Structure and Bonding 188
Series Editor: D.M.P. Mingos

D. Michael P. Mingos *Editor*

50th Anniversary of Electron Counting Paradigms for Polyhedral Molecules

Bonding in Clusters, Intermetallics and Intermetalloids

Springer

Structure and Bonding

Volume 188

Aims and Scope

Structure and Bonding is a publication which uniquely bridges the journal and book format. Organized into topical volumes, the series publishes in depth and critical reviews on all topics concerning structure and bonding. With over 50 years of history, the series has developed from covering theoretical methods for simple molecules to more complex systems.

Topics addressed in the series now include the design and engineering of molecular solids such as molecular machines, surfaces, two dimensional materials, metal clusters and supramolecular species based either on complementary hydrogen bonding networks or metal coordination centers in metal-organic framework materials (MOFs). Also of interest is the study of reaction coordinates of organometallic transformations and catalytic processes, and the electronic properties of metal ions involved in important biochemical enzymatic reactions.

Volumes on physical and spectroscopic techniques used to provide insights into structural and bonding problems, as well as experimental studies associated with the development of bonding models, reactivity pathways and rates of chemical processes are also relevant for the series.

Structure and Bonding is able to contribute to the challenges of communicating the enormous amount of data now produced in contemporary research by producing volumes which summarize important developments in selected areas of current interest and provide the conceptual framework necessary to use and interpret mega-databases.

We welcome proposals for volumes in the series within the scope mentioned above. Structure and Bonding offers our authors and readers:

- OnlineFirst publication. Each chapter is published online as it is finished, ahead of the print volume
- Wide dissemination. The chapters and the volume will be available on our platform SpringerLink, one of the largest collections of scholarly content in the world. SpringerLink attracts more than 50 million users at 15.000 institutions worldwide.
- Easy manuscript preparation. Authors do not have to spend their valuable time on the layout of their contribution. Springer will take care of all the layout related issues and will provide support throughout the complete process.

More information about this series at http://www.springer.com/series/430

D. Michael P. Mingos
Editor

50th Anniversary of Electron Counting Paradigms for Polyhedral Molecules

Bonding in Clusters, Intermetallics and Intermetalloids

With contributions by

S. Dehnen · T. F. Fässler · F. Gam · J.-F. Halet · S. Kahlal · W. Klein · Z. Lin · D. M. P. Mingos · F. Pan · J.-Y. Saillard · A. Schier · F. K. Sheong · J. Wei · B. Weinert · J.-X. Zhang

Springer

Editor
D. Michael P. Mingos
Chemistry Department
University of Oxford
Oxford, UK

ISSN 0081-5993 ISSN 1616-8550 (electronic)
Structure and Bonding
ISBN 978-3-030-84870-5 ISBN 978-3-030-84871-2 (eBook)
https://doi.org/10.1007/978-3-030-84871-2

This Springer imprint is published by the registered company Springer Nature Switzerland AG.
The registered company address is: Gewerbestrasse 11, 6330 Cham, Switzerland

Preface

2021 marks the 50th Anniversary of the publication by Ken Wade of "The structural significance of the number of skeletal bonding electron-pairs in carboranes, the higher boranes and borane anions, and various transition-metal carbonyl cluster compounds" in Chemical Communications. This paper played an important role in the subsequent growth of the main group and transition metal cluster chemistry and as it evolved into the related *isolobal* analogy it encouraged the appreciation of imaginative interconnections between the main group, transition metal and organic chemistry. The characterisation of increasingly large cluster molecules also led to the emergence of nano-chemistry and important connections to materials chemistry. It has been widely cited and the rules which resulted from this publication and related papers are described in most modern undergraduate inorganic textbooks. As the Series Editor of *Structure and Bonding* and someone who contributed to some of the developments, I thought it would be appropriate to publish a set of reviews that summarised and evaluated the influence of these generalisations on modern inorganic chemistry. I hope that the resulting volumes provide a better insight in how the origins and development of these ideas have evolved during the subsequent half-century. The resulting chapters not only celebrate these ideas but also indicate the limitations of the approach.

The first volume which is sub-titled "Historical and Recent Developments" opens with a chapter titled "Personal Historical Perspective on the Development of Electron Counting Rules for Boranes and Clusters and Ken Wade's Contribution". It gives a historical account of the experimental, spectroscopic and conceptual developments which provided an understanding of the bonding in boron hydrides and eventually led to the electron-counting approach summarised in Ken Wade's 1971 Chemical Communication. The chapter also summarises the subsequent papers which extended the applications of this approach in the 1970s and the early theoretical papers which began to provide an understanding of the theoretical concepts which were responsible for the rules which emerged.

A more general and robust theoretical framework was articulated in Anthony Stone's Tensor Surface Harmonic Theory published in the early 1980s. The chapter

"Introduction to Tensor Surface Harmonic Theory" provides an account of this theory and its subsequent applications. This molecular orbital model which was based on the development of the particle on a spherical surface problem was able to account not only for the electron counting generalisations, but also some of the exceptions which had been noted. Using frontier orbital concepts, it also provided a methodology for rationalising the polytopal rearrangements and reactivities of polyhedral molecules.

The influential contributions of Williams and Wade focussed primarily on deltahedral boranes and carboranes with 4–12 vertices. Sourav Kar and Sundargopal Ghosh's chapter "Polyhedra Beyond the Icosahedron" describes the synthesis of related polyhedral molecules with more than 12 vertices. This possible expansion of the field had been highlighted by theoretical studies from the 1970s but was not realised until the twenty-first century when significant experimental challenges had been overcome. Extensive research on supra-icosahedral borate dianions and their carbon and metal analogues has been reported in the last two decades and as a result, a significant number of supra-icosahedral clusters with 13–16 vertices have been characterised and studied. Before 2003, the absence of suitable precursors had limited progress in this important field. Modern synthetic methods and particularly the reduction-capitation methodology have resulted in the isolation of a significant number of novel supra-icosahedral clusters. For example, 15- and 16-vertex rhodium-based metallaboranes have been synthesised from the reactions of cyclopentadienyl metal halides with mono-borane reagents. The successful isolation of these large metallaboranes not only verifies earlier predictions of stable, large supra-icosahedral boranes clusters but has also resulted in a solid foundation for the subsequent expansion of supra-icosahedral borane chemistry.

Supra-icosahedral deltahedra with 14–16 vertices often adopt the Frank–Kasper deltahedra which have several degree 6 vertices. The theoretical implications of these novel structures are discussed by Alexandru Lupan, Amr Attia, Szabolcs Jákó, Attila-Zsolt Kun and Bruce King in the next chapter. This review discusses how transition metal atoms have the ability to utilise their d orbitals to stabilise deltahedra with higher degree vertices and describes how distortions from spherical *closo*-deltahedral geometries arise in such metalloboranes and metallocarbaboranes. This chapter also discusses the more substantial deviations from sphericality observed in the dirhenaboranes $Cp_2Re_2B_{n-2}H_{n-2}$ ($8 \leq n \leq 12$) which have oblate ellipsoidal structures. Specifically, they note that the rhenium atoms are antipodally situated at degree 6 or 7 vertices with relatively low local curvatures and the boron atoms are situated at degree 4 and 5 vertices with relatively high local curvatures.

Soon after the discovery of the icosahedral borane anion $[B_{12}H_{12}]^{2-}$ and the isoelectronic carborane $C_2B_{10}H_{12}$, it was realised that they exhibited aromatic-like properties. This led to the discovery of a wide range of substitution reactions and resulted in the incorporation of many substituents into these cage compounds. This opened up the possibility of developing families of compounds that matched those which had been developed previously for benzene and related aromatic organic molecules. Alan Welch's chapter "Bis(carboranes) and Related Species" discusses the syntheses, structures and reactivities of such compounds. The chemistries of these derivatives are reviewed with particular emphasis on 1,1′-bis(*ortho*-carborane).

Its reactivity is conveniently discussed with respect to the following: (a) as a κ^2-ligand with transition-metals; (b) 5-membered cyclic derivatives with non-metals; (c) deboronation-metalation chemistry and (d) reduction-metalation chemistry.

Catherine Housecroft's chapter "Borane and Carborane Clusters Meet Coordination Polymers and Networks: In the Hole or in the Backbone?" gives an overview of the different functions that borane and carbaborane clusters play in the assembly of coordination polymers and networks. The roles played by these polyhedral building blocks include "space fillers", rigid rods (linkers) and connecting nodes. The $[Co(C_2B_9H_{11})_2]$ metallocarborane provides a notable example of these clusters playing an important role as "space fillers". The templating effects of the spatially demanding polyhedral molecules are described. The ability of carbaborane clusters to act as scaffolds for the design of di-, tri- and tetra-topic multifunctional carboxylate linkers has proved to be particularly significant. These mimic arene-centred organic molecules are well established as linkers and connecting nodes in 2D- and 3D- metal-organic networks.

The second volume is sub-titled "Bonding in Clusters, Intermetallics and Intermetalloids" and begins with an introductory chapter titled "Electron Counting Rules for Gold Clusters Which Are Stereochemically Non-rigid and Exhibit Skeletal Isomerism". The electron counting methodology associated with the polyhedral skeletal electron pair theory (PSEPT) has proved to be particularly useful as an aide-memoire for teaching inorganic chemistry since it summarises economically a significant body of structural information. Its simplicity provided an easily applicable and reasonably reliable tool to enable synthetic chemists to target potential new clusters. A fundamental question remains however – "What do you do if the rules do not work?" This chapter provides an account of a methodology, which was developed when a significant group of gold cluster compounds was found not to comply with the rules. It also addresses the additional questions which arise when such compounds are stereochemically non-rigid either in the solid or in the solution state.

Jean-Yves Saillard, Jean-Francois Halet, Franck Gam, Jianyu Wei and Samia Kahlal's chapter "Electron Counting in Ligated High Nuclearity Late Transition Metal Clusters" develops this theme further by recounting the development of theoretical models for large ligated transition-metal clusters. The impressive synthetic and structural research which has led to the characterisation of these novel high nuclearity Group 10 and Group 11 metals have been accompanied by notable advances in the development of theoretical concepts, which have been assisted by major advances in computational techniques. The jellium model has proved to be particularly significant for chemists working in this area since it describes ligated noble metal nanoclusters as superatoms and supermolecules in a way that resonates with well-established chemical thinking. This review develops the basic theory and illustrates its applications for specific spherical and non-spherical ligand-protected nanoclusters containing platinum and coinage metals.

The extension of the electron counting rules to Zintl/Klemm polyhedral anions and cations of the main group elements marked a particularly significant development in the 1970s and in recent years research into these compounds has proved to be one of the most exciting areas of cluster chemistry. The chapter by Fuxing Pan, Bastian Weinert and Stefanie Dehnen titled "Binary Zintl Anions Involving Group

13–15 (Semi-) Metal Atoms, and the Relationship of Their Structures to Electron Count" provides a broad account of general developments in this field. They note that binary molecular Zintl anions based on either two different p-block atoms or combinations of p- and d-block atoms not only exhibit exceptional cage architectures, but they are important starting compounds for materials chemistry. Many of the structures can be satisfactorily described using structure-electron counting relationships, but there are also a significant number of exceptions. This review provides a comprehensive collection of representative examples and comments on their respective bonding patterns.

Wilhelm Klein, Annette Schier and Thomas Fässler's chapter "Molecules Meet Solids: From Wade-Mingos Clusters to Intermetalloid Clusters" develops this theme in the next chapter. They note that the atomic and electronic structures of Zintl/Klemm clusters place them right at the interface between that of molecules and the extended bulk state. As a result of these studies, a series of compounds – ranging from bare homoatomic Zintl clusters, through endohedral filled ones to examples of complex polyanions comprising metal atoms with high coordination numbers has been characterised which define the transition from molecules to intermetallic compounds. The examples also mark the transition in chemical bonding from molecular orbital theory to band structure calculations of extended solid and this has led to their description as inter-metalloid clusters.

Jing-Xuan Zhang, Fu Kit Sheong and Zhenyang Lin's chapter titled "Structure and Bonding of Group 14 Clusters: Wade's Rules and Beyond" discusses in more detail the complexities of the bonding in Group 14 clusters. These clusters bear many similarities to the borane clusters and have inspired chemists to understand their structure and bonding based on Wade's original electron counting proposals. The discovery of many new compounds in this area in recent years has revealed many challenges for structural and theoretical chemists. In this chapter, the authors discuss the structure and bonding for a wide variety of Group 14 clusters, including bare clusters, substituent decorated clusters, endohedral clusters, transition metal-doped clusters, and their mixtures. Analysing their electronic structures within the framework of molecular orbital theory has helped chemists appreciate their distinctive features and define new generalisations.

I shall be retiring as Series Editor of *Structure and Bonding* this year after 20 years in the post and I should like to thank not only those authors who have contributed to this volume but the volume editors and authors of the 87 volumes which have been published during my tenure. I should also like to express my sincere thanks to the senior editors, Marion Hertel, Elizabeth Hawkins, Judith Hinterberg and Charlotte Hollingworth along with the supporting editorial staff at Springer who have helped me and all the contributors in producing chapters that have a very professional appearance and are more easily appreciated by the reader because of their superior editorial skills and great attention to detail.

Oxford, UK D. Michael P. Mingos
July 2021

Contents

Struct Bond (2021) 188: 1–68
https://doi.org/10.1007/430_2021_87

Published online: 24 July 2021

Electron Counting Rules for Gold Clusters Which Are Stereochemically Non-rigid and Exhibit Skeletal Isomerism

D. Michael P. Mingos

Contents

Abstract The valence shell electron pair repulsion theory (VSEPR) added a three-dimensional interpretation of simple molecular inorganic compounds by proposing that bonds and lone pairs are both stereochemically active and together define a characteristic co-ordination polyhedron. The polyhedral skeletal electron pair theory (PSEPT) developed an analogous relationship for borane and metal carbonyl polyhedral molecules which is based on the total number of skeletal valence electrons in related *closo*-, *nido*- and *arachno*- deltahedral molecules. The historical development of the ideas which led to the PSEPT has been described in the Introductory

D. M. P. Mingos (✉)
Inorganic Chemistry Laboratory, Oxford University, Oxford, UK
e-mail: Michael.mingos@seh.ox.ac.uk

Chapter of Volume 1. The electron counting rules associated with this generalisation have proved to be useful as aide-memoire for teaching inorganic chemistry since they bring together a large body of structural information for polyhedral molecules. Their simplicity provided an easily applicable, but reasonably reliable, indicator for identifying potential new targets for synthetic chemists. The fundamental question remains – "What do you do if the rules do not work?". This chapter provides an account of the steps taken when a significant group of cluster compounds were found not to comply with the rules. The gold clusters discussed in this chapter were recognised as such a group in the 1970s, but they did not follow the pattern which had been recognised earlier for polyhedral boranes and transition metal carbonyl clusters. Furthermore, as their structures were revealed by X-ray crystallography it became apparent that they provided many examples of skeletal isomerism, i.e. more than one skeletal geometry was observed for seemingly isoelectronic molecules. In addition, spectroscopic studies showed that many of the clusters were stereochemically non-rigid especially in solution. The challenge of bringing these gold clusters within the scope of PSEPT when they do not share the same structures and electron counts as metal carbonyl clusters have multiple structures and are frequently stereochemically non-rigid was not trivial. Most importantly it was not sufficient to just tinker with the numerological aspects of PSEPT but a re-examination of the fundamental quantum mechanical assumptions underlying PSEPT and reformulating it in the new context.

Keywords Boranes · Zintl ions · Carbonyl clusters · Deltahedra · *closo-* · *nido-* *arachno* · Electron counting rules · Three-centre bonds · Capping principle skeletal isomers · Skeletal rearrangements

Abbreviations

CD	Circular dichromism
CNCs	Chiral nano-metre clusters
CPL	Circular polarised luminescence
dppe	Diphenylphosphinoethane
dppp	Diphenylphosphinopropane
HOMO	Highest occupied molecular orbital
HPLC	High-performance liquid chromatography
LUMO	Lowest unoccupied molecular orbital
mos	Molecular orbitals
NCs	Nanoclusters
PSEPT	Polyhedral skeletal electron pair theory
sec	Skeletal electron count
Tol	tolyl
VCD	Vibrational circular dichroism
VSEPR	Valence shell electron pair theory

1 Introduction

1.1 Are Clusters Stereochemically Rigid?

Technical and computational developments in the last 50 years have reduced the time and effort required to solve the structures of cluster compounds in the solid state [1, 2]. Solving the structure of a gold phosphine cluster compound in 1970 required several weeks to collect the data and solve the structure but in 2021 the structures of large clusters are determined on smaller crystals using automated algorithms in a matter of days. The structures of clusters with more than 100 metal atoms are regularly reported. Synchrotron X-ray sources and the use of programmes and techniques which were developed initially for protein structures have made the characterisation of these nano-sized clusters accessible if not completely routine. The excitement of seeing a three-dimensional representation of the cluster molecule for the first time is palpable. The pictorial representations which show the structure as spherical balls connected by rods intuitively suggest a very strong and rather rigid structure. When the observed structure can also be rationalised using simple electron counting formalisms then one can easily fall into a mindset which assumes that this structure represents a unique and very stable geometry [3–5]. It is appropriate at times to remind oneself that these single X-ray structural determinations do not provide any direct experimental information or even an indication as to whether the structure is stereochemically rigid in the solid state or in solution. If it is indeed stereochemically non-rigid, then further measurements are required to define the magnitude of the activation energies of the fluxional processes and provide evidence to support a specific mechanism for the polytopal rearrangement process. Further spectroscopic measurements are required both in the solid state and solution to resolve whether the fluxional state observed in solution persists in the solid state. It is also important to determine whether the stereochemical non-rigidity involves migratory process involving the ligands moving across the surface of the metal cluster, or rearrangements of the metal skeleton which may require the ligands to retain their links to the metals. Simultaneous rearrangements of the ligands and the metal skeleton represent a third possibility. For carbonyl and hydrido-clusters the activation energies for interconverting terminal and bridging carbonyls are generally quite small and these ligands frequently migrate over the surface of the cluster rapidly at room temperature. Hydrido-ligands have also been observed to migrate from the surface to interstitial sites within the cluster. In contrast phosphine ligands generally remain anchored to the metal atom and do not migrate readily over the surface of the cluster. These molecular processes are most effectively studied using spectroscopic techniques. N.M.R. experiments are particularly helpful for defining the permutation of nuclei in these rearrangement processes. Kinetic and mechanistic information has been obtained primarily for those clusters which have nuclei with nuclear isotopes which may be readily interrogated using N.M.R. techniques. X-ray crystal structural analyses may provide some circumstantial evidence for stereochemical non-rigidity of the metal skeleton. The temperature factors provide

evidence concerning the mean amplitudes of vibrations of atoms although they may also reflect disorder within the crystalline state. A cluster compound may crystallise in more than one crystalline modification. If the metal skeletal geometries differ significantly and the two forms interchange in solution, it suggests that the potential energy surface for the interconversion of the alternative skeletal geometries might be sufficiently soft to permit the occurrence of rearrangement processes in solution.

2 Gold Clusters [3, 4]

Chapter I of Volume I described how the theories which were developed in the early 1970s led to a better understanding of the electronic factors which influenced the geometries of main group and transition metal cluster compounds [5]. It established for the first-time general relationships between the observed geometry and total number of valence electrons [6–8]. These electron counting rules did not apply to all polyhedral compounds of the transition metals and worked best for the carbonyl clusters of the metals in Groups 6–9. It became apparent that the local symmetries of the individual metal fragments also played an important role in underpinning the relationships between main group and transition metal fragments. Specifically, pyramidal $M(CO)_3$ fragments were more reliable replacements for B–H and C–H fragments than the less symmetric $M(CO)_4$ and $M(CO)_2$ fragments [9–12] and we studied these differences using both theoretical and experimental studies. The clusters of the coinage metals were less obvious rule breakers since they were based on axially symmetric M-PPh_3 (M = Cu, Ag and Au) fragments. In 1976 I started working at Oxford University on the synthesis of gold cluster compounds and the research was funded by Imperial Chemical Industries (ICI) and the studentship was taken up by Brian Theobald. The research project suggested the possibility of synthesising cluster compounds containing metals from opposite ends of the transition metal series and studying their catalytic properties. Malatesta's group in Milan had reported the first examples of gold cluster compounds [13–16] stabilised by phosphine ligands in the late 1960s and the structures of $[Au_{11}(PPh_3)_7(SCN)_3]$ and $[Au_9(PTol_3)_8](PF_6)_3$ had been solved by the Milan group [17–20] and Ron Mason (helped by research student Mary McPartlin) in Sheffield [21]. They were the first examples of high-nuclearity metal clusters with interstitial metal atoms and their skeletal geometries are illustrated in Fig. 1. The structures were interpreted in terms of modifications of a putative regular centred icosahedron ($Au_{13}L_{12}$). $[Au_9(Ptol_3)_8]^{3+}$ [21] was described as an icosahedron with two pairs of *trans*-gold atoms removed and $[Au_{11}(PPh_3)_7(SCN)_3]$ was related to the icosahedron by the replacement of a triangle of gold atoms by a single gold atom [15, 17, 18]. This limited number of examples did not reproduce the *closo*-, *nido*- and *arachno*-relationships for metal clusters first described by Wade in 1971 [6] and their total valence electron counts did not follow the pattern which was beginning to emerge for the metal carbonyl clusters of the earlier metals [6, 7].

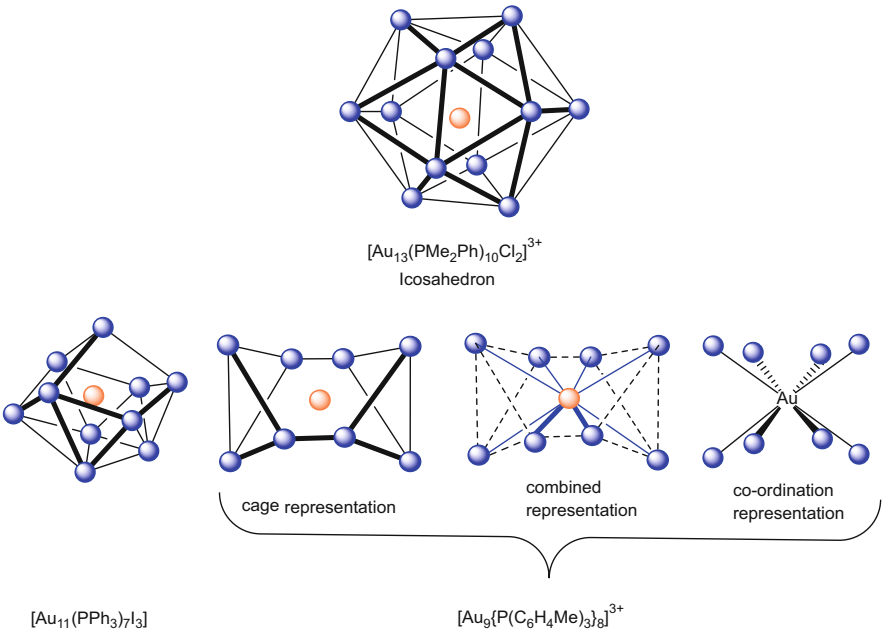

Fig. 1 Structures of the high nuclearity clusters synthesised by Malatesta and structurally characterised by Mason and Albano [20, 21] and their relationship to the icosahedral cluster synthesised later [22]. The interstitial gold atom is coloured differently

In these early publications there were discussions as to whether these compounds were best described as cages, representing fragments of a metallic structure, or as co-ordination compounds with 8 or 10 Au-L "ligands" bonded to the central gold atom. These limiting alternative representations are illustrated in Fig. 1 for $[Au_9(PTol_3)_8]^{3+}$ together with a hybrid representation. They were described sometimes as "porcupine clusters" to indicate this ambiguity [23]. The experimental metrics suggested that the combined structure is the more appropriate because both types of bonds (radial and surface) fall in the range anticipated for gold–gold bonds. The surface Au-Au lengths are somewhat longer than the radial Au-Au bonds [18, 21, 23]. The radial bonds of Malatesta's gold cluster compounds lay between 2.62 and 2.72 Å whereas the surface bond lengths varied from 2.80 to 3.10 Å. In metallic gold the Au-Au distance is 2.884 Å. The radial bonds of Malatesta's gold cluster compounds lay between 2.62 and 2.72 Å whereas the surface bond lengths varied from 2.80 to 3.10 Å. This is indicated in Fig. 1 by the use of continuous lines for radial and dotted lines for surface bonds. The initial bonding descriptions noted that the co-ordination description led to 18 and 16 electron configurations for the central gold atom which were well established in octahedral and square-planar complexes of the transition metals [21]. These unresolved bonding issues prompted me to extend the molecular orbital methodology we had developed for carbonyl clusters to see if we could understand the exceptional behaviour of gold clusters [24–26].

All of Malatesta's cluster compounds were made by the reduction of gold(I) phosphine complexes $[Au(PR_3)X]$ with sodium borohydride [13–20]. To further the aims of Brian Theobald's Ph.D. project we studied the reaction of gold(I) phosphine complexes with $[Ti(\eta\text{-}C_6H_6)_2]$, which was not a commercially available reagent, but was routinely synthesised in Malcolm Green's laboratory by Geoff Cloke using metal vapour synthesis techniques [22]. In our hands it did not result in the isolation of stable titanium-gold cluster compounds but it proved to be an effective reducing agent which resulted after work-up in the isolation of crystals of $[Au_{13}Cl_2(PMe_2Ph)_{10}][PF_6]_3$. The phosphine was chosen to have a smaller cone angle than PPh_3 in order to encourage the formation of higher nuclearity clusters and the importance of the steric requirements of the ligands led us subsequently to define a cluster cone angle [27, 28] based on Tolman's cone angle. The structure of $[Au_{13}Cl_2(PMe_2Ph)_{10}][PF_6]_3$ proved to be difficult to solve, because it had some critical disorder problems associated with the counterions which were overcome by Alan Welch. He solved the structure and established the presence of three counter-anions. The structure provided the first example of an icosahedral metal cluster with the geometry illustrated in Fig. 1. In common with other centred cluster compounds the radial Au–Au bonds are shorter 2.716(2)–2.789(2) Å than the peripheral Au–Au bonds 2.852(2)–2.949(3) Å. The spread of bond lengths indicated significant distortions away from the idealised icosahedral geometry and were attributed to the steric constraints imposed by the bulky phosphine ligands. The solution of this structure confirmed an earlier theoretical prediction we had made in 1976 [25] that 13 atom centred gold clusters, $[Au_{13}L_{12}]$, would have an icosahedral geometry and be associated with a 5+ charge (i.e. 160 valence electrons). I think that this represented the first example of a sizeable cluster compound being predicted and subsequently successfully synthesised and characterised [22, 25].

Taken together with the structures reported by Malatesta's group these gold clusters clearly did not follow the patterns proposed by Wade based on analogies with borane polyhedral molecules. The theoretical analysis we had published in 1976 provided an understanding of the bonding in these gold clusters [25] and explained the reasons for their aberrant behaviour. In subsequent years salts of the related ions $[Au_{13}X_4(PMe_2Ph)_8]^+$ (X = Cl, Br , I or SCN), $[Au_{13}Br_3(PMe_2Ph)_9]^{2+}$ and $[Au_{13}(SCN)_5(PMe_2Ph)_7]$ were synthesised. The icosahedral gold cluster compound was subsequently also synthesised by the photolysis of $[Au(N_3)(PMe_2Ph)]$ and also by the addition $[AuCl(PMe_2Ph)]$ to $[Au_{11}(PMe_2Ph)_{10}][PF_6]_3$, which has a bicapped square-antiprismatic skeletal geometry and this route was subsequently extended to synthesise mixed icosahedral cluster compounds containing silver and copper [3, 4]. These examples emphasised the importance of steric effects associated with the ligands and the cluster cone angle we had proposed provided a useful parameter for defining these effects [27, 28].

In the 1980s and 1990s the synthetic routes to gold cluster compounds were expanded and a large number of structures were reported by Steggerda's group in Nijmegen, Holland [29–41] and by the Oxford group [42–51]. From the turn of the century Konishi's group in Japan has contributed significantly to the range of such compounds [52–61]. Malatesta and Steggarda had recognised that bidentate

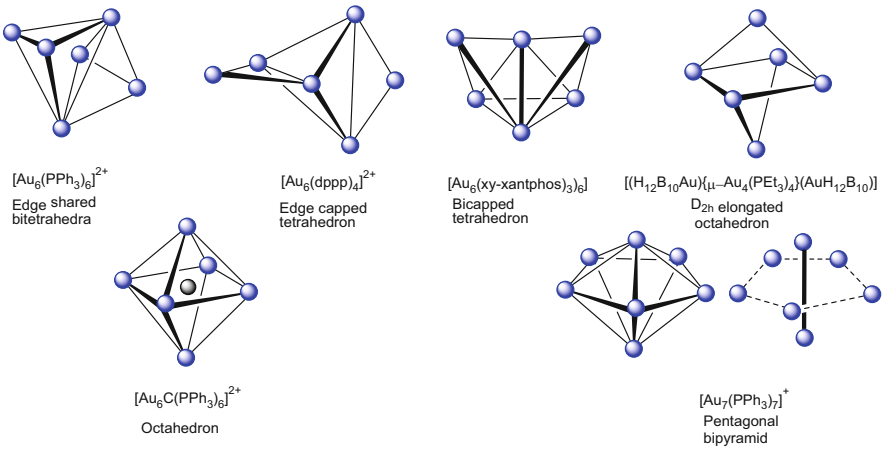

Fig. 2 Examples of gold phosphine clusters with six and seven gold atoms [19, 38, 47]

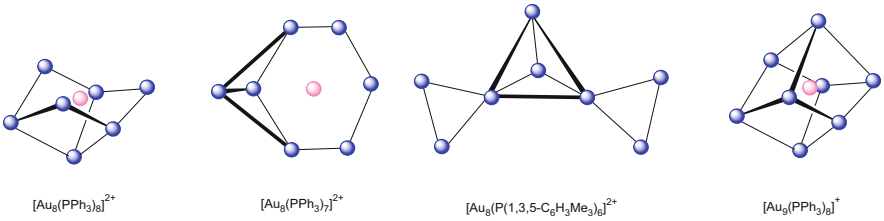

Fig. 3 Examples of gold phosphine clusters with eight gold atoms [30–32, 38, 41, 58]

phosphine ligands added extra rigidity and stability to gold clusters and Konishi has subsequently made a major contribution by his systematic studies based on the dppe and dppp ligands [52–61]. The structures of gold phosphine clusters which resulted from these studies are summarised and illustrated in Figs. 2, 3, 4, and 5 and organised according to the number of metal atoms. The examples are illustrative, rather than comprehensive, and the results reinforced the view that these clusters followed a very different pattern from those reported for the carbonyl clusters of the earlier transition metals. Specifically, there are numerous structures which are not based on deltahedra and very open structures are more common. The latter are not simply related by the *closo-*, *nido-* and *arachno-* deletions which had become familiar for carbonyl clusters and boranes.

In the early 1980s it became apparent that minor changes in the phosphine ligands could result in large changes in the skeletal geometry and suggested that a soft potential energy surface may connect alternative skeletal geometries for the gold clusters which did not have high symmetries and near spherical geometries. For example, $[Au_9\{P(C_6H_4OMe)_3\}_8](BF_4)_3$ was a minor variant of Malatesta's cluster shown in Fig. 1 with a distant replacement of Me by OMe but resulted in the isolation of crystals of a cluster with a very different skeletal geometry

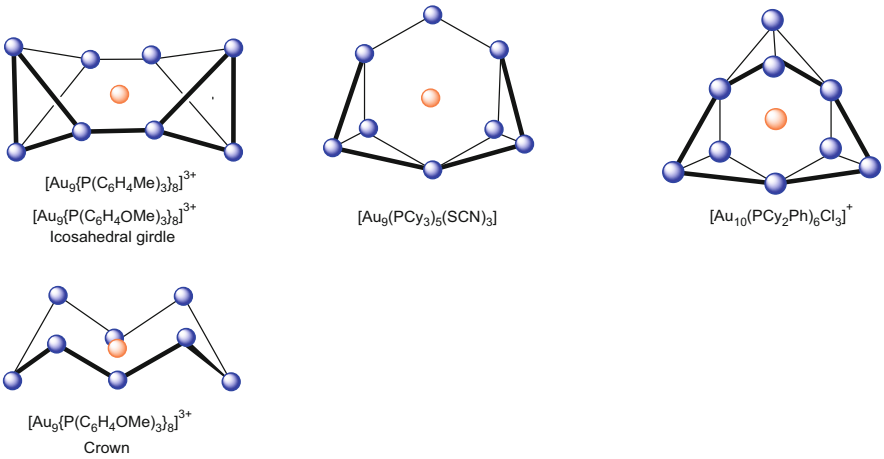

Fig. 4 Examples of gold clusters with nine gold atoms [21, 31, 35, 40, 41, 44]

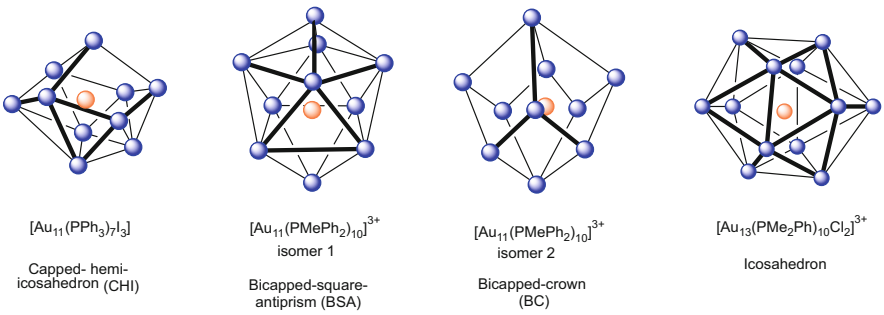

Fig. 5 Examples of clusters with 11 and 13 metal atoms [15, 17, 18, 22, 36, 37, 41, 43, 50, 53, 58, 59]

[44, 45]. Figure 4 illustrates the alternative geometries and shows it has an octagonal ring of gold atoms rather than being a fragment of an icosahedron. It is noteworthy that the crown geometry is related to a squashed square-antiprism but has longer Au–Au distances in the square planes. Later Kevin Hall, in a manner which Pasteur would have appreciated, manually separated two crystalline modifications of $[Au_9\{P(C_6H_4OMe)_3\}_8](NO_3)_3$ from the same solution and structural determinations of the two polymorphs exhibited the alternative skeletal geometries illustrated in Fig. 4. This separation was simplified because the two isomers have different colours, i.e. green and brown. A third geometry for these gold clusters was subsequently reported for $[Au_9\{PCy_3)_5(SCN)_3]$ and is also illustrated on the right-hand side of Fig. 4. This cluster is closely related to that observed for $[Au_{10}(PCy_2Ph)_6Cl_3]$ and both have a central hexagonal ring but the former has two and the latter three bridging gold atoms.

The structures of several gold clusters with 11 atoms have been reported and they fall into two major classes. $[Au_{11}\{P(C_6H_4F)_3\}_7I_3]$, $[Au_{11}\{P(C_6H_4Cl)_3\}_7I_3]$, $[Au_{11}\{P(C_6H_5)_3\}_7I_3]$, $[Au_{11}\{PPh_3\}_7(CNi\text{-}Pr)_2I]$ and $[Au_{11}(dppp))_5I_3]$ all share a skeletal structure based on an icosahedron with a triangle replaced by a single atom as shown in Fig. 5 (Capped-hemi-icosahedron). The importance of capping atoms in cluster chemistry had been recognised in 1973 [62] and amplified in later publications [63, 64]. With the smaller phosphine ligand $PMePh_2$ and the carborane $C_2B_9H_{11}^-$ as a counter anion two crystalline modifications were isolated and their geometries may be described either as a bicapped square-antiprism (isomer 1) or a bicapped octagonal ring (isomer 2) (see Fig. 5). In contrast the centred gold clusters with 13 gold atoms do not show inclinations to form skeletal isomers and all known examples have icosahedral geometries. The alternative cuboctahedral geometry which Lipscomb suggested may act as an intermediate in the rearrangements of icosahedral boranes and carboranes $[B_{12}H_{12}]^{2-}$ and $[C_2B_{10}H_{12}]$ has not been observed for phosphine clusters. Cuboctahedral clusters have been observed in larger poly-spherical gold thiolato-clusters and the geometries of these related clusters have been discussed in detail elsewhere [65–67].

Gold clusters stabilised by thiolato-ligands rather than phosphines have attracted considerable interest recently because of their potential applications in the area of nano-technology [3, 4, 65–67]. The rapid growth of the area has been stimulated by the development of a flexible general synthetic route which has led to the isolation of a number of crystalline solids and single crystal X-ray diffraction studies on some key compounds. The crystallographic determinations of $[Au_{102}(SC_6H_4CO_2H)_{44}]$ and $[Au_{25}(SC_2H_4Ph)_{18}]^-$ proved to be pivotal in developing an understanding of the important structural features. Specifically they established that there is a central core of gold atoms, which is approximately spherical and close packed, and is stabilised by an outer layer of either SR or organothiolato-gold(I) ligands, e.g. SR, $[Au(SR)_2]^-$ and $[Au_2(SR)_3]^-$. These gold-thiolato-ligands have been described as "staples" because they are considered to be essential for stabilising the gold core. Reviews in Refs. [3] and [4] give more comprehensive accounts of the developments in this related and rapidly expanding field [65–67].

The presence of interstitial atoms is not limited to these higher nuclearity clusters and there are examples of smaller clusters which encapsulate atoms, but since the central cavity is smaller in these clusters only atoms with smaller radii are accommodated. Figure 2 illustrates $[Au_6C(PPh_3)_6]^{2+}$ which has an octahedral gold cluster with a central carbon atom and therefore resembles $[Ru_6C(CO)_{17}]$. They are not isoelectronic since the former has 80 valence electrons and the latter has 86. The interstitial carbido-ligand in $[Au_6C(PTol_3)_6]^{2+}$ was initially not detected in the structure and it was formulated initially as $[Au_6(PTol_3)_6]^{2+}$, but molecular orbital calculations reported in 1976 suggested that such a molecule would be paramagnetic and suggested that it may actually be the carbido-cluster $[Au_6C(PR_3)_6]^{2+}$ [25]. Schmidbaur et al. developed a rational synthesis for the closely related compound $[Au_6C(PPh_3)_6]^{2+}$ a decade later and reformulated the earlier $PTol_3$ compound [19, 63]. Analogous compounds with other main group interstitial atoms were subsequently reported by his group [68–70].

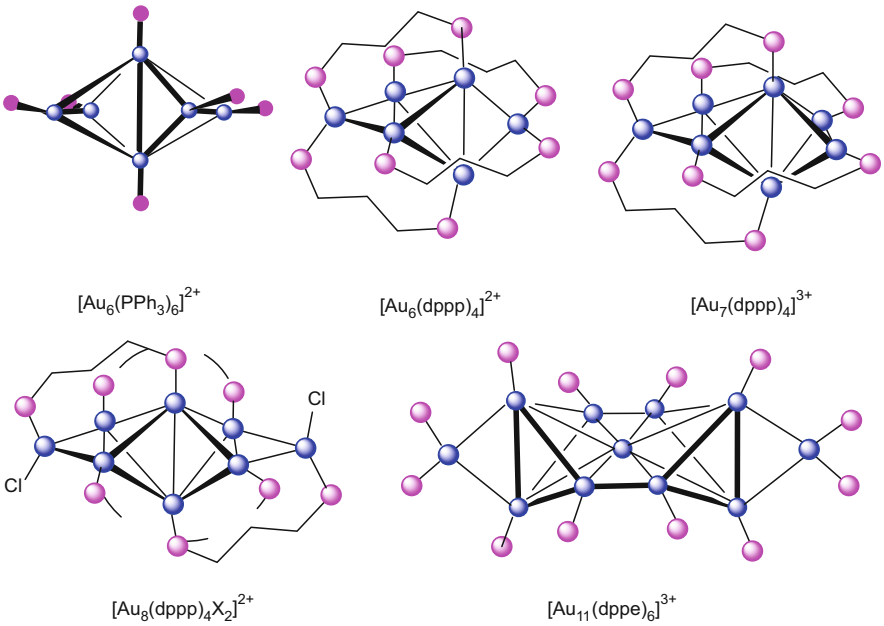

Fig. 6 Transformation of the geometries of Au_n clusters induced by introducing the bidentate phosphine dppp or dppe [16, 29, 51–53, 55]. The phosphorus atoms are shown in magenta and the gold atoms in blue

This emphasises once more that the gold cluster compounds constitute a separate class which did not adhere to the electron counting rules developed for metal carbonyls and boranes. Figures 2, 3, 4, and 5 show that these gold clusters do not have one characteristic geometry and small changes in the electronic and steric properties of the ligands give rise to alternative skeletal geometries. This variability suggested that the potential energy surface connecting the alternative geometries may be quite soft.

Another important difference between these clusters and the carbonyl clusters is that the geometry of gold clusters may be altered by introducing bidentate phosphine ligands. Konishi [52–61] has made a systematic study of gold clusters stabilised by bidentate phosphines and particularly dppp and some examples are illustrated in Fig. 6 and compared with $[Au_6(PPh_3)_6]^{2+}$. Specifically, dppp has just the correct bite angles to bridge three atom metal sequences [34, 52–61]. Replacing monodentate phosphine ligands with such ligands not only increases the gold coordination numbers for the peripheral gold atoms, but also initiates a change of skeletal geometry from two tetrahedra sharing an edge to a tetrahedron with two bridged edges. The two compounds are contrasted in Fig. 6. The coordination chemistry of gold(I) complexes is dominated by linear (14 electron) complexes, e.g. $[Au(CN)_2]^-$ and $[Au(PPh_3)_2]^+$, but trigonal and tetrahedral (16 and 18 electron) centres are

introduced when dppp is introduced. These *exo*- gold atoms bridge edges of the tetrahedral core [61].

Konishi has demonstrated that these clusters have unique spectral properties. The gold clusters with [core+*exo*]-type geometries (nuclearity = 6, 7, 8, and 11) commonly displayed characteristic single absorption bands in the visible region, which are absent in PR_3 analogues. Theoretical studies demonstrated that the HOMO and LUMO were shown to be localised around the polyhedral cores and the *exo*- gold atoms, respectively. Therefore, the HOMO–LUMO transitions responsible for the visible absorptions occur in the core → *exo* direction which is consistent with the *capping principle* [62–64]. The HOMO–LUMO gap energies showed no clear trends with respect to the nuclearity (size), indicating that the individual geometric features of the inorganic framework primarily govern the clusters' electronic structures and spectral properties. Structurally, they generally have a tetrahedral Au_4 or bitetrahedral Au_6 core with one or two *exo*-gold atoms (see Fig. 6). On the other hand, the use of bis(diphenylphosphino)ethane (dppe) resulted in the formation of a higher-nuclearity [core+*exo*]-type cluster, $[Au_{11}(dppe)_6]^{3+}$, which is composed of a butterfly-shaped Au_9 core and two *exo* gold atoms ([Au_9+2Au]-type). Steggerda and Konishi have also used bidentate phosphines to stabilise icosahedral gold clusters [29, 52].

A general characteristic of boranes and metal carbonyl clusters is that addition of electron pairs, either electrochemically or by ligand addition, results in an opening up of the skeleton of the cluster. For the boranes this is manifested in the *closo*-, *nido*- and *arachno*- triads $[B_nH_n]^{2-}$, $[B_nH_n]^{4-}$, $[B_nH_n]^{6-}$ and for the 3-connected polyhedral molecules more specific bond breakage processes result [6–8]. In contrast gold, platinum and related heteronuclear clusters adopt more compact structures when additional electron pairs are introduced. Some specific examples of this alternative behaviour are illustrated in Fig. 7 [6, 8, 42]. In the first example reduction of the gold cluster leads to a spherical cubic structure and in the second example the CO ligand co-ordinates to the interstitial platinum and although the **sec** (skeletal electron count) stays the same the geometry becomes hemi-spherical. This is discussed more fully in Sect. 5.

3 $^{31}P\{^1H\}$ N.M.R. Studies in Solution and the Solid State

3.1 Solution Studies [34–42, 50, 51]

Although the common isotopes of gold do not provide a basis for studying directly the geometries of gold clusters in solution and the solid state using N.M.R. techniques the $^{31}P\{^1H\}$ N.M.R. spectra of the phosphine ligands attached to the clusters have provided important circumstantial evidence concerning the fluxional behaviour of these clusters in the solution and solid states. The observed spectra in solution are simpler than that anticipated from the solid state crystal structure and suggested that the majority of $[Au_x(PR_3)_x]^{m+}$ and $[Au_{x+1}(PR_3)_x]^{m+}$

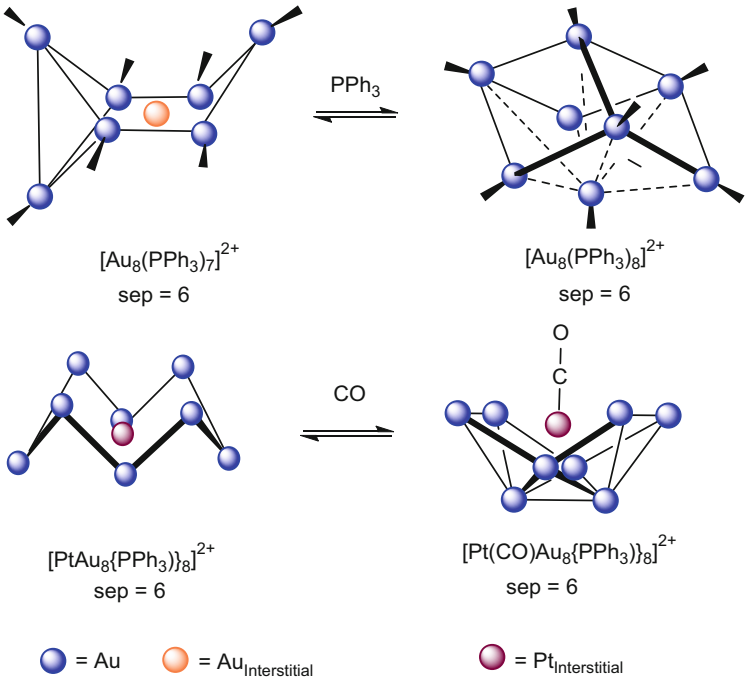

Fig. 7 Examples of reduction and ligand addition to gold clusters. In both examples the clusters become more spherical as a result of the increase in the total number of electrons [40]

clusters are stereochemically non-rigid in solution even at low temperatures and the $^{31}P\{^{1}H\}$ N.M.R. spectra frequently show only a single average resonance. In the solid state, magic angle techniques have been used to obtain reasonable high-resolution spectra with linewidths approximately 300 Hz and have proved more helpful for defining the solid-state structures. $^{31}P\{^{1}H\}$ N.M.R. studies provide more robust information when the cluster contains interstitial platinum or rhodium which are helpful for confirming the occurrence of intramolecular rearrangements. The presence of silver nuclei on the surface of the cluster may also provide additional information concerning which atoms are rearranging on the N.M.R. timescale.

The solution $^{31}P\{^{1}H\}$ N.M.R. of the uncentred and lower nuclearity clusters $[Au_6(dppp)_4]^{2+}$ [34] and $[Au_6(PPh_3)_6]^{2+}$ provide structural data consistent with the X-ray crystallographic analysis. The Nijmegen group was the first to recognise that polydentate phosphine ligands increase the rigidity of gold clusters and thereby obtain more accessible structural data. In recent years Konishi has exploited this property most effectively to expand the range of gold clusters [52–61]. The spectrum of $[Au_6(dppp)_4]^{2+}$ shows two quintets of equal intensity which is consistent with the solid-state structure shown in Fig. 6. The low temperature solution spectrum ($-90°C$) of $[Au_6(PPh_3)_6]^{2+}$ is consistent with the observed solid-state structure, i.e. the edge shared bitetrahedron shown in Fig. 6 [34, 47]. The low-temperature spectrum at $-40°C$ shows two singlets in the ratio of 2:4 but the P-P coupling pattern

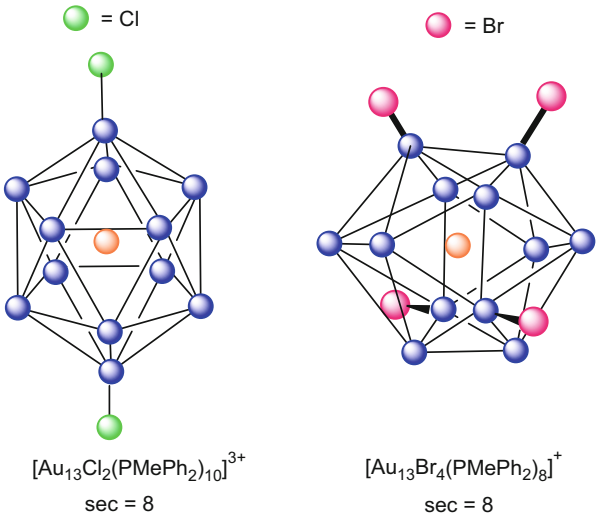

Fig. 8 Location of halide ions in icosahedral gold clusters based on the icosahedron. The structures are consistent with the $^{31}P\{^1H\}$ N.M.R. spectra in solution

was not resolved. As the temperature is raised the spectrum coalesces and at room temperature only a single resonance is observed. An intermolecular skeletal rearrangement has been proposed to account for the observed spectral changes and a bicapped tetrahedron was suggested as the possible transition state. The $[Au_7(PPh_3)_7]OH$ cluster [39] has the pentagonal bipyramidal geometry shown in Fig. 2 which resembles those observed for $[B_7H_7]^{2-}$ and $[C_2B_5H_7]$ but has a more compressed oblate structure because the apical gold atoms form a strong bond. Indeed this is the shortest Au–Au bond 2.584(4) Å, and is significantly shorter than the surface bonds (average Au_{axial}–Au_{equat} 2.82(8) Å ; Au_{equat}–Au_{equat} 2.95 (6) Å). It could also be described as an Au_2 dimer acting as a spindle to a planar pentagon of more weakly held gold atoms. The solution $^{31}P\{^1H\}$ N.M.R. spectrum at room temperature shows only a single resonance suggesting a fluxional process which interchanges the equatorial and axial gold atoms at a fast rate on the N.M.R. timescale [39].

The icosahedral $[Au_{13}Br_4(PMePh_2)_8]Br$ is stereochemically rigid in solution at room temperature [22, 51]. The solution spectrum has three resonances which is consistent with the isomer shown in Fig. 8. Three different phosphorus environments in the ratio 4:2:2. Despite some overlapping three resonances with similar chemical shifts to those noted in solution are observed. The icosahedral cluster $[Au_{13}Cl_2(PMePh_2)_{10}]PF_6\}_3$ shows a single phosphorus environment which is consistent with the solid state structure shown in Fig. 8. In this case there is no evidence for stereochemical non-rigidity.

The solution $^{31}P\{^1H\}$ N.M.R. spectra of the icosahedral $[Au_{13}X_4(PMe_2Ph)_8]Y$, (X = Br, I, SCN; Y = Br, I, SCN, PF_6, BPh_4) and $[Au_{13}Cl_2(PMe_2Ph)_{10}][PF_6]_3$ are consistent with isomeric structures shown in Fig. 8 [51]. All structures are based on an icosahedron with the total number of co-ordinated phosphines and halides bonded to the 12 surface gold atoms. In the first a singlet and two triplets of relative intensity

4:2:2 are observed and in the latter shows three lines of equal intensity. The ^{1}H N.M.R. spectra are also consistent with proposed structures. These observations suggest that the energy barriers separating the alternative isomeric possibilities for these clusters are sufficiently large that they are not fluxional at ambient temperatures. The energy barriers separating the alternative isomeric possibilities for the icosahedron are larger than those for other gold clusters without interstitial atoms [50].

The spectrum of $[Au_{11}(PAr_3)_7(SCN)_3]$ (Ar = *p*-C_6H_4Cl) showed only a single resonance even when the temperature was reduced to −90°C. When PPh_3 is added to a solution of $[Au_{11}(PAr_3)_7(SCN)_3]$ no exchange between free and co-ordinated phosphine was detected and similar results were obtained for other high nuclearity gold clusters. These results suggest that the four different ^{31}P environments predicted from the ground state structure shown in Fig. 4 (capped-hemi-icosahedron with C_{3v} symmetry) are exchanging rapidly on the N.M.R. timescale, but technically there are other possible interpretations, e.g. fortuitous accidental degenerate chemical shifts [31, 36, 37]. The phosphine/glutathione ligand exchange processes in these clusters have also been studied in detail [71]. The synthesis of $[Au_{11}(MePh_2)_{10}]\{C_2B_9H_{12}\}_3$ has resulted in two isomers crystallised both of which have structures based on a centred bicapped square-antiprisms or a bicapped crown (BSA and BC) rather than the C_{3v} geometry described above (see Fig. 5). The solution $^{31}P\{^{1}H\}$ N.M.R. spectrum of the isomers both show identical sharp singlets even at low temperatures [50]. The BSA and BC structures are anticipated to have spectra based on peaks in the ratio of 2:8 and suggesting the occurrence of an intramolecular skeletal rearrangement. A detailed analysis of the structures of the isomers lies on the least motion pathway between an idealised BSA and BC geometries and the C_{3v}structure and suggests a soft potential energy surface [50]. The marked difference in the room temperature solution and solid-state spectra has been attributed to faster intermolecular rearrangement processes in solution. $[Au_9\{P(C_6H_4OMe)_3\}_8](NO_3)_2$ also crystallises as two polymorphic isomers whose structures are illustrated in Fig. 4. They show identical $^{31}P\{^{1}H\}$ N.M.R. spectra and suggest that the two isomers interconvert rapidly in solution. Specifically, when the temperature is lowered the singlet does not broaden and separate into distinct resonances suggesting that these compounds are also stereochemically non-rigid on the N.M.R. timescale [35, 40, 44, 45].

3.2 Solid State N.M.R. Studies [39, 71–74]

The gold clusters have also been studied in the solid state using magic angle spinning N.M.R. techniques. The clusters show chemical shifts between 37 and 71 ppm relative to 45% H_3PO_4 and are associated with a series of side bands spaced at the spinning frequency. For the spinning speeds used in these studies the side band intensities are relatively small and represent less than 25% of the total signal intensity. The chemical shift anisotropies as revealed by the relative intensities of

the spinning sidebands were found to be similar for the different phosphine environments in a given cluster. The line widths of the resonances are generally typically 300 Hz in the solid state whereas related solution spectra have line widths of <5 Hz. Part of the line width in the solid state may be attributed to dipolar broadening effects due to ^{197}Au nuclei which are averaged-out in solution. It is not removed completely by magic angle spinning because the quadrupole interaction of the gold is comparable to the nuclear Zeeman interaction. Despite the broad lines many of the peaks are sufficiently well resolved in the solid state [71, 72].

The room temperature solid state $^{31}P\{^1H\}$ spectrum of $[Au_6\{P(C_6H_4OMe)_3\}_6](NO_3)_2$ has two well-resolved peaks with relative intensities of 2:4 and similar to the resonances observed when the compound was studied in solution at low temperature (−90°C) and is consistent with the structure (Fig. 6). The marked difference in the room temperature solution and solid-state spectra has been attributed to faster intermolecular rearrangement processes in solution. The $^{31}P\{^1H\}$ solid state NMR spectrum of $[Au_7(PPh_3)_7]OH$ [39], which has a squashed pentagonal D_{5h} structure, has two overlapping peaks at 47.6 and 57.4 ppm downfield relative to 85% H_3PO_4 consistent with the solid state structure. In solution at room temperature only a single sharp signal at 51.5 ppm is observed. Similar conclusions were reached for $[Au_8\{PPh_3\}_8](NO_3)_2$ and $[Au_8\{P(C_6H_4OMe)_3\}_8](NO_3)_2$, whose structures are illustrated in Figs. 3 and 4 . Its solid-state spectrum shows one completely resolved peak at low field and a number (at least two) overlapping peaks at higher field. The low field resonance has been assigned to the unique phosphine which has a significantly longer Au–P distance. The low temperature solution spectrum of $[Au_8\{PPh_3\}_8](NO_3)_2$ shows only a single low field peak and three overlapping resonances at high fields, which is consistent with the idealised C_{3v} symmetry observed in the crystal. In solution two distinct processes involving the equilibration of all the phosphorus atoms and the movement of the Au–P units around the central gold atom have been proposed [75].

The solid state $^{31}P\{^1H\}$ spectrum of $[Au_9\{P(C_6H_4OMe)_3\}_8](NO_3)_2$ shows two resonances at +48 and 68.7 ppm relative to 45% H_3PO_4 indicative of two environments and this is consistent with the D_{2h} skeletal geometry illustrated in Fig. 4. In solution it shows only a single resonance even at low temperatures. The second gold brown isomer gives rise to two peaks with an intensity ratio of 2:6. The idealised skeletal geometry has D_{4d} symmetry which has all phosphorus environments symmetry equivalent. The crystallographically imposed symmetry is C_{2v} which allows four distinct phosphorus environments which suggests overlapping of resonances of nearly equivalent sites with similar chemical shifts. In solution not only do the molecules undergoing interesting fluxional processes, but also a rapid interconversion of the two isomers on the N.M.R. timescale [76]. The application of pressures of up to 60 kbar on the green (D_{2h}) isomers of $[Au_9(PPh_3)_8]^{3+}$ in the solid state shows that it is converted reversibly into the brown isomer (D_{4d}) and the process was monitored using differences in their optical spectra. This pressure-induced reversible change in cluster geometry from the D_{2h} icosahedral-fragment form to the D_{4d} centred-crown form confirms the presence of a low energy intermolecular transformation. The change in the core skeletal geometries of the clusters may result from a

relatively minor "twist" of the "top" four Au atoms relative to the "bottom" four Au. The concomitant realignment of "bonding" Au-Au interactions is efficient and permits a low energy interconversion of the two forms. Similar pressure studies have been used to study rearrangements in rhodium gold clusters [77, 78].

In summary these solid state N.M.R. results suggest that in many, but not all cases, the distinct sites of the cluster framework may be resolved. A combination of solid state crystallographic, solution and solid state N.M.R. spectroscopic measurements and pressure studies are valuable for studying the ground state structures and dynamic properties of phosphine clusters. The utility of the solid-state N.M.R. technique is likely to be of unique importance in cases where crystal structures cannot be determined, particularly when suitable crystals cannot be obtained or when a molecule of interest is contained in non-crystalline environments, e.g. when it is absorbed on the surface or encapsulated in a molecular cavity.

4 Hetero-Metallic Gold Clusters

The incorporation of other metals inside the cages of gold clusters attracted considerable attention in the 1980s. Pignolet [70–81] and Steggerda [82, 83] reported the first examples of gold clusters with palladium and platinum interstitial atoms and Watson prepared the first example of gold cluster with an interstitial rhodium [84, 85]. Subsequently molybdenum, cobalt and other transition metals were incorporated. Strahle incorporated carbonyls of the earlier transition metals into gold clusters [86, 87] and Teo was the first to introduce silver into the surface locations of icosahedral gold clusters and we reported examples of linked icosahedral derivatives [88–92]. References [93] and [94] give examples of Ag/Au clusters and Ag/Cu clusters stabilised by thiolato-clusters. Silver, copper and mercury were subsequently incorporated into palladium and platinum gold clusters by Steggerda [82] and Pignolet [75] and they demonstrated that these clusters would undergo oxidative addition reactions with hydrogen and this could be utilised as the basis of catalytic processes. Examples of these clusters are illustrated in Figs. 9 and 10 [75]. Figure 9 provides examples of a range of heteronuclear clusters which are isostructural to the homonuclear gold clusters and are also isoelectronic. This permitted the interpretation of the bonding in both classes of cluster using the same bonding model. It is noteworthy that all the clusters in Fig. 9 have spherical geometries and triangular faces predominate. The radial Pt–Au bond lengths are 2.6–2.8 Å and the Au–Au distances in the periphery of the metal frame are 2.8–2.9 Å, i.e. the pattern established for the parent homonuclear gold clusters persists. The X-ray structure of $[Pt(AuPPh_3)_8(Hg)_2]^{4+}$ shows two Hg atoms in *trans*-positions and the crown configuration of the parent $[Pt(AuPPh_3)_8]^{2+}$ is largely unaffected (Fig. 15). The steric crowding associated with the phosphines plays an important deciding the nuclearity of the clusters. The addition of metal cations (e.g. Ag, or Hg^{2+} or M–X fragments, e.g. Ag–Cl, $AgNO_3$ and CuCl) are particularly effective capping groups with minimal steric demands [27, 28] and lead to coordination numbers as high as

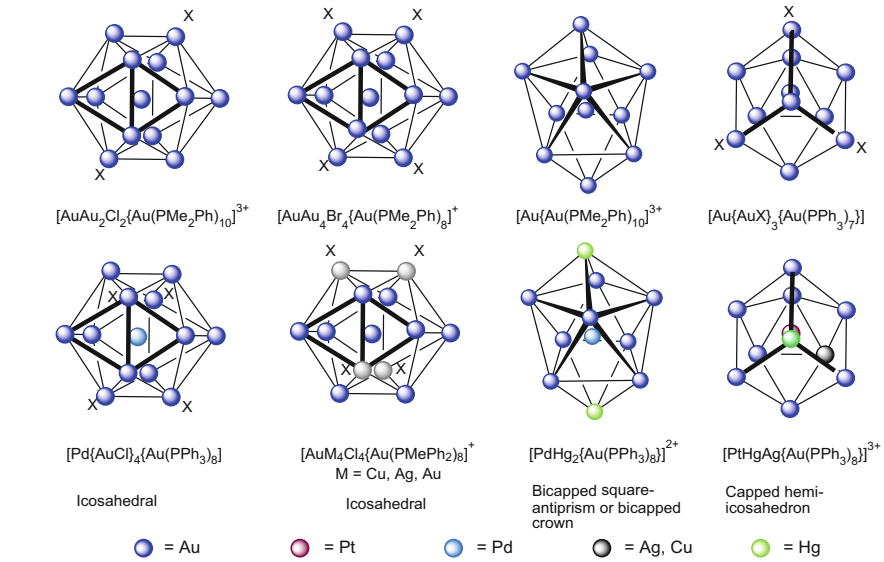

Fig. 9 Examples of isostructural and isoelectronic spherical heteronuclear gold clusters

12 for the interstitial atom. The substitution of the Hg-bonded NO_3^- by Cl^- has been shown to be a fast reaction.

Figure 10 provides another class of heteronuclear cluster compounds which may be described in terms of an incomplete icosahedron and indeed many of the larger examples may be described as hemi-spherical icosahedra. The lower nuclearity examples are more appropriately described in terms of pentagonal pyramids. It is also noteworthy that ring clusters undergoes a skeletal rearrangement to a more spherical shape when ligands are co-ordinated to the central atom. The interconversion of $[Pt\{Au_8(PPh_3)_8\}]^{2+}$ into $[Pt(CO)\{Au_8(PPh_3)_8\}]^{2+}$when CO is added provides a specific example in Fig. 10 of this skeletal rearrangement [74, 75]. The cluster compounds $[Au_7(PPh_3)_7\{Mo(CO)_3\}]^+$ and $[Au_7(PPh_3)_7\{Co_2(CO)_6\}]^+$ have been isolated when $[AuN_3(PPh_3)]$ is photolysed in the presence of either $Mo(CO)_6$ and $Co_2(CO)_8$ [86, 87]. The former has an interstitial molybdenum atom and both have structures which may be derived from the icosahedron and resembles the platinum and rhodium clusters described above. $[Au_7(PPh_3)_7\{Co_2(CO)_6\}]$ has two Au_4Co trigonal bipyramids linked by a common vertex. The icosahedral clusters which resemble $[Au_{13}Cl_2(PMePh_2)]^{3+}$ and have copper or silver partially replacing gold atoms on the surface have been synthesised by modifying the initial procedure. Specifically $[Au_9M_4Cl_4(PMePh_2)_8]^+$ (M = Cu or Ag) were made and structurally characterised [51].

The N.M.R. spectroscopic characterisation of these cluster compounds in solution was made more informative by the presence of ^{195}Pt, ^{103}Rh and ^{107}Ag and ^{109}Ag nuclei. $[PtAu_8(PPh_3)_8]^{2+}$ has the centred crown structure observed previously for the homo-nuclear gold clusters shown in Fig. 4. The platinum cluster reacts more readily

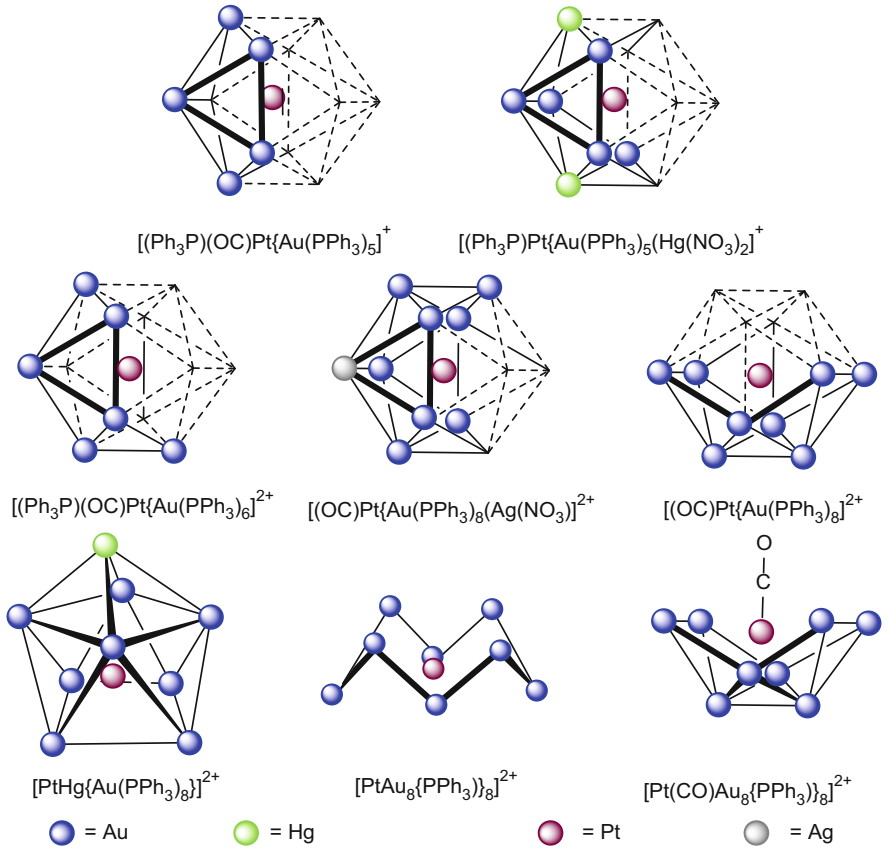

Fig. 10 Examples of heteronuclear gold clusters containing platinum silver and gold

with nucleophiles, e.g. CO, than the related gold cluster and on co-ordination to the interstitial gold atom increases the skeletal electron count by 2. As a result the skeletal geometry changes to a more hemi-spherical shape in the way illustrated in Figs. 7 and 10. A related cluster compound is observed in $[Rh(CNC_8H7_9)_2Au_8Cl_2(PPh_3)_8]^{2+}$ which has an interstitial rhodium atom. In the X-ray structure determinations Pt and Au cannot be readily distinguished because of their similar atomic numbers and the position of the Pt must be determined by careful analyses of ^{195}Pt, and ^{31}P NMR and/or ^{197}Au Mossbauer spectral studies. To date no isomer with a central Au and a peripheral Pt has been detected. In the 1980s Zhenyang and Mingos [94, 95] developed a theoretical model which accounted for the regioselectivities of these metals in heteronuclear gold clusters. In essence those metals which have the higher enthalpies of atomisation (Pd, Pt, Ir, Rh) favour interstitial locations and those with smaller enthalpies of atomisation favour surface locations (Ag, Cu, Hg). In all the examples studied to date the palladium and

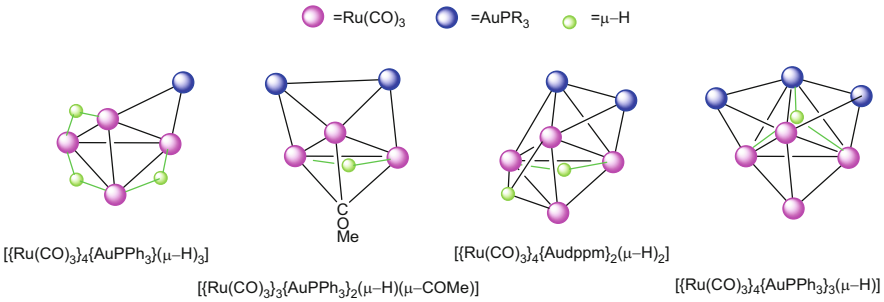

Fig. 11 Gives examples of cluster building based on the addition of $[Au(PR_3)]^+$ fragments to preformed metal carbonyl anions

platinum atoms occupy the interstitial sites. This is reminiscent of the segregation behaviour of gold/platinum alloys where platinum avoids occupation of surface sites. Those clusters which have different Au-P sites in the crystalline state show only a single Au-P resonance in the $^{31}P\{^1H\}$ N.M.R. spectra at room temperature. The intramolecular fluxionality in the platinum clusters can be confirmed by the retention of coupling between the phosphorus and platinum nuclei over the whole temperature range.

The Group 11 cations $[M(PPh_3)]^+$ (M = Cu, Ag and Au) have also been widely used in cluster aggregation reactions, because they are able to cap triangular faces or edges of nucleophilic metal carbonyl clusters [96–101]. As discussed in the Introductory chapter [5] the skeletal electron pairs of the parent carbonyl cluster are not altered by these capping processes. These properties have been utilised extensively by Bruce [96, 97], Salter [98], Lauher [99] and Housecroft [100, 101] and their reviews provide comprehensive compilations of the resulting compounds. Housecroft developed this strategy to encapsulate a boron atom into metal carbonyl cages. Similar reactions of $[M(PPh_3)]^+$ and H^+ have led to them being described as *isolobal* and theoretical calculations have revealed the electronic reasons for this analogy [10, 26]. Furthermore, the ability of H_2 to form dihydrogen complexes with transition metals has some similarities to the behaviour of $[M(PPh_3)]^+$ fragments when bonded to metal carbonyl clusters. Specifically, these fragments (especially when M = Au) tend to aggregate on the cluster surface. The ability of gold to participate in aurophilic interactions encourages these processes and Fig. 11 provides some specific ruthenium examples of these compounds. When two or more $[M(PPh_3)]$ fragments are bonded to the metal carbonyl cage N.M.R. studies in solution indicate that the capping fragments undergo skeletal rearrangements which lead to site exchange. The carbonyl segment of the cluster appears to remain rigid with the $[M(PPh_3)]$ fragments migrating over this more rigid cage. The fact that $[M(PPh_3)]^+$ is able to cap either faces or edges of the carbonyl cluster facilitates these migratory processes as do the aurophilic interactions which come into play when the gold-gold separation becomes less than 3 Å. These aurophilic interactions reduce the activation

energies for these dynamic processes. Dyson, Rossel, Braunstein, Orpen, and Shapley have reviewed the issues relating to skeletal isomerism in metal clusters [102–106].

5 A Flexible Bonding Model for Gold Clusters

5.1 Introduction

It became apparent from 1976 that the gold clusters did not follow the bonding patterns which had been defined in the early 1970s by Wade [6], Rudolph [7] and Mingos [8]. Specific calculations on platinum and gold clusters explained their errant behaviour and led to some alternative predictions for the closed shell requirements for gold clusters with interstitial atoms, e.g. icosahedral $[Au_{13}(PR_3)_{12}]^{5+}$ [24, 25] and octahedral $[Au_6C(PPh_3)_6]^{2+}$ [10, 11, 42]. These calculations identified that the $AuPR_3$ fragment was *isolobal* with H and the alkali metals [107–112] rather than the trigonal $M(CO)_3$ fragments commonly present in metal carbonyl clusters (see Fig. 12). This suggestion enabled synthetic chemists to use this relationship to develop an *aufbau* capping procedure to expand the range of carbonyl clusters by the addition of gold atoms, in the form of $[Au(PPh_3)]^+$ [96–101]. These semi-empirical calculations implied that the energy differences separating clusters with alternative skeletal geometries would be sufficiently large that the structure observed in the solid state is maintained in solution. The N.M.R. results discussed above showed this to be incorrect. Synthetic studies increased the number of examples of structurally characterised skeletal isomers. Continue with Isoelectronic gold clusters consequently highlighted a problem which had not been encountered for rationalising the structures of borane, hydrocarbon and carborane polyhedral molecules. Eventually the numerous alternative structures of gold clusters diminished the possibility of developing a model which was based on a single class of polyhedra. The structures generated a chimera which had a hint of an underlying pattern but not one that was not readily amenable to a simple interpretation. The combination of structural and N.M.R. data suggested these gold clusters represented an intermediate stage lying between a gold nugget based on rigid polyhedral structures and a more fluid model resembling a droplet of liquid gold. This raised fundamental issues and highlighted a general valency question for chemists – how could one develop a satisfactory model which applied to a body of clusters which were not defined by a single characteristic geometric feature? This resulted in the development of a more flexible model for gold clusters which was based initially on less specific topological features [113] and resembled a droplet model which permitted distortions from spheres into spheroids of lower symmetry [114]. The physics community had previously developed such flexible models for describing nuclear structures [114].

It is noteworthy that although the $[B_nH_n]^{2-}$ anions have characteristic deltahedral geometries not all examples are stereochemically rigid on the N.M.R. timescale. Examples of both rigid and fluxional polyhedral geometries had been noted and

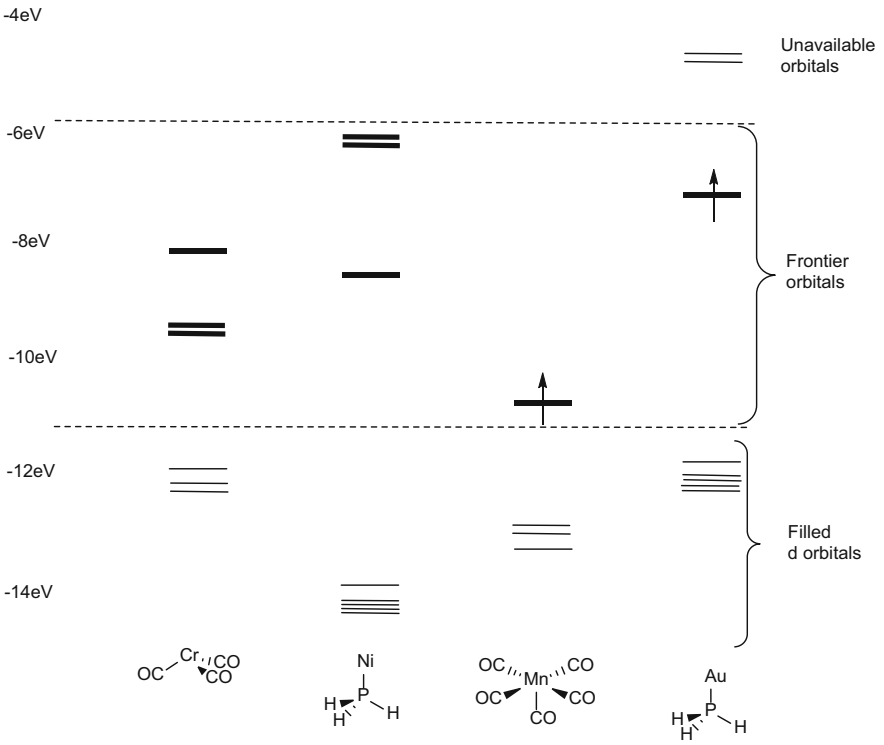

Fig. 12 Frontier orbitals of common fragments [10]

shown to depend on the number of boron atoms [5]. Subsequent studies showed that these differences did not depend solely on geometric and topological factors but were also influenced by orbital symmetry effects. In contrast the majority of phosphine stabilised gold cluster compounds are fluxional on the N.M.R. timescale but are made more rigid by dppp bidentate phosphine ligands [52–61]. An understanding of the structures and fluxional characteristics of gold clusters therefore requires a quantum mechanically based model but does not depend on a single geometric polyhedral class. Early analyses of the molecular orbitals of gold cluster compounds made it apparent that the skeletal molecular orbitals followed a particle in a sphere pattern, with nodal surfaces increasing in number as the molecular orbitals became less stable [24, 25, 107, 109]. In these early papers individual mos were classified by their point group symmetry labels, but their relationship to the orbitals of spherical atoms was implicit. The nodal characteristics of the mos did not show the degeneracies associated with spherical atom but clustered sufficiently to suggest that a spherical model may be a good starting point as long as it permitted distortions from the full rotation symmetry of spherical point groups. The Tensor Surface Harmonic Theory published by Stone in 1981 [115–118] articulated in an elegant and general way the relevance of the spherical free electron models and it provided a

useful notation for designating the mos in gold clusters. Indeed the greater simplicity of the frontier orbitals of the $[AuPR_3]^+$ fragment shown in Fig. 12 made the Stone methodology simpler to develop than that for borane and carbonyl clusters. This analysis proved to be a very flexible and appropriate general methodology for gold clusters when modified to incorporate non-spherical gold cluster shapes [3, 4, 107, 119, 120]. The analysis was simplified considerably by the recognition that although the molecular orbitals in borane clusters required an analysis of the radial and tangential molecular orbitals the gold skeletal molecular orbitals depended primarily on a consideration of the radial molecular orbitals. Indeed, the solutions of the quantum mechanical problem referenced to the particle in a spherical field resembled the graphical approaches introduced by King [121]. The publication of the closely related Jellium model reported by Knight and co-workers in 1984 [122] accounted for the relativity stabilities of sodium clusters observed in gas-phase molecular beam experiments proved timely and enabled us to connect the two areas. Clemenger in 1985 extended the Jellium model to prolate and oblate spheroids [123] and this was closely related the line we had taken for molecular gold clusters and reinforced the *isolobal* relationships between gold and the alkali metals [124–127]. Our conclusions were consistent with the ab initio calculations on sodium clusters reported by Koetecky and Fantucci [128].

5.2 *Bonding in Simple Gold Clusters [113, 120, 129, 130]*

The frontier orbitals of the $[Au(PR_3)]^+$ fragment are compared with related carbonyl and phosphine fragments in Fig. 12 and confirm that that the former has a single available frontier orbital. The bonding in phosphine cluster compounds of gold is dominated by a single frontier orbital and metal-metal bonding depends primarily on overlap between the 6s valence orbitals which hybridise with the $5d_{z^2}$ [68–70] and to a lesser extent with $6p_z$. The relative energies of the 5d, 6s and 6p valence orbitals are greatly affected by relativistic effects which place the 6s and 5d orbitals at similar energies and encourage effective hybridisation. A large 6s-6p energy separation minimises the participation of the 6p orbitals and the $6p^{\pi}$ orbitals do not form strong metal-metal bonds on the surface of the cluster sphere. Pyykkö [131, 132] made a particularly important contribution recognising the importance of these relativistic effects for gold resulting from the contraction of the 6s orbitals of gold. The bonding characteristics of the frontier orbitals of $[Au(PR_3)]^+$ fragments lead to the following generalisations:

1. The energies of the bonding skeletal molecular orbitals in single shell gold clusters are dominated primarily by bonding interactions between 6s orbitals. The number of nearest gold neighbours therefore plays an important role in defining the spectrum of cluster mos.

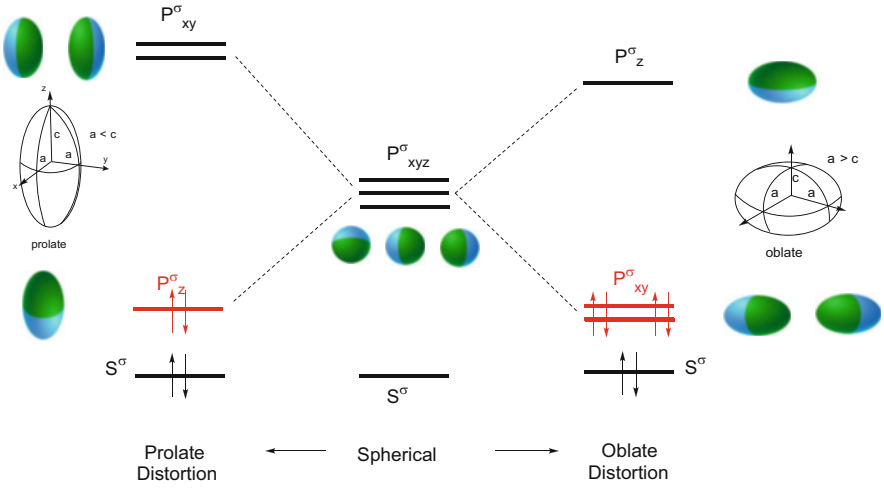

Fig. 13 Effect of prolate and oblate distortions on the energy levels of the particle in a sphere problem

2. Low nuclearity $[Au_nL_n]$ ($n = 2$–4) are characterised by a single bonding molecular orbital resulting from the in-phase overlap of 6s orbitals on the individual gold atoms. This in-phase combination has no angular nodes and therefore resembles an s atomic orbital and is designated the symbol S^{σ} (see Fig. 13).
3. For larger clusters $[Au_nL_n]$ ($n > 4$) additional P^{σ} skeletal molecular orbitals, which are singly noded become available and contribute significantly to the skeletal bonding. The radial bonding is enhanced by interstitial atoms. If the P^{σ} shell is occupied by 6 electrons, the total electron density is spherically symmetric and the cluster adopts a spherical geometry.
4. There are almost no phosphine gold clusters which are paramagnetic and consequently the filling of molecular orbitals can proceed in a pairwise *aufbau* fashion. If the P^{σ} shell is completely occupied by electrons, then the total electron density is spherical and the cluster adopts a geometry which is spheroidal and maximises the number of nearest neighbours. If the steric requirements of the ligands are significant, then distortions away from these ideal geometries may result.
5. When there are insufficient electron pairs to completely fill the P^{σ} shell then the cluster distorts in a manner which creates a stable partially filled shell. The distortion is sufficiently large that the electrons pair up to form a low spin ground state. The partial filling of P^{σ} molecular orbitals with a single electron pair leads to a preference for a prolate geometry and oblate shape is favoured when P^{σ} is occupied by 4 electrons (see Fig. 13).

Figure 13 illustrates the consequences of these simple molecular orbital arguments derived from the solutions of the Schrödinger equation for the particle in a spheroid. The methodology is limited to spheroids and is not based on detailed

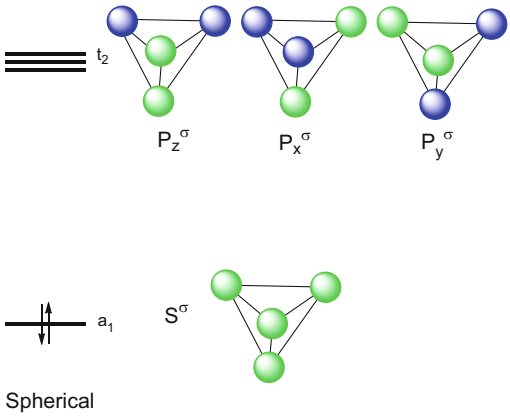

Fig. 14 The skeletal molecular orbitals of a tetrahedral gold cluster. The molecular orbitals are illustrated in terms of 6s orbitals on the gold atoms, but calculations indicate significant 6s/5d_z^2 hybridisation

geometric features of a specific cluster. Following the analysis developed by Stone [115–118] the solutions may be used to specify the coefficients of orbitals which form the basis set for the molecular orbitals from the locations of the atoms. This analysis suggests that the mos are most stable when the number of nearest neighbours is maximised. Ideally the clusters which are classified as spherical have the same connectivities for all the vertices and lie on the same spherical surface. Specific examples are the tetrahedron, the octahedron and the icosahedron which also have the maximum number of edges on a spherical surface because they have triangular faces exclusively. The vertices of the square-antiprism and the cuboctahedron have the same connectivities as deltahedra with the same number of atoms and also lie on a single spherical surface but have fewer edges because of the presence of some square faces.

$[Au_4(PBu^t_3)_4]^{2+}\{S^\sigma\}^2$ (Fig. 14 [133–135]), octahedral – $[Au_6C(PPh_3)_6]^{2+}$ $\{S^\sigma\}^2\{P^\sigma\}^6$ (Fig. 15 [68]) and $[Au_{13}Cl_2(PMe_2\ Ph)_{10}]^{3+}$ $\{S^\sigma\}^2\{P^\sigma\}^6$ (Fig. 16 [22]) provide specific examples of closed shell structures compatible with the energy levels shown in the centre of Fig. 13 for a sphere [133–135]. The square-antiprism and cuboctahedron have not been observed in simple phosphine complexes. The cuboctahedron has only been observed in a conjoined form with 25 gold atoms in thiolato-clusters [3, 4]. Stone's particle on a sphere equations may be used to define the wavefunctions for the molecular orbitals of specific clusters and these results are illustrated in Figs. 14, 15, and 16. The stabilities of the molecular orbitals depend on the overlap integrals and resonance integrals and in a Hückel approximation are maximised for deltahedral arrangements. Figure 17 gives a corresponding molecular orbital diagram for the cuboctahedron which has fewer edges but still reproduces a very similar molecular orbital diagram and closed shell structure.

In these figures the skeletal molecular orbitals have been designated by both point group symmetry labels and the pseudo-spheroidal symmetry labels, which emphasise the number of nodes associated with each molecular orbital. The number of nodes defines the relative energies of the molecular orbitals, *viz* S^σ which has no

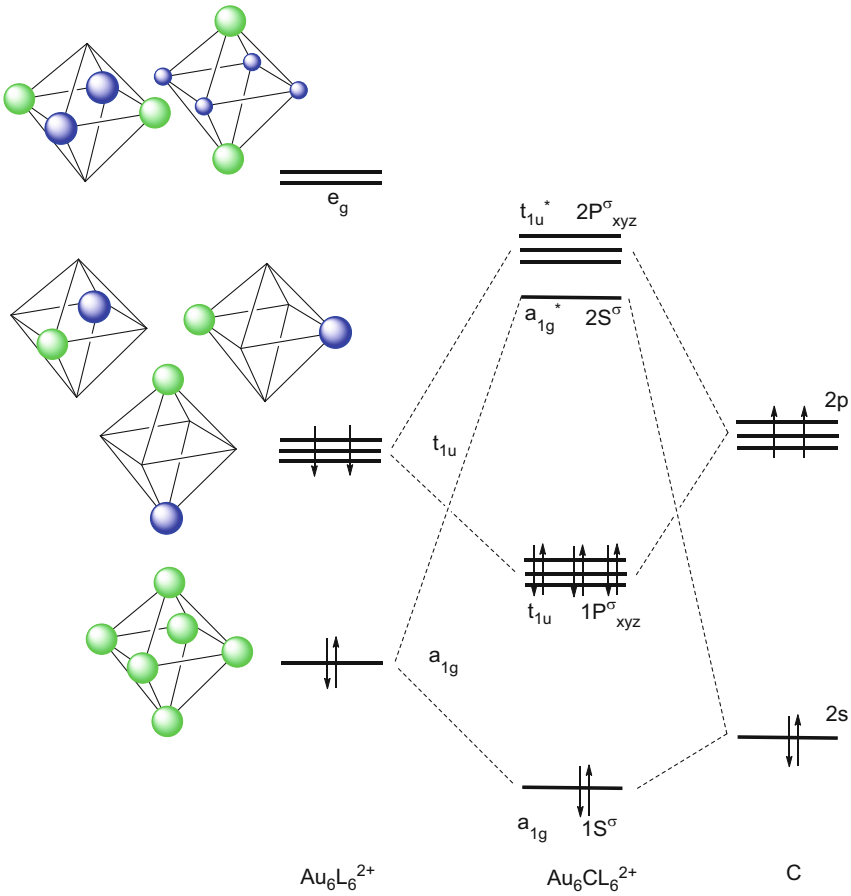

Fig. 15 Molecular orbital interaction diagram for $[Au_6C(PPh_3)_6]^{2+}$. Similar analyses may be constructed for trigonal bipyramidal $[Au_5P(PPh_3)_5]^{2+}$ and tetrahedral $[Au_4O(PPh_3)_4]^{2+}$

nodes along the tetrahedral edges is strongly bonding and the P^{σ}, which is noded along half the edges, is somewhat antibonding. At its simplest level a Hückel [70] interpretation suggests that the bonding molecular S^{σ} molecular orbital is stabilised by 3β (since it has three nearest neighbour gold atoms) and each component of the P^{σ} molecular orbitals is destabilised by –β. The triple degeneracy of P^{σ} leads to an equal spreading of the −3β antibonding character. Therefore a stable closed shell electronic configuration is associated with triangular $[Au_3L_3]^+$ and tetrahedral $[Au_4L_4]^{2+}$, which both have $\{S^{\sigma}\}^2$ configurations. Although triangular clusters of gold are not well established, there are several examples of tetrahedral gold clusters, viz $[Au_4(PBu^t_3)_4]^{2+}$, $[Au_4\{P(C_6H_3Me_3\text{-}1,3,5\}_4]^{2+}$, where each gold atom is associated with a single phosphine ligand. The stable $[Au_4]^{2+}$ entity may also be stabilised by a combination of phosphine ligands and anionic bridging ligands along two edges

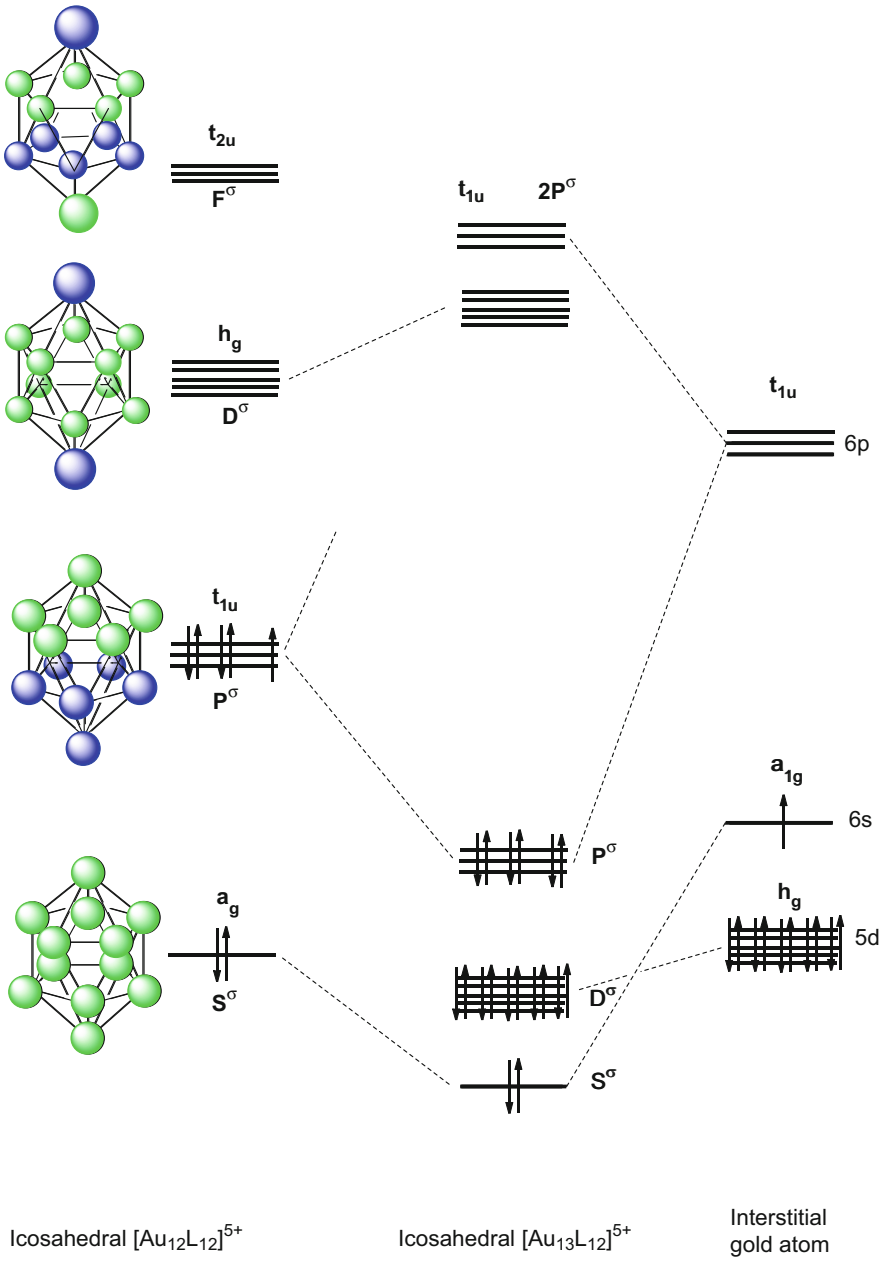

Fig. 16 Interaction molecular orbital diagram for metal-centred icosahedra. The numerous d orbitals localised on the peripheral gold atoms make a narrow band and have been excluded for reasons of clarity

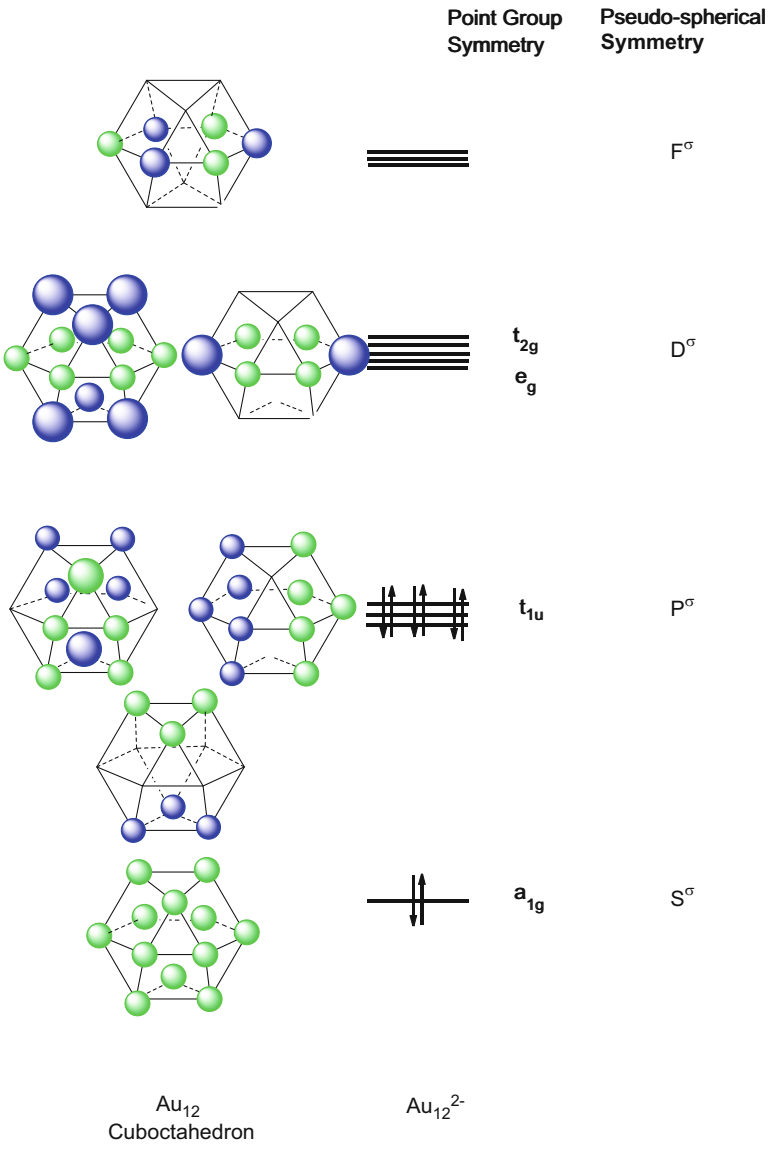

Fig. 17 Skeletal molecular orbitals for a centred cuboctahedral gold cluster

of the tetrahedron, namely $[Au_4(\mu\text{-}I)_2(PPh_3)_4]$ and $[Au_4(\mu\text{-}SnCl_3)_2(PPh_3)_4]$ [133–135]. Since these clusters have only one bonding skeletal mo then the covalent bonding is not strong between because only a single electron pair in S^{σ} is delocalised over the six edges of the tetrahedron.

Other deltahedral clusters constructed from equilateral triangles do not have the vertices lying on a single surface and the resultant spheroids are either prolate or

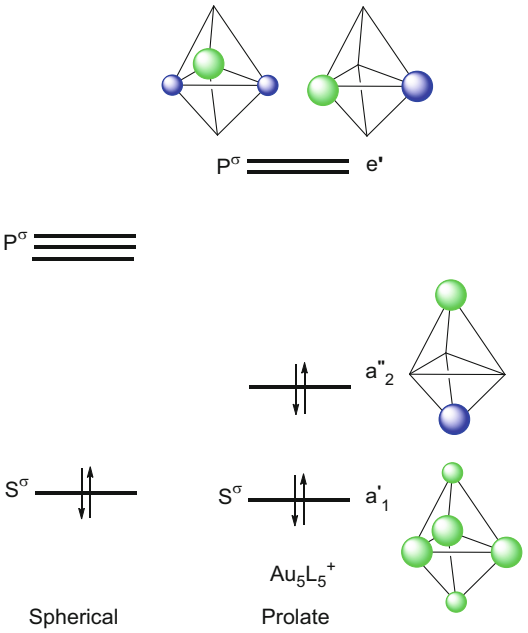

Fig. 18 The skeletal molecular orbitals of a trigonal-bipyramidal gold cluster. The molecular orbitals are illustrated in terms of 6s orbitals on the gold atoms. The prolate nature of this polyhedron results in a splitting

oblate. When $n = 5$, 8 and 10 (i.e. trigonal-bipyramids, dodecahedra and bicapped square-antiprisms) the spheroids are prolate and when $n = 7, 9$ and 11 (i.e. pentagonal bipyramid, the tricapped trigonal-prism and the octadecahedron) are oblate shaped. Therefore for these clusters the three components of the P^{σ} shell shown in Fig. 13 lose their degeneracy and the reduced symmetry $D_{\infty h}$ point group is appropriate for the resultant prolate and oblate spheroids. The $P^{\sigma}{}_{z}$ component is stabilised in the prolate sphenoid and if the distortion results in a stabilisation greater than the pairing energy a closed shell configuration for $\{S^{\sigma}\}^2\{P^{\sigma}\}^2$ becomes the ground state. In contrast an oblate distortion results in a stabilisation of the degenerate $P^{\sigma}{}_{x,y}$ components and favours a $\{S^{\sigma}\}^2\{P^{\sigma}\}^4$ closed shell. Figures 18 and 19 illustrate the LCAO molecular orbitals of $[Au_5L_5]^+$ (prolate-trigonal bipyramid) and $[Au_7L_7]^+$ (oblate-pentagonal bipyramid) and confirm these geometric consequences. The relationship between the distortions and the orbital splittings may be analysed using perturbation theory for the free electron model or by using the co-ordinates of the specific atoms of deltahedron to derive the linear combinations from which the energies may be derived from a Hückel approximation [122–127].

It follows that prolate geometries are favoured for clusters with $\{S^{\sigma}\}^2\{P^{\sigma}\}^2$ electronic configurations because the $P_{x,y}{}^{\sigma}$ components are destabilised relative to the $P_z{}^{\sigma}$ component as shown in Fig. 13. $[Au_6(PPh_3)_6]^{2+}$ has a pair of tetrahedra sharing a common edge and illustrates the prolate geometry. $[Au_6(dppp)_4]^{2+}$ which has a structure based on a di-edge bridged tetrahedron provides a second example. In both examples the $P_{x,y}{}^{\sigma}$ components are localised on the atoms lying in the equatorial plane and the nodal plane leads to antibonding next neighbour gold-gold

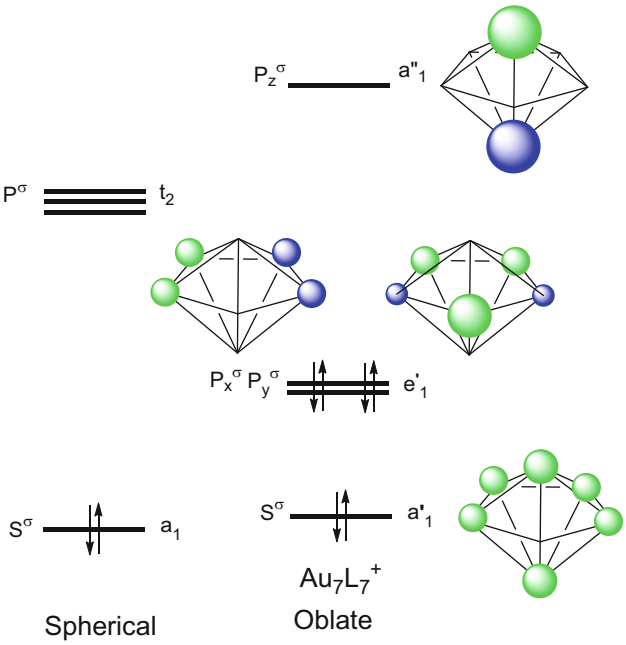

Fig. 19 The skeletal molecular orbitals of a pentagonal bipyramidal gold cluster

interactions. A prolate distortion, which pushes the equatorial atoms closer amplifies the splitting shown in Fig. 13. Konishi et al. [60] have reported a related tri-tetrahedral geometry $[Au_8(dppe)_4]^{2+}$ with 6 valence electrons which can be interpreted by an extension of this model.

In contrast an oblate distortion which pushes the polar atoms closer together results in a greater destabilisation of the P_z^{σ} component (see Fig. 13). The pentagonal bipyramidal cluster $[Au_7(PPh_3)_7]^+$ has an oblate structure and indeed the shortest bond in the cluster is between the two apical gold atoms. This structure is consistent with the closed subshell structure $\{S^{\sigma}\}^2\{P_{x,y}^{\sigma}\}^4$ shown in Fig. 19. It is noteworthy that the distortions described above create a sufficiently large HOMO–LUMO gap to ensure that the clusters adopt a low spin state which is diamagnetic. Strahle has reported that the $[Au_6(PPh_3)_6\{Mn(CO)_3\}]$ also has a pentagonal bipyramidal structure [86] and a similar spectrum of mos. In these examples the number bonding electrons in skeletal mos is either 4 or 6 which is significantly lower than that in the corresponding deltahedral boranes, i.e. 12 and 14, and do not result in a very strong bonding regime.

This analysis has proved sufficiently robust to account for the geometries of gold clusters stabilised by soft ligands such as phosphines, iodide and $SnCl_3$. It is important to recognise that the ligands play an important role in influencing the stabilities and geometries of the clusters. This influence is not limited to electronic effects and the steric effects introduced by the substituents on the phosphines and the anionic ligands also greatly influence the observed geometries. In the absence of

such ligands the bare clusters either adopt rather different geometries or decompose to the bulk metal. These structures of bare gold clusters have been established by careful spectroscopic studies in the gas phase and are supported by DFT calculations. The structures of these clusters are discussed in some detail by Woodham and Fielicke in "Gold Clusters in the Gas Phase" [136]. Their studies on clusters up to Au_{20} have shown that the smaller clusters generally favour close-packed planar structures and the 2D to 3D transition occurs at Au_{12} for anions.

5.3 Introduction of Interstitial Atoms

For gold clusters with eight atoms or more the central cavity can accommodate another metal atom with a slightly smaller radius. The interstitial metal atoms in gold clusters thereby have smaller effective radii [3, 4, 42, 120]. This property has resulted in a wide range of gold clusters with interstitial gold, rhodium, palladium and platinum atoms. The introduction of an interstitial metal with nd, (n+1)s and (n +1)p valence orbitals in a spherical cluster is represented diagrammatically in Fig. 16 for an icosahedral cluster. The s and p valence orbitals of the interstitial metal atom match the bonding skeletal molecular orbitals $\{S^{\sigma}\}$ and $[P^{\sigma}]$ in much the same way as that described above for carbon (see Fig. 15). The d orbitals of the gold atom are stabilised but to a lesser extent by a weaker interaction with the D^{σ} antibonding skeletal molecular orbitals. Therefore, a spherical cluster is characterised by the following filled molecular orbitals $\{S^{\sigma}\}^2$ $\{d\}^{10}$ $\{P^{\sigma}\}^6$ This leads to a total of 18 valence electrons, 10 of which are localised mostly as d orbitals on the interstitial gold atom, i.e. these clusters are characterised by 12n + 18 valence electrons if all the gold valence orbitals are included. Or 2n + 8 if the d shells on the gold atoms are excluded because of their smaller bonding contribution, i.e. $\{S^{\sigma}\}^2\{P^{\sigma}\}^6$ is the ground state electronic configuration. The relevant skeletal molecular orbitals for a cuboctahedron are shown in Fig. 17. The computed energies for $[Au_{13}]^{5+}$ icosahedral and cuboctahedral clusters are very similar. Both polyhedra have 12 strong radial interactions, but the icosahedron has marginally stronger tangential interactions because it has exclusively triangular faces. The radial bonding interactions with the interstitial atoms strengthen the cluster but only 8 electrons are involved in the radial and tangential bonding orbitals. This leads to relatively weak metal–metal bonds in these compounds and of course a softer potential energy surface for rearrangements. In the majority of the early publications we described the electron counts as $12n_s$ + 18 (spherical) and $12n_s$ + 16 (oblate/toroidal), where n_s is the number of surface gold atoms. The filled d shell was included to make them as similar as possible to the PSEPT description developed earlier for carbonyl clusters. The discovery of nanoclusters with more than 100 gold atoms made this impractical and we excluded the d shells and used a notation where only the skeletal electrons (**sec**) originating from the 6s and 6p gold valence orbitals were audited.

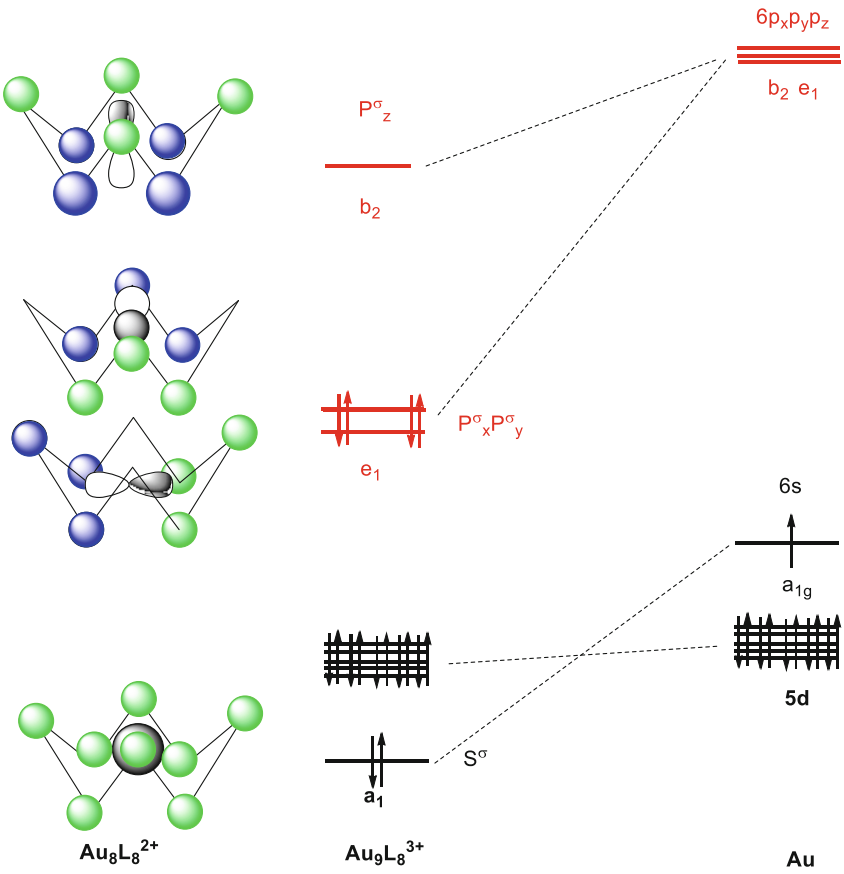

Fig. 20 Molecular orbital diagram for $[Au_9(PR_3)_8]^{3+}$ with a crown geometry (D_{4d} symmetry). The contributions of the interstitial gold atom are shown in black and white

Figure 20 illustrates a mo interaction diagram for 8 gold atoms with a crown geometry and their interactions with the atomic orbitals of an interstitial gold atom. The degeneracy of the $[P^\sigma]$ shell is removed in the oblate topology and the degenerate components $[P^\sigma_{xy}]$ interact with the orbitals of the ring more strongly. The $[P^\sigma_z]$ component is only weakly bonding and this leads to a substantial HOMO–LUMO gap. These oblate gold clusters are characterised by the closed shell $\{S^\sigma\}^2\{d\}^{10}\{P^\sigma_{xy}\}^4$, i.e. 16 electrons or 6 if the d shell is ignored, i.e. **sec** = 6. This model may be extended to related clusters with interstitial platinum and iridium [73, 75, 82, 120].

Gold clusters with more than 7 metal atoms invariably have interstitial metal atoms and their structures have been illustrated in Figs. 5, 7, 8, 9, and 10. The molecular orbital analysis suggests that the clusters fall into two classes – oblate $\{S^\sigma\}^2\{P^\sigma\}^6$ and spherical $\{S^\sigma\}^2\{P^\sigma\}^4$. These spheroidal shapes may be given more specific molecular descriptions by recognising that they are based either on centred

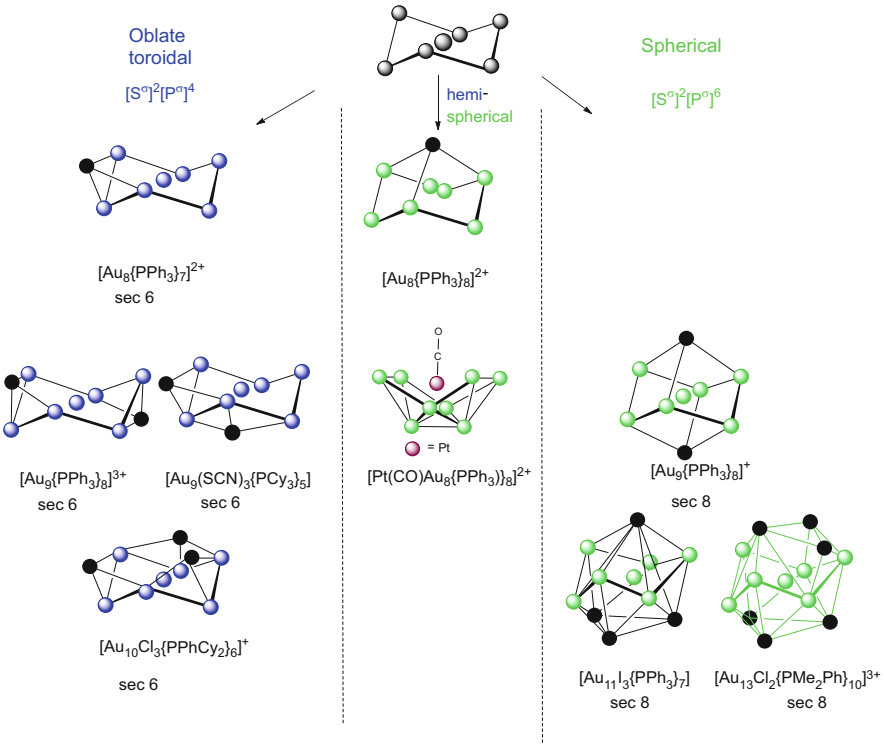

Fig. 21 Examples of spherical and oblate (toroidal) gold clusters with interstitial atoms. Hemispherical examples are shown in the middle column

hexagonal or crown cores. Examples based on the centred hexagon are given in Fig. 21 and those based on a centred crown in Fig. 22. The oblate geometries are associated with $\{S^{\sigma}\}^2\{P^{\sigma}\}^4$ skeletal mos and skeletal electron counts (**sec**) of 6, but the introduction of capping groups along the C_3 or C_4 axes leads to the spherical clusters with $\{S^{\sigma}\}^2\{P^{\sigma}\}^6$ closed electronic shells. The capping involves the addition of a single gold atom or a triangle of gold atoms along the three or fourfold axis and leads to spherical clusters with **sec** of 8. If additional gold atoms are not introduced along the major axis, but bridge edges of the hexagon then the oblate topology is maintained (see Fig. 21) and the $\{S^{\sigma}\}^2\{P^{\sigma}\}^4$ shell configuration is retained. Such clusters are characterised by **sec** of 6. Specific examples of these oblate clusters are shown on the left-hand side of Fig. 21. Addition of a single metal atom along the rotation axis above and below the interstitial atom leads to a distorted cube and addition of a pair of triangles leads to an icosahedron (see Fig. 21). This polar capping results in an increase in the number of skeletal bonding mos from 3 to 4 and an increase in the skeletal electron count (**sec**) from 6 to 8. Although the centred hexagonal ring has not been characterised as an independent species for gold cluster, it represents an important building block because it corresponds to the central girdle

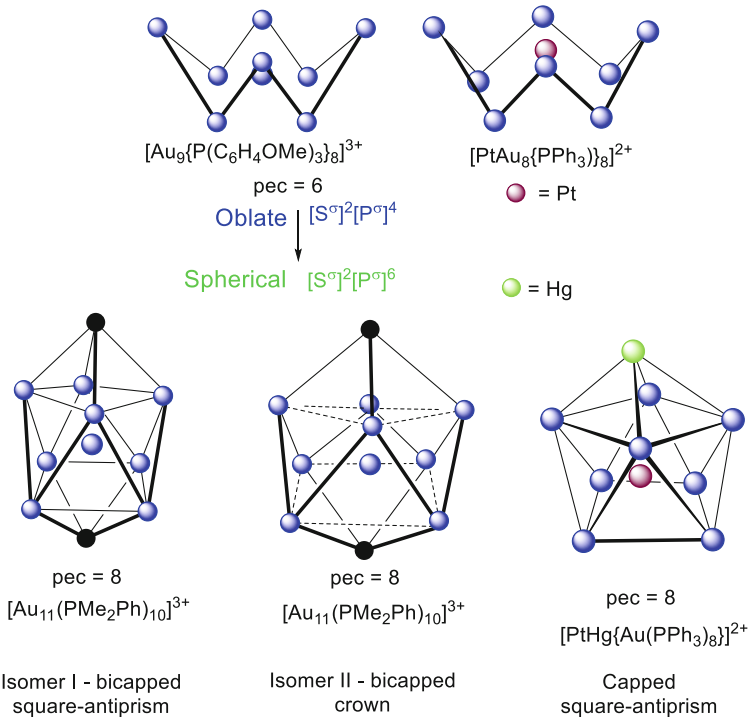

Fig. 22 Examples of oblate and spherical clusters gold based on a crown. The examples on the right have isoelectronic clusters with interstitial platinum atoms

of an icosahedron. The second important component is the oblate centred crown. The structure is converted into a more spherical geometry by adding atoms along the C_4 and if accompanied by a squeezing together the four metal atoms which define the planes above and below the interstitial atom results in the bicapped square-antiprism shown at the bottom of Fig. 22. If the original crown is kept, then the resultant capped structure is best described as a bicapped crown. Figure 22 also gives an example of a mono-capped capped square-antiprism which is also characterised by a **sec** of 8 electrons.

The LUMO of the oblate crown cluster is the $[P^{\sigma}_{z}]$ molecular orbital which has the appropriate symmetry to interact with lone pair orbital of a ligand. The addition of PPh_3 to $[Au_8(PPh_3)_7]^{2+}$ converts it into $[Au_8(PPh_3)_8]^{2+}$ and this results in a rearrangement of the cluster into a hemi-spherical cluster. A similar transformation has been observed when $[PtAu_8(PPh_3)_8]^{2+}$ reacts with CO to form $[Pt(CO)\text{-}Au_8(PPh_3)_8]^{2+}$ and the structures of the resultant clusters are illustrated in the centre of Fig. 21 and described as hemispherical.

5.4 Summary

The bonding model developed above represents a fusion of the free electron Jellium and Stone models. The former defines the overall topology of the clusters and the closed shell requirements and the latter provides a menu of reasonable structural possibilities for the molecule and gives rise to skeletal isomers. The Jellium establishes the following spheroid shapes for gold clusters with 2–8 skeletal electrons:

$\{S^{\sigma}\}^2$ – spherical ; $\{S^{\sigma}\}^2\{P^{\sigma}_z\}^2$ – prolate; $\{S^{\sigma}\}^2\{P^{\sigma}_{xy}\}^4$ – oblate; $\{S^{\sigma}\}^2\{P^{\sigma}_{xyz}\}^6$ – spherical

Within these geometric boundaries the greatest stabilisation of the surface molecular orbitals is achieved for atomic arrangements with the maximum number of nearest neighbours, i.e. triangulated arrangements. This stabilisation is diminished as the number of nearest neighbours is reduced. Connections between oblate and prolate clusters are made by capping gold atoms and triangles introduced along the major symmetry axis. These stabilisation energies fall in the same range as the sterically induced repulsion energies introduced by the ligands. This leads to the alternative geometric skeletal isomers described above. Figs. 21 and 22 provide more specific examples which illustrate the scope of these generalisations. These ideas have been extended to higher nuclearity phosphine and thiolato clusters of gold in other publications [3, 4, 63, 129, 130]. Other chapters also provide examples of subsequent developments of the Jellium model to clusters containing metals and non-metals in other groups of the periodic table. Addition of ligands to the interstitial atoms leads to hemi-spherical clusters which bridge the oblate and spherical categories by utilising the LUMO P^{σ}_z in metal ligand bond.

6 Possible Skeletal Rearrangement Mechanisms

6.1 DSD Mechanism in Borane and Carborane Deltahedral Molecules

Few of the gold clusters are isostructural with the *closo*- deltahedra which are characteristic of boranes and carboranes and there are almost no *nido*- and *arachno*-analogues. In addition they exhibit multiple isomeric structures for a given nuclearity which result from subtle changes in the electronic and steric properties of the ligands. In the early 1960s it was established that icosahedral 1,2-$[C_2B_{10}H_{12}]$ when heated above 450°C resulted in two isomeric molecules with the carbon atoms occupying more distant positions on the icosahedral cage. Clearly these rearrangement processes were associated with a high activation energy but subsequently detailed $^{11}B\{^1H\}$ N.M.R. studies showed that the boranes $[B_8H_8]^{2-}$ and $[B_{11}H_{11}]^{2-}$ rearranged even at low temperatures and the interconversion pathways were associated with low activation energies. The interpretation of these rearrangement processes represented

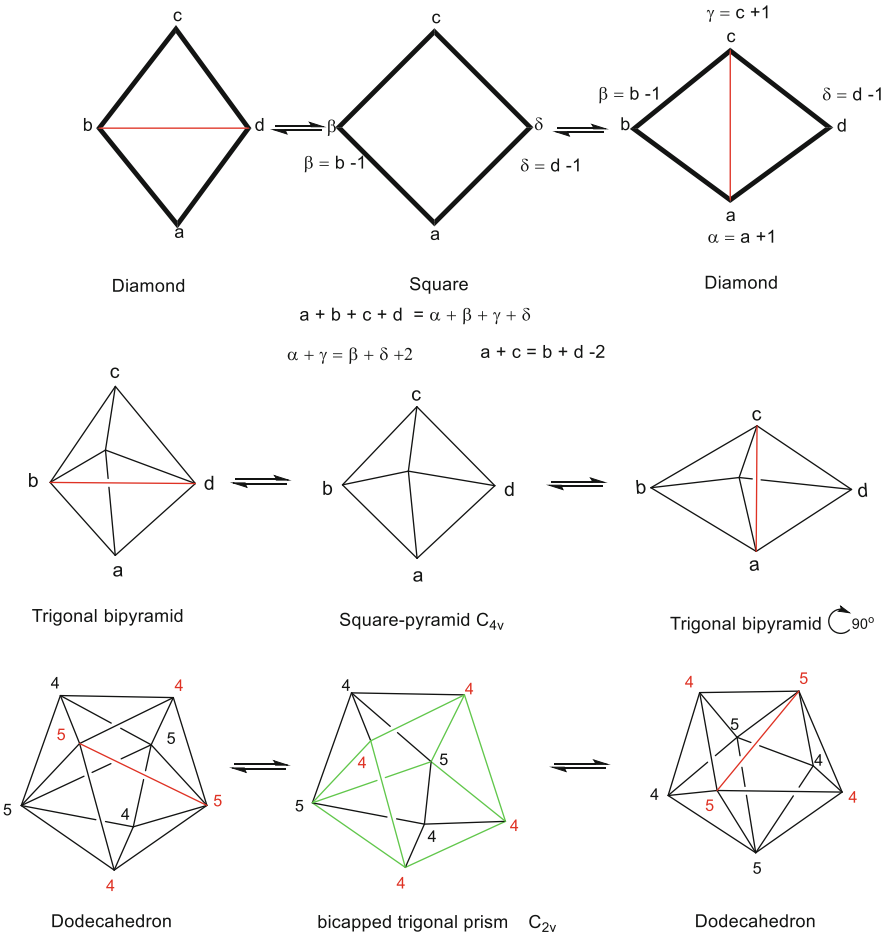

Fig. 23 Definition and specific illustrations of the diamond-square-diamond rearrangement pathway and the connectivities of the vertices involved. The bonds in red represent the bond broken and made in the DSD process those in green the trigonal prism

a considerable intellectual challenge since there was no precedence which could be adapted from organic chemistry.

In the 1960s Lipscomb proposed a general mechanism for the rearrangements of deltahedral borane structures [137–140]. It provided a conceptual basis for understanding the fluxional behaviour of some of the $[B_nH_n]^{2-}$ anions and the thermally induced isomerisation of the isoelectronic carboranes $[C_2B_nH_{n+2}]$ ([141–144] and references therein provide an entry into the relevant experimental literature). Lipscomb focussed attention on two adjacent triangular faces of the deltahedra and proposed that the diamond-square-diamond (DSD) rearrangement process, illustrated in Fig. 23 to explain such skeletal rearrangements. If the bond shared by the two triangular faces of the deltahedron is broken a square or rhombic face is

generated. When a new bond is made between the alternative vertices of the square a new diamond is reformed with an alternative combination of linked vertices. The rearrangement permutes the vertices although the bond length changes required are relatively small. The net result is a pseudo-rotation of the initial deltahedron by 90°. Lipscomb was drawn to the DSD mechanism because relatively small motions of the atoms were required to achieve the isomerisation and he argued that such a least motion pathway would facilitate a low activation energy for the skeletal rearrangement. His insight arose from a disorder problem which occurred whilst solving the crystal structure of the bicapped square-antiprismatic $Cu_2B_{10}H_{10}$. Lipscomb calculated that four boron atoms remain in the same position and the other six boron atoms move only 0.4 Å when the two isomeric forms are interconverted. If the DSD process occurs at a frequency faster than the N.M.R. experiment because of a low activation energy, then only an average signal is observed for the ^{11}B nuclei. Even in those cases where the activation energy for the DSD mechanism was large the analysis proved useful for accounting for the isomers formed when the carboranes $[C_2B_nH_{n+2}]$ are heated and isomerise. In this context he realised that for symmetrical deltahedra and specifically the icosahedron and the octahedron a single DSD rearrangement does not reproduce the original deltahedron but a less symmetric deltahedron. Several simultaneous and concerted DSD processes, however, may provide an alternative least motion pathway for interconverting isomeric forms. Specifically, he proposed that the formation of isomeric forms of icosahedral $[C_2B_{10}H_{12}]$, which required temperatures in excess of 450°C, could be explained by the concerted multiple DSD processes shown in Fig. 24. The figure also illustrates how the octahedron may be converted into a bicapped tetrahedron with a single DSD pseudo-rotation, but into trigonal prism as a result of a triple concerted DSD mechanism.

Alternative diamond combinations may be chosen for deltahedra where all the vertices do not have the same connectivities. Not all single DSD moves regenerate the original deltahedron with permuted locations of the vertices. King [145–148] was the first to systematically explore the geometric restraints associated with the DSD mechanism in deltahedral $[B_nH_n]^{2-}$. Although the DSD geometric methodology identified possible least-motion pathways, it did not evaluate the quantum mechanical effects which result from the evolution of molecular orbitals as the DSD process proceeds. The Woodward Hoffmann rules showed that the activation energies of pericyclic organic reactions are greatly influenced by the specific details of the stereochemistry of the rearrangement pathways and demonstrated that symmetry forbidden orbital crossings greatly influence their activation energies. Orbital crossings also play an important role in the DSD rearrangements of deltahedral borane anions [149–162]. King's graph theoretical and topological analysis [145–148] suggested that $[B_5H_5]^{2-}$, $[B_8H_8]^{2-}$, $[B_9H_9]^{2-}$ and $[B_{11}H_{11}]^{2-}$ may rearrange to an identical deltahedron via a single DSD pathway, but experimental and theoretical studies established that although $[B_8H_8]^{2-}$ and $[B_{11}H_{11}]^{2-}$ are indeed highly fluxional $[B_5H_5]^{2-}$ and $[B_9H_9]^{2-}$ are stereochemically rigid at ambient temperatures [140–144]. Theoretical analyses have demonstrated that this rigidity results because the DSD process for $[B_nH_n]^{2-}$ with $4p + 1$ ($p = 1, 2, \ldots$) is symmetry forbidden

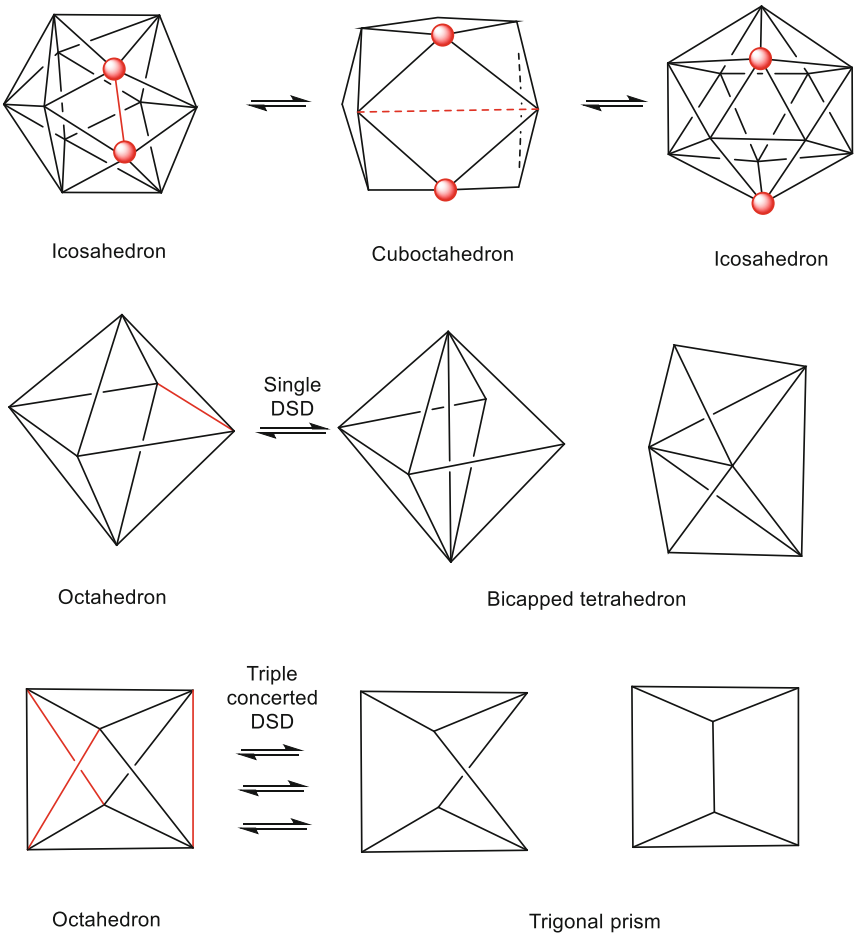

Fig. 24 The effect of a multiple DSD process for interconverting an icosahedron into a cuboctahedron. The consequences of a single DSD process on an octahedron which results in a bicapped tetrahedron, and a triple DSD process which interconverts an octahedron into a trigonal prism

because of an orbital crossing in the C_{4v} transition state, i.e. the Woodward Hoffmann principle of the conservation of orbital symmetry applies to these molecules which have spherical geometries in the same way that had been established previously for organic pericyclic reactions [149–163]. These orbital crossings involve the tangential L^{π} molecular orbitals defined by Stone's tensor surface harmonic theory. Gimarc [149–151], McKee [153–155] and Wales and Stone [160] have analysed the symmetry implications of these DSD rearrangements (see also [158–163]). Alternative pathways not based on the DSD process have also been identified in these theoretical studies and especially those addressing rearrangements of carboranes where the activation energies are significantly higher [152–157].

Although Lipscomb focussed his attention on the rearrangements in polyhedral molecules, the methodology was also developed to analyse possible rearrangement pathways in co-ordination compounds where deltahedral geometries were frequently used to define the ligand polyhedron although the atoms are not linked by bonds. Muetterties [164–166] who was very involved in studying the rearrangements of $[B_nH_n]^{2-}$ by N.M.R. extended his knowhow of the DSD mechanism to co-ordination compounds. He made inorganic chemists more aware of the wide range of coordination compounds which were stereochemically non-rigid and he identified co-ordination compounds which are described by deltahedral co-ordination polyhedral and suggested alternative pathways for their rearrangement [164–166]. Many complexes with co-ordination numbers greater than 6 are stereochemically non-rigid because simple small ligands, e.g. H and F, do not provide a rigid co-ordination polyhedron and may move in a concerted manner around the co-ordination sphere whilst maintaining strong radial bonds to the central metal [164–166]. These studies led to the re-evaluation of alternative mechanistic pathways which complemented those defined by the DSD rearrangements of the ligand co-ordination polyhedron. Muetterties was very influential in developing the Bürgi and Dunitz reaction co-ordinate mode of analysis to provide frozen frames of the rearrangement pathways of co-ordination compounds based on structural data [2, 164–175]. The group theoretical and symmetry implications of orbital symmetry effects associated with DSD pathways in polyhedral and co-ordination molecules have also been discussed in Refs. [159–163, 176–179]. These studies are relevant to gold clusters which require an ambiguous description between co-ordination compounds and polyhedral cages.

6.2 *Orbital Symmetry Constraints for Gold Clusters*

The gold clusters provided the first examples of skeletal isomerism in 1984 and led to the definition that such clusters have identical stoichiometries but with different skeletal geometries in the solid state [44, 45]. Later the definition was extended to clusters which share the same number of skeletal electron pairs although they do not have identical ligands [180–182]. A more recent review by Russel, Seco and Segales [102] has defined three types of related isomeric possibilities: skeletal, positional and ligand isomerism in cluster chemistry. They concluded that when skeletal isomers are obtained from a reaction then crystals may be obtained by changing the counter ion, solvent or rate of crystallisation. In addition, they noted that small changes in the steric or electronic effects may result in the preferential crystallisation of one of the isomers. The versatility of $AuPR_3$ fragment, which is *isolobal* with H, and the unsaturation of 16 electron platinum centres encourage the formation of skeletal isomers and the many examples of this phenomenon were noted [98, 106]. Dyson [103] has reviewed rearrangements which result as a consequence of ligand addition and elimination reactions and discussed their importance in catalytic processes.

The gold clusters do not conform to the structure/bonding generalisations developed for boranes, carboranes and metal carbonyl clusters in the early 1970s [5] and often have multiple isomeric structures for isoelectronic clusters. These result from subtle changes in the electronic and steric properties of the ligands. The denticity and bite angles of the polydentate ligands also play an important role in influencing the observed geometries in the solid state. Although there is no reason why the gold clusters should follow the same pattern of behaviour established for $[B_nH_n]^{2-}$ anions, it is pertinent to examine whether the DSD mechanism provides a useful basis for classification and interpretation.

The fluxional behaviour of higher nuclearity gold clusters has been recognised since the 1970s [3, 4, 13–21] but detailed analyses have been limited to rather unspecific statements suggesting that relatively minor movements of the gold atoms can result in facile rearrangements. This section tries to identify plausible intramolecular rearrangement pathways for gold clusters in addition to DSD. The analysis also makes use of conclusions derived from the bonding model developed above. This combined approach explores those processes which exchange all the gold-phosphine fragments and discards those which limit the exchange to sub-group of atoms within the cluster. It is possible to exchange all the gold atoms by combining several individual rearrangement steps, which involve different sub-groups, sequentially as long as all the individual steps have a low activation energy. Our analysis utilises the extensive structural database on gold clusters to benchmark the proposed pathways. This methodology draws on the Dunitz and Bürgi's structural correlation method [2, 165–169] which uses extensive structural data to track probable reaction pathways for rearrangements and nucleophilic reactions. This methodology was used to great effect for classifying the structures and rearrangement and structures of co-ordination compounds by Muetterties [164–172]. Orpen and Salter have reported a structural correlation analysis of heterometallic gold clusters of the platinum metals [98, 106]. They examined possible rearrangement pathways for M_3Au_2 cluster cores based on 16 crystal structures and concluded that the DSD mechanism shown in Fig. 25 was more consistent with the data than the alternative turnstile mechanism. The homoleptic gold clusters have a more limited database and so are less definitive. The basic premise is that if there are several structures with the same skeletal electron count and the potential energy surface is soft the structures represent local minima which give pointers to possible intermediates along the rearrangement co-ordinate.

The potential implications of orbital symmetry effects on polytopal rearrangements of homoleptic gold clusters are illustrated in Fig. 26, which also illustrates the relevant skeletal molecular orbitals for the rearrangement of a trigonal bipyramidal cluster via a DSD mechanism. The corresponding rearrangement for $[B_5H_5]^{2-}$ has been shown to be forbidden because of an orbital crossing involving the surface molecular orbitals derived from the p^{π} surface atomic orbitals [149–152, 156–163]. The corresponding rearrangement for the $[Au_5L_5]^{+}$ is also symmetry forbidden because the orbital crossing involves components of the incomplete P^{σ} subshell as shown in Fig. 26 rather than L^{π}/L^{π} surface mos. The topological feature underlying this orbital crossing results because the trigonal-bipyramid and

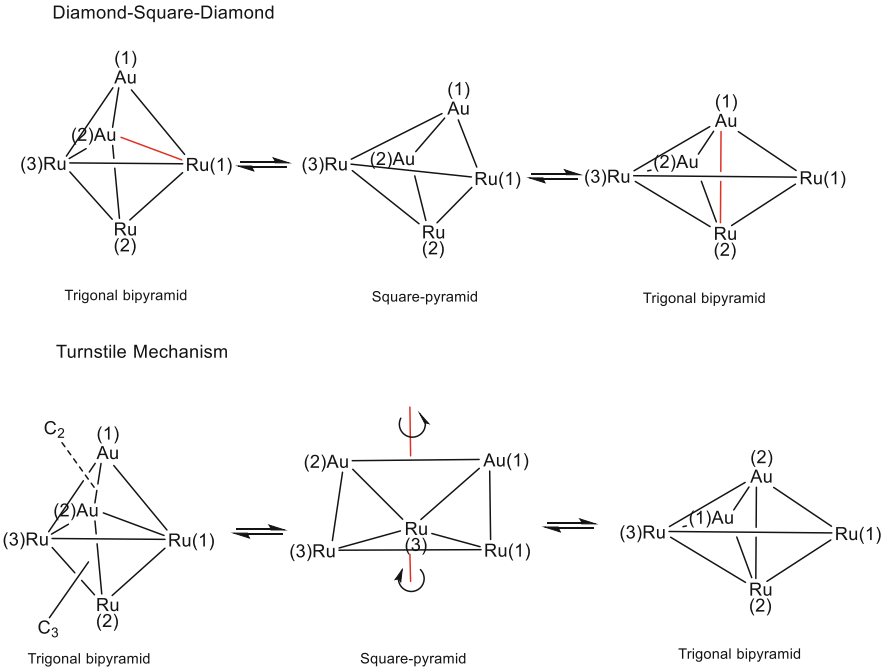

Fig. 25 DSD and turnstile mechanisms for the rearrangement of Ru_3Au_2 clusters

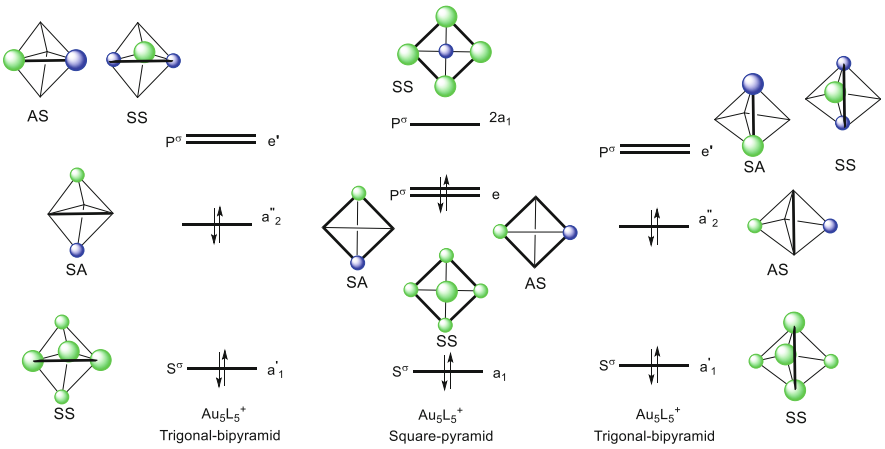

Fig. 26 DSD mechanism for the trigonal-bipyramidal $[Au_5L_5]^+$ cluster which proceeds through a square-pyramid

square-pyramid represent alternative prolate and hemi-spherical topologies and the DSD rearrangement causes a reversal of orbital energies of the components of the P^σ subshell. For the corresponding $[Au_5L_5]^{3+}$ cluster the pathway is symmetry allowed

because the $\{S^{\sigma}\}^2$ closed shell correlates along the reaction co-ordinate for the DSD rearrangement. A similar line of reasoning suggests that the trigonal bipyramidal cluster with an $\{S^{\sigma}\}^2\{P^{\sigma}\}^6$ ground state would similarly follow a symmetry allowed DSD pathway. Clusters with partially filled $\{P^{\sigma}\}^2$ and $\{P^{\sigma}\}^4$ sub-shells are allowed only if the same topology is maintained along the rearrangement pathway, i.e. maintain prolate or oblate spheroidal topologies along the pathway. Pathways which involve prolate → oblate → prolate, prolate → spherical → prolate, oblate → prolate → oblate and oblate → spherical → oblate would be orbitally **forbidden**, but prolate → prolate, oblate → oblate hemi-spherical → hemi-spherical and spherical → spherical are **allowed** processes.

The approach may be illustrated by considering a specific example, viz $[Au_6(PPh_3)_6]^{2+}$ which has the bitetrahedral edge sharing geometry illustrated in Fig. 27. In solution $^{31}P\{^1H\}$ N.M.R. spectrum at −40°C of this cluster is consistent with the observed solid state D_{2h} structure, but on raising the temperature the peaks coalesce and a single line is observed at room temperature. The solid state $^{31}P\{^1H\}$ N.M.R. spectrum is also consistent with the crystal structure and the (4:2 pattern) and chemical shifts replicate those observed in solution at low temperatures [43, 76]. Since the N.M.R. experiments suggest that all the phosphine ligands exchange this rules out some possible skeletal rearrangements. For example, a rearrangement which keeps the central pair of gold atoms (shown in red) stationary and has the outer atoms (shown in green in Fig. 27) rotate in opposite directions would not exchange all gold atoms and maintain the 4:2 pattern throughout and would not average the two symmetry distinct locations.

The conversion of the bitetrahedron into a bicapped tetrahedron shown at the top of Fig. 27 requires the formation of a new bond in the northern hemisphere of the molecule as shown in Fig. 27a, b and creates three tetrahedra sharing faces. This bicapped tetrahedral structure has been observed in $[Au_6(xant\text{-}phos)_6]^{2+}$ (see Fig. 2) but it does not exchange all the gold environments. If the two bonds shown in red in the bicapped tetrahedron are broken, then a bi-edged-tetrahedron results (27c) and this structure has been observed in $[Au_6(dppp)_4]^{2+}$ (see Fig. 2). If these edge bridging gold atoms pivot to form an alternative bicapped tetrahedron (27d), it no longer has both red gold atoms in 5-connected sites. Reforming a bitetrahedron (27e) from 27d results in an exchange of the central and peripheral gold atoms and when repeated results in the interchange of al gold atoms. Consequently, the sequence of reactions at the top of Fig. 27 provides a mechanism for exchanging all gold atoms, albeit by a rather circuitous route. It does nevertheless incorporate intermediates which have a precedence in the library of known structures and could reasonably represent minima in the soft potential energy surface.

The second row in Fig. 27 provides an alternative mechanism whereby the bitetrahedron (27f) is converted into a high symmetry octahedron (27g) by breaking the central Au–Au bond and making bonds between the two pairs of points of the tetrahedra connected by red dotted lines. The intermediate octahedron may reform to a bitetrahedron by reversing the bond making and breaking processes in the alternative axial directions of the octahedron 27g 27h. Early theoretical calculations on gold clusters indicate that an octahedral gold cluster would be an open shell molecule

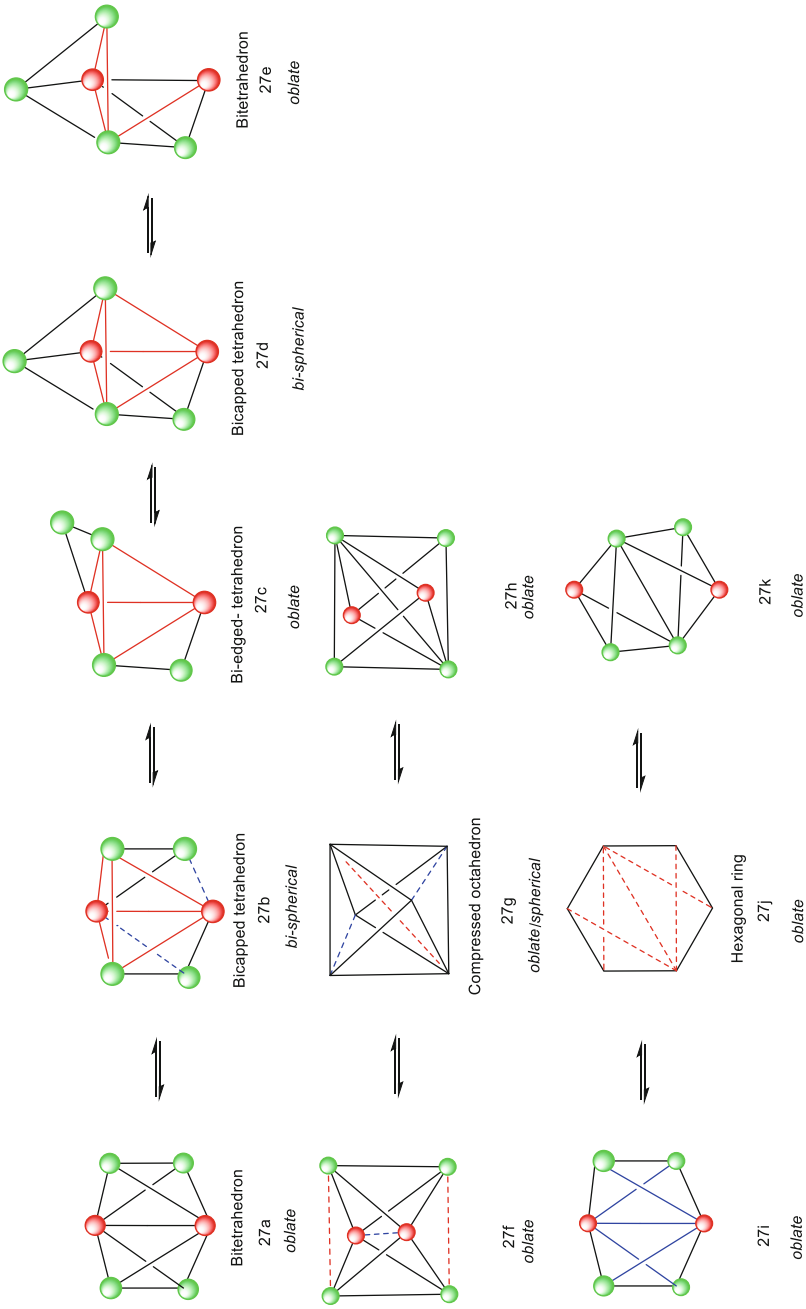

Fig. 27 Possible alternative mechanisms which enable the interchange of all nuclei in the bitetrahedron $[Au_6(PPh_3)_6]^{2+}$ cluster

and suggested that an octahedral $[Au_6(PPh_3)_6]^{2+}$ does not have a closed shell structure [24] but an elongated D_{2h} octahedron of gold atoms has been observed in the borane compound illustrated in Fig. 2. Nevertheless, a regular octahedron is unlikely to represent the transition state but the rearrangement may follow a path which skirts the around this potential energy surface.

The third possible mechanism involves forming a hexagonal ring Fig. 27i, j, by simultaneously breaking five bonds in Fig. 27i. This geometry is not required to be planar and indeed the centred chair arrangement of six gold atoms is commonly observed in phosphine gold clusters. The D_{3d} symmetry permits an alternative permutation of gold atoms when the bond making processes are reversed as shown in 27k. The last two mechanisms shift both gold atoms of the common bond in the bitetrahedron to *trans*-positions in the outer plane of atoms whereas the first one transfers only one of the atoms to the outer plane. This analysis suggests the possibility of distinguishing the mechanisms by variable temperature N.M.R. experiments and may also be explored further using theoretical calculations. The third rearrangement mechanism is the most plausible because it achieves a rearrangement of the isomers using the minimal number of steps and the same oblate topology is maintained throughout, whereas the second mechanism proceeds through a spherical octahedron.

The $[Au_7(PPh_3)_7]^+$ cluster has the pentagonal bipyramidal geometry shown in Figure 2. The skeleton has the same idealised D_{5h} symmetry as $[B_7H_7]^{2-}$ but has a very compressed oblate structure which results from the compression of the deltahedron along the fivefold axis. The apical gold atoms are connected by the shortest bond (2.584(4) Å; average Au_{axial}–Au_{equat} 2.82(8) Å ; Au_{equat}–Au_{equat} 2.95 (6) Å) [39, 141, 142]. The solution $^{31}P\{^1H\}$ N.M.R. spectrum at room temperature shows only a single resonance suggesting a fluxional process which interchanges the equatorial and axial gold atoms at a fast rate on the N.M.R. timescale, but the solid state N.M.R. is consistent with the solid state structure and shows two ^{31}P environments [39]. In contrast $[B_7H_7]^{2-}$, in common with $[B_9H_9]^{2-}$ and $[B_{10}H_{10}]^{2-}$, is stereochemically rigid and is not fluxional on the N.M.R. timescale [141, 142]. This property has been rationalised on geometric and orbital symmetry considerations. This reinforces the view that the different bonding in gold and borane clusters is reflected in their different fluxional properties. Figure 28 illustrates a DSD pathway involving two adjacent faces in the northern hemisphere which results in a capped octahedron with the cap in the southern hemisphere. A subsequent DSD involving two adjacent faces from the cap and the octahedron results in pseudo-rotated pentagonal bipyramid with apical-equatorial atom interchanged (i.e. red green interchange in the figure). For boranes it is geometrically and orbitally symmetry forbidden and accounts for the rigidity of $[B_7H_7]^{2-}$. The intermediate capped octahedron requires a significant lengthening of the short connecting bond between apical atoms and involves a significant change in topology from oblate to spherical.

The second mechanism illustrated in Fig. 28 recognises the short Au–Au axial bond in $[Au_7(PPh_3)_7]^+$ and the relatively long surface Au–Au bonds. The rearrangement may be viewed as the five equatorial atoms pivoting about this bond and opening one of the edges of the pentagon to enable one of the initial apical

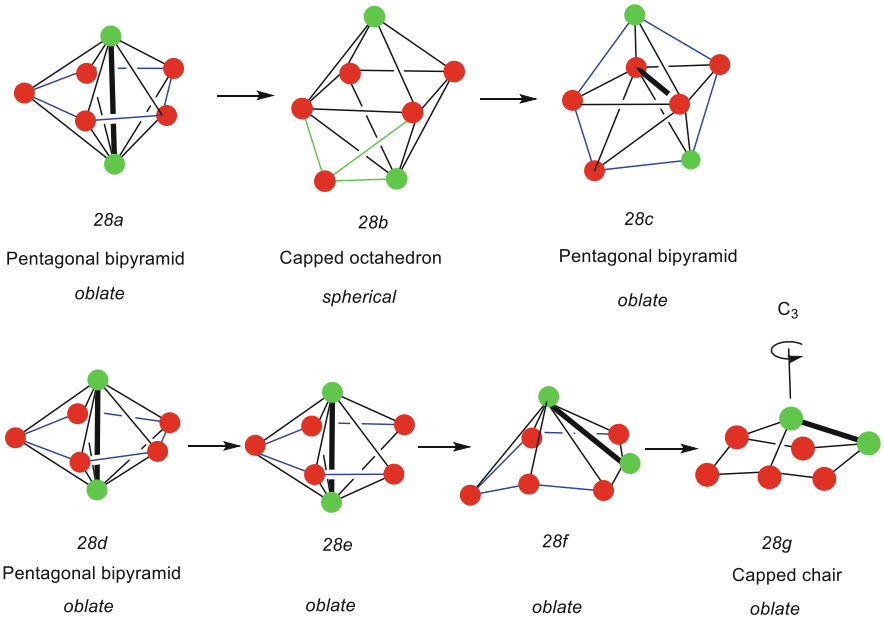

Fig. 28 Plausible alternative mechanisms which enable the interchange of nuclei in the $[Au_7(PPh_3)_7]^+$ cluster, which has a squashed pentagonal bipyramidal geometry. The DSD pathway for the top example involves three equatorial atoms and the northern axial atom

gold atoms to take up an equatorial site. The resulting capped chair of seven gold atoms shown in the figure is a common feature of gold clusters and is reminiscent of the hemi-spherical clusters shown in Fig. 21. The resulting intermediate has C_{3v} symmetry and if the process is reversed utilising one of the alternative chair gold atoms related by the C_3 axis then a new pentagonal bipyramid is formed which has one green and one red apical atom. This results in a different permutation of nuclei compared to the first example and more detailed N.M.R. studies have the potential of distinguishing between these alternative rearrangement pathways [168–172]. The sequential use of this pathway would result in the scrambling of all the gold atoms after several cycles. The second pathway maintains an oblate topology throughout and consequently is favoured on orbital symmetry considerations. Figure 29 illustrates the molecular orbitals for the pentagonal bipyramid and the capped hexagonal chair and suggests they can be interchanged without any forbidden orbital crossings.

It was noted above that $[Au_9\{P(C_6H_4OMe)_3\}_8](NO_3)_3$ may be co-crystallised as the crown and icosahedral girdle isomers and their crystallographic structures are illustrated in Figs. 4, 21, and 22. Solid state N.M.R. experiments have confirmed their independent structures. In solution the two isomers have identical spectra even at low temperatures, which suggests that these isomers interchange rapidly. The atom movements required to interchange these isomers are shown in Fig. 30. A four-atom metal sequence in the peripheral crown rearranges into a butterfly arrangement. Figure 31 summarises geometric transformations possible for an octagonal ring of

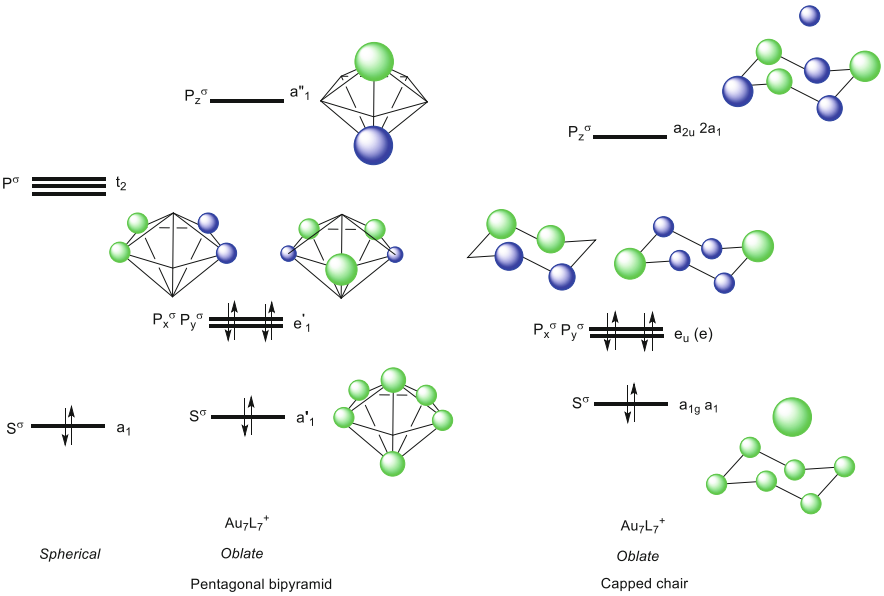

Fig. 29 Molecular orbitals for $[Au_7L_7]^+$ with pentagonal bipyramidal and capped chair geometries

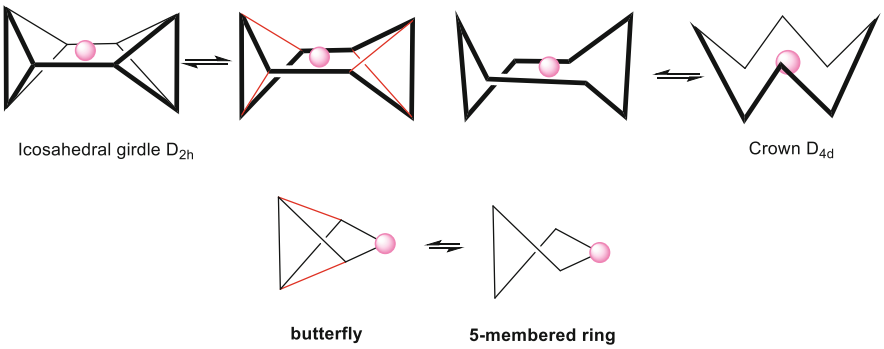

Fig. 30 Interconversion of the crown and icosahedral girdle isomers of $[Au_9\{P(C_6H_4OMe)_3\}_8](NO_3)_3$

gold atoms with an interstitial gold atom. For clarity it is represented as a planar projection of the octagonal crown and illustrates how the crown may be converted into alternative structures based on butterfly sequences shown in Fig. 30. Isomers of bicapped square-antiprismatic gold clusters $[Au_{11}\{PMePh_2\}_{10}]^{3+}$ have been shown to have structures lying on this putative reaction pathway (see Fig. 31). This figure also shows the possibility of forming a basket structure observed in crystals of $[Au_9(SCN)_3\{PCy_3\}_5]$. Therefore, there are representative experimental structures for all four possible intermediates shown in Fig. 31 and confirm the plausibility of

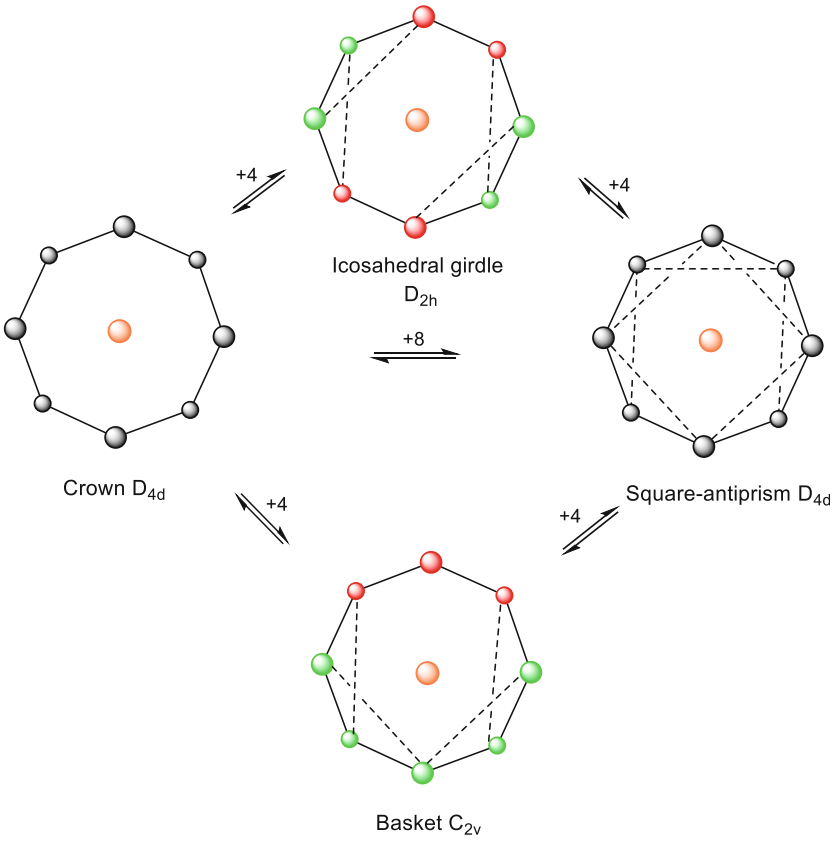

Fig. 31 Possible mechanism for polyhedral rearrangements which account for the N.M.R. spectra and the geometries observed for nine atom gold clusters having **sec** = 6. The crown geometry can be transformed into a square-antiprism by shortening the distances between atoms in the two square-planes. Intermediate structures with D_{2h} and C_{2v} symmetry may be generated by shortening only 4 of the inter-gold contacts and simultaneously rotating two of bonds (separated by two or three bonds) in the initial structure clockwise.

the cycle providing steps with low activation energies for averaging all the peripheral gold nuclei.

The Au_9 clusters discussed above share oblate topologies, but the known Au_{11} clusters are characterised by spherical skeletal geometries, i.e. bicapped square-antiprism, a bicapped crown and a capped hemi-icosahedron with C_{3v} symmetry shown in Figs. 5, 21, and 22. The spherical topologies are consistent with their $\{S^{\sigma}\}^2\{P^{\sigma}\}^6$ closed shell electronic configurations.

The capped hemi-icosahedron has C_{3v} symmetry and has three rhomboidal faces radiating from the single gold atom on the C_3 axis. Figure 31 illustrates how a square-antiprism and the crown may be inter-connected by concerted movements of all eight metal atoms whilst maintaining D_{4d} symmetry and an oblate topology. Their

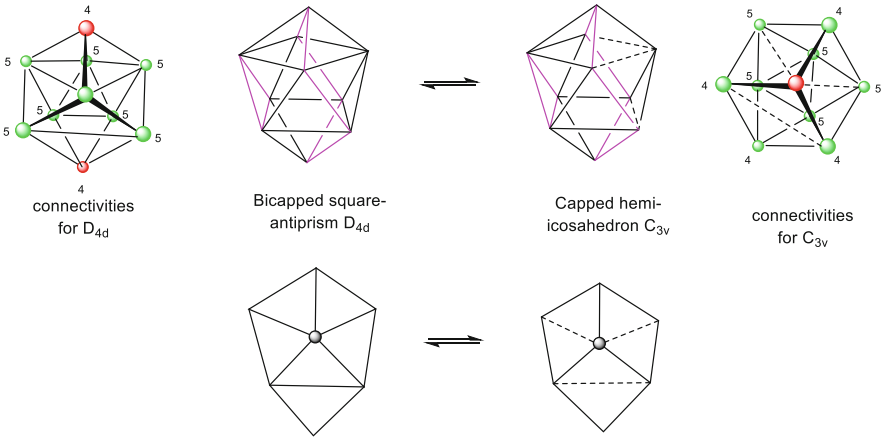

Fig. 32 Rearrangement of bicapped square-antiprism and a capped hemi-icosahedron

bicapped derivatives have been observed in the isomers of $[Au_{11}(PMePh_2)_{10}]^{3+}$ shown in Fig. 5. Figure 32 illustrates the changes in bond connectivities which are required to interconvert a bicapped square-antiprism and a capped hemi-icosahedron. If the three rhomboidal faces of the C_{3v} cluster are transformed into 6 triangular faces by concerted square-diamond transformations, then a bicapped square-antiprism results. This is equivalent to three simultaneous DSD processes. These clusters both have spherical geometries and their closed shell configurations are $\{S^{\sigma}\}^2\{P^{\sigma}\}^6$ and therefore the transformation interconverting them is not symmetry forbidden. The eight symmetry-equivalent equatorial vertices of the square-antiprism provide a pathway for exchanging the all ten vertices in the initial C_{3v} structure.

The solution $^{31}P\{^1H\}$ N.M.R. spectra of the icosahedral $[Au_{13}X_4(PMe_2Ph)_8]Y$, (X = Br, I, SCN; Y = Br, I, SCN, PF_6, BPh_4) and $[Au_{13}Cl_2(PMe_2Ph)_{10}][PF_6]_3$ are consistent with isomeric structures shown in Fig. 7 [51]. The observation that these icosahedral gold structures are stereochemically rigid on the N.M.R. timescale suggests that the alternative cuboctahedral structure is significantly less stable than the icosahedron in agreement with theoretical calculations. Both polyhedra are characterised by $\{S^{\sigma}\}^2\{P^{\sigma}\}^6$ closed shell electron configurations, but since the icosahedron has six more edges this leads to a significant increase in the total stabilising tangential bonding interactions.

The analysis illustrates how the Jellium model and a molecular orbital analysis derived from the Stone approach may be used to classify the wide ranges of structures observed for the gold phosphine cluster compounds. It also provides a sound basis for proposing plausible mechanisms for the interchange processes which occur in solution rapidly on the N.M.R time scale. The steric demands of the ligands play a very important role in diversifying the range of structures observed by weakening the tangential interactions between the gold atoms. They diminish the significance of the generalisation associated with boranes whereby the deltahedra

represent significant global minima on the potential energy surface. The most plausible mechanisms involve either simultaneous DSD processes or concerted bond making process involving centred hexagonal or octagonal rings.

6.3 *Polytopal Rearrangements in Other Metal Cluster Compounds*

In the great majority of carbonyl clusters of the earlier transition metals the carbonyl ligands migrate between the metal atoms by making and breaking bridge bonds. For carbonyls the terminal → bridge → terminal transformations are concerted and follow facile pathways with small activation energies for the individual steps across the soft potential energy surface [182–184]. In solution the majority of these migrations can be modelled in terms of ligand migrations over the surface of a rigid metal cage [182–184]. There are nevertheless some clusters where the carbonyl and metal envelopes both undergo rearrangements, leading to polytopal rearrangements of the ligand shell and the metal skeleton. The first examples of carbonyl clusters undergoing metal skeletal rearrangements were defined for rhodium and platinum which have isotopes with I = ½ nuclear spins and therefore the effects of the fluxional processes can be detected by changes in the spin multiplicities and line widths of the N.M.R. spectra [184, 185]. If the metal nuclei do not have isotopes which can be observed using this technique, then the skeletal rearrangements cannot be investigated directly and may appear invisible. In favourable circumstances evidence can be obtained through other nuclei with I = ½ which retain their bonds to specific metal atoms during the rearrangement processes.

High nuclearity rhodium clusters were observed to undergo polyhedral rearrangements on the NMR timescale at ambient temperature by the Union Carbide group led by Jose Vidal in the 1970s [186–191] and included $[Rh_{10}E(CO)_{22}]^{n-}$ (E = P or As, $n = 3$; E = S, $n = 2$) and $[Rh_9E(CO)_{21}]^{2-}$ (E = P or As) which have capped and bicapped square-antiprismatic geometries illustrated in Fig. 33. The presence of the interstitial ^{31}P (I = ½) nucleus and the coupling to the ^{103}Rh nuclei (I = ½) on the surface of the cluster provided ideal conditions for establishing that the rearrangement is intramolecular and results from the rhodium nuclei migrating around the phosphorus atom whilst remaining in bonding contact. The limiting low temperature N.M.R. spectra of these clusters agrees with the structures observed in the solid-state by single crystal X-ray diffraction (see Fig. 33), but at higher temperatures all the Rh atoms are observed as one averaged chemical environment. The $^{31}P\{^1H\}$ N.M.R. spectrum of $[Rh_9P(CO)_{21}]^{2-}$ showed the presence of a ten-line multiplet centred at 282.3 ppm and it becomes more complex as a result of inequivalent rhodium environments upon decreasing the temperature from +40 to −80°C. The square-diamond rearrangement of the rhodium skeleton which leads to a tricapped trigonal-prism is illustrated in Figs. 32 and 33 and accounts for these

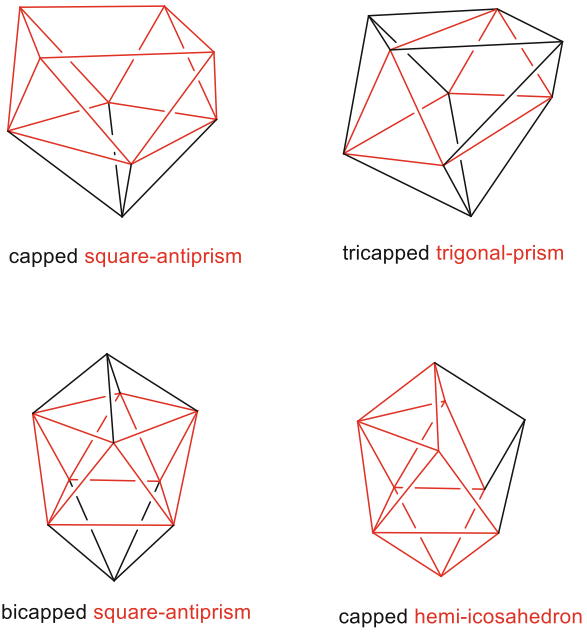

Fig. 33 The capped and bicapped square-antiprisms observed in the rhodium clusters $[Rh_9E(CO)_{21}]^{2-}$ (E = P or As) and $[Rh_{10}E(CO)_{22}]^{n-}$ (E = P or As, $n = 3$; E = S, $n = 2$) are shown on the left-hand side of the figure. Possible intermediates which account for the observed skeletal rearrangements are shown on the right-hand side

observations since the latter could rearrange back using the other two edges of the trigonal prism parallel to the threefold axis to create alternative permutations of the rhodium atoms in the initial capped square-antiprism. Similarities between the infrared spectra as a nujol mull and in solution negate the possibility of a change in the structure of the cluster on dissolution in the N.M.R. solvent. In common with the majority of known carbonyl clusters the carbon monoxide ligands simultaneously undergo a fluxional process around the surface of the rhodium skeleton. The group 14 Zintl anion clusters $[M_9]^{2-}$ (M = Sn, Pb) also have a capped square-antiprismatic geometries and exhibit similar fluxional characteristics and presumably also rearrange via a tricapped trigonal prism as shown in Fig. 33 [192].

The bicapped square-antiprismatic clusters $[Rh_{10}E(CO)_{22}]^{n-}$ (E = P or As, $n = 3$; E = S, $n = 2$) have also been structurally characterised and the $^{31}P\{^1H\}$ N.M.R. spectrum of the phosphide compound has a symmetric 11 line pattern at ca 40°C but more complex spectra at low temperatures consistent with the idealised D_{4d} structure with rhodium environments in the ratio of 2:8 [187, 188]. The isostructural *closo*-$[B_{10}H_{10}]^{2-}$ anion shows no evidence of skeletal fluxionality on the N.M.R. timescale and this has been attributed to the orbitally forbidden nature of the appropriate diamond-square-diamond rearrangement for a bicapped square-antiprism [159–163]. A double DSD process which results in two open faces sharing an edge is symmetry allowed but is not utilised because of the high barrier. The fluxional process for the rhodium anion may proceed as a result of the process shown in Fig. 32 and has been proposed to account for the fluxionality of the centred gold clusters, $[Au_{11}X_3(PR_3)_7]$. It proceeds via a capped hemi-icosahedral cluster which

may be formed from the bicapped square-antiprism by three Rh-Rh bond lengthening displacements. The skeleton in the icosahedral cluster $[Rh_{12}Sb(CO)_{27}]^{3-}$ has idealised I_h symmetry in the crystalline state and its N.M.R. spectrum is consistent with a fluxional polytopal rearrangement involving the carbonyl ligands. The high symmetry of the metal framework means that skeletal rearrangements of the metal cluster cannot be detected in the N.M.R. experiment [190].

The first example of a facile intramolecular skeletal rearrangement of homoleptic metal carbonyl clusters had resulted from a collaboration between Paulo Chini, Larry Dahl and Brian Heaton [193–197]. Booth and Chatt had observed that when base was added to $[PtCl_2(CO)_2]$ a range of brightly coloured solutions were observed and Longoni and Chini established that the compounds contained related $[\{Pt_3(CO)_6\}_m]^{2-}$ anions (m = 2, 3, 5, and 9) based on stacked $[Pt_3(\mu\text{-}(CO)_3(CO)_3]$ triangular clusters as illustrated in Fig. 34. These structures shown were determined by the Dahl group. The stacking does not result in a perfect column because the triangles are not perfectly eclipsed but show a slight twist perpendicular to the threefold symmetry axis. The metal-metal bonds within the triangular units are significantly shorter than those between the layers and suggest that triangular clusters may rotate relative to each other in solution. Since the oligomers bear the same 2-charge one may conclude that the column has multilayer bonding reminiscent of that established for $[Pt(CN)_4]^{2-}$. As the column grows the inter-triangle bonding becomes weaker and permits a rotation that would not be favourable for a trigonal prism. Elegant and detailed variable temperature ^{195}Pt and ^{13}C N.M.R. data have shown that platinum triangles undergo rapid rotations perpendicular to the C_3 axis which interconvert trigonal prismatic/antiprismatic moieties along the chain. Theoretical description of the bonding in these columnar clusters has been published by Hoffmann et al. [198]. ^{13}C and ^{195}Pt N.M.R. studies in solution established that for m = 3 the triangles not only rotate relative to each other but also interchange triangles between the columnar clusters. This added an additional dimension to that described above for the rhodium clusters which undergo only intramolecular skeletal rearrangements [183, 184].

More recent work [199–201] has demonstrated the possibility of functionalising the anionic Chini/Longoni platinum clusters using mono- and bi-dentate phosphine ligands. Structures and N.M.R. studies of the numerous compounds isolated have confirmed a high flexibility associated with the inter-triangular Pt−Pt interactions along the pseudo-C_3 axis. The overall trigonal prismatic structures present in the homoleptic clusters are readily deformed and transformed upon functionalisation. Such transformations result from both steric and electronic effects and may be described as local deformations along the conversion co-ordinate connecting the trigonal prism and octahedron. The structures $[Pt_9(CO)_{16}(dppe)]^{2-}$, $[Pt_9(CO)_{16}(R\text{-}dppp)]^{2-}$, $[Pt_{12}(CO)_{22}(PPh_3)_2]^{2-}$ and $[Pt_9(CO)_{16}(PPh_3)_2]^{2-}$ are represented in a simplified way in this figure. Conversion of the cage from trigonal-prismatic to octahedral was observed in $[Pt_6(CO)_{10}(dppe)]^{2-}$ and $[Pt_6(CO)_{10}(PPh_3)_2]^{2-}$. The reciprocal rotation of two trigonal prismatic units with the loss of a Pt−Pt contact was established for $[Pt_{12}(CO)_{20}(dppe)_2]^{2-}$. Taking a broader view these clusters represent a midpoint between the gold clusters and the

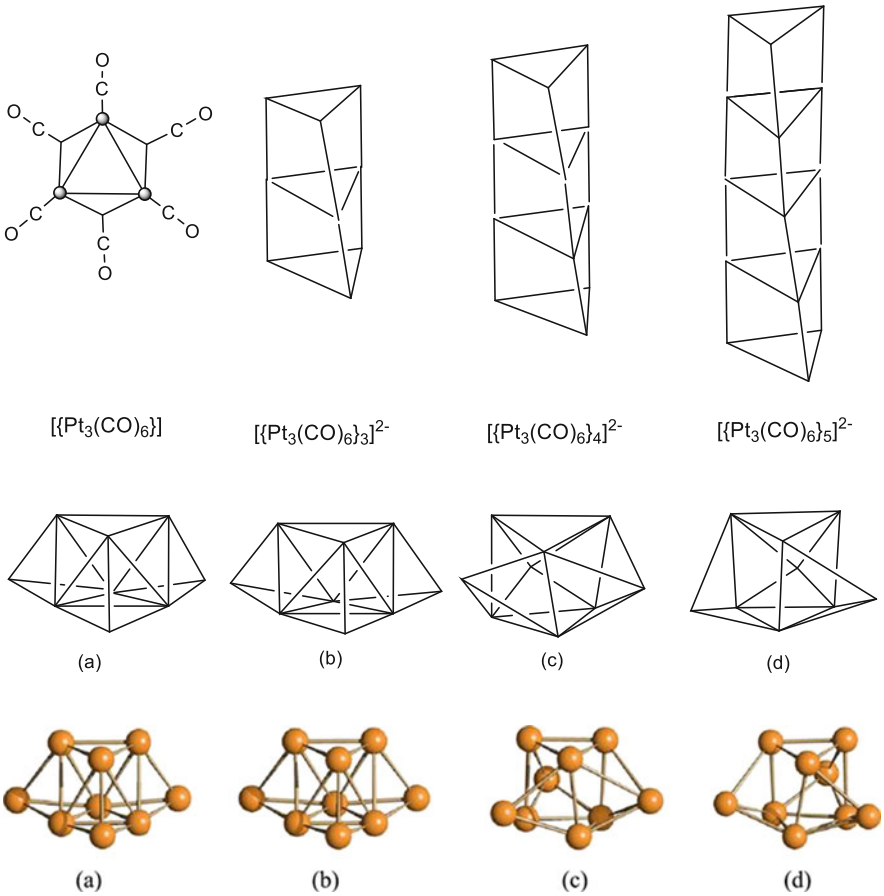

Fig. 34 Columnar clusters of platinum clusters $[\{Pt_3(CO)_6\}_m]^{2-}$ anions (m = 3, 4 and 5) and the tricapped octahedral and tricapped trigonal prism geometries observed for the central palladium cluster in $[HCo_{15}Pd_9C_3(CO)_{38}]^{2-}$. (**a**) to (**d**) indicate the way they define the transit between these high symmetry possibilities

more rigid carbonyl clusters of the earlier transition metals since the individual metal triangles remain rigid but intra- and inter- triangle motions lead to facile rotations and the transfer of triangles between the columnar clusters [199–201]. Skeletal isomerism has also been observed in the crystal structures of large molecular organometallic nanoclusters. Two isomers of the $[HCo_{15}Pd_9C_3(CO)_{38}]^{2-}$ nanocluster, referred to as TP-Pd_9 and O_h-Pd_9, have been structurally characterised by single-crystal X-ray crystallography as their organo-ammonium and phosphonium salts [202]. The cluster core of TP-Pd_9 is a tricapped trigonal prism, but a tricapped octahedron in O_h-Pd_9. The presence in the solid state of the O_h-Pd_9 or TP-Pd_9 isomers depends on the cation employed and/or the number and type of co-crystallised solvent molecules. Often, mixtures of the two isomers, within the

same single crystal or as mixtures of different crystals within the same crystallisation batch, are obtained.

References [202–210] provide more examples of skeletal isomerism which have been studied recently.

The last 20 years has resulted in the synthesis and characterisation of gold thiolato-clusters, e.g. $[Au_{38}(SR)_{24}]$, $[Au_{28}(SR)_{20}]$ and $[Au_{30}(SR)_{18}]$ [4, 65–67, 211] and has led to very high nuclearity clusters, e.g. $[Au_{102}(SR)_{44}]$ [212]. They are collectively described as molecular nanoclusters (NCs) to emphasise the step change which has marked the isolation of clusters with hundreds of atoms and thereby approach nano-metre dimensions. The smaller cone angles of the thiolato-ligands relative to organo-phosphines were important in facilitating this transition. Moreover, the combination of gold(I) atoms with thiolato- (SR^-) anions proved to be uniquely capable of self-assembling a spherical ligand shell with just the right dimensions and ligating properties to wrap around the central kernel of gold atoms. The spherical ligand is constructed from $[Au(SR)_2]^-$, $[Au_2(SR)_3]^-$ and $[Au_3(SR)_4]^-$ fragments which act like straps on the spherical surface and stabilise to the central gold kernel. The gold cluster located at the centre resembles the gold phosphine clusters described above and net charge follows the bonding model and electron counts introduced above. Many have a central icosahedral $[Au_{13}]^{5+}$ kernel with sec = 8 satisfying the closed shell $[S^{\sigma}]^2$ $[P^{\sigma}]^6$ [3, 4].

The thiolato- clusters have not been studied in detail by N.M.R. because neither Au or S have nuclei with I = ½ isotopes and consequently their dynamic properties are not as well defined. Nevertheless, several examples of skeletal isomerism have been established. This type of isomerism may prove to be important for understanding and design of gold new nanoclusters and their dynamic properties. Researchers in the field have identified three distinct mechanisms of structural isomerism (i.e. core isomerism, staple isomerism and complex isomerism) [3, 4]. The three-dimensional structures of NCs attracted considerable interest as nanoparticles with controlled structures are potentially useful for selectively detecting important bio-molecules [213–224]. This selectivity is enhanced if the NC is chiral. The first crystal structures of $[Au_{102}(SR)_{44}]$ and $[Au_{38}(SR)_{24}]$ revealed the intrinsic chirality of these clusters. This chirality arose primarily from the arrangement of the gold-thiolato- ligands on the surface of the cluster cores but other origins of asymmetry have been identified subsequently. Additional characterisation techniques, e.g. CD, VCD, N.M.R. and CPL confirmed the asymmetric and optical activity of CNCs (Chiral nano-metre clusters). Advances in synthetic methods and characterisation techniques have led to 50 distinct types of CNCs [213, 214]. Their chiral and optical properties have their origins in (1) the chirality transfer from chiral ligand; (2) the helical organic−inorganic interface, such as –SR–Au–SR– staples; (3) the asymmetric metal kernel and (4) the chiral arrangement of organic ligands [213, 214]. It is worth adding that these four bases of chirality are not mutually exclusive and a specific CNC may manifest optical properties representing the cumulative effect of multiple sources of chirality.

When achiral ligands are used to stabilize the clusters the resultant compounds are obtained as racemic mixtures. The separation of the enantiomers by HPLC

(high-performance liquid chromatography) was achieved and confirmed by the measurement of their CD spectra. Thermally induced inversion allows determination of the activation parameters for their racemisation. The inversion studies demonstrate that the gold–thiolate interface is anything but fixed and indeed suggest that it is rather flexible. N.M.R. spectroscopy has successfully probed the chirality of well-defined Au nanoclusters. The chiral $[Au_{38}(SCH_2CH_2Ph)_{24}]$ and nonchiral $[Au_{25}(SCH_2CH_2Ph)_{18}]$ nanoclusters have been used as benchmark examples of chiral and nonchiral gold nanoclusters, respectively. The single crystal X-ray diffraction of $[Au_{102}(SR)_{44}]$ in 2007 [212] provided an important stimulus for the development of nanoclusters of the coinage metals. The possible existence of chiral metal kernels among Au-GSH CNCs was initially proposed by Whetten et al. in 2000 but not established unambiguously by single-crystal diffraction studies [211].

Subsequently experimental results successfully proved that chiral ligands or helix staples could induce a chiral metal core [215–220]. The single-crystal diffraction study of $[Au_{52}(SR)_{32}]$ revealed that a DNA-like double-helical Au_{32} metal kernel was induced by four short $Au(SR)_2$ staples and eight long $Au_2(SR)_3$ staples, both arranged along a common helix direction [215]. In 2014 Wang et al. [216] reported $Au_{20}(PP_3)_4Cl_4$ nanoclusters whose chirality came from the intrinsically chiral metal kernel. The Au_{20} metal kernel has a centred Au_{13} icosahedron surrounded by a fan-like Au_7 motif in a helical arrangement but the racemic $[Au_{20}(PP_3)_4Cl_4]$ products available at that moment.

The separation of racemic clusters to obtain pure enantiomers proved to be challenging. Bürgi and co-workers achieved the enantio-separation of $[Au_{38}(SR)_{24}]$ [217, 218, 221] using HPLC. The enantio-separation of racemic $[Au_{40}(SR)_{24}]$, [217, 218] $[Au_{28}(SR)_{20}]$ [219] and $[Ag_{29}(SR)_{12}(PPh_3)_4]$ [220] was subsequently reported [218–220]. Ackerson *et al* reported a chiral ammonium bromide counterion induced phase transfer method that enantioenriched the left-handed and right-handed Au_{102} enantiomers in water and chloroform, respectively [221]. The enantiopure Au_{20} with an intrinsically chiral metal kernel has been separated using a supramolecular self-assembly method (α-cyclodextrin induced). Recently Zang *et al* achieved the enantio-separation of $[Ag_{30}(SR)_8\ (dppm)_6]$ NCs with helically arranged staples and chiral arrangement of ligands through the conglomerate crystallisation method in dimethylacetamide (DMAc) solvent [219]. Pasteur-like separation of silver nanocluster racemates by conglomerate crystallisation has also been reported [222–224].

7 Conclusions

Since the early part of the twentieth century chemists have used numerical rules as pedagogical aids and synthetic chemists found that they proved to be useful indicators for identifying possible new classes of compounds. The octet and 18 electron rules proposed by Lewis and Langmuir between 1916 and 1920 predated the development of the quantum mechanical description of the chemical bond. The

octet rule proved to be a cornerstone of both inorganic and organic chemistry for the subsequent 50 years especially after Pauling's quantum mechanical reformulation of Lewis' two electron covalent bond. Langmuir's 18 electron rule underwent a long period of hibernation as chemists developed the chemistries of the transition metals, lanthanides and actinides. Many of the compounds resulting from this research did not follow the 18 electron rule and its application was limited to transition metal carbonyls. The discovery of ferrocene in the 1950s propelled the growth of organometallic chemistry and led to an appreciation of the18 electron rule as a useful aid for synthesising a wide range of new molecular compounds.

The Hückel 4p + 2 rule for cyclic aromaticity was initially proposed in 1931 but had little influence on the development of organic chemistry until the 1950s when molecular orbital ideas began to percolate into the subject. The development of the Woodward-Hoffmann Rules in the early 1960s resulted in an important change in the way organic chemistry was practiced and taught. Its success was based on an appreciation of how the energies of orbitals in molecules evolved during the course of the reaction and the important role symmetry played in the process. The stereochemistries of pericyclic organic reactions were controlled by the electron delocalisation in cyclic transition states.

The valence shell electron pair repulsion theory (VSEPR) provided a three-dimensional interpretation of molecular inorganic compounds. It proposed that bonds and lone pairs are both stereochemically active and defined a polyhedron which locates them as far apart as possible and thereby minimise electron-electron repulsions. The polyhedral skeletal electron pair theory (PSEPT) developed an analogous relationship for borane and metal carbonyl polyhedral molecules which related the total number of valence electrons to *closo*-, *nido*- and *arachno*-deltahedral polyhedral geometries [5]. The electron counting rules associated with VSEPR and PSEPT provided a basis for organising a large body of structural information for molecular and polyhedral inorganic molecules. Gaining from the prior experience in organic chemistry concepts taken from molecular orbital theory were used to construct a theoretical framework for translating the numerology associated with the electron counting formalisms into a more scientifically based quantum mechanical orbital description.

This chapter provides a description of the steps which were taken when the rules failed when applied to gold clusters. They did not follow the same structural pattern which had been established for polyhedral boranes and transition metal carbonyl clusters. Furthermore, as more of their structures were revealed by X-ray crystallography it became apparent that they exhibited many examples of skeletal isomerism, i.e. more than one skeletal geometry was observed for seemingly isoelectronic molecules. Spectroscopic studies established that many of the clusters were stereochemically non-rigid in solution and some even in the solid state. The patterns associated with VSEPR and PSEPT were identified with ease because related molecules shared a common stereochemistry. A paradigm which can be traced back to Van't Hoff's deduction that organic compounds are built from tetrahedral carbon atoms and Werner's subsequent extension of these ideas to transition metal co-ordination compounds based on octahedra.

The exceptional behaviour of gold clusters was resolved by fusing two separate quantum mechanically based models. The Jellium model defined the overall topology of the gold clusters and their closed shell requirements in terms of the quantum mechanical wave equations of the Schrödinger equation for an electron constrained in a spheroidal ball. This gives rise to S^{σ}, P^{σ} and D^{σ} solutions which resemble the familiar solutions for the hydrogen atom. This occurs for 2, 8, 18, 20 electrons for spherical clusters. It does not, however, specify the locations of the metal atoms or the preferred geometric shapes. It does imply that when the S^{σ}, P^{σ} and D^{σ} are partially filled the shape may distort from the spherical shapes characteristic of filled shells. These deficiencies are partially resolved by using the wave functions for S^{σ}, to define the LCAO of the s functions on the individual gold atoms and estimate the relevant energies of these molecular orbitals. This draws on the approach developed by Stone in the Tensor Surface Harmonic Theory. It may also be used to define the dispersion of mos in the P^{σ} and D^{σ} shells as a result of transforming the spherical shape into oblate or prolate spheroids. The resulting sub-shells determine the closed shell requirements in the gold clusters. This approach provides a menu of reasonable structural possibilities for the cluster molecules which account for the skeletal isomers based on the following:

$\{S^{\sigma}\}^2$ – spherical , $\{S^{\sigma}\}^2\{P^{\sigma}\}^2$ – prolate , $\{S^{\sigma}\}^2\{P^{\sigma}\}^4$ – oblate , $\{S^{\sigma}\}^2\{P^{\sigma}\}^6$ – spherical

Within these geometric boundaries the greatest stabilisation of the surface molecular orbitals is achieved for atomic arrangements with the maximum number of nearest neighbours, i.e. deltahedral arrangements. This stabilisation is diminished somewhat as the number of nearest neighbours is reduced in order to minimise the repulsions between the sterically demanding ligands. Connections between oblate and spherical clusters are made by capping gold atoms and triangles introduced along the major symmetry axis. These stabilisation energies fall in the same range as the sterically induced repulsion energies introduced by the ligands. This leads to the alternative geometric skeletal isomers described above.

The resulting model is sufficiently flexible to give a broad topological representation of the structure and defines a range of structures which are accessible as a result of variations in the steric requirements of the ligands. This model since it is grounded in the orbital characteristics not only provides a basis for articulating the possible alternative structures but also provides insights into the nature of the fluxional behaviour of these clusters. In broad terms the fluxionality reflects the relative weakness of gold–gold bonds in these clusters because the small number of electrons constituting the closed shells and sub-shells. Plausible pathways for the fluxional processes may be proposed on the basis that orbital crossings are avoided. This model has been extended to describe the bonding in condensed and high nuclearity gold clusters [5, 129, 130].

The analysis of exceptions to the electron counting rules using molecular orbital theory became a theme of our research for the next decade and the following references provide a summary of the areas studied and appropriate references:

1. Triangular platinum cluster compounds [225–227].
2. Metalloboranes with PtL_2 fragments and slipped metallocarboranes [228–233].
3. Metalloboranes displaying alternative electron counts and unusual geometries [234, 235, 237, 241].
4. Metal clusters with ML_4 fragments [11, 12, 64].
5. Condensed cluster compounds [236, 237].
6. Clusters with interstitial atoms and molecules [238–241].
7. Bond breaking in electron rich clusters [242, 243].
8. Involvement of lone pairs in skeletal bonding [244].
9. Transition metal clusters of the earlier transition metals with π-donor ligands [245].

In each case the chasm left because of the failure of the electron counting rules was satisfactorily bridged using simple concepts developed from molecular orbital theory and associated perturbation theory arguments.

Acknowledgements I would like to thank Lin Zhenyang, Jean-Francois Halet and Katsuaki Konishi for their helpful comments and Jean-Yves Saillard and Steffano Zacchini for bringing to my attention the recent examples of skeletal isomerism.

References

1. Mingos DMP, Raithby PL (2020) 21st century challenges in chemical crystallography. Struct Bond 185:1–231
2. Mingos DMP, Raithby PL (2020) 21st century challenges in chemical crystallography. Struct Bond 186:1–278
3. Mingos DMP (2014) Gold clusters, colloids and nanoparticles. Struct Bond 161:1–282
4. Mingos DMP (2014) Gold clusters, colloids and nanoparticles. Struct Bond 162:1–231
5. Mingos DMP (2021) A personal historical perspective on the development of the electron counting rules for Boranes and Clusters and Ken Wade's contribution in a Half century of electron counting Rules Ed. Mingos D M P Struct Bond 187:1–66
6. Wade K (1971) The structural significance of the number of skeletal bonding electron pairs in carboranes, the higher boranes and borane anions and various transition metal-carbonyl cluster compounds. J Chem Soc D Chem Commun:792–793
7. Rudolph RW (1976) Boranes and heteroboranes: a paradigm for the electron requirements of clusters? Acc Chem Res 9:446–452
8. Mingos DMP (1972) A general theory for cluster and ring compounds of the main group and transition elements. Nat Phys Sci 236:99–102
9. Elian M, Chen MML, Mingos DMP, Hoffmann R (1976) A comparative study of conical fragments. Inorg Chem 15:1148–1155
10. Mingos DMP, Evans DG (1982) Molecular orbital analysis of the bonding in low nuclearity gold and platinum tertiary phosphine complexes and the development of *isolobal* analogies for the $M(PR_3)$ fragment. J Organomet Chem 232:171–191
11. Mingos DMP, Evans DG (1982) Polyhedral skeletal electron pair theory – its extension to non-conical fragments. J Organomet Chem 240:321–327
12. Mingos DMP, Evans DG (1983) Polyhedral skeletal electron pair theory – its extension to non-conical ML_4 fragments. Organometal 2:435–447

13. Naldini L, Cariati F, Simonetta G, Malatesta L (1966) Gold tertiary phosphine derivatives with intermetallic bonds. J Chem Soc D Chem Commun:647
14. Malatesta L (1975) Cluster compounds of gold. Gold Bull 8:48–52
15. Cariati F, Naldini L (1971) Trianionoeptakis(triarylphosphine)undecagold cluster compounds. Inorg Chim Acta 5:172–174
16. Cariati F, Naldini L, Simonetta G, Malatesta L (1967) Clusters of gold compounds with 1,2-Bis(diphenylphosphino)ethane. Inorg Chim Acta 1:315–318
17. Albano VG, Bellon PL, Manassero M, Sansoni M (1970) Intermetallic pattern in metal-atom clusters – structural studies on $Au_{11}X_3(PR_3)_7$ species. J Chem Soc D Chem Commun:1210–1211
18. Bellon P, Manassero M, Sansoni M (1972) Crystal and molecular structure of tri-iodoheptakis (tri-p-fluorophenylphosphine)undecagold. J Chem Soc Dalton Trans:1481–1487
19. Bellon P, Manassero M, Sansoni M (1973) An octahedral gold cluster: crystal and molecular structure of hexakis[tris-(p-tolyl)phosphine]-octahedro-hexagold bis(tetraphenylborate). J Chem Soc Dalton Trans:2423–2427
20. Manassero M, Naldini L, Sansoni M (1979) A new class of gold cluster compounds. Synthesis and X-ray structure of the octakis(triphenylphosphinegold) dializarinsulphonate $[Au_8(PPh_3)_8](aliz)_2$. J Chem Soc Chem Commun:385–386
21. McPartlin M, Mason R, Malatesta L (1969) Cluster compounds of gold(0)-gold(I). J Chem Soc D Chem Commun:334–335
22. Briant CE, Theobald BRC, White JW, Bell LK, Mingos DMP, Welch AJ (1981) Synthesis and X-ray structural characterization of the centred icosahedral gold cluster compound $[Au_{13}(PMe_2Ph)_{10}Cl_2](PF_6)_3$; the realization of a theoretical prediction. J Chem Soc D Chem Commun:201–202
23. King RB (1971) Transition metal cluster compounds. Prog Inorg Chem 15:287–465. (specifically pp. 453–454)
24. Mingos DMP (1974) Molecular orbital calculations for an octahedral cobalt cluster complex $[Co_6(CO)_{14}]^{4-}$. J Chem Soc Dalton Trans:124–138
25. Mingos DMP (1976) Bonding in gold clusters. J Chem Soc Dalton Trans:1163–1169
26. Mingos DMP (1977) Recent developments in theoretical organometallic chemistry. Adv Organomet Chem 15:1–51
27. Müller TE, Mingos DMP (1995) Determination of the Cone Angle in from crystallographic parameters and a statistical analysis using the crystallographic database. Transit Met Chem 20:533–539
28. Mingos DMP (1982) Steric effects in metal cluster compounds. Inorg Chem 21:464–466
29. van der Velden JWA, Vollenbroek FA, Bour JJ, Beurskens PT, Smits JMM, Bosnian WP (1981) Gold clusters containing bidentate phosphine ligands. Preparation and X-Ray structure investigation of $[Au_5(dppmH)_3(dppm)](NO_3)_2$ and $[Au_{13}(dppmH)_6](NO_3)_n$. Recl Trav Chim Pays-Bas 100:148–152
30. Vollenbroek FA, Bosman WP, Bour JJ, Noordik JH, Beurskens PT (1979) Reactions of gold phosphine cluster compounds. Preparation and X-ray structure determination of octakis (triphenylphosphine)octa-gold bis(hexafluorophosphate). J Chem Soc D Chem Commun:387–388
31. Vollenbroek FA, Bour JJ, van der Veden JWA (1980) Gold-phosphine cluster compounds: the reactions of $[Au_9L_8]^{3+}$ (L = PPh) with L, SCN^- and Cl^- to $[Au_8L_8]^{2+}$ $[Au_{11}L_8(SCN)_2]^+$ and $[Au_{11}L_8Cl_2]^+$. Recl Trav Chim Pays-Bas 99:137–141
32. van der Velden JWA, Bour JJ, Bosman WP, Noordik JH (1981) Synthesis and X-ray crystal structure determination of the cationic gold cluster compound $[Au_8(PPh_3)_7](NO_3)_2$. J Chem Soc D Chem Commun:1218–1219
33. Steggerda JJ, Bour JJ, van der Velden JWA (1982) Preparation and properties of gold cluster compounds. Recl Trav Chim Pays-Bas 101:164–170
34. van der Velden JWA, Bour JJ, Steggerda JJ, Beurskens PT, Roseboom M, Noordik M (1982) Gold cluster – Tetrakis [1,3-bis(diphenylphosphino)propane]hexagold dinitrate; preparation,

X-ray analysis and gold(197) Mössbauer and phosphorus $^{31}P\{^{1}H\}$ N.M.R. spectroscopy. Inorg Chem 21:4321–4324
35. Smits JMM, Beurskens PT, Bour JJ, Vollenbroek FA (1983) X-ray analysis of octakis(tri-p-tolylphosphine)enneagoldtris(hexafluorophosphate), $[Au_9\{P(p\text{-}MeC_6H_4)_3\}_8](PF_6)_3$: a redetermination. J Cryst Spect Res 13:365–372
36. Smits JMM, Beurskens PT, Velden JWA, Bour JJ (1983) Partial X-ray analysis of triiodoheptakis (triphenylphosphine)undecagold, $Au_{11}C_{126}H_{105}I_3P_7$. J Cryst Spect Res 13:373–379
37. Smits JMM, Bour JJ, Vollenbroek FA, Beurskens PT (1983) Preparation and X-ray structure determination of [pentakis{1,3-bis(diphenylphosphino)propane}]undecagoldtris(thiocyanate), $[Au_{11}\{PPh_2C_3H_6PPh_2\}_5(SCN)_3]$. J Cryst Spect Res 13:355–363
38. van der Velden JWA, Bour JJ, Bosman WP, Noordik JH (1983) Reactions of cationic gold clusters with Lewis bases. Preparation and X-ray structure investigation of $[Au_8(PPh_3)_7](NO_3)_2.2CH_2Cl_2$ and $Au_6(PPh_3)_4[Co(CO)_4]_2$. Inorg Chem 22:1913–1918
39. van der Velden JWA, Beurskens PT, Bour JJ, Bosman WP, Noordik JH, Kolenbrander M, Buskens JAKM (1984) Intermediates in the formation of gold clusters. Preparation and x-ray analysis of $[Au_7(PPh_3)_7]^+$ and synthesis and characterization of $[Au_8(PPh_3)_6I]PF_6$. Inorg Chem 23:146–151
40. van der Velden JWA, Bour JJ, Bosman WP, Noordik JH, Beurskens PT (1984) The electrochemical preparation of $[Au_9(PPh_3)_8]^+$. A comparative study of the structures and properties of $[Au_9(PPh_3)_8]^+$ and $[Au_9(PPh_3)_8]^{3+}$. Recl Trav Chim Pays-Bas 103:13–16
41. Bos W, Kanters RPF, Van Halen CJ, Bosman WP, Behm H, Smits JMM, Beurskens PT, Bour JJ, Pignolet LH (1986) Gold clusters: synthesis and characterization of $[Au_8(PPh_3)_7(CNR)]^{2+}$, $[Au_9(PPh_3)_6(CNR)_2]^{3+}$ and $[Au_{11}(PPh_3)_7(CNR)_2O]^{2+}$ and their reactivity towards amines. The crystal structure of $[Au_{11}(PPh_3)_7(CN\text{-}i\text{-}Pr)_2I](PF_6)_2$. J Organomet Chem 307:385–398
42. Hall KP, Mingos DMP (1984) Homo-and heteronuclear cluster compounds of gold. Prog Inorg Chem 32:237–325
43. Briant CE, Hall KP, Mingos DMP, Wheeler AC (1986) Synthesis and structural characterisation of hexakis(triphenylphosphine(hexagold(2+))), $[Au_6(PPh_3)_6]^{2+}$ and related clusters with edge shared tetrahedra. J Chem Soc Dalton Trans:687–692
44. Hall KP, Theobald BRC, Gilmour DI, Mingos DMP, Welch AJ (1982) Synthesis and structural characterization of $[Au_9\{P(p\text{-}C_6H_4OMe)_3\}_8](BF_4)_3$; a cluster with a centred crown of gold atoms. J Chem Soc D Chem Commun:528–530
45. Briant CE, Hall KP, Mingos DMP (1984) Structural characterisation of two crystalline modifications of $[Au_9\{P(C_6H_4OMe\text{-}p)3\}_8](NO_3)_3$: the first example of skeletal isomerism in metal cluster chemistry. J Chem Soc D Chem Commun:290–292
46. Briant CE, Hall KP, Wheeler AC, Mingos DMP (1984) Structural characterisation of $[Au_{10}Cl_{l3}(PCy_2Ph)_6](NO_3)$(Cy = cyclohexyl) and the development of a structural principle for high nuclearity gold clusters. J Chem Soc D Chem Commun:248–250
47. Briant CE, Hall KP, Mingos DMP (1983) Synthesis and structural characterisation of hexakis (triphenyl phosphine)hexagold(2+) $[Au_6(PPh_3)_6][NO_3]_2$, and related clusters with an edge shared bitetrahedral gold clusters. J Organomet Chem 254:C18–C19
48. Cheetham GMT, Harding MM, Haggitt JL, Mingos DMP, Powell HR (1993) Synthesis and microcrystal structure determination of $[Au_{10}(PPh_3)_7\{S_2C_2(CN)_2\}_2]$ with monochromatic synchrotron radiation. J Chem Soc D Chem Commun:1000–1001
49. Mingos DMP, Briant CE, Hall KP (1982) Unusual degradation reaction of icosahedral cluster compounds of gold with chelating diphosphanes and the X-ray structure of di-bis (diphenylphosphido)methanidogold(I) $Au_2\{(Ph_2P)CH\}_2$. J Organomet Chem 229:C5–C6
50. Copley RCB, Mingos DMP (1996) The novel structure of the $[Au_{11}(PMePh_2)_{10}]^{3+}$ cation: crystal structures of $[Au_{11}(PMePh_2)_{10}][C_2B_9H_{12}]$3.4thf and $[Au_{11}(PMePh_2)_{10}][C_2B_9H_{12}]_3$(thf = tetrahydrofuran). J Chem Soc Dalton Trans:479–489
51. Copley RCB, Mingos DMP (1996) Synthesis and characterization of the centred icosahedral cluster series $[Au_9M_4Cl_4(PMePh_2)_8][C_2B_9H_{12}]$, where M =Au, Ag or Cu. J Chem Soc Dalton Trans:491–500

52. Konishi K (2014) Phosphine co-ordinated pure-gold clusters: diverse geometrical structures and unique optical properties/responses in Gold clusters, colloids and nanoparticles I. Struct Bond 161:49–86
53. Shichibu Y, Kamei Y, Konishi K (2012) Unique [core+two] structure and optical property of a dodeca-ligated undecagold cluster: critical contribution of the *exo*- gold atoms to the electronic structure. J Chem Soc D Chem Commun 48:7559–7561
54. Shichibu Y, Konishi K (2010) HCl-induced nuclearity convergence in diphosphineprotected ultrasmall gold clusters: a novel synthetic route to "magic-number" Au_{13} clusters. Small 6:1216–1220
55. Shichibu Y, Suzuki K, Konishi K (2012) Facile synthesis and optical properties of magic-number Au_{13} clusters. Nanoscale 4:4125–4129
56. Kamei Y, Shichibu Y, Konishi K, Chen J, Zhang QF, Bonaccorso TA, Williard PG, Wang LS (2014) Controlling gold-nanoclusters by diphospine ligands. J Am Chem Soc 136:92–95
57. Sugiuchi M, Shichibu Y, Nakanishi T, Hasegawa Y, Konishi K (2015) Cluster-π electronic interaction in a superatomic Au_{13} cluster bearing σ-bonded acetylide ligands. J Chem Soc D Chem Commun 51:13519–13522
58. Shichibu Y, Zhang M, Iwasa T, Ono Y, Taketsugu T, Omagari S, Nakanishi T, Hasegawa Y, Konishi K (2019) Photoluminescence properties of [Core+exo]-type Au_6 clusters: insights into the effect of ligand environments on the excitation dynamics. J Phys Chem C 123:6934–6939
59. Shichibu Y, Ogawa Y, Sugiuchi M, Konishi K (2021) Chiroptical activity of Au_{13} clusters: experimental and theoretical understanding of the origin of helical charge movements. Nano Adv 3:1005–1011
60. Kamei Y, Shichibu Y, Konishi K (2011) Generation of small gold clusters with unique geometries through cluster-to-cluster transformations: octanuclear clusters with edge-sharing gold tetrahedron motifs. Angew Chem Int Ed 50:7580–7583
61. Konishi K, Iwasaki W, Shichibu Y (2018) Phosphine-ligated gold clusters with *core+exo* geometries: Unique properties and interactions at the ligand–cluster interface. Acc Chem Res 51:3125–3133
62. Mason R, Thomas KM, Mingos DMP (1973) Stereochemistry of octadecacarbonyl hexaosmium(0) – a novel hexanuclear complex based on a bicapped tetrahedron of metal atoms. J Am Chem Soc 95:3802–3804
63. Johnston RL, Mingos DMP (1987) Group theoretical paradigm for describing the skeletal molecular orbitals of cluster compounds. Part II – Bispherical clusters. J Chem Soc Dalton Trans:1445–1456
64. Mingos DMP (1982) Comment: Edge bridging in clusters, Royal Society Meeting for discussion – metal clusters in chemistry. Proc R Soc A308:14–15
65. Zeng C, Jin R (2014) Gold nanostructures: size controlled syntheses and crystal structures, gold clusters, colloids and nanoparticles I. Struct Bond 161:87–116
66. Lu Y, Chen W (2014) Progess in the synthesis and characterisation of gold nanoclusters gold clusters, colloids and nanoparticles I. Struct Bond 161:117–154
67. Kumara C, Jupally VR, Dass A (2014) Gold thiolate nanomolecules: synthesis mass spectrometry and characterisation gold clusters, colloids and nanoparticles I. Struct Bond 161:155–188
68. Scherbaum F, Grohmann A, Huber B, Kruger C, Schmidbaur H (1988) "Aurophilicity" as a consequence of relativistic effects: the Hexakis(triphenylphosphaneaurio)methane dication [(Ph3PAu)6C]2+. Angew Chem Int Ed Engl 27:1544–1546
69. Górling A, Rósch N, Ellis EI, Schmidbaur H (1991) Electronic structure of main-group-element-centered octahedral gold clusters. Inorg Chem 30:3986–3994
70. Schmidbaur H (1995) Ludwig Mond lecture: high carat gold compounds. Chem Soc Rev:391–400
71. McKenzie LC, Zaikova TO, Hutchison JE (2014) Structurally similar triphenylphosphine stabilized undecagolds $[Au_{11}(PPh_3)_7Cl_3]$ and $[Au_{11}(PPh_3)_8Cl_2]Cl$, exhibit distinct ligand exchange pathways with glutathione. J Am Chem Soc 136:13426–13435

72. Diesfeld JW, Menger EM, Edzes HT, Veeman WS (1980) High-resolution solid-state phosphorus-31 nuclear magnetic resonance of some triphenylphosphine transition-metal complexes. J Am Chem Soc 102:7935–7936
73. Hansen BE, Sullivan MJ, Davis RJ (1984) Direct evidence for bridge-terminal carbonyl exchange in solid dicobalt octacarbonyl by variable-temperature magic angle spinning carbon-13 NMR spectroscopy. J Am Chem Soc 106:251–253
74. Watson MJ, Mingos DMP (1991) Recent developments in the homo- and hetero- metallic cluster compounds of gold. Transit Met Chem 16:285–287
75. Mingos DMP (1982) Some theoretical and structural aspects of gold clusters in chemistry. Proc R Soc A308:75–80
76. Pignolet LH, Krogstad DA (1998) Schmidbaur H (ed) Molecular compounds of gold with main group and transition metals in gold-progress in chemistry, biochemistry and technology. Wiley, Chichester, pp 429–492
77. Clayden NJ, Dobson CM, Hall KP, Mingos DMP, Smith DJ (1985) Studies on gold cluster compounds using high resolution ^{31}P solid-state nuclear magnetic resonance spectroscopy. J Chem Soc Dalton Trans:1811–1814
78. Coffer JL, Drickamer HG, Shapley JR (1990) Pressure-induced skeletal isomerization of octakis (triphenylphosphine)nonagold (3+) hexafluorophosphate in the solid state. Inorg Chem 29:3900–3901
79. Bray KL, Drickhamer HG, Mingos DMP, Watson JM, Shapley JR (1991) Pressure-induced isomerization of a heterometallic rhodium-gold cluster compound $[Rh_2Cl_2(CNC_8H_9)_4(AuPPh_3)]_2(PF_6)_2$. Inorg Chem 30:864–866
80. Pignolet LH, Aubsert MA, Criagheas KL, Gould RAT, Krogstad DA, Wiley JS (1995) Phosphine-stabilized, platinum-gold and palladium-gold cluster compounds and applications in catalysis. Coord Chem Rev 143:219–263
81. Alexander BL, Mueting BL, Pignolet LH (1990) Synthesis and characterization of cationic gold-rhodium phosphite cluster complexes. X-ray crystal and molecular structure of $\{Au_4Rh(H)_2[P(O\text{-}iso\text{-}C_3H_7)_3]_2\}$. Inorg Chem 29:1313–1319
82. Steggerda JJ (1991) Platinum-gold cluster compounds. Comment Inorg Chem 11:113–129
83. Kappen TGMM, van der Broek ACM, Schlebos PPJ, Bour JJ, Bosman WP, Smits JMM, Beurskens PT, Steggarda JJ (1992) New transition metal-gold clusters: synthesis and characterization of the tungsten-gold clusters $[W(CO)_4(AuPPh_3)_5](PF_6)$ and $[W(CO)_3(AuPPh_3)_7](PF_6)$. Inorg Chem 31:4075–4080
84. Bott SG, Fleischer H, Leach M, Mingos DMP, Powell H, Watkin DJ, Watson MJ (1991) Synthesis of heteronuclear gold-rhodium cluster compounds and structural characterization of $[Rh(CNC_8H_9)_3(AuPPh_3)_5]^{2+}$ and $[Rh(CCNC_8H_9)_2(AuPPh_3)_6(AuCl)_2]^+$. J Chem Soc Dalton Trans:2569–2578
85. Bott SG, Mingos DMP, Watson MJ (1989) Synthesis and structural characterisation of $[Au_8Cl_2(PPh_3)_6Rh(CNC_8H_9)_2]PF_6$: a novel heterometallic cluster of gold with a hemispherical topology. J Chem Soc D Chem Commun:1192–1193
86. Mielcke J, Strahle J (1992) $[(Ph_3PAu)_6Mn(CO)_3]^+$ – a cluster with a pentagonal-bipyr amidal structure. Angew Chem Int Ed Engl 31:464–466
87. Strahle J (1995) Braunstein P, Oro LA, Raithby PL (eds) Homonuclear and heteronuclear cluster compounds of gold in metal clusters in chemistry, vol 1. Wiley VCH, Chichester, pp 535–560
88. Teo BK, Keating KJ (1984) Novel tri-icosahedral structure of the largest metal alloy cluster: hexachlorododecakis(triphenylphosphine)-gold-silver cluster $[(Ph_3P)_{12}Au_{13}Ag_{12}Cl_6]^{m+}$. J Amer Chem Soc 106:2224–2226
89. Teo BK, Zhang H (1995) Polyicosahedricity: icosahedron to icosahedron of icosahedra growth pathway for bimetallic (Au-Ag) and trimetallic (Au-Ag-M; M =Pt, Pd,Ni) supraclusters, synthetic studies , site preferences and stereochemical principles. Coord Chem Rev 143:611–636

90. Yan J, Teo BK, Zheng N (2018) Surface chemistry of atomically precise coinage-metal nanoclusters: from structural control to surface reactivity and catalysis. Acc Chem Res 51:3084–3093
91. Teo BK, Shi X, Zhang H (1992) Pure gold cluster of 1:9:9:1:9:9:1 layered structure: a novel 39- metal-atom cluster $[(Ph_3P)_{14}Au_{39}Cl_6]Cl_2$ with an interstitial gold atom in a hexagonal antiprismatic cage. J Am Chem Soc 114:2743–2745
92. Teo BK (2014) A perspective on the science of clusters. J Clust Sci 25:5–28
93. Yan J, Su H, Yang C, Hu S, Malola S, Lin S, Teo BK, Häkkinen H, Zheng N (2016) Asymmetric synthesis of chiral bimetallic $[Ag_{28}Cu_{12}(SR)_{24}]^{4-}$ nanoclusters via ion pairing. J Am Chem Soc 138:12751–12754
94. Mingos DMP, Lin Z (1989) Site preference effects in heterometallic clusters. Comment Inorg Chem 9:95–122
95. Walter M, Moseler M (2009) Ligand-protected gold alloy clusters: doping the superatom. J Phys Chem C 113:15834–15837
96. Bruce MI (2007) RSC specialist per reports. Organo-transition metal cluster compounds. 27:151-220
97. Bruce MI, Nicholson BK (1983) Cluster chemistry: XXIII. Mono-, di-and tri-auration of $H_4Ru_4(CO)_{12}$ with $[\{Au(PPh_3)\}_3O][BF_4]$: X-ray crystal structure of $HRu_4Au_3(CO)_{12}(PPh_3)_3$. J Organomet Chem 252:243–255
98. Salter ID (1989) Heteronuclear cluster chemistry of copper, silver and gold. Adv Organomet Chem 29:243–343
99. Lauher JW, Wald K (1981) Synthesis and structure of triphenylphosphinegold-dodecacarbonyltricobaltiron $[FeCo_3(CO)_{12}AuPPh_3]$: a trimetallic trigonal-bipyramidal cluster. Gold derivatives as structural analogs of hydrides. J Am Chem Soc 103:7648–7650
100. Housecroft CE (1995) Transition metal boride clusters at the molecular level. Coord Chem Rev 143:297–330
101. Housecroft CE (1995) Denuding the boron atom of B-H interactions in transition metal-boron clusters. Chem Soc Rev:215–222
102. Rossell O, Seco M, Segalé G (1999) Braunstein P, Oro LA, Raithby PL (eds) Skeletal isomerism in transition metal clusters, clusters in chemistry. Wiley, Chichester, pp 1053–1072
103. Dyson P (2004) Braunstein P, Oro LA, Raithby PL (eds) Reversible skeletal rearrangements in transition metal clusters, clusters in chemistry. Wiley, Chichester, pp 1028–1051
104. Sculfort S, Braunstein P (2011) Intramolecular d^{10}–d^{10} interactions in heterometallic clusters of the transition metals. Chem Soc Rev 40:2741–2760
105. Ma L, Wilson SR, Shapley JR (1994) Polyhedral skeletal isomerization in the octanuclear cluster $[Re_7IrC(CO)_{23}]^{2-}$. J Am Chem Soc 116:787–788
106. Orpen AG, Salter ID (1991) Structural systematics. 2. Metal framework rearrangements in cluster compounds containing the Au_2Ru_3 fragment. Organometallics 10:11–117
107. Mingos DMP, Johnston RL (1987) Theoretical models of cluster bonding. Struct Bond 68:31–82
108. Mingos DMP (1980) Theoretical and structural aspects of metal cluster compounds. Pure Appl Chem 52:705–712
109. Hall KP, Gilmour DI, Mingos DMP (1984) Molecular orbital analysis of the bonding in high nuclearity gold cluster compounds. J Organomet Chem 268:275–293
110. Mingos DMP (1984) Structure and bonding in cluster compounds of gold. Polyhedron 3:1289–1297
111. Gilmour GI, Mingos DMP (1986) Molecular orbital calculations on platinum-gold heterometallic clusters. J Organomet Chem 302:127–146
112. Evans DG, Mingos DMP (1985) Molecular orbital analysis of the bonding in penta- and heptanuclear gold tertiary phosphine clusters. J Organomet Chem 295:389–400
113. Mingos DMP (1996) Gold – a flexible friend in cluster chemistry. J Chem Soc Dalton Trans:561–566
114. Bertulani C (2007) Nuclear physics in a nutshell. Princeton University Press, Princeton

115. Stone AJ (1980) A new approach to bonding in transition metal clusters theory. Mol Phys 41:1339–1354
116. Stone AJ (1981) New approach to bonding in transition-metal clusters and related compounds. Inorg Chem 20:563–571
117. Stone AJ, Alderton MJ (1982) A new model of structure and bonding in the boron hydrides. Inorg Chem 21:2297–2302
118. Stone AJ (1984) The bonding in boron and transition-metal cluster compounds. Polyhedron 3:1299–1306
119. Mingos DMP (2014) A historical introduction to gold clusters and colloids in gold clusters, colloids and nanoparticles I. Struct Bond 161:1–52
120. Dyson PJ, Mingos DMP (1999) Schmidbaur H (ed) Homonuclear clusters and colloids of gold: synthesis, reactivity, structural and theoretical considerations in gold. Progress in chemistry, biochemistry and technology. Wiley, New York, pp 511–556
121. King RB (1986) Metal cluster topology 2. Gold clusters. Inorg Chim Acta 116:109–117
122. Knight WD, Strahle K, de Heer WA, Saunders WA, Chou My Cohen I (1984) Electronic shell structure and abundances of sodium clusters. Phys Rev Lett 54:2141–2143
123. Clemenger K (1985) Ellipsoidal shell structure in free-electron metal clusters. Phys Rev B 32:1359–1362
124. Mingos DMP, Slee T, Lin Z (1990) Structural jellium model of cluster electronic structure. Chem Phys 142:321–334
125. Mingos DMP, Lin Z, Slee T (1990) Bonding models for ligated and bare clusters. Chem Rev 90:383–402
126. Mingos DMP, Lin Z (1989) Structural consequences of the jellium model for alkali metal clusters. Chem Phys 137:15–24
127. Wales DJ, Mingos DMP (1989) Splitting of cluster crbitals. Inorg Chem 28:2748–2754
128. Koetecky J, Fantucci P (1986) Theoretical aspects of metal atom clusters. Chem Rev 86:539–587
129. Mingos DMP (2016) Structural and bonding issues in clusters and nano-clusters in gold clusters, colloids and nanoparticles I. Struct Bond 162:1–66
130. Mingos DMP (2015) Structural and bonding patterns in gold clusters. Dalton Trans 44:6680–6695
131. Pyykkö P (2004) Theoretical chemistry of gold I. Angew Chem Int Ed 43:4412–4456
132. Pyykkö P (2008) Theoretical chemistry of gold III. Chem Soc Rev 16:1967–1997
133. Mingos DMP, Powell HR, Stolberg TA (1992) Synthesis and characterisation of the tetrahedral cluster $[Au_4(PPh_3)_4(SnCl_3)_2]$. Transit Met Chem 17:334–337
134. Zeller E, Beruda H, Schmidbaur H (1993) Tetrahedral gold cluster $[Au_4]^{2+}$: crystal structure of $\{[(tert\text{-}Bu)_3PAu]_4\}^{2+}(BF_4^-)_2{\cdot}2CHCl_3$. Inorg Chem 32:3203–3204
135. Demartin F, Manassero M, Naldini L, Ruggeri R, Sansoni MJ (1981) Synthesis and X-ray characterization of an iodine-bridged tetranuclear gold cluster, di-μ-iodo-tetrakis (triphenylphosphine)-tetrahedro-tetragold. J Chem Soc D Chem Commun:222–223
136. Woodham AP, Fielcke A (2014) Gold clusters in the gas phase in gold clusters, colloids and nano-particles I. Struct Bond 161:243–277
137. Lipscomb WN (1966) Framework rearrangement in boranes and carboranes. Science 53:373–378
138. Lipscomb WN, Britton DJ (1960) Valence structures of the higher borides. Chem Phys 33:275–280
139. Kaczmarczyk A, Dobrott RD, Lipscomb WN (1962) Reactons of $B_{10}H_{10}^{2-}$ anion. Proc Nat Acad Sci U S A 48:729–733
140. Eaton GR, Lipscomb WN (1969) NMR studies of boron hydrides and related compounds. Benjamin Press, New York
141. Schlüter F, Bernhardt E (2011) Syntheses and crystal structures of the closo-borates $M_2[B_7H_7]$ and $M[B_7H_8]$ (M = PPh_4, PNP, and N(n-Bu_4)): the missing crystal structure in the series $[B_nH_n]^{2-}$ (n = 6−12). Inorg Chem 50:2980–2989. and references therein

142. Schlüter F, Bernhardt E (2012) Syntheses and crystal structures of the *closo*-borate $M[B_8H_9]$ ($M = [PPh_4]$ and $[N(n\text{-}Bu_4)]$). Inorg Chem 51:511–517
143. Muetterties EL, Beier BF (1975) Structural form and non-rigidity in 6, 7, 8, and 9-atom polyhedral boranes-molecular orbital calculations. Bull Soc Chimiq Belges 84:397–406
144. Klanberg F, Muetterties EL (1966) Chemistry of boranes. XXVII.1 New polyhedral borane anions, $B_9H_9^{2-}$ and $B_{11}H_{11}^{2-}$. Inorg Chem 50:2980–2989
145. King RB (1981) Chemical applications of topology and group theory – degenerate edges as a source of inherent fluxionality in deltahedra. Inorg Chim Acta 49:239–247
146. King RB (1984) Chemical applications of group theory and topology X. Topological representations of hyperoctahedrally restricted eight-coordinate polyhedral rearrangements. Theor Chim Acta 64:439–452
147. King RB (1981) Chemical applications of topology and group theory 18. Polyhedral isomerizations of seven-coordinate complexes. Inorg Chem 24:1716–1719
148. King RB (1983) Chemical applications of topology and graph theory. Elsevier, Amsterdam, p 99
149. Gimarc BN, Ott JJ (1987) Isomerization of the carboranes $C_2B_6H_8$, $C_2B_8H_{10}$, and $C_2B_9H_{11}$ by the diamond-square-diamond rearrangement. J Am Chem Soc 109:1388–1392
150. Gimarc BN, Ott JJ (1986) Isomers of $C_2B_3H_5$ and the diamond-square-diamond rearrangement mechanism. Inorg Chem 25:83–85
151. Brown CA, Gimarc BN, Ott JJ (1989) Diamond-square-diamond isomerization of heptahydrodicarbaheptaborane. Inorg Chem 28:4269–4273
152. Gimarc BM (1979) Molecular structure and bonding. Academic Press, New York
153. McKee ML (1988) Ab initio study of the mechanisms of rearrangements in $C_2B_4H_6$ and $C_2B_5H_7$. J Am Chem Soc 110:5317–5321
154. Kleier DA, Bicerano J, Lipscomb WN (1980) Stereochemical rigidity and isomerization in tetraborane (4) and tetrafluorotetraborane (4). A theoretical study. Inorg Chem 19:216–218
155. McKee ML, Lipscomb WN (1981) Theoretical study of the isomerization of hypothetical tetraborane(4). Inorg Chem 20:4148–4151
156. Halgreen TA, Pepperberg IM, Lipscomb WN (1975) Computational evidence for a stable intermediate in the rearrangement of 1, 2-dicarbahexaborane (6) to 1,6-dicarbahexaborane(6). J Am Chem Soc 97:1248–1250
157. Kleie DA, Lipscomb WN (1979) Fluxional behavior in octahydrooctaborate (2-). A theoretical study. Inorg Chem 18:1312–1318
158. Kleier DA, Dixon DA, Lipscomb WN (1978) Fluxional behavior in $B_{11}H_{11}^{2-}$: a theoretical study. Inorg Chem 17:166–167
159. Mingos DMP, Wales DJ (1990) An introduction to cluster chemistry. Prentice-Hall, Englewood Cliffs, pp 218–248
160. Wales DJ, Stone AJ (1987) Theoretical Study of rearrangements in boranes. Inorg Chem 26:3845–3850
161. Mingos DMP, Johnston RL (1988) Allowed and forbidden nature of diamond-square-diamond degenerate rearrangements in polyhedral boranes – a general topological analysis. Polyhedron 7:2437–2439
162. Wales DJ, Mingos DMP, Lin Z (1989) Skeletal rearrangements in clusters II. Inorg Chem 28:2754–2764
163. Wales DJ, Mingos DMP (1989) Skeletal rearrangements in clusters III – application of vibrational symmetry analysis. Polyhedron 8:1933–1938
164. Muetterties EL, Wright GM (1967) Molecular polyhedra of high co-ordination numbers. Quart Rev (London) 21:109–194
165. Muetterties EL (1972) Stereochemical non-rigidity. Int Rev Sci Inorg Chem Ser One 9:37–85
166. Guggenberger LJ, Muetterties EL (1976) Reaction path analysis. 2. The nine-atom family. J Amer Chem Soc 98:7221–7225
167. Bürgi HB, Dunitz JD (1983) From crystal statics to chemical dynamics. Acc Chem Res 16:153–161

168. Muetterties EL (1969) Topological representation of stereoisomerism. I. Polytopal rearrangements. J Am Chem Soc 91:1636–1643
169. Muetterties EL (1969) Topological representation of stereoisomerism. II. The five-atom family. J Am Chem Soc 91:4115–4122
170. Muetterties RL (1968) Intramolecular rearrangement of six-coordinate structures. J Am Chem Soc 90:5097–5102
171. Guggenberger LJ, Muetterties EL (1976) Reaction path analysis. 2. The nine-atom family. J Am Chem Soc 98:7221–7225
172. Muetterties EL (1970) Stereochemically non-rigid structures. Acc Chem Res 3:266–273
173. Holmes RR (1972) Spectroscopy and structure of pentacoordinated molecules. Acc Chem Res 5:296–303
174. Kepert DL (1979) Aspects of the stereochemistry of seven-coordination. Prog Inorg Chem 25:41–144
175. Clare BW, Kepert DL (2006) Coordination numbers & geometries. encyclopedia of inorganic and bioinorganic chemistry. Wiley, Chichester
176. King RB (2001) Three-dimensional aromaticity in polyhedral boranes and related molecules. Chem Rev 101:1119–1152
177. King RB, Rouvray DH (1977) Chemical applications of group theory and topology. 7. A graph theoretical interpretation of the bonding in boranes, carboranes and metal clusters. J Am Chem Soc 99:7834–7840
178. Woodward RB, Hoffmann R (1970) The conservation of orbital symmetry. Verlag Chemie Weinheim, Germany
179. Mingos DMP, Wales DJ (1991) Structural rearrangements in clusters: some new insights involving Lipscomb's diamond square diamond mechanism. In: Olah GA, Williams RE, Wade K (eds) Electron deficient boron and carbon clusters. Wiley, New York, pp 143–163
180. Braunstein P, deMric de Bellefon C, Bouaoud S-E, Grandjean D, Halet J-F, Saillard J-Y (1991) Cluster core isomerization from planar to tetrahedral: experimental and theoretical aspects. Steric control by the ligands of cluster geometry. Synthesis and crystal structure. J Am Chem Soc 113:5282–5292
181. Taylor NJ, Chieh PC, Carty AJ (1975) Platinum cluster compounds: X-ray structures of phosphido-bridged bi-and tri-nuclear complexes with strong metal–metal bonds derived from $[Pt(PPh_3)_4]$. J Chem Soc Chem Commun:448–449
182. Johnson BFG, Rodgers A (1990) Shriver DF, Kaesz HF, Adams RD (eds) The chemistry of metal cluster complexes. VCH, Weinheim, pp 303–325
183. Johnson BFG, Rodgers A (1988) Polyhedral rearrangements in clusters. Polyhedron 7:1107–1120
184. Heaton BT (1988) Structural, bonding, and mechanistic rearrangement information on transition metal carbonyl clusters from multinuclear magnetic resonance studies. Pure Appl Chem 60:1757–1761
185. Heaton BT, Grachova EV, Tunik SP, Podkorytov S (2015) The ligand polyhedral model approach to the mechanism of complete carbonyl exchange in $[Rh_4(CO)_{12}]$ and $[Rh_6(CO)_{16}]$. J Chem Soc Dalton Trans 44:16611–16613
186. Vidal JL, Schoening RC (1983) On the thermal growth and decomposition of rhodium carbonyl clusters. J Organomet Chem 241:395–416
187. Garlaschelli L, Fumagalli A, Martinengo S, Heaton BT, Smith DO, Strona L (1978) The synthesis and nuclear magnetic resonance spectroscopic study of $[Rh_{10}S(CO)_{22}]^{2-}$. J Chem Soc Dalton Trans:2265–2267
188. Gansow OA, Gill DS, Bennis FJ, Hutchinson JR, Vidal JL, Schoening RC (1980) Rhodium-103-NMR evidence for charge separation and fluxionality among rhodium atoms in metal clusters. J Am Chem Soc 102:2449–2450
189. Vidal JL, Walker WE, Schoening RC (1981) $[Rh_{10}P(CO)_{22}]^{3-}$: a transition-metal carbonyl cluster with a metal polyhedron based on the bicapped square-antiprism as illustrated by the structural study of the benzyltriethylammonium salt. Inorg Chem 20:238–242

190. Vidal JL, Troup JM (1981) $[Rh_{12}Sb(CO)_{27}]^{3-}$: an example of encapsulation of antimony by a transition metal carbonyl cluster. J Organomet Chem 213:51–63
191. Heaton BT, Strona L, Della Pergolla R, Vidal JL, Schoening R (1982) Multinuclear variable-temperature nuclear magnetic resonance study of rhodium carbonyl clusters containing encapsulated heteroatoms: ligand and metal polyhedral rearrangements. J Chem Soc Dalton Trans:1941–1947
192. Eichhorn B, Kocak S (2011) Dynamic properties of the group 14 Zintl ions and their derivatives in zintl ions – principles and recent developments. Struct Bond 140:59–89. and references therein
193. Heaton BT (2002) NMR studies of metal complexes and clusters with carbonyls and phosphines in modern co-ordination chemistry. In: Leigh GJ, Winterton N (eds) The legacy of Joseph Chatt. Royal Society of Chemistry, London, pp 89–100
194. Chini P, Longoni G (1976) Synthesis and chemical characterization of platinum dicarbonyl dianions $[Pt_3(CO)_6]_m^{2-}$ (m = 10, 6, 5, 4, 3, 2, 1). A new series of inorganic oligomers. J Am Chem Soc 78:7225–7231
195. Brown C, Heaton BT, Towl ADC, Chini P, Fumagalli A, Longoni G (1979) Stereochemical nonrigidity of a metal polyhedron; carbon-13 and platinum-195 Fourier-transform nuclear magnetic resonance spectra of the platinum dicarbonyls $[Pt_n(CO)_{2n}]^{2-}$ (n = 3, 6, 9, 12, or 15). J Organomet Chem 181:233–254
196. Heaton BT (1982) Nuclear magnetic resonance studies in cluster chemistry. Philos Trans R Soc Lond Ser A Math Phys Eng Sci 308:95–102
197. Brown C, Heaton BT, Chini P, Fumagalli A, Longoni G (1977) Stereochemical nonrigidity of a metal polyhedron; Fourier transform platinum-195 nuclear magnetic resonance spectra of $[Pt_n(CO)_{2n}]^{2-}$ (n = 3, 6, or 9). J Chem Soc D Chem Commun:309–311
198. Underwood DJ, Hoffmann R, Tatsumi K, Nakamura A, Yamamoto Y (1985) Triangular platinum and nickel clusters: the "Tinker-Toy" construction of chains with high nuclearity platinum carbonyl clusters. J Am Chem Soc 107:5968–5980
199. Ciabatti I, Femoni C, Iapalucci MC, Longoni G, Lovato T, Zacchini S (2013) PPh_3-derivatives of $[Pt_{3n}(CO)_{6n}]^{2-}$ (n = 2–6) Chini's clusters: syntheses, structures, and ^{31}P NMR studies. Inorg Chem 52:4384–4395
200. Cesari C, Ciabatti I, Femoni C, Iapalucci MC, Mancini F, Zacchini S (2017) Heteroleptic Chini-type platinum clusters: synthesis and characterization of bis-phosphine derivatives of $[Pt_{3n}(CO)_{6n}]^{2-}$ (n = 2–4). Inorg Chem 56:1655–1668
201. Berti B, Cesari C, Conte F, Ciabatti I, Femoni C, Iapalucci MC, Vacca F, Zacchini S (2018) Synthesis of $[Pt_{12}(CO)_{20}(dppm)_2]_{2-}$ and $[Pt_{18}(CO)_{30}(dppm)_3]_{2-}$ heteroleptic Chini-type platinum clusters by the oxidative oligomerization of $[Pt_6(CO)_{12}(dppm)]^{2-}$. Inorg Chem 57:7578–7590
202. Berti B, Ciabatti I, Femoni C, Iapalucci MI, Zacchini S (2018) Molecular cluster core isomerism induced by crystal packing effects in the $[HCo_{15}Pd_9C_3(CO)_{38}]^{2-}$ molecular nanocluster nanocluster. ACS Omega 3:13239–13250
203. Capacci C, Cesari C, Femoni C, Iapalucci MC, Mancini F, Ruggieri S, Zacchini S (2020) Structural diversity in molecular nickel phosphide carbonyl nanoclusters. Inorg Chem 59:16016–16026
204. Fu J, Morshedi M, Moxey GJ, Barlow A, Cifuentes MP, Humphrey MG (2016) Dynamic permutational isomerism in a *closo*-cluster. Chem Eur J 22:5128–5132
205. Adams RD, Captain B, Pellechia PJ, Zhu J (2004) Addition of $Pt(PBut_3)$ groups to $Ru_5(CO)_{12}(\eta^6\text{-}C_6H_6)(\mu^5\text{-}C)$. Synthesis, structures, and dynamical activity. Inorg Chem 43:7243–7249
206. Calderoni F, Iapualucci MC, Longoni G (1996) Compounds of post transition elements of groups 12-14 containing $Fe(CO)_4$ and related carbonyl ligands. In: Metal-ligand interactions. NATO ASI series, vol 474. Springer ASIC, New York, pp 85–103

207. Berti B, Bortoluzzi M, Cesar C, Femoni C, Iapalucci MC, Mazzoni R, Vacca F, Zacchini S (2020) Thermal growth of Au–Fe heterometallic carbonyl clusters containing N-heterocyclic carbene and phosphine ligands. Inorg Chem 59:2228–2240
208. Berti B, Bortoluzzi M, Cesari C, Femoni C, Iapalucci MC, Soleri L, Zacchini S (2020) Synthesis, structural characterization, and DFT investigations of $[M_xM'_5\text{-}xFe_4(CO)_{16}]^{3-}$ (M, M′ = Cu, Ag, Au; M ≠ M′) 2-D molecular alloy clusters. Inorg Chem 59:15936–15952
209. Gam F, Wei J, Kahlal Saillard J-F, Halet J-F (2021) Electron counting in ligated high nuclearity later transition metal clusters in 50 years of electron counting rules. Struct Bond 190:1–34
210. Chiu T-H, Liao J-H, Gam F, Chantrenne I, Kahlal S, Saillard J-Y, Liu CW (2019) Homoleptic platinum/silver superatoms protected by dithiolates: linear assemblies of two and three centered icosahedra isolobal to Ne_2 and I_3^-. J Am Chem Soc 141:12957–12961
211. Schaaff TG, Whetten RL (2000) Giant gold-glutathione cluster compounds: intense optical activity in metal-based transition. J Phys Chem B 104:2630–2641
212. Jadzinsky PD, Calero G, Ackerson CJ, Bushnell DA, Kornberg RD (2007) Structure of a thiol monolayer-protected gold nanoparticle at 1.1 Å resolution. Science 318:430–433
213. Zhu Y, Guo J, Qiu X, Zhao S, Tang Z (2021) Optical activity of chiral metal nanoclusters. Acc Mater Res 2:21–35
214. Ma W, Xu LG, de Moura AF, Wu XL, Kuang H, Xu CL, Kotov N (2017) Chiral inorganic nanostructures. Chem Rev 117:8041–8093
215. Zeng CJ, Chen YX, Liu C, Nobusada K, Rosi NL, Jin RC (2015) Gold tetrahedra coil up: Kekule-like and double helical superstructures. Sci Adv 1:e1500425
216. Wan XK, Yuan S-F, Lin ZW, Wang QMA (2014) Chiral gold nanocluster Au_{20} protected by tetradentate phosphine ligands. Angew Chem Int Ed Engl 53:2923–2926
217. Dolamic I, Knoppe S, Dass A, Bürgi T (2012) First enantioseparation and circular dichroism spectra of Au_{38} clusters protected by achiral ligands. Nat Commun 3:798–800
218. Knoppe S, Dolamic I, Dass A, Bürgi T (2012) Separation of enantiomers and CD spectra of $Au_{40}(SCH_2CH_2Ph)_{24}$: spectroscopic evidence for intrinsic chirality. Angew Chem Int Ed Engl 51:7589–7591
219. Zeng CJ, Li T, Das A, Rosi NL, Jin RC (2013) Chiral structure of thiolate-protected 28-gold-atom nanocluster determined by X-ray crystallography. J Am Chem Soc 135:10011–10013
220. Yoshida H, Ehara M, Priyakumar UD, Kawai T, Nakashima T (2020) Enantioseparation and chiral induction in Ag_{29} nanoclusters with intrinsic chirality. Chem Sci 11:2394–2400
221. Knoppe S, Wong OA, Malola S, Hakkinen H, Bürgi T, Verbiest T, Ackerson CJ (2019) Chiral phase transfer and enantio-enrichment of thiolate-protected Au_{102} cluster. J Am Chem Soc 136:4129–4132
222. Huang J-H, Wang Z-Y, Zang S-Q, Mak TCW (2020) Spontaneous resolution of chiral multi-thiolate protected Ag_{30} nanoclusters. ACS Cent Sci. https://doi.org/10.1021/acscentsci.0c01045
223. Yao Q-F, Xie J-P (2020) Pasteur-like separation of silver nanocluster racemates by conglomerate crystallization. ACS Cent Sci. https://doi.org/10.1021/acscentsci.0c01301
224. Zhu YF, Wang H, Wan KW, Guo J, He CT, Yu Y, Zhao L, Zhang Y, Lv J, Shi L (2018) Enantioseparation of $Au_{20}(PP_3)_4Cl_4$ clusters with intrinsically chiral cores. Angew Chem Int Ed Engl 57:9059–9063
225. Slee T, Mingos DMP (1990) A molecular orbital study of trinuclear platinum clusters. J Organomet Chem 394:679–698
226. Mingos DMP, Wardle RWM (1985) Homonuclear cluster compounds of platinum. Transit Met Chem 10:441–459
227. Burrows AD, Mingos DMP (1996) The chemistry of Group 10 metal *triangulo*- clusters. Coord Chem Rev 154:19–69
228. Mingos DMP (1977) Molecular orbital calculations on metalloboranes: Part I. J Chem Soc Dalton Trans:602–610

229. Mingos DMP, Forsyth MI, Welch AJ (1977) X-ray crystallographic and theoretical studies on "Slipped" metallocarboranes. J Chem Soc D Chem Commun:605–607
230. Mingos DMP, Forsyth MI, Welch AJ (1978) Molecular and crystal structure of 3,3-bis (triethylphosphine)-1,2-dicarba-3-platinadodecarborane, and molecular orbital analysis of the "Slip" distortion in metallocarboranes. J Chem Soc Dalton Trans:1363–1374
231. Mingos DMP, Forsyth MI (1978) M.O. analysis of the "Slip" distortion in electron rich sandwich complexes derived from the 1,2-$C_2B_9H_{11}$ ligand. J Organomet Chem 146:C37–C42
232. Mingos DMP, Welch AJ (1980) Molecular orbital calculations on carbometalloboranes and related polyhedra. J Chem Soc Dalton Trans:1674–1681
233. Mingos DMP, Calhorda MJ, Welch AJ (1982) Theoretical comparison of the 'Slip' distortion in comparable seven and twelve vertex carboplatinaboranes. J Organomet Chem 228:309–320
234. Mingos DMP, Calhorda MJ (1982) Extended Hückel molecular orbital calculations on fused pentagonal bipyramidal metallocarboranes containing wedge ligands such as BH, Sn or Ge. J Organomet Chem 229:229–245
235. Johnston RL, Mingos DMP, Sherwood P (1991) Bonding and electron counting in hyper closo metalloboranes and metallocarboranes. New J Chem 15:831–841
236. Mingos DMP (1983) Polyhedral skeletal electron pair theory – a generalised principle for condensed polyhedra. J Chem Soc D Chem Commun:706–708
237. Mingos DMP, Evans DG (1983) Bonding in condensed polyhedral cluster compounds of platinum. J Organomet Chem 251:C13–C16
238. Mingos DMP, Weisberger S, Heeb S (1993) Molecular orbital analysis of main group clusters with interstitial transition metal atoms. New J Chem 17:531–543
239. Halet JF, Mingos DMP (1988) Molecular orbital analysis of dicarbido transition metal cluster compounds. Organometal **7**:51–58
240. Halet JF, Evans DG, Mingos DMP (1988) Effect of cavity size on the charge distribution in carbido-metal carbonyl clusters and its possible catalytic implications. J Am Chem Soc 110:87–90
241. Mingos DMP, Kanters RPF (1990) Molecular orbital analysis of mono and di-carbido gold cluster compounds. J Organomet Chem 384:405–415
242. Lyne PD, Mingos DMP, Ziegler T (1992) A theoretical study of Te_6^{2+} and $Te_4S_4^{2+}$. J Chem Soc Dalton Trans:2743–2747
243. Lyne PD, Mingos DMP (1992) Systematics of electron rich polyhedral molecules: an econium to linus pauling-molecules in natural. Sci Med:395–430
244. Mingos DMP, Modrego J (1991) Exceptions to the polyhedral skeletal electron pair theory in heterometallic naked clusters. New J Chem 15:9–16
245. Johnston RL, Mingos DMP (1986) Theoretical analysis of the bonding in octahedral transition metal clusters containing π-donor ligands and their *nido*- and *arachno*- derivatives. Inorg Chem 25:1661–1671

Struct Bond (2021) 188: 69–102
https://doi.org/10.1007/430_2021_81

Published online: 30 March 2021

Electron Counting in Ligated High Nuclearity Late Transition Metal Clusters

Franck Gam, Jianyu Wei, Samia Kahlal, Jean-Yves Saillard, and Jean-François Halet

Dedicated to the memory of our great friend Roy Johnston, an important contributor to cluster chemistry understanding.

Contents

Abstract Over the years, the development of large ligated transition metal clusters has been accompanied by the development of theories using conceptual ideas and models which resulted in a range of electron-counting rules. All of them aimed to understand and rationalize the relationship between the structure and the electron count. Among these rules, those relying on the *spherical jellium* approximation, initially employed to study simple spherical alkali clusters, have shown to be very

F. Gam, J. Wei, S. Kahlal, and J.-Y. Saillard (✉)
Univ Rennes, CNRS, UMR 6226, Institut des Sciences Chimiques de Rennes (ISCR), Rennes, France
e-mail: Jean-Yves.Saillard@univ-rennes1.fr

J.-F. Halet (✉)
Univ Rennes, CNRS, UMR 6226, Institut des Sciences Chimiques de Rennes (ISCR), Rennes, France

CNRS-Saint Gobain-NIMS, IRL 3629, Laboratory for Innovative Key Materials and Structures (LINK), National Institute for Materials Science (NIMS), Tsukuba, Japan
e-mail: Jean-Francois.Halet@univ-rennes1.fr

powerful to chemists interested in viewing ligated noble metal nanoclusters as *superatoms*, *supermolecules* or specific nano-objects with "magic" electron counts. This review develops the basic theory and illustrates its applications for specific spherical and non-spherical ligand-protected nanoclusters containing metals from groups 10 and 11.

Keywords Clusters · Copper · Electron-counting rules · Gold · Jellium model · Nanoclusters · Palladium · Platinum · Polyhedral skeletal electron pair theory · Silver · Superatoms · Supermolecules

Abbreviations

AO	Atomic orbital
Cp*	Pentamethylcyclopentadienyl
cve	Cluster valence electron
DFT	Density functional theory
dmf	Dimethylformamide
Dppp	1,3-bis(diphenylphosphino)propane
dtp	Dithiophosphate
EAN	Effective atomic number
Et	Ethyl
GUM	Grand unified model
HOMO	Highest occupied molecular orbital
LUMO	Lowest unoccupied molecular orbital
Me	Methyl
MO	Molecular orbital
Ph	Phenyl
PR_3	Organophosphine
PSEPT	Polyhedral skeletal electron pair theory
SR	Organothiolato
tol	4-Methylphenyl
Tr	Tropylium
TSH	Tensor surface harmonic

1 Introduction

Ken Wade's seminal paper "*The structural significance of the number of skeletal bonding electron-pairs in carboranes, the higher boranes and borane anions, and various transition-metal carbonyl cluster compounds*" published in *Chemical Communications* in 1971 [1] certainly paved the way and influenced the way cluster chemistry has developed during the last 50 years. Wade's rules were initially setup to

link the shape of the skeletal polyhedral borane and carborane clusters to the number of electron pairs [2–7]. Rapidly, interconnections between these boranes and carboranes and main group and/or ligated transition metal clusters were established [3, 8–12]. Encouraged by the *isolobal* analogy [13, 14], a flurry of contributions resulted, which expanded the impact of the ideas presented in this original paper and which constitute today the basis of the so-called *Polyhedral Skeletal Electron Pair Theory* (PSEPT) – also known as the Wade–Mingos rules [2, 3, 15–17]. The reader is directed to Mingos' introductory chapter of this volume for the historical development of these electron-counting rules. Although their relevance is sometimes considered to be limited to the area of organometallic clusters the power of PSEPT originates from the fact it is able to cover a very large field of structural chemistry from small clusters to sub-nanometre sized (even nano-sized) metal particles.

Several years after Wade's publication, Stone developed the elegant *Tensor Surface Harmonic* (TSH) theory to theoretically underpin Wade's rules [18–24] (see Fowler's chapter in this volume). In short, TSH theory is related to the problem of an electron gas constrained to remain *over* the surface of a sphere, and this is why the original rules apply only to hollow pseudo-spherical (*closo*, *nido*, *arachno*, etc.) clusters, although PSEPT is able to extend them to other cluster families [25] through *aufbau* processes based on capping and condensation principles. In the case of non-hollow, compact pseudo-spherical clusters, one has to rely on a somewhat different conceptual model, the so-called *spherical jellium* model, which is based on the problem of an electron gas constrained to remain *inside* a sphere. Although well known within the physics community [26] for a long time, the *jellium* model is not so familiar to chemists. It was initially used to interpret mass spectrometry experiments on sodium Na_n clusters and other alkali clusters [27], which exhibited particular abundance for specific numbers of alkali atoms (2, 8, 20, 40 . . .), which were called "magic numbers" [27–30]. The *spherical jellium* model views a cluster of atoms as a single large pseudo-atom with electron shell closings for 2, 8, 18, 20, 34, 40, 58, etc. electrons. This model was subsequently adapted to gold phosphine clusters by Mingos et al. in the 1980s [22, 31–37]. In the 1990s the relationships between the *spherical jellium* model and the TSH theory were also used to interpret the geometries of clusters derived from ab initio calculations [23, 24].

Today, with the increasing development of noble metal nano-chemistry, the *jellium* model is commonly used to rationalize nanoclusters as "giant atoms" with magic electron counts [38, 39]. The following discussion will illustrate how this *jellium* model can help to understand the structural and electronic properties of spherical or nearly spherical ligand-protected nanoclusters. Given the huge amount of published literature in this area during the past decades, many examples are available to illustrate these applications. We have had to be selective and the examples chosen are somewhat illustrative rather than exhaustive – a collection of "portraits" which we think is educationally helpful.

2 The *Spherical Jellium* Model

Before entering into the business of electron counting in high nuclearity late transition metal clusters – the objective of this chapter – let us briefly summarize initially the basic principles of the *spherical jellium* model, with a special emphasis on the comparison with the polyelectronic atom problem, which will lead to the concept of *superatom*.

The Hamiltonian operator for a polyelectronic atom is recalled on the left side of Fig. 1. The solutions of the Schrödinger equation for such a spherical system are polyelectronic functions that can be written on the basis of simple monoelectronic functions, the so-called atomic orbitals, which are the product of a spherical harmonic and a radial function. In the case of a molecule (middle of Fig. 1), several nuclei (Z_p) are present. Thus, the spherical symmetry is broken and the polyelectronic solutions of the Schrödinger equation can no longer be written on the basis of atomic orbitals, all of them centred on the same nucleus. However, in the very specific case of a pseudo-spherical close-packed (compact) arrangement of the nuclei, the approximation of replacing the dense cloud of nuclei point charges by a smoothened (average) uniform positive potential of radial symmetry, $\nu(r)$, can be made (Fig. 1, right side). This is the *spherical jellium* approximation. Thus, the resulting approximate Hamiltonian somewhat resembles that of the polyelectronic atom. Both reflect the spherical symmetry of their respective systems and have their electron/nucleus (nuclei) interactions described by a radial potential. It follows that, as for the polyelectronic atom case, the solutions of the Schrödinger equation resulting from the *spherical jellium* approximation can be written on the basis of monoelectronic functions which are the product of a spherical harmonic and a radial function (Fig. 1). These $\Psi_{n,l,m}$ functions are called "*jellium orbitals*" in the following

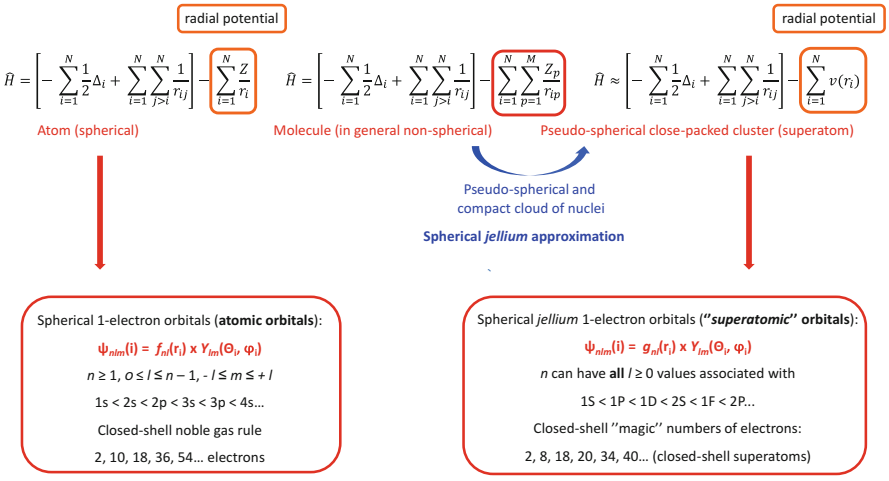

Fig. 1 Main features of the *spherical jellium* approximation and *superatom* concept

sections. Their S, P, D, F... designation for $l = 0, 1, 2, 3...$, respectively, was coined by Mingos et al. in the beginning of the 1980s [40]. Three important remarks should be made at this point.

1. One should keep in mind that the *spherical jellium* approximation is based on the assumption of pseudo-spherical symmetry *and* cluster compactness. Both conditions have to be satisfied simultaneously. Applying such a model to non-spherical clusters and/or to clusters with hollow cages is likely to lead to erroneous conclusions. In some cases, however, clusters with lower symmetries can be treated from the point of view of Jahn–Teller distorted spheres.
2. Although the Hamiltonian operators of the polyelectronic atom and that of the *spherical jellium* approximation have related expressions, they differ by the nature of their radial potential. In the atomic case, it is in $1/r$, whereas in the *spherical jellium* formalism it is generally approximated to a rounded square potential, i.e., having a certain value inside the sphere, another one outside and some continuous function connecting these two regions (Woods–Saxon potential) [41]. The *jellium* orbitals thus differ from the atomic orbitals by their radial functions. In particular, their principal number n conventionally starts at $n = 1$, regardless of the associated value of the angular momentum number l. The shell level ordering $1S < 1P < 1D < 2S < 1F < 2P < 1G < 2D < 1H...$ is rather independent of the mathematical expression and parameterization given to the radial potential $\nu(r)$. It is thus largely independent from the cluster nature, in the same way as the $1s < 2s < 2p < 3s < 3p...$ shell ordering in polyelectronic atoms is quasi-independent from the atom nature.
3. Since the *jellium* approximation consists of replacing the atomic nuclei by an average potential, there are no nuclei, no atoms, thus no atomic orbitals within the framework of this approximation. Thus, the *stricto sensu jellium* orbitals are not combinations of atomic orbitals. In fact, the S, P, D, F... *jellium* orbitals have similar shapes as $s, p, d, f...$ atomic orbitals, except that they expand significantly over a much larger space, that is, within a volume of the order of magnitude of the cluster sphere. Nowadays in cluster chemistry, the *spherical jellium* approximation model is most often used at a qualitative level for the purpose of electron counting (see below). Modern quantum chemical calculations – usually performed at the density functional theory (DFT) level – are based on the linear combination of atomic orbitals (LCAO) approach. The question which arises after such calculations is to identify among all the computed molecular (Kohn–Sham) orbitals (MOs) those that would have been obtained from quantitative calculations assuming the *spherical jellium* approximation, i.e., the *jellium* orbitals. Indeed, regular LCAO calculations on a given cluster will provide an orbital spectrum containing much more MOs than that corresponding to the *jellium orbitals*, such as those associated with atomic cores or ligand orbitals, for instance. The DFT-computed orbital diagram of a bare centred icosahedral I_h $[Ag_{13}]^{5+}$ cluster is shown as an example in Fig. 2, with its lowest *jellium* orbitals lying among and above the non-*jellium* 4*d* (Ag) combinations.

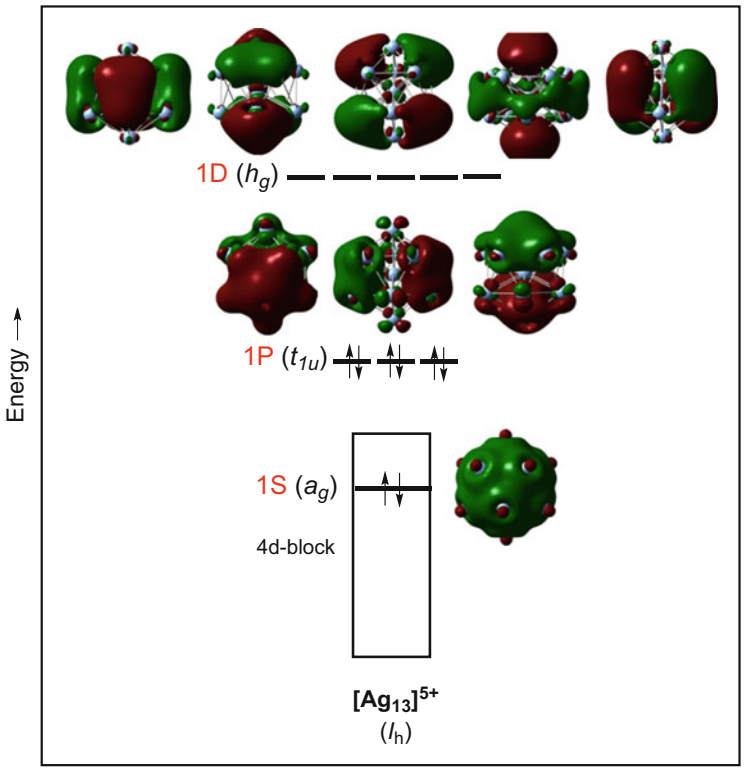

Fig. 2 DFT-computed MO diagram of I_h $[Ag_{13}]^{5+}$ ($1S^2$ $1P^6$ configuration). Note that the 1S orbital is buried within the block of the *non-jellium* 4*d* combinations

The chemical parentage in terms of their shell electronic structures and associated one-electron orbitals between polyelectronic atoms and clusters that can be described within this framework has been largely deepened at the turn of the last century, leading to the word of *superatom* to designate the latter species [42–48]; their *jellium* orbitals being often referred as *superatomic orbitals*. As for any molecule, chemical stability (viability [49]) of a *superatom* is expected to be reached when it will satisfy the closed-shell requirement with a significant HOMO–LUMO gap. The following configurations result from the successive filling of *jellium shells*:

$1S^2$ (2 electrons)
$1S^2$ $1P^6$ (8 electrons)
$1S^2$ $1P^6$ $1D^{10}$ (18 electrons)
$1S^2$ $1P^6$ $1D^{10}$ $2S^2$ (20 electrons)
$1S^2$ $1P^6$ $1D^{10}$ $2S^2$ $1F^{14}$ (34 electrons)
$1S^2$ $1P^6$ $1D^{10}$ $2S^2$ $1F^{14}$ $2P^6$ (40 electrons)
$1S^2$ $1P^6$ $1D^{10}$ $2S^2$ $1F^{14}$ $2P^6$ $1G^{18}$ (58 electrons)
etc.

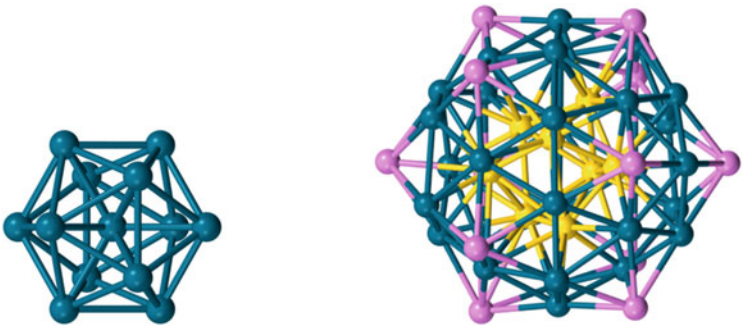

Fig. 3 Structural arrangement of bare $[Al_{13}]^-$ (left) [42, 44] and $Al_{50}Cp^*_{12}$ [described as $Al_8@Al_{30}@(AlCp^*)_{12}$] (right) [51] aluminium *superatoms*. Yellow, blue and pink spheres are Al atoms of the Al_8, Al_{30} and Al_{12} shells, respectively. Surrounding Cp* groups are omitted for clarity

The closed-shell *jellium* electron numbers (2, 8, 18, 20, 34, 40, 58. . .) are referred to as the so-called magic numbers which provide the *superatom* with chemical stability. The similarity with the noble gas configurations (2, 10, 18, 36, 54. . . electrons), which confers stability to a neutral or ionic atom, is obvious.

Before addressing electron counting in specific late transition metal clusters, we would like to briefly illustrate the basic concepts with two historical milestones. Both are taken from aluminium cluster chemistry and show how the *superatom* concept can be applied to both bare and ligated cluster species. The first one concerns $[Al_{13}]^-$, which adopts the close-packed centred icosahedral structure $Al@Al_{12}$ (Fig. 3, left), a common motif in *superatom* chemistry. Its peculiar stability was first recognized by Castleman from mass spectrometry experiments [42]. This bare cluster, which possesses (13 x 3) + 1 = 40 valence electrons was shown by Khanna and Jena to be a closed-shell *superatom* of *jellium* configuration $1S^2\ 1P^6\ 1D^{10}\ 2S^2\ 1F^{14}\ 2P^6$ [44]. The same authors computed the electron affinity of the neutral Al_{13} species (outer configuration $2P^5$) to show that it was comparable to that of a halogen [45] and defined this cluster as a *superhalogen* [50]. The second example is the large ligated $Al_{50}Cp^*_{12}$ compound ($Cp^* = \eta^5\text{-}C_5Me_5$), synthesized by Schnöckel and co-workers [51]. This cluster exhibits a rather compact pseudo-spherical structure (Fig. 3, right) consisting of an inner Al_8 square antiprism encapsulated within an Al_{30} icosidodecahedron, the 12 pentagonal faces of which are capped by AlCp* units (onion-like structure $Al_8@Al_{30}@(AlCp^*)_{12}$). Assuming the Cp* ligands to be formally anionic, one is left with (50 x 3) – 12 = 138 aluminium electrons, which is a *superatom* magic number. Indeed, DFT calculations performed later on by Clayborne et al. confirmed the $1S^2\ 1P^6\ 1D^{10}\ 2S^2\ 1F^{14}\ 2P^6\ 1G^{18}\ 2D^{10}\ 1H^{22}\ 3S^2\ 2F^{14}\ 3P^6\ 1I^{26}$ *superatomic* configuration, secured by a surprisingly large HOMO–LUMO gap [52]. Other *superatom* examples can be found in the rich metalloid-type chemistry developed by Schnöckel and collaborators [53].

Some time ago, Mingos [54–60] and Teo [61, 62] showed that this *jellium* model could also be particularly effective for understanding the structure and closed-shell electronic configuration of the large class of spherical or near-spherical ligated

inorganic gold clusters. This is mostly due to the fact that in these species the metal–metal bonding is principally ensured by the 6*s* (Au) orbitals, whereas the participation of the occupied 5*d* (Au) ones can be neglected. Today, the *superatom* model is largely employed in the field of ligand-protected noble metal nanoclusters (not only gold, but also other coinage metals) [63–67]. Recently, it has been also used to rationalize the bonding and stability of spherical ligated group 10 nanoclusters, despite the apparent zero-electron count for many of them [68]. Some specific examples are discussed in the following sections.

3 Ligated Group 11 Nanoclusters

3.1 Pseudo-Spherical Nanoclusters

3.1.1 Pseudo-Spherical Homometallic Clusters

Among the group 11 metal triad, gold is certainly the most widely encountered in ligated nanocluster chemistry. In fact, as said above, the pioneering work in this field started in the 1980s, with substantial contributions from Mingos' [54–60] and Teo's [61, 62] groups. But the booming of gold cluster and nanocluster chemistry really started at the beginning of this century, in particular (but not only) with the general use of thiolate ligands as metal core-protecting ligands [69–84]. In terms of structure rationalization, the major contributions have come from Häkkinen and co-workers who have shown that the stability of these species can be interpreted within the framework of the *superatom* concept [63, 64, 85]. This unified view of ligand-protected gold clusters applies as well to the silver and copper nano-species which were characterized subsequently. At the risk of oversimplifying, one can conceptually divide a given ligated coinage cluster into two components:

1. The compact pseudo-spherical M_x (M = Cu, Ag, Au) cluster core, which is the *superatomic* part of the nano-molecules. Most often, the average oxidation state of M in the core is comprised between 0 and +I ($[M_x]^{m+}$, $0 \leq m < x$). If it was +I for all M atoms, then they all would have a nd^{10} $(n + 1)s^0$ configuration and hardly any M–M bonding would be possible since all the *d* orbital combinations are formally occupied. Thus $(n + 1)s$ valence electrons are needed for ensuring M–M bonding, but not too many to avoid filling antibonding $(n + 1)s$ combinations. This is why the M average oxidation state is generally slightly higher than zero. Thus, in the case of group 11 clusters, the number of metallic $(n + 1)s$ electrons can be identified as the number of *jellium* electrons (sometimes called *free* electrons), i.e., those responsible for cluster bonding [16, 55]. Consistently, in a first approximation, the combinations of the metallic $(n + 1)s$ AOs can be identified as counterpart MOs of *jellium* (or *superatomic*) orbitals, independently from their occupation number. Of course, these $(n + 1)s$ combinations afford some mixing with metallic occupied *nd* and vacant $(n + 1)p$ AOs, but as far as

electron counting is concerned, the $(n + 1)s$ combinations of the metallic core can be considered as corresponding to *jellium* orbitals. In many cases, a simple 3-dimensional Hückel calculation of the $[M_x]^{m+}$ core (i.e., considering isotropic *s* orbitals) can provide the favoured *superatomic jellium* configuration. At this point, it is easy to understand why in the $[M_x]^{m+}$ core the M average oxidation state cannot be lower than zero. With M(0) atoms, $x/2$ = half of the $(n + 1)s$ combinations are occupied. This is the limit case where the number of bonding and antibonding $(n + 1)s$ combinations are equal. In general, in such close-packed spherical systems the number of bonding combinations is lower than $x/2$, all the other ones being antibonding.

2. The peripheral protecting (passivating) ligand shell. As a whole, its total formal charge is generally negative to compensate the formal cationic charge of the metal core. This negative charge comes generally from ligands that are considered as formally anionic from the point of view of oxidation states, i.e., hydrides (H^-), halogenides (X^-), thiolates (SR^-), alkynyls (CCR^-), etc. Neutral ligands such as phosphines or N-heterocyclic carbenes (NHCs) can also be present. The metal atoms that belong to the $[M_x]^{m+}$ *superatomic* core and that lie on its interface are generally bonded to one ligand. An important point to notice is that, as far as thiolates are present, in many cases the peripheral protecting "ligand" shell contains also supplementary metal centres. These metal atoms can be considered as being in their +I oxidation state. They are generally only weakly bonded to the $[M_x]^{m+}$ *superatomic* core (mainly via metallophilic interactions) and strongly bonded to two or three sulphur atoms, making the so-called staples (vide infra). Their role is to satisfy the nucleophilic demand of extra sulphur lone pairs and/or to participate to the total charge balance, owing to the fact that the charge of an isolable inorganic molecule is most often equal or close to zero.

Thus, the structure and chemical composition of such atom-precise nanoclusters is the result of a non-trivial compromise between M–M bonding within the *superatomic* core, M–ligand bonding, charge balance and steric requirements. To illustrate this complexity, we discuss below the structures and electron counts of two related nanocluster species, namely $[Au_{25}(SR)_{18}]^-$ ($R = CH_2CH_2Ph$) [86], Me [87]) and $[Ag_{21}[S_2P(OR)_2\}_{12}]^+$ ($R = {}^iPr$) [88] (Fig. 4). The *superatomic* cores of both clusters are similar, i.e., exhibiting a close-packed centred icosahedral M_{13} ($M@M_{12}$) arrangement (M = Ag, Au) of ideal I_h symmetry, with a formal charge of +5. These $[M_{13}]^{5+}$ cores are 8-electron *superatoms* with $1S^2\ 1P^6$ closed-shell configuration (see Fig. 2). It is of note that combining 13 *s*-type AOs in I_h symmetry leads to 4 bonding MOs ($a_g + t_{1u}$) and 9 antibonding MOs ($h_g^* + a_g^* + t_{2u}^*$). Thus, the most favoured closed-shell electron number for such a system is 8. The 1S, 1P, 1D and 2S *jellium* orbitals can be identified as the a_g, t_{1u}, h_g^* and a_g^* combinations, respectively, whereas the t_{2u}^* level can be associated with a part of the seven-fold 1F manifold (the number of *jellium* orbitals is infinite, while that of the $(n + 1)s$ combinations is not).

The peripheral shell of $[Au_{25}(SR)_{18}]^-$ is composed of 18 formally anionic thiolate ligands and 12 formally cationic gold atoms, leading to the global composition

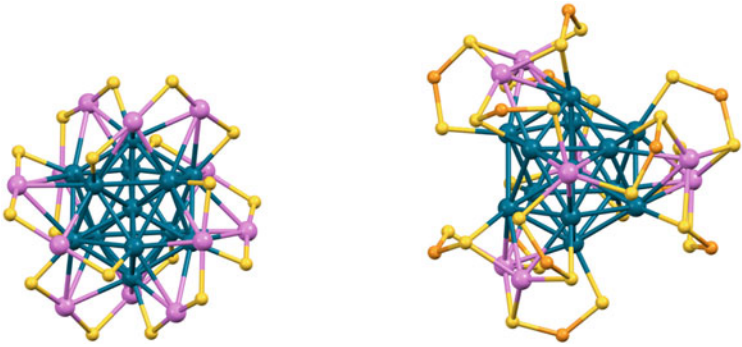

Fig. 4 Structural arrangement of $[Au_{25}(SR)_{18}]^{-}$ (R = CH_2CH_2Ph [86], Me [87]) (left) and $[Ag_{21}\{S_2P(OR)_2\}_{12}]^{+}$ (R = ^{i}Pr) [88] (right). R and OR groups are omitted for clarity. Atoms forming the *superatomic* icosahedral $[M_{13}]^{5+}$ core are in blue. Outer M(I), S and P atoms are in purple, yellow and orange, respectively

$[Au_{12}(SR)_{18}]^{6-}$ for the protecting shell. Each of the 12 peripheral Au(I) atoms is bonded to two sulphur atoms in an approximately linear coordination, making a local stable 14-electron centre. With the sulphur atoms they are bonded to, these peripheral metal atoms form –S–Au–S–Au–S– staples that are clipped onto the central icosahedral Au_{13} core, making each of its 12 Au vertices radially bonded to one sulphur atom (see Fig. 4). From a structural point of view, the 12 outer Au(I) centres are capping 12 of the 20 icosahedral faces of the Au_{13} core, via weak interactions being mainly of aurophilic nature.

The peripheral shell of $[Ag_{21}\{S_2P(OR)_2\}_{12}]^{+}$ is composed of 12 formally monoanionic dithiophosphate (dtp = $S_2P(OR)_2$) ligands and 8 peripheral formally cationic silver atoms, leading to the global composition $[Ag_8\{S_2P(OR)_2\}_{12}]^{4-}$ for the protecting shell. Each of these peripheral Ag(I) atoms is bonded to three sulphur atoms in an approximately planar trigonal coordination, making local stable 16-electron centres. These 8 peripheral Ag(I) atoms are capping in a *metallophilic* bonding fashion 8 out of the 20 icosahedral faces of the Ag_{13} icosahedral core. Finally, each of the 12 Ag atoms of the icosahedral core is radially monocoordinated to a sulphur atom. The orbital diagram of the $[Ag_{21}\{S_2PH_2\}_{12}]^{+}$ model used to mimic $[Ag_{21}\{S_2P(OR)_2\}_{12}]^{+}$ is shown in Fig. 5. A comparison with that of its $[Ag_{13}]^{5+}$ core (Fig. 2) indicates that the peripheral shell does not destroy the *superatomic* nature of the cluster [88].

Thus, although being related through their 8-electron *superatomic* nature, $[Au_{25}(SR)_{18}]^{-}$ and $[Ag_{21}\{S_2P(OR)_2\}_{12}]^{+}$ differ substantially by their peripheral protecting shells due to the different nature of their ligands. Although both thiolate and dtp ligands are formally mono-anions, they differ from their number of coordinating S centres (one vs. two) and by their space occupancy (assuming similar R groups, one dtp ligand is less bulky than two thiolate ones). The two clusters differ also from the preference of Au(I) for a linear coordination and Ag(I) for a trigonal coordination. It is also noteworthy that the peripheral shells are subject to potential

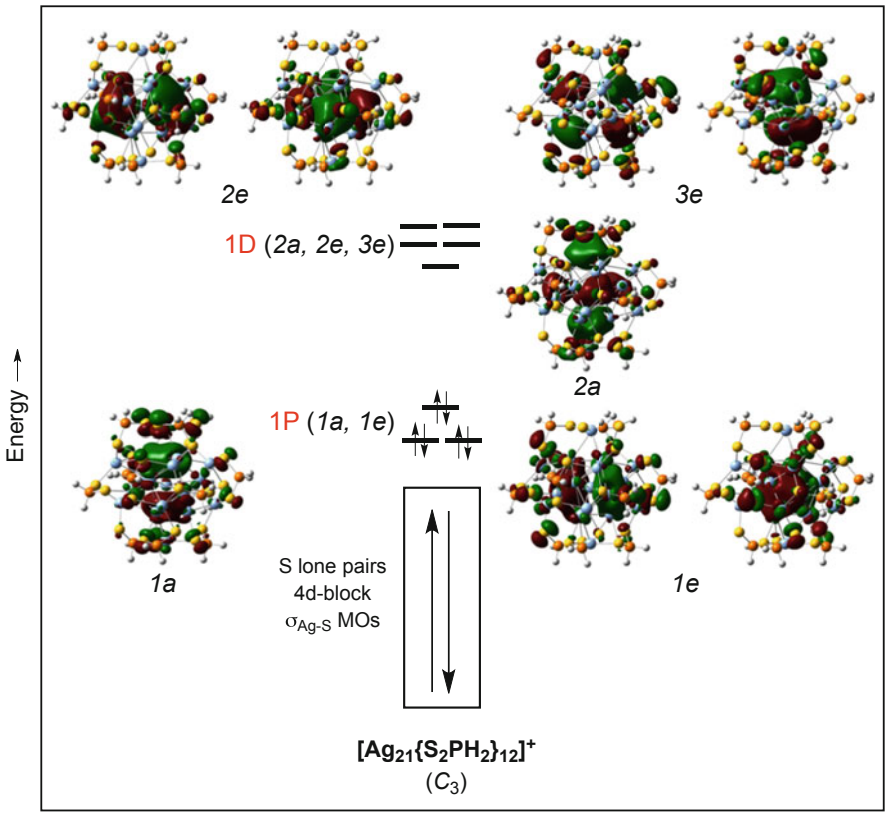

Fig. 5 DFT-computed MO diagram of the model $[Ag_{21}\{S_2PH_2\}_{12}]^+$ of C_3 symmetry. MO plots correspond to the 1P (*1a* + *1e*) and 1D (*2a* + *2e* + *3e*) *jellium* (*superatomic*) orbitals. See Fig. 2 for a comparison with I_h $[Ag_{13}]^{5+}$. Adapted with permission from Ref. [88]. Copyright (2015) WILEY-VCH Verlag GmbH

isomerism [89–92], leading to different topologies, all of them maintaining the major bonding features discussed above.

Apart from the singularity of their peripheral protecting shell, group 11 nanoclusters are most often easy to identify with respect to the nature of their *superatomic* core and their *jellium* electron count. A few selected examples are provided in Table 1. To this list, one could add the bare (non-ligated) neutral Au_{20} cluster of tetrahedral symmetry [93], which illustrates the Au(0) lowest limit case of metal oxidation state. This gas phase species is of course metastable with respect to aggregation. Very large ligand-protected Au and Ag clusters have been so far structurally characterized (up to more than 300 metal atoms) [84, 94–101]. Such huge species do not always obey the "magic" *jellium* electron number rule. Several reasons can be invoked to explain these exceptions.

Table 1 Selected examples of structurally characterized closed-shell homometallic group 11 *superatomic* clusters

Compound	*Jellium* electron number	*Jellium* configuration	*Superatomic* core
$[Cu_{13}\{S_2CNR_2\}_6(CCR')_4]^+$ [104]	2 (13 – 6 – 4 – 1)	$1S^2$	$[Cu_{13}]^{11+}$ centred cuboctahedron
$[Cu_{25}H_{22}(PR_3)_{12}]^+$ [105]	2 (25 – 22 – 1)	$1S^2$	$[Cu_{13}]^{11+}$ centred icosahedron
$[Au_{13}(PR_3)_{10}Cl_2]^{3+}$ [56]	8 (13 – 2 – 3)	$1S^2\ 1P^6$	$[Au_{13}]^{5+}$centred icosahedron
$[Ag_{44}(SR)_{30}]^{4-}$ [106, 107]	18 (44 – 30 + 4)	$1S^2\ 1P^6\ 1D^{10}$	Icosahedral $[Ag_{12}@Ag_{20}]^{14+}$
$[Ag_{46}(PR_3)_8(SR)_{24}]^{2+}$ [108–110]	20 (46 – 24 – 2)	$1S^2\ 1P^6\ 1D^{10}\ 2S^2$	*fcc*-related $[Ag_{38}]^{18+}$
$Au_{68}(SR)_{34}$ [111, 112]	34 (68 – 34)	$1S^2\ 1P^6\ 1D^{10}\ 2S^2\ 1F^{14}$	$[Au_{19}@Aug_{30}]^{15+}$ Marks-decahedron
$Au_{102}(SR)_{44}$ [96]	58 (102 – 44)	$1S^2\ 1P^6\ 1D^{10}\ 2S^2\ 1F^{14}\ 2P^6\ 1G^{18}$	$[Au_{80}]^{22+}$ Marks-decahedron-like

1. The cluster shape is not spherical enough for the strict application of the *spherical jellium* approximation. However, in some cases, the electron count can be rationalized from the point of view of the removal of *jellium* shell degeneracies by specific geometries with lower symmetry.
2. The cluster charge is not always precisely known. In particular, it can be difficult to clearly identify in the X-ray structure the (possibly disordered) small counterions in the vicinity of the huge nanocluster. One could remark, for example, that the X-ray characterized compound $Ag_{211}(SR)_{71}(PPh_3)_6Cl$ (139 electrons) [94] when computed as a cationic species presents a significant HOMO–LUMO gap for the 138-electron count, which is by the way (and perhaps accidentally) a "magic" electron number.
3. When the metal core increases in size, the favoured HOMO–LUMO gap tends to decrease, leading to a "metallic" situation over a certain size limit [102, 103]. In other words, the *superatomic jellium* levels start to coalesce developing a *band structure*. This limit is not clear-cut, since it depends on several parameters such as the metal and ligand nature and the intimate structure of the core. The metallic or near-metallic situation is often accompanied with a plasmonic behaviour. For example, $Au_{246}(SR)_{80}$ has been reported to be non-metallic with a small band gap, based on UV/Vis and femtosecond transient absorption spectroscopic as well as electrochemical measurements [99]. Later, the same authors found a non-metallic-to-metallic transition when going from $Au_{246}(SR)_{80}$ to $Au_{279}(SR)_{84}$ with nascent surface plasmonic resonance [100]. Similarly, calculations on the structurally related $[Ag_{136}(SR)_{64}Cl_3]^-$ and $Ag_{374}(SR)_{113}Br_2Cl_2$ nanoclusters have shown that the former exhibits a significant HOMO–LUMO gap, whereas it is closed for the latter. Conversely, both show plasmonic behaviour [101].

3.1.2 Heterometallic Pseudo-Spherical Group 11-Rich Nanoclusters

When a *superatomic* heterometallic nanocluster is made of two (or more) group 11 metals [113–116], such as the 18-electron nanoalloys $[AuAg_{24}(SR)_{18}]^-$ [117] or $[AuAg_{20}\{S_2P(OR)_2\}_{12}]^+$ [118], for instance, the electron-counting rules hold in exactly the same way as their homometallic relatives [119–122]. The only additional question is metal site occupancy. Alloying group 11 elements with other electron-rich transition metals has been also commonly reported [113–115, 123–131]. In the case of alloys containing group 10 or group 12 metal atoms, one can assume that, as for the group 11 elements, they participate to the cluster bonding with only their $(n + 1)s$ orbitals, contributing to the *jellium* count with 0 and 2 electrons, respectively. Some care should be taken however with less electron-rich metals, for which the *nd* AOs might participate to the bonding, as we discuss below [2].

One of the major interests of such alloy nanoclusters is that their properties can be modulated upon tuning their metal ratio. Another peculiarity of metal heterogeneity is that it favours structural diversity. New structures can arise, as it is observed for the tetracapped tetrahedral Cu_4Zn_4 core in the 8-electron *superatom* $Cu_4(\mu_3\text{-}ZnCp^*)_4(CNR)_4$ [132]. The $[Cu@Cu_{12}@Cu_{30}@Al_{12}]Cp^*_{12}$ icosahedral Mackay-type [133] structure of $Cu_{43}Al_{12}Cp^*_{12}$ is even more original [134]. DFT calculations indicate that this nanocluster is a 67-electron open-shell *superatom* of configuration $1S^2\ 1P^6\ 1D^{10}\ 2S^2\ 1F^{14}\ 2P^6\ 1G^{18}\ 1D^9$. In this specific case, the Cp* ligands form a tight protecting shell to kinetically protect the open-shell core.

3.2 *Non-spherical Nanoclusters*

3.2.1 Unconventional Electron Counts Stabilized by Lowering of Symmetry

In the same way as simple transition metal complexes can afford Jahn–Teller distortion away from ideal symmetry when their electron count deviates from that satisfying the *effective atomic number* (EAN) rule, *superatoms* can also distort away from sphericity when their *jellium* electron count is not equal to a *superatom* closed-shell *magic* number. In such cases, simple oblate (flattening) or prolate (elongating) distortions come obviously to mind. The 6-electron $MAu_{24}(SR)_{18}$ (M = Pd, Pt) species constitute nice examples of oblate distorted structures. Indeed, their structure is related to the 8-electron dianionic forms $[MAu_{24}(SR)_{18}]^{2-}$ which are isoelectronic and isostructural to the homometallic $[Au_{25}(SR)_{18}]^-$ cluster [86, 87]. Whereas the centred icosahedral $[M@Au_{12}]^{4+}$ *superatomic* core in the dianions adopts a regular icosahedral shape, their neutral 6-electron counterparts exhibit a flattened centred icosahedral $[M@Au_{12}]^{6+}$ core [128, 135]. This oblate distortion was first predicted by DFT calculations [128] and later proven by X-ray diffraction measurements [135]. It causes a two-below-one splitting of the three nearly degenerate 1P HOMOs in the undistorted core (of idealized t_{1u} symmetry; see Fig. 2), thus opening

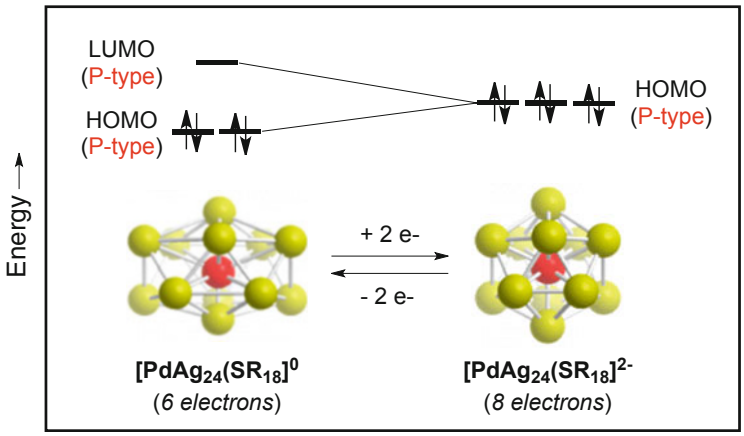

Fig. 6 Jahn–Teller distortion associated with the stabilization of the 6-electron cluster $Pd@Au_{12}(SR)_{18}$. Adapted with permission from Ref. [128]. Copyright (2015) American Chemical Society

a HOMO–LUMO gap which allows stabilizing the *non-magic* 6-electron $1S^2\ 1P^4$ closed-shell configuration (Fig. 6). However, both the flattening distortion and HOMO–LUMO gap are moderate, indicative of some cluster frustration with respect to not reaching the *magic* 8-electron count [22, 31–37].

Clusters with structures much farther away from sphericity can still sometimes be described as distorted *superatoms* with unconventional *jellium* configuration. This is the case, for example, of the very prolate 6-electron cluster $[Cu_{10}Zn_2](mesitylene)_6(Cp^*)_2$, the *jellium* configuration of which was shown by DFT calculations to be $1S^2\ 1P^2\ 2S^2$ [136]. It should be noted that oblate or prolate distortions are not necessary for inducing removal of *jellium* shell degeneracy. The sphere is more symmetrical than any finite (even "pseudo"-spherical) molecular object. A typical example is the 12-electron $Au_{36}(SR)_{24}$ cluster, which possesses a tetrahedral Au_{28} core. In T_d symmetry, the 1D shell splits into two components (e below t_2), leading to the closed-shell configuration $1S^2\ 1P^6\ 1D_e^{\ 4}\ 1D_{t2}^{\ 0}$ [137]. In this particular case, the deviation away from sphericity is sufficiently large for inducing a degeneracy splitting that is strong enough to favour an unconventional electron count. This is of course not a general case.

There are also a few cases that still escape from any general electron counting scheme that could be related in a simple way to the *spherical jellium* model, as exemplified by the very nice oblate 30-electron cluster $[Au_8Ag_{57}(Dppp)_4(C_8H_{11}S)_{32}Cl_2]^+$ (Dppp = 1,3-bis(diphenylphosphino)propane) [138]. DFT calculations found the closed-shell *jellium* configuration $1S^2\ 1P^6\ 1D^8\ 2S^2\ 2P^4\ 1F^4\ 1G^4$, which suggests an intermediate situation between the spherical (3D) and planar (2D) *jellium* approximations [139].

3.2.2 Assemblies of Superatoms (Supermolecules)

There is a rapid growing family of definitely non-spherical group 11-rich nanoclusters where the structure can be described as resulting from the assembly of several pseudo-spherical (mainly icosahedral) basis units. Teo and co-workers noticed it a long time ago and proposed the concept of *clusters of clusters* for its rationale [140, 141]. In fact, in many cases it is possible to describe such assemblies of pseudo-spherical *superatomic* units as "*supermolecules*" [80], in the same way as one looks at molecules as being composed of electron-sharing atoms with electron counts related the bond order, i.e., to the degree of fusion between the atoms/*superatoms* [60, 70, 142–154].

With respect to gold-rich clusters made of two fused centred icosahedra, Mingos elegantly proposed in 2015 [60] to extend the Mulliken's *united atom* model used for diatomics [155–159] to clusters to show the analogy between their total *jellium* electron numbers and the valence electron counts of stable main-group diatomic orbitals. Indeed, fusion of polyhedra provides the equivalent of compression (i.e., bond order) for simple diatomic molecules [60]. The major conceptual developments of what he called a *united cluster* approach are illustrated for a series of homo- and heterometallic nanoclusters in Table 2 and Fig. 7. Consider first the closed-shell $Au_{38}(SR)_{24}$ cluster, for example [160]. Its total number of *jellium* (6*s* (Au)) electrons is 38–24 = 14. These 14 *jellium* electrons are associated to the $[Au_{23}]^{9+}$ core of the cluster made of two $Au@Au_{12}$ icosahedra that share a triangular face (see Table 2 and Fig. 7). The other 15 Au atoms are peripheral Au(I) centres, mainly bonded to sulphur atoms and belonging to the protecting shell, together with the 24 formally anionic thiolate ligands. The analogy with the 14-electron closed-shell F_2 molecule is straightforward. It can be shown in turn that in the bare $[Au_{23}]^{9+}$ core, the combinations of the 6*s* (Au) orbitals can be described as combinations of the *superatomic* (or *jellium*) 1S and 1P orbitals of the two individual icosahedral *superatoms*, in the same way as the 2*s* and 2p AOs of fluorine combine in F_2, leading to the same $1\sigma_g^2\ 1\sigma_u^2\ \pi_u^4\ 2\sigma_g^2\ \pi_g^4\ 2\sigma_u^0$ electron configuration. Such *supermolecular* orbitals can still be identified in the entire $Au_{38}(SR)_{24}$ cluster.

An important parameter affecting the *supermolecule* electron count is its degree of fusion (vertex-sharing, face-sharing or interpenetrating) in a similar way as the bond order does for main group molecules [60]. For example, $[Au_{17}Ag_2(NO_3)_9(PMe_2Ph)_{10}]^+$ [161] has an $[Au_{17}Ag_2]^{9+}$ core made of two interpenetrating icosahedra (Table 2 and Fig. 7) and its *jellium* electron count is similar to the electron count of the triply bonded N_2 molecule. Conversely, the much less compact $[Au_{13}Ag_{12}]^{9+}$ core in $[Au_{13}Ag_{12}Br_8(Ptol_3)_{10}]^+$ [151] consists of two icosahedra sharing one vertex and its *jellium* electron count is that of a van der Waals $(Ne)_2$ molecule (bond order = 0) (Table 2 and Fig. 7). To the best of our knowledge, no intermediate 12-electron bis-icosahedral *supermolecule* with an open-shell configuration analogous to that of O_2 has been reported so far. Interestingly however, Tsukuda and co-workers reported recently the 12-electron $MM'Au_{36}(SR)_{24}$ species (M, M' = Pd, Pt) which exhibits an $[MM'Au_{21}]^{9+}$ core made of two centred

Table 2 Mingos' analogy between diatomic molecules and group 10 clusters made of two fused centred icosahedra

Diatomic molecule	N_2	O_2	F_2	$(Ne)_2$
Number of electrons	10 = 2 x 8 – 6	12 = 2 x 8 – 4	14 = 2 x 8 – 2	16 = 2 x 8
Bond order	3	2 (triplet state)	1	0 (van der Waals)
Example of analogous cluster	$[Au_{17}Ag_2(NO_3)_9(PMe_2Ph)_{10}]^+$ [152]	So far unknown	$Au_{38}(SR)_{24}$ [151]	$[Au_{13}Ag_{12}Br_8(Ptol_3)_{10}]^+$ [147]
Electron configuration[a]	$1\sigma_g^2\ 1\sigma_u^2\ \pi_u^4\ 2\sigma_g^2\ \pi_g^0\ 2\sigma_u^0$	$1\sigma_g^2\ 1\sigma_u^2\ \pi_u^4\ 2\sigma_g^2\ \pi_g^2\ 2\sigma_u^0$	$1\sigma_g^2\ 1\sigma_u^2\ \pi_u^4\ 2\sigma_g^2\ \pi_g^4\ 2\sigma_u^0$	$1\sigma_g^2\ 1\sigma_u^2\ \pi_u^4\ 2\sigma_g^2\ \pi_g^4\ 2\sigma_u^2$
Core structure[b]	Interpenetrated 2 x 13 – 5 – 1 – 1 = 19 atoms $[Au_{17}Ag_2]^{9+}$		Face-sharing 2 x 13 – 3 = 23 atoms $[Au_{23}]^{9+}$	Edge-sharing 2 x 13 – 1 = 25 atoms $[Au_{13}Ag_{12}]^{9+}$

[a]The energy ordering of the occupied levels is arbitrary

[b]Encapsulated and shared atoms are in green and red, respectively

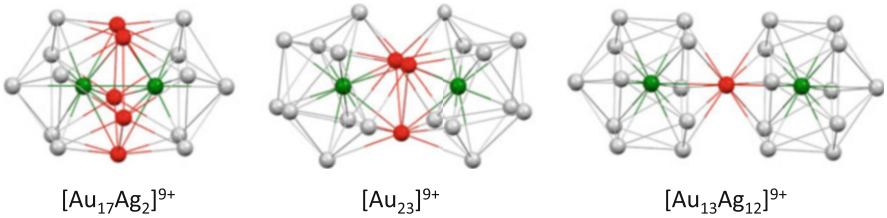

Fig. 7 Core structures of some clusters resulting from the condensation of centred icosahedral clusters via vertex-sharing ($[Au_{13}Ag_{12}Br_8(Ptol_3)_{10}]^+$, right), face-sharing ($Au_{38}(SR)_{24}$, middle) and interpenetration ($[Au_{17}Ag_2(NO_3)_9(PMe_2Ph)_{10}]^+$, left). Encapsulated and shared atoms are in green and red, respectively

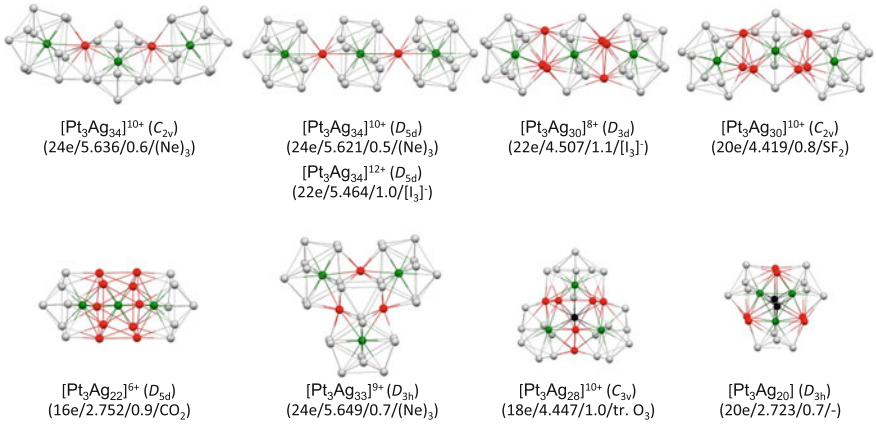

Fig. 8 Stable closed-shell assemblies made of three fused icosahedra [139]. Pt atoms are in green, and silver atoms in red and black are shared between two and three icosahedra, respectively. Electron count, $d_{Pt\text{-}Pt}$ (Å), HOMO–LUMO gap (eV) and *isolobal* molecule are given in brackets

icosahedra sharing one face [162]. However, its structure is somewhat C_{2v} Jahn–Teller distorted, resulting in a splitting of the *superatomic* π_g level and a $\pi_g(x)^2\,\pi_g(y)^0$ closed-shell situation.

Such a molecular analogy which is in a way a variation of the well-known *isolobal* analogy [13, 14] can be extended to assemblies made of more than two *superatoms*. This is illustrated in Fig. 8, for instance, for some cluster *supermolecular* cores that are computed to be *isolobal* to simple triatomic molecules [139]. It is noteworthy that the fusion of icosahedra allows non-linear "bond" angles between them upon "hybridization" requirement similarly as in polyatomic molecules. Indeed some nanoclusters containing such cluster cores have already been characterized, as exemplified with $Pt_3Ag_{44}(dtp)_{22}$ which contains a $[Pt_3Ag_{34}]^{12+}$ *supermolecular* assembly *isolobal* to the $[I_3]^-$ anion, as shown in Fig. 9 [130].

It is likely that the library of *supermolecules* made of the assembly of more than two *superatomic* (mostly but not exclusively icosahedral) subunits will develop in the next future. Stable *supermolecules* analogous to unknown or unstable molecules

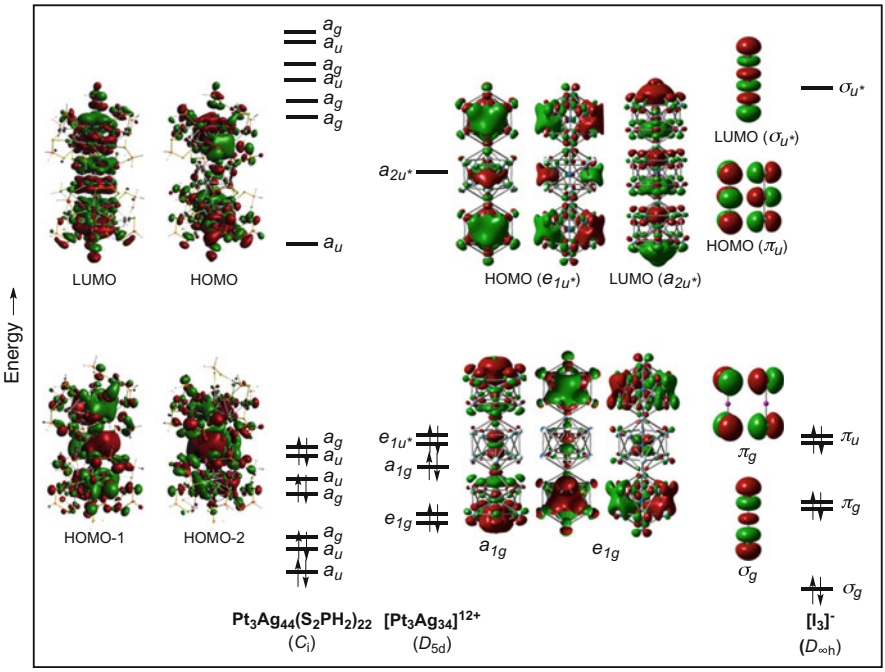

Fig. 9 DFT-computed MO diagrams of $Pt_3Ag_{44}(dtp)_{22}$ (left), its 22-electron $[Pt_3Ag_{34}]^{12+}$ core (middle) and $[I_3]^-$ (right). Note that the MO diagram of the ligated cluster $Pt_3Ag_{44}(dtp)_{22}$ is comparable to that of the bare cluster $[Pt_3Ag_{34}]^{12+}$ with (minor) additional orbital mixing/splitting due to lower symmetry. Adapted with permission from Ref. [130]. Copyright (2019) American Chemical Society

(such as cyclic O_3 [139]) could be designed. However, the *isolobal* analogy between assemblies of atoms and *superatoms* should not be pushed too far. There are obvious differences (among them the presence of 1D *superatomic* orbitals [150]), which can add up when the number of considered atoms/*superatoms* increases. Closed-shell non-spherical group 11 nanoclusters exist, the complex structures of which has not been yet rationalized on the basis of simple electron-counting rules, even those made from fused icosahedral units [139].

4 Group 10 Ligated Clusters

The chemistry of large low valence ligated transition metal nanoclusters is not restricted to coinage metals. Group 10 metals (Ni, Pd, Pt) also tend to aggregate in a compact fashion to produce close-packed metal cores protected by an outermost shell of ligands (mostly phosphines and/or carbonyls) [163–167]. As for group 11 clusters, although various shapes are encountered there are more and more

examples of pseudo-spherical species. This is the case, for instance, of the Dahl's emblematic Matryoshka-like nanoclusters $Pd_{55}(P^iPr_3)_{12}(\mu_3\text{-}CO)_{20}$ [168], $Pd_{145}(CO)_{60}(PEt_3)_{30}$ [169] or $Pd_{164\text{-}x}Pt_{x\,+\,1}(CO)_{72}(PPh_3)_{20}$ [170]. In these examples the Pd oxidation state is formally zero (Pd(0) $4d^{10}\ 5s^0$). Looking at them within the concept of *superatom* in a straight similar way as for their group 11 relatives leads to an apparent *jellium* electron count of zero. Indeed, if the 4*d* (Pd) shell is fully occupied, its electrons are not supposed to ensure M–M bonding. This result is of course contradictory with the existence of substantial M–M bonding within the $[Pd_n]^0$ cluster core of these species. In fact, s*uperatomic* bonding exists in these compounds, with occupation of 5*s* (Pd) bonding combinations (*jellium* orbitals), reaching *magic* electron counts due to level crossing with 4*d* (Pd) combinations [68]. In other words, Pd(0) is in an average $4d^{10\text{-}x}\ 5s^x$ configuration in these clusters. This complex situation is discussed below.

4.1 Pseudo-Spherical Nanoclusters

As said above, although most of the largest spherical Pd nanoclusters are neutral with formal metal oxidation state being zero, it is likely that they all can be depicted as *superatoms*, as demonstrated with $Pd_{55}(P^iPr_3)_{12}(\mu_3\text{-}CO)_{20}$, for instance [68, 168]. Its core structural arrangement consists of a Mackay hard-sphere [133] icosahedral close-packed assembly $Pd@Pd_{12}@Pd_{42}$, i.e., a "Matryoshka doll sequence" with one Pd atom located at the centre of a Pd_{12} icosahedron, which is further encapsulated within a Pd_{42} polyhedron. This metal core is protected by a ligand shell, which is made of 20 triply bridging carbonyls and 12 terminal phosphine groups (Fig. 10).

DFT calculations carried out on related model analogues $Pd_{55}(L)_{12}(\mu_3\text{-}CO)_{20}$ ($L = PH_3$, CO) found a triplet ground state with a nice singlet ground state for its dianion, secured by a substantial HOMO–LUMO gap [68]. Analysis of their Kohn–Sham orbital diagrams revealed that both neutral triplet and dianionic singlet exhibit a *jellium* configuration of $1S^2\ 1P^6\ 1D^{10}\ 2S^2$ (Fig. 11), with closed-shell "magic" electron count of 20. These 20 *jellium* electrons are formally transferred from 4*d* (Pd) orbital combinations to 5*s* (Pd) orbital combinations (*jellium* levels), the former becoming vacant and destabilized by ligand orbitals. Note that in the neutral clusters the open-shell configuration is associated with 4*d*-type singly occupied MOs, located deeply in the metal kernel, in such a way that the stability of the clusters is not affected [68].

The above-described level crossing is sketched on the left side of Fig. 12. For the sake of comparison, a related hypothetical situation corresponding to a 20-electron group 10 cluster is shown on the right side. Major differences come from the fact that (i) the bare group 10 metal core possesses a substantial HOMO–LUMO gap for the proper "magic" *superatomic* electron number, whereas the Pd_{55} core in $Pd_{55}(P^iPr_3)_{12}(\mu_3\text{-}CO)_{20}$ exhibits an open-shell behaviour (if really stable for the considered Mackay architecture) and (ii) the Pd core uses some of its 4*d*

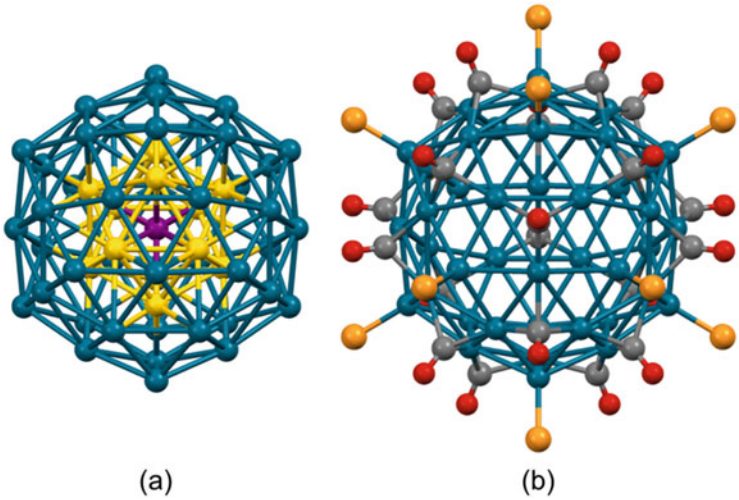

Fig. 10 Structural arrangement of $Pd_{55}(P^iPr_3)_{12}(\mu_3\text{-}CO)_{20}$ [168]: (**a**) "Matryoshka doll sequence" of the $Pd@Pd_{12}@Pd_{42}$ metal kernel and (**b**) outer Pd_{42} shell with surrounding ligands (isopropyl groups are not shown for clarity). The purple, yellow, dark blue, orange, grey and red spheres are central Pd, inner-shell Pd, outer-shell Pd, P, C and O atoms, respectively

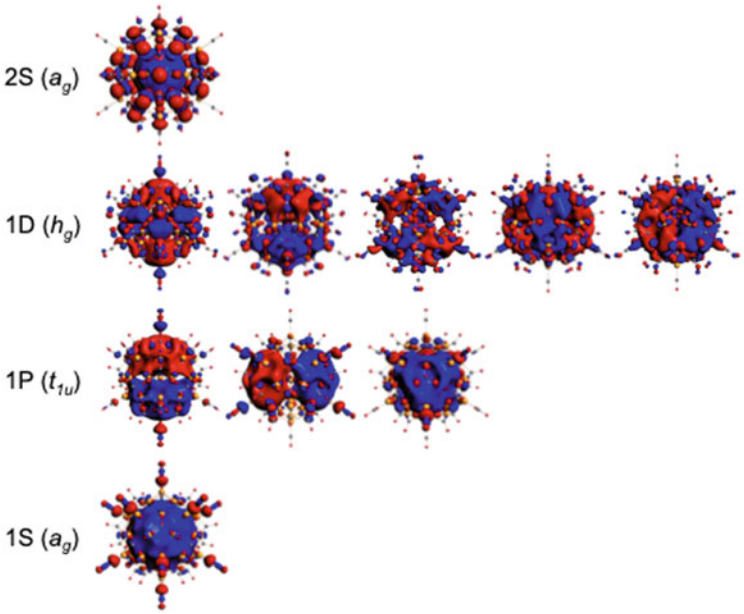

Fig. 11 Occupied *superatomic* orbitals of $[Pd_{55}(CO)_{12}(\mu_3\text{-}CO)_{20}]^{2-}$ of I_h symmetry [68]

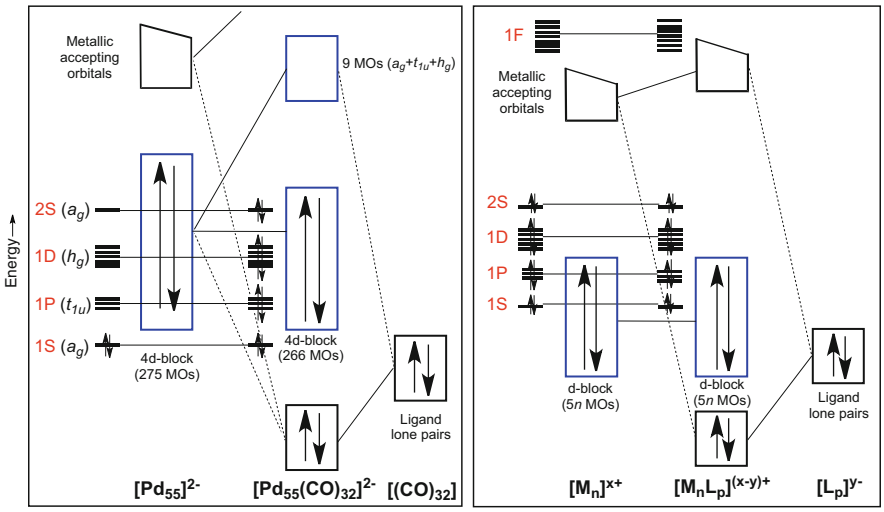

Fig. 12 Simplified MO diagram of $[Pd_{55}(CO_{12})(\mu_3\text{-}CO)_{20}]^{2-}$ obtained on the basis of the interaction between the $[Pd_{55}]^{2-}$ and $[(CO)]_{32}$ fragments (left) and simplified general MO diagram for ligated group 11 closed-shell $[M_nL_p]^{(x-y)+}$ *superatom* with an arbitrarily chosen 20-electron "magic" count (right). Ligands are considered as 2-electron donors. Adapted with permission from Ref. [68]. Copyright (2020) WILEY-VCH Verlag GmBH

combinations (9 in that case) to interact with the peripheral ligands, whereas in the group 11 case the ligands interact only with the accepting *ns*/*np* hybrid orbitals. The fact that some Pd *d*-type orbitals participate to the bonding with the ligands (i.e., are destabilized and depopulated to the benefit of *superatomic* orbitals) is likely not to be uncommon in the Ni-triad cluster chemistry. In particular, we suggest that large spherical icosahedral Mackay clusters such as $Pd_{145}(CO)_{60}(PEt_3)_{30}$ [169] and $Pd_{164-x}Pt_x(\mu_{12}\text{-}Pt)(CO)_{72}(PPh_3)_{20}$ ($x \approx 7$) [170] are indeed *superatoms* characterized by (at least approximately) specific "magic" electron counts, these electrons occupying *s* states and resulting from electron transfer from *d* states due to interaction with the ligand-protecting shell. The difficulty lies in getting the *jellium* electron count with M(0) atoms, since the number of *d*-electrons transferred to the *jellium* orbitals cannot be anticipated without theoretical calculations and no simple rules have been established yet.

Spherical group 10 clusters of smaller size that are known so far generally possess formal anionic charge on the metal core and/or staples clipped around it, rendering these clusters electronically similar to group 11 nanoclusters. For instance, the structure of $[Pt_{13}(CO)_{12}\{Cd_5(\mu\text{-}Br)_5Br_2\text{-}(dmf)_3\}_2]^{2-}$ [171] and $Pt_{13}(Pt_2(\mu_2\text{-}CO)(PPh_3)_2)_2(\mu_2\text{-}CO)_2CO_8(PPh_3)_4$ [172] consists of a Pt-centred $[Pt_{13}(CO)_{12}]^{8-}$ *superatom* with a *jellium* configuration $1S^2\ 1P^6$ similar to that of the isoelectronic species $[Au_{13}(PR_3)_{10}Cl_2]^{3+}$ [56] discussed earlier. The 8 *jellium* electrons can be formally considered as coming from the anionic charge or the staples, thus filling the proper *superatomic* orbitals and leaving the *d*-block fully occupied. A somewhat

similar situation occurs in $[Pd_{13}(\mu_4\text{-}Tr)_6]^{2+}$ (Tr = C_7H_7) [173]. This closed-shell cluster exhibits a centred cuboctahedral core (fcc-like) protected by six tropylium ligands. Tropylium is generally considered as formally an aromatic $(C_7H_7)^+$ cation, i.e., a 6 π-electron ligand. However, calculations show that in this particular cluster the ligand shell is better described as a partly reduced $[(C_7H_7)_6]^{4+}$ system interacting with a $[Pd_{13}]^{2-}$ core, the two electrons provided by the charge filling the low-lying 1S orbital [174].

4.2 Non-spherical Nanoclusters

Most of the ligated group 10 clusters that have been characterized are far from spherical and therefore cannot be approximated to spherical shapes [163–167]. Some of them can however be rationalized within the framework of the PSEPT theory [2, 3, 16, 38, 39]. We also believe that despite their oblate or prolate distorted structures, most of them possess a *supermolecular* nature, which means that they can be viewed as fused assemblies of *superatoms*, in the same way as for non-spherical group 11 species discussed previously. In common with the large spherical Pd species discussed above, only valence *s*-type electrons can ensure strong metal−metal bonding in these species. This implies, assuming cluster neutrality, level crossing (and electron transfer) between occupied *d*-type orbitals and vacant *s*-type (*jellium*) bonding. It follows that without the help of quantum chemical calculations, it is difficult to determine their "hidden" *supermolecular* electronic structure, despite the fact that some group 10 clusters exhibit metal cores that are strongly reminiscent of those of group 11 *supermolecules*.

A certain number of the Ni-triad nanoclusters exhibit core structures based on interpenetrated icosahedra or cuboctahedra, especially with platinum [166, 167]. $[Pt_{19}(CO)_{17}]^{8-}$ [171] and $[Pt_{19}(CO)_{22}]^{4-}$ [175] provide typical examples of such clusters. The former, which constitutes the anionic moiety of the complex salt $[Pt_{19}(CO)_{17}\{Cd_5(\mu\text{-}Br)_5Br_3(Me_2CO)_2\}\{Cd_5(\mu\text{-}Br)_5Br(Me_2CO)_4\}]^{2-}$ exhibits an interpenetrated bis-icosahedral Pt_{19} core, whereas that of the latter consists of two interpenetrated bi-capped pentagonal prisms (Fig. 13).

Recent DFT calculations revealed that $[Pt_{19}(CO)_{17}]^{8-}$ is a 10-electron *supermolecule* with corresponding $1\sigma_g^2\ 1\sigma_u^2\ \pi_u^4\ 2\sigma_g^2\ \pi_g^0\ 2\sigma_u^0$ electron configuration, i.e., analogous to the diatomic molecule N_2 (Table 2) [176]. Interestingly, similarly to $Pd_{55}L_{12}(\mu_3\text{-}CO)_{20}$ [68] (see above), its degenerate 5*d*-type HOMO is half-occupied leading to a triplet state. With two more electrons, a substantial HOMO–LUMO gap allows stabilizing a singlet ground state (Fig. 14). Thus, as in the spherical $[Pt_{13}(CO)_{12}]^{8-}$ *superatom* discussed above the anionic charge of $[Pt_{19}(CO)_{17}]^{10-}$ provides all the cluster *jellium* electrons (no level crossing). The "real" $[Pt_{17}(\mu_{12}\text{-}Pt)_2(CO)_{17}]^{8-}$ cluster is simply lacking two 5*d* (Pt) electrons to reach a closed-shell configuration.

The situation is different for $[Pt_{19}(CO)_{22}]^{4-}$, which is a closed-shell 14-electron *supermolecule*, thus analogue to F_2 with the $1\sigma_g^2\ 1\sigma_u^2\ \pi_u^4\ 2\sigma_g^2\ \pi_g^4\ 2\sigma_u^0$ electron

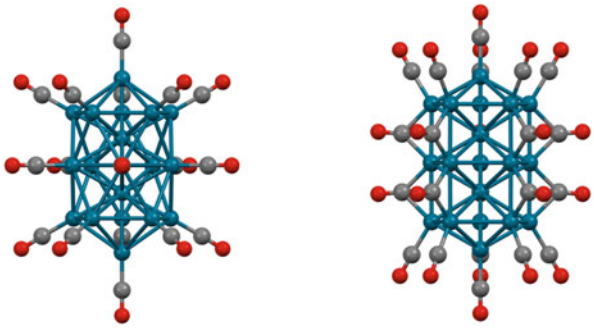

Fig. 13 Structural arrangement of $[Pt_{19}(CO)_{17}]^{8-}$ [171] (left) and $[Pt_{19}(CO)_{22}]^{4-}$ [175] (right)

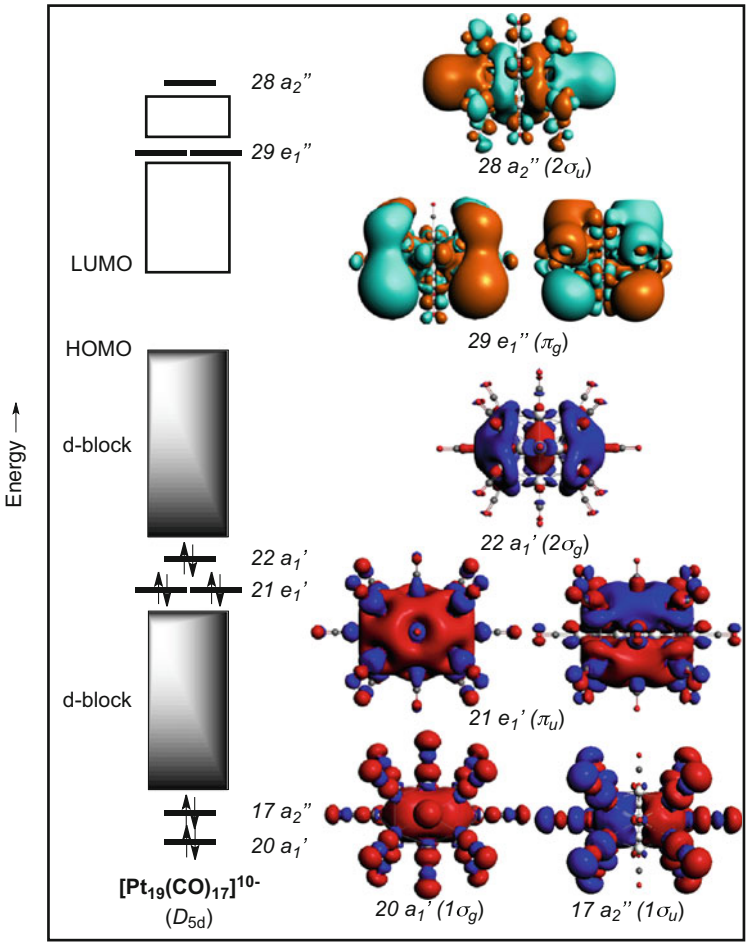

Fig. 14 Electronic structure of $[Pt_{19}(CO)_{17}]^{10-}$ (DFT BP86/TZP calculations). With two less electrons, the "real" $[Pt_{19}(CO)_{17}]^{8-}$ anion has a triplet ground state. The *supermolecular* orbitals are plotted on the right side. Both $[Pt_{19}(CO)_{17}]^{10-}$ and $[Pt_{19}(CO)_{17}]^{8-}$ are 10-electron species [176]

configuration (Table 2) [176]. Considering the tetra-anionic charge of the cluster, a level crossing occurs between five 6*s* (Pt) and five 5*d* (Pt) combinations. The $Pt_{19}(CO)_{17}]^{8-/10-}$ and $[Pt_{19}(CO)_{22}]^{4-}$ differ by their number of *supermolecular* electrons. The total cluster valence electron (cve) counts (232/234 and 238, respectively) follow the same trend and are consistent with the fact that the metallic core of the more electron-rich prismatic cluster $[Pt_{19}(CO)_{22}]^{4-}$ is less compact than that of the antiprismatic cluster $Pt_{19}(CO)_{17}]^{8-/10-}$ due to a 36° rotation of the central pentagonal ring when going from the former to the latter.

5 Conclusion

We hope that this pragmatic but illustrative account will stimulate the reader's appetite to explore more the extensive and diverse readings in the vibrant field of ligand-stabilized high-nuclearity clusters. It is clear that, despite increasingly accurate DFT calculations performed today to analyse electronic structures of nanoclusters, the concepts and ideas which Wade initiated 50 years ago [1] have been a valuable source of inspiration for the development of qualitative models. Indeed, over the years, the increasing number of large ligated transition metal clusters has been accompanied by the development of conceptual ideas and theoretical models aiming at understanding and rationalizing the relationships existing between the structure and the electron count [2–12, 15–25 59–62, 177, 178]. It turns out that the most useful characteristic of the electron-counting rules and that which distinguishes it from numerology is the incitement to understand the origins of the structural patterns using an orbital description developed from quantum mechanics. The definition of the electronic structure of a specific (nano)cluster is also important for defining the magnitude of a specific spectroscopic measurement but rarely leads to a deeper understanding of a general pattern. Interestingly, the development of qualitative models continues to be active today. For instance, Gao and co-workers developed recently the so-called *Grand Unified Model* (GUM) which proposes that any ligand-protected gold cluster is made of locally closed-shell elementary blocks (two-electron triangles and tetrahedra and eight-electron centred icosahedra) [179, 180]. A variant of the *jellium* model developed by Teo and Yang [181, 182], the so-called *jelliumatic* model, which separates nanoclusters in several atomic shells has also been used to rationalize the electron count of unusual shapes and compositions.

Chemists find that electron-counting rules which are based on the *jellium* approximation are particularly helpful. The perspective that noble metal nanoclusters are giant *superatoms* or giant *supermolecules* associated with electron counts can be simply derived from the oxidation states of the various cluster components. Application of this model to ligated non-coinage transition metal nanoclusters seems to be possible, assuming more and more involvement of *nd* orbitals as one moves to the left of the Periodic Table. This involvement can take two different forms. One is *nd* to $(n + 1)s$ electron transfer (and level crossing), as discussed above in the case of Pd

clusters. The other one is the possible *nd* participation to *jellium* orbitals, that is, inclusion of some *d*-electrons in the *superatom* electron count [183]. The *jellium* approximation is particularly flexible since it is also applicable to non-spherical shaped clusters, not only to oblate and prolate ellipsoidal species [31, 184] as discussed above, but also to clusters with cubic or cuboidal shapes, for instance [185, 186].

Finally, we would like to remind the reader that any electron-counting rule is based on the *closed-shell principle*, i.e., it requires the existence of a sizeable HOMO–LUMO gap. Although there are exceptions (e.g., Au_{20}, see above), the rules should not be applied to neutral bare metal clusters, which usually exhibit metal-like density of states, as well as, to very large ligated metal nanoclusters. The latter, having non-specific magic electron counts, lose their major reason to be exactly atom-precise. Exploring the boundaries between the world of large discrete clusters and their non-atom-precise nanoparticle counterparts is nowadays a very active field of research [66, 102–104, 187].

Acknowledgments J.W. thanks the China Scholarship Council for a Ph.D. grant. Prof. D. M. P. Mingos is warmly acknowledged for helpful discussions.

References

1. Wade K (1971) The structural significance of the number of skeletal bonding electron-pairs in carboranes, the higher boranes and borane anions, and various transition-metal carbonyl cluster compounds. J Chem Soc D Chem Commun:792–793
2. Mingos DMP, Wales DJ (1990) Introduction to cluster chemistry. Prentice-Hall, Englewood Cliffs
3. Fehlner TP, Halet J-F, Saillard J-Y (2007) Molecular clusters. In: A bridge to solid state chemistry. Cambridge University Press, Cambridge
4. Williams RE (1971) Carboranes and boranes; polyhedra and polyhedral fragments. Inorg Chem 10:210–214
5. Rudolph RW (1976) Boranes and heteroboranes: a paradigm for the electron requirements of clusters? Acc Chem Res 9:446–452
6. Rudolph RW, Pretzer WR (1972) Hückel-type rules and the systematization of borane and heteroborane chemistry. Inorg Chem 11:1974–1978
7. Williams RE (1992) The polyborane, carborane, carbocation continuum: architectural patterns. Chem Rev 92:177–207
8. Wade K (1980) Some bonding considerations. In: Johnson BFG (ed) Transition metal clusters. Wiley, Chichester, pp 193–264
9. Mingos DMP (1972) A general theory for cluster and ring compounds of the main group and transition elements. Nat Phys Sci 236:99–102
10. Wade K (1972) Skeletal electron counting in cluster species. Some generalisations and predictions. Inorg Nucl Chem Lett 8:559–562
11. Wade K (1972) Skeletal electron counting in cluster species. Applications to metal-hydrocarbon π-complexes. Inorg Nucl Chem Lett 8:563–566
12. Wade K (1976) Skeletal bond orders in borane anions $B_nH_n^{2-}$ and related closo-cluster species. Adv Inorg Chem Radio Chem 18:1–66
13. Elian M, Chen MM-L, Mingos DMP, Hoffmann R (1976) Comparative bonding study of conical fragments. Inorg Chem 15:1148–1155

14. Hoffmann R (1982) Building bridges between inorganic and organic chemistry. Angew Chem Int Ed 21:711–724
15. Mason R, Thomas KM, Mingos DMP (1973) Stereochemistry of octadecacarbonylhexaosmium(0). Novel hexanuclear complex based on a bicapped tetrahedron of metal atoms. J Am Chem Soc 95:3802–3804
16. Mingos DMP, Johnston RL (1987) Theoretical models of cluster bonding. Struct Bond 68:29–87
17. Mingos DMP (1991) Theoretical aspects of metal cluster chemistry. Pure Appl Chem 63:807–812
18. Stone AJ (1980) A new approach to bonding in transition metal clusters theory. Mol Phys 41:1339–1354
19. Stone AJ (1981) New approach to bonding in transition-metal clusters and related compounds. Inorg Chem 20:563–571
20. Stone AJ, Alderton MJ (1982) A new model of structure and bonding in the boron hydrides. Inorg Chem 21:2297–2302
21. Stone AJ (1984) The bonding in boron and transition-metal cluster compounds. Polyhedron 3:2051–2068
22. Wales DJ, Mingos DMP (1989) Splitting of cluster orbitals. Inorg Chem 28:2748–2754
23. Wales DJ, Mingos DMP, Slee T, Lin Z (1990) Clusters in inorganic and molecular beam chemistry, some unifying principles. Acc Chem Res 23:17–22
24. Johnston RL (1997) Mathematical cluster chemistry. Struct Bond 87:1–34
25. Mingos DMP, Lin Z (1988) A theoretical analysis of high-nuclearity metal carbonyl clusters. J Chem Soc Dalton Trans:1657–1664
26. Mayer MG, Jensen JHD (1955) Elementary theory of nuclear shell structure. Wiley, New York
27. Knight WD, Clemenger K, Heer WA, Saunder WA, Chou MY, Cohen ML (1984) Electronic shell structure and abundances of sodium clusters. Phys Rev Lett 52:2141–2144
28. Ekardt W (1985) Size-dependent photoabsorption and photoemission of small metal particles. Phys Rev B 31:6360–6370
29. Ekardt W (1985) Collective multipole excitations in small metal particles: critical angular momentum lcr for the existence of collective surface modes. Phys Rev B 32:1961–1970
30. de Heer WA (1993) The physics of simple metal clusters: experimental aspects and simple models. Rev Mod Phys 65:611–676
31. Lin Z, Slee T, Mingos DMP (1990) A structural jellium model of cluster electronic structure. Chem Phys 142:321–334
32. Lin Z, Kanters RFP, Mingos DMP (1991) Closed-shell electronic requirements for condensed clusters of the group 11 elements. Inorg Chem 30:91–93
33. Mingos DMP (1985) Theoretical analyses and electron counting rules for high nuclearity clusters. J Chem Soc Chem Commun:1352–1354
34. Mingos DMP, Johnston RL (1987) A group theoretical paradigm for describing the skeletal molecular orbitals of cluster compounds. Part 1. Deltahedral clusters. J Chem Soc Dalton Trans:647–656
35. Mingos DMP, Johnston RL (1987) A group theoretical paradigm for describing the skeletal molecular orbitals of cluster compounds. Part 2. Bispherical clusters. J Chem Soc Dalton Trans:1445–1456
36. Mingos DMP, Slee T, Lin Z (1990) Bonding models for ligated and bare clusters. Chem Rev 90:383–402
37. Johnston RL (2002) Atomic and molecular clusters. Taylor and Francis, New York
38. Saillard J-Y, Halet J-F (2016) Structure and bonding patterns in large molecular ligated metal clusters. Struct Bond 169:157–180
39. Frapper G, Halet J-F (2019) Rationalising and predicting the structure and bonding of bare and ligated transition metal clusters and nanoparticles. In: Oganov AR, Kvashnin AG, Saleh G (eds) Computational materials discovery. Royal Society of Chemistry, London, pp 320–351

40. Hall KP, Theobald BRC, Gilmour DI, Mingos DMP, Welch AJ (1982) Synthesis and structural characterization of $[Au_9\{P(p\text{-}C_6H_40Me)_3\}_8](BF_4)_3$; a cluster with a centered crown of gold. J Chem Soc Chem Commun:528–530
41. Woods RD, Saxon DS (*1954*) *Diffuse surface optical model for nucleon-nuclei scattering*. Phys Rev *95:577–578*
42. Leuchtner RE, Harms AC, Castleman Jr AW (1989) Thermal metal cluster anion reactions: behavior of aluminum clusters with oxygen. J Chem Phys 91:2753–2754
43. Khanna SN, Jena P (1992) Assembling crystals from clusters. Phys Rev Lett 69:1664–1667
44. Khanna SN, Jena P (1995) Atomic clusters: building blocks for a class of solids. Phys Rev B 51:13705–13716
45. Jena P, Khanna SW, Rao BK (1996) Designing clusters as superelements. Surf Rev Lett 3:993–999
46. Bergeron DE, Roach PJ, Castleman Jr AW, Jones NO, Khanna SN (2005) Al cluster superatoms as halogens in polyhalides and as alkaline earths in iodide salts. Science 307:231–235
47. Castleman AW, Khanna SN (2009) Clusters, superatoms, and building blocks of new materials. J Phys Chem C 113:2664–2675
48. Luo Z, Castleman AW (2014) Special and general superatoms. Acc Chem Soc 47:2931–2940
49. Hoffmann R, Schleyer PVR, Schaefer HFIII (2008) Predicting molecules-more realism, please! Angew Chem Int Ed 47:7164–7167
50. Bergeron DE, Castleman Jr AW, Morisato T, Khanna SN (2004) Formation of $Al_{13}I^-$: evidence for the superhalogen character of Al_{13}. Science 304:84–87
51. Vollet J, Hartig JR, Schnöckel H (2004) $Al_{50}C_{120}H_{180}$: a pseudofullerene shell of 60 carbon atoms and 60 methyl groups protecting a cluster core of 50 aluminum atoms. Angew Chem Int Ed 43:3186–3189
52. Clayborne PA, Lopez-Acevedo O, Whetten RL, Grönbeck H, Häkkinen H (2011) The $Al_{50}Cp^*_{12}$ cluster - a 138-electron closed shell (L = 6) superatom. Eur J Inorg Chem 2011:2649–2652
53. Schnöckel H (2010) Structures and properties of metalloid Al and Ga clusters open our eyes to the diversity and complexity of fundamental chemical and physical processes during formation and dissolution of metals. Chem Rev 110:4125–4163
54. Mingos DMP (1976) Molecular-orbital calculations on cluster compounds of gold. J Chem Soc Dalton Trans:1163–1169
55. Mingos DMP (1984) Gold cluster compounds are they metals in miniature? Gold Bull 17:5–12
56. Briant CE, Theobald BRC, White JW, Bell LK, Mingos DMP, Welch AJ (1981) Synthesis and X-ray structural characterization of the centred icosahedral gold cluster compound $[Au_{13}(PMe_2Ph)_{10}Cl_2](PF_6)_3$; the realization of a theoretical prediction. J Chem Soc Chem Commun:201–202
57. Briant CE, Hall KP, Mingos DMP (1984) Structural characterisation of two crystalline modifications of $[Au_9\{P(C_6H_4OMe\text{-}p)_3\}_8](NO_3)_3$: the first example of skeletal isomerism in metal cluster chemistry. J Chem Soc Chem Commun:290–291
58. Copley RCB, Mingos DMP (1996) The novel structure of the $[Au_{11}(PMePh_2)_{10}]^{3+}$ cation: crystal structures of $[Au_{11}(PMePh_2)_{10}][C_2B_9H_{12}]_3{\cdot}4thf$ and $[Au_{11}(PMePh_2)_{10}][C_2B_9H_{12}]_3$ (thf = tetrahydrofuran). J Chem Soc Chem Commun:479–489
59. Mingos DMP (2014) Structural and bonding issues in clusters and nano-clusters. Struct Bond 162:1–65
60. Mingos DMP (2015) Structural and bonding patterns in gold clusters. Dalton Trans 44:6680–6695
61. Teo BK, Shi X, Zhang H (1992) Pure gold cluster of 1:9:9:1:9:9:1 layered structure: a novel 39-metal-atom cluster $[(Ph_3P)_{14}Au_{39}Cl_6]Cl_2$ with an interstitial gold atom in a hexagonal antiprismatic cage. J Am Chem Soc 114:2743–2745
62. Teo BK (2014) A perspective on the science of clusters. J Clust Sci 25:5–28

63. Häkkinen H (2008) Atomic and electronic structure of gold clusters: understanding flakes, cages and superatoms from simple concepts. Chem Soc Rev 37:1847–1859
64. Walter M, Akola J, Lopez-Acevedo O, Jadzinsky PD, Calero G, Ackerson CJ, Whetten RL, Grönbeck H, Häkkinen H (2008) A unified view of ligand-protected gold clusters as superatom complexes. Proc Natl Acad Sci U S A 105:9157–9162
65. Reimers JR, Wang Y, Cankurtaran BO, Ford MJ (2010) Chemical analysis of the superatom model for sulfur-stabilized gold nanoparticles. J Am Chem Soc 132:8378–8384
66. Häkkinen H (2012) Louis C, Pluchery O (eds) Theoretical studies of gold nanoclusters in various chemical environments: when the size matters, in from gold nanoparticles for physics, chemistry and biology. Imperial College Press, London, p 233
67. Weerawardene KD, Häkkinen H, Aikens CM (2018) Connections between theory and experiment for gold and silver nanoclusters. Annu Rev Phys Chem 69:205–229
68. Wei J, Marchal R, Astruc D, Saillard JY, Halet JF, Kahlal S (2020) Theoretical analysis of the Mackay icosahedral cluster $Pd_{55}(P\mathit{i}Pr_3)_{12}(\mu_3\text{-}CO)_{20}$: an open-shell 20-electron superatom. Chem Eur J 26:5508–5514
69. Jin R, Zeng C, Zhou M, Chen Y (2016) Atomically precise colloidal metal nanoclusters and nanoparticles: fundamentals and opportunities. Chem Rev 116:10346–10413
70. Chakraborty I, Pradeep T (2017) Atomically precise clusters of noble metals: emerging link between atoms and nanoparticles. Chem Rev 117:8208–8271
71. Yao Q, Chen T, Yuan X, Xie J (2018) Toward total synthesis of thiolate-protected metal nanoclusters. Acc Chem Rev 51:1338–1348
72. Sakthivel NA, Dass A (2018) Aromatic thiolate-protected series of gold nanomolecules and a contrary structural trend in size evolution. Acc Chem Rev 51:1774–1783
73. Lei Z, Wan X-K, Yuan S-F, Guan Z-J, Wang Q-M (2018) Alkynyl approach toward the protection of metal nanoclusters. Acc Chem Rev 51:2465–2474
74. Higaki T, Li Q, Zhou M, Zhao S, Li Y, Li S, Jin R (2018) Toward the tailoring chemistry of metal nanoclusters for enhancing functionalities. Acc Chem Rev 51:2764–2773
75. Yan J, Teo BK, Zheng N (2018) Surface chemistry of atomically precise coinage-metal nanoclusters: from structural control to surface reactivity and catalysis. Acc Chem Rev 51:3084–3093
76. Sharma S, Chakrahari KK, Saillard J-Y, Liu CW (2018) Structurally precise dichalcogenolate-protected copper and silver superatomic nanoclusters and their alloys. Acc Chem Res 51:2475–2483
77. Smith CA, Narouz MR, Lummis PA, Singh I, Nazemi A, Li CH, Crudden MC (2019) N-heterocyclic carbenes in materials chemistry. Chem Rev 119:4986–5056
78. Du Y, Sheng H, Astruc D, Zhu M (2019) Atomically precise noble metal nanoclusters as efficient catalysts: a bridge between structure and properties. Chem Rev 120:526–622
79. Kang X, Zhu M (2019) Tailoring the photoluminescence of atomically precise nanoclusters. Chem Soc Rev 48:2422–2457
80. Omoda T, Takano S, Tsukuda T (2020) Toward controlling the electronic structures of chemically modified superatoms of gold and silver. Small. https://doi.org/10.1002/smll.202001439
81. Kang X, Li Y, Zhu M, Jin R (2020) Atomically precise alloy nanoclusters: syntheses, structures, and properties. Chem Soc Rev 49:6443–6514
82. Hirai H, Ito S, Takano S, Koyasu K, Tsukuda T (2020) Ligand-protected gold/silver superatoms: current status and emerging trends. Chem Sci 11:12233–12248
83. Esma K, Pradeep T (2021) New routes for multicomponent atomically precise metal nanoclusters. ACS Omega 6:1–6
84. Mingos DMP (ed) (2014) Gold clusters, colloids and nanoparticles I. Structure and bonding, vol 161. Springer, Berlin
85. Häkkinen H (2015) Electronic structure: Shell structure and the superatom concept. In: Tsukuda T, Häkkinen H (eds) Frontiers of nanoscience. Protected metal clusters: from fundamentals to applications, vol 9. Elsevier, Amsterdam, pp 189–222

86. Heaven MW, Dass A, White PS, Holt KM, Murray RW (2008) Crystal structure of the gold nanoparticule $[N(C_8H_{17})_4][Au_{25}(SCH_2CH_2Ph)_{18}]$. J Am Chem Soc 130:3754–3755
87. Akola J, Walter M, Whetten RL, Häkkinen H, Grönbeck H (2008) On the structure of thiolate-protected Au_{25}. J Am Chem Soc 130:3756–3757
88. Dhayal RS, Liao J-H, Liu Y-C, Chiang M-H, Kahlal S, Saillard J-Y, Liu CW (2015) $[Ag_{21}\{S_2P(OiPr)_2\}_{12}]^+$: an eight-electron superatom. Angew Chem Int Ed 54:3702–3706
89. Kang X, Zhu M (2021) Structural isomerism in atomically precise nanoclusters. Chem Mater 33:39–62
90. Yan J, Zhang J, Chen X, Malola S, Zhou B, Selenius E, Zhang X, Yuan P, Deng G, Liu K, Su H, Teo BK, Häkkinen ZL, Zheng N (2018) Thiol-stabilized atomically precise, superatomic silver nanoparticles for catalysing cycloisomerization of alkynyl amines. Natl Sci Rev 5:694–702
91. Dhayal RS, Lin Y-R, Liao J-H, Chen Y-J, Liu Y-C, Chiang M-H, Kahlal S, Saillard J-Y, Liu CW (2016) $[Ag_{20}\{S_2P(OR)_2\}_{12}]$: a superatom complex with a chiral metallic core and high potential for isomerism. Chem Eur J 22:9943–9947
92. Kalenius E, Malola S, Matus MF, Kazan R, Bürgi T, Häkkinen (2021) Experimental confirmation of a topological isomer of the ubiquitous $Au_{25}(SR)_{18}$ cluster in the gas phase. J Am Chem Soc 143:1273–1277
93. Li J, Li X, Zhai H-J, Wang L-S (2003) Au_{20}: a tetrahedral cluster. Science 299:864–867
94. Liu J-Y, Alkan F, Wang Z, Zhang Z-Y, Kurmoo M, Yan Z, Zhao Q-Q, Aikens CM, Tung C-H, Sun D (2019) Different silver nanoparticles in one crystal: $Ag_{210}(^i PrPhS)_{71}(Ph_3P)_5Cl$ and $Ag_{211}(^i PrPhS)_{71}(Ph_3P)_6Cl$. Angew Chem Int Ed 58:195–199
95. Hu F, Li J-J, Guan Z-J, Yuan S-F, Wang Q-M (2020) Formation of an alkynyl-protected Ag_{112} silver nanocluster as promoted by chloride released in situ from CH_2Cl_2. Angew Chem Int Ed 59:5312–5315
96. Jadzinsky PD, Calero G, Ackerson CJ, Bushnell DA, Kornberg RD (2007) Structure of a thiol monolayer-protected gold nanoparticle at 1.1 Å resolution. Science 318:430–433
97. Higaki T, Liu C, Zhou M, Luo T-Y, Rosi NL, Jin R (2017) Tailoring the structure of 58-electron gold nanoclusters: $Au_{103}S_2(S\text{-nap})_{41}$ and its implications. J Am Chem Soc 139:9994–10001
98. Lei Z, Li J-J, Wan X-K, Zhang W-H, Wang Q-M (2018) Isolation and total structure determination of an all-alkynyl-protected gold nanocluster Au_{144}. Angew Chem Int Ed 57:8639–8643
99. Zhou M, Zeng C, Song Y, Padelford JW, Wang G, Sfeir MY, Higaki T, Jin R (2017) On the non-metallicity of 2.2 nm $Au_{246}(SR)_{80}$ nanoclusters. Angew Chem Int Ed 56:16257–16261
100. Higaki T, Zhou M, Lambright KJ, Kirschbaum K, Sfeir MY, Jin R (2018) Sharp transition from nonmetallic Au_{246} to metallic Au_{279} with nascent surface plasmon resonance. J Am Chem Soc 140:5691–5695
101. Yang H, Wang Y, Chen X, Zhao X, Gu L, Huan H, Yan J, Xu C, Li G, Wu J, Edwards AJ, Dittrich B, Tang Z, Wang D, Lehtovaara H, Zheng N (2016) Plasmonic twinned silver nanoparticles with molecular precision. Nat Commun 7:12809
102. Malola S, Häkkinen H (2015) How many gold atoms make gold metal? Europhys News 46:23–26
103. Chakraborty I, Erusappan J, Govindarajan A, Sugi KS, Udayabhaskarano T, Ghosh A, Pradeep T (2014) Emergence of metallicity in silver clusters in the 150 atoms regime: a study of differently sized silver clusters. Nanoscale 6:8024–8031
104. Chakrahari KK, Liao J-H, Kahlal S, Liu Y-C, Chiang M-H, Saillard J-Y, Liu CW (2016) $[Cu_{13}\{S_2CN^nBu_2\}_6(acetylide)_4]^+$: a two-electron superatom. Angew Chem Int Ed 55:14704–14708
105. Nguyen T-AD, Jones ZR, Goldsmith BR, Buratto WR, Wu G, Scott SL, Hayton TW (2015) A Cu_{25} nanocluster with partial Cu(0) character. J Am Chem Soc 137:13319–13324

106. Yang H, Wang Y, Huang H, Gell L, Lehtovaara L, Malola S, Häkkinen H, Zheng N (2013) All-thiol-stabilized Ag_{44} and $Au_{12}Ag_{32}$ nanoparticles with single-crystal structures. Nat Commun 4:2422
107. Desireddy A, Conn BE, Guo J, Yoon B, Barnett RN, Monahan BM, Kirschbaum K, Griffith WP, Whetten RL, Landman U, Bigioni TP (2013) Ultrastable silver nanoparticles. Nature 501:399–402
108. Chai J, Yang S, Lv Y, Chen T, Wang S, Yu H, Zhu M (2018) A unique pair: Ag_{40} and Ag_{46} nanoclusters with the same surface but different cores for structure-property correlation. J Am Chem Soc 140:15582–15585
109. Bodiuzzaman M, Ghosh A, Sugi KS, Nag A, Khatun E, Varghese B, Paramasivam G, Antharjanam S, Natarajan G, Pradeep T (2019) Camouflaging structural diversity: co-crystallization of two different nanoparticles having different cores but the same shell. Angew Chem Int Ed 58:189–194
110. Bodiuzzaman M, Dar WA, Pradeep T (2020) Cocrystals of atomically precise noble metal nanoclusters. Small. https://doi.org/10.1002/smll.202003981
111. Dass A (2009) Mass spectrometric identification of $Au_{68}(SR)_{34}$ molecular gold nanoclusters with 34-electron shell closing. J Am Chem Soc 131:11666–11667
112. Xu WW, Gao Y (2015) Unraveling the atomic structures of the $Au_{68}(SR)_{34}$ nanoparticles. J Phys Chem C 119:14224–14229
113. Wang S, Li Q, Kang X, Zhu M (2018) Customizing the structure, composition, and properties of alloy nanoclusters by metal exchange. Acc Chem Res 51:2784–2792
114. Ghosh A, Mohammed OF, Bakr OM (2018) Atomic-level doping of metal clusters. Acc Chem Res 51:3094–3103
115. Hossain S, Niihori Y, Nair LV, Kumar B, Kurashige W, Negishi Y (2018) Alloy clusters: precise synthesis and mixing effects. Acc Chem Res 51:3114–3124
116. Takano S, Tsukuda T (2021) Chemically modified gold/silver superatoms as artificial elements at nanoscale: design principles and synthesis challenges. J Am Chem Soc 143:1683–1698
117. Bootharaju MS, Joshi CP, Parida MR, Mohammed OF, Bakr OM (2016) Templated atom-precise galvanic synthesis and structure elucidation of a $[Ag_{24}Au(SR)_{18}](-)$ nanocluster. Angew Chem Int Ed 55:922–926
118. Chang W-T, Lee P-Y, Liao J-H, Chakrahari KK, Kahlal S, Liu Y-C, Chiang M-H, Saillard J-Y, Liu CW (2017) Eight-electron silver and mixed gold/silver nanoclusters stabilized by selenium donor ligands. Angew Chem Int Ed 56:10178–10182
119. Guan Z-J, Zeng J-L, Yuan S-F, Hu F, Lin Y-M, Wang Q-M (2018) $Au_{57}Ag_{53}(C{\equiv}CPh)_{40}Br_{12}$: a large nanocluster with C_1 symmetry. Angew Chem Int Ed 57:5703–5707
120. Zeng J-L, Guan Z-J, Du Y, Nan Z-A, Lin Y-M, Wang Q-M (2016) Chloride-promoted formation of a bimetallic nanocluster $Au_{80}Ag_{30}$ and the total structure determination. J Am Chem Soc 138:7848–7851
121. Zou X, Li Y, Jin S, Kang X, Wei X, Wang S, Meng X, Zhu M (2020) Doping copper atoms into the nanocluster kernel: Total structure determination of $[Cu_{30}Ag_{61}(SAdm)_{38}S_3](BPh_4)$. J Phys Chem Lett 11:2272–2276
122. Wang S, Jin S, Yang S, Chen S, Song Y, Zhang J, Zhu M (2015) Total structure determination of surface doping $[Ag_{46}Au_{24}(SR)_{32}](BPh_4)_2$ nanocluster and its structure-related catalytic property. Sci Adv 1:e1500441
123. Kawawaki T, Imai Y, Suzuki D, Kato S, Kobayashi I, Suzuki T, Kaneko R, Hossain S, Negishi Y (2020) Atomically precise alloy nanoclusters. Chem Eur J 26:16150–16193
124. Lin Y-R, Kishore PVVN, Liao J-H, Kahlal S, Liu Y-C, Chiang M-H, Saillard J-Y, Liu CW (2018) Synthesis, structural characterization and transformation of an eight-electron superatomic alloy, $[Au@Ag_{19}\{S_2P(OPr)_2\}_{12}]$. Nanoscale 10:6855–6860
125. Hirai H, Takano S, Nakamura T, Tsukuda T (2020) Understanding doping effects on electronic structures of gold superatoms: a case study of diphosphine-protected $M@Au_{12}$(M = Au, Pt, Ir). Inorg Chem 59:17889–17895

126. Bhat S, Baksi A, Mudedla SK, Natarajan G, Subramanian V, Pradeep T (2017) $Au_{22}Ir_3(PET)_{18}$: an unusual alloy cluster through intercluster reaction. J Phys Chem Lett 8:2787–2793
127. Yao C, Lin Y-J, Yuan J, Liao L, Zhu M, Weng L-H, Yang J, Wu Z (2015) Mono-cadmium vs mono-mercury doping of Au_{25} nanoclusters. J Am Chem Soc 137:15350–15353
128. Kwak K, Tang Q, Kim M, Jiang D-E, Lee D (2015) Interconversion between superatomic 6-electron and 8-electron configurations of $M@Au_{24}(SR)_{18}$ clusters (M = Pd, Pt). J Am Chem Soc 137:10833–10840
129. Negishi Y, Igarashi K, Munakata K, Ohgake W, Nobusada K (2012) Palladium doping of magic gold cluster $Au_{38}(SC_2H_4Ph)_{24}$: formation of $Pd_2Au_{36}(SC_2H_4Ph)_{24}$ with higher stability than $Au_{38}(SC_2H_4Ph)_{24}$. Chem Commun 48:660–662
130. Chiu T-H, Liao J-H, Gam F, Chantrenne I, Kahlal S, Saillard J-Y, Liu CW (2019) Homoleptic platinum/silver superatoms protected by dithiolates: linear assemblies of two and three centered icosahedra isolobal to Ne_2 and I_3-. J Am Chem Soc 141:12957–12961
131. Kumara C, Aikens CM, Dass A (2014) X-ray crystal structure and theoretical analysis of $Au_{25-X}Ag_X(SCH_2CH_2Ph)_{18}$-alloy. J Phys Chem Lett 5:461–466
132. Freitag K, Banh H, Gemel C, Seidel RW, Kahlal S, Saillard J-Y, Fischer RA (2014) Molecular brass: Cu_4Zn_4, a ligand protected superatom cluster. Chem Commun 50:8681–8684
133. Mackay AL (1962) A dense non-crystallographic packing of equal spheres. Acta Cryst 15:916–918
134. Weßing J, Ganesamoorthy C, Kahlal S, Marchal R, Gemel C, Cador O, Da Silva ACH, Da Silva JLF, Saillard J-Y, Fischer RA (2018) The Mackay-type cluster $[Cu_{43}Al_{12}](Cp^*)_{12}$: open-shell 67-electron superatom with emerging metal-like electronic structure. Angew Chem Int Ed 57:14630–14634
135. Suyama M, Takano S, Nakamura T, Tsukuda T (2019) Stoichiometric formation of open-shell $[PtAu_{24}(SC_2H_4Ph)_{18}]^-$ via spontaneous electron proportionation between $[PtAu_{24}(SC_2H_4Ph)_{18}]^{2-}$ and $[PtAu_{24}(SC_2H_4Ph)_{18}]^0$. J Am Chem Soc 141:14048–14051
136. Schütz M, Maximilian M, Freitag K, Gemel C, Kahlal S, Saillard J-Y, Da Silva ACH, Da Silva JLF, Fässler TF, Fischer RA (2020) Contrasting structure and bonding of a copper-rich and a zinc-rich intermetalloid Cu/Zn cluster. Inorg Chem 59:9077–9085
137. Zeng C, Qian HQ, Li T, Li G, Rosi NL, Yoon B, Barnett RN, Whetten RL, Landman U, Jin R (2012) Total structure and electronic properties of the gold nanocrystal $Au_{36}(SR)_{24}$. Angew Chem Int Ed Engl 51:13114–11318
138. Jin S, Zhou M, Kang X, Li X, Du W, Wei X, Chen S, Wang S, Zhu M (2020) Three-dimensional octameric assembly of icosahedral M_{13} units in $[Au_8Ag_{57}(Dppp)_4(C_6H_{11}S)_{32}Cl_2]Cl$ and its $[Au_8Ag_{55}(Dppp)_4(C_6H_{11}S)_{34}][BPh_4]_2$ derivative. Angew Chem Int Ed 59:3891–3895
139. Gam F, Liu CW, Kahlal S, Saillard J-Y (2020) Electron counting and bonding patterns in assemblies of three and more silver-rich superatoms. Nanoscale 12:20308–20316
140. Teo BK, Zhang H, Shi X (1990) Cluster of clusters: a modular approach to large metal clusters. Structural characterization of a 38-atom cluster $[(p\text{-}Tol_3P)_{12}Au_{18}Ag_{20}Cl_{14}]$ based on vertex-sharing triicosahedra. J Am Chem Soc 112:8552–8562
141. Teo BK, Shi X, Zhang H (1991) Cluster of clusters. Structure of a novel gold-silver cluster $[(Ph_3P)_{10}Au_{13}Ag_{12}Br_8][SbF_6]$ containing an exact staggered-eclipsed-staggered metal configuration. Evidence of icosahedral units as building blocks. J Am Chem Soc 113:4329–4331
142. Saito S, Ohnishi S (1987) Stable $(Na_{19})_2$ as a giant alkali-metal-atom dimer. Phys Rev Lett 59:190–193
143. Cheng L, Yang J (2013) Communication: new insight into electronic shells of metal clusters: analogues of simple molecules. J Chem Phys 138:141101–141104
144. Goicoechea JM, Sevov SC (2005) $[(Pd\text{-}Pd)@Ge_{18}]^{4-}$: a palladium dimer inside the largest single-cage deltahedron. J Am Chem Soc 127:7676–7677
145. Sun Z-M, Xiao H, Li J, Wang L-S (2007) $Pd_2@Sn_{18}^{4-}$: fusion of two endohedral stannaspherenes. J Am Chem Soc 129:9560–9561

146. Kang X, Xiang J, Lv Y, Du W, Yu H, Wang S, Zhu M (2017) Synthesis and structure of self-assembled $Pd_2Au_{23}(PPh_3)_{10}Br_7$ nanocluster: exploiting factors that promote assembly of icosahedral nano-building blocks. Chem Mater 29:6856–6862
147. Teo BK, Shi X, Zhang H (1993) Bond valence sum analysis of metal-ligand bond lengths in metalloenzymes and model complexes. 2. Refined distances and other enzymes. Inorg Chem 32:3987–3988
148. Jena P, Sun Q (2018) Super atomic clusters: design rules and potential for building blocks of materials. Chem Rev 118:5755–5870
149. Muñoz-Castro A (2019) Single, double, and triple intercluster bonds: analyses of $M_2Au_{36}(SR)_{24}$ (M = Au, Pd, Pt) as 14-, 12- and 10-ve superatomic molecules. Chem Commun 55:7307–7310
150. Muñoz-Castro A (2020) Triple 1D≡1D superatomic bonding. $Au_{22}(dppp)_6$ as a $\prod^4$- and Δ^2-triply bonded cluster based on Au_{11} assembled units. Phys Chem Chem Phys 22:1422–1426
151. Teo BK (1988) Novel triicosahedral structure of the largest metal alloy cluster: hexachlorododecakis(triphenylphosphine)-gold-silver cluster $[(Ph_3P)_{12}Au_{13}Ag_{12}Cl_6]^{m+}$. J Am Chem Soc 106:2224–2226
152. Liu Q, Xu C, Wu X, Cheng L (2019) Electronic shells of a tubular Au_{26} cluster: a cage-cage superatomic molecule based on spherical aromaticity. Nanoscale 11:13227–13232
153. Cheng L, Ren C, Zhang X, Yang J (2013) New insight into the electronic shell of $Au_{38}(SR)_{24}$: a superatomic molecule. Nanoscale 5:1475–1478
154. Liu L, Li P, Yuan L-F, Cheng L, Yang J (2016) From isosuperatoms to isosupermolecules: new concepts in cluster science. Nanoscale 8:12787–12792
155. Herzberg G (1967) Molecular spectra and molecular structure, volume 3: electronic spectra and electronic structure of polyatomic molecules. Van Nostrand, New York, USA, 276–419
156. Mulliken RS (1932) Electronic structures of polyatomic molecules and valence. Phys Rev 40:55–62
157. Mulliken RS (1932) Electronic structures of polyatomic molecules and valence. II. General considerations. Phys Rev 41:49–71
158. Mulliken RS (1932) Electronic structures of polyatomic molecules and valence. II. Quantum theory of the double bond. Phys Rev 41:751–758
159. Lowe JR (1978) Quantum chemistry. Academic Press, New York, pp 167–192
160. Qian H, Eckenhoff WT, Zhu Y, Pintauer T, Jin R (2010) Total structure determination of thiolate-protected Au_{38} nanoparticles. J Am Chem Soc 132:8280–8281
161. Nunokawa K, Ito M, Sunahara T, Onaka S, Ozeki T, Chiba H, Funahashi Y, Masuda H, Yonezawa T, Nishihara H, Nakamoto M, Yamamoto M (2005) A new 19-metal-atom cluster $[(Me_2PhP)_{10}Au_{12}Ag_7(NO_3)_9]$ with a nearly staggered-staggered M_5 ring configuration. Dalton Trans:2726–2730
162. Ito E, Takano S, Nakamura T, Tsukuda T (2021) Controlled dimerization and bonding scheme of icosahedral $M@Au_{12}$ (M = Pd, Pt) superatoms. Angew Chem 133:645–649
163. Belyakova OA, Slovokhotov YL (2003) Structures of large transition metal clusters. Russ Chem Bull Int Ed 52:2299–2327
164. Femoni C, Iapalucci MC, Kaswalder F, Longoni G, Zacchini S (2006) The possible role of metal carbonyl clusters in nanoscience and nanotechnologies. Coord Chem Rev 250:1580–1604
165. Mednikov EG, Dahl LF (2010) Syntheses, structures and properties of primarily nanosized homo/heterometallic palladium CO/PR_3-ligated clusters. Philos Trans R Soc A (Lond) 368:1301–1332
166. Ciabatti I, Femoni C, Iapalucci MC, Longoni G, Zacchini S (2014) Platinum carbonyl clusters chemistry: four decades of challenging nanoscience. J Clust Sci 25:115–146

167. Berti B, Cesari C, Femoni C, Funaioli T, Iapalucci MC, Zacchini S (2020) Redox active Ni–Pd carbonyl alloy nanoclusters: syntheses, molecular structures and electrochemistry of $[Ni_{22-x}Pd_{20+x}(CO)_{48}]^{6-}$ (x = 0.62), $[Ni_{29-x}Pd_{6+x}(CO)_{42}]^{6-}$ (x = 0.09) and $[Ni_{29+x}Pd_{6-x}(CO)_{42}]^{6-}$ (x = 0.27). Dalton Trans 49:5513–5522
168. Erickson JD, Mednikov EG, Ivanov SA, Dahl LF (2016) Isolation and structural characterization of a Mackay 55-metal-atom two-shell icosahedron of pseudo-I_h symmetry, $Pd_{55}L_{12}(\mu_3\text{-}CO)_{20}$ (L = PR_3, R = isopropyl): comparative analysis with interior two-shell icosahedral geometries in capped three-shell Pd_{145}, Pt-centered four-shell Pd-Pt M_{165}, and four-shell Au_{133} nanoclusters. J Am Chem Soc 138:1502–1505
169. Tran NT, Powell DR, Dahl LF (2000) Nanosized $Pd_{145}(CO)_x(PEt_3)_{30}$ containing a capped three-shell 145-atom metal-core geometry of pseudo icosahedral symmetry. Angew Chem Int Ed 39:4121–4125
170. Mednikov EG, Jewell MC, Dahl LF (2007) Nanosized $(\mu_{12}\text{-}Pt)Pd_{164-x}Pt_x(CO)_{72}(PPh_3)_{20}$ (x ≈ 7) containing Pt-centered four-shell 165-atom Pd-Pt core with unprecedented intershell bridging carbonyl ligands: comparative analysis of icosahedral shell-growth patterns with geometrically related $Pd_{145}(CO)_x(PEt_3)_{30}$ (x ≈ 60) containing capped three-shell Pd_{145} core. J Am Chem Soc 129:11619–11630
171. Femoni C, Iapalucci MC, Longoni G, Zacchini S, Zarra S (2011) Icosahedral Pt-centered Pt_{13} and Pt_{19} carbonyl clusters decorated by $[Cd_5(\mu\text{-}Br)_5Br_{5-x}(solvent)_x]^{x+}$ rings reminiscent of the decoration of Au-Fe-CO and Au- thiolate nanoclusters: a unifying approach to their electron counts. J Am Chem Soc 133:2406–2409
172. de Silva N, Dahl LF (2005) Synthesis and structural analysis of the first nanosized platinum-gold carbonyl/phosphine cluster, $Pt_{13}[Au_2(PPh_3)_2]_2(CO)_{10}(PPh_3)_4$, containing a Pt-centered $[Ph_3PAu\text{-}AuPPh_3]$-capped icosahedral Pt_{12} cage. Inorg Chem 44:9604–9606
173. Teramoto M, Iwata K, Yamaura H, Kurashima K, Miyazawa K, Kurashige Y, Yamamoto K, Murahashi T (2018) Three-dimensional sandwich nanocubes composed of 13-atom palladium core and hexakis-carbocycle shell. J Am Chem Soc 140:12682–12686
174. Wei J, Kahlal S, Halet J-F, Saillard J-Y (2019) Elucidating the electronic structure of the ligated cuboctahedral palladium cluster $[Pd_{13}(\mu_4\text{-}C_7H_7)_6]^{2+}$. J Clust Sci 30:1227–1233
175. Washecheck DM, Wucherer EJ, Dahl LF, Ceriotti A, Longoni G, Manassero M, Sansoni M, Chini P (1979) Synthesis, structure, and stereochemical implication of the $[Pt_{19}(CO)_{12}(\mu_2\text{-}CO)_{10}]^{4-}$ tetraanion: a bicapped triple-decker all-metal sandwich of idealized fivefold (D5h) geometry. J Am Chem Soc 101:6110–6112
176. Wei J, Kahlal S, Saillard J-Y, Halet J-F (2021) Superatoms and supermolecules in ligand-protected platinum nanocluters. Unpublished results
177. Jemmis ED, Balakrishnarajan MM, Pancharatna PD (2001) A unifying electron-counting rule for macropolyhedral boranes, metallaboranes, and metallocenes. J Am Chem Soc 122:4313–4323
178. Jemmis ED, Balakrishnarajan MM, Pancharatna PD (2002) Electronic requirements for macropolyhedral boranes. Chem Rev 102:93–144
179. Xu WW, Zhu B, Zeng XC, Gao Y (2015) A grand unified model for liganded gold clusters. Nat Commun 7:13574
180. Xu WW, Zeng XC, Gao Y (2018) Application of electronic counting rules for ligand-protected gold nanoclusters. Acc Chem Res 51:2739–2747
181. Teo BK, Yang SY (2015) Jelliumatic shell model. J Clust Sci 26:1923–1941
182. Teo BK, Yang H, Yan J, Zheng N (2017) Supercubes, supersquares, and superrods of face-centered cubes (FCC): atomic and electronic requirements of $[M_m(SR)_l(PR_3)_8]^q$ nanoclusters (M = coinage metals) and their implications with respect to nucleation and growth of FCC metals. Inorg Chem 56:11470–11479
183. Mingos DMP, Modrego J (1991) Exceptions to the polyhedral skeletal electron pair theory in heterometallic naked clusters. New J Chem 15:9–16
184. Clemenger K (1985) Ellipsoidal shell structure in free-electron metal clusters. Phys Rev B 32:1359–1362

185. Zeng C, Chen Y, Iida K, Nobusada K, Kirschbaum K, Lambright KJ, Jin R (2016) Gold quantum boxes: on the periodicities and the quantum confinement in the Au_{28}, Au_{36}, Au_{44}, and Au_{52} magic series. J Am Chem Soc 138:3950–3953
186. Yang H, Yan J, Wang Y, Su H, Gell L, Zhao X, Xu C, Teo BK, Häkkinen H, Zheng N (2017) Embryonic growth of face-center-cubic silver nanoclusters shaped in nearly perfect half-cubes and cubes. J Am Chem Soc 139:31–34
187. Pillay MN, van Zyl WE, Liu CW (2020) A construction guide for high-nuclearity ($\geq$50 metal atoms) coinage metal clusters at the nanoscale: bridging molecular precise constructs with the bulk material phase. Nanoscale 12:24331–24348

Struct Bond (2021) 188: 103–148
https://doi.org/10.1007/430_2021_88

Published online: 7 August 2021

Binary Zintl Anions Involving Group 13–15 (Semi-)Metal Atoms, and the Relationship of Their Structures to Electron Count

Fuxing Pan, Bastian Weinert, and Stefanie Dehnen

Dedicated to the memory of Professor Kenneth Wade.

Contents

Abstract Binary molecular Zintl anions, which consist of either two different p-block atoms or one type of p- and d-block atoms each do not only exhibit exceptional cage-type architectures, but they have also served as starting materials for a variety of derivatives. Like their homoatomic cousins, they can be treated in regard of the structure-electron count relationship by application of either the 8 – *N* rule or Wade-Mingos rules. This review article provides a full collection of representative known examples and comments on the respective bonding situations and

F. Pan, B. Weinert, and S. Dehnen (✉)
Fachbereich Chemie, Philipps-Universität Marburg, Marburg, Germany
e-mail: dehnen@chemie.uni-marburg.de

structures, also in the context of contemporary inorganic synthesis and materials chemistry.

Keywords Binary · Electron count · Heterometallic · Wade-Mingos rules · Zintl anions

1 Introduction

1.1 General Remarks on Zintl Anions and Electron Counting Rules

Anions that comprise purely metal or semimetal atoms have been a fascinating species of molecules since their early discovery at the end of the nineteenth century by Kraus and Joannis [1, 2] and the more detailed studies and finally confirmation of their nature by Zintl in the early 1930s [3]. Ever since, the exploration of their properties in the solid state, in solution and in the gas phase, and their potential use as precursors for multimetallic cluster synthesis [4–18], or as precursors for new materials by mild oxidative conditions [19–21], has greatly expanded. As a consequence, Zintl chemistry is a well-established field of inorganic and materials chemistry even more than 100 years after the astonishing observations by the pioneers in this field.

However, while full credit needs to be given to Zintl, who has become the patron saint of this chemistry posthumously, being awarded this honor by Laves [22], he had no knowledge of the anions' structures or bonding properties owing to their lack of crystallinity or appropriate techniques to investigate his samples. He therefore suggested wrong molecular architectures of the highly uncommon polyanions, which required another 40 years to be finally elucidated upon crystallization and X-ray diffraction studies on corresponding salts by Kummer and Strähle [23], as well as Corbett [24].

It should be mentioned that Zintl anions do not need to be molecular, but can appear in extended structures also. Most of them can be easily understood in terms of a *pseudo*-element consideration, at least regarding the connectivity of the atoms involved in them. This means that the atoms of the one-dimensional, two-dimensional, or three-dimensional polyanionic substructure of corresponding solids form $8 - N$ bonds, with N being the number of s and p valence electrons of the respective atom plus its (formal) charge. In some cases, the resulting structures even exactly resemble the element structure of an element with the same number of valence electrons (hence being the strictest interpretation of the *pseudo*-element consideration), yet variations exist as well, especially if the anions are not homoatomic. In rare cases, the bonding of extended Zintl anions cannot be understood in terms of the $8 - N$ rule, particularly if the anionic substructures are

electron-deficient. This property is much more frequently found in molecular anions, however, which then form deltahedra or fragments of deltahedra. It is thus also possible to classify discrete (semi-)metal polyanions either as electron-precise or as electron-deficient species.

1.2 Outline of This Chapter

In this chapter we particularly survey binary molecular anions involving p-block (semi-)metal elements, which also usually follow one of the two possible modes of appearance. Either they are electron-precise, thus strictly following the 8 – *N* rule, or they are electron-deficient, thus require the application of Wade-Mingos rules in order to explain the relationship of their molecular structures to their electron count. Naturally, many of the anions adopt structures that are known from neutral valence compounds of p-block elements or simple anions, or the (hypothetical) structures of boranes on the other hand. However, owing to the elemental combinations covered in this overview, all of them can be regarded as binary Zintl anions involving group 13–15 elements.

In Sect. 2, we will refer to the underlying concepts of how to interpret the structures and bonding of the two classes of compounds. For this, homoatomic anions or neutral valance compounds will be used as examples, hence molecules that are isoelectronic cousins of the ones on which this chapter is focused. In the subsequent sections, we will present a comprehensive overview of all known binary molecular anions, in which the core structures contain exclusively p-block elements of groups 13–15 (Sect. 3), thereby discriminating between electron-precise and electron-deficient clusters, and illustrating the different structural motives in each of these groups. Section 4 is dedicated to binary anions, in which atoms of a group 13–15 element are combined with d-block or f-block metal atoms.

Finally, it should be noted that this survey focuses on anions or neutral valance compounds that cannot be understood as endohedral clusters, which were comprehensively reviewed elsewhere [4–18]. The presented anions resemble either empty cage-type compounds or coordination compounds with the atoms coordinating a central atom while being unconnected among themselves.

2 Brief Overview of Structures and Bonding of Homoatomic Molecular Zintl Anions

2.1 Electron-Precise Zintl Anions and the 8 – N Rule

Molecular Zintl anions that can be written down in a Lewis diagram with all lines representing 2-electron-2-center bonds are considered as being electron-precise.

They are not in need of 2-electron multicenter bonding, hyperconjugation, or hypercoordination, but they may include multiple-bonding. Hence, each atom in such molecules comprises 8–*N* bonds to its neighboring atoms. In contrast to this rule being applied to normal valence compounds of the p-block elements, however, N does not simply equal the natural valence electron count of the respective main group, but equals this number plus the formal charge of the respective atom, hence referring to the group of a respective *pseudo*-element. This may be as simple as in the tetrahedral anion Si_4^{4-}, in which each of the "Si^{-}" atoms behaves like a group 15 atom, for which they are called *pseudo*-group 15 atoms that form 8 – (4 + 1) = 8 – 5 = 3 bonds to three next Si atoms each. But there are also cases, in which the atoms carry different (formal) charges. One example is the nortricyclane-type P_7^{3-} anion, in which three atoms behave like (two-bonded) group 16 atoms, according to 8 – (5 + 1) = 8 – 6 = 2, while 4 P atoms remain neutral and are three-bonded as typical for a group 15 atom. Therefore, they are analogs of P_4S_3. Another example is the butterfly-shaped Si_4^{6-} anion, with its two three-bonded *pseudo*-group 15 atoms, "Si^{-}", and 2 two-bonded "Si^{2-}" sites behaving like a *pseudo*-group 16 atom. The latter is the only case that may also be viewed as an electron-deficient anion, as outlined in the next section. This concept has been known under a variety of names, most commonly as the Zintl-Klemm concept, referring to the pioneers in this field, but also other denominations, like Zintl-Klemm-Busmann concept or Klemm concept, have been used in the literature [25, 26].

2.2 Electron-Deficient Anions and the Wade-Mingos Rules

Electron-deficient molecular anions need to share electrons in a ratio smaller than 2:2 between their atoms. Most of them form deltahedral molecular architectures, which allow for a high degree of electron delocalization (also denoted as three-dimensional aromaticity), which can be precisely described in terms of a superatomic electronic situation by means of cluster orbitals. However, to classify the structures in correlation with the respective electron number, the application of Wade-Mingos rules has proven a fantastic tool for getting a quick answer [27–32]. The most convenient way of using these rules in the context of Zintl anions starts out with summing up the valence electron number (VEN) of the cluster (including the negative charge) and deriving the skeleton electron number (SEN) from this number. The SEN is key to the cluster type according to the correlation developed for borane clusters, including heteroboranes and metallaboranes. It is received from the VEN by subtracting two "exo-electrons" for each of the *n* main group atoms of the cluster skeleton and 12 "exo-electrons" for each of the *m* transition metal atoms that are part of the deltahedron, see Eq. (1). While in boranes the exo-electrons are used to build the external B-H bond (or to bind other ligands, like CO ligands in metallaboranes, for instance), they usually represent the lone pairs directing outward of the cluster cage in the case of Zintl anions.

$$\mathrm{SEN} = \mathrm{VEN} - n \cdot 2 - m \cdot 12 \quad (1)$$

The correlation of the SEN with the number of cluster atoms (n or $n + m$) allows an assignment of the cluster to the different classes, according to the correlation $2{\cdot}n + x$ known from boranes. Hence, for a purely main group atom cluster, SEN = $2{\cdot}n + 2$ indicates a *closo*-cluster that adopts the shape of a complete deltahedron, SEN = $2{\cdot}n + 4$ indicates a *nido* cluster that adopts the shape of a deltahedral fragment that is derived from a complete deltahedron with $n + 1$ vertices by removal of 1 vertex, SEN = $2{\cdot}n + 6$ indicates an *arachno* cluster that adopts the shape of a deltahedral fragment that is derived from a complete deltahedron with $n + 2$ vertices by removal of 2 vertices, and so on. A few examples of Zintl clusters can even be discussed in terms of *hypho*-type architectures, with SEN = $2{\cdot}n + 8$, but to the best of our knowledge, no electron-deficient Zintl anions have been known to date with a skeleton electron count of SEN > $2{\cdot}n + 8$. Very prominent examples for the named types of clusters are Sn_9^{4-} (*nido*) [33] and Si_4^{6-} (*arachno*) [34]. All of these considerations also apply to clusters, in which n main group atoms and m transition metal atoms are combined, so that the "$2{\cdot}n + x$" expressions are to be simply replaced by "$2{\cdot}(n + m) + x$" for the final electron counts to classify the cluster types.

As mentioned above, there are some rare cases, in which also extended anionic substructures are electron deficient and require a description in the Wade-Mingos formalism, such as the all-vertex-linked B_6^{2-} octahedra that form a network of *closo* clusters in CaB_6 [35]. To receive the necessary SEN of $2{\cdot}n + 2$, the calculation is done for the linked cages as follows: SEN = 6·3 (three valence e^- of each of the B atoms) + 6·1 (one e^- from each of the neighboring B atoms) + 2 (negative charge) – 6·2 (two exo-electrons per B atom) = $14 = 2{\cdot}n + 2$.

The following section will give an overview of all known molecular, homoatomic Zintl anions as a basis of the discussion of the binary ones, and as a reference that will be used for the description of the binary architectures. It should be noted that some of the binary anions presented below rather resemble neutral compounds, such as the tetrahedral P_4 and As_4 molecules or the dimeric Al_2Cl_6 molecule formed by edge-sharing of tetrahedral complexes, or they share the structure with common atom-centered binary anions, such as the carbonate $[CO_3]^{2-}$ or silicate $[SiO_4]^{4-}$ anion. We will refer to such well-known species directly at the respective places in Sect. 3.

2.3 *Molecular Structures of Homoatomic Molecular Zintl Anions*

The structures of known homoatomic molecular Zintl anions of group 13, group 14, and group 15 (semi-)metal atoms are illustrated in Figs. 1, 2, and 3, respectively.

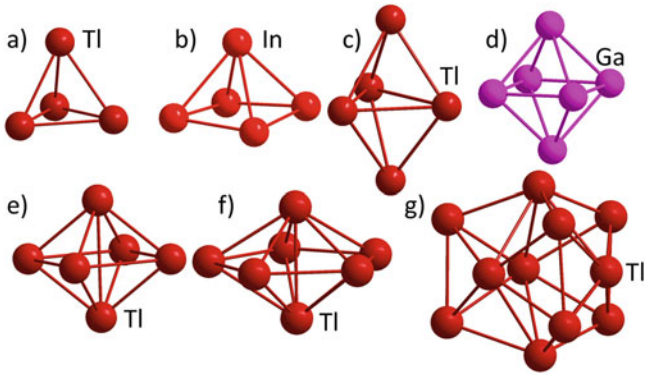

Fig. 1 Structures of molecular Zintl anions containing group 13 atoms: (**a**) Tl_4^{8-}, (**b**) In_5^{9-}, (**c**) Tl_5^{7-}, (**d**) Ga_6^{8-}, (**e**) Tl_6^{6-}, (**f**) Tl_7^{7-}, (**g**) Tl_{11}^{7-} [36–56]

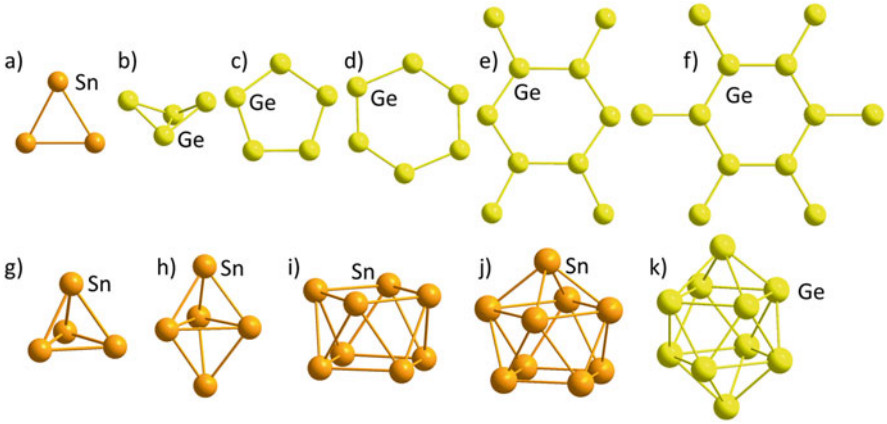

Fig. 2 Structures of molecular Zintl anions containing group 14 atoms: (**a**) Sn_3^{2-}, (**b**) Ge_4^{6-}, (**c**) Ge_5^{6-}, (**d**) Ge_6^{10-}, (**e**) Ge_{10}^{20-}, (**f**) Ge_{12}^{21-} (**g**) Sn_4^{4-}, (**h**) Sn_5^{2-}, (**i**) Sn_8^{6-}, (**j**) Sn_9^{4-}, (**k**) Ge_{10}^{2-} [26, 33, 34, 57–125]

The color codes of the different atom types are indicated in the figure captions and used throughout this chapter in a consistent way.

3 Binary Zintl Anions of p-Block Atoms of Groups 13–15

Generally, the transfer from homoatomic to binary Zintl anions can be viewed as isoelectronic replacement of one atom with another one [186]. However, it was shown in some cases that not only the electron count alone, but also the specific properties of the involved atoms define the stability of the observed structures

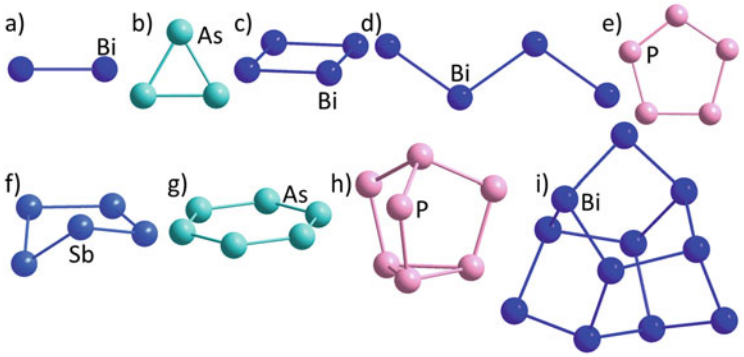

Fig. 3 Structures of molecular Zintl anions containing group 15 atoms: (**a**) Bi_2^{2-}, (**b**) As_3^{3-}, (**c**) Bi_4^{2-}, (**d**) Bi_4^{4-}, (**e**) P_5^{-}, (**f**) Sb_5^{5-}, (**g**) As_6^{4-}, (**h**) P_7^{3-}, (**i**) Bi_{11}^{3-} [126–185]

[187]. Moreover, the presence of different types of atoms always provides the opportunity of forming isomers, which may coexist – at least in solution, but also in the solid state – and may show different chemical and physical properties. A very important issue is the resulting charge upon isoelectronic replacement. Solubilities, crystallization, and the isolation of corresponding anions and their respective salts are greatly influenced by the total charge. Given that the solution dynamics of corresponding anionic cages allow for exchange reactions, which was proven to be the case [188, 189], binary systems can easily react on the demand of a subsequent heterometallic or intermetalloid cluster to form in reactions with d-block or f-block compounds [190]. Thus, the introduction of one (or more) additional atom types always increases the variability, and thus represents a fantastic means of realizing cluster structures in general, which are not accessible with one atom type only.

3.1 Electron-Precise p-Block-p-Block Anions

3.1.1 P_4-Type Anions

The chemistry of white phosphorus (P_4) proved to be a blossoming research field for chemists [181–195]. P_4 possesses a tetrahedral molecular symmetry in all states of matter, and it represents the most reactive and least stable allotrope of elemental phosphorus under ambient conditions. Its flexible coordination modes have resulted in a number of activation pathways. The heavier congener of P_4, yellow arsenic (As_4), shows an even more unstable character, so it readily turns into the thermodynamic stable, air-insensitive gray allotrope, which seriously hinders further use for coordination chemistry [196]. As a result, As_4 chemistry faces much more challenges, as it requires extreme conditions for in-situ preparation, potential storage, and finally application of the tetrahedral molecule for chemical reactions. To facilitate the use of both pnictogens, new methods were developed recently to stabilize

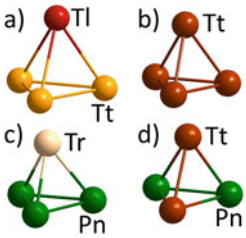

Fig. 4 Structures of all types of electron-precise binary p-block-p-block (semi-)metal anions with *pseudo*-tetrahedral shape: (**a**) $(TlSn_3)^{5-}$, (**b**) $(Tt^1_{4-x}Tt^2_x)^{4-}$, (**c**) $(TrPn_3)^{2-}$, (**d**) $(Tt_2Pn_2)^{2-}$

both P_4 and As_4, including the reversible coordination of P_4 or As_4 to transition metals or the encapsulation of them as molecular guest in porous materials [195, 197–200]. In 2009, a facile way was reported for the synthesis of the binary molecule AsP_3 in the condensed phase. Its structure has been confirmed by coordination to a corresponding transition metal complex fragment in $[Mo(\eta^1\text{-}P_3As)(CO)_3(P^iPr_3)_2]$ (^{i}Pr = *iso*-propyl) [201].

Beside the aforementioned approaches, another method to investigate group 13–15 (*pseudo*-)tetrahedral units was realized by partial or full isoelectronic replacement of the pnictogen atoms in Pn_4 (Pn = P, As) with (formally) negatively charged atoms of group 13 or 14 elements, yielding Zintl-type binary p-block anions together. The negative charge of the anions is defined by the elemental combination, hence is highest in the binary triel-tetrel *pseudo*-tetrahedra $(TrTt_3)^{5-}$ (Tr: group 13 (triel) element, Tt: group 14 (tetrel) element). Only one such anion has been established to date, namely $(TlSn_3)^{5-}$ (Fig. 4a), that occurs in the alloy $Na_5(TlSn_3)$ [202]. However, the high negative charge of this anion leads to extremely poor solubility, which inhibits further use of the salt for solution chemistry. Follow-up chemistry of this anion is thus limited to high temperature flux reactions. Alloys and salts comprising Tt_4^{4-} and its derivatives $(Tt^1_{4-x}Tt^2_x)^{4-}$ (Fig. 4b), with slightly lower charge, can be dissolved in liquid ammonia. Examples of subsequent reactions have led to the formation of the coordination compounds $[(MesCu)_2(\eta^3\text{-}Tt_4)]^{4-}$ (Tt = Si, Ge, Si/Ge; Mes = mesitylene), $[Zn\{\eta^2\text{-}(Si/Ge)_4\}_2]^{6-}$, $[(\eta^2\text{-}Sn_4)Zn(\eta^3\text{-}Sn_4)]^{6-}$, and $[Au(\eta^2\text{-}Sn_4)_2]^{7-}$, which form in and crystallize from ammonia solutions [203–208]. The high overall charges of the heteroatomic $(TrTt_3)^{5-}$ and homoatomic Tt_4^{4-} species can be further reduced by isoelectronic replacement of (formally) charged triel or tetrel atoms, Tt(–I) or Tr(–II), by (formally) neutral pnictogen atom(s), Pn(0). Various related anions have been reported in the meantime as [K(crypt-222)]$^+$ salts (crypt-222 = 4,7,13,16,21,24-hexaoxa-1,10-diazabicyclo[8.8.8]hexacosane): $(GaBi_3)^{2-}$, $(InBi_3)^{2-}$, $(TlBi_3)^{2-}$, $(Ge_2P_2)^{2-}$, $(Ge_2As_2)^{2-}$, $(Sn_2Sb_2)^{2-}$, $(Sn_2Bi_2)^{2-}$, $(Pb_2Sb_2)^{2-}$, and $(Pb_2Bi_2)^{2-}$ (Fig. 4c, d) [188, 209–215], and several further binary *pseudo*-tetrahedral anions, $(TrTt_3)^{5-}$ (Tr = Al, Ga; Tt = Ge, Sn, Pb), $(InTt_3)^{5-}$ (Tt = Sn, Pb), $(TlPb_3)^{5-}$, $(TrPn_3)^{2-}$ (Tr = Al, Ga; Pn = As, Sb), $(TlSb_3)^{2-}$, $(Si_2Pn_2)^{2-}$ (Pn = P, As), and $(Ge_2Sb_2)^{2-}$, were predicated synthesizable, although their isolation in condensed phase still has to be proven [216]. The reduced charge of the $(TrBi_3)^{2-}$ and $(Tt_2Pn_2)^{2-}$ anions significantly enhances the solubility of the corresponding salts, which allows their application for solution chemistry in room-temperature solvents such as ethane-1,2-diamine (en), pyridine (py), or

Table 1 Overview of known or predicted electron-precise binary p-block-p-block (semi-)metal anions with *pseudo*-tetrahedral shape

Formula	Parent compound/source	Ref.	Figure no.
$(TlSn_3)^{5-}$	$Na_5(TlSn_3)$	[202]	4a
$(Si_{4-x}Ge_x)^{4-}$ $x = 1–3$	$NaRb_7(Si_{4-x}Ge_x)_2$, $K_{12}Si_{17-x}Ge_x$	[203, 204]	4b
$(TrBi_3)^{2-}$ Tr = Ga, In, Tl	$[K(crypt\text{-}222)]_2(TrBi_3)\cdot en$	[209, 210]	4c
$(Ge_2Pn_2)^{2-}$ Pn = P, As	$[K(crypt\text{-}222)]_2(Ge_2Pn_2)\cdot en$	[188–211]	4d
$(Tt_2Pn_2)^{2-}$ Tt = Sn, Pb; Pn = Sb, Bi	$[K(crypt\text{-}222)]_2(Tt_2Pn_2)\cdot en$	[212–215]	4d
$(TrTt_3)^{5-}$ Tr = Al, Ga; Tt = Ge, Sn, Pb	Calculated	[216]	–
$(InTt_3)^{5-}$ Tt = Sn, Pb	Calculated	[216]	–
$(TlPb_3)^{5-}$	Calculated	[216]	–
$(TrPn_3)^{2-}$ Tr = Al, Ga; Pn = As, Sb)	Calculated	[216]	–
$(TlSb_3)^{2-}$	Calculated	[216]	–
$(Si_2Pn_2)^{2-}$ Pn = P, As	Calculated	[217]	–
$(Ge_2Sb_2)^{2-}$	Calculated	[216]	–

dimethylformamide (dmf). An overview of known electron-precise binary p-block-p-block (semi-)metal anions with *pseudo*-tetrahedral shape is listed in Table 1.

In the past decades, said binary *pseudo*-tetrahedral anions have thus been shown to be excellent starting materials for the formation of a large variety of heterometallic and intermetalloid Zintl clusters. While in most of the reaction products the anionic structure is heavily modified by fragmentation and rearrangement steps, these *pseudo*-tetrahedral units have been maintained in some of the resulting anions. These may occur in the original version, like in $[Au(Sn_2Sb_2)_2]^{3-}$ [217], or in a form resulting from an atom-exchange reaction, like in $[Cd_3(Ge_3P)_3]^{3-}$ [188], or both, for example in $[Au_6(Ge_3As)(Ge_2As_2)_3]^{3-}$ [189].

3.1.2 Nortricyclane-Type Anions

Homoatomic nortricyclane-type Zintl anions possess the formula Pn_7^{3-}. They have been known from all pnictogen atoms (except N), specifically P_7^{3-}, As_7^{3-}, Sb_7^{3-}, and Bi_7^{3-} [9, 175], yet the heaviest congener was identified as late as in 2015 – hence, more than 50 years later than the first of its congeners, Sb_7^{3-} in Cs_3Sb_7 [157]. According to the *pseudo*-element consideration, the two-bonded atoms in this cage carry a (formal) charge of 1–, which complies well with the position of real group 16 elements in the corresponding structure of P_4S_3 [218], the relative proximity of the counterions in the salts of Pn_7^{3-}, and the selective substitution of these

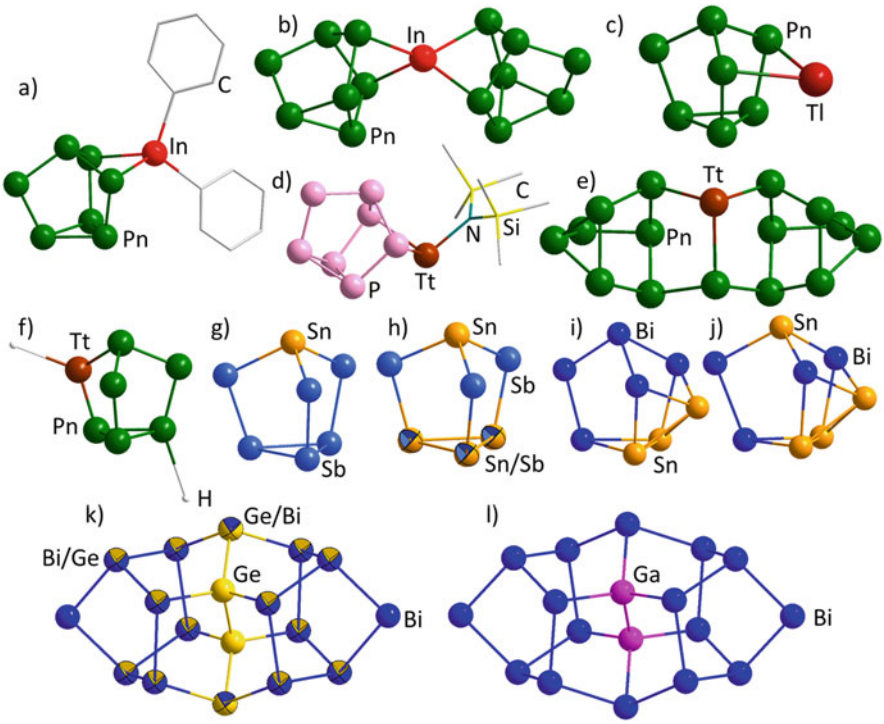

Fig. 5 Structures of all known electron-precise binary p-block-p-block (semi-)metal anions adopting or involving nortricyclane-type structures: (**a**) $(Pn_7InPh_2)^{2-}$, (**b**) $[In(Pn_7)_2]^{3-}$, (**c**) $(TlPn_7)^{2-}$, (**d**) $[P_7TtN(SiMe_3)_2]^{2-}$ (Tt = Ge, Sn, Pb), (**e**) $(TtPn_{15})^{3-}$ (Tt = Sn, Pb, Pn = P; Tt = Sn, Pn = As), (**f**) $(TtPn_6H_2)^{2-}$ (Tt = Si, Pn = P, As; Tt = Ge, Pn = P), (**g**) $(SnSb_6)^{4-}$, (**h**) $(Sn_3Sb_4)^{6-}$, (**i**) $(Sn_3Bi_5)^{3-}$, (**j**) $(Sn_4Bi_4)^{4-}$, (**k**) $(Ge_4Bi_{14})^{4-}$, (**l**) $(Ga_2Bi_{16})^{4-}$. H atoms are omitted for clarity in Fig. 5a, c

sites with H^+ or organic groups [219–221]. Furthermore, the Pn_7^{3-} cages were found to act as electron donors to other Tr or Tt metal atoms via two of these negatively charged atoms to form adducts such as $(Pn_7InPh_2)^{2-}$ (Pn = P, As; Fig. 5a), $[In(Pn_7)_2]^{3-}$/$(TlPn_7)^{2-}$ (Pn = P, As; Fig. 5b, c) and $[P_7TtN(SiMe_3)_2]^{2-}$ (Tt = Ge, Sn, Pb; Fig. 5d) [222–224]. In addition, a related, larger anion, P_{16}^{2-}, can be viewed as fusion of two nortricyclane-type P_7^{3-} anions via a P_2 dumbbell [225]. Replacement of one P atom in this dumbbell with one Tt atom generates isoelectronic anions $(TtP_{15})^{3-}$ (Tt = Sn, Pb; Fig. 5e) [222]. Binary p-block-p-block nortricyclane-type anions could also be realized. The extraction of ternary K/Si/P, K/Ge/P, or K/Si/As solids possessing corresponding stoichiometries with en/crypt-222 afforded compounds with (partially protonated) binary anions of the respective group 14/15 elemental combinations, $(SiPn_6H_2)^{2-}$ (Pn = P, As) and $(GeP_6H_2)^{2-}$ (Fig. 5f) [226]. Owing to these species' intrinsically poor crystallinity and low solubility, it was difficult to establish the identity of these species. However, the combination of all analytical results available, including single-crystal X-ray diffraction (SC-XRD),

energy-dispersive X-ray (EDX) spectroscopy, electrospray ionization mass spectrometry (ESI-MS), and nuclear magnetic resonance (NMR) spectroscopy, with quantum chemical studies confirmed said compositions and their doubly protonated character. These molecules have been the first examples of binary Zintl anions of the Si/P and Si/As elemental combinations, which added to the recent efforts to synthesize p-block-p-block binary Zintl anions.

An (unprotonated) heavier homolog, $(SnSb_6)^{4-}$, was identified in a corresponding alloy (Fig. 5g) [227], and another variant was obtained by extraction of the ternary compound $K_8[SnSb_4]$ (see also below) with liquid ammonia as a salt of the $(Sn_3Sb_4)^{6-}$ anion – with an even higher average charge on each of its atoms (Fig. 5h) [212]. It was thus understandable that this anion required close cation–anion interactions in the K^+-ammoniate salt, while the more commonly used en/crypt-222 counterion stabilization did not work for this system. As it was not possible to distinguish between Sn and Sb atoms with conventional SC-XRD studies, EDX spectroscopy served as an auxiliary tool for confirming the given composition. The result was in full accordance with the total 6– charge of $(Sn_3Sb_4)^{6-}$ obtained from application of the Zintl-Klemm concept, with charge assignments according to $[Sb(Sb^-)_3(Sn^-)_3]^{6-}$.

Two further anions that can be derived from nortricyclane units are $(Sn_3Bi_5)^{3-}$ and $(Sn_4Bi_4)^{4-}$ (Fig. 5i, j) [228, 229]. They were synthesized by extraction of "RbSnBi" and "CsSnBi," respectively, in liquid ammonia. The two isostructural and isoelectronic anions were described as $\{Sn_2Bi_5\}$ and $\{Sn_3Bi_4\}$ nortricyclane-like structures, which are monocapped by an additional Sn atom on one side. Both of the two anions possess a VEN of 40, in accordance with a (hypothetical) molecule comprising eight pnictogen atoms and no charges.

A structurally more complex binary main group polyanion that is still related to nortricyclane cages, $(Ge_4Bi_{14})^{4-}$ (Fig. 5k), was obtained by extracting a solid with the nominal composition "K_2GeBi" with en/crypt-222 [230]. Notably, while the first compound to crystallize from this solutions was $[K(crypt\text{-}222]_2Bi_4$ [231], after 2 months at room temperature (or 90 days at 5 °C), the initially blue solution turned green, then red-brown, and crystals of $[K(crypt\text{-}222)]_4(Ge_4Bi_{14})\cdot solv$ (solv = en, tol) formed at last. Topologically, the anion can be viewed either as two nortricyclane-type $\{Bi_7\}$ cages that are connected by a linear $\{Ge_4\}$ chain, or alternatively, as a fusion of one nortricyclane-type $\{Bi_7\}$ cage with a binary $\{Bi_7Ge_4\}$ 11-atom cage, which exhibits the Bi_{11}^{3-} "ufosane"-type architecture. According to the *pseudo*-element concept, the structure and bonding situation of the tetraanion can be explained as follows: 2 four-bonded Ge(0) atoms are located around the inversion center of the cluster, while 2 three-bonded Ge(–I) atoms are located at the two ends of the $\{Ge_4\}$ chain. 12 Bi(0) atoms are connected to this central unit, with 2 two-bonded Bi(−I) sites found at the outmost vertices of the anion. Besides its extension and the large number of connected Bi atoms, the anion is also unique in another way: apart from some indication for mixed Ge/Bi site-occupancies in some of the atomic positions in the crystal structure, the two different types of atoms clearly show a strong separation tendency within the molecule, in contrast to a maximum number of heteroatomic bonds being preferred in most of the other binary

Table 2 Overview of known electron-precise binary p-block-p-block (semi-)metal anions adopting or involving nortricyclane-type structures

Formula	Parent compound	Ref.	Figure no.
$(Pn_7InPh_2)^{2-}$ Pn = P, As	$[K(crypt\text{-}222)]_2(Pn_7InPh_2)$	[224]	5a
$(TlPn_7)^{2-}$ Pn = P, As	$[K(crypt\text{-}222)]_2(TlP_7)\cdot py$	[222]	5c
$[In(Pn_7)_2]^{3-}$ Pn = P, As	$[K(crypt\text{-}222)]_3[In(Pn_7)_2]\cdot n$ solv Pn = P, n solv = 3.5py; Pn = As, n solv = none	[222]	5b
$(SiPn_6H_2)^{2-}$ Pn = P, As	$[K(crypt\text{-}222)]_2(SiPn_6H_2)\cdot n$ solvPn = P, solv = en·0.7H_2O; Pn = As, solv = none	[226]	5f
$(GeP_6H_2)^{2-}$	$[K(crypt\text{-}222)]_2(Ge_xP_{7-x}H_{2-x})_{1-n}(Ge_{9-y}P_yH_{2-y})_n$	[226]	5f
$(Sn_3Sb_4)^{6-}$	$[K_6(NH_3)_9](Sn_3Sb_4)$	[212]	5h
$(SnSb_6)^{4-}$	Rb_4SnSb_6	[227]	5g
$(Sn_3Bi_5)^{3-}$	$[Rb(crypt\text{-}222)]_3(Sn_3Bi_5)\cdot 8.87NH_3$	[228]	5i
$(Sn_4Bi_4)^{4-}$	$[Cs(18\text{-}crown\text{-}6)]_4(Sn_4Bi_4)\cdot 12NH_3$	[229]	5j
$(TtP_{15})^{3-}$ Tt = Sn, Pb	$[K(crypt\text{-}222)]_3(TtP_{15})\cdot en$	[222]	5e
$(SnAs_{15})^{3-}$	$[K(crypt\text{-}222)]_3(SnAs_{15})\cdot 2en$	[222]	5e
$[P_7TtN(SiMe_3)_2]^{2-}$ Tt = Ge, Sn, Pb	$[K(18\text{-}crown\text{-}6)]_2[P_7TtN(SiMe_3)_2]\cdot 2py$	[223]	5d
$(Ge_4Bi_{14})^{4-}$	$[K(crypt\text{-}222)]_4(Ge_4Bi_{14})$	[230]	5k
$(Ga_2Bi_{16})^{4-}$	$[K(crypt\text{-}222)]_3(Ga_2Bi_{16})(\cdot 4py)$	[232]	5l

anions reported to date. However, this unusual finding is in agreement with the immiscibility of Ge and Bi in the solid state, which could also explain why it has not been possible to isolate the *pseudo*-tetrahedral anion $(Ge_2Bi_2)^{2-}$ originally targeted in the corresponding experiment. While anions including the Ga/Bi elemental combination, like $[Bi@Ga_8(Bi_2)_6]^{q-}$ (q = 3, 5), have been known to form with more heteroatomic bonds, an anion with an isoelectronic situation, $(Ga_2Bi_{16})^{4-}$ (Fig. 5l) [232], was found that is reminiscent of the isoelectronic anion $(Ge_4Bi_{14})^{4-}$ – with a similar tendency for element segregation at the molecular scale. Corresponding to the slightly different composition, a "Ga_2^{2-}" dumbbell is placed in the center of the $(Ga_2Bi_{16})^{4-}$ anion, while all other sites are clearly occupied by Bi atoms; two outmost atoms again are formally Bi(–I). The bonding situation of all atoms thus complies with the Zintl-Klemm concept in this anion, too. The $(Ga_2Bi_{16})^{4-}$ anion contains the largest number of consecutively linked Bi atoms in a binary main group cluster to date. An overview of known electron-precise binary p-block-p-block (semi-)metal anions adopting or involving nortricyclane-type structures is given in Table 2.

3.1.3 $[SiO_4]^{4-}$-Type, $[Be_2Cl_6]^{2-}$-Type, CO_2-Type and $[CO_3]^{2-}$-Type Anions

Partial or full isoelectronic replacement of Si and O atoms of the orthosilicate ion $[SiO_4]^{4-}$ with Tt and Pn elements, respectively, provides us with isoelectronic Zintl anions $[TtPn_4]^{8-}$ (Tt = Si, Ge; Pn = P, As) and $[SnSb_4]^{8-}$, respectively (Fig. 6a) [233–236], with the same centered, tetrahedral structure. These anions were reported to be stabilized by dications (Ca^{2+}, Sr^{2+}, Ba^{2+}) or by a combination of Na^+ with dications (Ca^{2+}, Sr^{2+}, Eu^{2+}) in a 2:1 ratio. Corresponding sum formulae are $A_4[TtP_4]$ (A = Ca, Sr, Ba; Tt = Si, Ge), $Ba_4[TtAs_4]$ (Tt = Si, Ge), $Sr_4[TtAs_4]$ (Tt = Si, Ge), $Na_8[SnSb_4]$, and $A^1{}_4A^2{}_2[SnPn_4]$ (A^1 = Na, K; A^2 = Ca, Sr, Ba; Pn = P, As, Sb, Bi), respectively. Attempts to replace the dications completely with Na^+, K^+, or Cs^+ ions failed, yet caused the formation of salts comprising anions that adopt the shape of several other regular valence compounds or complex anions. These are the CO_2-type anions $[BPn_2]^{3-}$ (Pn = P, As) or $[P\text{-}B\text{-}As]^{3-}$ in the salts $A_3[BPn_2]$ (A = Na, K, Rb, Cs) and $Cs_3[P\text{-}B\text{-}As]$ (Fig. 6b) [237, 238], the $[CO_3]^{2-}$-type anions in compounds $Na_5[TtPn_3]$ (Tt = Si, Ge; Pn = P, As), $Rb_5[SiAs_3]$, $Rb_5[GeP_3]$, $Cs_5[TtPn_3]$ (Tt = Si, Ge; Pn = P, As), $Na_2K_3[SnPn_3]$ (Pn = P, Bi), and $Na_2Cs_3[SnP_3]$ [239–242], or the $[Be_2Cl_6]^{2-}$-type anions in $Na_{10}[Tt_2As_6]$ (Tt = Ge, Sn), $K_{10}[Sn_2Pn_6]$ (Pn = As, Sb, Bi), and $Na_8K_2[Sn_2Sb_6]$, respectively (Fig. 6c, d) [243–246].

All of the aforementioned compounds comprising anions resembling $[SiO_4]^{4-}$, CO_2, $[CO_3]^{2-}$, or $[Be_2Cl_6]^{2-}$ were obtained in neat solids that do not show notable solubility in any room-temperature solvent, and none of them can be dissolved in liquid ammonia without decomposition (see the formation of $(Sn_3Sb_4)^{6-}$ from $K_8[SnSb_4]$ described above). However, another approach worked for one particular case: A soluble salt of a $[CO_3]^{2-}$-type anion, $[SnBi_3]^{5-}$, was successfully synthesized from reactions of K_3Bi_2 with either K_4Sn_9 or $K_{12}Sn_{17}$ in liquid ammonia [247]. In the presence of crypt-222, crystals with the composition $K_5SnBi_3{\cdot}9NH_3$ were isolated. A related reaction of K_3Bi_2 with $K_{12}Sn_{17}$, yet in the presence of 18-crown-6 instead of crypt-222, yielded $K_9[K(18\text{-crown-}6)][SnBi_3]_2{\cdot}15NH_3$. As for the compounds quoted above, the anion of these two salts, $[SnBi_3]^{5-}$, possesses

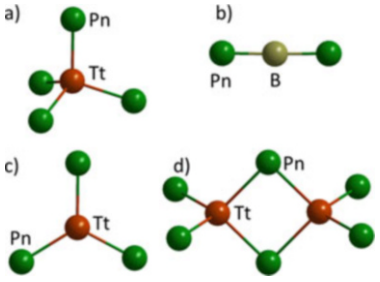

Fig. 6 Structures of all known electron-precise binary p-block-p-block (semi-)metal anions representing isoelectronic analogs of $[SiO_4]^{4-}$, CO_2, $[CO_3]^{2-}$, or $[Be_2Cl_6]^{2-}$: (**a**) $[TtPn_4]^{8-}$(Tt = Si, Ge, Sn; Pn = P, As, Sb, Bi), (**b**) $[BPn_2]^{3-}$ (Pn = P, As), (**c**) $[TtPn_3]^{5-}$ (Tt = Si, Ge, Sn; Pn = P, As, Bi), (**d**) $[Tt_2As_6]^{10-}$ (Tt = Si, Ge, Sn; Pn = As, Sb, Bi)

Table 3 Overview of known electron-precise binary p-block-p-block (semi-)metal anions representing isoelectronic analogs of $[SiO_4]^{4-}$, CO_2, $[CO_3]^{2-}$, or $[Be_2Cl_6]^{2-}$

Formula	Parent compound	Type	Ref.	Figure no.
$[BPn_2]^{3-}$ (Pn = P, As)	$A_3[BPn_2]$ A = Na, K, Rb, Cs	CO_2	[237]	6b
$[TtPn_3]^{5-}$ Tt = Si, Ge; Pn = P, As	$A_5[TtPn_3]$ A = Na, Rb, Cs	$[CO_3]^{2-}$	[239, 240, 242]	6c
$[SnPn_3]^{5-}$ Pn = P, Bi	$A_5[SnPn_3]$ A = Na/K, Na/Cs; $K_9[K(18\text{-crown-}6)][SnBi_3]_2 \cdot 15NH_3$	$[CO_3]^{2-}$	[241, 247]	6c
$[SnPn_4]^{8-}$ Pn = P, As, Sb, Bi	$A^1{}_4A^2{}_2[SnPn_4]$ A^1 = Na, K; A^2 = Ca, Sr, Ba; Pn = P, As, Sb, Bi)	$[SiO_4]^{4-}$	[236]	6a
$[TtPn_4]^{8-}$ Tt = Si, Ge; Pn = P, As	$A_4[TtPn_4]$ A = Ca, Sr, Ba	$[SiO_4]^{4-}$	[233, 234, 248]	6a
$[SnSb_4]^{8-}$	$Na_8[SnSb_4]$	$[SiO_4]^{4-}$	[235]	6a
$[Tt_2As_6]^{10-}$ Tt = Si, Ge, Sn	$Na_{10}[Tt_2As_6]$	$[Be_2Cl_6]^{2-}$	[244, 245]	6d
$[Sn_2Pn_6]^{10-}$ Pn = Sb, Bi	$A_{10}[Sn_2Pn_6]$ A = Na, K, Na/K	$[Be_2Cl_6]^{2-}$	[243, 246]	6d

24 valence electrons and adopts a trigonal planar structure, in which a central Sn atom covalently bonds to three Bi atoms. It represents the first $[CO_3]^{2-}$ analog containing exclusively metal atoms that was obtained from solution. The anion shows the same type of electron delocalization as known from $[CO_3]^{2-}$ (Fig. 6c), confirmed by a considerable Sn-Bi bond shortening, in spite of the atoms stemming from higher period elements. An overview of known electron-precise binary p-block-p-block (semi-)metal anions representing isoelectronic analogs of $[SiO_4]^{4-}$, CO_2, $[CO_3]^{2-}$, or $[Be_2Cl_6]^{2-}$ is summarized in Table 3.

3.2 *Electron-Deficient p-Block-p-Block Anions Which Follow the Wade-Mingos Rules*

Most of the p-block-p-block anions following Wade-Mingos rules correspond with *nido* or *closo* cages comprising 5, 9, or 10 cluster atoms. The solubility of solids of the type $A_{12}Si_{17-x}Ge_x$ (A = K, Rb; $x = 1, 5, 9, 12$), which could not be obtained as single crystals suitable for structure determination by XRD, was investigated in liquid ammonia. Anionic cages of the compositions $(Si_{9-x}Ge_x)^{4-}$ ($x = 1.2, 1.5$; Fig. 7a) [249] and $(Si_{9-x}Ge_x)^{3-}$ ($x = 4.4, 6.6, 6.7, 6.8$; Fig. 7b) [250] were isolated as ammoniate salts and characterized. While the anions $(Si_{9-x}Ge_x)^{4-}$ clearly possess

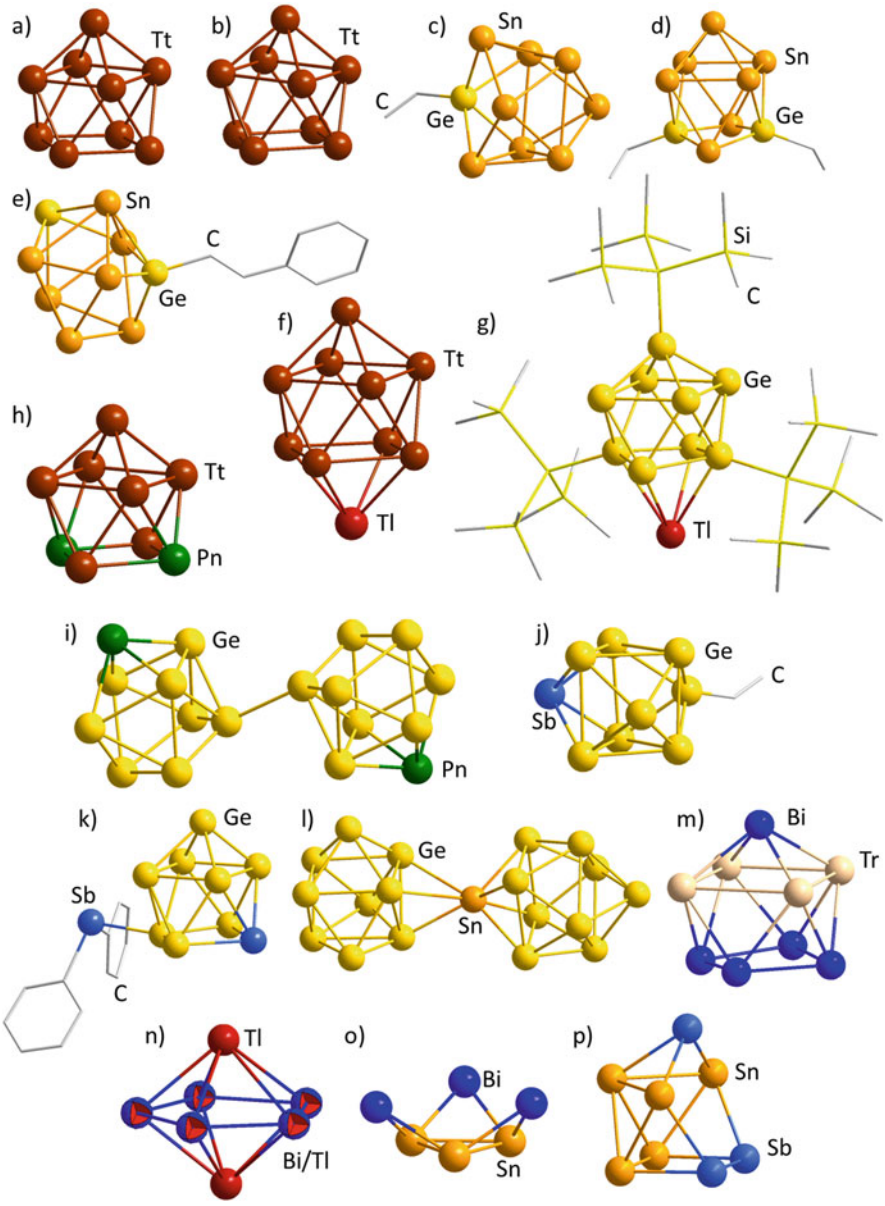

Fig. 7 Structures of all known electron-deficient binary p-block-p-block (semi-)metal anions adopting molecular structures that accord with Wade-Mingos rules: (**a**) $(Si_{9-x}Ge_x)^{4-}$, (**b**) $(Si_{9-x}Ge_x)^{3-}$, (**c**) $(GeSn_8\text{-}HC{=}CH_2)^{3-}$, (**d**) $[Ge_2Sn_7\text{-}(HC{=}CH_2)_2]^{2-}$, (**e**) $(Ge_2Sn_7\text{-}HC{=}CHPh)^{2-}$, (**f**) $(TlTt_9)^{3-}$ (Tt = Ge, Sn), (**g**) Hyp_3Ge_9Tl, (**h**) $(Tt_7Pn_2)^{2-}$ (Tt = Sn, Pb, Pn = Bi; Tt = Ge, Pn = P, As, Sb), (**i**) $[(SbGe_8)\text{-}(Ge_8Sb)]^{4-}$, (**j**) $[(SbGe_8)\text{-}CH_2 = CH_2]^{2-}$, (**k**) $[(SbGe_8)\text{-}SbPh_2]^{2-}$, (**l**) $[Sn(Ge_9)_2]^{4-}$, (**m**) $(Tr_4Bi_5)^{3-}$ (Tr = In, Tl), (**n**) $(Tl_4Bi_3)^{3-}$, (**o**) $(Sn_3Bi_3)^{5-}$, (**p**) $(Sn_5Sb_3)^{3-}$. H atoms are omitted for clarity

nido-type structures, the $(Si_{9-x}Ge_x)^{3-}$ species with lower negative charge need to be regarded as intermediates between the *closo*- and the *nido*-type species.

Reactions of the ternary alloy $K_4Ge_{9-x}Sn_x$ with alkynes in en resulted in the following structurally characterized compounds with alkenylated heteroatomic *nido*-type clusters: $(GeSn_8\text{-}R)^{3-}$ (R = HC=CH_2, HC=CHC_{pr}), $[Ge_2Sn_7\text{-}(HC{=}CH_2)_2]^{2-}$, and $(Ge_2Sn_7\text{-}HC{=}CHPh)^{3-}$ (Fig. 7c–e) [251]. Alternatively, capping of the *nido*-Tt_9^{4-} anion (Tt = Ge, Sn) by a formally Tl^+ Lewis acid, upon reaction of Tt_9^{4-} with TlCp ($Cp^- = (C_5H_5)^-$), yielded a corresponding *closo*-type cluster anion, $(TlTt_9)^{3-}$ (Figs. 7f) [252]. A threefold substitution of $(TlGe_9)^{3-}$ with hypersilyl groups ({$(SiMe_3)_3Si$} = Hyp) affords a corresponding neutral cluster, *closo*-(Hyp_3Ge_9Tl) [253] (Fig. 7g), which has a different substitution pattern compared to previously reported tetra-substituted {Ge_9} cages. Further Hyp-decorated Tt-d-block anions will be discussed in Sect. 4.2.2.

Partial replacements of the Tt(–I) atoms in the *closo*-type or *nido*-type anions Tt_9^{x-} ($x = 2, 4$) by atoms of group 15 elements, formally Pn(0), result in isoelectric anions of binary composition, namely *nido*-$(Ge_7Pn_2)^{2-}$ (Pn = P, As; Fig. 7h) [188, 211], and *nido*-$(Tt_7Bi_2)^{2-}$ (Tt = Sn, Pb; Fig. 7h) [214, 254]. Several derivatives of $(Tt_7Pn_2)^{2-}$ have also been studied. These include a series of species with the general formula $(Ge_7P_2R_3)^+$ (R = CH_3, C_2H_5 and C_3H_3) which were theoretically predicted based on the experimentally known *nido*-$(Ge_7P_2)^{2-}$ anion [255]. The theoretical design of the derivatives $[Ge_7Pn_2(CH_3)_3]^+$ was extended by replacing P atoms with As, Sb, or Bi atoms. A simple and efficient method for experimentally replacing Ge atoms in deltahedral Ge_9^{4-} clusters with either Sb or Bi atoms has been realized by reactions of Ge_9^{4-} with $PnPh_3$ (Pn = Sb, Bi) at certain temperatures or under sonication. Structure elucidations revealed "n-doped" deltahedral Zintl ions $[(PnGe_8)\text{-}(Ge_8Pn)]^{4-}$ (Pn = Sb, Bi), $(Ge_7Sb_2)^{2-}$, $[(SbGe8)\text{-}CH{=}CH_2]^{2-}$ and $[(SbGe_8)\text{-}SbPh_2]^{2-}$ (Fig. 7h–k) [256].

The formation of 10-atom *closo*-type cages can also be realized by bridging of 9-atom units via p-block metal atoms. For example, $[(Ge_9)Sn(Ge_9)]^{4-}$ (Fig. 7l) [257] consists of two Ge_9^{4-} clusters, which coordinate an Sn(II) atom in an η^4- or η^3-mode, respectively. Owing to shorter Sn-Ge distances (on average) between the central Sn atoms and the atoms of the η^4-coordinating cage, this "side" is viewed as a *closo*-type 10-atom cluster according to Wade-Mingos rules, with the SEN being 22 ($= 2{\cdot}n + 2$). In contrast, the η^3-type coordination and the distances found within the remaining part of the structure refer to a *closo*-type 9-atom cage. In summary, $[(Ge_9)Sn(Ge_9)]^{4-}$ can be treated as a combination of a *closo*-$(Ge_9Sn)^{2-}$ and a *closo*-$(Ge_9)^{2-}$ connected via a Lewis acid-base interaction.

The combination of Tr and Pn atoms has further enriched the spectrum of *closo*- or *nido*-type anions. $(In_2Sb_3)^-$ and $(Tr_2Bi_3)^-$ (Tr = Al, Ga, In) [258], which were reported to exist in the gas phase, are isoelectronic and isostructural with *closo*-Tt_5^{2-} (Tt = Si, Ge, Sn, Pb) [89, 91]. The 9-atom cages $(Tr_4Bi_5)^{3-}$ (Tr = In, Tl; Fig. 7m) [209, 210], resembling binary analogs of *nido*-Tt_9^{4-} [91], were observed as minor products upon extraction of "$K_5In_2Bi_4$" with en/crypt-222, or as side products during the synthesis of $[K(crypt\text{-}222)]_2[Tl_2Bi_6\{Ru(cod)\}]{\cdot}2tol$ (cod = 1,5-cyclooctadiene). Solid mixtures of the elemental combination K/Tl/Bi indicate the presence of

multiple Zintl phases. Extractions with en in the presence of crypt-222 afforded single crystals comprising $[K(crypt\text{-}222)]^+$ salts of several novel binary anions, including $(Tl_4Bi_3)^{3-}$ (Fig. 7n) [259], among others. $(Tl_4Bi_3)^{3-}$shows a rare pentagonal bipyramidal structure. It represents the first binary cage of this topology and the first 7-atom *closo*-type p-block cluster. Its SEN amounts to 16 ($= 2{\cdot}n + 2$), which is thus different from the pentagonal bipyramidal cluster anion Tl_7^{7-} in the neat solid $K_{10}Tl_7$: with an SEN of $14 = 2{\cdot}n$, this homoatomic cluster falls in the category of the so-called *pre-closo* cages, with an even larger electron deficiency [49].

As discussed above, many binary *closo*-type or *nido*-type Zintl clusters were isolated to date – most of them as their respective salts through solution chemistry. In striking contrast, there has been only one example so far of a *hypho*-cluster anion obtained this way: $(Sn_3Bi_3)^{5-}$ (Fig. 7o) [228] was synthesized through extraction of "$RbSn_2/Rb_3Bi_2$" in liquid ammonia. The high charge density of this anion is balanced by close contacts with adjacent Rb^+ cations in $Rb_6[Sn_3Bi_3][Sn_4]_{1/4}{\cdot}6.75NH_3$. With VEN = (3·4 + 3·5 + 5) = 32 and SEN = (32–6·2) = 20, this 6-vertex anion correlates with the expectations for a *hypho*-type cluster. It was suggested that $(Sn_3Bi_3)^{5-}$ might represent an intermediate in the reaction pathway toward two related anions, $(Sn_3Bi_5)^{3-}$ and $(Sn_4Bi_4)^{4-}$ [228, 229].

Some more species have been reported that correspond with an electron count expected for *arachno*-type cages. The synthesis and crystallization of the $[K(crypt\text{-}222)]^+$ salt of *arachno*-$(Sn_5Sb_3)^{3-}$ (Fig. 7p) [187] demonstrated that not only the electron count of a specific anion determines its structure. In addition, different chemical composition within an isoelectronic series of binary Zintl anions can lead to different isomeric structures. The general structural classification as an *arachno*-type is matched by the SEN of 22 ($= 2{\cdot}n + 6$) here from eight Sn/Sb atoms occupying the vertices of a polyhedral fragment that can indeed be derived from the corresponding *closo*-10-vertex deltahedron. However, unlike the strict rules followed in borane chemistry regarding the removal of directly adjacent vertices when going from *nido*-type to *arachno*-type cages, (semi-)metal clusters allow for variations here: instead of the removal of two directly adjacent vertices, Zintl anions also allow for the removal of next but one or even opposite vertices, which is actually preferred here and denoted as *iso-arachno* in the literature. Hence, the structural motif found for $(Sn_5Sb_3)^{3-}$ is rare, as compared to the square anti-prismatic architecture reported for several isoelectronic ions: $(Tl_2Bi_6)^{2-}$ in $[Tl_2Bi_6\{Ru(cod)\}]^{2-}$ [210], Bi_8^{2+} in $[CuBi_8]^{3+}$ [260], Sn_8^{6-} in $Rb_4Li_2Sn_8$ and $[\{K_2ZnSn_8(ZnMes)\}_2]^{4-}$ [261, 262], and $(Sn_4Sb_4)^{2-}$ in $[Co@Sn_6Sb_6]^{3-}$ [263]. Interestingly, however, the global minimum isomer of two recently reported heterometallic dimers, $[(Sn_5Sb_3M)_2]^{4-}$ (M = Cu, Au) [189, 190], comprises related $(Sn_5Sb_3)^{3-}$ fragments with a slightly different isomeric form of the *arachno*-cage. As the isolated version of $(Sn_5Sb_3)^{3-}$ represents the global minimum structure for this composition, according to DFT calculations, it was suggested that the slightly different isomer is more reactive and thus acts as a precursor to the formation of the ternary anions $[(Sn_5Sb_3M)_2]^{4-}$ (M = Cu, Au; see Sect. 4.2.4). Another heterometallic cluster, $[Sb_6(RuCp^*)_2]^{2-}$ ($Cp^* = C_5Me_5$; Fig. 15e) [264], has a remarkably similar 8-vertex core, which will be discussed in more detail in Sect. 4.2.3. An overview

of known electron-deficient binary p-block-p-block (semi-)metal anions adopting molecular structures that accord with Wade-Mingos rules is provided in Table 4.

3.3 Ternary Analogs

The existence of several ternary p-block Zintl ions is also worth noting herein. One example is the dimeric deltahedral cluster $[(Sn_6Ge_2Bi)_2]^{4-}$ (Fig. 8) [265], with Ge-Ge inter-cluster bonds, which was obtained either by reacting bimetallic clusters $(Sn_{9-x}Ge_x)^{4-}$ ($x = 4.5$, for instance) with $BiPh_3$ or by direct extraction of a quaternary precursor with the nominal composition "$K_4Ge_4Sn_4Bi$" with en and subsequent layering with crypt-222/toluene. Each of the subunits is best described as distorted tricapped trigonal prisms of six tin atoms, with the two Ge atoms and one Bi atom capping the three rectangular faces; this description is in accordance with the interpretation of the subunits as *closo*-type cages with SEN = 8·4 (Ge, Sn) + 5 (Bi) + 2 (charge) + 1 (Ge-Ge bond) – 9·2 (exo e^- Ge, Bi) = 40 – 18 = 22 = 2·*n* + 2. This way, the anion compares well with the known dimers $[(Ge_9)_2]^{6-}$ and $[(PnGe_8)_2]^{4-}$ (Pn = Sb, Bi), respectively [253, 266]. The alternative description as a highly distorted monocapped square antiprism, with the open square defined by one Ge atom, one Bi atom, and two Sn atoms, deviates more from the observed architecture, and it disagrees with the SEN. The ESI mass spectrum of the reactive solution obtained from $BiPh_3$ + "$K_4Sn_{4.5}Ge_{4.5}$" in en revealed $(Sn_6Ge_2Bi)^-$ as producing the predominant peak. Calculations showed that no structural changes are present in the lowest-energy isomers when $(Sn_6Ge_2Bi)^{3-}$ is initially oxidized to $(Sn_6Ge_2Bi)^{2-}$, which is anticipated to subsequently dimerize to form $[(Sn_6Ge_2Bi)_2]^{4-}$ [267]. The related examples of this category are listed in Table 5.

4 Binary Zintl Anions of p-Block and d-Block Atoms

The remarks made at the outset of Sect. 3, that is, the concept of isoelectronic replacement of atoms, also apply to binary anions composed of p-block and d-block atoms. However, the variability is even larger in this case. Naturally, the reactions yielding the clusters usually require other synthetic protocols, and d-block atoms show a distinct tendency to occupy an endohedral position within main group (semi-)metal cages; however, such endohedral, "intermetalloid" [268] clusters (unless closely related with species discussed herein) will not be addressed in this chapter, which aims at focusing on cages without interstitial atoms – so-called "heterometallic clusters" – on the one hand, and on centered anions with no bonds between the substituents on the other hand. The distinctly different electronic nature of d-block metal atoms can also have another effect, owing to these atoms' higher flexibility regarding their coordination environment. Hence, the transition metal atoms can stabilize main group (semi-)metal units that would not be stable as

Table 4 Overview of known electron-deficient binary p-block-p-block (semi-)metal anions adopting molecular structures that accord with Wade-Mingos rules

Formula	Parent compound/source	Type	Ref.	Figure no.
$(TlTt_9)^{3-}$ Tt = Ge, Sn	$[K(crypt\text{-}222)]_3(Ge_9Tl)\cdot 2py$ $[K(crypt\text{-}222)]_{6-}[(Ni@Sn_9Tl)_x(Ni@Sn_9)_{(1-x)}]_2\cdot 2en$	*closo*	[252]	7f
Hyp_3Ge_9Tl	Hyp_3Ge_9Tl	*closo*	[253]	7g
$(Si_{9-x}Ge_x)^{4-}$ $x = 1.2, 1.5$	$Rb_4(Si_{7.8}Ge_{1.2})(NH_3)_5$ $[Rb(18\text{-crown-}6)Rb_3](Si_{7.5}Ge_{1.5})(NH_3)_4$	*nido*	[249]	7a
$(Si_{9-x}Ge_x)^{3-}$ $x = 4.4, 6.6, 6.7, 6.8$	$[Rb(crypt\text{-}222)]_3(Si_{2.2(1)}Ge_{6.8(1)})(NH_3)_8$ $[K(crypt\text{-}222)]_3(Si_{2.4(1)}Ge_{6.6(1)})(NH_3)_{8.5}$ $[K(crypt\text{-}222)]_3(Si_{4.6(1)}Ge_{4.4(1)})(NH_3)_{8.5}$	Between *closo*- and *nido*	[250]	7b
$[Sn(Ge_9)_2]^{4-}$	$[K(18\text{-crown-}6)]_4[(Ge_9)Sn(Ge_9)]\cdot 4.5\,en$	*closo*	[257]	7l
$(GeSn_8\text{-}R)^{3-}$ $R = HC{=}CH_2$, $HC{=}CHC_{pr}$	$[K(crypt\text{-}222)]_3(GeSn_8\text{-}CH{=}CH_2)\cdot en\cdot tol$ $[K(crypt\text{-}222)]_3(GeSn_8\text{-}CH{=}CHC_{pr})\cdot en$	*nido*	[251]	7c
$[Ge_2Sn_7\text{-}(HC{=}CH_2)_2]^{2-}$	$[K(crypt\text{-}222)]_4[Ge_2Sn_7(CH{=}CH_2)_2]_2\cdot en$	*nido*	[251]	7d
$(Ge_2Sn_7\text{-}HC{=}CHPh)^{2-}$	$[K(crypt\text{-}222)]_3(Ge_2Sn_7\text{-}CH{=}CHPh)\cdot 2en$	*nido*	[251]	7e
$(In_2Sb_3)^-$	Gas phase	*closo*	[258]	–
$(Tr_2Bi_3)^-$ Tr = Al, Ga, In	Gas phase	*closo*	[258]	–
$(Tl_4Bi_3)^{3-}$	$[K(crypt\text{-}222)]_3(Tl_4Bi_3)$	*closo*	[259]	7n
$(Tr_4Bi_5)^{3-}$ Tr = In, Tl	$[K(crypt\text{-}222)]_6(In_4Bi_5)(In_4Bi_5)\cdot 1.5en\cdot 0.5tol$ $[K(crypt\text{-}222)]_3(Tl_4Bi_5)\cdot 2en$	*nido*	[209, 210]	7m
$(Sn_5Sb_3)^{3-}$	$[^nBu_4P]_3(Sn_5Sb_3)$	*arachno*	[187]	7p
$(Sn_3Bi_3)^{5-}$	$Rb_6(Sn_3Bi_3)(Sn_4)_{0.25}\cdot 6.75\,NH_3$	*hypho*	[228]	7o
$(Ge_7Pn_2)^{2-}$ Pn = P, As, Sb	$[K(crypt\text{-}222)]_2(Ge_7Pn_2)$ Pn = P, As $[Rb(18\text{-crown-}6)]_2(Ge_7Sb_2)\cdot en$ $[K(crypt\text{-}222)]_2(Ge_7Sb_2)\cdot tol$; $[^nBu_4N]_2(Ge_7Sb_2)\cdot tol$	*nido*	[188, 211, 256]	7h
$[Ge_7P_2(R)_3]^+$ $R = CH_3, C_2H_5, C_3H_3$	Calculated	*closo*	[255]	–

(continued)

Table 4 (continued)

Formula	Parent compound/source	Type	Ref.	Figure no.
$(Tt_7Bi_2)^{2-}$ Tt = Sn, Pb	$[K(crypt\text{-}222)]_2(Sn_7Bi_2)\cdot en\cdot tol$, $[K(crypt\text{-}222)]_2(Pb_7Bi_2)\cdot 1.36en$	*nido*	[214, 254]	7h
$[(SbGe_8)\text{-}R]^{2-}$ R = $SbPh_2$, $CH{=}CH_2$	$[K(crypt\text{-}222)]_2[(SbGe_8)\text{-}SbPh_2]$ $[K(crypt\text{-}222)]_2[(SbGe_8)\text{-}CH{=}CH_2]$	*nido*	[256]	7k 7j
$[(SbGe_8)\text{-}(Ge_8Sb)]^{4-}$	$[K(crypt\text{-}222)]_4[(SbGe_8)\text{-}(Ge_8Sb)]\cdot 3en$ $[K(18\text{-}crown\text{-}6)]_4[(SbGe_8)\text{-}(Ge_8Sb)]\cdot 4en$ $[K(18\text{-}crown\text{-}6)]_4[(BiGe_8)\text{-}(Ge_8Bi)]\cdot 5en$	*nido*	[256]	7i

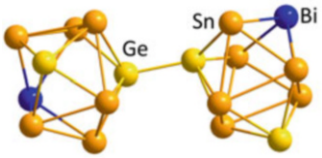

Fig. 8 Structure of $[(Sn_6Ge_2Bi)_2]^{4-}$, an electron-deficient ternary p-block-p-block-p-block (semi-) metal anion, in which the molecular structural subunits adopt cage structures that accord with Wade-Mingos rules

Table 5 Overview of known ternary p-block-p-block-p-block (semi-)metal anion adopting a molecular structures that accord with Wade-Mingos rules

Formula	Parent compound/source	Type	Ref.	Figure no.
$[(Sn_6Ge_2Bi)_2]^{4-}$	$[K(crypt\text{-}222)]_4[(Sn_6Ge_2Bi)_2]\cdot 1.5en$	*closo*	[265]	8
$[Sn_6Ge_2Bi]^{3-}$	Calculated	*closo*	[267]	–
$[Sn_{9-x-y}Ge_xBi_y]^{(4-y)-}$ $y = 1\text{–}4$, $x = 0 - (9 - y)$	Calculated	*nido*	[267]	–

isolated homoatomic Zintl anions. In summary, the binary anions that result from the combinations of d-block and p-block atoms, which will be presented in the subsequent sections (again distinguished by their electron-precise or electron-deficient nature, respectively), show a larger variation of resulting geometric and electronic structures, and also of concomitant chemical and physical properties.

4.1 Electron-Precise p-Block-d-Block Anions

4.1.1 Binary Cages Involving Group 13 Atoms

Examples of heterometallic clusters involving solely group 13 atoms in addition to d-block metal atoms that were isolated from solution-based syntheses are rare. One example is given by the neutral compound $[(Cp^*AlCu)_6H_4]$ (Fig. 9) [269], which was discussed in the context of embryonic states of Hume−Rothery phases, owing to their elemental combination. The cluster is based on a Cu_6 core (a bicapped tetrahedron), which is surrounded by six {Cp*Al} fragments that are arranged in an octahedral manner. The compound was shown to provide an inexpensive intermediate in the synthesis of selective catalysts for the semihydrogenation of alkynes to alkenes.

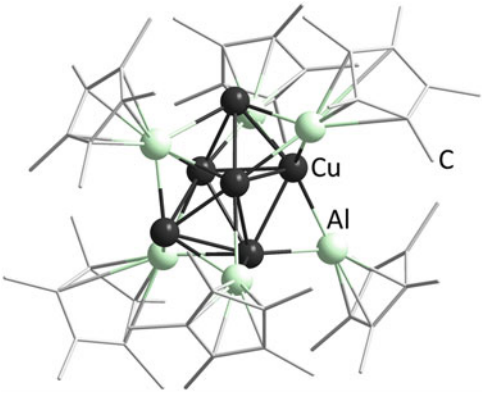

Fig. 9 Structure of $[(Cp^*AlCu)_6H_4]$. H atoms are omitted for clarity

4.1.2 Anions Based on Cyclohexane-Type and S_8-Type Units

$[Nb(\eta^6\text{-}C_6H_5Me)_2]$ was reacted with K_4Sn_9 in en/crypt-222 to yield $[(\eta^6\text{-}C_6H_5Me)NbSn_6Nb(\eta^6\text{-}C_6H_5Me)]^{2-}$ (Fig. 10) as its $[K(crypt\text{-}222)]^+$ salt [270]. In contrast to homoatomic polystannide ions isolated from solution, namely *nido*-Sn_9^{4-}, paramagnetic Sn_9^{3-}, or *closo*-Sn_5^{2-}, and in contrast to metal-stabilized Zintl ions including *closo*-Sn_6^{2-} in $[Sn_6\{Cr(CO)_5\}_6]^{2-}$ [271], and Sn_8^{6-} in *closo*-$Li_2Sn_8^{4-}$ [261] or $\{[K_2ZnSn_8(ZnMes)]_2\}^{4-}$ [262], all of which accord with Wade-Mingos rules, the heterometallic cluster in $[(\eta^6\text{-}C_6H_5Me)NbSn_6Nb(\eta^6\text{-}C_6H_5Me)]^{2-}$ can be regarded as a *cyclo*-Sn_6^{12-} ion, which is stabilized by two $[(\eta^6\text{-}C_6H_5Me)Nb]^{5+}$ fragments on both sides. This anion is related to intermetalloid anions of the type $(MPn_8)^{n-}$ (M = Nb, Mo; Pn = Sb, As; n = 2, 3) [272–274], yet with the difference that in the latter, the $\{Pn_8\}$ "crown" is centered around an interstitial d-block ion, hence does not form a cage-type structure together with it. While the formal charge assignments (i.e., the assigned oxidation states) appear extreme, they serve to describe well the bonding within the $\{E_n\}$ rings: the formal 12− charge of the $\{Sn_6\}$ ring in $[(\eta^6\text{-}C_6H_5Me)NbSn_6Nb(\eta^6\text{-}C_6H_5Me)]^{2-}$ is structurally consistent with a cyclohexane structure, and thus in accordance with short 2e2c Sn-Sn single bonds; similarly, the Pn_8 rings of the $(MPn_8)^{2-}$ anions, with an S_8-type shape, are in good agreement with this electron-transfer model, too. Still, it should be emphasized that this formalism does not reflect accurate oxidation states; as for most of the known mixed p-block-d-block clusters, it just serves to formally rationalize the structure and bonding observed in the p-block substructure.

4.1.3 Nortricyclane-Type Anions

Compared to norbornadiene-type electron-precise p-block-p-block anions [9], nortricyclane-type anions Pn_7^{3-} show a larger tendency to act as ligands for coordinating d-block metal ions. Among them, P_7^{3-} and As_7^{3-}, exhibiting relatively strong bonds within the cages, do not tend to undergo extensive fragmentation and

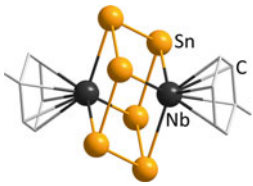

Fig. 10 Structure of $[(\eta^6\text{-}C_6H_5Me)NbSn_6Nb(\eta^6\text{-}C_6H_5Me)]^{2-}$. H atoms are omitted for clarity

rearrangement processes; partial bond cleavage is observed in some cases though, resulting in rare examples with fragments of the cages serving as donor ligands, for instance in $[Co(\eta^5\text{-}P_5)\{\eta^2\text{-}P_2H(Mes)\}]^{2-}$ and $[Co(\eta^3\text{-}As_3)\{\eta^4\text{-}As_4(Mes)_2\}]^{2-}$ [275, 276]. Most often however, P_7^{3-} and As_7^{3-} cages coordinate to d-block metal complex fragments as a whole, thereby forming a series of related anions, such as $[P_7Ni(CO)]^{3-}$, $[Fe(HP_7)_2]^{2-}$, $[M(Pn_7)_2]^{4-}$ (M = Zn, Pn = P, As, Sb; M = Cd, Pn = P, As), and $[Au_2(As_7)_2]^{4-}$ (Figs. 11a–d) [280–281]. A comprehensive list of examples is provided in Table 6 [224, 280–288]. The Pn-Pn bond strength decreases with the increase of the metallicity of Pn, which is reflected in a lower overall stability of such cages. Thus, besides relatively rare examples of $\{Sb_7\}$ cages retained in a heterometallic cluster, $[Sb_7M(CO)_4]^{3-}$ (M = Cr, Mo) and $[Zn(Sb_7)_2]^{4-}$ (Fig. 11c, e) [289–290], a bimetallic norbornadiene-like dimeric anion, $[(ZnSb_6)_2]^{4-}$ (Fig. 11f) [288], was prepared by direct extraction of a ternary alloy of the nominal composition "K_6ZnSb_5" with en in the presence of crypt-222 (it should be noted, however, that it is not secured whether the extract contained the Sb_7^{3-} anion at all). The structure represents a new type of coupled norbornadiene-type fragments. However, distortions decrease the overall molecular symmetry. It is worth noting that the Zn^{2+} ions formally possess a $16e^-$ configuration within their nearly perfect triangular $\{ZnSb_3\}$ coordination pattern.

Although having been predicted to exist by Zintl himself, the lack of a rational experimental approach of polycyclic polybismuthides has long inhibited their isolation. However, this was finally realized with the combination of suitable synthetic and crystallization conditions which resulted in the synthesis of Bi_{11}^{3-} from $(GaBi_3)^{2-}$ and the release of elemental Ga(0) [185], and the synthesis of Bi_7^{3-} from K_5Bi_4 in the presence of $[(C_6H_6)Cr(CO)_3]$ [175]. The first heterometallic polyanion with nortricyclane-type polybismuthide cages coordinating a transition metal atom, $[(Bi_7)Cd(Bi_7)]^{4-}$ (Fig. 11g), was reported 5 years later [289]. Similar to the homologous compounds with lighter Pn_7^{3-} ligands (Pn = P, As, Sb), the two Bi_7^{3-} nortricyclane cages bind to the central Cd^{2+} ion via two of their two-bonded Bi atoms each. Overall, this leads to a tetrahedral coordination of the central ion. Based on a DFT study on the stability of the whole series of $[(Pn_7)M(Pn_7)]^{4-}$ species, it was assumed that slight variations of the reaction conditions might in fact allow for the successful synthesis and isolation of the homologous complex $[(Bi_7)Zn(Bi_7)]^{4-}$, but unfortunately this anion has not been isolated to date. In a report prior to this, the formation of the heterometallic cluster anion $[Bi_9\{Ru(cod)\}_2]^{3-}$ has already proven that another *pseudo*-tetrahedral anion, $(TlBi_3)^{2-}$, can also serve as an excellent starting material for the formation of polybismuthide architectures in reactions

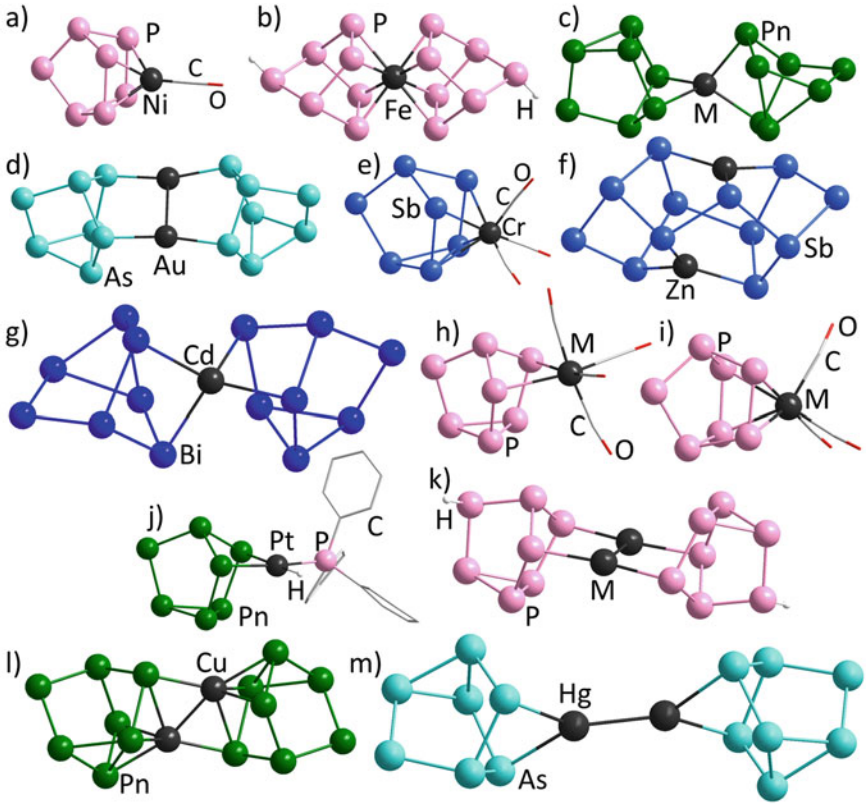

Fig. 11 Selected structures of known electron-precise binary p-block-d-block (semi-)metal anions adopting ring-type and cage-type structures: (**a**) $[P_7Ni(CO)]^{3-}$, (**b**) $[Fe(HP_7)_2]^{2-}$, (**c**) $[M(Pn_7)_2]^{4-}$ (M = Zn, Pn = P, As, Sb; M = Cd, Pn = P, As), (**d**) $[Au_2(As_7)_2]^{4-}$, (**e**) $[Sb_7Cr(CO)_4]^{3-}$, (**f**) $[(ZnSb_6)_2]^{4-}$, (**g**) $[Cd(Bi_7)_2]^{4-}$, (**h**) $[P_7M(CO)_4]^{3-}$ (M = Cr, Mo, W), (**i**) $[HP_7M(CO)_4]^{2-}$ (M = Cr, Mo, W), (**j**) $[Pn_7PtH(PPh_3)]^{2-}$ (Pn = P, As), (**k**) $[M_2(HP_7)_2]^{2-}$ (M = Ag, Au), (**l**) $[Cu_2(Pn_7)_2]^{4-}$ (Pn = P, As), (**m**) $[Hg_2(As_7)_2]^{4-}$. H atoms are omitted for clarity in (**j**)

with transition metal compounds [210]. An overview of known electron-precise binary p-block-d-block (semi-)metal anions adopting cage-type structures is given in Table 6.

4.1.4 SiS_2 and CO_2-Type Anions

In contrast to the orthosilicate ion $[SiO_4]^{4-}$, SiS_2 consists of $_\infty{}^1[SiS_{4/2}]$ chains. Isoelectronic heterometallic architectures were realized in the one-dimensionally extended Zintl anions $_\infty{}^1[ZnPn_2]^{4-}$ (Pn = P, As, Sb, Bi; Fig. 12a) included in $Ba_2[ZnPn_2]$ [290], which were synthesized from corresponding element mixtures in

Table 6 Overview of known electron-precise binary p-block-d-block (semi-)metal anions adopting cage-type structures

Formula	Parent compound	Ref.	Figure no.
$[P_7Ni(CO)]^{3-}$	$[K(crypt\text{-}222)][(n\text{-}C_4H_9)_4P]_2[P_7Ni(CO)]$	[277]	11a
$[P_7M(CO)_4]^{3-}$ M = Cr, Mo, W	$[K(crypt\text{-}222)]_3[\eta^2\text{-}P_7M(CO)_4]\cdot en$	[278]	11h
$[HP_7M(CO)_4]^{2-}$ M = Cr, Mo, W	$[K(crypt\text{-}222)]_2[\eta^2\text{-}HP_7M(CO)_4]\cdot en$	[278]	11i
$[Fe(HP_7)_2]^{2-}$	$[K(crypt\text{-}222)]_2[Fe(HP_7)_2]$	[279]	11b
$[M(Pn_7)_2]^{4-}$ M = Zn; Pn = P, As, Sb M = Cd; Pn = P, As	$[K(crypt\text{-}222)]_4[Zn(Pn_7)_2]$ $[K(crypt\text{-}222)]_4[Cd(P_7)_2]\cdot 6py$ $[K(crypt\text{-}222)]_4[Cd(As_7)_2]\cdot en$ $[K(crypt\text{-}222)]_4[Zn(Sb_7)_2]\cdot 8NH_3$	[224, 280, 281]	11c
$[Pn_7PtH(PPh_3)]^{2-}$ Pn = P, As	$[K(crypt\text{-}222)]_2[P_7PtH(PPh_3)]$	[282]	11j
$[M_2(HP_7)_2]^{2-}$ (M = Ag, Au)	$[K(crypt\text{-}222)]_2[M(HP_7)_2]$	[283]	11k
$[Au_2(As_7)_2]^{4-}$	$[K(crypt\text{-}222)]_4[Au_2(As_7)_2]$	[284, 285]	11d
$[Cu_2(Pn_7)_2]^{4-}$ Pn = P, As	$[K(crypt\text{-}222)]_4[Cu_2(Pn_7)_2]$	[224]	11l
$[Hg_2(As_7)_2]^{4-}$	$[K(crypt\text{-}222)]_4[Hg_2(As_7)_2]$	[286]	11m
$[Sb_7M(CO)_4]^{3-}$ M = Cr, Mo	$[K(crypt\text{-}222)]_3[Sb_7M(CO)_4]$	[287]	11e
$[(ZnSb_6)_2]^{4-}$	$[K(crypt\text{-}222)][(ZnSb_6)_2]\cdot 0.65tol$	[288]	11f
$[Cd(Bi_7)_2]^{4-}$	$[K(crypt\text{-}222)]_4[(Bi_7)Cd(Bi_7)]\cdot en$	[289]	11g

a lead flux. The anions are constructed by *trans*-edge-sharing of $\{ZnPn_4\}$ tetrahedra, which replace the $\{SiS_4\}$ tetrahedra in the archetypical SiS_2.

When including alkali metal cations instead of Ba^{2+} in such p-block element mixtures, molecular units are observed that may be understood as a product of a cleavage of the chains and disconnection of the $\{MPn_2\}$ units. Selected examples include $[BePn_2]^{4-}$ (Pn = P, As, Sb), $[BPn_2]^{3-}$ (Pn = P, As), $[MPn_2]^{4-}$ (M = Zn, Cd, Hg; Pn = P, As), $[AuPn_2]^{5-}$ (Pn = P, As), $[CuPn_2]^{5-}$ (Pn = As, Sb), and $[ZnBi_2]^{4-}$ (Fig. 12b), which are stabilized by Na^+, Na^+/K^+, K^+, Rb^+, or Cs^+ cations, respectively, in corresponding alloys [291–296]. The linear triatomic anions are isoelectronic with CO_2. The same applies to $[Sn\text{-}Zn\text{-}Sn]^{6-}$ (Table 7, Fig. 12c) [297], present in the alloys Na_6ZnSn_2 and $Na_{20}Zn_8Sn_{11}$, in which Tt atoms are included instead of Pn atoms. Notably, one of these very highly charged anions, $[Bi\text{-}Zn\text{-}Bi]^{4-}$, was even obtained from solution: Reactions between $[Zn_2(Mesnacnac)_2]$ (Mesnacnac = $[(2,4,6\text{-}Me_3C_6H_2)NC(Me)]_2CH$) and K_3Bi_2/18-crown-6 or K_5Bi_4/crypt-222 in liquid ammonia result in the formation and isolation of $K_4[ZnBi_2](NH_3)_{12}$ [298]. The linear $[Bi\text{-}Zn\text{-}Bi]^{4-}$ unit in it represents the first triatomic 16-valence electron species that can alternatively adopt another allotropic form of TtE_2 (Tt = C, Si; E = O, S; Scheme 1). In addition, the anion $[Bi\text{-}Zn\text{-}Bi]^{4-}$ indeed represents the first (and so far only) metal-atom-based CO_2 analog obtained from

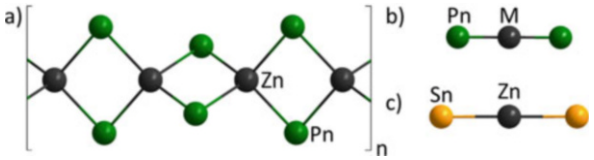

Fig. 12 Structures of all known electron-precise binary p-block-d-block (semi-)metal anions representing isoelectronic analogs of CO_2: (**a**) $_{\infty}^{1}[ZnPn_2]^{4-}$ (Pn = P, As, Sb, Bi), (**b**) $[BePn_2]^{4-}$ (Pn = P, As, Sb), $[BPn_2]^{3-}$ (Pn = P, As), $[MPn_2]^{4-}$ (M = Zn, Cd, Hg; Pn = P, As), $[AuPn_2]^{5-}$ (Pn = P, As), $[CuPn_2]^{5-}$ (Pn = As, Sb), and $[ZnBi_2]^{4-}$, (**c**) [Sn-Zn-Sn]$^{6-}$

Table 7 Overview of electron-precise binary p-block-d-block (semi-)metal anions representing isoelectronic analogs of CO_2 or SiS_2

Formula	Parent compound	Type	Ref.	Figure no.
$_{\infty}^{1}[ZnPn_2]^{4-}$ Pn = P, As, Sb, Bi	$Ba_2[ZnPn_2]$	SiS_2	[290]	12a
[Sn-Zn-Sn]$^{6-}$	$Na_6[ZnSn_2]$, $Na_{20}Zn_8Sn_{11}$	CO_2	[297]	12c
$[MPn_2]^{4-}$ M = Zn, Cd, Hg; Pn = P, As	$A_4[MPn_2]$ A = Na^+, Na^+/K^+, K^+, Rb^+, Cs^+	CO_2	[291–294]	12b
$[AuPn_2]^{5-}$ (Pn = P, As)	$K_5[AuPn_2]$	CO_2	[296]	12b
$[CuPn_2]^{5-}$ Pn = As, Sb	$K_5[CuPn_2]$	CO_2	[296]	12b
$[ZnBi_2]^{4-}$	$K_4[ZnBi_2]$	CO_2	[295]	12b
[Bi-Zn-Bi]$^{4-}$	$K_4(ZnBi_2)(NH_3)_{12}$	CO_2	[298]	12b

solution. An overview of electron-precise binary p-block-d-block (semi-)metal anions representing isoelectronic analogs of CO_2 or SiS_2 is summarized in Table 7.

4.2 Electron-Deficient p-Block-d-Block Anions

4.2.1 Tt-d-Block Anions

Early NMR studies of reaction mixtures containing $[Pt(PPh_3)_4]$ and Tt_9^{4-} ions (Tt = Sn, Pb) in en confirmed highly fluxional properties of the products. However, the lack of single crystals had prevented its definitive structural assignment and further analysis for a while [299]. The synthesis and crystallization of *closo*-$[Sn_9Cr(CO)_3]^{4-}$ (Fig. 13a) finally evidenced the first member of a new class of polyhedral clusters, and thus opened up a new gate for mixed-metallic d-block-p-block Zintl chemistry [300]. In the meantime, a huge number of such *closo*-type d-block-p-block Zintl anions have been isolated and identified, holding the record of numbers among all different types of Zintl clusters. The formation of these species, e.g., $[\eta^4\text{-}Tt_9M(CO)_3]^{4-}$ (Tt = Sn, Pb; M = Cr, Mo, W) [300–305] (Fig. 13a), can be viewed as the addition of a neutral $\{M(CO)_3\}$ fragment to the open square face of a *nido*-Tt_9^{4-} ion, thus generating a *closo*-10-atom deltahedron according to Wade-Mingos

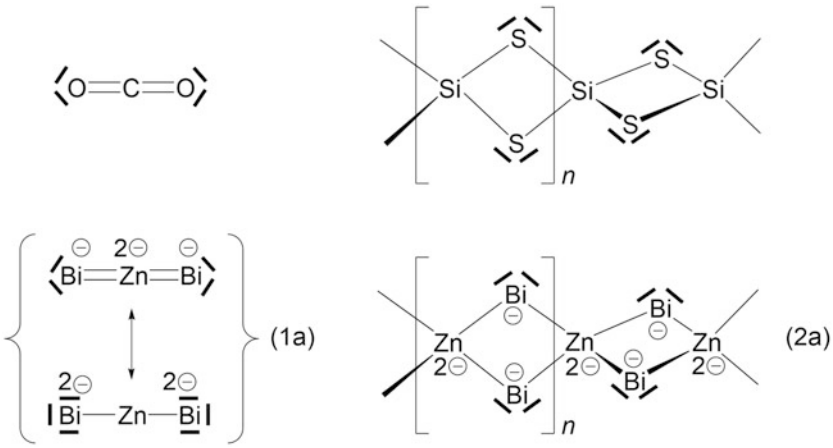

Scheme 1 Diagram of the two modifications of $[Bi\text{-}Zn\text{-}Bi]^{4-}$, drawn with formal charges to emphasize the isoelectronic analogy to CO_2 on the one hand (**1a**) and to SiS_2 on the other hand (**2a**). Reproduced with permission of Wiley-VCH

rules. The $\{M(CO)_3\}$ unit possesses 12 valence electrons (VE), isolobal to a 2-electron $(BH)^{2+}$ fragment. Consequently, it does not contribute to cluster bonding, as all of the VE are considered as exo-electrons. According to the Wade-Mingos formalism, one calculates SEN = 9·4 (VE Tt) + 12 {VE $M(CO)_3$} + 4 (charge) – 9·2 (*exo*-e^- Tt) – 1·12 (*exo*-e^- $\{M(CO)_3\}$) = 52 – 30 = 22 = 2·(*n* + *m*) + 2. Analogous considerations apply to the related anions $[\eta^4\text{-}Tt_9ML_x]^{3-}$ shown in Table 8 and Figs. 13b–e, such as $[Ge_9Ni\text{-}CO]^{3-}$ [306], $[\eta^4\text{-}Tt_9Ir(cod)]^{3-}$ (Tt = Sn, Pb) [307, 308], $[Cu(\eta^4\text{-}Ge_9)(PR_3)]^{3-}$(R = Cy = cyclohexane or R = ^{i}Pr) [309], and $[\eta^4\text{-}Tt_9ZnR]^{3-}$ (Tt = Si, Ge, Sn, Pb; R = Et, Mes, ^{i}Pr, Ph) [310, 311, 314].

A capping of *nido*-type cages with transition metal fragments to form *closo*-type d-block-p-block Zintl anions can alternatively be realized by transition metals connecting two *nido*-type 9-atom cages. Similar to the hybrid *closo-nido*-type anion $[(Ge_9)Sn(Ge_9)]^{4-}$, the Zn-centered cluster $\eta^4{:}\eta^3\text{-}[Zn(Ge_9)_2]^{6-}$ (Fig. 13f) [257] might be regarded as being composed of a $(Ge_9Zn)^{2-}$ *closo*-cluster comprising 22 skeleton electrons and nine lone pairs (18 exo-electrons), with an acceptor orbital being located at the Zn atom that further interacts with a filled orbital of a *closo*-type nine-atom anion $D_{3h}\text{-}Ge_9^{4-}$. Furthermore, several investigations have been devoted to synthesize compounds containing low-valent Zn atoms ever since the first Zn (I) compound, $[Zn_2Cp^*_2]$ with a covalent Zn-Zn bond, was reported in 2004 [318]. This has also been applied to the isolation of *closo*-Zintl anions by replacing the Cp* ligands in $[Zn_2Cp^*_2]$ with *nido*-type Zintl cages through different synthetic strategies. The resulting anions, $(Ge_9Zn\text{-}ZnGe_9)^{6-}$ and the structurally related $(Pb_9Cd\text{-}CdPb_9)^{6-}$ (Fig. 13g) [312, 313], can be regarded as dimers of *closo*-$(Tt_9M)^{3-}$ bearing an unpaired electron at their respective Zn or Cd vertex, which is paired in the M-M bond. Notably, in addition to the formation of $(Ge_9Zn\text{-}$

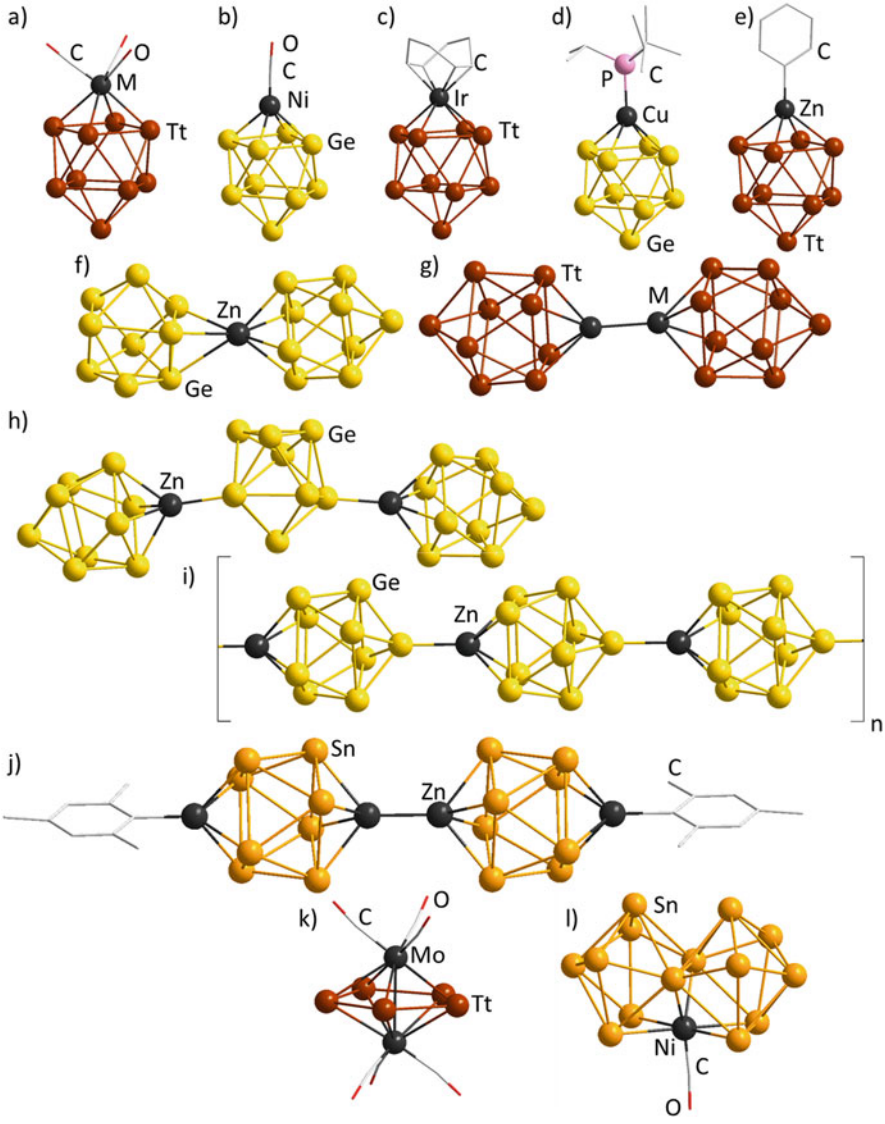

Fig. 13 Structures of all known electron-deficient binary Tt-d-block (semi-)metal anions: (**a**) $[\eta^4\text{-}Tt_9M(CO)_3]^{4-}$ (Tt = Sn, Pb; M = Cr, Mo, W), (**b**) $[Ge_9Ni\text{-}CO]^{3-}$, (**c**) $[\eta^4\text{-}Tt_9Ir(cod)]^{3-}$ (Tt = Sn, Pb), (**d**) $[Cu(\eta^4\text{-}Ge_9)(PR_3)]^{3-}$(R = Cy, ^{i}Pr), (**e**) $[\eta^4\text{-}Tt_9ZnR]^{3-}$ (Tt = Si, Ge, Sn, Pb; R = Et, Mes, ^{i}Pr, Ph), (**f**) $[Zn(Ge_9)_2]^{6-}$, (**g**) $[Tt_9M\text{-}MTt_9]^{6-}$ (Tt/M = Ge/Zn, Pb/Cd), (**h**) $[(Ge_9Zn)\text{-}(Ge_9)\text{-}(ZnGe_9)]^{8-}$, (**i**) $_\infty{}^1[-(Ge_9Zn)^{2-}\text{-}]_1$, (**j**) $\{[K_2ZnSn_8(ZnMes)]_2\}^{4-}$, (**k**) $[Tt_5\{M(CO)_3\}_2]^{4-}$, (**l**) $[Sn_{14}Ni(CO)]^{4-}$. H atoms are omitted for clarity

Table 8 Overview of known electron-deficient binary Tt-d-block (semi-)metal anions without Hyp-substitution

Formula	Parent compound/source	Type	Ref.	Figure no.
$[\eta^4\text{-}Tt_9M(CO)_3]^{4-}$ Tt = Sn, Pb; M = Cr, Mo, W	$[K(crypt\text{-}222)]_4[\eta^4\text{-}Tt_9M(CO)_3]$	*closo*	[300–305]	13a
$[Ge_9Ni\text{-}CO]^{3-}$	$[K(crypt\text{-}222)]_3[Ge_9Ni\text{-}CO]$	*closo*	[306]	13b
$[\eta^4\text{-}Tt_9Ir(cod)]^{3-}$ Tt = Sn, Pb	$[K(crypt\text{-}222)]_3[\eta^4\text{-}Tt_9Ir(cod)]$	*closo*	[307, 308]	13c
$[Cu(\eta^4\text{-}Ge_9)(PR_3)]^{3-}$ R = Cy, ^{i}Pr	$[K(crypt\text{-}222)]_3[Cu(\eta^4\text{-}Ge_9)(PR_3)]\cdot n$ solv R/n solv = Cy/2.5dmf, ^{i}Pr/13NH$_3$	*closo*	[309]	13d
$[\eta^4\text{-}Tt_9ZnR]^{3-}$ Tt = Si, Ge, Sn, Pb R = Mes, ^{i}Pr, Ph	$[K(crypt\text{-}222)]_3[\eta^4\text{-}Tt_9ZnR]\cdot n$ solv Tt/R/n solv = Si/Ph/2py, Ge/Mes/none, Ge/^{i}Pr/en·2tol, Ge/Ph/2en·tol, Sn/Mes/tol, Sn/^{i}Pr/0.5en, Sn/Ph/tol, Pb/Mes/none, Pb/Ph/2en·tol	*closo*	[310, 311]	13e
$[Zn(Ge_9)_2]^{6-}$	$K_2[K(crypt\text{-}222)]_4[Zn(Ge_9)_2](NH_3)_{21.6}$	*closo* unit	[257]	13f
$[(Ge_9Zn)\text{-}(Ge_9)\text{-}(ZnGe_9)]^{8-}$	$K_4[K(crypt\text{-}222)]_{4-}[(Ge_9Zn)\text{-}(Ge_9)\text{-}(ZnGe_9)](NH_3)_{29}$	*closo* unit	[312]	13h
$_\infty{}^1[-(Ge_9Zn)^{2-}\text{-}]$	$[K(crypt\text{-}222)]_2(ZnGe_9)(en)_{0.9}$	*closo* unit	[312]	13i
$[Tt_9M\text{-}MTt_9]^{6-}$ Tt/M = Ge/Zn, Pb/Cd	$K_2[K(crypt\text{-}222)]_{4-}[Ge_9Zn\text{-}ZnGe_9](NH_3)_{26}$ $[K(crypt\text{-}222)]_6[Pb_9Cd\text{-}CdPb_9]\cdot 2en$	*closo* unit	[312, 313]	13g
$[(\eta^4\text{-}Ge_9)(ZnEt)]^{3-}$	$[K(crypt\text{-}222)]_3[(\eta^4\text{-}Ge_9)(ZnEt)]\cdot 7.4NH_3$	*closo*	[314]	
$[Pb_5\{Mo(CO)_3\}_2]^{4-}$	$K_2[K(crypt\text{-}222)]_2[Pb_5\{Mo(CO)_3\}_2]\cdot 3en$	*closo*	[315]	13k
$[Tt_5\{M(CO)_3\}_2]^{4-}$ Tt = Si, Ge, Sn, Pb M = Cr, Mo, W	Calculated	*closo*	[316]	–
$\{[K_2ZnSn_8(ZnMes)]_2\}^{4-}$	$[K(crypt\text{-}222)]_4\{[K_2ZnSn_8(ZnMes)]_2\}$	*closo* unit	[262]	13j
$[Sn_{14}Ni(CO)]^{4-}$	$[K(crypt\text{-}222)]_4[Sn_{14}Ni(CO)]\cdot dmf$	*closo* unit	[317]	13l

$ZnGe_9)^{6-}$ (Fig. 13g), another compound consisting of three $\{Ge_9\}$ clusters that are connected via two Zn^{2+} ions, $[(Ge_9Zn)\text{-}(Ge_9)\text{-}(ZnGe_9)]^{8-}$ (Fig. 13h), was observed as a side product. Variation of the reaction conditions afforded $_\infty{}^1[-(Ge_9Zn)^{2-}\text{-}]$ (Fig. 13i) as a polymeric strand of *closo*-$(Ge_9Zn)^{2-}$ anions. Very recently, an inverse sandwich-type cluster dimer, $\{[ZnSn_8(ZnMes)]_2\}^{8-}$ (Fig. 13j), was reported as the anionic substructure of $\{[K_2ZnSn_8(ZnMes)]_2\}^{4-}$ [262]. Here, a highly charged

Sn_8^{6-} anion coordinates to mixed-valence Zn(I)/Zn(II) sites to form dimeric {*closo*-$[Zn_2Sn_8]$}$_2$ moieties centering around a Zn-Zn bond.

A *quasi-closo*-type structure has been discovered in a rare example of a 7-atom p-block-d-block Zintl anion, $[Pb_5\{Mo(CO)_3\}_2]^{4-}$ (Fig. 13k) [315]. As is shown in Fig. 13k, *cyclo*-Pb_5^{4-} acts as an η^5-ligand to two neutral $\{Mo(CO)_3\}$ fragments in a sandwich-type manner. According to Wade-Mingos rules, the structure is based on a cage with SEN = 16 = 5·4 (VE Pb) + 2·12 {VE $Mo(CO)_3$} + 4 (charge) – 5·2 (*exo*-e^- Pb) – 2·12 (*exo*-e^- $\{Mo(CO)_3\}$) = 48 – 34 = 14, which differs from the expected number of $2\cdot(n + m) + 2 = 16$ skeleton electrons to bind a 7-vertex *closo*-type polyhedron. However, if the $\{Pb_5\}$ ring is alternatively treated as a π-antiaromatic Pb_5^{4-} ligand coordinating the neutral $\{Mo(CO)_3\}$ fragments to form $[Pb_5\{Mo(CO)_3\}_2]^{4-}$, the cyclic anion can be regarded as an analog to 4π-antiaromatic cyclobutadiene in the half-sandwich complex $[(C_4H_4)Fe(CO)_3]$. A third interpretation considers the five-ring as a 6π-aromatic Pb_5^{6-}, assuming that it receives two electrons from the $\{Mo(CO_3\}$ units; indeed, DFT calculations indicate a considerable diatropic ring current to occur in Pb_5^{6-} as a hint toward aromaticity [319]. The general accessibility of a series of $[\eta^4\text{-}Tt_5M(CO)_3]^{4-}$ (Tt = Sn, Pb; M = Cr, Mo, W) with this structure type has also been proposed through DFT calculations [316].

The first example of a face-fused 9-atom anion was reported with $[Sn_{14}Ni(CO)]^{4-}$ (Fig. 13l) [317]. Formally, two *nido*-$[Sn_8Ni(CO)]^{6-}$ clusters exhibiting identical, elongated, tricapped trigonal prisms are oxidatively fused to share a triangular $\{Sn_2Ni\}$ face. With the {Ni(CO)} 12-electron fragment (ten electrons from the d^{10} atom and two electrons from the CO ligand), the required total number of 62 valence electrons is met for a face-fused $[Sn_{14}Ni(CO)]^{4-}$ cage; according to Wade-Mingos rules, the $(BH)^{2+}$-analogous {Ni(CO)} fragment again does not contribute to cluster bonding, as all electrons of the transition metal unit are considered as exo-electrons. Hence, each of the formally fused, underlying *nido*-type cages $\{Sn_8Ni(CO)\}^{6-}$possesses 8·4 (VE Sn) + 12 (VE {Ni(CO)}) + 6 (charge) – 8·2 (exo-e^- Sn) – 12 (exo-e^- {Ni(CO)}) = 22 = 2 $(n + m)$ + 4 skeletal electrons. An overview of known electron-deficient binary Tt-d-block (semi-)metal anions (without Hyp-substitution; cf. next section) is listed in Table 8.

4.2.2 Hyp-Substituted Tt-d-Block Anions

A group a Zintl clusters with lower or even no charge is represented by the series of cages with Hyp groups as substituents, which recently added a new branch to Zintl chemistry that is dealing with readily soluble Tt-based cluster species. Such compounds can be accessed from molecular building blocks [320] or from Zintl anions [321], which in the first step allowed for a rational synthesis of $(Ge_9Hyp_3)^-$ anions and subsequently for the generation and isolation of the first tetra-substituted – and thus neutral – cluster, $[Hyp_3Ge_9\{SnPh_3\}]$ (Fig. 14a) [322]. From this anion, a few heterometallic Tt-d-block cages were derived that follow Wade-Mingos rules. The first examples were $[Hyp_3Ge_9M(CO)_3]^-$ (M = Cr, Mo, W; Fig. 14b) [326–327] and $[Hyp_3EtGe_9Pd(PPh_3)]$ (Fig. 14c) [323], followed by $[Hyp_3EtGe_9M(PPh_3)]$ (M = Ni,

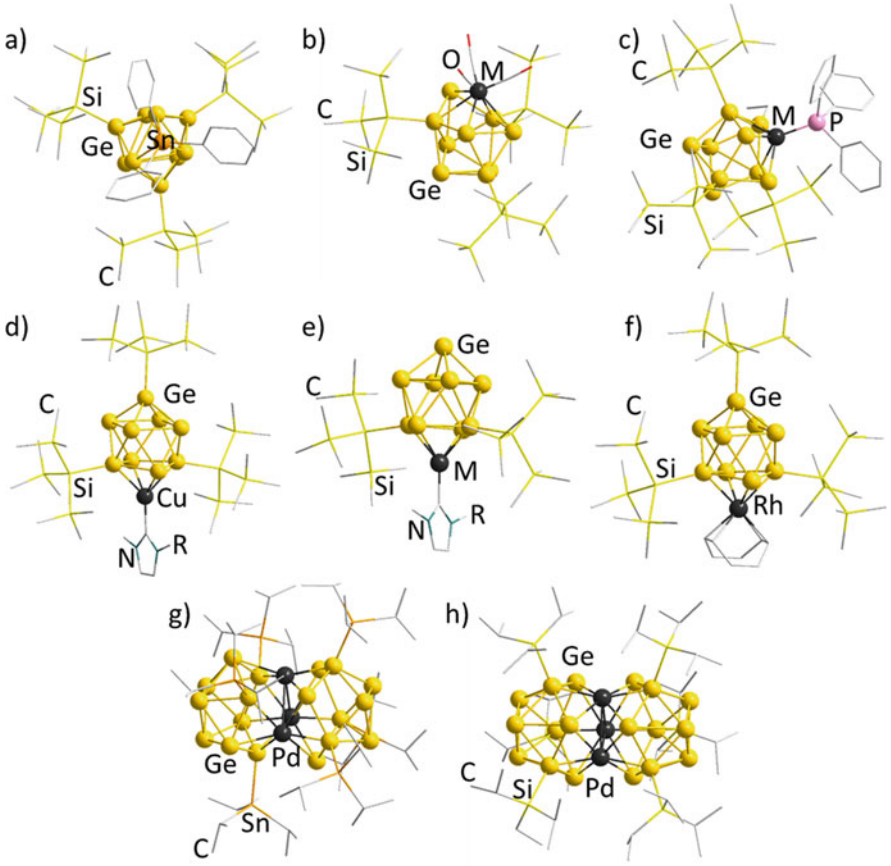

Fig. 14 Structures of all known Hyp-, $^{i}Pr_3Si$- or $^{i}Pr_3Si$-substituted electron-deficient binary Tt-d-block (semi-)metal anions: (**a**) $[Hyp_3Ge_9\{SnPh_3\}]$, (**b**) $[Hyp_3Ge_9M(CO)_3]^-$ (M = Cr, Mo, W), (**c**) $[Hyp_3EtGe_9M(PPh_3)]$ (M = Ni, Pd, Pt), (**d**) $[NHC^{i}PrCu(\eta^4\text{-}Ge_9Hyp_3)]$, (**e**) $[NHC^{R}M(\eta^4\text{-}Ge_9Hyp_2)]^-$ (M = Cu; R = ^{i}Pr, Mes, Dipp or M = Ag/Au; R = Dipp), (**f**) $[\eta^4\text{-}Ge_9(Hyp)_3Rh(cod)]$, (**g**) $[Ge_{18}Pd_3(Sn^{i}Pr_3)_6]^{2-}$, (**h**) $[Ge_{18}Pd_3\{Si^{i}Pr_3\}_6]^{2-}$. H atoms are omitted for clarity

Pt; Fig. 14c) [324], $[NHC^{iPr}Cu(\eta^4\text{-}Ge_9Hyp_3)]$ and $[NHC^{R}M(\eta^4\text{-}Ge_9Hyp_2)]^-$ ((NHC = N-heterocyclic carbene; M = Cu, R = ^{i}Pr, Mes, Dipp; M = Ag/Au, R = Dipp; Dipp = 2,6-diisopropylphenyl; Fig. 14d, e) [325] later on. These clusters can be treated as *closo*-deltahedra based on $\{Ge_9M\}$ cores that are functionalized in different ways with organic groups. Notably, an alkane-soluble Zintl cluster of this type, *closo*-$[\{\eta^4\text{-}Ge_9(Hyp)_3\}Rh(cod)]$ (Fig. 14f), was recently reported as the first example of a well-defined Zintl cluster to be used in homogeneous catalysis for the hydrogenation of cyclic alkenes, such as 1,5-cyclooctadiene and *cis*-cyclooctene [326].

Analogous clusters with Tt = Sn were synthesized by reactions of acetonitrile suspensions of K_4Ge_9 with $^{i}Pr_3SnCl$ or HypCl, producing tristannylated or

Table 9 Overview of known Hyp-substituted electron-deficient binary Tt-d-block (semi-)metal anions

Formula	Parent compound	Type	Ref.	Figure no.
$[Hyp_3Ge_9\{SnPh_3\}]$	$[Hyp_3Ge_9\{SnPh_3\}]$	*closo*	[320]	14a
$[Hyp_3Ge_9M(CO)_3]^-$ M = Cr, Mo, W	$[Li(thf)_4][Hyp_3Ge_9M(CO)_3]$	*closo*	[328, 329]	14b
$[\eta^4\text{-}Ge_9(Hyp)_3Rh(cod)]$	$[\eta^4\text{-}Ge_9(Hyp)_3Rh(cod)]$	*closo*	[326]	14f
$[NHC^iPrCu(\eta^4\text{-}Ge_9Hyp_3)]$	$[NHC^iPrCu(\eta^4\text{-}Ge_9Hyp_3)]$	*closo* unit	[324]	14d
$[NHC^RM(\eta^4\text{-}Ge_9Hyp_2)]^-$ M = Cu, R = *i*Pr, Mes, Dipp M = Ag/Au, R = Dipp	$[K(crypt\text{-}222)][NHC^RM(\eta^4\text{-}Ge_9Hyp_2)]$	*closo* unit	[325]	14e
$[Hyp_3EtGe_9M(PPh_3)]$ M = Pd, Ni, Pt	$[Hyp_3EtGe_9M(PPh_3)]$	*closo*	[323, 324]	14c
$[Ge_{18}Pd_3\{Si^iPr_3\}_6]^{2-}$	$[K(crypt\text{-}222)]_2[Ge_{18}Pd_3\{Si^iPr_3\}_6]\cdot 2thf$	*hypho* unit	[330]	14h
$[Ge_{18}Pd_3(Sn^iPr_3)_6]^{2-}$	$[K(crypt\text{-}222)]_2[Ge_{18}Pd_3\{Sn^iPr_3\}_6]\cdot {}^iPr_2O$	*hypho* unit	[331]	14g

trisilylated 9-atom clusters $[Ge_9\{Sn^iPr_3\}_3]^-$ or $[Ge_9Hyp_3]^-$, respectively, in a first step. Subsequent addition of $[Pd(PPh_3)_4]$ to the reaction mixtures yielded $[Ge_{18}Pd_3\{Sn^iPr_3\}_6]^{2-}$ or $[Ge_{18}Pd_3\{Si^iPr_3\}_6]^{2-}$ (Fig. 14g, h) [330–331], respectively. Either of these two anions can be viewed as dimers of face-fused icosahedra ("twinned icosahedra") sharing a triangular Pd_3-face, which resembles (but is not isoelectronic with) the known borate $[B_{21}H_{18}]^-$ [327]. Each of the two $[Ge_9\{Sn^iPr_3\}_3]^-/[Ge_9Hyp_3]^-$ units, thus lacking the Pd_3 triangle, can topologically be derived from a (hypothetical) icosahedral Ge_{12}^{2-} anion by cutting three Ge atoms, thus resulting in *hypho*-$[Ge_9\{Sn^iPr_3\}_3]^-/[Ge_9Hyp_3]^-$. Interestingly, the two highly related binary $\{Ge_{18}Pd_3\}$ clusters show a different situation regarding their substitution patterns: the staggered positions of the $^iPr_3Sn$ ligands in $[Ge_{18}Pd_3\{Sn^iPr_3\}_6]^{2-}$ is attributed to the known mobility of Sn-based ligands on the surface of Ge_9 clusters, while the positions of the Hyp ligands in the other cluster cousin remain eclipsed. An overview of known Hyp-substituted electron-deficient binary Tt-d-block (semi-)metal anions is provided in Table 9.

4.2.3 Pn-d-Block Anions

The relatively strong P-P and As-As bonding in P_7^{3-} and As_7^{3-} and their relative electron-rich character generally inhibits the formation of heterometallic P-based or As-based Zintl anions from such anions that follow Wade-Mingos rules. In contrast, this has been observed for the heavier homologs comprising Sb and Bi atoms. A

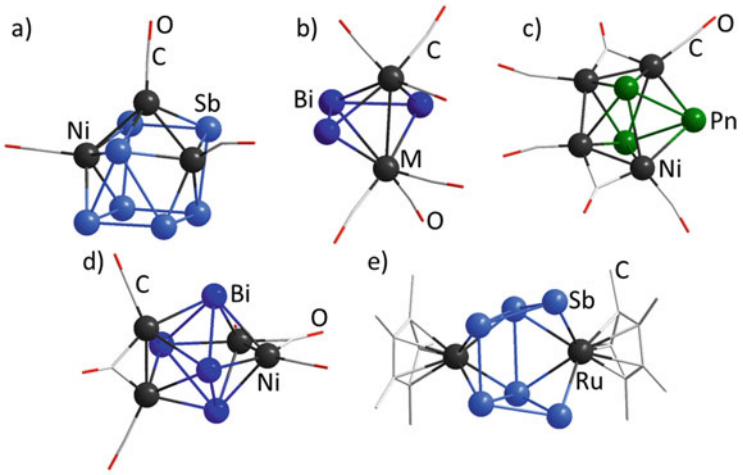

Fig. 15 Structures of all known electron-deficient binary Pn-d-block (semi-)metal anions: (**a**) $[Sb_7Ni_3(CO)_3]^{3-}$, (**b**) $[Bi_3M_2(CO)_6]^{3-}$ (M = Cr, Mo), (**c**) $[Pn_3Ni_4(CO)_6]^{3-}$ (Pn = Sb, Bi), (**d**) $[Bi_4Ni_4(CO)_6]^{2-}$, (**e**) $[Sb_6(RuCp^*)_2]^{2-}$. H atoms are omitted for clarity

reaction of K_3Sb_7 with $[Ni(CO)_2(PPh_3)_2]$ in en/crypt-222 afforded *nido*-$[Sb_7Ni_3(CO)_3]^{3-}$ (Fig. 15a), which can be derived from a rare 11-vertex deltahedron by removal of one vertex under formation of a square face [332]. Furthermore, dissolving of K_5Bi_4 in polar solvents like en causes fragmentation and rearrangement of the Bi_x substructure comprised in the binary solid into smaller or larger oligomers Bi_n^{n-}, such as Bi_{2n}^{-}, Bi_3^{n-}, Bi_4^{n-}, and Bi_5^{n-}. These (potentially co-existing) units remarkably broadened the spectrum of binary p-block-d-block Zintl anions to be obtained through coordination of transition metal complex fragments. Isolated products from these reactions were *closo*-$[Bi_3M_2(CO)_6]^{3-}$ (M = Cr, Mo; Fig. 15b), *closo*-$[Bi_3Ni_4(CO)_6]^{3-}$ (Fig. 15c) and an isostructural *closo*-$[Sb_3Ni_4(CO)_6]^{3-}$ (Fig. 15c), as well as *closo*-$[Bi_4Ni_4(CO)_6]^{2-}$ (Fig. 15d) [332–333]. Here, we use *closo*-$[Bi_3Ni_4(CO)_6]^{3-}$ for demonstrating that they follow the Wade-Mingos rules. The structure of the 7-atom cluster core is similar to that of *closo*-$(Tl_4Bi_3)^{3-}$ [259] and $[Pb_5\{Mo(CO)_3\}_2]^{4-}$ [315], hence constructed from a $\{BiNi_4\}$ pentagon that is bicapped by two Bi atoms. The *closo*-type cage of $[Bi_3Ni_4(CO)_6]^{3-}$ contains a total number of 70 cluster valence electrons (VEN = 3·5 (VE Bi) + 4·10 (VE Ni) + 6·2 (donor-e$^-$ CO) + 3 (charge) = 70), and consequently possesses a skeleton electron number of 16 (SEN = 70 – 3·2 (exo-e$^-$ Bi) – 4·12 (exo-e$^-$ Ni) = 16), which matches the SEN required for a 7-atom *closo*-cluster, 2·(n + m) + 2 = 16. Similar to the *cyclo*-Sn_6^{12-} unit described in Sect. 4.1.2, a six-membered ring of group 15 atoms, *cyclo*-Sb_6, was found to coordinate $\{RuCp^*\}$ fragments in the heterometallic *arachno*-type cluster $[Sb_6(RuCp^*)_2]^{2-}$ (Fig. 15e) [264], mentioned briefly in Sect. 3.2. There are different ways of describing the comparably unsymmetrical structure of $[Sb_6(RuCp^*)_2]^{2-}$; the most plausible one derives the 8-vertex cluster from a monocapped square anti-prismatic (hence,

Table 10 Overview of known electron-deficient binary Pn-d-block (semi-)metal anions

Formula	Parent compound	Type	Ref.	Figure no.
$[Sb_7Ni_3(CO)_3]^{3-}$	$[K(crypt\text{-}222)]_3[Sb_7Ni_3(CO)_3]\cdot 2en$	*nido*	[332]	15a
$[Sb_3Ni_4(CO)_6]^{3-}$	$[K(crypt\text{-}222)]_3[Sb_3Ni_4(CO)_6]\cdot en\cdot tol$	*closo*	[333]	15c
$[Sb_6(RuCp^*)_2]^{2-}$	$[K(crypt\text{-}222)]_3[Sb_6(RuCp^*)_2]\cdot 2tol$	*arachno*	[264]	15e
$[Bi_3M_2(CO)_6]^{3-}$ M = Cr, Mo	$K[K(crypt\text{-}222)]_3[Bi_3M_2(CO)_6]_2\cdot 3en$	*closo*	[333]	15b
$[Bi_3Ni_4(CO)_6]^{3-}$	$[K(crypt\text{-}222)]_3[Bi_3Ni_4(CO)_6]\cdot en\cdot tol$	*closo*	[334]	15c
$[Bi_4Ni_4(CO)_6]^{2-}$	$[K(crypt\text{-}222)]_2[Bi_4Ni_4(CO)_6]\cdot 0.5tol$	*closo*	[334]	15d

nido-type) polyhedron that is missing one atom in the uncapped square face. Indeed, with SEN = 6·5 (VE Sb) + 2·13 (VE {RuCp*}) + 2 (charge) – 6·2 (exo-e^- Sb) – 2·12 (exo-e^- {RuCp*}) = 22 = 2·(n + m) + 6, the electron count is in agreement with its interpretation as an *arachno*-type cluster according to Wade-Mingos rules. An overview of known electron-deficient binary Pn-d-block (semi-)metal anions is given in Table 10.

4.2.4 Ternary Analogs and Special Cases

Interactions of Zintl anionic cages with d-block metal complex fragments in most cases result in the formation of electron-precise architectures, such as observed upon coordination of two As_7^{3-} units to a Hg_2^{2+} dumbbell in $[Hg_2(\eta^2\text{-}As_7)_2]^{4-}$ [286], or in the formation of electron-deficient clusters like the aforementioned *closo*-$[(\eta^4\text{-}Tt_9)(ZnPh)]^{3-}$ anion [310]. The electron-richer group 15 atoms tend to form electron-precise cages, while group 14 atoms, exhibiting the same electron count as a {B-H} unit, most often arrange themselves in borane-related deltahedral cages to overcome their electron-deficiency. Some exceptions from this very general assignment have been mentioned above, some more will be given below. However, upon transferring this concept from binary to ternary systems including atoms of different main groups, it can generally not be predicted, which of the two intrinsic demands would be dominating the course of the cluster formation reactions. Here, the transition metal atoms, ions, or complex fragments play an important role, as to whether they would rather give extra electrons to the main group skeleton, or whether they would withdraw electrons from the latter to themselves.

The Sn/Sb system, for example, formed an electron-precise anion, $[Sn_2Sb_5(ZnPh)_2]^{3-}$, in combination with $(ZnPh)^+$ units, (Fig. 16a) [212]. The anion's {Sn_2Sb_5} core can be rationalized by means of the Zintl-Klemm concept, by formally replacing two Sb(0) atoms in Sb_7^{3-} with two Sn^- atom, thus resulting in a formally $(Sn_2Sb_5)^{5-}$ anion overall. Coordination of two $(ZnPh)^+$ fragments in a η^2:η^2-fashion through the lone pairs of two of the two-bonded Sb atoms defines the entire anion. The homologous $[Sn_2Bi_5(ZnPh)_2]^{3-}$ has been theoretically predicted [335], but has not been isolated to date.

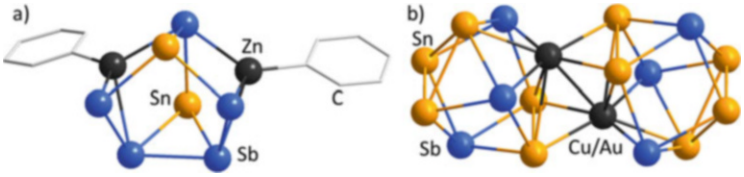

Fig. 16 Structures of ternary electron-precise or electron-deficient p-block-d-block (semi-)metal anions: (**a**) $[Sn_2Sb_5(ZnPh)_2]^{3-}$, (**b**) $[(Sn_5Sb_3M)_2]^{4-}$ (M = Cu, Au). H atoms are omitted for clarity

However, the same elemental combination can also take a different path. For instance, ternary 9-vertex cages form dimers in the aforementioned clusters $[(Sn_5Sb_3M)_2]^{4-}$ (M = Cu, Au) (Fig. 16b) [189, 190], with three-center bonding between the monomeric "$(Sn_5Sb_3M)^{2-}$" units according to DFT calculations. These monomeric units are related to the homoatomic Sn_9^{4-} parent clusters, yet comprise (5·4 + 3·5 + 1·1 + 2) = 38 valence electrons only, which would make them *closo*-type cages like the Sn_9^{2-} anion. However, as the Cu^+ ion has no exo-electrons (besides the d electrons that were ignored in this sum for easier comparison with the $\{Sn_9\}$ cases), the SEN is 22, like in Sn_9^{4-}. Indeed, an interpretation according to Wade-Mingos rules is difficult here – in accordance with the observation that structure is neither "*closo*-like" nor "*nido*-like," and in agreement with the dimerization that needs to be additionally taken into consideration.

These two results serve to illustrate that binary units of different p-block element (semi-)metal atoms bear an even higher flexibility, relative to homoatomic systems, for adjusting both the cluster structures and the coordination environment to match the requirements of the d-block or f-block metal atoms or complex fragments.

As exemplified above, beside the large number of either electron-precise or Wade-Mingos-type p-block-d-block Zintl anions, there are also several cases, to which none of the classical concepts apply. Another, yet binary, example was observed with the anion $[TiCp(\eta^4\text{-}Sn_8)]^{3-}$ (Fig. 17a) [336]. It is based on a 9-atom $\{TiSn_8\}$ metal atom core, which comprises a total VEN of 44, which according to Eq. (1) in Sect. 2.2 would result in an SEN = 16, thus, in no correlation with any electron-counting rule. However, a combination of the information that a) the $\{TiSn_8\}$ core can be regarded as a derivative of icosahedral Sn_{12}^{2-}, b) the replacement of one Cp ligand of the underlying $\{TiCp_2\}$ moiety with an $\{Sn_8\}$ fragment would actually result in a complex of the type $[TiCp(\eta^4\text{-}Sn_8)]^{3-}$, and c) the release of all organic ligands in other reports resulted in endohedral clusters like $[Ir@Sn_{12}]^{2-}$ [307] served to suggest that $[TiCp(\eta^4\text{-}Sn_8)]^{3-}$ should be regarded as an intermediate on the way toward larger endohedral clusters.

As an SEN of 22 is expected for a *closo*-type 10-vertex anion, the cluster $[Ge_8Mo_2(CO)_6]^{4-}$ (Fig. 17b) [337] is lacking two electrons. DFT calculations indicated this arrangement to be highly unstable, hence its observation is surprising. Further 10-vertex "hybrids" of the general composition $[Bi_7M_3(CO)_3]^{2-}$ (M = Co, Rh; Fig. 17c) [338] represent unusual adducts of Bi_7^{3-}, as compared to $[(Bi_7)Cd(Bi_7)]^{4-}$ [289]. In these clusters, the VEN of 70 again mismatches the number

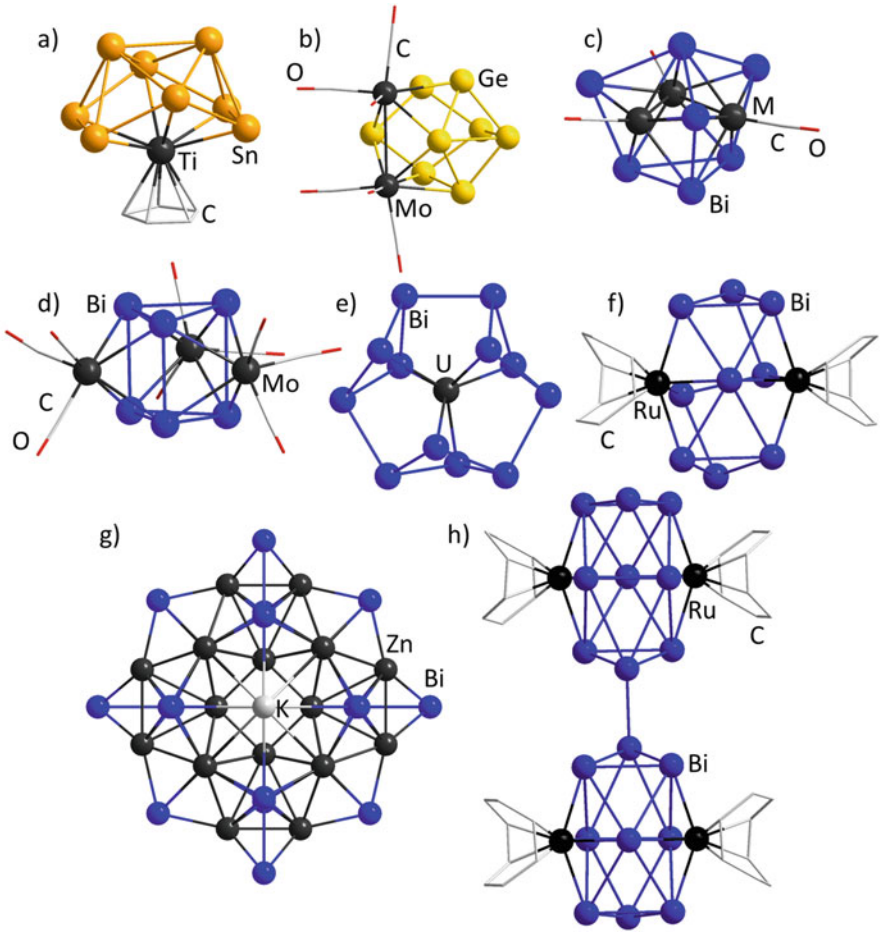

Fig. 17 Structures of binary p-block-d-block (semi-)metal anions that do not accord with any of the classical concepts of correlating the electron count with the structure: (**a**) $[Ti(\eta^4\text{-}Sn_8)Cp]^{3-}$, (**b**) $[Ge_8(Mo(CO)_3)_2]^{4-}$, (**c**) $[Bi_7M_3(CO)_3]^{2-}$ (M = Co, Rh), (**d**) $[Bi_6Mo_3(CO)_9]^{4-}$, (**e**) $[U@Bi_{12}]^{3-}$, (**f**) $[\{Ru(cod)\}_2Bi_9]^{3-}$, (**g**) $[K_2Zn_{20}Bi_{16}]^{6-}$, (**h**) $[\{Ru(cod)\}_4Bi_{18}]^{4-}$. H atoms are omitted for clarity

required for a *closo*-type anion by a 2-electron deficiency. An adduct of a distorted $\{Bi_6\}$ triangular prism was found in $[Bi_6Mo_3(CO)_9]^{4-}$ (Fig. 17d) [339]. The VEN of the underlying Bi_6^{4-} units amounts to 5·6 (VE Bi) + 4 (charge) = 34; as a consequence, the entire 9-atom anion $[Bi_6Mo_3(CO)_9]^{4-}$ comprising the same electron count (as the 12 electrons of each of the $\{Mo(CO)_3\}$ units are exo-electrons) represents neither a *closo*-type nor a *nido*-type cluster, which required 38 or 40 electrons, respectively. These examples illustrate the notably higher flexibility of metal clusters toward deviation from "ideal" electron counts in comparison with corresponding compounds of non-metal atoms, such as boranes. This intrinsic

Table 11 Overview of binary or ternary p-block-d-block (semi-)metal anions that do not accord with any of the classical concepts of correlating the electron count with the structure

Formula	Parent compound	Ref.	Figure no.
$[Ti(\eta^4\text{-}Sn_8)Cp]^{3-}$	$[K([18]crown\text{-}6)]_2(\eta^5{:}\eta^5\text{-}Cp)]_4[K([18]crown\text{-}6)(NH_3)_2][TiCp_2(NH_3)_2][TiCp_2(\eta^1\text{-}Sn_9)(NH_3)]\text{-}[Sn_8TiCp](NH_3)_{63}$	[336]	17a
$[Ge_8(Mo(CO)_3)_2]^{4-}$	$K[K(18\text{-}crown\text{-}6)]_3[Ge_8(Mo(CO)_3)_2]\cdot en$	[337]	17b
$[Bi_7M_3(CO)_3]^{2-}$ (M = Co, Rh)	$[K(crypt\text{-}222)]_2[Bi_7M_3(CO)_3]\cdot 1tol$	[338]	17c
$[Bi_6Mo_3(CO)_9]^{4-}$	$[K(crypt\text{-}222)]_4[Bi_6Mo_3(CO)_9]$	[339]	17d
$[U@Bi_{12}]^{3-}$	$[K(crypt\text{-}222)]_3[U@Bi_{12}]\cdot tol\cdot 1.5en$	[340]	17e
$[Th@Bi_{12}]^{4-}$	$[K(crypt\text{-}222)]_4[Th@Bi_{12}]\cdot 2en$	[319]	–
$[K_2Zn_{20}Bi_{16}]^{6-}$	$[K(crypt\text{-}222)]_6[K_2Zn_{20}Bi_{16}]$	[341]	17g
$[\{Ru(cod)\}_2Bi_9]^{3-}$	$[K(crypt\text{-}222)]_3[Bi_9\{Ru(cod)\}_2]\cdot 1.5\,en$	[210]	17f
$[\{Ru(cod)\}_4Bi_{18}]^{4-}$	$[K(crypt\text{-}222)]_4[\{Ru(cod)\}_4Bi_{18}]_2(\cdot 4.63thf\cdot 2en)$	[232]	17h

property needs to be taken into account whenever discussing the clusters in terms of the classical concepts.

As mentioned above, $(GaBi_3)^{2-}$ and $(TlBi_3)^{2-}$ have a distinct tendency to release elemental Tr(0) (Tr = Ga, Tl) during heterometallic cluster formation. This property was also used to synthesize several binary anions comprising polybismuthide units, such as $[U@Bi_{12}]^{3-}$ with a formally $\{Bi_{12}\}^{8-}$ unit surrounding a U^{5+} cation [340] (Fig. 17e), or $[\{Ru(cod)\}_2Bi_9]^{3-}$ (Fig. 17f), in which localized and delocalized bonding coexist, thus again placing the anion with its unique structure in between an electron-precise and an electron-deficient cluster [210]. As the $[K(crypt\text{-}222)]^+$ salts of $(GaBi_3)^{2-}$ and $(TlBi_3)^{2-}$ have a limited reactivity, another synthetic approach was chosen for cases that require an even higher reductive power. Here, the ternary solid with the formal composition "$K_5Ga_2Bi_4$", which actually serves as a source of $[K(crypt\text{-}222)]_2(GaBi_3)$, was applied directly. With "$K_5Ga_2Bi_4$", it was possible to reduce $ZnPh_2$ and form the heterometallic mixed-valence cluster $[K_2Zn_{20}Bi_{16}]^{6-}$ (Fig. 17g) [341]. A low-valent $\{Zn_{12}\}$ core, constructed from four corner-sharing $\{Zn_4\}$ tetrahedra, is embedded within a 24-membered $\{Zn_8Bi_{16}\}$ unit, with a high degree of electron delocalization. From a topological point of view (and considering a similar VEN), the surrounding unit additionally shows a close relationship to the organic, aromatic macrocycle porphine, yet – owing to its much larger size – it embeds a 12-a.u. instead of a single ion, while additionally coordinating two K^+ cations above and below the molecular "disc." Notably, the cluster also exhibits weak aromaticity according to DFT calculations, hence does not accord with any known model for the description of binary (semi-)metal anions to date. The "$K_5Ga_2Bi_4$" solid also served to access several further anions that will not be detailed here, among them the endohedral cluster $[Bi@Ga_8(Bi_2)_6]^{3-}$ [232], the $[Th@Bi_{12}]^{4-}$ analog of $[U@Bi_{12}]^{3-}$ mentioned above, exhibiting the largest

reported ring current per electron of a π-aromatic molecule described so far [319, 340], and a dimer of the $[\{Ru(cod)\}_2Bi_9]^{3-}$ anion, $[\{Ru(cod)\}_4Bi_{18}]^{4-}$, which includes the largest number of all-connected Bi atoms within a molecule published to date (Fig. 17h) [232]. An overview of binary or ternary p-block-d-block (semi-)metal anions that do not accord with any of the classical concepts of correlating the electron count with the structure is given in Table 11.

5 Summary, Outlook, and Concluding Remarks

In this chapter, we provided an overview of binary (semi-)metal anions and some selected ternary examples. We indicated their close similarity to anionic or neutral non-metal compounds, where models have been developed to rationalize their structures based on bonding schemes which related the structures to the total number of valence electrons. We also have shown that (semi-)metal cages can deviate from these precise correlations because of their much higher tendency to incorporate a certain degree of electron deficiency. Nevertheless, it is indeed remarkable how many of the presented examples actually follow the rules that were originally set up for "normal" valence compounds of the mostly non-metallic electron-rich p-block elements or for boranes.

The interesting "hybrid" structures and electronic situation of the anions surveyed in this chapter make them exciting objects for fundamental research. However, beyond that, they are gaining more and more attention also in regard of their potential in various fields. One of the current research activities aims at exploring the catalytic activity of the molecular anions or extended materials obtained from them. It is very probable that such monodisperse, mostly unprotected (semi-)metal nano-architectures activate even relatively strong bonds, although their selectivity remains a challenge. Moreover, the heteroatomic nature of the cluster enables fine-tuning of the electronic and geometric structures, which makes such binary anions interesting candidates for tailor-made intermetallic phases. Overall, a thorough understanding of the properties will serve to predict the behavior of the anions in all regards, which can ultimately lead to a knowledge-based design of nanostructured multi-(semi-)metal materials.

References

1. Joannis A, Hebd CR (1891) Seances Acad Sci 113:795–799
2. Kraus CA (1924) Trans Am Electrochem Soc 45:175–186
3. Zintl E, Goubeau J, Dullenkopf W (1931) Z Phys Chem A 154:1–46
4. Scharfe S, Kraus F, Stegmaier S, Schier A, Fässler TF (2011) Angew Chem Int Ed 50:3630–3670
5. Mayer K, Weßing J, Fässler TF, Fischer RA (2018) Angew Chem Int Ed 57:14372–14393
6. Fässler TF (2001) Coord Chem Rev 215:347–377

7. González-Gallardo S, Bollermann T, Fischer RA, Murugavel R (2012) Chem Rev 112:3136–3170
8. González-Gallardo S, Prabusankar G, Cadenbach T, Gemel C, von Hopffgarten M, Frenking G, Fischer RA (2010) Struct Bond 136:147–188
9. Turbervill RSP, Goicoechea JM (2014) Chem Rev 114:10807–10828
10. Sevov SC, Goicoechea JM (2006) Organometallics 25:678–5692
11. Wilson RJ, Lichtenberger N, Weinert B, Dehnen S (2019) Chem Rev 119:8506–8554
12. Peters B, Lichtenberger N, Dornsiepen E, Dehnen S (2020) Chem Sci 11:16–26
13. Weinert B, Mitzinger S, Dehnen S (2018) Chem Eur J 24:8470–8490
14. Wilson RJ, Weinert B, Dehnen S (2018) Dalton Trans 47:14861–14869
15. Weinert B, Dehnen S (2017) Struct Bond 174:99–134
16. Zhao J, Du Q, Zhou S, Kumar V (2020) Chem Rev 120:9021–9163
17. Wang Y, McGrady JE, Sun Z-M (2021) Acc Chem Res 54:1506–1516
18. Liu C, Sun Z-M (2019) Coord Chem Rev 382:32–56
19. Guloy AM, Ramlau R, Tang Z, Schnelle W, Baitinger M, Grin Y (2006) Nature 443:320–323
20. Bentlohner MM, Waibel M, Zeller P, Sarkar K, Müller-Buschbaum P, Fattakhova-Rohlfing D, Fässler TF (2016) Angew Chem Int Ed 55:2441–2445
21. Geier S, Jung R, Peters K, Gasteiger HA, Fattakhova-Rohlfing D, Fässler TF (2018) Sustain Energy Fuels 2:85–90
22. Laves F (1941) Naturwissenschaften 29:244–255
23. Kummer D, Diehl L (1970) Angew Chem Int Ed Engl 9:895–895
24. Corbett D, Adolphson DG, Merryman DJ, Edwards PA, Armatis FJ (1975) J Am Chem Soc 97:6267–6268
25. Klemm W (1958) P Chem Soc:329–364
26. Busmann E (1961) Z Anorg Allg Chem 313:90–106
27. Wade K (1971) J Chem Soc D 0:792–793
28. Wade K (1976) Adv Inorg Chem Radiochem 18:1–66
29. Mingos DMP (1984) Acc Chem Res 17:311–319
30. Mingos DMP, Johnston RL (1987) Struct Bond 68:29–87
31. Lin Z, Slee T, Mingos DMP (1990) Chem Phys 142:321–334
32. Mingos DMP, Slee T, Zhenyang L (1990) Chem Rev 90:383–402
33. Corbett JD, Edwards PA (1975) J Chem Soc Chem Commun:984–985
34. Eisenmannm B, Janzon KH, Schafer H, Weiss A (1969) Z Naturforsch B 24:457–458
35. Otani S (1998) J Crystal Growth 192:346–349
36. Sevov SC, Corbett JD (1993) J Solid State Chem 103:114–130
37. Dong ZC, Corbett JD (1996) Inorg Chem 35:3107–3112
38. Cordier G, Ludwig M, Stahl D, Schmidt P, Kniep R (1995) Angew Chem Int Ed Engl 34:1761–1763
39. Schlechte A, Prots Y, Niewa R (2004) Z Kristallogr NCS 219:349–350
40. Dong ZC, Corbett JD (1994) J Am Chem Soc 116:3429–3435
41. Zhao JT, Corbett JD (1995) Inorg Chem 34:378–383
42. Saltykov V, Nuss J, Wedig U, Prasad DLVK, Jansen M (2011) Z Anorg Allg Chem 637:834–839
43. Dong ZC, Corbett JD (1993) J Am Chem Soc 115:11299–11303
44. Dong ZC, Corbett JD (1996) Inorg Chem 35:2301–2306
45. Liu Q, Hoffmann R, Corbett JD (1994) J Phys Chem 98:9360–9364
46. Henning RW, Leon-Escamilla EA, Zhao JT, Corbett JD (1997) Inorg Chem 36:1282–1285
47. Dong ZC, Corbett JD (1996) Angew Chem Int Ed 35:1006–1009
48. Blase W, Cordier G, Corbett JD (1990) Z Kristallogr 193:319–320
49. Kaskel S, Corbett JD (2000) Inorg Chem 39:778–782
50. Henning RW, Corbett JD (1997) Inorg Chem 36:6045–6049
51. Blase W, Cordier G (1991) Z Kristallogr 194:150–151
52. Sevov SC, Corbett JD (1991) Inorg Chem 30:4875–4877

53. Blase W, Cordier G, Müller V, Häußermann U, Nesper R (1993) Z Naturforsch B 48b:754–760
54. Dong ZC, Corbett JD (1995) J Clust Sci 6:187–201
55. Dong ZC, Corbett JD (1996) Inorg Chem 35:1444–1450
56. Dong ZC, Corbett JD (1995) Inorg Chem 34:5042–5048
57. Fässler TF, Kronseder C (1997) Angew Chem Int Ed Engl 36:2683–2686
58. Witte J, von Schnering HG, Klemm W (1964) Z Anorg Allg Chem 327:260–273
59. Goebel T, Prots Y, Haarmann F (2008) Z Kristallogr NCS 223:187–187
60. von Schnering HG, Schwarz M, Chang JH, Peters K, Peters EM et al (2005) Z Kristallogr NCS 220:525–527
61. Hoch C, Wendorff M, Röhr C (2003) J Alloys Compd 361:206–221
62. Queneau V, Todorov E, Sevov SC (1998) J Am Chem Soc 120:3263–3264
63. von Schnering HG, Schwarz M, Nesper R (1986) Angew Chem Int Ed 25:566–567
64. Janzon KH, Schäfer H, Weiss A (1970) Z Anorg Allg Chem 372:87–99
65. Eisenmann B, Riekel C, Schäfer H, Weiss A (1970) Z Anorg Allg Chem 372:325–331
66. von Schnering HG, Llanos J, Chang JH, Peters K, Peters EM et al (2005) Z Kristallogr NCS 220:324–326
67. Carrillo-Cabrera W, Cardoso Gil R, Somer M, Persil Ö, von Schnering HG (2003) Z Anorg Allg Chem 629:601–608
68. von Schnering HG, Baitinger M, Bolle U, Carrillo-Cabrera W, Curda J et al (1997) Z Anorg Allg Chem 623:1037–1039
69. Llanos J, Nesper R, von Schnering HG (1983) Angew Chem Int Ed 22:998
70. von Schnering HG, Llanos J, Grin Y, Carrillo-Cabrera W, Peters EM et al (1998) Z Kristallogr NCS 213:661
71. Betz A, Schäfer H, Weiss A, Wulf R (1968) Z Naturforsch B 23:878
72. Müller W, Volk K (1977) Z Naturforsch B 32:709–710
73. Grin Y, Baitinger M, Kniep R, von Schnering HG (1999) Z Kristallogr NCS 214:453–454
74. Hewaidy IF, Busmann E, Klemm W (1964) Z Anorg Allg Chem 328:283–293
75. Baitinger M, Grin Y, Kniep R, von Schnering HG (1999) Z Kristallogr NCS 214:457–458
76. Hoch C, Wendorff M, Röhr C (2003) Z Anorg Allg Chem 629:2391–2397
77. Marsh RE, Shoemaker DP (1953) Acta Cryst 6:197–205
78. Röhr C (1995) Z Naturforsch B 50:802–808
79. Baitinger M, Peters K, Somer M, Carrillo-Cabrera W, Grin Y et al (1999) Z Kristallogr NCS 214:455–456
80. Bobev S, Sevov SC (2002) Polyhedron 21:641–649
81. Ponou S, Fässler TF (2007) Z Anorg Allg Chem 633:393–397
82. Queneau V, Sevov SC (1997) Angew Chem Int Ed 36:1754–1756
83. Hoch C, Wendorff M, Röhr C (2002) Acta Cryst C 58:I45–I46
84. Queneau V, Sevov SC (1998) Inorg Chem 37:1358–1360
85. Todorov E, Sevov SC (1998) Inorg Chem 37:3889–3891
86. Wiesler K, Brandl K, Fleischmann A, Korber N (2009) Z Anorg Allg Chem 635:508–512
87. Joseph S, Suchentrunk C, Korber N (2010) Z Naturforsch B 65:1059–1065
88. Goicoechea JM, Sevov SC (2004) J Am Chem Soc 126:6860–6861
89. Campbell J, Schrobilgen GJ (1997) Inorg Chem 36:4078–4081
90. Suchentrunk C, Korber N (2006) New J Chem 30:1737–1739
91. Edwards PA, Corbett JD (1977) Inorg Chem 16:903–907
92. Somer M, Carrillo-Cabrera W, Peters EM, Peters K, Kaupp M, von Schnering HG (1999) Z Anorg Allg Chem 625:37–42
93. Joseph S, Suchenrunk C, Kraus F, Korber N (2009) Eur J Inorg Chem 2009:4641–4647
94. Suchentrunk C, Daniels J, Somer M, Carrillo-Cabrera W, Korber N (2005) Z Naturforsch B 60:277–283
95. Somer M, Carrillo-Cabrera W, Peters EM, Peters K, von Schnering HG (1998) Z Anorg Allg Chem 624:1915–1921

96. Carrillo-Cabrera W, Aydemir U, Somer M, Kircali A, Fässler TF, Hoffmann SD (2007) Z Anorg Allg Chem 633:1575–1580
97. Belin CHE, Corbett JD, Cisar A (1977) J Am Chem Soc 99:7163–7169
98. Downie C, Mao JG, Guloy AM (2001) Inorg Chem 40:4721–4725
99. Diehl L, Khodadadeh K, Kummer D, Strähle J (1976) Z Naturforsch B 31:522–524
100. Diehl L, Khodadadeh K, Kummer D, Strähle J (1976) Chem Ber 109:3404–3418
101. Korber N, Fleischmann A (2001) J Chem Soc Dalton Trans:383–385
102. Corbett JD, Edwards PA (1977) J Am Chem Soc 99:3313–3317
103. Hauptmann R, Fässler TF (2003) Z Kristollogr NCS 218:455–457
104. Burns RC, Corbett JD (1985) Inorg Chem 24:1489–1492
105. Fässler TF, Hoffmann R (1999) Angew Chem Int Ed 38:543–545
106. Benda CB, Waibel M, Köchner T, Fässler TF (2014) Chem Eur J 20:16738–16746
107. Hauptmann R, Fässler TF (2002) Z Anorg Allg Chem 628:1500–1504
108. Hauptmann R, Fässler TF (2003) Z Kristollogr NCS 218:458–460
109. Hauptmann R, Hoffmann R, Fässler TF (2001) Z Anorg Allg Chem 627:2220–2224
110. Yong L, Hoffmann SD, Fässler TF (2006) Inorg Chim Acta 359:4774–4778
111. Fässler TF, Hoffmann R (1999) J Chem Soc Dalton Trans:3339–3340
112. Campbell J, Dixon DA, Mercier HPA, Schrobilgen GJ (1995) Inorg Chem 34:5798–5809
113. Fässler TF, Hunziker M (1994) Inorg Chem 33:5380–5381
114. Fässler TF, Schütz U (1999) Inorg Chem 38:1866–1870
115. Hauptmann R, Fässler TF (2003) Z Kristallogr NCS 218:461–463
116. Angilella V, Belin C (1991) J Chem Soc Faraday Trans 87:203–204
117. Suchentrunk C, Korber N (2006) Inorg Chim Acta 359:267–272
118. Critchlow SC, Corbett JD (1983) J Am Chem Soc 105:5715–5716
119. Fässler TF, Hunziker M (1996) Z Anorg Allg Chem 622:837–844
120. Fässler TF, Hoffmann R (2000) Z Kristallogr NCS 215:139–142
121. Yong L, Hoffmann SD, Fässler TF (2005) Z Kristallogr NCS 220:49–52
122. Goicoechea JM, Sevov SC (2005) Inorg Chem 44:2654–2658
123. Åkerstedt J, Ponou S, Kloo L, Lidin S (2011) Eur J Inorg Chem 2011:3999–4005
124. Belin C, Mercier H, Angilella V (1991) New J Chem 15:931–938
125. Spiekermann A, Hoffmann SD, Fässler TF (2006) Angew Chem Int Ed 45:3459–3462
126. Gascoin F, Sevov SC (2000) J Am Chem Soc 122:10251–10252
127. von Schnering HG, Hartweg M, Hartweg U, Hönle W (1989) Angew Chem Int Ed 28:56–58
128. Gascoin F, Sevov SC (2001) Inorg Chem 40:5177–5181
129. Somer M, Hartweg M, Peters K, von Schnering HG (1991) Z Kristallogr NCS 195:103–104
130. von Schnering HG, Wittmann M, Sommer D (1984) Z Anorg Allg Chem 510:61
131. Deller K, Eisenmann B (1976) Z Naturforsch B 31:1023–1027
132. Deller K, Eisenmann B (1977) Z Naturforsch B 32:1368–1370
133. Emmerling F, Petri D, Röhr C (2004) Z Anorg Allg Chem 630:2490–2501
134. Abicht HP, Hönle W, von Schnering HG (1984) Z Anorg Allg Chem 519:7–23
135. von Schnering HG, Meyer T, Hönle W, Schmettow W, Hinze U et al (1987) Z Anorg Allg Chem 553:261–279
136. Schmettow W, Lipka A, von Schnering HG (1974) Angew Chem Int Ed Engl 13:345
137. Hönle W, Krogull G, Peters K, von Schnering HG (1999) Z Kristallogr NCS 214:17–18
138. Eisenmann B, Jordan H, Schafer H (1985) Z Naturforsch B 40:1603–1606
139. Manriquez V, Hönle W, von Schnering HG (1986) Z Anorg Allg Chem 539:95–109
140. Santandrea RP, Mensing C, von Schnering HG (1986) Thermochim Acta 98:301–311
141. Meyer T, Hönle W, von Schnering HG (1987) Z Anorg Allg Chem 552:69–80
142. Dahlmann W, von Schnering HG (1972) Naturwissenschaften 59:420
143. Hönle W, Buresch J, Peters K, Chang JH, von Schnering HG (2002) Z Kristallogr NCS 217:485–486
144. Hönle W, Buresch J, Peters K, Chang JH, von Schnering HG (2002) Z Kristallogr NCS 217:487–488

145. Emmerling F, Röhr C (2002) Z Naturforsch 57b:963–975
146. Hönle W, Buresch J, Wolf J, Peters K, Chang JH et al (2002) Z Kristallogr NCS 217:489–490
147. Derrien G, Tillard M, Manteghetti A, Belin C (2003) Z Anorg Allg Chem 629:1601–1609
148. Schmettow W, von Schnering HG (1977) Angew Chem Int Ed Engl 16:857
149. Dorn FW, Klemm W (1961) Z Anorg Allg Chem 309:189–203
150. Hirschle C, Röhr C (2000) Z Anorg Allg Chem 626:1992–1998
151. Wichelhaus W, von Schnering HG (1973) Naturwissenschaften 60:104
152. von Schnering HG, Somer M, Kliche G, Hönle W, Meyer T et al (1991) Z Anorg Allg Chem 601:13–30
153. Emmerling F, Röhr C (2003) Z Anorg Allg Chem 629:467–472
154. Hönle W, von Schnering HG, Schmidpeter A, Burget G (1984) Angew Chem Int Ed Engl 23:817–818
155. Korber N, Daniels J (1996) Helv Chim Acta 79:2083–2087
156. Kraus F, Korber N (2005) Chem Eur J 11:5945–5959
157. Korber N, Daniels J (1999) Z Anorg Allg Chem 625:189–191
158. Korber N, Daniels J (1996) J Chem Soc Dalton Trans:1653–1658
159. Korber N, Daniels J (1996) Acta Cryst C 52:2454–2457
160. Korber N, von Schnering HG (1996) Chem Ber 129:155–159
161. Kraus F, Hanauer T, Korber N (2006) Inorg Chem 45:1117–1123
162. Bashall A, Beswick MA, Choi N, Hopkins AD, Kidd SJ et al (2000) J Chem Soc Dalton Trans:479–486
163. Hanauer T, Grothe M, Reil M, Korber N (2005) Helv Chim Acta 88:950–961
164. Somer M, Hönle W, von Schnering HG (1989) Z Naturforsch B 44:296–306
165. Driess M, Merz K, Pritzkow H, Janoschek R (1996) Angew Chem Int Ed Engl 35:2507–2510
166. Hübler K, Becker G (1998) Z Anorg Allg Chem 624:483–496
167. Korber N, von Schnering HG (1997) Z Kristallogr NCS 212:85–86
168. Castleman AW, Khanna SN, Sen A, Reber AC, Qian M, Davis KM, Peppernick SJ, Ugrinov A, Merritt MD (2007) Nano Lett 7:2734–2741
169. Beswick MA, Choi N, Harmer CN, Hopkins AD, McPartlin M, Wright DS (1998) Science 281:1500–1501
170. Adolphson DG, Corbett JD, Merryman DJ (1976) J Am Chem Soc 98:7234–7239
171. Diehl L, Khodadadeh K, Kummer D, Strähle J (1976) Z Naturforsch 31b:522–524
172. Critchlow SC, Corbett JD (1984) Inorg Chem 23:770–774
173. Breunig HJ, Ghesner ME, Lork E (2005) Z Anorg Allg Chem 631:851–856
174. Mutzbauer F, Korber N (2011) Acta Cryst E 67:m1551
175. Perla LG, Oliver AG, Sevov SC (2015) Inorg Chem 54:872–875
176. Korber N, Daniels J, von Schnering HG (1996) Angew Chem Int Ed Engl 35:1107–1110
177. Knettel D, Reil M, Korber N (2001) Z Naturforsch 56b:965–969
178. Korber N, Daniels J (1996) Z Anorg Allg Chem 622:1833–1838
179. Korber N, Daniels J (1996) Polyhedron 15:2681–2688
180. Dai FR, Xu L (2007) Chin J Struct Chem 26:45
181. Hanauer T, Korber N (2006) Z Anorg Allg Chem 632:1135–1140
182. Bolle U, Tremel W (1992) J Chem Soc Chem Commun:91–93
183. Jun Z, Xu L (2011) Chin J Struct Chem 30:1091
184. García F, Less RJ, Naseri V, McPartlin M, Rawson JM, Tomas MS, Wright DS (2008) Chem Commun:859–861
185. Weinert B, Eulenstein AR, Ababei R, Dehnen S (2014) Angew Chem Int Ed 53:4704–4708
186. Seifried C, Longo L, Pollak P, Weigend F (2017) J Chem Phys 146:034304
187. Wilson RJ, Weigend F, Dehnen S (2020) Angew Chem Int Ed 59:14251–14255
188. Mitzinger S, Bandemehr J, Reiter K, McIndoe SJ, Xie X, Weigend F, Corrigan JF, Dehnen S (2018) Chem Commun 54:1421–1424
189. Pan F, Guggolz L, Weigend F, Dehnen S (2020) Angew Chem Int Ed 59:16638–16643

190. Wilson RJ, Broeckaert L, Spitzer F, Weigend F, Dehnen S (2016) Angew Chem Int Ed 55:11775–11780
191. Jupp AR, Beijer S, Narain GC, Schipper W, Slootweg JC (2021) Chem Soc Rev 50:87–101
192. Scheer M, Balázs G, Seitz A (2010) Chem Rev 110:4236–4256
193. Cossairt BM, Piro NA, Cummins CC (2010) Chem Rev 110:4164–4177
194. Hoidn CM, Scott DJ, Wolf R (2021) Chem Eur J 27:1886–1902
195. Seidl M, Balázs G, Scheer M (2019) Chem Rev 119:8406–8434
196. Spitzer F, Sierka M, Latronico M, Mastrorilli P, Virovets AV, Scheer M (2015) Angew Chem Int Ed 54:4392–4396
197. Schwarzmaier C, Schindler A, Heindl C, Scheuermayer S, Peresypkina EV, Virovets AV, Neumeier M, Gschwind R, Scheer M (2015) Angew Chem Int Ed 52:10896–10899
198. Seitz AE, Hippauf F, Kremer W, Kaskel S, Scheer M (2018) Nat Commun 9:361
199. Schmidt M, Seitz AE, Eckhardt M, Balázs G, Peresypkina EV, Virovets AV, Riedlberger F, Bodensteiner M, Zolnhofer EM, Meyer K, Scheer M (2017) J Am Chem Soc 139:13981–13984
200. Schoo C, Bestgen S, Egeberg A, Seibert J, Konchenko SN, Feldmann C, Roesky PW (2019) Angew Chem Int Ed 58:4386–4389
201. Cossairt BM, Diawara M-C, Cummins CC (2009) Science 323:602
202. Cordier G, Blase W (1991) Z Kristallogr 196:207–211
203. Waibel M, Pecher O, Mausolf B, Haarmann F, Fässler TF (2013) Eur J Inorg Chem:5541–5546
204. Waibel M, Henneberger T, Jantke L-A, Fässler TF (2012) Chem Commun 48:8676–8678
205. Waibel M, Gabriele Raudaschl-Sieber Fässler TF (2011) Chem Eur J 17:13391–13394
206. Waibel M, Kraus F, Scharfe S, Wahl B, Fässler TF (2010) Angew Chem Int Ed 49:6611–6615
207. Stegmaier S, Waibel M, Henze A, Jantke LA, Karttunen AJ, Fässler TF (2012) J Am Chem Soc 134:14450–14460
208. Benda CB, Waibel M, Kochner T, Fässler TF (2014) Chem Eur J 20:16738–16746
209. Xu L, Sevov SC (2000) Inorg Chem 39:5383–5389
210. Lichtenberger N, Spang N, Eichhofer A, Dehnen S (2017) Angew Chem Int Ed 56:13253–13258
211. Mitzinger S, Broeckaert L, Massa W, Weigend F, Dehnen S (2016) Nat Commun 7:10480–10490
212. Lips F, Schellenberg I, Pöttgen R, Dehnen S (2009) Chem Eur J 15:12968–12973
213. Critchlow SC, Corbett JD (1982) Inorg Chem 21:3286–3290
214. Ababei R, Heine J, Hołyńska M, Thiele G, Weinert B, Xie X, Weigend F, Dehnen S (2012) Chem Commun 48:11295–11297
215. Friedrich U, Neumeier M, Kochb C, Korber N (2012) Chem Commun 48:10544–10546
216. Guggolz L, Dehnen S (2020) Chem Eur J 26:11819–11828
217. Pan F-X, Li LJ, Sun ZM (2016) Chin J Struct Chem 35:1099–1106
218. Leung YC, Waser J, Houten SV, Vos A, Wiegers GA, Wiebenga EH (1957) Acta Cryst 10:574–582
219. Korber N, von Schnering H-G (1995) J Chem Soc Chem Commun:1713–1714
220. Turbervill RSP, Goicoechea JM (2012) Organometallics 31:2452–2462
221. Mattamana SP, Promprai K, Fettinger JC, Eichhorn BW (1998) Inorg Chem 37:6222–6228
222. Knapp CM, Large JS, Rees NH, Goicoechea JM (2011) Dalton Trans 40:735–745
223. Quintero GE, Paterson-Taylor I, Rees NH, Goicoechea JM (2016) Dalton Trans 45:1930–1936
224. Knapp C, Zhou B, Denning MS, Rees NH, Goicoechea JM (2010) Dalton Trans 39:426–436
225. von Schnering HG, Manriquez V, Honle W (1981) Angew Chem Int Ed 20:594–595
226. Mitzinger S, Guggolz L, Massa W, Dehnen S (2019) Z Anorg Allg Chem 645:153–157
227. Asbrand M, Eisenmann B (1992) Z Kristallogr 198:309–310
228. Friedrich U, Korber N (2016) ChemistryOpen 5:306–310
229. Friedrich U, Neumeier M, Koch C, Korber N (2012) Chem Commun 48:10544–10546

230. Wilson RJ, Dehnen S (2017) Angew Chem Int Ed 56:3098–3102
231. Cisar A, Corbett JD (1977) Inorg Chem 16:2482–2487
232. Pan F, Wei S, Guggolz L, Eulenstein A, Tambornino F, Dehnen S (2021) J Am Chem Soc 143:7176–7188
233. Eisenmann B, Jordan H, Schäfer H (1981) Z Anorg Allg Chem 475:74–80
234. Eisenmann B, Jordan H, Schaefer H (1982) Mat Res Bull 17:95–99
235. Eisenmann B, Klein J (1988) Z Naturforsch 43b:69–71
236. Eisenmann B, Rößler U (2000) Z Anorg Allg Chem 626:1373–1379
237. von Schnering H-G, Somer M, Hartweg M, Peters K (1990) Angew Chem Int Ed Engl 29:65–67
238. Somer M (2000) Z Anorg Allg Chem 626:897–904
239. Eisenmann B, Klein J (1991) Z Kristallogr 197:263–264
240. Eisenmann B, Klein J (1991) Z Kristallogr 197:273–274
241. Asbrand M, Eisenmann B, Engelhardt H, Rößler U (1998) Z Naturforsch 53b:405–410
242. Eisenrnann VB, Klein J, Somer M (1990) Angew Chem Int Ed Engl 29:87–88
243. Asbrand M, Eisenmann B (1993) Z Kristallogr 205:323–324
244. Eisenmann B, Klein J (1991) Z Kristallogr 197:265–266
245. Eisenmann B, Klein J (1991) Z Kristallogr 197:267–268
246. Eisenmann B, Klein J (1991) Z Kristallogr 196:213–229
247. Mayer K, Dums JV, Klein W, Fässler TF (2017) Angew Chem Int Ed 56:15159–15163
248. Eisenmann B, Jordan H, Schäfer H (1981) Angew Chem Int Ed Engl 20:197–198
249. Waibel M, Benda CB, Wahl B, Fässler TF (2011) Chem Eur J 17:12928–12931
250. Waibel M, Fässler TF (2013) Inorg Chem 52:5861–5866
251. Gillett-Kunnath MM, Petrov I, Sevov SC (2010) Inorg Chem 49:721–729
252. Rios D, Gillett-Kunnath MM, Taylor JD, Oliver AG (2011) Inorg Chem 50:2373–2377
253. Li F, Sevov SC (2014) J Am Chem Soc 136:12056–12063
254. Lips F, Dehnen S (2009) Angew Chem Int Ed 48:6435–6438
255. Reddya GN, Paridaa R, Muñoz-Castroc A, Janab M, Giri S (2020) Chem Phys Lett 759:137952
256. Gillett-Kunnath MM, Oliver AG, Sevov SC (2011) J Am Chem Soc 133:6560–6562
257. Bentlohner MM, Jantke L-A, Henneberger T, Fischer C, Mayer K, Klein W, Fässler TF (2016) Chem Eur J 22:13946–13952
258. Gupta U, Reber AC, Melko JJ, Khanna SN, Castleman Jr AW (2011) Chem Phys Lett 505:92–95
259. Lichtenberger N, Franzke Y, Massa W, Weigend F, Dehnen S (2018) Chem Eur J 24:12022–12030
260. Knies M, Kaiser M, Isaeva A, Müller U, Doert T, Ruck M (2018) Chem Eur J 24:127–132
261. Xu H-L, Tkachenko NV, Muñoz-Castro A, Boldyrev AI, Sun Z-M (2021) Angew Chem Int Ed 60:9990–9995
262. Wilson RJ, Hastreiter F, Reiter K, Büschelberger P, Wolf R, Gschwind R, Weigend F, Dehnen S (2018) Angew Chem Int Ed 57:15359–15363
263. Bobev S, Sevov SC (2000) Angew Chem Int Ed 39:4108–4110
264. Wang Y, Zavalij P, Eichhorn B (2018) Chem Commun 54:11917–11920
265. Gillett-Kunnath MM, Muñoz-Castrob A, Sevov SC (2012) Chem Commun 48:3524–3526
266. Xu L, Sevov SC (1999) J Am Chem Soc 121:9245–9246
267. Muñoz-Castro A, Sevov SC (2013) Phys Chem Chem Phys 15:986–991
268. Fässler TF, Hoffmann SD (2004) Angew Chem Int Ed 43:6242–6247
269. Ganesamoorthy C, Weßing J, Kroll C, Seidel RW, Gemel C, Fischer RA (2014) Angew Chem Int Ed 53:7943–7947
270. Kesanli B, Fettinger J, Eichhorn B (2001) Angew Chem Int Ed 40:2300–2302
271. Schiemenz B, Huttner G (1993) Angew Chem Int Ed Engl 32:297–298
272. von Schnering H-G, Wolf J, Weber D, Ramirez R, Meyer T (1986) Angew Chem Int Ed Engl 25:353–354

273. Kesanli B, Fettinger J (2003) Eichhorn B J Am Chem Soc 125:7367–7376
274. Kesanli B, Fettinger J, Scott B, Eichhorn B (2004) Inorg Chem 43:3840–3846
275. Knapp CM, Westcott BH, Raybould MAC, McGrady JE, Goicoechea JM (2012) Angew Chem Int Ed 51:9097–9100
276. Knapp CM, Westcott BH, Raybould MAC, McGrady JE, Goicoechea JM (2012) Chem Commun 48:12183–12185
277. Charles S, Fettinger JC, Bott SG, Eichhorn BW (1996) J Am Chem Soc 118:4713–4714
278. Charles S, Fettinger JC, Eichhorn BW (1996) Inorg Chem 35:1540–1548
279. Knapp CM, Large JS, Rees NH, Goicoechea JM (2011) Chem Commun 47:4111–4113
280. Mandal S, Reber AC, Qian M, Liu R, Saavedra HM, Sen S, Weiss PS, Khanna SN, Sen A (2012) Dalton Trans 41:12365–12377
281. Kaas M, Korber N (2017) Z Anorg Allg Chem 643:1331–1334
282. Kesanli B, Charles S, Lam Y-F, Bott SG, Fettinger J, Eichhorn BW (2000) J Am Chem Soc 122:11101–11107
283. Knapp CM, Jackson CS, Large JS, Thompson AL, Goicoechea JM (2011) Inorg Chem 50:4021–4028
284. Qian M, Reber AC, Ugrinov A, Chaki NK, Mandal S, Saavedra HM, Khanna SN, Sen A, Weiss PS (2010) ACS Nano 4:235–240
285. Chaki NK, Mandal S, Reber AC, Qian M, Saavedra HM, Weiss PS, Khanna SN, Sen A (2010) ACS Nano 4:5813–5818
286. Mandal S, Reber AC, Qian M, Liu R, Saavedra HM, Sen S, Weiss PS, Khanna SN, Sen A (2012) Dalton Trans 41:5454–5457
287. Charles S, Eichhorn BW, Rheingold AL, Bott SG (1994) J Am Chem Soc 116:8077–8086
288. Wang Y, Zavalij P, Eichhorn B (2017) Chem Commun 53:11600–11602
289. Lichtenberger N, Massa W, Dehnen S (2019) Angew Chem Int Ed 58:3222–3226
290. Saparov B, Bobev S (2010) Inorg Chem 49:5173–5179
291. Balvanz A, Baranets S, Bobev S (2020) Acta Cryst C76:869–873
292. Eisenmann B, Klein J (1991) Z Kristallogr 197:271–272
293. Prots Y, Aydemir U, Öztürk SS, Somer M (2007) Z Kristallogr 222:163–164
294. Lidin S, Popp T, Somer M, von Schnering HG (1992) Angew Chem Int Ed Engl 31:924–927
295. Qin Q, Zhou L, Wang Y, Sang R, Xu L (2014) Dalton Trans 43:5990–5993
296. Eisenmann B, Klein J (1992) J Alloys Compd 178:431–439
297. Kim S-J, Kraus F, Fässler TF (2009) J Am Chem Soc 131:1469–1478
298. Benda CB, Köchner T, Schäper R, Schulz S, Fässler TF (2014) Angew Chem Int Ed 53:8944–8948
299. Teixidor F, Luetkens ML, Rudolph RW (1983) J Am Chem Soc 105:149–150
300. Eichhorn BW, Haushalter RC (1988) J Am Chem Soc 110:8704–8706
301. Eichhorn BW, Haushalter RC (1990) J Chem Soc Chem Commun:937–938
302. Kesanli B, Fettinger J, Eichhorn B (2001) Chem Eur J 7:5277–5285
303. Yong L, Hoffmann SD, Fässler TF (2005) Z Kristallogr 220:53–57
304. Yong L, Hoffmann SD, Fässler TF (2005) Eur J Inorg Chem 18:3663–3669
305. Campbell J, Mercier HPA, Franke H, Santry DP, Dixon DA, Schrobilgen GJ (2002) Inorg Chem 41:86–107
306. Goicoechea JM, Sevov SC (2006) J Am Chem Soc 128:4155–4161
307. Wang J-Q, Stegmaier S, Wahl B, Fässler TF (2010) Chem Eur J 16:1793–1798
308. Downing DO, Zavalij P, Eichhorn BW (2010) Eur J Inorg Chem 2010:890–894
309. Scharfe S, Fässler TF (2010) Eur J Inorg Chem:1207–1213
310. Goicoechea JM, Sevov SC (2006) Organometallics 25:4530–4536
311. Zhou B, Denning MS, Jones C, Goicoechea JM (2009) Dalton Trans:1571–1578
312. Mayer K, Jantke L-A, Schulz S, Fässler TF (2017) Angew Chem Int Ed 56:2350–2355
313. Zhou B, Denning MS, Chapman TAD, McGrady JE, Goicoechea JM (2009) Chem Commun:7221–7223
314. Wallach C, Mayer K, Henneberger T, Klein W, Fässler TF (2020) Dalton Trans 49:6191–6198

315. Yong L, Hoffmann SD, Fässler TF, Riedel S, Kaupp M (2005) Angew Chem Int Ed 44:2092–2096
316. Gholiee Y, Salehzadeh S, Khodaveisi S (2019) New J Chem 43:7797–7805
317. Perla LG, Sevov SC (2016) Angew Chem Int Ed 55:6721–6724
318. Resa I, Carmona E, Gutierrez-Puebla E, Monge A (2004) Science 305:1136–1138
319. Eulenstein AR, Franzke YJ, Lichtenberger N, Wilson RJ, Deubner L, Kraus F, Clérac R, Weigend F, Dehnen S (2021) Nat Chem 13:149–155
320. Schnepf A (2003) Angew Chem Int Ed 42:2624–2625
321. Li F, Sevov SC (2012) Inorg Chem 51:2706–2708
322. Li F, Muñoz-Castro A, Sevov SC (2012) Angew Chem Int Ed 124:8709–8712
323. Li F, Muñoz-Castroc A, Sevov SC (2016) Angew Chem Int Ed 55:8630–8633
324. Frischhut S, Kaiser F, Klein W, Drees M, Kühn FE, Fässler TF (2018) Organometallics 37:4560–4567
325. Geitner FS, Fässler TF (2020) Inorg Chem 59:15218–15227
326. Townrow OPE, Chung C, Macgregor SA, Weller AS, Goicoechea JM (2020) J Am Chem Soc 142:18330–18335
327. Bernhardt E, Brauer DJ, Finze M, Willner H (2007) Angew Chem Int Ed 46:2927–2930
328. Schenkb C, Schnepf A (2009) Chem Commun:3208–3210
329. Henke F, Schenkb C, Schnepf A (2011) Dalton Trans 40:6704–6710
330. Perla LG, Muñoz-Castroc A, Sevov SC (2017) J Am Chem Soc 139:15176–15181
331. Perla LG, Sevov SC (2016) J Am Chem Soc 138:9795–9798
332. Charles S, Eichhorn BW, Bott SG (1993) J Am Chem Soc 115:5837–5838
333. Xu L, Ugrinov A, Sevov SC (2001) J Am Chem Soc 123:4091–4092
334. Goicoechea JM, Hull MW, Sevov SC (2007) J Am Chem Soc 129:7885–7893
335. Raupach M, Dehnen S, Tonner R (2014) J Comput Chem 35:1045–1057
336. Benda CB, Waibel M, Fässler TF (2015) Angew Chem Int Ed 54:522–526
337. Wang Y, Qin Q, Wang J, Sanga R, Xu L (2014) Chem Commun 50:4181–4183
338. Li Z, Ouyang D, Xu L (2019) Chem Commun 55:6783–6786
339. Qiao L, Chen D, Zhu J, Muñoz-Castro A, Sun Z-M (2021) Chem Commun 57:3656–3659
340. Lichtenberger N, Wilson RJ, Eulenstein AR, Massa W, Clérac R, Weigend F, Dehnen S (2016) J Am Chem Soc 138:9033–9036
341. Eulenstein AR, Franzke YJ, Bügel P, Massa W, Weigend F, Dehnen S (2020) Nat Commun 11:5122

Struct Bond (2021) 188: 149–196
https://doi.org/10.1007/430_2021_82

Published online: 17 March 2021

Molecules Meet Solids: From Wade–Mingos Clusters to Intermetalloid Clusters

Wilhelm Klein, Annette Schier, and Thomas F. Fässler

Contents

Abstract The common feature of molecular deltahedral borane clusters, molecules with a set of multiple bonds and metals is their electron deficiency, and they are all connected with the term "electron delocalization," although with different meanings. The atomic and electronic structure of atom clusters is right between that of molecules and the extended bulk, and thus these clusters meet at the interface of molecules and solids.

In recent years intriguing examples of bare anionic homoatomic tetrel element clusters and more complex molecular metal clusters have been obtained from the reaction of tetrel element Zintl clusters in solution, and in the course of these studies a series of compounds has been established that describes the transition from molecules to intermetallic compounds. In this context the term intermetalloid clusters was coined. On the one hand, these clusters play a dominant role at the interface of molecular clusters and intermetallic solids, since they cover the entire area from rather simple borane-type species to intermetalloid clusters and intermetallic

W. Klein, A. Schier, and T. F. Fässler (✉)
Department of Chemistry, Technical University of Munich, Munich, Germany
e-mail: thomas.faessler@lrz.tum.de

compounds, whose chemical bonding is so far hardly understood. On the other hand, there are extraordinary intermetallic compounds based on large intermetalloid clusters like $[Sn@Cu_{12}@Sn_{20}]^{12-}$ that demand for an extension of the 8-N rule of Zintl phases which is derived from a superatom approach.

In this review, examples of borderline cases at the transition from "locally delocalized electrons" to delocalized electronic systems are summarized, with a special focus on examples that occur as anions in solution and in extended solids. The chosen cases allow a step-wise extension of the description of the chemical bond, starting from delocalized bonds in organic molecules, to delocalized bonds in deltahedral molecules, bare metal atom clusters, and rather complex intermetalloid clusters. The structural relationships between boranes $B_nH_m^{x-}$ and tetrel element clusters $[E_n]^{x-}$ are defined and applied to their derivatives, which include transition metal complexes. The similarities between the protonated species $B_9H_{12}^-$ and $[Si_9H_2]^{2-}$ and the bare tetrel clusters are emphasized. The introduction of ligand-stabilized transition metal fragments for cluster vertex expansion $[E_nTL]^{x-}$ as well as the inclusion of metal atoms under formation of endohedral species $[T@E_n]^{x-}$ is highlighted. The intriguing similarity of the local coordination environment of the transition metal atoms in $[T@E_n]^{x-}$ clusters with $n = 9$ and 10 and in ternary Zintl phases and bare binary alloys with special emphasis on the oxidation state of the endohedral guest atom is discussed. The final part is dedicated to intermetalloid clusters with icosahedral structure. Using selected examples, possible reaction pathways to icosahedral building units are depicted. Specifically their relationship to compounds with highly coordinated atoms in intermetallic compounds is explored, and the formation of discrete and interpenetrating icosahedra is summarized. Even though the electronic structures of typical molecular units and larger intermetalloid clusters are different, the structures of boranes/carboranes like the *tricommo*$\{Ge_9Pd_3\}$ and the *tricommo*-B_{12} unit in elemental boron are related, and the unit $[Pd_2@E_{18}]^{4-}$ (E = Ge, Sn) can be described as a "macropolyhedral" species. Finally, the transition from large intermetalloid clusters such as $[Au_{12}Pb_{44}]^{8-}$ to Frank–Kasper phases is discussed.

Keywords Cluster compounds · Endohedral clusters · Intermetalloid clusters · Superatom approach · Zintl anions

1 Introduction

The term "electron delocalization" is used with rather different meanings for molecules and for extended metals. In molecules it is generally applied to describe resonance structures of conjugated and aromatic π systems. In metals, however, electrons are delocalized over the entire system, and in solid state physics, "electron delocalization" refers to "free electrons," that facilitate electrical conduction or – using the most simple concept – to the picture of a "free electron gas." In general "electron delocalization" addresses those electrons in molecules, molecular ions,

solid metals, or intermetallic compounds, that are not directly associated with a specific atom either in form of a localized covalent bond or a lone pair, and it is associated with the aggregation of electron-deficient atoms that cannot fulfill the valence rules.

Electron deficiency increases gradually from typical molecules via molecular clusters to bulk metals or intermetallic compounds. The atomic and electronic structure of clusters, which in chemistry are defined as aggregates of atoms hold together by non-classical bonds, is right between that of molecules and the extended bulk, and therefore clusters meet at the interface of molecules and solids. For molecular metal clusters which contain both ligand-bearing and naked metal atoms that are only bonded to other metal atoms, the term "metalloid clusters" was introduced in 2002 [1]. The term was expanded to "intermetalloid clusters" in 2004 for the description of the rapidly growing class of molecular, metal-centered heteroatomic clusters (endohedral clusters) [2]. Such cluster species, generally obtained from chemical syntheses in solution, show striking structural similarities to condensed or interpenetrating clusters as they occur in intermetallic compounds. Selected examples of cage molecules, metal clusters, and related coordination polyhedra in metals and intermetallic compounds are shown in Fig. 1. It was pointed out that *"following the original motivation for the usage of the suffix "oid" in the term metalloid, a heterometallic cluster addressed as intermetalloid ideally bears some structural resemblance to a related intermetallic's solid-state structure. A characteristic structural feature of typical intermetallics (such as Laves or Hume-Rothery phases) is the occurrence of high coordination numbers. Thus, clusters with endohedral atoms are seen as exemplary intermetalloid species. Among the ligand-free heterometallic clusters that comprise semi(metallic) p block element atoms, species with endohedral d block atoms constitute one of the prevalent groups"* [3]. In intermetallic compounds the cluster approach is used to describe the local coordination sphere of the metal atoms, however, the polyhedral clusters are not discrete, but each cluster atom represents the center of neighboring interpenetrating clusters. Nonetheless, in specific Zintl phases as a subgroup of intermetallic compounds, in which a large difference in electronegativity between the involved metals occurs, discrete clusters appear in the solid. The structure of Zintl phases can be explained by a formal transfer of all valence electrons to the electronegative component (salt-like description). The bonding of the resulting polyanions follows molecular valence concepts (octet rule). In some cases the polyanions form polyhedral metal cluster anions (Zintl clusters) that follow typical skeletal electron counting rules as outlined below, and these Zintl phases are called "electron precise" [4, 5]. Since there are some examples, where such clusters can be brought into solution without a structural change, they mark the borderline between molecular (inter)metalloid clusters and intermetallic solids.

The most numerous examples are derived from the intermetallic compounds K_4Sn_9 and K_4Pb_9. In both cases the two components are typical metals, but they contain nine-atomic tin and lead clusters, respectively. In a salt-like description the tin and lead atoms form $[Sn_9]^{4-}$ and $[Pb_9]^{4-}$ polyanions, charge-balanced by

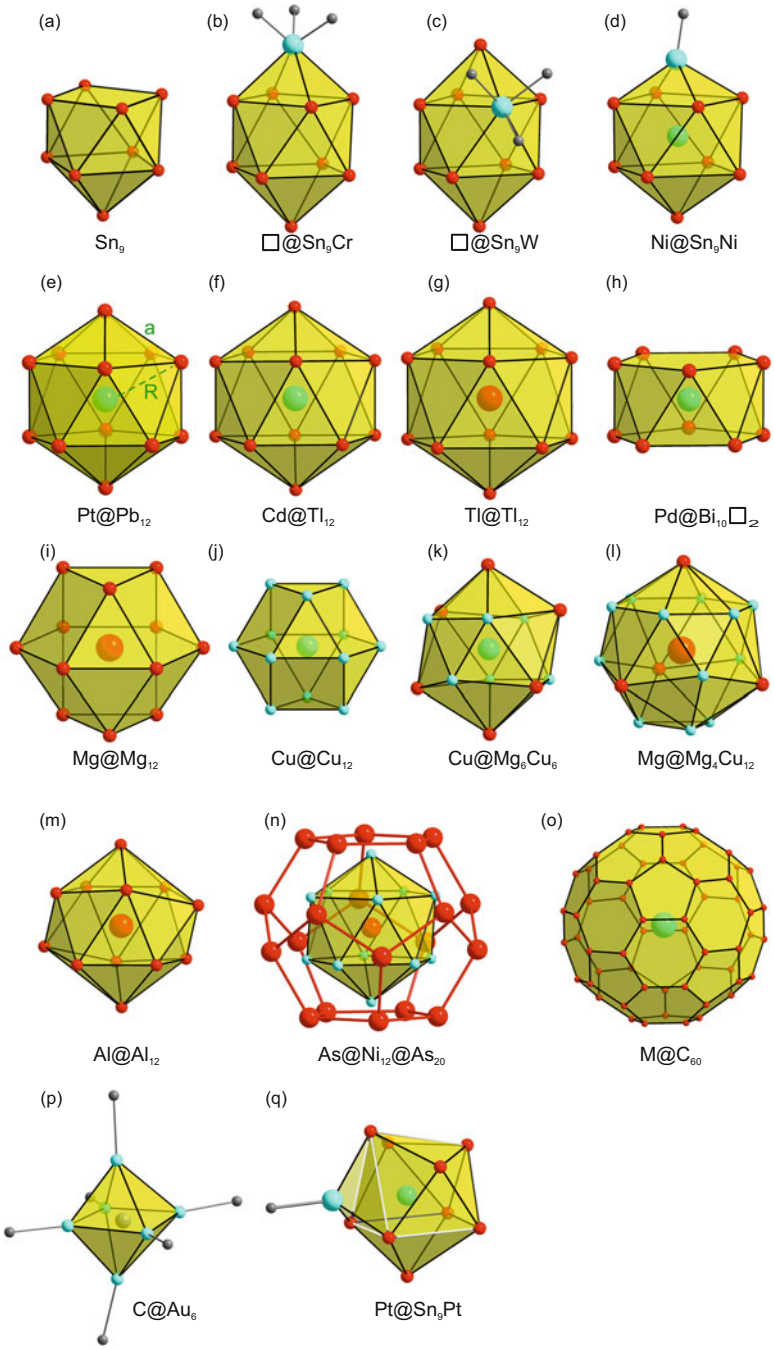

Fig. 1 Selected examples of cage molecules, metal clusters, and related coordination polyhedra in metals and intermetallic compounds. (**a**) Sn_9^{4-}; (**b**) $[Sn_9Cr(CO)_3]^{4-}$ [6], (**c**) $[Sn_9W(CO)_3]^{4-}$ [6], (**d**) $[NiSn_9Ni(CO)]^{3-}$ [7], with the C atoms of the CO ligands drawn in gray; (**e**) $[PtPb_{12}]^{2-}$ [8]; (**f**) $[CdTl_{12}]^{12-}$ in $Na_{14}K_6Tl_{18}Cd$ [9]; (**g**) $[Tl_{13}]^{11-}$ in $Na_3K_8Tl_{13}$ [9]; (**h**) $[PdBi_{10}]^{4+}$ in $Bi_{14}PdBr_{16}$ [10];

Table 1 Examples of electron deficiency in molecules

Fragment	Stabilization	Example	Bond type
⋮N:	Dimer	N_2 molecule	π bonds
:CH_2	Dimer	Ethene	π bond
	Rings	Cyclohexane C_6H_{12}	σ bond
	Chain	Polyethylene	σ bond
⋮CH	Dimer	Ethine (acetylene)	2π bonds
	Ring + multiple bond	Benzene	π bond (π delocalization) or Wade rule
	Chain + multiple bond	Polyacetylene	π bond (conjugated)
	Cage molecule	Tetrahedrane	σ bond or Wade rules
⋮C	Cage molecule + double bond	Fullerenes	π bond (conjugated)
BH_3	Dimer	B_2H_6, cyclohexasilane	3c-2e bond, σ delocalization
:BH	Cluster	$B_nH_n^{m-}$ polyanion	Multi-center bond, σ delocalization (Wade rules)
:Si:	Cluster	Si_n^{m-} polyanion	Multi-center bond, σ delocalization (Wade rules)

potassium cations. These intermetallic compounds are semiconductors, and the electrons may be considered as "locally delocalized" within the nine-atomic clusters.

Electron deficiency in molecules with lighter atoms leads to the formation of multiple bonds, and electron delocalization refers to resonances in conjugated or aromatic π systems (Table 1 and Fig. 2). In this context graphite is a nice example of a molecular polymer, in which delocalized π bonds are directly associated with electrical conductivity along the directions of the sheets in bulk graphite. The dimeric BH_3 provides the textbook example of electron deficiency. The formation of 3c-2e bonds (three-center-two-electron bonds), and the resulting B-H-B unit can also be interpreted as a resonance structure resulting from a delocalization of σ bonds. Small clusters such as tetrahedral B_4Cl_4 with its eight disposable electrons for six B-B contacts are described by four 3c-2e bonds. For the larger deltahedral borane anions, e.g. $B_6H_6^{2-}$, the electron deficiency involves 14 electrons for cluster bonding, i.e. seven 3c-2e bonds for eight triangular faces of the octahedron, and consequently mesomeric 3c-2e BBB bonds (Fig. 2) are required. For larger clusters a bonding picture with fully delocalized electrons in molecular orbitals is more

Fig. 1 (continued) (**i**) part of the structure of elemental Cu; (**j**) part of the structure of elemental Mg; (**k** and **l**) coordination polyhedra of Cu and Mg, respectively, in the Laves phase $MgCu_2$ [11]; (**m**) coordination sphere of the central Al atom in $[Al_{77}\{N(SiMe_2)_2\}_{20}]^{2-}$ [12]; (**n**) $[AsNi_{12}As_{20}]^{2-}$ [13]; (**o**) endohedral fullerene; (**p**) $[CAu_6(PPh_3)_6]^{2+}$ [14]; (**q**) $[PtSn_9Pt(PPh_3)]^{2-}$ [7], with the P atoms of the PPh_3 ligands drawn in gray. *From Angew. Chem* [2]., *copyright Wiley-VCH GmbH. Reproduced with permission*

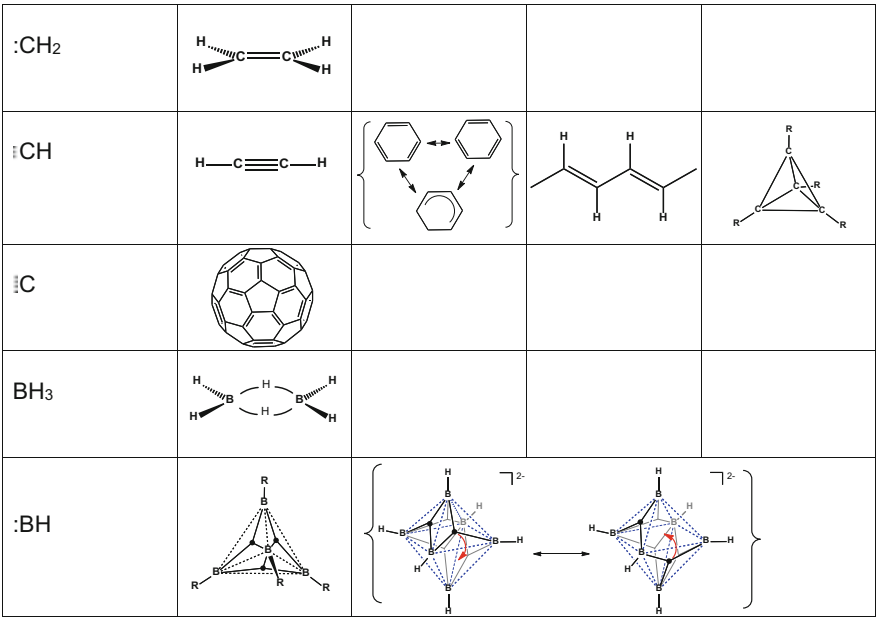

Fig. 2 Molecular structures arising from fragments with electron deficiency (Table 1)

appropriate, which flows into the easy-to-handle Wade rules for deltahedral borane clusters and its extension to cage molecules including transition metal fragments in the Wade–Mingos rules [15–18]. When the clusters are metal-richer and larger and contain more transition metals, the situation becomes more complex, and the concepts must be expanded to include three-dimensional aromaticity and the superatom approach.

The review article summarizes borderline cases that mark the transition from "locally delocalized electrons" to "delocalized electronic systems."

2 The Wade–Mingos Rules: Homoatomic Deltahedra and the Isolobal Concept

For the description of cage molecules with deltahedral faces and consequently higher coordination numbers than four for the cluster vertex atoms, Wade rules have developed into a powerful tool. In main group element clusters such as boranes, electron deficiency leads to a full delocalization of electrons as expressed by delocalized molecular orbitals. In a simple picture the valence orbitals of each cluster vertex can be assumed to be sp^3 hybridized. One of the four sp^3 hybrid orbitals is then used for an *exo* cluster bond, whereas the remaining orbitals are available for

cluster bonding, and *closo* clusters are stable, if $n + 1$ out of the $3n$ combinations of hybrid orbitals are filled with electrons.

The concept can be expanded to bare main group element clusters ("Zintl anions") in which an *exo* bond is formally replaced by a lone pair of electrons. The octahedral cage of $CB_5H_6^-$ (**1**, Fig. 3) features six *exo* bonds, whereas the iso-valence electronic $[Sn_6]^{2-}$ has one lone pair at each Sn atom that radially points to the outside of the cluster, thereby allowing, e.g., the coordination of $Cr(CO)_5$ fragments (**2**) [19]. Even though there are striking similarities between (carbo)-boranes and Zintl ions, there are also some differences. The iso-valence electronic *nido* structures $B_9H_{12}^-$ (**3**) and $[Si_9]^{4-}$ (**4**) adapt different structures upon the removal of different vertex atoms from their corresponding bi-capped square-antiprismatic *closo* cluster (**5**).

On the other hand, (carbo)boranes and deltahedral Zintl anions show remarkable similarities regarding the attachment of H atoms. $B_9H_{12}^-$ (**3**) carries beside the nine *exo*-bonded H atoms three bridging H atoms at the B atoms of the open five-membered ring (not shown in the picture), which are fluctional [20]. The same feature is observed for the H atoms of the protonated anion $[Si_9H_2]^{2-}$ (**4a**, Fig. 4). Even though the proton of the mono-protonated $[Si_9H]^{3-}$ cluster (**4b**) in the solid state structure of $[K(18\text{-crown-6})]_3[Si_9H]\cdot 2\ NH_3\cdot 2$ thf is *exo*-bonded [89], the ^1H NMR spectrum of **4a** shows only one multiplet indicative of equivalent protons, which are in contact with all nine Si atoms, and suggesting a fast exchange of their positions at the cluster surface (Fig. 4) [21]. Similarly, NMR spectroscopic investigations of $[Si_9H]^{3-}$ reveal a dynamic process with Si-H scrambling [22].

Another striking similarity is the addition of metal-organic fragments to *nido*-type structures of boranes and homoatomic tetrel clusters. The readily available *nido*-$[E_9]^{4-}$ (E = Si – Pb) and the *nido*-$C_2B_9H_9^{2-}$ clusters are the most prominent participants from the Zintl and (carbo)borane series, respectively, and result in intermetalloid clusters and metallacarbaboranes, respectively. Both *nido* structures can be considered as six electron donors (**6** and **7**), and the addition, e.g., of the fragment $(\eta^6\text{-}C_6H_6)Ru^{2+}$ to **7** leads to *closo*-$[(\eta^6\text{-}C_6H_6)Ru(\eta^5\text{-}C_2B_9H_9)]$ (**8**), whereas the interaction of $NHCCu^+$ with the open square of the $[Si_9)]^{4-}$ unit **6** gives *closo*-$[NHCCu(\eta^4\text{-}Si_9))]^{3-}$ (**9**, **10**, Fig. 5) [23].

The isolobal principle introduced by Roald Hoffmann [24] provided an astonishingly simple concept that gave a bonding description of many heteroatomic cage molecules including transition metals [25] and offered a flexible conceptual framework for synthetic chemists. The equivalence of hybrid orbitals between main group element fragments like the two skeletal electron fragment B-H and transition metal fragments is outlined in Fig. 6 [26]. The corresponding number of electrons is given in the three hybrid orbitals that are available for skeletal bonding.

Due to the convenient accessibility of the *nido* clusters $[Ge_9]^{4-}$, $[Sn_9]^{4-}$, and $[Pb_9]^{4-}$ a large number of products of their reactions with transition metal complexes have been reported. A typical reaction of a *nido* cluster is the addition of another cluster vertex that contributes zero electrons to the skeletal bonding. The first such reaction was reported by *Eichhorn* in which the zero-electron fragment $Cr(CO)_3$ was attached to the $[Sn_9]^{4-}$ unit, resulting in the *closo* cluster $[(\eta^4\text{-}Sn_9)Cr(CO)_3]^{4-}$ (**11**,

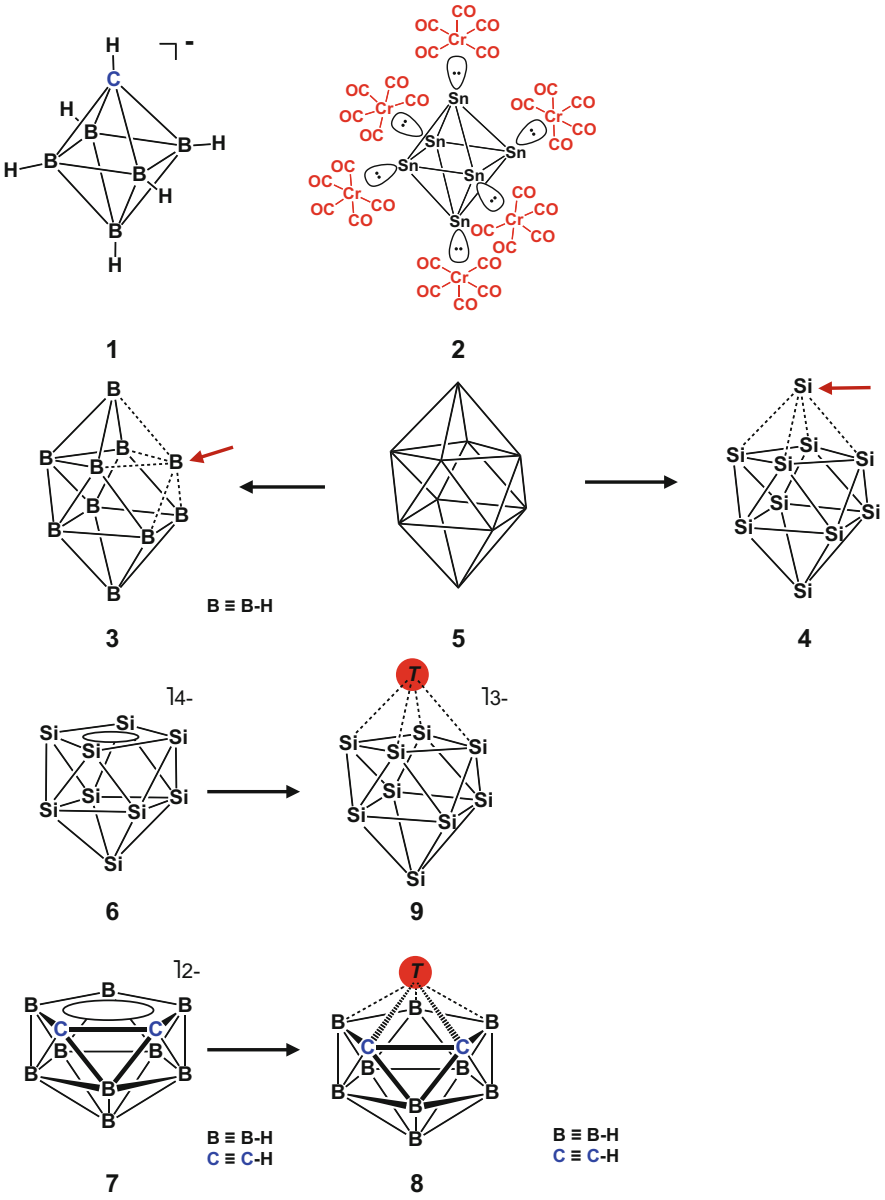

Fig. 3 Relationship between borane and Zintl clusters

Fig. 5), and subsequently the $[(\eta^4\text{-}E_9)T(CO)_3]^{4-}$ series was completed for E = Sn, Pb and T = Cr, Mo [6, 27–30]. As for (carbo)boranes, where the C position in a cluster can vary with respect to the B position, there exist isomers also in the clusters with the newly attached $T(CO)_3$ group, which can be found either as a cap of the

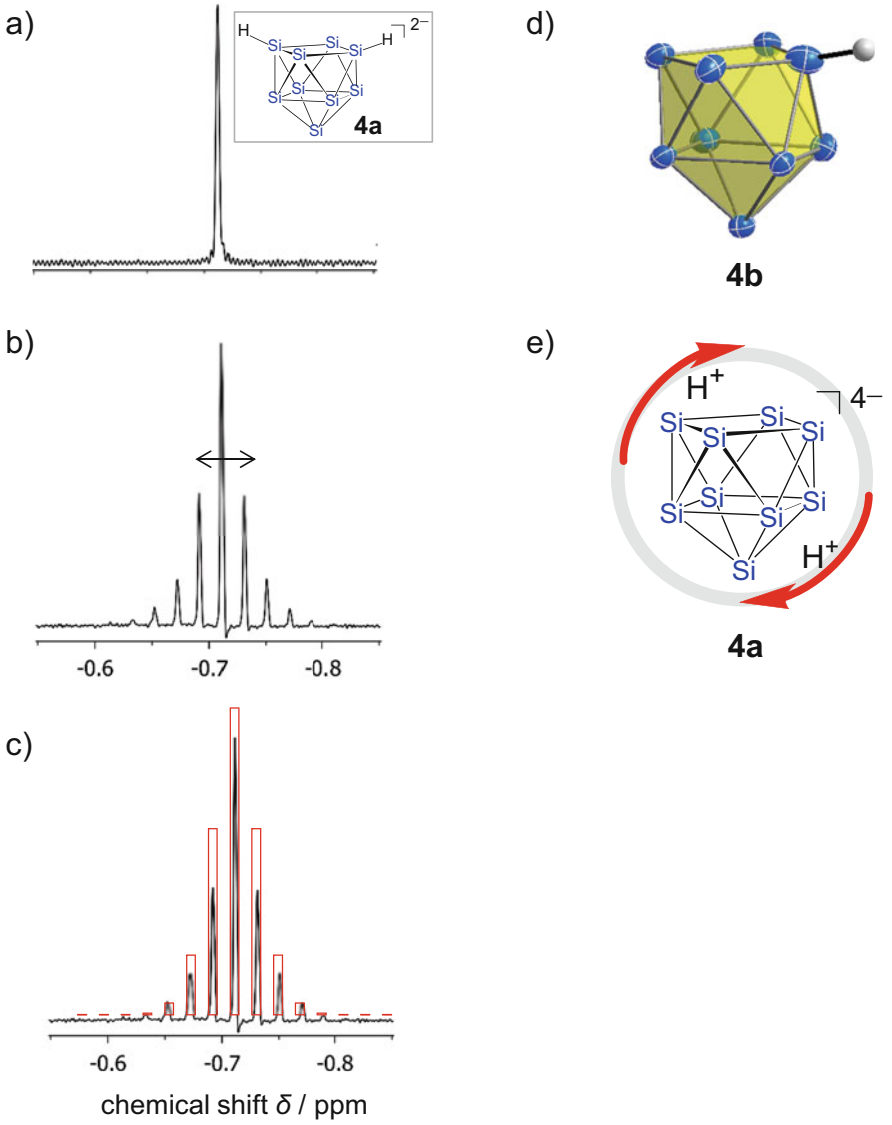

Fig. 4 ^{1}H NMR spectrum of the $[Si_9H_2]^{2-}$ dianion (**4a**, shown as insert). (**a**) ^{29}Si-decoupled; (**b**) *J* (^{1}H-^{29}Si) = 19.7 Hz; (**c**) spectrum with the simulated pattern for the 15% ^{29}Si-enriched sample; (**d**) the structure of the $[Si_9H]^{3-}$ cluster (**4b**) as determined in the salt $[K(18\text{-crown-6})]_3[\mathbf{HSi_9}]\cdot 2\ NH_3\cdot 2$ *thf*; (**e**) representation of protons of **4a** which are highly fluctional over the cluster surface [21]

square antiprism with a coordination number of four (**11**), or as a vertex of the square antiprism with a coordination number of five, as observed in $[(\eta^5\text{-}Sn_9)W(CO)_3]^{4-}$ [6] and $[(\eta^5\text{-}Pb_9)Mo(CO)_3]^{4-}$ (**12**), respectively [30]. Subsequently a large number of *closo* clusters with zero-electron fragments of late- and post-transition metals have

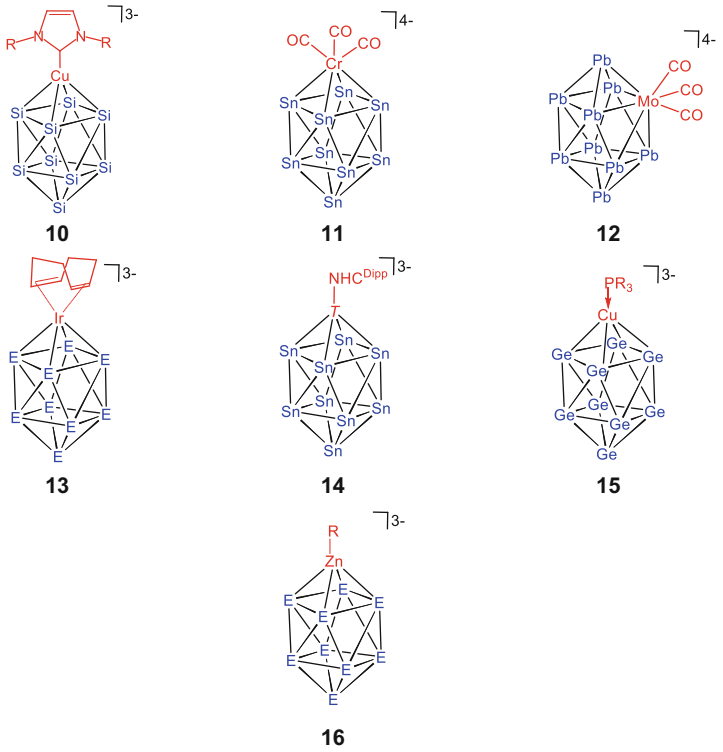

Fig. 5 Selected examples for the attachment of transition metal fragments to $[E_9]^{4-}$ Zintl clusters

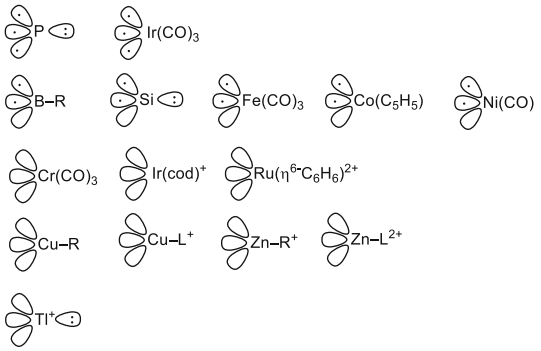

Fig. 6 Selected examples for the isolobal relationship of main group element and organo-metal fragments that contribute three, two, and zero skeletal electrons to a polyhedral cluster framework

been described. They include $[E_9\text{Ir(cod)}]^{3-}$ (E = Sn, Pb) (**13**) [31, 32], $[\text{NHCCu}(\eta^4\text{-Si}_9)]^{3-}$ (**10**), and the related $[\text{Sn}_9T(\text{NHC}^{\text{Dipp}})]^{3-}$ species (T = Cu, Ag, Au) (**14**) [33], as well as $[\text{Ge}_9\text{Cu(PR}_3)]^{3-}$ (R = ^{i}Pr, Cy) (**15**) [34] and $[\text{Ge}_9\text{Pd(PPh}_3)]^{3-}$ [35],

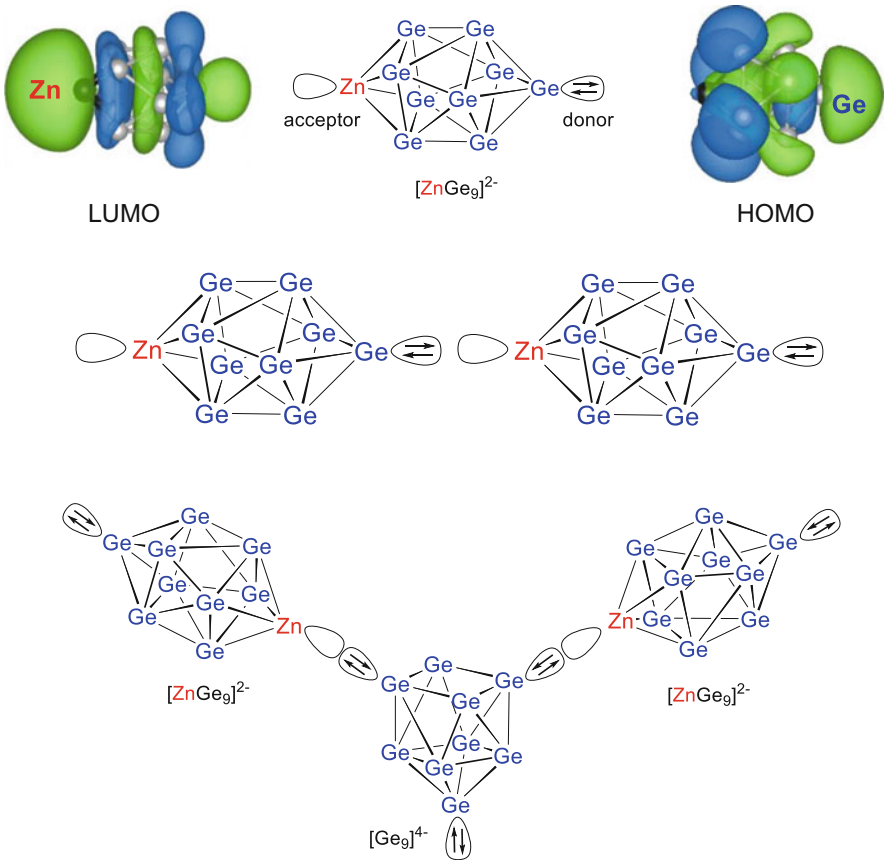

Fig. 7 Interaction between Ge_9Zn cluster units

$[E_9ZnPh]^{3-}$ [36], E = Si–Pb; R = ^{i}Pr, Mes, E = Ge–Pb) (**16**) [37], and the analogous $[E_9CdPh]^{3-}$ (E = Sn, Pb) species, as well as $[Sn_9Cd(Sn^{n}Bu_3)]^{3-}$ [38].

Aiming for even larger cluster aggregates the addition of a second Zintl cluster unit to a transition metal atom is of special interest, which paves the way towards intermetallic compounds (Fig. 7). In this case the electron-donating ligand L of the isolobal transition metal fragment is a second homoatomic cluster, leading to, e.g., $[(\eta^4\text{-}Ge_9)Cu(\eta^1\text{-}Ge_9)]^{7-}$ (**17**, Fig. 8) [34] and $[(\eta^4\text{-}Sn_9)Ag(\eta^1\text{-}Sn_9)]^{7-}$ [33], where $\{Cu\text{-}[\eta^1\text{-}Ge_9]\}^{3-}$ and $\{Ag\text{-}[\eta^1\text{-}Sn_9]\}^{3-}$, respectively, act as fragments with zero skeletal electrons.

The introduction of a Zn vertex atom under formation of a $[Ge_9Zn]^{2-}$ *closo* cluster gives access to two other interesting intermetalloid anions. A closer look at the LUMO of the $[Ge_9Zn]^{2-}$ unit reveals that the Zn atom located at a capping position of the square antiprism acts as electron acceptor (formally from the addition of Zn^{2+} to the *nido* cluster $[Ge_9]^{4-}$), whereas the HOMO has a high contribution from the opposing Ge cap, indicating a donor function for this position (Fig. 7). As a

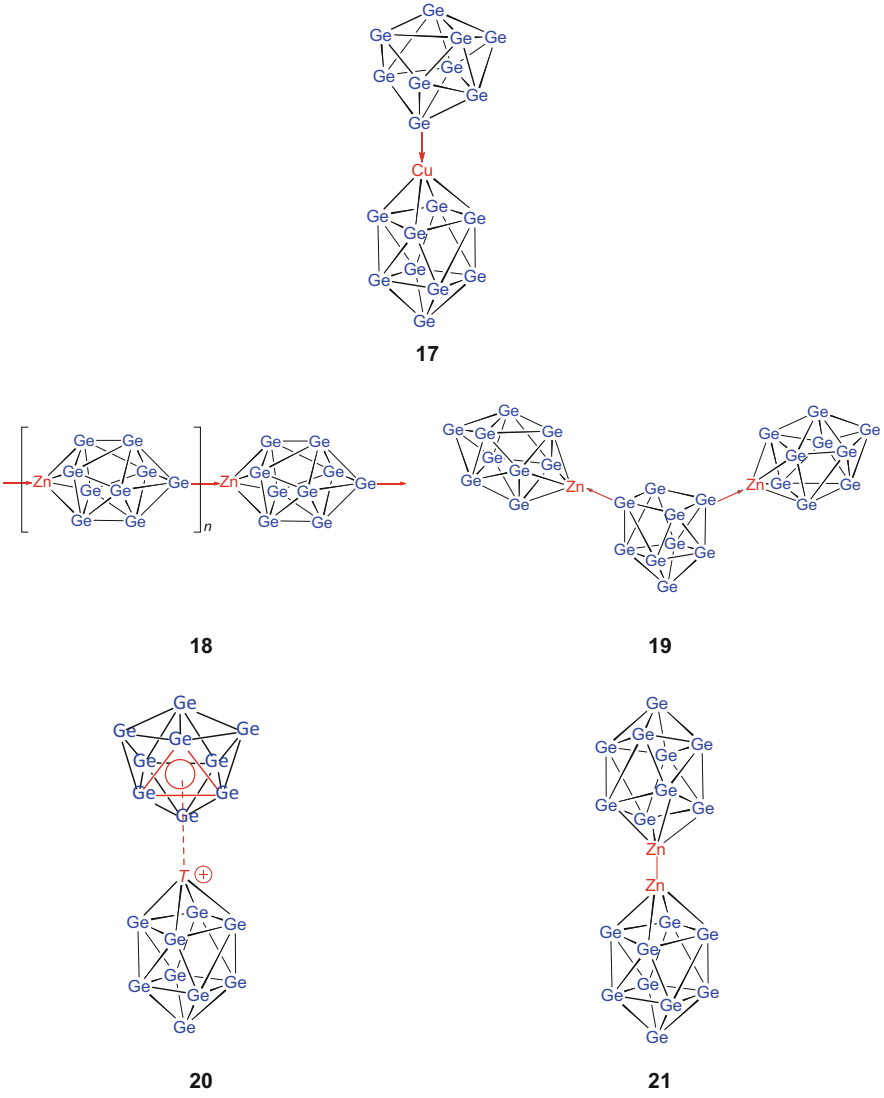

Fig. 8 Selected examples for the coordination modes of a second and a third Zintl cluster ($T = \mathrm{Zn}$, Sn)

consequence a head-to-tail arrangement of these ten-atomic *closo* clusters $[(Ge_9Zn)]^{2-}$ is observed, which leads to the formation of the linear polymer ${}^{1}_{\infty}\{Zn[\mu_2(\eta^4 : \eta^1 Ge_9)]\}2^-$ (**18**, Fig. 8). The coordination of two $[Ge_9Zn]^{2-}$ units to two Ge atoms of a $[Ge_9]^{4-}$ cluster yields the oligomer $[(Ge_9Zn)\text{-}(\eta{:}\eta^1\text{-}Ge_9)\text{-}(ZnGe_9)]^{8-}$ (**19**) [39]. Such a donor–acceptor liaison reminds of frustrated Lewis

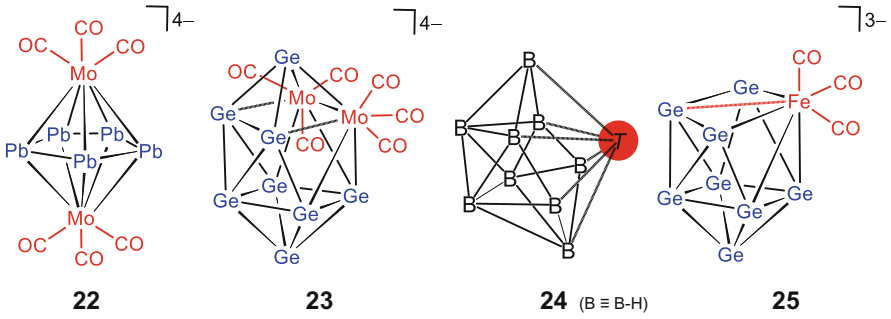

Fig. 9 Clusters with $2n$ and $2n + 3$ skeletal electrons [T= Ru(η^6-C_6Me_6)]

acid base pairing which has recently been discussed for boryl-substituted Ge_9 clusters [40].

Alternatively, the coordination of a second Zintl cluster to the heteroatom can take place through a triangular cluster face, and is realized in $[(\eta^4\text{-}Ge_9)Zn(\eta^3\text{-}Ge_9)]^{6-}$ and $[(\eta^4\text{-}Ge^9)Sn(\eta^3\text{-}Ge_9)]^{4-}$ (**20**). Molecular orbital analyses show that the Zn and Sn atoms of the Ge_9Zn and Ge_9Sn fragments, respectively, coordinate to a second $[Ge_9]$ cluster in different ways. $[Ge_9Zn]^{2-}$ acts – as shown above – as electron acceptor when it interacts with the triangular face of a $[Ge_9]^{4-}$ unit, whereas the Sn atom of the $[Ge_9Sn]^{2-}$ unit donates two electrons to the triangular face of a second cluster which is considered as $[Ge_9]^{2-}$ [41].

In another variant a second *closo* cluster is attached via a covalent bond through the heteroatom. In this case *R* in the isolobal fragment Zn-*R* refers to a second heteroatomic cluster by forming a bond between the two heteroatoms, which is realized in $[Ge_9Zn\text{-}ZnGe_9]^{6-}$ [39] (**21**) and in the structurally analogous $[Pb_9Cd\text{-}CdPb_9]^{6-}$ [42]. In both cases Zn and Cd, respectively, adopt the low-valent oxidation state of +1.

Interestingly, there are cases which deviate from the Wade–Mingos rules. The cluster anions $[Pb_5\{Mo(CO)_3\}_2]^{4-}$ [43] (**22**, Fig. 9) and $[Ge_8\{Mo(CO)_3\}_2]^{4-}$ (**23**) [44] possess $5 \times 2 + 4 = 14$ and $8 \times 2 + 4 = 20$ electrons, respectively, corresponding to $2n$ electron-deficient clusters [$14 = 2n$ ($n = 7$) and $20 = 2n$ ($n = 10$)]. Such clusters with less electrons are also known for boranes, e.g. in *closo*-$[(\eta^6\text{-}C_6Me_6)RuB_9H_9)]$ (**24**) [45].

In $[Ge_8Fe(CO)_3]^{3-}$ [44] (**25**) one Ge vertex with two skeletal electrons is formally replaced by the isolobal fragment $Fe(CO)_3$, and thus **25** is isoelectronic and isostructural to the known paramagnetic 21-electron cluster $[Ge_9]^{3-}$ with a structure between that of a nine-atomic *closo* cluster (20 skeletal electrons) and a nine-atomic *nido* cluster (22 skeletal electrons). Similarly, $[Ge_9Ni(CO)]^{3-}$ [46] with an additional two-electron Ni(CO) vertex corresponds to a ten-atomic 23-electron cluster and thus also has a structure between a *closo* and a *nido*-type cluster.

3 Condensed and Discrete Intermetalloid Clusters in Intermetallic Compounds: From Wade–Mingos Rules to the Superatom Approach

A characteristic feature of intermetallic compounds is that all metal atoms have high coordination numbers. Frank und Kasper [47, 48] introduced a defined number of coordination polyhedra that allow a close packing of atoms of different sizes with coordination polyhedra, reaching coordination numbers of the hosting atoms between 12 and 16. On the other hand, Sn-rich intermetallics form a number of compounds with transition metals, *T*-Sn, in which the transition metals have a lower coordination number and are exclusively connected to tin atoms (Fig. 10). A coordination number of eight is predominant for *T*:Sn ratios of 1:2, 1:2.33, 1:3,

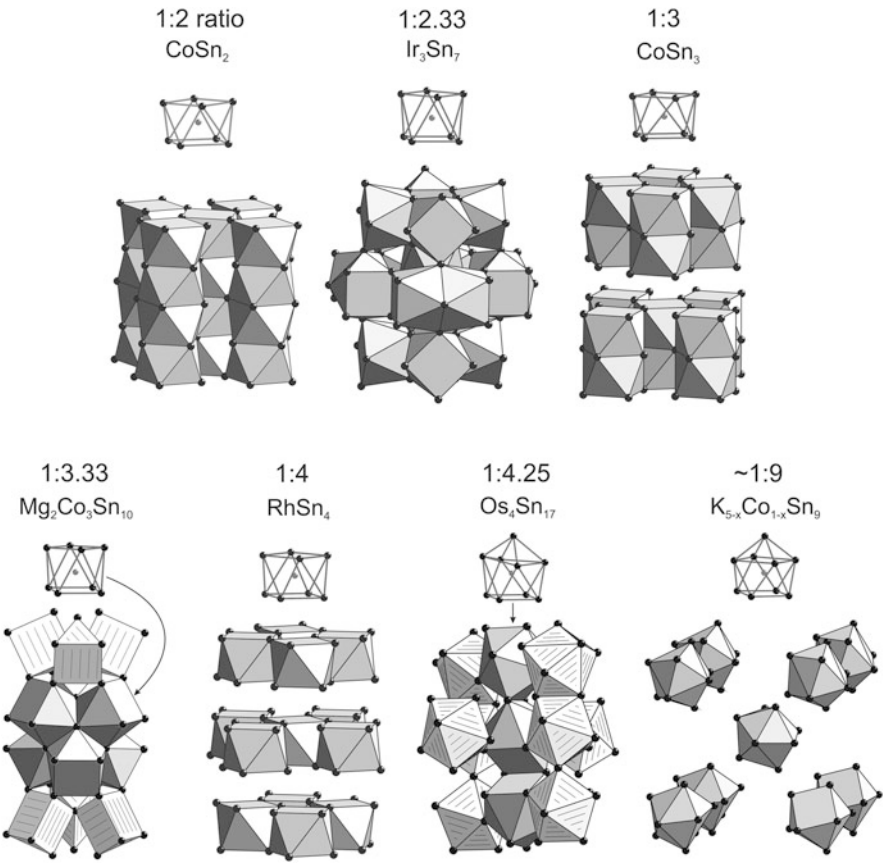

Fig. 10 The structures of binary and ternary Sn-rich intermetallic compounds containing transition metal (*T*)-centered tetragonal Sn_8-antiprisms. The respective ratio of *T* to Sn is shown. *From Chemistry – A European Journal* [50], *copyright Wiley-VCH GmbH. Reproduced with permission*

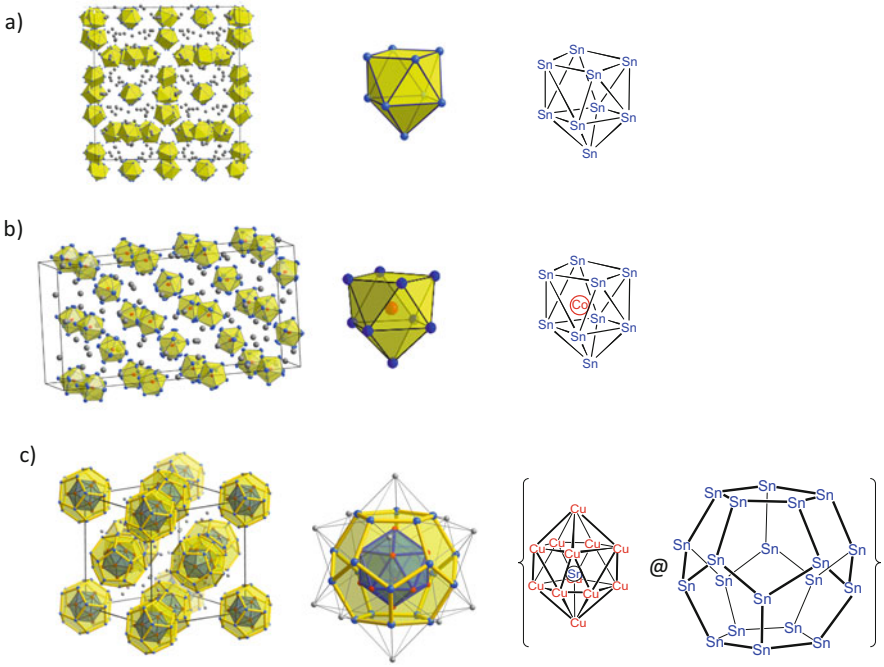

Fig. 11 Solid state compounds which contain discrete intermetalloid clusters. a) K_4Sn_9 and two representations of $[Sn_9]^{4-}$; b) $K_{13-x}Co_{1-x}Sn_{17}$ and two representations of $[Co@Sn_9]^{5-}$; c) $K_{12}Cu_{12}Sn_{21}$ and two representations of $[Sn@Cu_{12}@Sn_{20}]^{12-}$ with and without K atoms. Sn, Cu/Co, and K atoms are shown in blue, red, and gray, respectively

1:3.33, and 1:4, as in $CoSn_2$, Ir_3Sn_7, $CoSn_3$, $Mg_2Co_3Sn_{10}$, and $RhSn_4$, respectively, in which the *T* atoms are located at the center of a tetragonal prism or antiprism (Fig. 10). The $[T@Sn_8]$ cages are closely related to that of molecular transition metal complexes or molecular endohedral tin cluster anions, however, with the crucial difference that the Sn clusters in intermetallic compounds share edges and faces. Compounds with a slightly higher *T*:Sn ratio of 1:4.25 contain polyhedra with nine vertices, which are less condensed, as shown in Fig. 10 for Os_4Sn_{17} with its edge-sharing, nine-atomic $[T@Sn_9]$ clusters.

The presence of electropositive elements gives the ensemble a strong ionic character, and the polyhedra are separated, as it is observed for Zintl phases like $[T@Sn_n]$. In such phases a salt-like description can be used by a formal transfer of all valence electrons of the electropositive to the electronegative metal component. Thus, K_4Sn_9 consists of K cations and the anionic Zintl clusters $[Sn_9]^{4-}$ (Fig. 11a). Upon their reaction with bulk metals or alloys the alkali metals act as "*metal scissors*" [49], since they cut the bulk into smaller individual cluster units. The number of Zintl phases, which contain tetrel element clusters with larger discrete deltahedral units ($n > 4$) is rather limited (Table 2), whereas there are more examples for deltahedral triel element clusters in intermetallic compounds. They carry much

Table 2 Solids with larger, empty and filled, discrete tetrel element clusters

Cluster	Compound
$[Ge_9]^{4-}$	K_4Ge_9 [52], Cs_4Ge_9 [53]
$[Sn_9]^{4-}$	K_4Sn_9 [54]
$[Pb_9]^{4-}$	K_4Pb_9 [55], Rb_4Pb_9 [56], Cs_4Pb_9 [57], $Cs_{10}K_6Pb_{36}$ [56]
$[Si_9]^{4-}/[Si_4]^{4-}$ (1:2)	$K_{12}Si_{17}$ [58], $Rb_{12}Si_{17}$ [59]
$[Ge_9]^{4-}/[Ge_4]^{4-}$ (1:2)	$Na_{12}Ge_{17}$, $K_{12}Ge_{17}$ [60]
$[Sn_9]^{4-}/[Sn_4]^{4-}$ (1:2)	$K_{12}Sn_{17}$, $Rb_{12}Sn_{17}$ [58]
$[Sn_9]^{4-}/[Sn_4]^{4-}$ (6:7)	$K_{52}Sn_{82}$ [61], $Cs_{52}Sn_{82}$ [61]
$[Co@Sn_9]^{5-}$	$K_{5-x}Co_{1-x}Sn_9$ [50]
$[Co@Sn_9]^{5-}/[Sn_4]^{4-}$ (1:2)	$K_{13-x}Co_{1-x}Sn_{17}$ [51]
$[Ni@Sn_9]^{4-}/[Sn_4]^{4-}$ (1:2)	$Na_{12}Ni_{1-x}Sn_{17}$ [51]
$[Pd@Sn_9]^{4-}/[Sn_4]^{4-}$ (1:2)	$K_{12}Pd_{1-x}Sn_{17}$ [49]
$[Rh@Pb_9]^{4-}$	K_4RhPb_9 [49]
$[Sn@Cu_{12}@Sn_{20}]^{12-}$	$A_{12}Cu_{12}Sn_{21}$ (A = Na–Cs) [3]

higher negative charges, can generally not be isolated as molecular units, and are not included in this review. A comprehensive overview has been published elsewhere [9].

Electron-precise Zintl phases are primarily restricted to intermetallic compounds of main group elements. However, the concept of *metal scissors* can also be applied for transition metal-containing alloys. Two-step syntheses of pre-formed binary Co-Sn, Ni-Sn, Pd-Sn, and Rh-Pb alloy mixtures with the respective alkali metals potassium or sodium yield the compounds $K_{5-x}Co_{1-x}Sn_9$ [50], $K_{13-x}CoSn_{17}$ [51], $Na_{12}Ni_{1-x}Sn_{17}$ [51], $K_{12}Pd_{1-x}Sn_{17}$, and K_4RhPb_9 [49] which contain the polyanions $[Co@Sn_9]^{5-}$, $[Ni@Sn_9]^{4-}$, $Pd@Sn_9]^{4-}$, and $[Rh@Pb_9]^{4-}$, respectively (Table 2, Fig. 11).

The ternary compounds with nine-atomic clusters can be regarded as filled variants of the binary phases K_4Sn_9 [54], $K_{12}Sn_{17}$ [58, 59], or K_4Pb_9 [55]. In all cases the ion packing and the structure type are retained despite the filling of the clusters with a transition metal atom. With a desired electron configuration of d^{10} for the transition metal, the negative charge of the $[Sn_9]^{4-}$ polyanion is increased by 1 for d^{10}-Co^- and remains unchanged for d^{10}-Ni^0 and d^{10}-Pd^0 (Table 3). The correlation between the occupancy of the positions of the potassium and the transition metal atoms in $K_{5-x}Co_{1-x}Sn_9$ and $K_{13-x}Co_{1-x}Sn_{17}$ shows that the species are electron-precise valence compounds, which are well established for Zintl phases. The presence of electron-precise Zintl phases is well documented for $K_{13-x}Co_{1-x}Sn_{17}$ for which – due to its diamagnetism – MAS-NMR spectra were recorded. As depicted in Fig. 12 the ^{119}Sn NMR spectrum shows three groups of signals corresponding to $[Sn_4]^{4-}$ and the simultaneously present $[Sn_9]^{4-}$ and $[Co@Sn_9]^{5-}$ units.

Raman spectroscopy can be used to prove the presence of filled clusters in ternary alloys. In this case the spectra show characteristic Raman modes at higher wave

Table 3 Selected ordered $[T@Sn_9]^{n-}$ units (T = Ni, Co, Pd) in ternary intermetallic compounds and their relation to the empty $[Sn_9]^{4-}$ cluster

Compound	Cluster	Approximate symmetry	Occupancy of T/% [a]
K_4Sn_9 [62]	$[Sn_9]^{4-}$	C_{4v}	0
$Na_{12}Ni_{1-x}Sn_{17}$ ($x \approx 0.07$) [51]	$[Ni@Sn_9]^{4-}$ [b]	C_{4v} D_{3h}	95 93
$K_{5-x}Co_{1-x}Sn_9$ ($x \approx 0.2$) [50]	$[Co@Sn_9]^{5-}$ [c]	C_{4v} D_{3h} D_{3h} D_{3h}	82 80 76 79
$K_{13-x}Co_{1-x}Sn_{17}$ ($x = 0$, $x \approx 0.05$) [51]	$[Co@Sn_9]^{5-}$	C_{4v}	100
$K_{12}Pd_{1-x}Sn_{17}$ ($x \approx 0.53$) [49]	$[Pd@Sn_9]^{4-}$ [d]	C_{4v} C_{4v} D_{3h}	56 26 54

Adapted from Ref. [49]
[a]With respect to $[Sn_9]^{4-}$
[b]Two
[c]Four
[d]Three independent clusters per unit cell

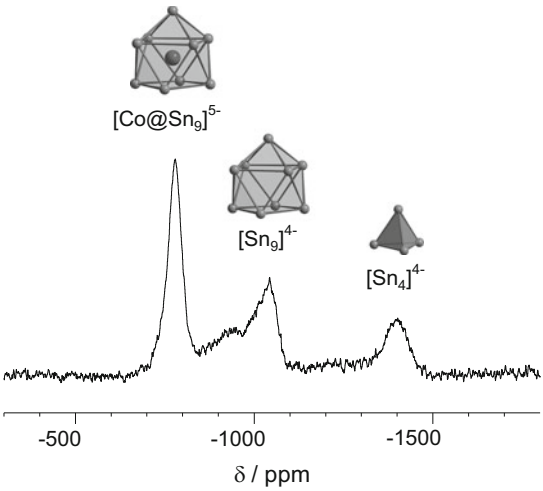

Fig. 12 ^{119}Sn MAS-NMR spectrum of $K_{13-x}Co_{1-x}Sn_{17}$ [51]

numbers (A and B in Fig. 13) in the range of 360 cm^{-1}, whereas the typical modes of the empty cages appear in the range of 100–250 cm^{-1} [63].

Like the empty Zintl clusters, the filled variants also tend to be disordered, and they show structures between that of a mono-capped square antiprism (C_{4v}) and a tri-capped trigonal prism (D_{3h}). Since the structure types allow a certain degree of empty alkali metal positions, filled and empty clusters may appear superimposed ($x > 0$). Nine-atomic clusters are among the smallest possible discrete deltahedral clusters, and the incorporation of transition metal atoms only leads to a slight

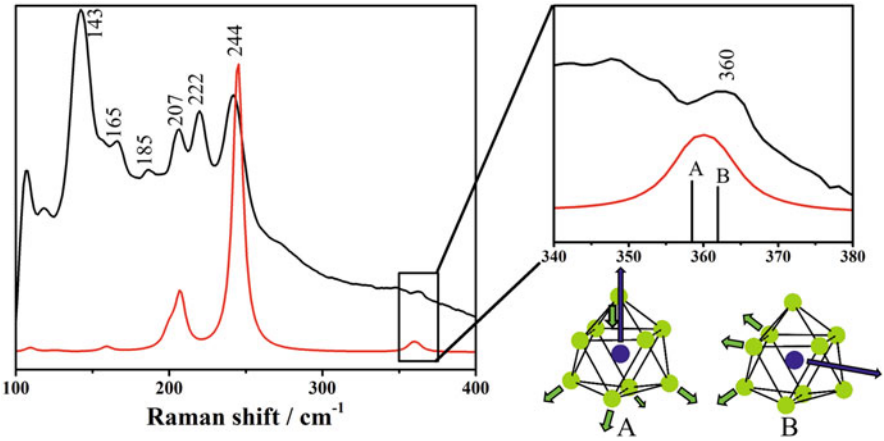

Fig. 13 The Raman spectrum of the precursor "$K_5Co_{1.2}Ge_9$" (black lines) and the calculated Raman spectrum of $[Co@Ge_9]^{5-}$ (red lines); the enlarged section shows the resonances of the vibration modes "**A**" and "**B**". *From Angewandte Chemie* [63], *copyright Wiley-VCH GmbH. Reproduced with permission*

increase of their volume. Since empty and full clusters appear superimposed, this increase reflects an average of empty and filled clusters, and thus the largest increase of ca. 15% corresponds to the highest filling degree of the cluster with a transition metal.

The application of the electron counting rules for Zintl phases ("8-N rule") in combination with the Wade–Mingos rules has proved to be extremely powerful tools for the understanding of intermetallic compounds comprising discrete clusters [9], and there is no comparable straightforward concept for the rationalization of transition metal-containing intermetallic compounds. A pre-formed Cu-Sn alloy reacts with the alkali metals A = Na, K, Rb, and Cs to the ternary species $A_{12}Cu_{12}Sn_{21}$ [3], that represent a new type of intermetallic compound with a multi-shell Matryoshka-type cluster $[Sn@Cu_{12}@Sn_{20}]$. Its electron count can be traced back to a Zintl-type salt-like approach, but not fulfilling 8-N or Wade–Mingos rules. These transition metal-rich species mark a new borderline between Zintl phases and typical intermetallic compounds. In this case the multi-shell clusters, otherwise used for a topological description of complex structures of alloys, represent discrete building blocks, which are in a salt-like manner exclusively surrounded by alkali metal cations, and their electronic structure can be treated by an isolated cluster approach. The compounds $A_{12}Cu_{12}Sn_{21}$ are diamagnetic and possess a small band gap, and thus a salt-like description $\{(A^+)_{12}[Sn@Cu_{12}@Sn_{20}]^{12-}\}$ by analogy with Zintl phases is justified. Similar anionic multi-shell clusters can also be obtained in solution-based reactions. E.g. the iso-valence electronic polyanion $[As@Ni_{12}@As_{20}]^{3-}$ was synthesized from As_7^{3-} and $Ni(COD)_2$ in ethylenediamine solution [13], and the recently described species $[Sb@T_{12}@Sb_{20}]^{3-}$ (T = Ni, Pd) [64, 65] were also obtained from solution.

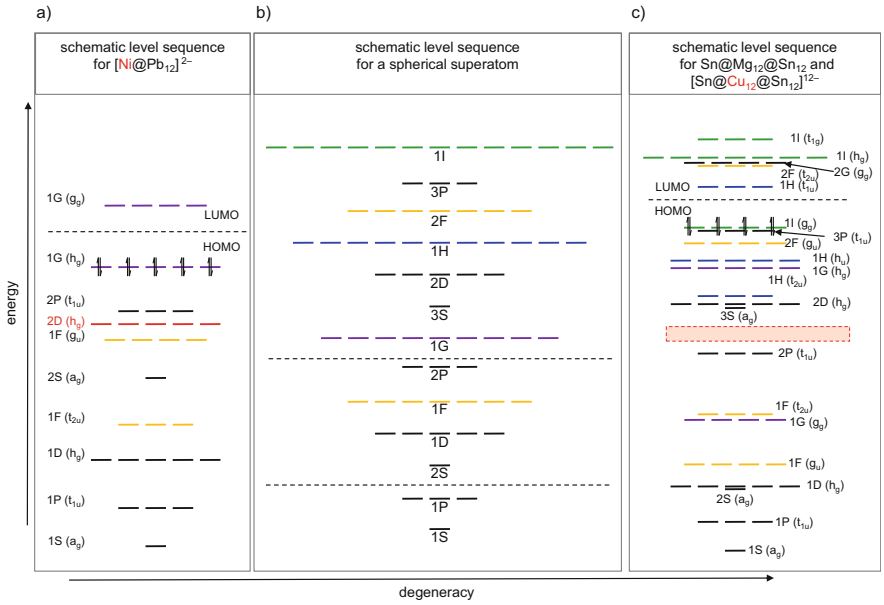

Fig. 14 Schematic orbital level sequences and degeneracies for (**a**) the cluster $[Ni@Pb_{12}]^{2-}$, (**b**) the spherical superatom cluster (jellium model) with lower and upper dashed lines representing filled levels for $[Mg_4]$ and $[Al_{13}]^-$, respectively, and (**c**) hypothetical $[Sn@Mg_{12}@Sn_{20}]$ with d orbitals of Cu atoms in $[Sn@Cu_{12}@Sn_{20}]^{12-}$ shown as a red block between the 2P and 3S levels and in accordance with the calculated levels shown in Fig. 15. Energy is given in arbitrary units. Electron filling in (**b** and **c**) is shown only for the highest occupied orbitals (HOMOs). Level sequences are adapted from Refs. [68–70]

The "superatom approach," originally developed for spherical bare atom clusters, reveals the presence of "locally delocalized electrons" in solid $A_{12}Cu_{12}Sn_{21}$. In this approach, the electrons are regarded as fully delocalized but constrained in "a box" defined by the atom cores, which leads to quantized electronic states, some of them with high degeneracy as they are known and labeled for electrons in (spherical) atoms, but with the difference that for all shells the full degeneracy S, P, D, F, G, etc., is possible (Fig. 14b). Clusters are stable when the number of valence electrons coincides with a closed-shell structure based on the jellium model [66, 67].

The superatom approach was developed many years ago for metal clusters observed in mass spectra [68]. An assembly of 4 Mg atoms or 13 Al atoms carrying one negative charge, $[Mg_4]$ and $[Al_{13}]^-$, comprises 8 and 40 valence electrons, respectively, which allow for the filling of the energy levels of a superatom (cluster) according to $[1S^2\ 1P^6]$ and $[1S^2\ 1P^6\ 1D^{10}\ 2S^2\ 1F^{14}\ 2P^6]$, respectively (see dashed lines in Fig. 14b) [68]. However, the idea of filling the electronic states according to the degeneracy arising from the spherical symmetry of "free atoms" is not restricted to filled or multi-shell clusters, but can also be applied to cage molecules. The degeneracy of levels is overturned in multi-electron systems, as it is known from the atomic orbitals of free atoms with more than one electron. In clusters the orbital

sequences are changed, and a level splitting of the electronic orbitals occurs due to lower structural symmetries. Interestingly, the cages $[E_9]^{4-}$ (E = Si–Pb) and $[Al@Al_{12}]^-$ both possess 40 valence electrons and thus have the same favorable jellium closed-shell configuration, although they have completely different structures. It is well known that $[E_9]^{4-}$ and also their filled variants such as $[Cu@E_9]^{3-}$ show a fluctional behavior in solution (see below), and on average over time their structures correspond to a spherical atom arrangement.

The structures of the filled icosahedral Zintl ion clusters $[T@Pb_{12}]^{2-}$ (T = Ni, Pd, Pt), $[Rh@Pb_{12}]^{3-}$, and $[Ir@Sn_{12}]^{3-}$, which are exclusively obtained in solution from the reaction of $[E_9]^{4-}$ (E = Ge – Pb), are similar to that of $[Al@Al_{12}]^-$, but they have a different number of electrons, and they host transition metal atoms T with a d^{10} electron configuration. The orbitals of the T atoms either do not at all interact with the orbitals of the outer atoms, or the contribution of bonding and anti-bonding interactions cancels each other out. Figure 14a shows the schematic orbital diagram of $[Ni@Pb_{12}]^{2-}$ [62], and the relation to the levels of a superatom is depicted in Fig. 14b. The levels 1F and 1G shown in yellow and pink in Fig. 14a, b, respectively, are split due to the icosahedral symmetry and represent the HOMO and LUMO of $[Ni@Pb_{12}]^{2-}$. Therefore, clusters with 50 valence electrons are stable, even though 50 do not correspond to a "magic number" in the superatom approach. The levels of the centering transition metal are located between the cluster levels in the bonding region, as indicated in red in Fig. 14a. Bare tetrel atom clusters are thus stable with a charge of 2- ($12 \times 4 + 2 = 50$), and additional charges of the cluster units can occur from the quest of the endohedral transition metal atom to achieve a stable d^{10} configuration. Including the contributions of the inert d^{10} metals T, all clusters $[T@Pb_{12}]^{2-}$ (T = Ni, Pd, Pt), $[Rh@Pb_{12}]^{3-}$ and $[Ir@Sn_{12}]^{3-}$ have 60 valence electrons, and all of them are almost perfectly icosahedral.

All Matryoshka-type clusters comprise 108 valence electrons which fit nicely in the degenerate orbitals of a superatom considering the symmetry reduction of point group I_h of the clusters. This model takes into account that the atoms in the Matryoshka-type clusters $[Sn@Cu_{12}@Sn_{20}]^{12-}$ and $[As@Ni_{12}@As_{20}]^{3-}$ have, on the one hand, filled d shells [($3d^{10}$)-Cu, ($4d^{10}$)-Sn, ($3d^{10}$)-Ni, ($3d^{10}$)-As] which then act as inert shells, and, on the other hand, have remaining 108 outer electrons [($4s^1$)-Cu, ($5s^25p^2$)-Sn, ($4s^0$)-Ni, ($5s^25p^3$)-As with additional 12 and 3 electrons according to the cluster charge], that fill the expected number of states derived for the jellium sphere. Thus, hypothetical $[Sn@Mg_{12}@Sn_{20}]$ serves as an appropriate model (Fig. 14b). According to the energetic sequence and the nodal shape of the sequence, the superatom orbitals arise in the order 1S, 1P, 2S, 1D, 1F, 2P, 1G, 3S, 2D, 1H, 2F, 3P, 1I, corresponding to the 54 lowest-lying valence molecular orbitals, that take up 108 valence electrons. In the icosahedral ligand field the 1H, 2F, and 1I superatom orbitals are split (in Fig. 14 highlighted in blue, yellow, and green, respectively), and the lowest 1I orbital (g_g) is the HOMO of the superatom, whereas the triply degenerate middle 1H (t_{1u}) orbital is the LUMO [61]. The inert d orbitals of the Cu atom appear as narrow block, as indicated by the red field in Fig. 14c.

Since the $[Sn@Cu_{12}@Sn_{20}]^{12-}$ unit is part of the intermetallic compound $K_8Cu_{12}Sn_{21}$, a single point calculation of the anion can directly be compared to

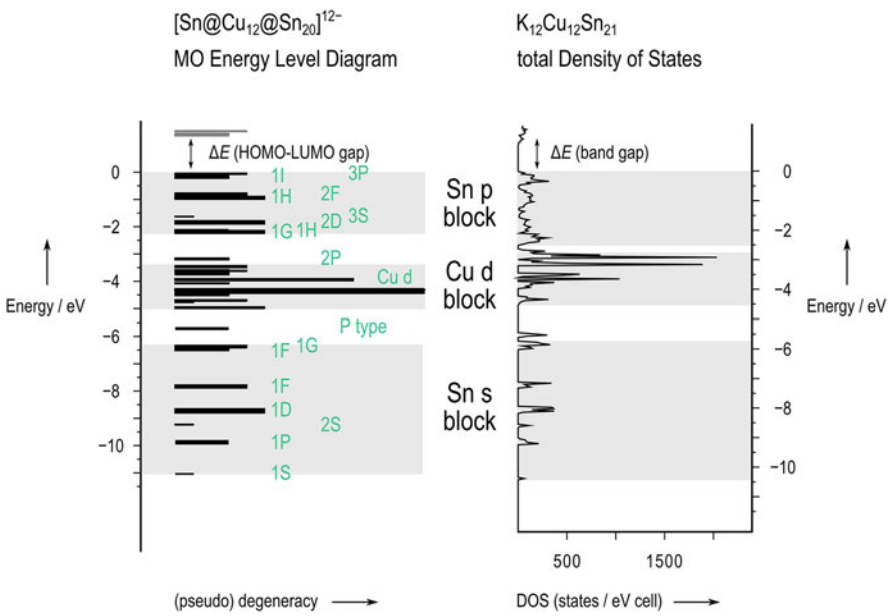

Fig. 15 (**a**) MO energy level diagram for the $[Sn@Cu_{12}@Sn_{20}]^{12-}$ cluster anion (single point calculation); (**b**) total density of states for $K_{12}Cu_{12}Sn_{21}$ (band structure calculation). The HOMO energy and the Fermi level were set to 0 eV. Reprinted from Ref. [3] with permission from the American Chemical Society. Copyright American Chemical Society, 2011

the density of states calculated for $K_8Cu_{12}Sn_{21}$ with inclusion of the alkali metal atoms. The calculated density of states (DOS) plot from DFT band structure calculations approves that the $A_{12}Cu_{12}Sn_{21}$ phases provide a textbook example for a molecular unit within a solid state compound, since its gaps and pseudo-gaps are completely analogous to the energetic ordering of the cluster MOs (Fig. 15). The calculated cluster MOs also match nicely the schematic picture developed in Fig. 14.

The molecular orbitals of $[Sn@Cu_{12}@Sn_{20}]^{12-}$ shown in Fig. 16 can be classified with labels indicating the numbers of radial and angular nodes as expected for spherical shell models of clusters in Fig. 14. The highest degeneracy I reflects further angular nodes, whereas *s*-, *p*-, *d*-, and *f*-type orbitals are known from atomic orbitals.

It has to be mentioned that there are also deviations from the electron-precise clusters like the molecular ionic examples $[E_9]^{3-}$ (E = Si–Pb) and $[Sb@Pd_{12}@Sb_{20}]^{4-}$ [64] as well as the unit $[Rh@Pb_9]^{4-}$ in K_4RhPb_9 [49], all of which are open-shell representatives.

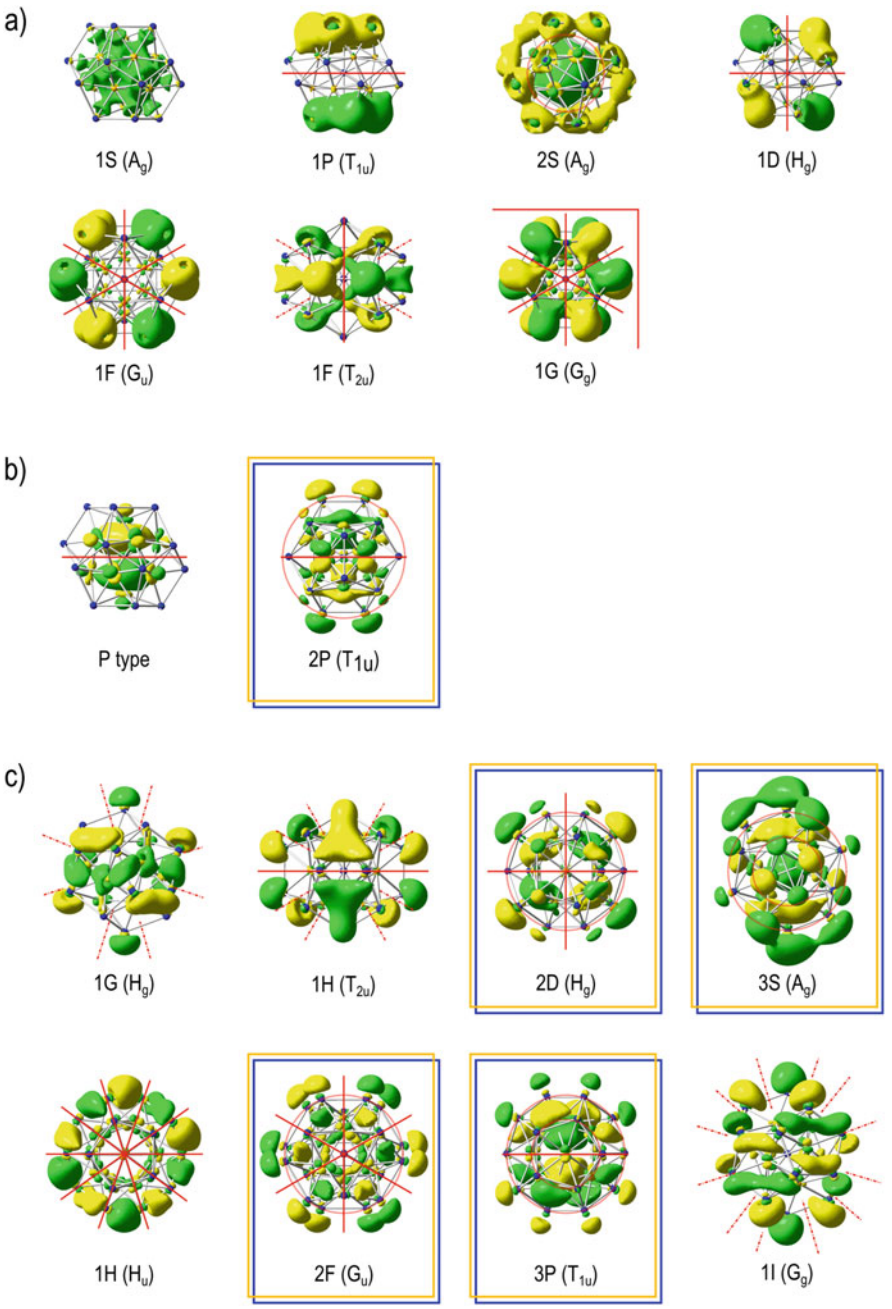

Fig. 16 Selected molecular orbitals (MOs) of the $[Sn@Cu_{12}@Sn_{20}]^{12-}$ cluster anion with emphasis on radial and angular nodes with (**a**) mainly Sn s-type atomic contributions, (**b**) P-type MOs with p contributions from the central Sn atom, and (**c**) Sn p-type contributions from the Sn atoms of the $\{Sn_{20}\}$ shell. Red circles indicate radial nodal surfaces, red solid lines show angular nodes perpendicular or parallel to the plane of projection, red dotted lines symbolize conical angular

4 Endohedral Intermetalloid Clusters

4.1 Building Principles of Intermetalloid Clusters in Solution

As outlined in Sect. 3 there are only a few intermetallic compounds with discrete endohedral or discrete multi-shell tetrel atom clusters, but reactions of the most abundant homoatomic $[E_9]^{4-}$ clusters lead to a large variety of intermetalloid clusters [71–76], and the formation of their transition metal complexes has already been described in Sect. 1. Possible reaction pathways yielding clusters with transition metal atoms encapsulated inside deltahedral nine-, ten-, or twelve-atomic cages leading to endohedral clusters are summarized in Fig. 17. Even though a large variety of filled clusters are known, a straightforward reaction sequence for the

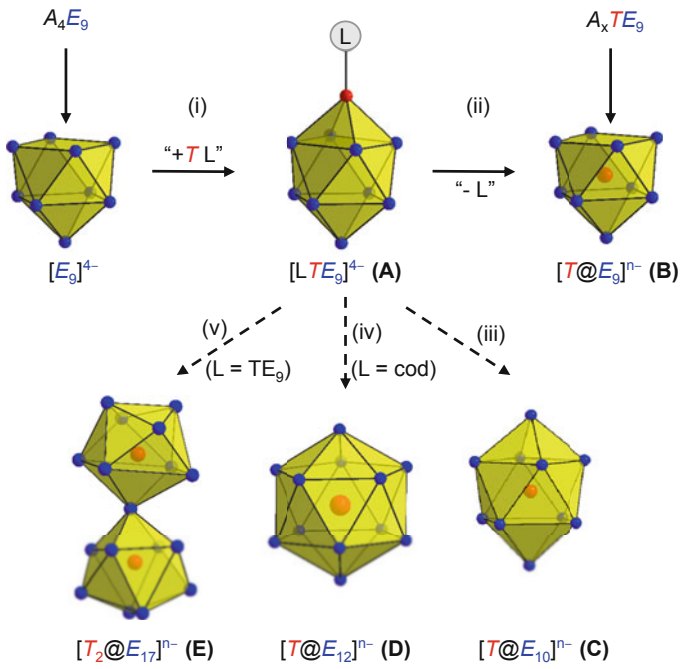

Fig. 17 Reaction of the mono-capped square-antiprismatic $[E_9]^{4-}$ Zintl clusters with organometallic compounds and principle pathways for a step-by-step cluster growth to endohedral clusters $[T@E_9]^{n-}$ (n = 3–6), $[T_2@E_{17}]^{n-}$ (n = 4–6), $[T@E_{10}]^{n-}$ (n = 2, 3), and $[T@E_{12}]^{n-}$ (n = 2, 3). Dashed arrows stand for dimerization, fragmentation, and rearrangement of cluster vertices that lead to larger intermetalloid clusters. *E* atoms are drawn in blue, *T* atoms in red, and clusters are shown as yellow polyhedra

Fig. 16 (continued) nodes. Reprinted from Ref. [3] with permission from the American Chemical Society. Copyright American Chemical Society, 2011

migration of the transition metal into the cluster is still missing. However, the isolation of a few striking examples of structurally characterized anions points towards a step-wise reaction as pointed out in Fig. 17. On the one hand, the formation of **15** (Fig. 5), in which the Cu atom of a $Cu(PR_3)$ fragment is attached to the open square of a $[Ge_9]^{4-}$ cluster (**A**), can be seen as the first step according to reaction path (i). On the other hand, the formation of **17** (Fig. 8) indicates that the PR_3 unit in **15** might act as a labile leaving group, thus allowing the ligand-free Cu atom to migrate into the cluster (ii) to give a filled cluster (**B**). Ligand replacement may as well lead to the attachment of a second empty cluster to the Cu atom. Thus, **17** can also be seen as a precursor for cluster growth which after fragmentation leads to filled ten- (**C**) and twelve-atomic (**D**) clusters following reaction paths (iii) and (iv), respectively (Fig. 17). A direct formation of a twelve-atomic cluster from a precursor complex **A** has only been reported for $[Ir@Sn_{12}]^{3-}$, starting from the preliminarily formed unit $[(cod)Ir(\eta^4\text{-}Sn_9)]^{3-}$ (**13**) (cod = 1,5-cyclooctadiene, Fig. 5), which, however, must be accompanied by a subsequent fragmentation reaction. The attachment of a second filled cluster to the transition metal atom through ligand exchange in complexes of type **15** (v) might be intermediates on the way to $[T_2@E_{17}]^{n-}$ clusters, in which two endohedral nine-atomic clusters share one cluster vertex (**E**).

4.2 *Endohedral Clusters Formed in Solution and as Building Blocks in Intermetallic Compounds*

Despite their expected stability based on the Wade–Mingos rules or the superatom approach, empty icosahedral $[E_{12}]^{2-}$ clusters are completely unknown. However, in case of the smaller nine- and ten-atomic deltahedral clusters both, filled and empty representatives, are known, and thus the role of the centering transition metal atoms can be examined in more detail. As shown in Fig. 14 the electronic states of an encapsulated d^{10} transition metal in $[T@E_{12}]^{n-}$ appear as an inert shell which does not significantly contribute to the skeletal electron number, indicating a steric template effect for the transition metal ion. Since nine- and ten-atomic clusters are considerably smaller, a stronger orbital interaction between the centering and the cluster vertex atoms is most likely, but interestingly most of the known examples comprise d^{10} transition metal guest atoms.

4.2.1 Filled Nine-Atomic Clusters

The reactions of $[E_9]^{4-}$ (E = Ge, Sn, Pb) with metal-organic compounds lead to endohedral clusters $[T@E_9]^{n-}$, with a charge n depending on the encapsulated transition metal atom. The known examples obtained this way together with examples $[T@E_9]^{n-}$ prepared via solid state reactions are summarized in Table 4. The

Table 4 Cluster volumes of various ordered $[T@Sn_9]^{n-}$ units calculated with VESTA [77] and their relation to the empty $[Sn_9]^{4-}$ cluster

Compound	Cluster[a]	Approx. symm.	Occupancy of *T*/%	Min./max. *TM-E* distance/Å ((A = Angström))	Av. cluster vol./Å^3	Volume increase/%	Ref.
$K_5Ge_9(OH)(NH_3)_{11}$	$[Ge_9]^{4-}$	C_{4v}	–	–	22.1	–	[78]
$K_6CoGe_9(OH)(NH_3)_{16}$	$[Co@Ge_9]^{5-}$	D_{3h}	100	2.331/2.374	26.4	19.9	[63]
(K[222] crypt)$_3$NiGe$_9$(en)$_{1.5}$	$[Ni@Ge_9]^{3-}$ [c]	C_{4v} C_{4v}	100 100	2.254/2.406 2.302/2.410	25.2 25.7	14.5 16.8	[79]
$K_5Sn_9(OH)(NH_3)_{11}$	$[Sn_9]^{4-}$	C_{4v}	–	–	32.6	–	[80]
$K_{13}CoSn_{17}$	$[Co@Sn_9]^{5-}$ [d]	C_{4v}	100	2.581/2.680	35.9	10.0	[51]
$K_{12.92}Co_{0.95}Sn_{17}$	$[Co@Sn_9]^{5-}$ [d]	C_{4v}	100	2.563/2.670	35.5	8.8	[51]
$K_{5-x}Co_{1-x}Sn_9$ ($x \approx 0.2$)	$[Co2@Sn_9]^{5-}$ $[Co1@Sn_9]^{5-}$ $[Co4@Sn_9]^{5-}$ $[Co3@Sn_9]^{5-}$	C_{4v} D_{3h} D_{3h} D_{3h}	82 80 79 76	2.517/2.693 2.561/2.660 2.542/2.702 2.561/2.683	35.3 35.4 35.4 35.4	8.2 8.5 8.5 8.5	[50]
(K[222]crypt)$_3$KCo$_{0.87}$Sn$_9$	$[Co@Sn_9]^{4-}$ [c]	C_{4v}	87	2.579/2.866	36.1	10.6	[81]
(K[222]crypt)$_3$KCo$_{0.68}$Sn$_9$	$[Co@Sn_9]^{4-}$ [c]	C_{4v}	68	2.553/2.886	35.4	8.5	[82]
$Na_{12}Ni_{1-x}Sn_{17}$ ($x \approx 0.07$)	$[Ni1@Sn_9]^{4-}$ $[Ni2@Sn_9]^{4-}$	C_{4v} D_{3h}	95 93	2.568/2.754 2.564/2.704	36.2 36.2	10.9 10.9	[51]
(K[222]crypt)$_3$KNiSn$_9$	$[Ni@Sn_9]^{4-}$	C_{4v}	100	2.580/2.732	36.1	10.6	[83]
(K[18]c6)$_3$KNiSn$_9$(benz)$_3$	$[Ni@Sn_9]^{4-}$	C_{4v}	60	2.522/2.738	34.8	6.7	[83]
(K[18]c6)$_4$NiSn$_9$(en)$_{1.5}$	$[Ni@Sn_9]^{4-}$	C_{4v}	32	2.486/2.784	33.8	3.6	[83]
(K[222] crypt)$_3$CuSn$_9$(dmf)$_3$	$[Cu@Sn_9]^{3-}$	D_{3h}	100	2.610/2.700	37.3	14.3	[84]
(K[18]c6)$_3$CuSn$_9$(mes)(thf)(NH$_3$)	$[Cu@Sn_9]^{3-}$	D_{3h}	100	2.599/2.701	37.0	13.4	[85]
$K_7RuSn_9(OH)(NH_3)_{10}$	$[Ru1@Sn_9]^{6-}$	D_{3h}	100	2.612/2.717	38.3	17.4	[63]
	$[Ru2@Sn_9]^{6-}$	D_{3h}	100	2.641/2.699	38.8	18.9	

(continued)

Table 4 (continued)

Compound	Cluster[a]	Approx. symm.	Occupancy of *T*/%	Min./max. *TM-E* distance/Å ((A = Angström))	Av. cluster vol./Å^3	Volume increase/%	Ref.
$K_{12}Pd_{1-x}Sn_{17}$	$[Pd1@Sn_9]^{4-}$ [d] $[Pd2@Sn_9]^{4-}$ [d] $[Pd3@Sn_9]^{4-}$ [d]	C_{4v} D_{3h} C_{4v}	56 54 26	2.561/2.792 2.554/2.765 2.470/2.782	36.0 36.2 34.0	10.3 10.9 4.3	[49]
(K[222] crypt)$_5Co_2Sn_{17}(en)_n$ [b]	$\{Co1@Sn_9\}$ $\{Co2@Sn_9\}$	C_{2v} C_{2v}	100 100	2.383/2.713 2.391/2.749	36.4 36.6	11.6 12.2	[50]
(K[222]crypt)$_5Co_2Sn_{17}$(en)(tol) [b]	$\{Co1@Sn_9\}$ $\{Co2@Sn_9\}$	C_{2v} C_{2v}	100 100	2.406/2.721 2.406/2.770	36.5 36.4	11.9 11.6	[82]
(K[222] crypt)$_4Ni_2Sn_{17}(en)_2$ [b]	$\{Ni1@Sn_9\}$ $\{Ni2@Sn_9\}$	C_{2v} C_{2v}	100 100	2.387/2.732 2.382/2.740	36.6 36.5	12.2 11.9	[86]
(K[222] crypt)$_3K_3Rh_2Sn_{17}(en)_4$ [b]	$\{Rh1@Sn_9\}$ $\{Rh2@Sn_9\}$	C_{2v} C_{2v}	100 100	2.497/2.760 2.497/2.761	38.6 38.5	18.3 18.0	[87]
$Li_4Pb_9(NH_3)_{17}$	$[Pb_9]^{4-}$	C_{4v}	–	–	37.5	–	[88]
K_4RhPb_9	$[Rh1@Pb_9]^{4-}$ $[Rh2@Pb_9]^{4-}$	C_{4v} C_{4v}	100 100	2.730/2.844 2.642/2.886	43.3 44.2	15.7 17.9	[49]
(K[222] crypt)$_3CuPb_9(dmf)_3$	$[Cu@Pb_9]^{3-}$	D_{3h}	100	2.708/2.802	41.7	11.3	[84]

Formula in bold correspond to clusters in ternary intermetallic compounds

[a]More than one listed anion, if more than one independent cluster is present in the unit cell

[b]Cluster type **E** (Fig. 17) of two vertex-sharing $\{T@Sn_9\}$ clusters

[c]Non-electron precise cluster

[d]Beside this ordered clusters there are other disordered ones

shapes of the clusters can be assigned more or less clearly to one of the possible idealized cage geometries, a mono-capped square antiprism with C_{4v} symmetry, and a tri-capped trigonal prism with D_{3h} symmetry. As pointed out previously, these structures are closely related, and a conversion is associated with rather small energy barriers. Notice, as outlined below, even though the tri-capped trigonal prism corresponds to a *closo* cluster, an elongation of the prism allows a lowering of the LUMO of a bare metal atom cluster, and therefore stability arises also for $4n + 4$ electrons [72]. Special cases are the filled "3D *spiro*" anions $[T_2@Sn_{17}]^{n-}$ consisting of two $[T@Sn_9]$ clusters with a common cage atom, which according to the borane nomenclature are called *commo*-bis$[T@Sn_9]$ (Fig. 17, **E**). None of the halves of these pairs adopts C_{4v} nor D_{3h} symmetry, but are best described as C_{2v}-symmetric nine-atomic cages.

All known representatives of filled nine-atomic tetrel clusters contain a metal atom of groups 8 to 11, all of which are able to adapt a d^{10} electron configuration with relatively low formal ion charges of −2 (Ru), −1 (Co, Rh), ±0 (Ni, Pd), and + 1 (Cu). Usually the total charge in such a filled cluster is simply obtained by adding this formal d^{10} ion charge and the charge of the empty cluster, $[E_9]^{4-}$, but a few exceptions of this rule, like the non-electron-precise clusters $[Ni@Ge_9]^{3-}$ [79] and $[Co@Sn_9]^{4-}$, [81, 82], have also been found, and can be derived from the known empty, partially oxidized Ge_9^{3-}/Sn_9^{3-} clusters.

A comparison of these filled clusters with their empty analogs reveals some differences, leading to the question of how far the filling of the clusters influences the interaction between the cage atoms and the endohedral transition metal atom. For instance, the *E-E* cluster bonds in $[Cu@Sn_9]^{3-}$ and $[Cu@Pb_9]^{3-}$ are 0.1 Å longer than in the empty cages $[Sn_9]^{4-}$ and $[Pb_9]^{4-}$, respectively [84]. This size effect can roughly be quantified considering the cluster volumes as summarized in Table 4. Empty, nine-atomic clusters are known for the tetrel elements Si–Pb, and the volume generally increases with the atomic number of the cage element (and, of course, with the number of cage atoms). To date the smallest hosts for endohedral atoms are the Ge_9 entities. However, only two representatives of filled germanium clusters are known, and while the corresponding Si_9 clusters seem to be too small to host any atom at all [89], a large number of Sn_9-based endohedral clusters has been characterized to date.

There are three main factors that determine the volume of the clusters, a) the size of the cluster-forming tetrel element, b) the size of the endohedral transition metal atom, and c) the number of the endohedral transition metal atoms. References for the empty Ge_9, Sn_9, and Pb_9 clusters in Table 4 are such compounds, whose structures were determined very accurately, and for which the cluster shapes are not compromised by following a high point group symmetry, superimposed orientational disorder, strong interactions with coordinating metal atoms, or attached functional groups. At first, for a given endohedral transition metal the volume increase of the cluster is larger for the lighter the cluster-forming tetrel element is, as can be seen from comparison of $[Co@Ge_9]^{5-}$ (+20%) and $[Co@Sn_9]^{5-}$ (~ +10%) or $[Cu@Sn_9]^{3-}$ (+14%) and $[Cu@Pb_9]^{3-}$ (+11%). Secondly, 4*d* transition metals trigger a distinctly higher increase than 3*d* elements, as indicated, e. g. by the larger

cluster halves of $Rh_2@Sn_{17}$ compared to the ones of its Co analog. Finally, if the site occupation of the endohedral transition metal atom is less than 100%, the site occupation rate is roughly proportional to the volume increase, as shown by the different Co, Ni, and Pd representatives. Note that in all cases in which the *T* atom site is not fully occupied the [*T*@E_9] cluster is superimposed with the corresponding empty [E_9] cluster. Thus, the calculated volume is a weighted average, and in consequence the calculated volume is smaller than expected (see, for example, $[Co@Sn_9]^{5-}$ and $[Co@Sn_9]^{4-}$ in Table 4 with less than 10% volume increase).

To a lesser but still significant extent the volume increase of filled E_9 clusters seems to be larger for the "3D *spiro*" anions [$T_2@Sn_{17}$] than for the corresponding single [*T*@Sn_9] clusters, seen from the slightly larger values for the respective Co and Ni compounds. Within this context it has to be noticed that the coordination number of the connecting *spiro* Sn atom is eight and, thus, larger than for all remaining cage atoms, and the longer Sn-Sn bonds resulting from this fact should cause a larger cluster volume. The observation that a larger coordination number leads to an increase of the interatomic distances is known for intermetallic compounds and is a consequence of the so-called pressure distance paradoxon [90]. Interestingly, there seems to be no significant influence of the charge and thus of the skeletal electron number, since the values for the paramagnetic $[Ni@Ge_9]^{3-}$ or $[Co@Sn_9]^{4-}$ are in the same range as those for the electron-precise examples.

While the volume effects can easily be attributed to quite simple geometrical reasons, the resulting symmetry is more difficult to explain. As stated above, the borderline cases of mono-capped square antiprisms with C_{4v} and tri-capped trigonal prisms with D_{3h} symmetry represent the expected polyhedra according to the Wade rules, i. e. a *nido* cluster for $2n + 4$ and a *closo* cluster for $2n + 2$ electrons. The distance between the centering *T* atom and the cage atoms can be used as an indicator (Table 4 and Fig. 18) to distinguish between the different symmetries. For filled E_9 clusters a D_{3h} symmetric tri-capped trigonal prism represents the best fit of nine atoms on a sphere, and consequently all *T*-*E* distances are very similar. By contrast, in a centered C_{4v}-symmetric mono-capped antiprism the coordination number of the central atoms is eight and determined by the underlying square antiprism, and the *T*-*E* distance to the capping atoms is considerably longer as, for example, in the case of $[Ni@Sn_9]^{4-}$ (2.78 Å, see Fig. 18a). The latter is thus rather similar to the coordination of *T* atoms in binary intermetallic compounds which predominantly have this coordination polyhedron, as outlined in Fig. 18. The same holds for centered ten-atomic clusters $[T@E_{10}]^{n-}$ with the shape of a bi-capped square antiprism and two longer interatomic distances between the centering atom and the two opposing prism caps (Fig. 17, C and Fig. 18b).

The clusters follow the trend that the *T*-*E* distances in discrete intermetalloid clusters are slightly shorter, but their longest bonds are in the range of the *T*-*E* distances in the corresponding intermetallic compounds. Considering the fact that in intermetallic compounds the distances are generally longer due to the much higher coordination numbers of the *E* atoms, this congruence in distances is very remarkable, and it supports the idea of an "intermetalloid" cluster.

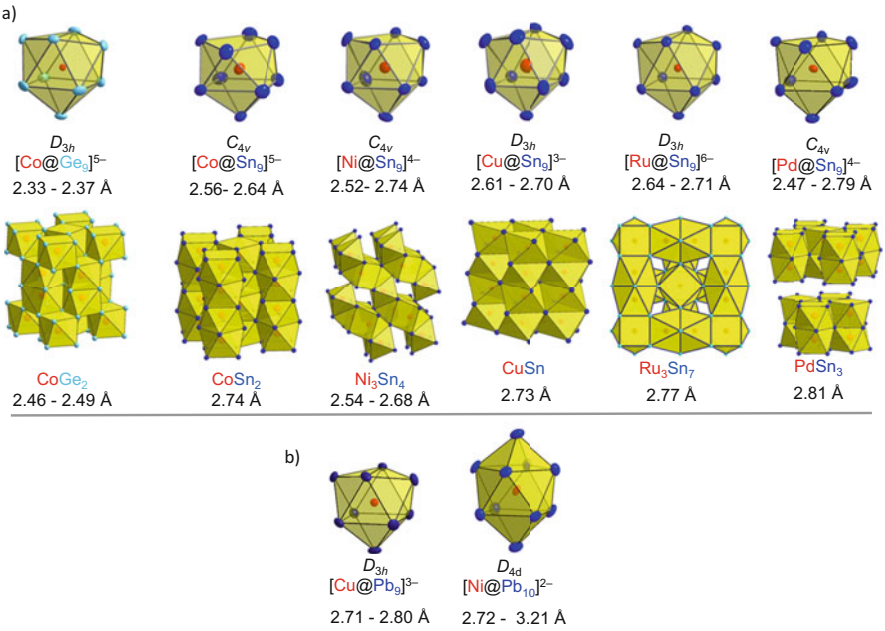

Fig. 18 Comparison of endohedral intermetalloid clusters with corresponding binary alloys. (**a**) Representatives with known binary intermetallic compounds. (**b**) In case of the Cu-Pb and Ni-Pb clusters binary intermetallic compounds or alloys are unknown. Tetrel element atoms and transition metal atoms are shown as blue and red spheres, respectively

However, the assigned point group symmetries have to be regarded with care, because deviations from a perfect shape are common, and some cases remain unclear, where some disorder or "packing effects" have to be taken into account, as shown for the different symmetries of the independent $[Co@Sn_9]^{5-}$ units in $K_{5-x}Co_{1-x}Sn_9$. The negatively charged ions Co^- and Ru^{2-} are the so far largest endohedral atoms in Ge_9 and Sn_9 clusters, and the respective clusters $[Co@Ge_9]^{5-}$ and $[Ru@Sn_9]^{6-}$ both adopt D_{3h} symmetry [63]. With respect to the fact that a sphere provides the maximum volume of a body with a given surface, the shape of a capped trigonal prism should be favored, and this finding might be assigned to a "balloon effect." Notice, a D_{3h}-symmetric nine-atomic deltahedron represents a *closo* type that requires 38 electrons for stability. However, the low-lying LUMO of the D_{3h}-symmetric clusters facilitates the uptake of two more electrons. Furthermore, a tri-capped trigonal prism with D_{3h} symmetry is a prerequisite for the application of the superatom approach, since such E_9 polyhedra possess an almost spherical shape: the Cu-*E* contacts are, for example, in the very narrow range between 2.611(7) and 2.700(7) Å for $[Cu@Sn_9]^{3-}$ and 2.71(1) Å and 2.802(11) Å for $[Cu@Pb_9]^{3-}$, with only slightly longer contacts to the capping atoms. The "sphere radii" are given by the mean Cu–*E* distances of 2.645 and 2.759 Å, respectively. Assuming the best fit of nine atoms on the surface of a sphere with

equalized interatomic distances of 1, the sphere radius geometrically determines to $r = 1/2\ \sqrt{3}$, arising in ideal interatomic distances of 3.054 and 3.186 Å for $[Cu@Sn_9]^{3-}$ and $[Cu@Pb_9]^{3-}$, respectively. These values are very close to the average experimental *E-E* contacts between the vertex atoms of 3.067 and 3.183 Å, respectively [84].

This could be similar to conditions corresponding to those in intermetallic compounds where valence electrons are considered to be completely delocalized, and the allocation of oxidation states to individual atoms is not possible or discussed controversially. Therefore the question arises if the situation changes in intermetalloid clusters despite the rather similar coordination polyhedra. In the highly negatively charged clusters $[Co@Ge_9]^{5-}$ and $[Ru@Sn_9]^{6-}$, a d^{10} configuration of Co^- and Ru^{2-} is anticipated [63]. If the same d^{10} electron configuration applies for the Cu atoms in $[Cu@Sn_9]^{3-}$ and $[Cu@Pb_9]^{3-}$, a positively charged Cu atom is required inside the highly negatively charged, surrounding $[Sn_9]^{4-}$ and $[Pb_9]^{4-}$ units, respectively. That this is actually the case gets support from NMR spectroscopic investigations (Fig. 19). The ^{119}Sn NMR spectrum exhibits one single resonance signal at −1,440 ppm split by Cu–Sn coupling, indicative of the presence of nine identical, structurally flexible Sn atoms in the cage anion. Due to the high quadrupolar momentum of the ^{63}Cu nucleus ($I = 3/2$), small electric field gradients are required for sharp signals and thus a highly symmetric environment for the Cu atom. In $[Cu@Sn_9]^{3-}$ the Cu atom is thus surrounded by a Sn_9 cluster of highest possible symmetry, which in this case, due to the scrambling of all Sn atoms, resembles a perfect sphere. As a consequence one sharp ^{63}Cu NMR resonance signal at $\delta = -332$ ppm in acetonitrile (−287 ppm in *N,N*-dimethylformamide) can be detected. The splitting pattern arises from different isotopomers $[Cu@^{119/117}Sn_mSn_{(9-m)}]^{3-}$ ($m = 0, 1, 2, 3, 4$) with 16% of the Sn atoms according to the natural isotope distribution having spin $I = ½$ arising in the intensity distribution of the observed seven peaks and in full agreement with magnetically equivalent atoms in the Sn_9 cluster core [84]. The same holds for $[Cu@Pb_9]^{3-}$ with a ^{63}Cu NMR resonance signal low-field shifted to $\delta = 248$ ppm in dmf solution and again with a splitting pattern according to time-averaged Pb atoms (^{207}Pb with $I = ½$ and 22.6% abundance) and the isotopomers $[Cu@^{207}Pb_mPb_{(9-m)}]^{3-}$ ($m = 0, 1, 2, 3, 4$). The ^{207}Pb NMR spectrum exhibits a resonance signal at −4,144 ppm split by Cu–Pb coupling in agreement with a structural flexibility of the cage anion [91]. A similar observation has been made for $[Rh_9E'(CO)_{21}]^{2-}$ and $[Rh_{10}E'(CO)_{22}]^{3-}$ ($E' =$ P, As) which can be regarded as "inverse"clusters, the main group elements P and As encapsulated inside a transition metal cage. However, whereas in the rhodium clusters the fluctional behavior of the carbonyl ligands and the rearrangement of the metal atoms in the polyhedron cannot be unequivocally separated from one another, the dynamic behavior of the ligand-free tetrel atom clusters arises from the rearrangement of the framework atoms [92].

As pointed out for the examples $[Cu@Sn_9]^{3-}$, $[Cu@Pb_9]^{3-}$, $[Co@Ge_9]^{5-}$, and $[Ru@Sn_9]^{6-}$, the empty D_{3h}-symmetric nine-atomic $[E_9]^{4-}$ cluster also corresponds to a 40-electron cluster within the model of the spherical atom approach according to

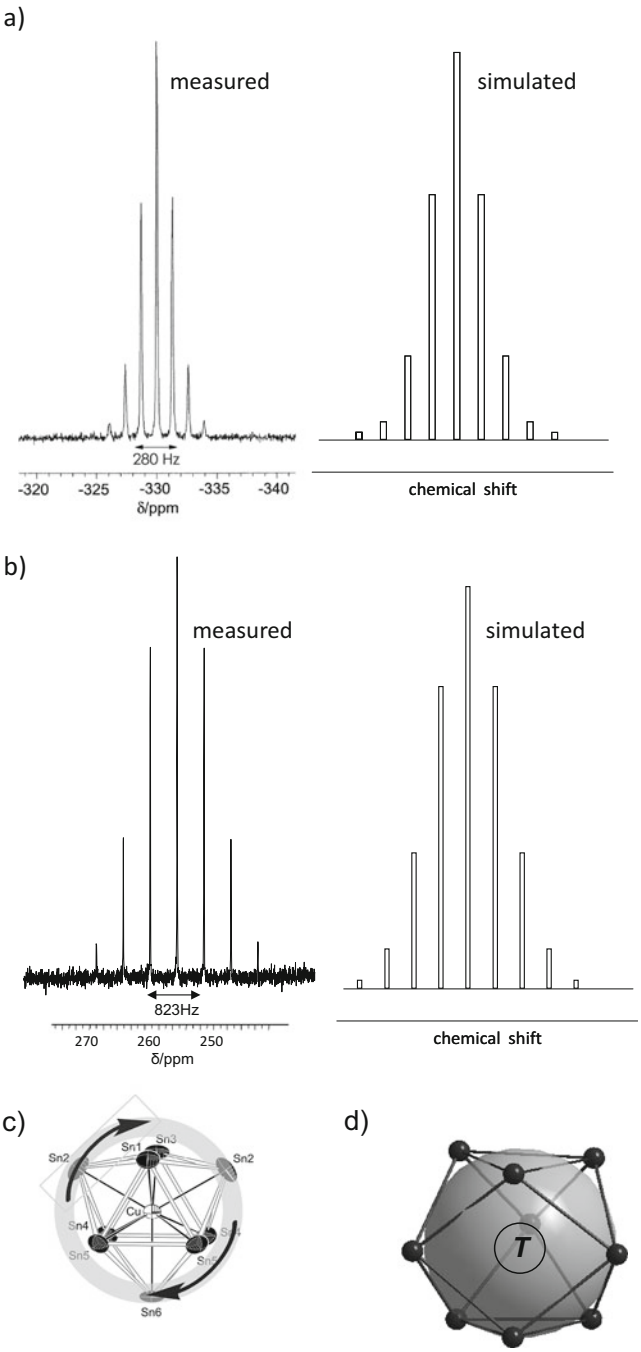

Fig. 19 Experimental and simulated ^{63}Cu NMR spectrum of (**a**) $[Cu@Sn_9]^{3-}$ in acetonitrile and (**b**) $[Cu@Pb_9]^{3-}$ in dimethylformamide. Simulated spectra of different isotopomers with m = 0, 1, 2, 3, 4 for $[Cu@^{119/117}Sn_mSn_{(9-m)}]^{3-}$ and $[Cu@^{207}Pb_mPb_{(9-m)}]^{3-}$, respectively. (**c**) Scrambling of

the electron configuration $1S^2\ 1P^6\ 1D^{10}\ 2S^2\ 1F^{14}\ 2P^6$ (Fig. 14), with bonding and anti-bonding interactions of the *d* orbitals of the centering transition metals cancelling each other out, as elaborated for icosahedral $[E_{12}]^{2-}$ in Chapter 3. Similarly, the oxidation state of Ag in $[Ag@Pb_{11}]^{3-}$ is +1, allowing the Wade–Mingos description of a *nido* cluster $[Pb_{11}]^{4-}$ filled with Ag^+ [93]. The general question whether metal atoms in heteronuclear clusters occupy internal or external locations was considered before [94].

4.2.2 Filled Ten-Atomic Clusters

Within the group of discrete tetrel element clusters the ten-atomic entities count by far the smallest number of representatives to date, and also their filled variants, all listed in Table 5, represent an exclusive, but nevertheless highly interesting family of compounds.

Empty $[E_{10}]^{2-}$ clusters are known for Ge [95] and Pb [96], and both form a bi-capped square antiprism with D_{4d} symmetry, a deltahedral *closo* cluster according to the Wade–Mingos rules. The rare examples of filled clusters include $[Co@Ge_{10}]^{3-}$ [97] and $[Ni@Pb_{10}]^{2-}$ [98] with endohedral $3d^{10}$ transition metal atoms as well as the non-electron-precise $[Fe@Ge_{10}]^{3-}$ [99]. Surprisingly, for Sn_{10} which shows by far the largest number of compounds including filled nine-atomic clusters, only one structurally characterized example has been reported, $[Rh@Sn_{10}]^{3-}$ [87]. $[Fe@Sn_{10}]$ has been detected in ESI-MS experiments, but its structure has not been determined yet [100].

As expected, the cluster volumes are slightly larger than those of their nine-atomic analogs, and the volume increase of the filled entities, as can be seen by comparison of the respective Ge and Pb compounds, is significant, but consistently to a lower extent. Interestingly, only the $[Ni@Pb_{10}]^{2-}$ cluster adopts the – maybe at a first sight also expected – D_{4d} symmetry with two significantly longer Ni–Pb distances (in average 3.21 vs. 2.72 Å) and an [8 + 2] coordination of the Ni atom. By contrast, the Co and Fe compounds take the shape of a pentagonal prism without any deltahedral faces and with ten almost equal *T*–Ge distances. Quantum chemical calculations on different levels of theory [97, 100, 102–104] showed that for the bare $[Ge_{10}]^{2-}$ unit and the corresponding and to date hypothetical $[Ni@Ge_{10}]^{2-}$ cluster, a bi-capped square antiprism with D_{4d} symmetry should be favored, while for an arrangement of ten Ge atoms hosting Co^- or Fe^- a pentagonal prism with D_{5h} symmetry was found as the structure of lowest energy, indeed. Again the size of the endohedral transition metal atom was considered as an influencing factor for the shape of the resulting polyhedron, as Ni^0 prefers an eightfold coordination by Ge, whereas the larger Co and Fe anions require larger coordination polyhedra with

Fig. 19 (continued) the atoms of the E_9 cage around the central Cu atom. (**d**) Nine-atomic cages with D_{3h} symmetry represent the best fit of the atoms to a sphere

Table 5 Discrete $[T@E_{10}]^{n-}$ cluster units

Compound	Cluster	Approx. symm.	Occupancy of *T*/%	Min./max. *TM-E* distance/Å ((A = Angström))	Av. cluster vol./Å^3	Volume increase/%	Ref.
(Rb[222]crypt)$_2$Ge$_{10}$(en)$_{1.5}$	$[Ge_{10}]^{2-}$	D_{4d}	–	–	26.9	–	[95]
(K[222]crypt)$_3$FeGe$_{10}$(en)$_2$ [a]	$[Fe@Ge_{10}]^{3-}$	D_{5h}	100	2.509/2.535	29.0	7.8	[99]
(K[222]crypt)$_4$[CoGe$_{10}$][Co(cod)]	$[Co@Ge_{10}]^{3-}$	D_{5h}	100	2.479/2.525	28.5	5.9	[97]
(K[222]crypt)$_3$CoGe$_{10}$(en)	$[Co@Ge_{10}]^{3-}$	D_{5h}	100	2.488/2.514	28.5	5.9	[101]
(K[222]crypt)$_3$RhSn$_{10}$(en)$_2$	$[Rh@Sn_{10}]^{3-}$ [b]	C_{2v}	100	2.679/2.888	45.2	–	[87]
(K[222]crypt)$_5$Rh$_3$Sn$_{24}$(dmf)$_2$(Tol)	{Rh1@Sn$_{10}$}	C_{2v}	100	2.681/2.919	47.0	–	[87]
	{Rh2@Sn$_{10}$}	C_{2v}	100	2.659/2.984	46.9	–	
	{Rh3@Sn$_{10}$}	C_{2v}	100	2.657/3.059	46.9	–	
(K[222]crypt)$_2$Pb$_{10}$	$[Pb_{10}]^{2-}$	D_{4d}	–	–	45.8	–	[96]
(K[222]crypt)$_2$NiPb$_{10}$	$[Ni@Pb_{10}]^{2-}$	D_{4d}	100	2.715/3.210	48.5	5.9	[98]

[a]Non-electron precise cluster

[b]Major component of two orientationally disordered, superposing clusters

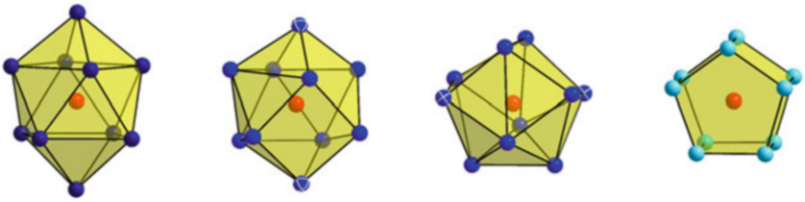

Fig. 20 Different shapes of the $[T@E_{10}]^{n-}$ clusters: $[Ni@Pb_{10}]^{2-}$ with D_{4d} symmetry (left); $[Co@Ge_{10}]^{3-}$ with D_{5h} symmetry (right); $[Rh@Sn_{10}]^{3-}$ with C_{2v} symmetry shown in two orientations to emphasize the partial similarities to D_{4d} and D_{5h}. The two opposite Sn atoms with the longest Rh–Sn distances are drawn with octant lines. Tetrel element atoms and transition metal atoms are shown as blue and red spheres, respectively

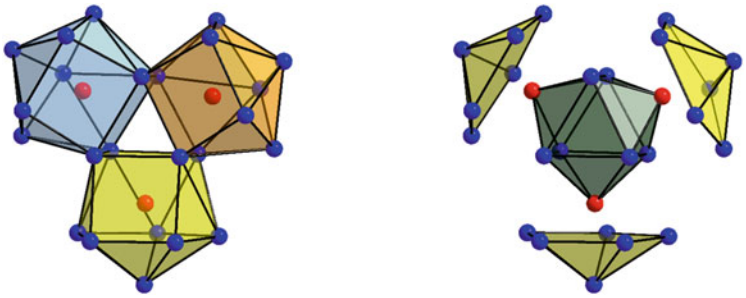

Fig. 21 Different views of the $[Rh_3@Sn_{24}]^{5-}$ cluster: Rh-centered C_{2v}-symmetric Sn_{10} units fused via common edges (left); Rh-capped Sn_6 prism with D_{3h} symmetry with an icosahedron fragment covering each Rh atom (right). Tetrel element atoms and transition metal atoms are shown as blue and red spheres, respectively

higher coordination numbers. However, similar to the findings for the C_{4v} and D_{3h} symmetries of the E_9 clusters, energetic differences between these cases are small. An intermediate structure with C_{2v} symmetry, mainly deltahedral but with two square faces, and with the longest Rh–Sn distances to two opposite cage atoms, is realized in $[Rh@Sn_{10}]^{3-}$ [87], see Fig. 20.

Another unique kind of fused endohedral E_{10} clusters was found in the Rh/Sn system [87]. Even though the underlying polyhedra contain also rectangular and not only deltahedral faces, the volume of the unit is within the range of that of other filled ten-atomic stannides. In $[Rh_3@Sn_{24}]^{5-}$ (Fig. 21) three of the C_{2v}-symmetric $\{Rh@Sn_{10}\}$ units share one edge with each neighbor under formation of a central trigonal Sn_6 prism so that one square face of each ten-membered cage represents a face of the prism. The remaining square faces are oriented towards the same side of the cluster, and thus, the whole $[Rh_3@Sn_{24}]^{5-}$ unit is approximately C_{3v}-symmetric. Alternatively, this unit can be described as an almost D_{3h}-symmetric Rh_3Sn_6 core with a triply-Rh-capped trigonal Sn_6 prism, in which every cap is covered by a semi-icosahedron, a capped pentagonal ring of Sn atoms.

Although obviously viable, endohedral E_{10} clusters still represent rare peculiarities in the chemistry of tetrel element clusters. The reason may be their low stability relative to the neighboring cluster species E_9 and E_{12}. While the latter can easily be described as closed-shell complexes according to the superatom approach, this is not possible for the ten-atomic 42-electron clusters.

4.3 Intermetalloid Clusters Comprising Icosahedra

Filled $[T@Sn_{12}]^{2-}$ and $[T@Pb_{12}]^{2-}$ clusters (Fig. 22a) are more frequent than the ten-atomic species (Table 6). According to the superatom approach these clusters resemble filled-shell representatives with very little influence of the endohedral d^{10} atom (Fig. 14). Due to the lack of empty icosahedral tetrel element clusters, filled clusters of the same atom type E are compared with respect to the centering atom. For $[T@Sn_{12}]$, Rh^- and Ir^- centering does not change the volume of 63 Å^3, and for the $[T@Pb_{12}]$ clusters the variation of the volume is less than 3% for $T = Co^-$, Ir^-, Ni^0, Pd^0, and Pt^0 as well as for Au^-, the latter comprising a $6s^2\ 5d^{10}$ electron configuration (Table 6). Even a substitution of 1 Pb atom of the icosahedron by 1 Au atom does not significantly change the volume of the icosahedral heteroatomic $\{Au@AuPb_{11}\}$ unit (Table 6). Based on geometrical arguments, only weak interactions between the endohedral atom and the cluster vertex atoms are assumed, as it was also the case for endohedral fullerene molecules (Fig. 1o) [2].

As pointed out, icosahedral discrete intermetalloid Zintl clusters only exist in the presence of endohedral atoms. However, $[Pd_3Ge_{18}(Sn(^iPr)_3)_6]^{2-}$ [110], in which six Ge atoms carry an external $Sn(^iPr)_3$ ligand, contains two empty $\{Ge_9Pd_3\}$ icosahedra connected via the Pd_3 triangle (Fig. 22h), and this *tricommo* $\{Ge_9Pd_3\}$ unit – named according to the borane nomenclature for polyhedral borane cages with three atoms in common – is the only example of an empty tetrel element-rich icosahedron (Table 7). The stabilizing role of the Pd atoms through donor−acceptor interactions with the frontier orbitals of the Ge_9R_3 cages via principal interacting orbital (PIO) has been suggested [111]. The smaller cluster volume if compared to the filled Sn and Pb variants originates from significant shorter Ge–Ge distances. Due to the distortion the shortest distance to the calculated center of gravity of the $\{Ge_9Pd_3\}$ unit of 2.23 Å is smaller than the shortest distance in $[Co@Ge_9]^{5-}$ [63]. Thus, the significantly larger icosahedron in $[Co@Ge_{12}]^{3-}$ with slightly longer Ge–Ge distances [101], similar as in $[Co@Ge_9]^{5-}$, and a larger volume of 44 Å^3 in contrast to ca. 40 Å^3 in $\{Ge_9Pd_3\}$ hints at a templating effect of the Co^- ion. Interestingly, empty *tricommo*-B_{12} icosahedra occur as building units in the β-rhombohedral boron allotrope, in which three B_{12} icosahedra each shares a trigonal face resulting in one common boron vertex atom (Fig. 22i).

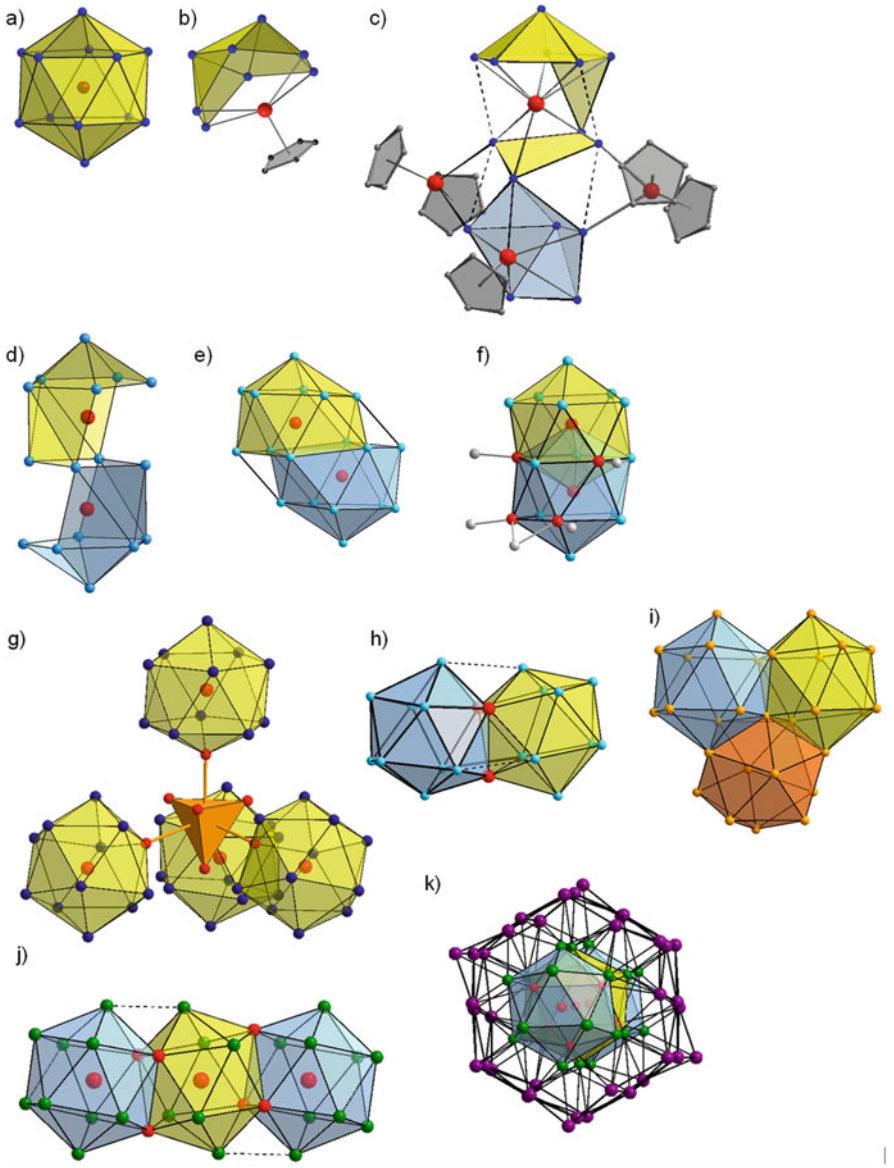

Fig. 22 (**a**) $[Ir@Sn_{12}]^{3-}$; (**b**) $[CpTi(\eta^4\text{-}Sn_8)]^{3-}$; (**c**) $[Ti_4Sn_{15}Cp_5]^{n-}$; (**d**) β-$[Co_2@Ge_{16}]^{4-}$; (**e**) $[Pd_2@Ge_{18}]^{4-}$; (**f**) $[Ge_{13}Ni_6(CO)_5]^{4-}$; (**g**) assembly of four $[Au@(Pb_{11}Au)]$ clusters around a central Au_4 unit in $[Au_{12}Pb_{44}]^{8-}$, (**h**) the $\{Ge_9Pd_3Ge_9\}$ core as part of $[Pd_3Ge_{18}(Sn(^iPr)_3)_6]^{2-}$ (Sn(^{i}Pr)$_3$ ligands are omitted), (**i**) building block in β-rhombohedral boron, (**j**) $\{Pd_{33}\}$ core as part of (**k**) $[Pd_{69}(CO)_{36}(PEt_3)_{18}]$ (CO and PEt_3 ligands are omitted). Orange, light and dark blue spheres correspond to B, Ge, and Sn atoms, respectively, Ti, Co, and Ni atoms are shown as red spheres, Pd atoms with red, green, or violet color. C atoms of C_5H_5 and CO groups are shown in gray.

Table 6 Discrete icosahedral $[T@E_{12}]^{n-}$ cluster units

Compound	Cluster	Approx. symm.	Occupancy of *T*/%	min./max. *T*-*E* distance/Å ((A = Angström))	Av. cluster vol./Å^3	Ref.
(K[222]crypt)$_3$CoGe$_{12}$(en)	[Co@Ge$_{12}$]$^{3-}$	D_{5d} [a]	100	2.494/2.781	44.0	[101]
(K[222]crypt)$_3$RhSn$_{12}$(dmf)	[Rh@Sn$_{12}$]$^{3-}$	I_h	100	2.898/2.952	63.2	[87]
(K[222]crypt)$_3$RhSn$_{12}$(tol)$_2$	[Rh1@Sn$_{12}$]$^{3-}$ [Rh2@Sn$_{12}$]$^{3-}$	I_h I_h	100 100	2.878/2.950 2.914/2.915	62.7 62.8	[87]
(K[222]crypt)$_3$IrSn$_{12}$(tol)	[Ir1@Sn$_{12}$]$^{3-}$ [Ir2@Sn$_{12}$]$^{3-}$ [b]	I_h I_h	100 100	2.883/2.942 2.880/2.972	63.2 63.2	[31]
(K[222]crypt)$_3$MnPb$_{12}$(en)	[Mn@Pb$_{12}$]$^{3-}$	D_{2h} [c]	100	2.875/3.278	72.8	[105]
(K[222]crypt)$_3$CoPb$_{12}$	[Co1@Pb$_{12}$]$^{3-}$ [Co2@Pb$_{12}$]$^{3-}$ [Co3@Pb$_{12}$]$^{3-}$ [d]	I_h I_h I_h	100 100 100	2.951/3.040 2.956/3.065 2.945/3.035	68.2 69.2 68.4	[106]
(K[18]c6)$_3$RhPb$_{12}$(en)$_2$	[Rh@Pb$_{12}$]$^{3-}$ [e]	I_h	100	2.984/3.028	69.3	[107]
(K[18]c6)$_3$IrPb$_{12}$	[Ir@Pb$_{12}$]$^{3-}$ [e]	I_h	100	3.009/3.019	69.4	[106]
(K[222]crypt)$_2$NiPb$_{12}$(en)	[Ni@Pb$_{12}$]$^{2-}$ [b]	I_h	100	2.924/3.034	67.2	[108]
(K[222]crypt)$_2$PdPb$_{12}$(tol)	[Pd@Pb$_{12}$]$^{2-}$	I_h	100	2.980/3.076	70.8	[108]
(K[222]crypt)$_2$PtPb$_{12}$	[Pt@Pb$_{12}$]$^{2-}$	I_h	100	3.056/3.059	72.5	[8]
(K[222]crypt)$_3$AuPb$_{12}$(py)$_2$	[Au@Pb$_{12}$]$^{3-}$	D_{5d} [f]	100	2.846/3.095	70.5	[109]
(K[222]crypt)$_3$AgPb$_{11}$(en)$_{0.5}$	[Ag@Pb$_{11}$]$^{3-}$	C_{5v}	100	3.007/3.118	62.1 [g]	[93]
(K[222]crypt)$_6$Au$_8$Pb$_{33}$(en)	{Au1@AuPb$_{11}$}	C_{5v}	100	Au-Au 2.783 Au-Pb 2.963/3.189	71.3	[93]
	{Au2@AuPb$_{11}$}	C_{5v}	100	Au-Au 2.779 Au-Pb 2.973/3.341	72.0	
	{Au3@AuPb$_{11}$}	C_{5v}	100	Au-Au 2.798 Au-Pb 2.964/3.165	71.4	
(K[222]crypt)$_8$Au$_{12}$Pb$_{44}$	{Au1@AuPb$_{11}$}	C_{5v}	100	Au-Au 2.821 Au-Pb 2.984/3.173	71.7	[93]
	{Au2@AuPb$_{11}$}	C_{5v}	100	Au-Au 2.811 Au-Pb 2.969/3.174	71.4	

(continued)

Table 6 (continued)

Compound	Cluster	Approx. symm.	Occupancy of *T*/%	min./max. *T*-*E* distance/Å ((A = Angström))	Av. cluster vol./Å^3	Ref.
	{Au3@AuPb$_{11}$}	C_{5v}	100	Au-Au 2.803 Au-Pb 2.981/3.164	71.6	
	{Au4@AuPb$_{11}$}	C_{5v}	100	Au-Au 2.816 Au-Pb 2.983/3.160	71.5	

[a]Icosahedron elongated along the five-fold axis
[b]Major component of two orientationally disordered, superposing cluster units
[c]Icosahedron compressed along two-fold axes
[d]Orientational disorder of three identical, superposing cluster units
[e]Orientational disorder of two identical, superposing cluster units
[f]Icosahedron compressed along the five-fold axis
[g]Smaller volume due to an eleven-atomic *nido* structure

Table 7 Empty *tricommo* heteroatomic icosahedral clusters

Compound	Cluster	min./max. *T-T*, *T-E* and *E-E* distance/Å ((A = Angström))	Av. cluster vol./Å^3	Ref.
(K[222]crypt)$_2$[Pd$_3$Ge$_{18}$(Sn(^{i}Pr)$_3$)$_6$](^{i}Pr$_2$O)	[Ge$_9$Pd$_3$Ge$_9$]$^{8-}$	Pd-Pd 2.871/2.891 Pd-Ge 2.440/2.730 Ge-Ge 2.566/2.892	39.9 40.5	[110]
[(CH$_3$CN)Cu(PPh$_3$)$_3$] [Pd$_3$Ge$_{18}$(Sn(^{i}Pr)$_3$)$_7$]	[Ge$_9$Pd$_3$Ge$_9$]$^{8-}$	Pd-Pd 2.879/2.894 Pd-Ge 2.440/2.727 Ge-Ge 2.558/2.881	39.5 40.6	[110]
(K[222]crypt)$_2$[Pd$_3$Ge$_{18}$(Si(^{i}Pr)$_3$)$_6$]	[Ge$_9$Pd$_3$Ge$_9$]$^{8-}$	Pd-Pd 2.839/2.844 Pd-Ge 2.457/2.741 Ge-Ge 2.573/2.874	40.7 40.6	[112]
(K[222]crypt)$_2$[Pd$_3$Ge$_{18}$(Sn(*c*-hex)$_3$)$_6$](thf)$_2$	[Ge$_9$Pd$_3$Ge$_9$]$^{8-}$	Pd-Pd 2.885/2.910 Pd-Ge 2.443/2.728 Ge-Ge 2.570/2.893	40.8 40.4	[112]

4.4 Intermetalloid Clusters Comprising Icosahedral Building Blocks

Since larger discrete tetrel atom clusters E_n are not observed in intermetallic compounds, the formation of clusters with $n > 9$ requires dissociation reactions followed by atom aggregation in solution. Due to the relatively high abundance of icosahedral and the absence of empty clusters a templating effect of the *T* atom during the formation of [*T*@E$_{12}$] clusters must be considered. In fact there are some examples of intermetalloid tetrel atom clusters that give clues of how endohedral icosahedra as well as interpenetrating clusters, as they frequently occur in intermetallic compounds, might be formed in solution. The reaction of bare tetrel atom clusters with organometallic compounds leads to intermediates that may coexist at the chemical equilibrium. Several different reaction products have been detected, for example, during the reaction of [Cp$_2$(NH$_3$)$_2$Ti]$^+$ with [Sn$_9$]$^{4-}$ clusters [113]. The formation of [Cp$_2$Ti(η^1-Sn$_9$)(NH$_3$)]$^{3-}$ shows the line of attack of the Ti atom to the cluster through the coordination to the lone pair in analogy to **2** or **19**, the fragmentation of [Sn$_9$]$^{4-}$, and a higher coordination of the Ti atom is realized in [CpTi(η^4-Sn$_8$)]$^{3-}$, in which eight Sn atoms form a pocket-type fragment of an icosahedron that coordinates to the Ti atom (Fig. 22b). Cluster growth with two icosahedral fragments in one species (yellow Sn$_{10}$ and blue Sn$_6$ in Fig. 22c) that coordinate to a Ti atom is realized in the complex structure of [Ti$_4$Sn$_{15}$Cp$_5$]$^{n-}$ ($n = 4$ or 5), as well as a stepwise ligand exchange in [Cp$_2$(NH$_3$)$_2$Ti]$^+$ by the coordination of Sn atoms to [Cp$_2$Ti], [CpTi], and finally a ligand-free Ti atom is realized in one anion. Similarly, fragments of icosahedra are observed around the Rh atoms in [Rh$_3$@Sn$_{24}$]$^{5-}$ [87]. The pentagonal six-atomic cap, representing one half of an icosahedron, is closed by a Sn$_4$ square, and the aggregation of three such Sn$_{10}$ units leads to a central trigonal prism (Fig. 21).

Table 8 Intermetalloid clusters with icosahedral building blocks

Compound	Cluster	Min./max. *T-E* distance/Å ((A = Angström))	Ref.
$(K[222]crypt)_4Co_2Ge_{16}(en)$	α-$[Co_2@Ge_{16}]^{4-}$ β-$[Co_2@Ge_{16}]^{4-}$ [a]	2.514/2.627 2.449/2.654	[114]
$(K[222]crypt)_4Pd_2Ge_{18}(Tol)_2$	$[Pd_2@Ge_{18}]^{4-}$	2.605/2.646	[115]
$(K[222]crypt)_4Pd_2Sn_{18}(en)_3$	$[Pd_2@Sn_{18}]^{4-}$		[116]
$(K[222]crypt)_4Pd_2Sn_{18}(en)_3$	$[Pd_2@Sn_{18}]^{4-}$		[117]
$(K[222]crypt)_4[Ge_{13}Ni_{6(}CO)_5](en)_{1.5}$	$[Ge_{13}Ni_6(CO)_5]^{4-}$	Ge-Ni 2.381/2.668 Ni-Ni 2.450/2.771 Ge-Ge 2.634/2.906	[118]

[a]Major component of two orientationally disordered, superposing clusters

In β-$[Co_2@Ge_{16}]^{4-}$ [114] (Table 8), two filled icosahedral fragments comprising nine out of twelve atoms of an icosahedron are merging to an intermetalloid cluster (Fig. 22d). Clusters composed of such merged polyhedra representing a concave curvature are frequent among *nido*-boranes. Aggregates of two or more cages, in which individual cages are joined or fused to each other with two or more atoms held in common, are often referred as "macropolyhedral" species. Compounds of the type $[Pd_2@E_{18}]^{4-}$ (E = Ge [115], Sn [116, 117]) are generally described as ellipsoid clusters that encapsulate two T atoms, similarly represent two filled icosahedral fragments of 11 E atoms at a preliminary stage on the way to interpenetrating clusters (Fig. 22e). Finally two interpenetrating clusters $\{Ni@Ge_{10}Ni_2\}$ are formed from nine-atomic clusters in solution indeed and are observed in $[Ge_{13}Ni_6(CO)_5]^{4-}$ [118] (Table 8) with one Ni vertex of each icosahedron acting as the center of the second icosahedron. In the latter case the coordination sphere of the Ni atoms at the surface is completed by CO ligands (Fig. 22f). The transition to an intermetallic compound with exclusively tetrahedral units is realized in the molecular anion $[Au_{12}Pb_{44}]^{8-}$ [93]. As in Frank–Kasper phases, the unit contains centered heterometallic icosahedra connected by metal atom tetrahedra. Notice, that the centered icosahedra itself form tetrahedral units. The coordination of the Au atoms which are part of the icosahedron to the trigonal faces of the central Au_4 tetrahedron results again in Au_4 tetrahedra (Table 6, Fig. 22g).

Examples of molecules with icosahedral units that are centered and share trigonal faces are in general rare and completely unknown for main group metals, but they represent important intermediates between intermetalloid clusters and intermetallic compounds. Interestingly, there is one case of a metalloid Pd cluster, in which three face-sharing *tricommo*-icosahedra form a Pd_{33} unit [119]. All icosahedra are centered by Pd atoms. The Pd_{33} unit as part of the structure of $[Pd_{69}(CO)_{36}(PEt_3)_{18}]$ is embedded in a hexagonally shaped Pd_{36} tube, and like the Ni atoms in $[Ge_{13}Ni_6(CO)_5]^{4-}$, the surface Pd atoms are coordinately saturated by CO and PEt_3 donor ligands (Fig. 22j, k).

5 Summary

The equivalence of hybrid orbitals in main group element fragments, like the two skeletal electron fragment B-H with an *exo* cluster B-H bond, and in a bare tetrel element *E* in a cluster with an *exo*-oriented lone pair of electrons draws an easy-to-understand relationship between boranes $B_nH_m^{x-}$ and bare tetrel element clusters, the so-called Zintl clusters $[E_n]^{x-}$. The analogy covers a large number of structures with different *n*, but it also applies to protonated species, transition metal complexes, and vertex expansions of boranes/carboranes and Zintl clusters. Despite the intriguing similarity of the chemical bond based on the Wade–Mingos rules, there are also some differences. Zintl clusters $[E_n]^{x-}$ with *n* up to 10 nicely complement boranes and carboranes, and the chemical bonding in such clusters and their transition metal complexes can be described in analogy to that of boranes. Regarding the fluctional behavior of cluster frameworks, it appears at much lower temperatures in tetrel atom clusters, and Zintl clusters of the heavier elements Sn and Pb show a strong tendency towards fragmentation in solution, thereby causing a higher reactivity under formation of, e.g., complex intermetalloid clusters of high nuclearity. Endohedral nine- and ten-atomic clusters can be compared to a number of binary intermetallic compounds. However, the oxidation state of a centering transition metal in intermetalloid clusters can easily be assigned on the basis of its d^{10} electron configuration, whereas the oxidation state of transition metals in intermetallic compounds is less well defined.

The coordination of transition metals in larger intermetalloid clusters isolated from solution is still very similar to that in intermetallic compounds, but it allows for a larger variety of structures since there are no restrictions concerning translational symmetry. Therefore, icosahedral building units, which do not allow translational symmetry in solids, are quite abundant in species isolated from solution, and in solution, transition metal atoms can play the role of templating atoms on the way to larger cluster units.

References

1. Schnepf A, Schnöckel H (2002) Metalloid aluminum and gallium clusters: element modifications on the molecular scale? Angew Chem Int Ed 41:3533–3552
2. Fässler TF, Hoffmann SD (2004) Endohedral Zintl ions: intermetalloid clusters. Angew Chem Int Ed 43:6242–6247
3. Stegmaier S, Fässler TF (2011) A bronze Matryoshka: the discrete intermetalloid cluster $[Sn@Cu_{12}@Sn_{20}]^{12-}$ in the ternary phases $A_{12}Cu_{12}Sn_{21}$ (A=Na,K). J Am Chem Soc 133:19758–19768
4. Fässler TF (2011) Zintl phases: principles and recent developments. In: Structure and bonding, vol 139. Springer, Heidelberg
5. Fässler TF (2011) Zintl ions: principles and recent developments. In: Structure and bonding, vol 140. Springer, Heidelberg

6. Kesanli B, Fettinger JC, Eichhorn BW (2001) The *closo*-$[Sn_9M(CO)_3]^{4-}$ Zintl ion clusters where M=Cr,Mo,W: two structural isomers and their dynamic behavior. Chem Eur J 7:5277–5285
7. Kesanli B, Fettinger JC, Gardner DR, Eichhorn BW (2002) The $[Sn_9Pt_2(PPh_3)]^{2-}$ and $[Sn_9Ni_2(CO)]^{3-}$ complexes: two markedly different Sn_9M_2L transition metal Zintl ion clusters and their dynamic behavior. J Am Chem Soc 124:4779–4786
8. Esenturk EN, Fettinger JC, Lam Y-F, Eichhorn BW (2004) $[Pt@Pb_{12}]^{2-}$. Angew Chem Int Ed 43:2132–2134
9. Corbett JD (2000) Polyanionic clusters and networks of the early p-element metals in the solid state: beyond the Zintl boundary. Angew Chem Int Ed 39:670–690
10. Ruck M, Dubenskyy V, Söhnel T (2003) Structure and bonding of $Pd@[Bi_{10}]^{4+}$ in the subbromide $Bi_{14}PdBr_{16}$. Angew Chem Int Ed 42:2978–2982
11. Hume-Rothery W, Smallman RE, Haworth CW (1969) The structure of metals and alloys (5th edn). Metals & Metallurgy Trust, London
12. Ecker A, Weckert E, Schnöckel H (1997) Synthesis and structural characterization of an Al_{77} cluster. Nature 387:379–381
13. Moses MJ, Fettinger JC, Eichhorn BW (2003) Interpenetrating As_{20} fullerene and Ni_{12} icosahedra in the onion-skin $[As@Ni_{12}@As_{20}]^{3-}$ ion. Science 300:778–780
14. Schmidbaur H, Scherbaum F, Huber B, Müller G (1988) Polyauriomethane compounds. Angew Chem Int Ed Engl 27:419–421
15. Wade K (1971) The structural significance of the number of skeletal bonding Electron-pairs in Carboranes, the higher Boranes and Borane anions, and various transition-metal carbonyl cluster compounds. J Chem Soc D:792–793
16. Wade K (1976) Structural and bonding patterns in cluster chemistry. In: Emeléus HJ, Sharpe AG (eds) Adv inorg chem radiochem, vol 18. Academic Press, London
17. Mingos DMP (1984) Polyhedral skeletal electron pair approach. Acc Chem Res 17:311–319
18. Mingos DMP, Johnston RL (1987) Theoretical-models of cluster bonding. In: Theoretical approaches. structure and bonding, vol 68. Springer, Heidelberg
19. Schiemenz B, Huttner G (1993) The first octahedral Zintl ion: $[Sn_6]^{2-}$ as a ligand in $[Sn_6(Cr(CO)_5)_6]^{2-}$. Angew Chem Int Ed 32:297–298
20. Kennedy JD (1986) The polyhedral Metallaboranes part II. Metallaborane clusters with eight vertices and more. Prog Inorg Chem 34:211–434
21. Schiegerl LJ, Karttunen AJ, Tillmann J, Geier S, Raudaschl-Sieber G, Waibel M, Fässler TF (2018) Charged Si_9 clusters in neat solids and the detection of $[H_2Si_9]^{2-}$ in solution: a combined NMR, Raman, mass spectrometric, and quantum chemical investigation. Angew Chem Int Ed 57:12950–12955
22. Lorenz C, Hastreiter F, Hioe J, Lokesh N, Gartner S, Korber N, Gschwind RM (2018) The structure of $[HSi_9]^{3-}$ in the solid state and its unexpected highly dynamic behavior in solution. Angew Chem Int Ed Engl 57:12956–12960
23. Grimes RN (2016) Carboranes.3rd edn. Elsevier, Amsterdam
24. Elian M, Chen MML, Mingos DMP, Hoffmann R (1976) Comparative bonding study of conical fragments. Inorg Chem 15:1148–1155
25. Mingos DMP, Slee T, Lin Z (1990) Bonding models for ligated and bare clusters. Chem Rev 90:383–402
26. Hoffmann R (1982) Building bridges between inorganic and organic chemistry (Nobel lecture). Angew Chem Int Ed Engl 21:711–724
27. Eichhorn BW, Haushalter RC, Pennington WT (1988) Synthesis and structure of *closo*-$[Sn_9Cr(CO)_3]^{4-}$: the first member in a new class of polyhedral clusters. J Am Chem Soc 110:8704–8706
28. Eichhorn BW, Haushalter RC (1990) closo-$[CrPb_9(CO)_3]^{4-}$: a 100 year history of the nonaplumbide tetra-anion. J Chem Soc Chem Commun:937–938
29. Campbell J, Mercier HPA, Franke H, Santry DP, Dixon DA, Schrobilgen GJ (2002) Syntheses, crystal structures, and density functional theory calculations of the *closo*-[1-$M(CO)_3(\eta^4$-

$E_9)]^{4-}$ (E=Sn,Pb; M=Mo,W) cluster anions and solution NMR spectroscopic characterization of [1-$M(CO)_3(\eta^4$-$Sn_9)]^{4-}$ (M=Cr,Mo,W). Inorg Chem 41:86–107
30. Yong L, Hoffmann SD, Fässler TF (2005) Crystal structures of [K(2.2.2-crypt)]$_4$[$Pb_9Mo(CO)_3$] – isolation of the novel isomers [(η^5-Pb_9)$Mo(CO)_3]^{4-}$ beside [(η^4-Pb_9)$Mo(CO)_3]^{4-}$. Eur J Inorg Chem 2005:3663–3669
31. Wang J-Q, Stegmaier S, Wahl B, Fässler TF (2010) Step-by-step synthesis of the Endohedral Stannaspherene $[Ir@Sn_{12}]^{3-}$ via the capped cluster anion $[Sn_9Ir(cod)]^{3-}$. Chem Eur J 16:1793–1798
32. Downing DO, Zavalij P, Eichhorn BW (2010) The *closo*-$[Sn_9Ir(cod)]^{3-}$ and $[Pb_9Ir(cod)]^{3-}$ Zintl ions: isostructural Ir(I) derivatives of the *nido*-$[E_9]^{4-}$ anions (E=Sn,Pb). Eur J Inorg Chem 2010:890–894
33. Geitner FS, Klein W, Fässler TF (2017) Formation of the intermetalloid cluster $[AgSn_{18}]^{7-}$ – the reactivity of coinage metal NHC compounds towards $[Sn_9]^{4-}$. Dalton Trans 46:5796–5800
34. Scharfe S, Fässler TF (2010) Varying bonding modes of the Zintl ion $[Ge_9]^{4-}$ in Cu^I complexes: syntheses and structures of [Cu(η^4-Ge_9)$(PR_3)]^{3-}$ (R=^{i}Pr, Cy) and [Cu(η^4-Ge_9)(η^1-Ge_9)]$^{7-}$. Eur J Inorg Chem:1207–1213
35. Sun Z-M, Zhao Y-F, Li J, Wang L-S (2009) Diversity of functionalized germanium Zintl clusters: syntheses and theoretical studies of $[Ge_9PdPPh_3]^{3-}$ and $[Ni@(Ge_9PdPPh_3)]^{2-}$. J Clust Sci 20:601–609
36. Goicoechea JM, Sevov SC (2006) Organozinc derivatives of deltahedral zintl ions: synthesis and characterization of *closo*-$[E_9Zn(C_6H_5)]^{3-}$ (E=Si,Ge,Sn,Pb). Organometallics 25:4530–4536
37. Zhou B, Denning MS, Jones C, Goicoechea JM (2009) Reductive cleavage of Zn–C bonds by group 14 Zintl anions: synthesis and characterisation of $[E_9ZnR]^{3-}$ (E=Ge,Sn,Pb; R=Mes, ^{i}Pr). Dalton Trans:1571–1578
38. Zhou B, Denning MS, Chapman TAD, Goicoechea JM (2009) Coupling reactions of functionalized Zintl ions $[E_9Cd(C_6H_5)]^{3-}$ (E=Sn,Pb) with tributyltinhydride: synthesis and isolation of $\{Sn_9CdSn[(CH_2)_3CH_3]_3\}^{3-}$. Inorg Chem 48:2899–2907
39. Mayer K, Jantke L-A, Schulz S, Fässler TF (2017) Retention of the Zn-Zn bond in [Ge_9Zn-Zn$Ge_9]^{6-}$ and formation of [(Ge_9Zn)-(Ge_9)-(ZnGe_9)]$^{8-}$ and polymeric [−($Ge_9Zn)^{2-}$-]. Angew Chem Int Ed 56:2350–2355
40. Wallach C, Geitner FS, Karttunen AJ, Fässler TF (2021) Boranyl-functionalized [Ge_9] clusters: providing the idea of Intramolecular Ge/B frustrated Lewis pairs. Angew Chem Int Ed 60:2648–2653
41. Bentlohner MM, Jantke LA, Henneberger T, Fischer C, Mayer K, Klein W, Fässler TF (2016) On the nature of bridging metal atoms in Intermetalloid clusters: synthesis and structure of the metal-atom-bridged Zintl clusters $[Sn(Ge_9)_2]^{4-}$ and $[Zn(Ge_9)_2]^{6-}$. Chem Eur J 22:13946–13952
42. Zhou B, Denning MS, Chapman TAD, McGrady JE, Goicoechea JM (2009) $[Pb_9CdCdPb_9]^{6-}$: a Zintl cluster anion with an unsupported cadmium-cadmium bond. Chem Commun 45:7221–7223
43. Yong L, Hoffmann SD, Fässler TF, Riedel S, Kaupp M (2005) $[Pb_5\{Mo(CO)_3\}_2]^{4-}$: a complex containing a planar Pb_5 unit. Angew Chem Int Ed 44:2092–2096
44. Wang Y, Qin Q, Wang J, Sang R-L, Xu L (2014) $[Ge_8(Mo(CO)_3)_2]^{4-}$: an unprecedented 20-electron empty ten-vertex Zintl cluster. Chem Commun 50:4181–4183
45. Brown M, Fontaine XLR, Greenwood NN, Kennedy JD (1991) Organoruthenaborane chemistry. IX. The reactions of $[\{(\eta^6$-$C_6Me_6)RuCl_2\}_2]$ and $[\{(\eta^6$-MeC_6H_4-4-^{i}Pr)$RuCl_2\}_2]$ with the [*nido*-$B_9H_{12}]^-$ anion. Z Anorg Allg Chem 598(/599):45–52
46. Goicoechea JM, Sevov SC (2006) Deltahedral germanium clusters: insertion of transition-metal atoms and addition of organometallic fragments. J Am Chem Soc 128:4155–4161
47. Frank FC, Kasper JS (1958) Complex alloy structures regarded as sphere packings. I. Definitions and basic principles. Acta Crystallogr 11:184–190

48. Frank FC, Kasper JS (1959) Complex alloy structures regarded as sphere packings. II. Analysis and classification of representative structures. Acta Crystallogr 12:483–499
49. Boyko M, Hlukhyy V, Jin H, Dums JV, Fässler TF (2020) Extracting $[Pd@Sn_9]^{4-}$ and $[Rh@Pb_9]^{4-}$ clusters from their binary alloys using "metal scissors". Z Anorg Allg Chem 646:1575–1582
50. Hlukhyy V, He H, Jantke L-A, Fässler TF (2012) The neat ternary solid $K_{5-x}Co_{1-x}Sn_9$ with Endohedral $[Co@Sn_9]^{5-}$ cluster units: a precursor for soluble Intermetalloid $[Co_2@Sn_{17}]^{5-}$ clusters. Chem Eur J 18:12000–12007
51. Hlukhyy V, Stegmaier S, Van Wüllen L, Fässler TF (2014) Endohedrally filled $[Ni@Sn_9]^{4-}$ and $[Co@Sn_9]^{5-}$ clusters in the neat solids $Na_{12}Ni_{1-x}Sn_{17}$ and $K_{13-x}Co_{1-x}Sn_{17}$: crystal structure and ^{119}Sn solid-state NMR spectroscopy. Chem Eur J 20:12157–12164
52. Ponou S, Fässler TF (2007) Crystal growth and structure refinement of K_4Ge_9. Z Anorg Allg Chem 633:393–397
53. Queneau V, Sevov SC (1997) $[Ge_9]^{4-}$: a deltahedral Zintl ion now made in the solid-state. Angew Chem Int Ed Engl 36:1754–1756
54. Hoch C, Wendorff M, Röhr C (2002) Tetrapotassium nonastannide, K_4Sn_9. Acta Crystallogr C 58:i45–i46
55. Queneau V, Sevov SC (1998) Synthesis and structure of the Zintl-phase K_4Pb_9 containing isolated $[Pb_9]^{4-}$ clusters of two different geometries. Inorg Chem 37:1358–1360
56. Bobev S, Sevov SC (2002) Isolated deltahedral clusters of lead in the solid state: synthesis and characterization of Rb_4Pb_9 and $Cs_{10}K_6Pb_{36}$ with $[Pb_9]^{4-}$, and $A_3A'Pb_4$ (A=Cs,Rb,K; A'=Na, Li) with $[Pb_4]^{4-}$. Polyhedron 21:641–649
57. Todorov E, Sevov SC (1998) Deltahedral clusters in neat solids: synthesis and structure of the Zintl phase Cs_4Pb_9 with discrete $[Pb_9]^{4-}$ clusters. Inorg Chem 37:3889–3891
58. Hoch C, Wendorff M, Röhr C (2003) Synthesis and crystal structure of the tetrelides $A_{12}M_{17}$ (A=Na,K,Rb,Cs; M=Si,Ge,Sn) and A_4Pb_9 (A=K,Rb). J Alloys Compd 361:206–221
59. Quéneau V, Todorov E, Sevov SC (1998) Synthesis and structure of isolated silicon clusters of nine atoms. J Am Chem Soc 120:3263–3264
60. Von Schnering HG, Baitinger M, Bolle U, Carrillo-Cabrera W, Curda J, Grin Y, Heinemann F, Llanos J, Peters K, Schmeding A, Somer M (1997) Binary alkali metal compounds with the Zintl anions $[Ge_9]^{4-}$ and $[Sn_9]^{4-}$. Z Anorg Allg Chem 623:1037–1039
61. Hoch C, Wendorff M, Röhr C (2003) Neue binäre Stannide $A_{52}Sn_{82}$ (A=K,Cs) mit $[Sn_4]^{4-}$- und $[Sn_9]^{4-}$-Cluster-Anionen. Z Anorg Allg Chem 629:2391–2397
62. Hoch C, Wendorff M, Rohr C (2002) Tetrapotassium nonastannide, K_4Sn_9. Acta Crystallogr C 58:I45–I46
63. Witzel BJL, Klein W, Dums JV, Boyko M, Fässler TF (2019) Metallocages for metal anions: highly charged $[Co@Ge_9]^{5-}$ and $[Ru@Sn_9]^{6-}$ clusters featuring spherically encapsulated co^{-} and Ru^{2-} anions. Angew Chem Int Ed 58:12908–12913
64. Li Z, Ruan H, Wang L, Liu C, Xu L (2017) Counterion-induced crystallization of intermetalloid *Matryoshka* clusters $[Sb@Pd_{12}@Sb_{20}]^{3-,4-}$. Dalton Trans 46:3453–3456
65. Wang Y, Moses-Debusk M, Stevens L, Hu J, Zavalij PY, Bowen KH, Dunlap BI, Glaser ER, Eichhorn BW (2017) $Sb@Ni_{12}@Sb_{20}{}^{-/+}$ and $Sb@Pd_{12}@Sb_{20}{}^{n}$ cluster anions, where $n = +1$, -1, -3, -4: multi-oxidation-state clusters of interpenetrating platonic solids. J Am Chem Soc 139:619–622
66. Lin Z, Slee T, Mingos DMP (1990) A structural jellium model of cluster electronic structure. Chem Phys 142:321–334
67. Sheong FK, Zhang J-X, Lin Z (2017) Localized bonding model for coordination and cluster compounds. Coord Chem Rev 345:42–55
68. Khanna SN, Jena P (1995) Atomic clusters: building blocks for a class of solids. Phys Rev B Condens Matter 51:13705–13716
69. Huang X, Zhao J, Su Y, Chen Z, King RB (2014) Design of Three-shell Icosahedral Matryoshka Clusters $A@B_{12}@A_{20}$ (A=Sn,Pb; B=Mg,Zn,Cd,Mn). Sci Rep 4:6915

70. Jin X, McGrady JE (2019) Structure and bonding in endohedral transition metal clusters. In: van Eldik R, Puchta R (eds) Computational chemistry. Advances in inorganic chemistry, vol 73. Elsevier, London
71. Corbett JD (1985) Polyatomic Zintl anions of the post-transition elements. Chem Rev 85:383–397
72. Fässler TF (2001) The renaissance of homoatomic nine-atom polyhedra of the heavier carbon-group elements Si-Pb. Coord Chem Rev 215:347–377
73. Sevov SC, Goicoechea JM (2006) Chemistry of deltahedral Zintl ions. Organometallics 25:5678–5692
74. Scharfe S, Kraus F, Stegmaier S, Schier A, Fässler TF (2011) Zintl ions, cage compounds, and intermetalloid clusters of group 14 and group 15 elements. Angew Chem Int Ed 50:3630–3670
75. Wilson RJ, Lichtenberger N, Weinert B, Dehnen S (2019) Intermetalloid and heterometallic clusters combining p-block (semi)metals with d- or f-block metals. Chem Rev 119:8506–8554
76. Liu C, Sun Z-M (2019) Recent advances in structural chemistry of group 14 Zintl ions. Coord Chem Rev 382:32–56
77. Momma K, Izumi F (2011) VESTA 3 for three-dimensional visualization of crystal, volumetric and morphology data. J Appl Crystallogr 44:1272–1276
78. Benda CB, He H, Klein W, Somer M, Fässler TF (2015) Bisvinylated [R–Ge_9–Ge_9–R]$^{4-}$ cluster dimers. Z Anorg Allg Chem 641:1080–1086
79. Goicoechea JM, Sevov SC (2005) [(Ni-Ni-Ni)@$(Ge_9)_2$]$^{4-}$: a linear triatomic nickel filament enclosed in a dimer of nine-atom germanium clusters. Angew Chem Int Ed 44:4026–4028
80. Mayer K, Dums JV, Klein W, Fässler TF (2017) [$SnBi_3$]$^{5-}$ -a carbonate analogue comprising exclusively metal atoms. Angew Chem Int Ed 56:15159–15163
81. Liu C, Jin X, Li L-J, Xu J, McGrady JE, Sun Z-M (2018) Reactivity studies of [Co@Sn_9]$^{4-}$ with transition metal reagents: bottom-up synthesis of ternary functionalized Zintl clusters. Inorg Chem 57:3025–3034
82. He H, Klein W, Jantke L-A, Fässler TF (2014) Metal-centered Zintl ions isolated by direct extraction from Endohedral intermetallic precursor: [Co_{1-x}@Sn_9]$^{4-}$ (x≈0.32) and [Co_2@Sn_{17}]$^{5-}$. Z Anorg Allg Chem 640:2864–2870
83. Gillett-Kunnath MM, Paik JI, Jensen SM, Taylor JD, Sevov SC (2011) Metal-centered deltahedral Zintl ions: synthesis of [Ni@Sn_9]$^{4-}$ by direct extraction from intermetallic precursors and of the vertex-fused dimer [{Ni@Sn_8(μ-Ge)$_{1/2}$}$_2$]$^{4-}$. Inorg Chem 50:11695–11701
84. Scharfe S, Fässler TF, Stegmaier S, Hoffmann SD, Ruhland K (2008) [Cu@Sn_9]$^{3-}$ and [Cu@Pb_9]$^{3-}$: intermetalloid clusters with Endohedral Cu atoms in spherical environments. Chem Eur J 14:4479–4483
85. Benda CB, Waibel M, Köchner T, Fässler TF (2014) Reactivity of liquid Ammonia solutions of the Zintl phase $K_{12}Sn_{17}$ towards Mesitylcopper(I) and Phosphinegold(I) chloride. Chem Eur J 20:16738–16746
86. Esenturk EN, Fettinger JC, Eichhorn BW (2006) Synthesis, structure, and dynamic properties of [Ni_2Sn_{17}]$^{4-}$. J Am Chem Soc 128:12–13
87. Liu C, Jin X, Li L-J, Xu J, McGrady JE, Sun Z-M (2019) Synthesis and structure of a family of rhodium polystannide clusters [Rh@Sn_{10}]$^{3-}$, [Rh@Sn_{12}]$^{3-}$, [Rh_2@Sn_{17}]$^{6-}$ and the first triply-fused stannide, [Rh_3@Sn_{24}]$^{5-}$. Chem Sci 10:4394–4401
88. Korber N, Fleischmann A (2001) Synthesis and crystal structure of [$Li(NH_3)_4$]$_4$[Sn_9] x NH_3 and [$Li(NH_3)_4$]$_4$[Pb_9] x NH_3. J Chem Soc Dalton Trans:383–385
89. Henneberger T, Klein W, Fässler TF (2018) Silicon containing nine atom clusters from liquid Ammonia solution: crystal structures of the first protonated clusters [HSi_9]$^{3-}$ and [H_2{Si/Ge}$_9$]$^{2-}$. Z Anorg Allg Chem 644:1018–1027
90. Kleber W (1967) Das "Druck-Abstands-Paradoxon". Krist Tech 2:13–14
91. Scharfe S (2010) Untersuchungen zur Reaktivität von Zintl-anionen der tetrele in Lösung. Dissertation Technische Universiät München
92. Heaton BT, Strona L, Della Pergola R, Vidal JL, Schoening RC (1983) Multinuclear variable-temperature nuclear magnetic resonance study of rhodium carbonyl clusters containing

encapsulated heteroatoms: ligand and metal polyhedral rearrangements. J Chem Soc Dalton Trans 1983:1941–1947
93. Shu C-C, Morgan HWT, Qiao L, McGrady JE, Sun Z-M (2020) A family of lead clusters with precious metal cores. Nat Commun 11:3477
94. Mingos DMP, Lin Z (1989) Site preference effects in Heterometallic clusters. Comments Inorg Chem 9:95–122
95. Bentlohner MM, Fischer C, Fässler TF (2016) Synthesis and characterization of pristine *closo*-$[Ge_{10}]^{2-}$. Chem Commun 52:9841–9843
96. Spiekermann A, Hoffmann SD, Fässler TF (2006) The Zintl ion $[Pb_{10}]^{2-}$: a rare example of a homoatomic *closo* cluster. Angew Chem Int Ed 45:3459–3462
97. Wang J-Q, Stegmaier S, Fässler TF (2009) $[Co@Ge_{10}]^{3-}$: an intermetalloid cluster with Archimedean pentagonal prismatic structure. Angew Chem Int Ed 48:1998–2002
98. Esenturk EN, Fettinger JC, Eichhorn BW (2005) The *closo*-$[Pb_{10}]^{2-}$ Zintl ion in the $[Ni@Pb_{10}]^{2-}$ cluster. Chem Commun 41:247–249
99. Zhou B, Denning MS, Kays DL, Goicoechea JM (2009) Synthesis and isolation of $[Fe@Ge_{10}]^{3-}$: a pentagonal prismatic Zintl ion cage encapsulating an interstitial Iron atom. J Am Chem Soc 131:2802–2803
100. Krämer T, Duckworth JCA, Ingram MD, Zhou B, McGrady JE, Goicoechea JM (2013) Structural trends in ten-vertex endohedral clusters, $M@E_{10}$ and the synthesis of a new member of the family, $[Fe@Sn_{10}]^{3-}$. Dalton Trans 42:12120–12129
101. Liu C, Li L-J, Popov IA, Wilson RJ, Xu C-Q, Li J, Boldyrev AI, Sun Z-M (2018) Symmetry reduction upon size mismatch: the non-icosahedral Intermetalloid cluster $[Co@Ge_{12}]^{3-}$. Chin J Chem 36:1165–1168
102. Uta MM, Cioloboc D, King RB (2012) Cobalt-centered ten-vertex germanium clusters: the pentagonal prism as an alternative to polyhedra predicted by the Wade-Mingos rules. Inorg Chem 51:3498–3504
103. Uta MM, Cioloboc D, King RB (2012) Iron-centered ten-vertex germanium clusters: the ubiquity of low energy pentagonal prismatic structures with various skeletal electron counts. J Phys Chem A 116:9197–9204
104. King RB, Silaghi-Dumitrescu I, Uta MM (2009) Endohedral nickel, palladium, and platinum atoms in 10-vertex germanium clusters: competition between Bicapped Square Antiprismatic and pentagonal prismatic structures. J Phys Chem A 113:527–533
105. Zhou B, Krämer T, Thompson AL, McGrady JE, Goicoechea JM (2011) A highly distorted open-Shell Endohedral Zintl cluster: $[Mn@Pb_{12}]^{3-}$. Inorg Chem 50:8028–8037
106. Li A-M, Wang Y, Downing DO, Chen F, Zavalij P, Munoz-Castro A, Eichhorn BW (2020) Endohedral plumbaspherenes of the group 9 metals: synthesis, structure and properties of the $[M@Pb_{12}]^{3-}$ (M=Co,Rh,Ir) ions. Chem Eur J 26:5824–5833
107. Wang Y, Wang L-L, Ruan H, Luo B-L, Sang R-L, Xu L (2015) Synthesis and characterization of the endohedral plumbaspherene $[Rh@Pb_{12}]^{3-}$. Chin J Struct Chem 34:1253–1258
108. Esenturk EN, Fettinger JC, Eichhorn BW (2006) The $[Pb_{12}]^{2-}$ and $[Pb_{10}]^{2-}$ Zintl ions and the $[M@Pb_{12}]^{2-}$ and $[M@Pb_{10}]^{2-}$ cluster series where M=Ni,Pd,Pt. J Am Chem Soc 128:9178–9186
109. Li L-J, Pan F-X, Li F-Y, Chen Z-F, Sun Z-M (2017) Synthesis, characterization and electronic properties of an endohedral plumbaspherene $[Au@Pb_{12}]^{3-}$. Inorg Chem Front 4:1393–1396
110. Perla LG, Sevov SC (2016) A stannyl-decorated Zintl ion $[Ge_{18}Pd_3(Sn^iPr_3)_6]^{2-}$: twinned icosahedron with a common Pd_3-face or 18-vertex *Hypho*-deltahedron with a Pd_3-triangle inside. J Am Chem Soc 138:9795–9798
111. Zhang J-X, Sheong FK, Lin Z (2019) Remote bonding in clusters $[Pd_3Ge_{18}R_6]^{2-}$: modular bonding model for large clusters via principal interacting orbital analysis. Inorg Chem 58:3473–3478
112. Perla LG, Munoz-Castro A, Sevov SC (2017) Eclipsed- and staggered-$[Ge_{18}Pd_3\{E^iPr_3\}_6]^{2-}$ (E=Si,Sn): positional isomerism in Deltahedral Zintl clusters. J Am Chem Soc 139:15176–15181

113. Benda CB, Waibel M, Fässler TF (2015) On the formation of Intermetalloid clusters: Titanocene(III) diammin as a versatile reactant toward Nonastannide Zintl clusters. Angew Chem Int Ed 54:522–526
114. Liu C, Popov IA, Li L-J, Li N, Boldyrev AI, Sun Z-M (2018) $[Co_2@Ge_{16}]^{4-}$: localized versus delocalized bonding in two isomeric intermetalloid clusters. Chem Eur J 24:699–705
115. Goicoechea JM, Sevov SC (2005) $[(Pd-Pd)@Ge_{18}]^{4-}$: a palladium dimer inside the largest single-cage deltahedron. J Am Chem Soc 127:7676–7677
116. Sun Z-M, Xiao H, Li J, Wang L-S (2007) $[Pd_2@Sn_{18}]^{4-}$: fusion of two endohedral stannaspherenes. J Am Chem Soc 129:9560–9561
117. Kocak FS, Zavalij P, Lam Y-F, Eichhorn BW (2008) Solution dynamics and gas-phase chemistry of $[Pd_2@Sn_{18}]^{4-}$. Inorg Chem 47:3515–3520
118. Esenturk EN, Fettinger JC, Eichhorn BW (2006) Synthesis and characterization of the $[Ni_6Ge_{13}(CO)_5]^{4-}$ and $[Ge_9Ni_2(PPh_3)]^{2-}$ Zintl ion clusters. Polyhedron 25:521–529
119. Tran NT, Dahl LF (2003) Nanosized $[Pd_{69}(CO)_{36}(PEt_3)_{18}]$: metal-core geometry containing a linear assembly of three face-sharing centered Pd_{33} icosahedra inside of a hexagonal-shaped Pd_{30} tube. Angew Chem Int Ed 42:3533–3537

Struct Bond (2021) 188: 197–258
https://doi.org/10.1007/430_2021_84

Published online: 24 April 2021

Structure and Bonding of Group 14 Clusters: Wade's Rules and Beyond

Jing-Xuan Zhang, Fu Kit Sheong, and Zhenyang Lin

Contents

Abstract Clusters of group 14 elements show plenty of similarities with borane clusters. As such, chemists often try to understand their structure and bonding on the basis of Wade's rules to predict and classify various clusters. Such practice, albeit very common, often faces challenges and difficulties due to significant differences in

J.-X. Zhang and Z. Lin (✉)
Department of Chemistry, The Hong Kong University of Science and Technology, Hong Kong, People's Republic of China
e-mail: jzhangbm@connect.ust.hk; chzlin@ust.hk

F. K. Sheong (✉)
Department of Chemistry, The Hong Kong University of Science and Technology, Hong Kong, People's Republic of China

Institute for Advanced Study, The Hong Kong University of Science and Technology, Hong Kong, People's Republic of China
e-mail: fksheong@connect.ust.hk

the bonding abilities between group 13 and 14 atoms, as well as the changes in the ionization energies and radial characteristics of atomic orbitals as the groups are descended. In this chapter, we have extensively discussed the structure and bonding of a wide variety of group 14 clusters, including bare clusters, substituent-decorated clusters, endohedral clusters, transition metal doped clusters, and their combinations. By thoroughly analyzing their electronic structures within the framework of molecular orbital theory, we have summarized their bonding patterns and explored the factors that affect the applicability of Wade's rules in various group 14 clusters.

Keywords Bare cluster · Cluster assembly · Endohedral cluster · Modular bonding picture · Wade-Mingos rules

Abbreviations

AdNDP	Adaptive natural density partitioning
HOMO	Highest occupied molecular orbital
Hyp	Hypersilyl, $Si(SiMe_3)_3$
LUMO	Lowest unoccupied molecular orbital
MSA	Monocapped square antiprism
*n*c-2e	*n*-center-2-electron
PIO	Principal interacting orbital
PSEPT	Polyhedral skeletal electron pair theory
SEP	Skeletal electron pair
TSH	Tensor surface harmonics
TTP	Tricapped trigonal prism

1 Introduction

Group 14 of the periodic table is arguably the most important group of elements in chemistry. Lead and tin are well known for their use in the production of alloys and devices, silicon and germanium are important semi-conductors that established the foundation of modern technology, and needless to say carbon constitutes the very basis of the living world. Because group 14 crosses the dividing line between metals and non-metals, elements in this group feature a wide variety of physical and chemical properties, bringing a rich context into material science.

Being main group elements with 4 valence electrons, group 14 elements are predominantly tetravalent as a straightforward implication of the octet rule, and thus they are often termed "tetrel elements." Indeed, the dominance of four-connected diamond structure in the bulk state allotropes of tetrel elements, and the wide existence of tetrel dioxides and tetrahalides, both demonstrate the predominant tetravalency of tetrel elements, especially for lighter ones. For the heavier tetrel

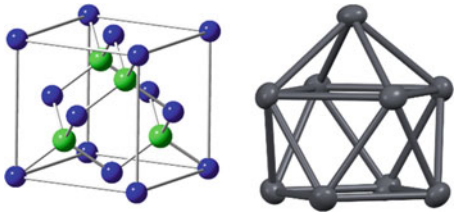

Fig. 1 Structures of diamond and the Zintl ion cluster $[Pb_9]^{4-}$ [1]

elements, inert pair effect gives rise to the possibility of divalent tetrel atoms, mostly seen in lead but sometimes also tin, as exemplified by a wide range of ionic compounds and coordination complexes with the metals formally in the +2 oxidation state.

In addition to the above-mentioned classic main group chemistry, however, tetrel elements can also exist in completely different forms. A clear counterexample is the Zintl compound, which is a class of simple binary compounds formed between alkali metals and heavy tetrel elements. The earliest synthesized Zintl compound is Na_4Pb_9, which greatly mystified chemists because it did not conform to simple valency rules. If we assume the sodium is present as the monovalent Na(I), we might be forced to assign the lead atoms with fractional negative charges or mixed oxidation states. In-depth examination of its crystal structure (Fig. 1), however, reveals that the lead atoms exist in the form of Pb_9^{4-} clusters, one of the earliest examples of what are later termed Zintl ion clusters.

The presence of clustered units in bulk phase indicates a new chemistry of tetrel elements, and understanding the electronic structures of these clusters would build an important bridge between molecules and bulk materials. The failure of tetrel elements to form four bonds and conform to octet rule hints a completely different bonding behavior in Zintl clusters. This raises the very fundamental question of this book: how to describe the structure and bonding of a cluster compound?

Encouraged by the fundamental importance and interesting chemistry of cluster compounds, numerous experimental and theoretical efforts have been made to understand the geometric and electronic structures of these nanoclusters. Experimentally, a great number of group 14 cluster compounds have been synthesized and characterized, together with their derivatives with different compositions and properties. A straightforward and extensively studied approach is to start from bulk materials and break the bulk into pieces of cluster units by reducing reagents. On the other hand, the bottom-up production of nanoclusters from molecular substances has also received lots of recent attentions as an alternative to the traditional top-down approach, as it allows more precise control of geometric and electronic structures of cluster compounds for further experimental analyses and development. Through this bottom-up approach, syntheses of group 14 clusters are no longer limited to Zintl phase compounds, but enter into the realm of molecular chemistry, allowing chemists to understand the structure and bonding of cluster compounds from a molecular perspective.

While individual atoms in cluster compounds do not necessarily follow the octet rule, bonding among these atoms is far from arbitrary. When we pay attention to cluster units instead of individual atoms, each cluster would exhibit certain patterns in electron counts, as first observed in borane clusters by Wade [2]. Wade's electron-counting rules were later extended into other main group and transition metal clusters by Mingos, now known as the polyhedral skeletal electron pair theory (PSEPT) [3, 4]. These electron-counting rules can relate the geometries of clusters with their electron counts, thus serve as versatile rules of thumb and play the central role in cluster chemistry similar to that of the octet rule in traditional inorganic chemistry.

In addition to electron-counting approaches, detailed analysis on electronic structures in terms of orbitals is essential for chemists to establish an in-depth yet generalizable understanding of clusters, especially when simple electron-counting rules do not apply. Stone's tensor surface harmonics (TSH) theory [5], for example, describes the underlying model that relates the geometric structures and electron counts within the framework of orbital interactions (*vide infra*) and rationalizes apparent "exceptions" to electron-counting rules.

This chapter is dedicated to revealing the structure and bonding of group 14 clusters that may or may not follow the prediction of Wade's electron-counting rules. We will go through representative examples, understand how the electron-counting rules work and how they would be affected under different cases, and show how new bonding patterns could arise from orbital interactions among chemical fragments.

Because of the importance of Wade's rules and PSEPT in cluster chemistry and their relevance in group 14 clusters, in Sect. 2, we will first give a brief review on Wade's rules and why they work in borane clusters. By making use of the isolobal analogy, we will then show by examples how Wade's rules play a guiding role in helping us understand group 14 clusters despite important differences between tetrel atoms and BH units (Sect. 3). With these established rules and patterns, we will present a wide variety of endohedral clusters that can be understood within the framework of Wade's rules, despite the existence of quite a number of exceptions (Sect. 4). More complicated clusters will be introduced in Sect. 5, which may fall out of the scope of Wade's rules at first glance, but can still be understood with the established knowledge through an in-depth analysis. Nevertheless, cluster chemistry is after all a rapidly developing field, and there are still many clusters out there that do not fit into any of the aforementioned classes, as will be introduced in Sect. 6. Via such an organization, we hope that readers can not only get familiar with the discovered group 14 clusters to date and the applicability of electron-counting rules, but more importantly, also understand the underlying concepts that bridge one with another. A brief conclusion and perspective discussion will be given in Sect. 7 to close this chapter.

2 A Brief Review of Wade's Rules and the Underlying Principles

While Wade's rules are convenient rules of thumb that can be easily applied in practice in determining overall charge or electron counts of clusters from their geometries without going into detailed electronic structures, there are more rigorous theoretical models that can better explain the electron counts of borane clusters predicted by Wade's rules [6]. One representative example of these mathematical models is the Stone's tensor surface harmonics (TSH) theory based on the framework of orbital interactions [5]. To be specific, let us consider one of the [BH] units distributed on a spherical surface and take a local coordinate system to orient its orbitals. Each [BH] unit has a localized B-H bond between the hydrogen 1s orbital and a boron s-p hybridized orbital, leaving three boron orbitals available for skeletal bonding with other [BH] units, one with σ symmetry and two with π symmetry (with respect to the center of the sphere). For a deltahedral borane, orbital interactions among these $3n$ orbitals contribute $(n + 1)$ skeletal electron pairs (SEPs) in total (Fig. 2), and hence Wade's rule for *closo* clusters is sometimes also referred to as the $(n + 1)$ rule [4]. Based on the same framework, we can also derive the $(n + 2)$ rule for *nido* clusters and $(n + 3)$ rule for *arachno* clusters.

Understanding the $(n + 1)$ rule from the orbital interaction perspective would help us understand some apparent "exceptions" to Wade's rules in a unified framework. A famous example is the $[B_4Cl_4]$ cluster, which has a tetrahedral geometry and hence appears to be *closo*, but has a SEP count of n instead of $(n + 1)$. As mentioned before, each boron vertex contributes three valence orbitals (1 σ and 2 π) to skeletal bonding.

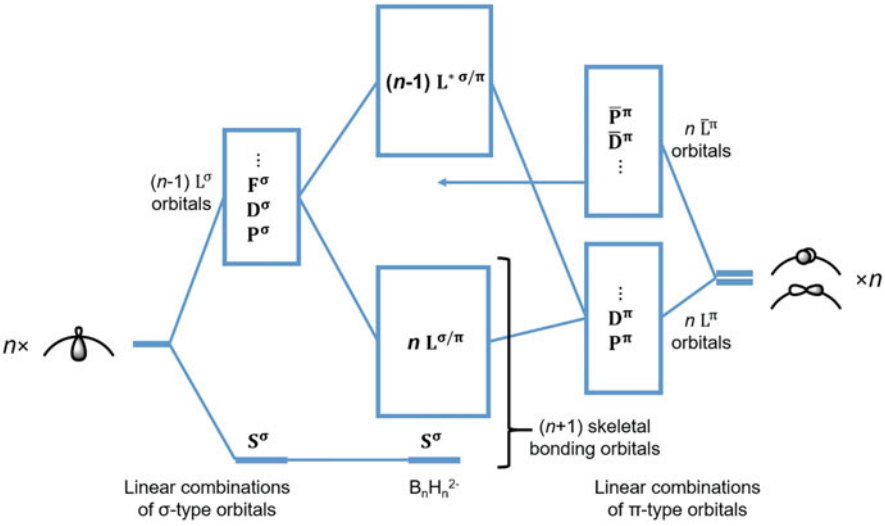

Fig. 2 Schematic orbital interaction diagram for general Wadean clusters showing the origin of the $(n + 1)$ rule

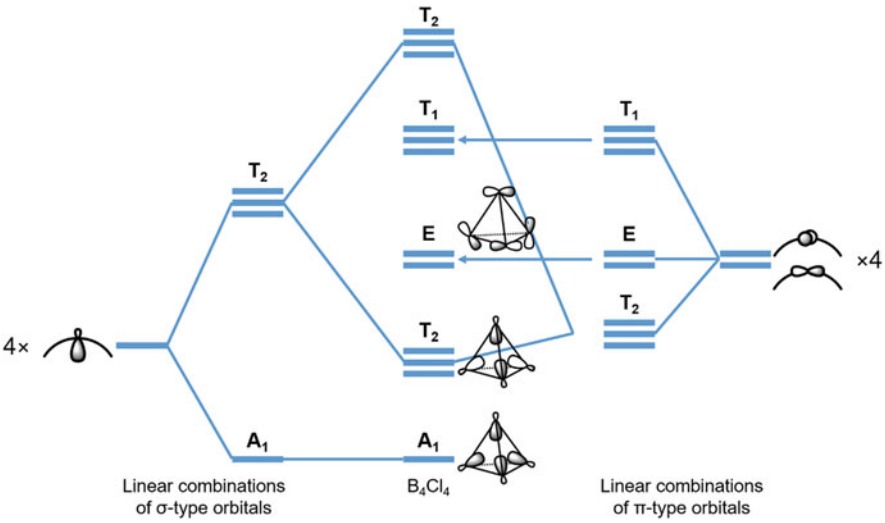

Fig. 3 Schematic orbital interaction diagram showing the skeletal molecular orbitals for tetrahedral clusters

The symmetry-adapted linear combinations of the four σ-type orbitals span $A_1 + T_2$ irreducible representations while the eight π-type orbitals span $E + T_1 + T_2$. Because there are two sets of orbitals with the same T_2 irreducible representations, they would further interact with each other to give rise to the skeletal bonding orbitals as in Fig. 3, in addition to orbitals in other irreducible representations. This orbital interaction diagram immediately eliminates the possibility of applying $(n + 1)$ rule in the B_4Cl_4 cluster ($n = 4$) since the $(n + 1)$-th orbital is degenerate with the $(n + 2)$-th orbital.

It should however be noted that, in molecular orbital calculations, the skeletal bonding orbitals and the external B-H σ bonding orbitals are always extensively mixed with each other, so the canonical molecular orbitals will not be able to clearly exhibit pure skeletal nature, as illustrated by calculation on the $[B_4H_4]$ molecule shown in Fig. 4. The two sets of $A_1 + T_2$ orbitals are actually in-phase and out-of-phase combinations of the skeletal bonding orbitals and the symmetry-adapted linear combinations of the external B-H σ bonding orbitals.

While electrons only fill up to the n-th orbital in the boron cluster $[B_4Cl_4]$ which contains relatively electropositive boron atoms, the tetrahedrane molecule $[C_4H_4]$ actually follows the $(n + 2)$ rule with six SEPs (each vertex having 3 electrons involved in bonding with the other three vertices, totaling 12 skeletal electrons). Such a delocalized view that correlates well to the $[B_4Cl_4]$ case is in fact equivalent with the usual localized view for tetrahedrane, which describes their skeletal bonding as having six localized C-C bonds, for which reason tetrahedrane is sometimes called an "electron-precise" cluster.

The inadequacy of Wade's rules for tetrahedral clusters is not a single exception. In fact, it has been found that in clusters which have a threefold axis and a single

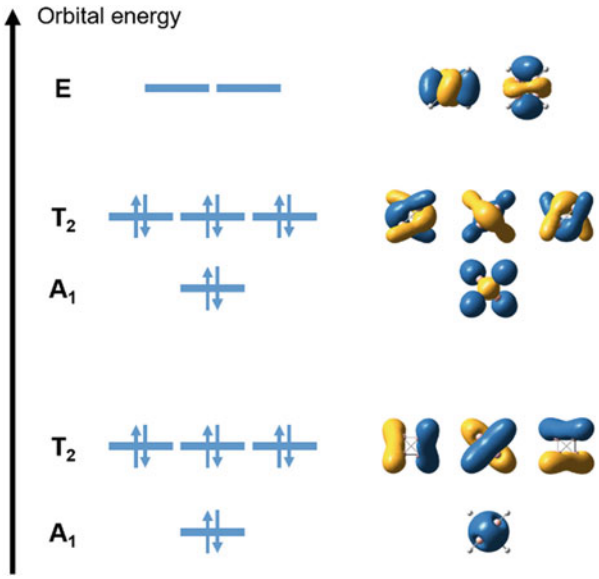

Fig. 4 Molecular orbital diagram of the tetrahedral $[B_4H_4]$ molecule computed using PBE0/def2TZVP model chemistry based on geometries optimized at the same level

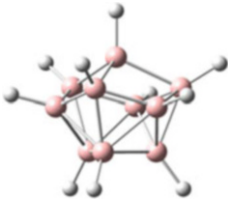

Fig. 5 Structure of the hypothetical cluster $[B_{10}H_{10}]$ [7]

vertex on this axis (e.g. tetrahedron), the $(n + 1)$-th and the $(n + 2)$-th skeletal bonding orbital will be degenerate as discussed above [7, 8]. In such case, a cluster with $(n + 1)$ SEPs will distort from a highly symmetric structure due to (first-order) Jahn-Teller effect, arising from the incomplete occupation of degenerate orbitals. Hence deviation from $(n + 1)$ rule is expected for such clusters. Apart from the aforementioned tetrahedral cluster $[B_4Cl_4]$, the hypothetical $[B_{10}H_{10}]$ cluster is also said to violate Wade's rules due to such a degeneracy. $[B_{10}H_{10}]$ might appear to have a closed deltahedral structure (Fig. **5**), but is very different from the bicapped square antiprismatic geometry for typical *closo* 10-vertex clusters. At the same time, this neutral cluster has only n SEPs, instead of $(n + 1)$ SEPs as seen in the bicapped square antiprismatic borane cluster $[B_{10}H_{10}]^{2-}$. Relevant examples with this kind of unusual electron count and geometry include some metallaboranes as well as some

other cases (*vide infra*) that are sometimes termed "*hyper-closo*" clusters [7, 8]. These apparent exceptions to Wade's rules have been extensively studied and become a part of the more generalized Wade-Mingos rules, or the PSEPT, which considers not only removal of vertices from *closo* clusters to generate *nido*, *arachno,* or *hypho* structures, but also vertex capping and other extensions [4].

3 Group 14 Clusters Which Conform to Wade's Rules

As mentioned in the Introduction section, Wade's rules are handy empirical rules that bridge the electron count and the geometry of borane clusters. The most typical boranes that fulfill Wade's rules are *closo* clusters in the form of $[B_nH_n]^{2-}$ with deltahedral geometries. The valence electron count associated with this kind of clusters is $4n + 2$ ($3n$ from n B atoms, n from n H atoms, and 2 from the negative charge). Although Wade's rules are originally proposed for borane clusters, this $(4n + 2)$ rule has been extended to $(14n + 2)$ rule in PSEPT for transition metal clusters by taking into consideration the d-shell of each vertex atom, and can also serve as an important guiding principle for group 14 clusters [9–12]. Despite the general applicability of Wade's rules, there are still striking differences between boranes and group 14 clusters that are worth careful examination. In this section, we will discuss the applicability of Wade's rules in group 14 clusters with a number of examples, especially those that are synthesized and characterized in solution or solid phases.

3.1 Bare Clusters $[E_n]^{q-}$ and Their Derivatives

Let us begin with the simplest group 14 cluster compounds in the formula of $[E_n]^{q-}$, E being a tetrel element hereafter, to demonstrate the general applicability of Wade's rules on group 14 clusters. In such a bare cluster $[E_n]^{q-}$, the orbital interaction among tetrel atoms is similar to that among [BH] units in boranes, by noting that a tetrel atom is not only isoelectronic (having the same number of valence electrons), but also isolobal (having the same number of available valence orbitals with similar symmetries and shapes) to a [BH] unit in borane clusters. Hence the same scenario as introduced in the previous section for borane clusters also holds in general for bare group 14 clusters.

Specifically, if we consider each atom having a lone pair pointing outwards, in analogy with an external B-H σ bond in a borane cluster, each tetrel atom is left with two valence electrons and three valence orbitals available for skeletal bonding, making itself isolobal with a [BH] unit. Hence a similar orbital interaction pattern is expected, giving rise to the same electron-counting rules.

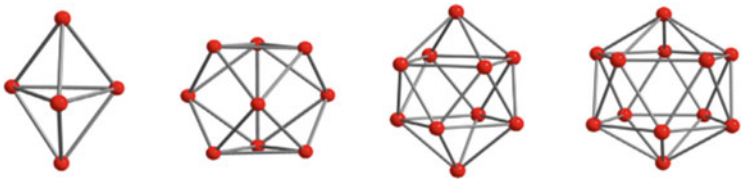

Fig. 6 *Closo* group 14 clusters $[E_5]^{2-}$, $[E_9]^{2-}$, $[E_{10}]^{2-}$, and $[E_{12}]^{2-}$ [12] (Adapted from [12], Copyright (2019), with permission from Elsevier)

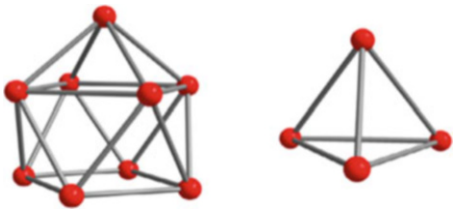

Fig. 7 *Nido* clusters $[E_9]^{4-}$ and *hyper-closo* clusters $[E_4]^{4-}$ [12] (Adapted from [12], Copyright (2019), with permission from Elsevier)

Because of the aforementioned isolobal analogy, Wade's rules would predict that group 14 clusters $[E_n]^{2-}$ will also adopt a *closo* geometry, similar to their analogous borane clusters with the same number of vertices. Indeed, there are many clusters following this prediction. Examples include $[E_5]^{2-}$ [13–18], $[E_9]^{2-}$ [19, 20], and $[E_{10}]^{2-}$ [21] (Fig. **6**), all of which have similar shapes with the corresponding borane clusters $[B_5H_5]^{2-}$, $[B_9H_9]^{2-}$, and $[B_{10}H_{10}]^{2-}$. $[E_{12}]^{2-}$ clusters have also been found to be particularly stable by theoretical studies, although they have only been detected in gas phase [22–24].

Group 14 clusters in *nido* geometries also exist. A notable example is the $[E_9]^{4-}$ (E = Ge, Sn, Pb) unit which exists in monocapped square antiprismatic geometry in A_4E_9 (A = alkali metals) compounds [17, 25–29] (Fig. **7**). The Na_4Pb_9 Zintl phase introduced earlier is one of the earliest examples that features this structure.

Similar to boranes, exceptions to Wade's rules could also be found in group 14 clusters. For example, $[E_4]^{4-}$ clusters have been reported [27, 30] (Fig. **7**), which have a similar orbital interaction diagram as $[B_4Cl_4]$ and thus clearly cannot fulfill Wade's rules. Instead, there are two more pairs of electrons filling into the non-bonding E-type orbitals, giving rise to $n + 2$ SEPs. Note that this description is equivalent to a localized picture in which there is a lone pair on each tetrel atom and a two-center-two-electron (2c-2e) bond associated with each neighboring atom pair. This equivalence can be immediately revealed by introducing a proton on each vertex to form an E-H bond and noting that the resulting species $[E_4H_4]$ is isoelectronic with tetrahedrane C_4H_4. Alternatively, one can also consider the isoelectronic relationship between an anionic tetrel atom $[E^-]$ and a pnictogen atom, say, P, and the cluster will simply be isoelectronic with the white phosphorous molecule P_4. This slightly higher tendency for group 14 clusters to fulfill octet, when compared to

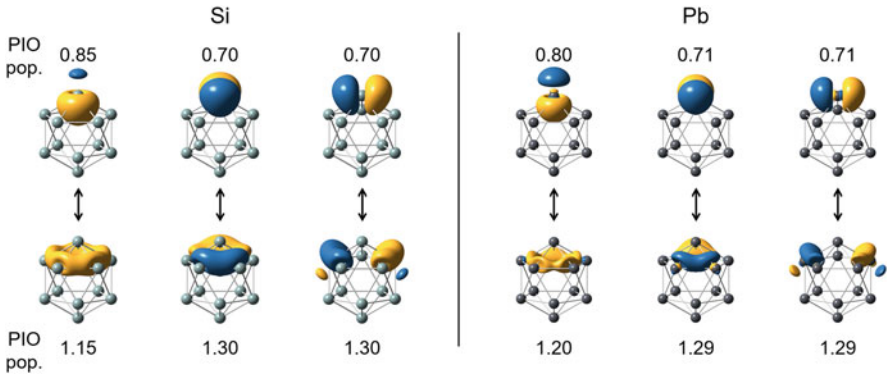

Fig. 8 Principal interacting orbital analysis on $[Si_{12}]^{2-}$ and $[Pb_{12}]^{2-}$ clusters, with one of the vertices as one fragment and the rest of cluster as the other fragment

group 13 counterparts, gives rises to some difference in bonding behaviors, which will be elaborated later in Sect. 6.

Apart from comparisons across groups, we may also make intra-group comparison among different periods. For heavy tetrel atoms like germanium, tin and lead, their atomic *n*s-*n*p energy gaps are large due to strong shielding effect. Thus, the s-p hybridization is not that significant when compared to carbon. Hence, we would expect that the lone pairs of tetrel atoms in a group 14 cluster are largely contributed by electrons in their *n*s orbitals, especially when the tetrel element goes down the group. To illustrate such difference, we can perform a principal interacting orbital (PIO) analysis [31, 32] on the $[Si_{12}]^{2-}$ cluster, to investigate the most important orbitals that each vertex utilizes to interact with other vertices. Indeed, the PIO analysis identifies three pairs of orbital interactions, consistent with our previous descriptions based on Wade's rules and TSH theory (Fig. **8**). The PIO analysis on the $[Pb_{12}]^{2-}$ cluster reveals a similar picture, except that the σ-type PIO of the Pb vertex is obviously of more p character compared to the Si analog, leaving the Pb 6s orbital for holding the lone pair. The unusual stability of *n*s orbitals (especially for lead because of the inert pair effect) is essential for a heavy tetrel atom to hold a lone pair of electrons, so that it does not significantly participate in skeletal bonding.

Compared to heavy tetrel elements, carbon has a much smaller s-p gap than heavier tetrel elements, and thus disfavors a localized lone pair that resembles a B-H σ bond in borane. This explains the fact that while there exist numerous examples of silicon, germanium, tin, and lead clusters that have close resemblance to boranes, we cannot find any similar electron-deficient clusters that consist of only carbon atoms. Instead, carbon has a bonding behavior very different from heavy tetrels. The out-of-plane π-type interactions between carbon 2p orbitals are much stronger than those between p orbitals of heavier tetrel atoms. Hence the commonly seen carbon "clusters" are fullerenes, which have completely different geometries from deltahedral borane clusters.

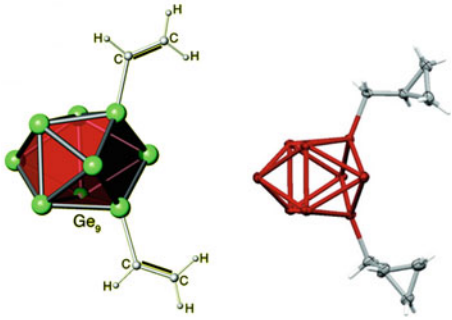

Fig. 9 Crystal structure of $[Ge_9R_2]^{2-}$, where R = C_2H_3 and C_4H_7 [37, 38] (Adapted with permission from [37, 38]. Copyright (2007) and (2009) American Chemical Society)

Fig. 10 Crystal structure of $[C_6Me_6]^{2+}$ [45] (Reprinted from [45], Copyright (2016), with permission from John Wiley and Sons)

Other than the aforementioned bare clusters, a larger number of their derivatives have been synthesized by introducing various substituents on some of the vertices of a cluster, ranging from monosubstituted, disubstituted, trisubstituted to tetrasubstituted clusters [33–42]. These clusters can be easily understood in a similar way, noting the isoelectronic/isolobal relationship among [BH], [E], and $[ER]^+$ units.

For example, the cluster $[Ge_9R_2]^{2-}$ (R = aliphatic groups) has 40 valence electrons (4 × 9 from Ge atoms, 1 × 2 from R substituents, and 2 from the negative charge), which is isoelectronic with the bare cluster $[Ge_9]^{4-}$ and the borane cluster $[B_9H_9]^{4-}$. Hence the skeletal bonding of the cluster $[Ge_9R_2]^{2-}$ should resemble its analogs. Indeed, the $[Ge_9R_2]^{2-}$ cluster adopts a monocapped square antiprismatic geometry (Fig. **9**), falling into the class of *nido* clusters as predicted by Wade's rules.

In fact, with an R-group substitution turning the "lone pair" of electrons on carbon into a σ bonding pair, electron-deficient carbon clusters become possible in some very rare cases. A worth-noting example is the dicationic "benzene," $[C_6Me_6]^{2+}$, which has a skeletal electron count of 16 (3 × 6 from carbon atoms minus 2 from positive charge), isoelectronic with $[B_6H_6]^{4-}$ in terms of skeletal bonding [43–45]. Unlike the neutral benzene in which all six carbon atoms lie on a plane, this molecule is electron-deficient and forms a three-dimensional cluster. As there are 6 vertices with a SEP count of 8 (= n + 2), Wade's rules predict a *nido* geometry similar to $[B_6H_6]^{4-}$, i.e. a pentagonal pyramid, which is indeed the case (Fig. **10**).

3.2 *Electronic Structure of [E_9] Clusters and Its Deviation from Wade's Rules*

Although many group 14 clusters could be easily understood with Wade's rules, they also show significant differences from borane clusters in terms of structure and bonding. One notable discrepancy can be seen from the observation that although $[B_6H_6]^{2-}$ and $[B_{12}H_{12}]^{2-}$ are representative structures of borane clusters, they are rarely observed in group 14 clusters. Instead, the most commonly seen group 14 cluster consists of 9 tetrel atoms, with two commonly associated electron counts, $[E_9]^{2-}$ and $[E_9]^{4-}$, which are seldom seen for borane compounds. Moreover, open-shell $[E_9]^{3-}$ species have also been reported to be stable [15, 28, 46, 47], which clearly falls out of the prediction of Wade's rules. All of these indicate that, apart from a simple analogy, there are still fundamental differences between group 14 clusters and boranes.

Some theoretical studies have been devoted to understand the origin of the extraordinary stability of the above-mentioned $[E_9]$ clusters. Adaptive natural density partitioning (AdNDP) analysis [48] has been performed to decipher the bonding by partitioning the electron density into 1c-2e bonds (lone pairs), 2c-2e bonds, and *n*c-2e (multi-centered) bonds [49] (Fig. **11**). The results show that the analyzed nine-vertex clusters seem to have special σ-aromaticity that stabilizes the skeletal bonding. As there are not yet systematic studies that perform parallel comparisons, how this aromatic behavior translates to the overall stability is still not so clear.

Another interesting attempt should be attributed to King and coworkers who viewed this problem from a different angle [50]. Note that in the aforementioned models, group 14 clusters are described as having out-pointing lone pairs localized at each vertex separated from skeletal bonding. But unlike borane clusters in which the B-H bonds are pointing away from each other, in group 14 clusters, the out-pointing lone pairs have stronger s characters and thus they can overlap with each other as well as with skeletal bonding orbitals. Hence an alternative model that could also be applied to understand the electronic structure of group 14 clusters is the Jellium model [50], which was originally proposed for alkali metal clusters and later extended to group 11 clusters [51–53]. Making use of the fact that a large class of clusters are approximately spherical, the Jellium model considers a cluster made up of many atoms as a "superatom," and the molecular orbitals of a cluster will resemble "superatomic orbitals" that can be well described with angular quantum numbers and hence can be labelled as S, P, D, F, etc. The 2-electron rule, 8-electron rule, and 18-electron rule become applicable, and the related magic numbers continue with 20, 34, 40, etc. Note that in this model, all of the valence electrons of a group 14 cluster are included in the electron counting. For example, the occupied orbitals for the $[E_{12}]^{2-}$ cluster are considered as a 50-electron species having its superatomic 1S, 1P, 1D, 2S, 1F, 2P, and 2D orbitals occupied.

Note that a $[E_9]^{4-}$ cluster has 40 (4×9 from tetrel atoms and 4 from the negative charge) valence electrons and thus conforms to the magic number (40). Without going into details, its corresponding occupied superatomic orbitals are 1S, 1P, 1D,

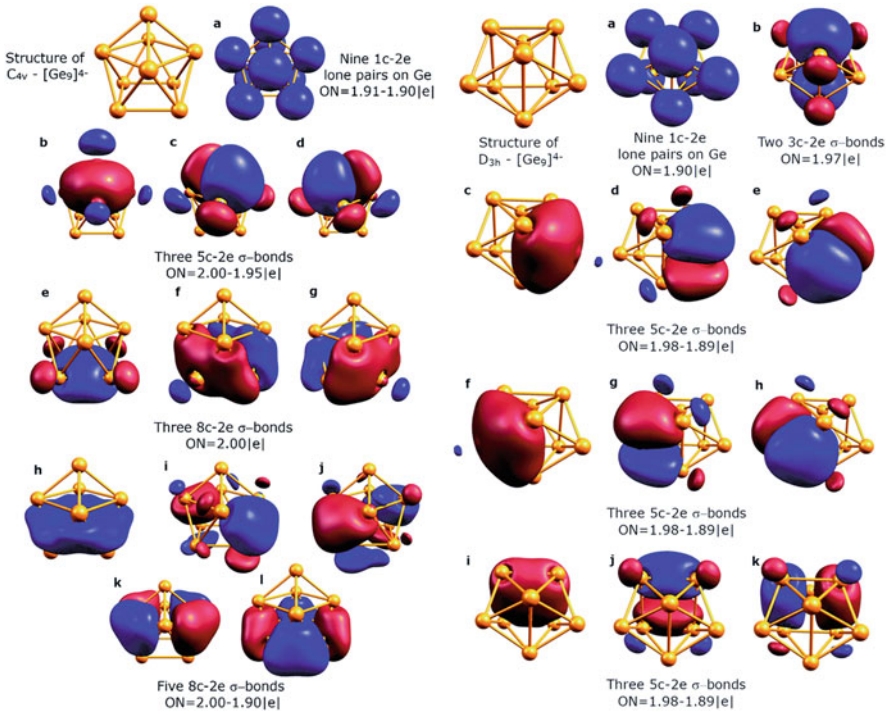

Fig. 11 Multi-centered bonding picture of $[Ge_9]^{4-}$ at C_{4v} and D_{3h} structures depicted by AdNDP analysis [49] (Reproduced from [49] – Published by The Royal Society of Chemistry, used under CC BY-NC 3.0)

2S, 1F, and 2P (Fig. **12**). Such "closed-shell" superatomic configuratiion described in the Jellium model might explain why $[E_9]^{4-}$ clusters (with or without substituents) are so common, even more common than *closo* $[E]^{2-}$ clusters, as well as the extraordinary stability of the open-shell species $[E_9]^{3-}$.

The $[E_9]^{4-}$ cluster is particularly interesting not only due to its surprising stability, but also because of its structural flexibility. If we follow the prediction of Wade's rules, $[E_9]^{4-}$ have $n + 2$ pairs of skeletal electrons and hence should adopt a *nido* structure, that is, a monocapped square antiprism (MSA).

However, there exist a number of examples showing that substituent-decorated $[E_9]^{4-}$ clusters can also be stable in a *closo* structure, that is, tricapped trigonal prism (TTP), as exemplified by the threefold-symmetric trisubstituted cluster $[Ge_9(Hyp)_3]^-$ (Hyp = hypersilyl, $Si(SiMe_3)_3$) [54] (Fig. **13**). To understand this observation, one has to first note that the MSA and TTP structures do not differ much in geometry. In fact, the MSA structure can be viewed as elongating one of the prismatic edges of the TTP geometry and opening up a square face (Fig. **14**). While the TTP structure of $[E_9]^{4-}$ does have an imaginary frequency according to gas phase calculation [12], this distortion is so small that the energy gain has been found to be very little. Therefore, the most stable geometry of $[E_9]^{4-}$ could be regulated by solvent, counterions, and substituents [55].

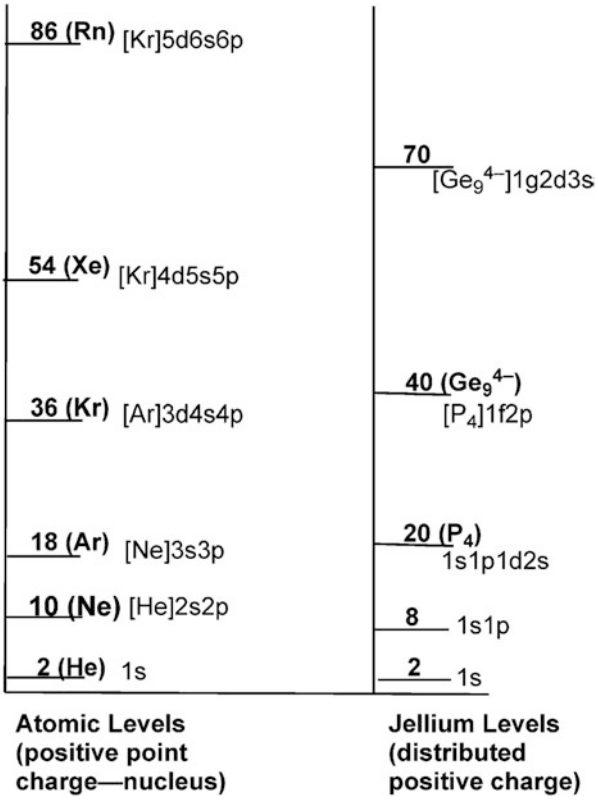

Fig. 12 Schematic MO diagram predicted by Jellium model and comparison with ordinary atomic levels [50] (Reproduced from Ref. [50] with permission from The Royal Society of Chemistry)

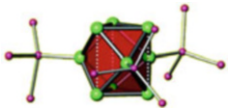

Fig. 13 Crystal structure of the trisubstituted $[Ge_9(Hyp)_3]^-$ cluster with threefold symmetry [54] (Adapted with permission from [54]. Copyright (2012) American Chemical Society)

From the electronic structure viewpoint, we may again see the close relationship between $[E_9]^{2-}$ and $[E_9]^{4-}$ at TTP and MSA geometries. Based on the aforementioned Jellium model, we can easily predict the shapes of the molecular orbitals of $[E_9]^{2-}$ at a TTP geometry. According to the Jellium model, the lowest occupied valence orbitals of $[Ge_9]^{2-}$ are expected to be 1S, 1P, 1D, and 2S orbitals, respectively (Fig. **12**). The subsequent 1F and 2P orbitals are higher in the valence region and are interlaced, with the $2P_z$ orbital being the HOMO and $1F_{z3}$ orbital being the LUMO (Fig. **15**). Note that this LUMO has slight bonding character among capping

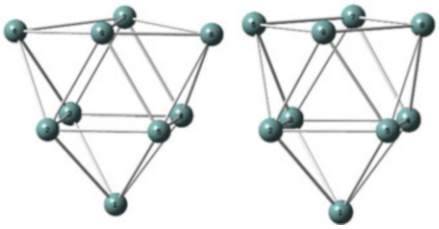

Fig. 14 Comparison between D_{3h} (left) and C_{4v} (right) structures of $[E_9]$ clusters in which shortening of the distance for a diagonal pair in the basal square face of the C_{4v} structure (top part of the shown structure) leads to the D_{3h} structure while an elongation leads back to the C_{4v} structure

atoms and anti-bonding character among those base atoms across the vertical edges. Hence in an $[E_9]^{4-}$ cluster, occupation of this $1F_{z3}$ orbital induces a second-order Jahn-Teller instability that could bring two of the capping atoms together while elongating a lateral edge, causing the cluster to deform from TTP to MSA geometry.

It should however be noted that, while Jellium model offers a distinct viewpoint for group 14 clusters, it does not predict different electronic structures but rather provides a different interpretation of the occupied orbitals of the clusters. In particular, for a $[E_9]$ cluster, Jellium model describes its molecular orbitals as superatomic orbitals and thus predicts a "closed-shell" configuration with 40 electrons. Wade's rules and Stone's TSH theory, on the other hand, separate skeletal bonding from external lone pairs and predict a *closo* configuration with 38 electrons. These two models should not be taken as contradictory to each other, but rather demonstrate the flexibility of the $[E_9]$ moiety in its electron count. The preferred configuration might vary with chemical environment, and the open-shell species $[E_9]^{3-}$, which lies between the two "closed-shell" electronic structures with different electron counts, can also exist. In fact, it has been found that this cluster can undergo electron exchange in solvent and reach a redox equilibrium among $[E_9]^{2-}$ and $[E_9]^{4-}$, as well as the intermediate state $[E_9]^{3-}$ [56].

Apart from the different possible electron counts shown above in a nine-vertex group 14 cluster, Wade's rules also have discrepancies in predicting the preferred geometries of 8, 11, and 14-vertex boranes and germanium clusters (Fig. **16**). While borane clusters tend to adopt deltahedral structures in which most if not all of the vertices have 4–5 neighboring vertices, germanium clusters prefer more an omnicapped polyhedral structure in which all the faces of a kernel polyhedron are capped with an extra atom. Such omnicapped polyhedral clusters show bispherical feature in geometry and have been systematically studied by Johnston and Mingos based on group theory [57].

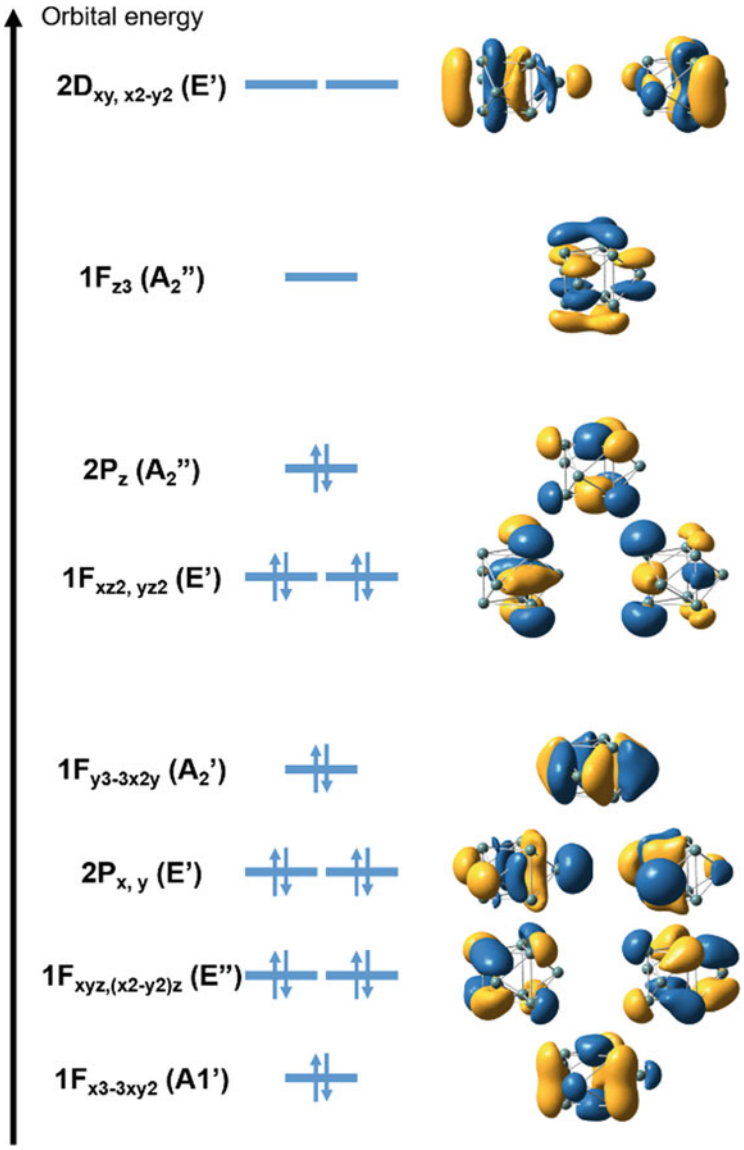

Fig. 15 Frontier molecular orbitals of $[Ge_9]^{2-}$ at a TTP geometry with corresponding superatomic orbital labels

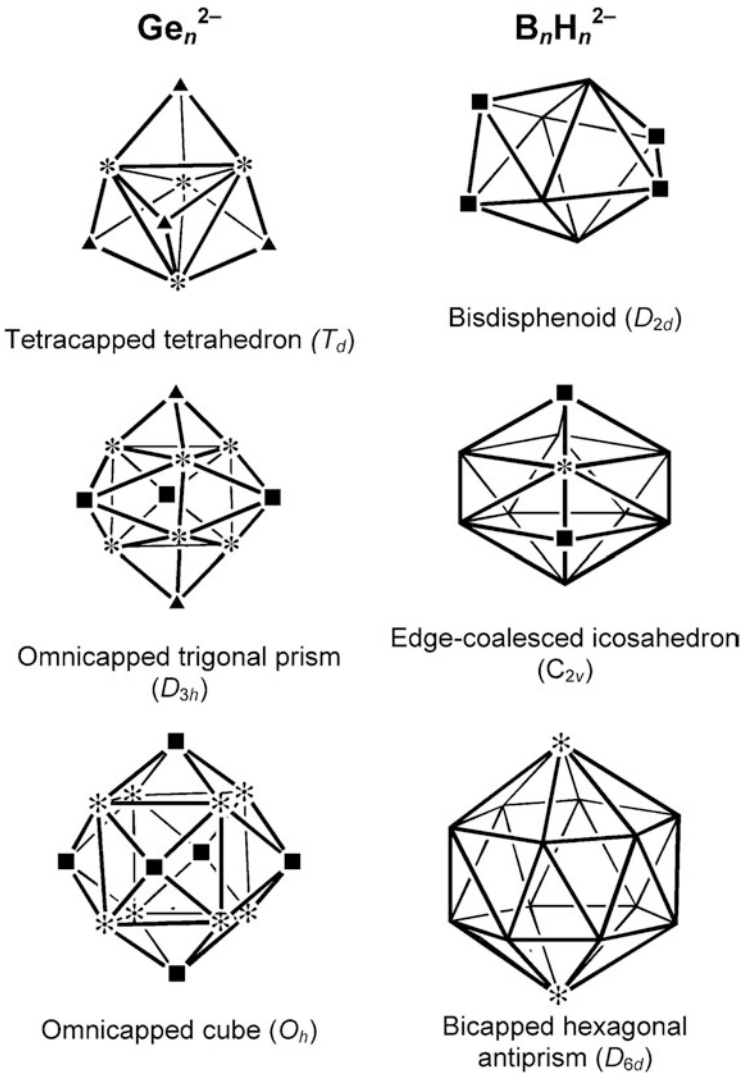

Fig. 16 Comparison between geometries of group 14 and borane clusters that have same electron counts [50] (Reproduced from Ref. [50] with permission from The Royal Society of Chemistry)

4 Endohedral Clusters

As mentioned above, group 14 clusters are mostly formed by heavy tetrel elements. Heavy element implies large atomic radius and thus the cavity inside polyhedral clusters could be large enough to encapsulate another atom, forming the so-called endohedral clusters [58–61]. Still, the electronic structure of endohedral clusters can be understood under the framework of Wade's rules in many cases.

4.1 Wadean Endohedral Clusters

Let us take $[PtPb_{12}]^{2-}$ as our first example. Compared to the bare cluster $[Pb_{12}]^{2-}$, this cluster has an additional Pt center in the cavity of the $[Pb_{12}]$ skeleton (Fig. 17), and is often denoted as $[Pt@Pb_{12}]^{2-}$ to show the endohedral relationship. The effect of the central metal atom on the electronic structure can be revealed via an orbital interaction diagram between the endohedral center and the peripheral atoms as shown in Fig. 18.

Let us consider the orbital interactions between the valence orbitals of Pt, namely 5d, 6s, and 6p, and the skeletal orbitals of $[Pb_{12}]^{2-}$ with the H_g, A_g, and T_{1u} irreducible representations, respectively. The consequence of the orbital interactions is that the A_g and T_{1u} skeletal bonding orbitals are stabilized by the empty metal s and p orbitals, while the H_g orbitals interact with metal d orbitals to form bonding and anti-bonding orbitals as shown in Fig. 18. For late transition metals, the metal d

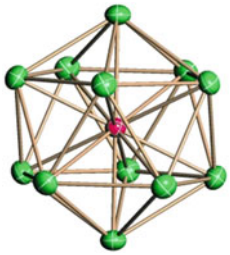

Fig. 17 Crystal structure of $[Pt@Pb_{12}]^{2-}$ [62] (Reprinted from [62], Copyright (2004), with permission from John Wiley and Sons)

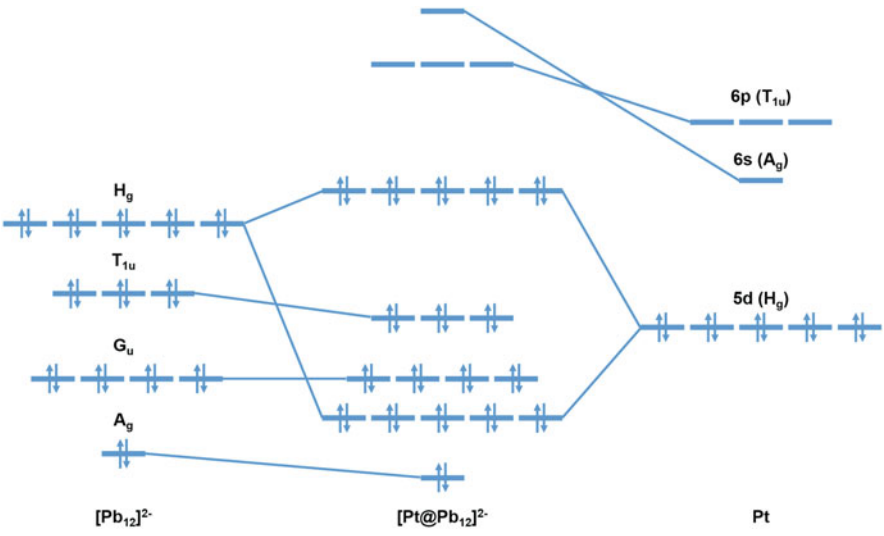

Fig. 18 Orbital interaction diagram for $[Pt@Pb_{12}]^{2-}$. For the $[Pb_{12}]^{2-}$ fragment, only the 13 skeletal bonding orbitals are shown for clarity [62]

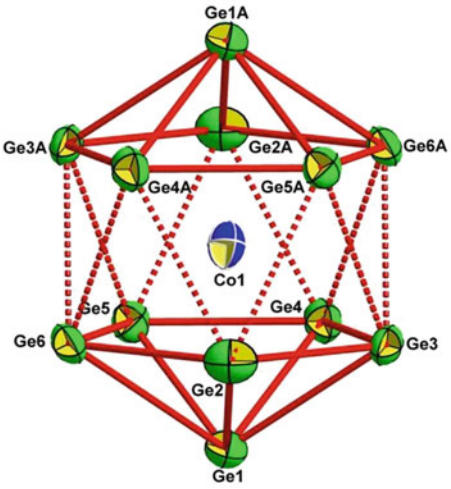

Fig. 19 Crystal structure of $[Co@Ge_{12}]^{3-}$ [69] (Reprinted from [69], Copyright (2018), with permission from John Wiley and Sons)

orbitals are low-lying in energy and relatively contracted in size, in which case the destabilization of the skeletal H_g set will be insignificant. Hence the existence of an endohedral center often will not affect the electron count: the peripheral atoms will still follow the established rules for bare clusters while the endohedral center has a closed-shell d^{10} configuration. In such a scenario, if we take into account both the $4n + 2$ valence electrons of the Wadean cluster and the 10 d electrons of the interstitial transition metal center, one would come up with the $(4n + 12)$ rule for transition metal doped endohedral cluster compounds.

This observation applies to a variety of endohedral clusters, including structurally characterized clusters $[M@Pb_{12}]^{2-}$ (M = Ni, Pd, Pt), $[Rh@Pb_{12}]^{3-}$, and $[Ir@Sn_{12}]^{3-}$ [62–65], as well as spectroscopically detected $[M@Pb_{12}]^{-}$ (M = Cu, Ag, Au), $[M@Sn_{12}]^{-}$ (M = Cu, Au) and $[Zn@E_{12}]$ (E = Sn, Pb) in gas phase [66–68]. Note that these examples all have a d^{10} endohedral center fit into an external icosahedral skeleton following Wade's $(n + 1)$ rule for *closo* cluster.

It is not surprising that not all clusters can have a central atom. The cavity size must match the size of the endohedral atom to avoid significant destabilization from the occupied H_g orbitals. For an icosahedral cluster, the distance between central atom and a peripheral atom is not much different from that between two peripheral atoms, suggesting that the central atom and peripheral atoms should have comparable atomic radius for the endohedral cluster to be stable.

This argument is clearly evidenced by the $[Co@Ge_{12}]^{3-}$ cluster [69] (Fig. **19**). A simple electron counting shows that this cluster has 60 valence electrons $(4 \times 12 + 9 + 3)$, isoelectronic with the $[Pt@Pb_{12}]^{2-}$ cluster. However, this Co-centered cluster does not have the expected perfect icosahedral geometry. Instead, both the crystal structure and computational optimization suggest a distorted icosahedral structure in D_{5d} point group. Such an observation can be explained by the size mismatch between the central atom and the cage cavity. Ge has a much smaller radius than Pb, giving rise to a smaller cavity that is incompatible with the

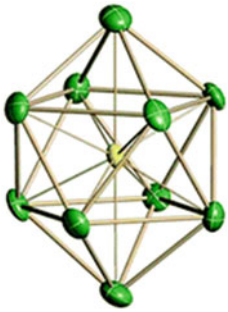

Fig. 20 Crystal structure of $[Ni@Pb_{10}]^{2-}$ [70] (Reproduced from Ref. [70] with permission from The Royal Society of Chemistry)

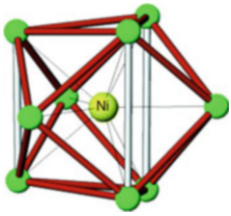

Fig. 21 Crystal structure of $[Ni@Ge_9]^{3-}$ [79] (Adapted with permission from [79]. Copyright (2006) American Chemical Society)

Co center. Thus the cluster has to undergo an expansion that reduces its symmetry through second-order Jahn-Teller distortion.

Endohedral clusters with fewer peripheral atoms have a similar bonding pattern as the $[PtPb_{12}]^{2-}$ cluster, but with a smaller cavity. Hence the possible number of peripheral atoms is usually limited. In addition to aforementioned 12-vertex endohedral clusters, a representative 10-vertex endohedral cluster is $[Ni@Pb_{10}]^{2-}$ (Fig. **20**), which also features a d^{10} center enclosed by a Wadean cluster, albeit its isoelectronic analogs $[M@Pb_{10}]^{2-}$ (M = Pd, Pt) have only been detected in gas phase [63, 70].

Nine-vertex endohedral clusters are also known, including $[Cu@E_9]^{3-}$ (E = Sn, Pb), $[Ni@Sn_9]^{4-}$, $[Co@E_9]^{5-}$ (E = Ge, Sn) and $[Ru@Sn_9]^{6-}$ [36, 71–77]. Electron counting reveals that these compounds all have 50 valence electrons, featuring a d^{10} center enclosed by an $[E_9]^{4-}$ cage. However, both the tricapped trigonal prismatic and monocapped square antiprismatic structures have been reported, demonstrating the previously discussed geometric flexibility of the $[E_9]^{4-}$ cage. The electronic flexibility of $[E_9]$ cages is also reflected by the existence of the 49-electron endohedral clusters $[Ni@E_9]^{3-}$ (E = Ge, Sn) (Fig. **21**) and $[Co@Sn_9]^{4-}$ [36, 78–80].

4.2 Icosahedral Clusters That Do Not Conform to Wade's Rules

Endohedral clusters discussed in the previous subsection all followed a simple electron-counting rule: a d^{10} endohedral center enclosed by a Wadean shell.

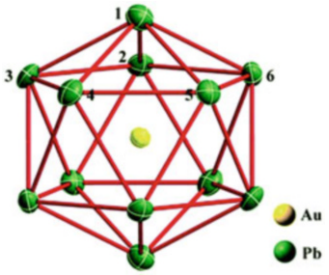

Fig. 22 Crystal structure of $[Au@Pb_{12}]^{3-}$ [81] (Reproduced from Ref. [81] with permission from The Royal Society of Chemistry)

However, there are cases that the electron counts of the core and the shell are not so easily separated, and more detailed examination is necessary.

For example, the outer cage of the cluster $[Au@Pb_{12}]^{3-}$ also has an icosahedral shape but only the symmetry of a D_{3d} point group (Fig. **22**) [81]. At first glance, the icosahedral cage resembles a typical Wadean cluster and is supposed to follow Wade's rules. But if one tries to perform electron counting, one would find that the total number of valence electrons in this cluster is 62 ($4 \times 12 + 11 + 3$). When compared to the typical endohedral cluster $[Pt@Pb_{12}]^{2-}$ with 60 valence electrons, one might suggest a $[(Au^{-})@(Pb_{12}{}^{2-})]$ assignment which formally retains the high symmetry in its electronic structure by putting the two extra valence electrons to the Au 6s orbital. However, computational study indicates that the HOMO of this cluster is completely of skeletal nature (with a_{2g} symmetry in D_{3d} point group and its nodal characteristics resembling the superatomic G_{x3z} orbital, see ref. [81] for its exact shape) and that the HOMO-LUMO gap of $[Au@Pb_{12}]^{3-}$ (2.10 eV) is also close to that of the hypothetical bare cluster $[Pb_{12}]^{4-}$ (1.90 eV) while the *closo* $[Pb_{12}]^{2-}$ cluster has a much larger HOMO-LUMO gap (3.26 eV) [81]. This scenario is not completely unexpected based on the observed distorted icosahedral geometry. One should note that the LUMOs of the (hypothetical) Wadean cluster $[Au@Pb_{12}]^{-}$ or $[Pb_{12}]^{2-}$ are expected to be degenerate. Therefore, addition of two extra electrons would lead to the observed symmetry-breaking. These results hint that the assignment $[(Au^{+})@(Pb_{12})^{4-}]$ is more appropriate for describing the electronic structure of the whole cluster. In this case, the Au 6s orbital is too high to be occupied with another pair of electrons because it interacts strongly with the skeletal bonding orbital and becomes high-lying in energy.

The $[Mn@Pb_{12}]^{3-}$ cluster shown in Fig. **23** provides another example of icosahedral clusters that do not exactly conform to Wade's rules. Again, this cluster has 58 ($4 \times 12 + 7 + 3$) valence electrons in total and is distorted in a D_{2h} manner. If this cluster follows the bonding pattern of typical endohedral clusters and has a d^{10} endohedral center, the icosahedral shell would be left with $48 = 4n$ electrons as opposed to the $4n + 2$ electron count expected for *closo* clusters. Alternatively, if we consider Mn as an early transition metal adopting its highest oxidation state +7 with d^0 configuration, or a half-filled d shell (d^5), the skeletal bonding would involve $58 = 4n + 10$ or $53 = 4n + 5$ electrons, respectively, none of which follows Wade's rules.

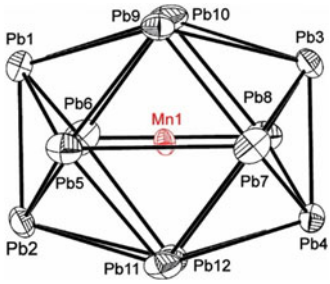

Fig. 23 Crystal structure of $[Mn@Pb_{12}]^{3-}$ [82] (Reprinted with permission from [82]. Copyright (2011) American Chemical Society)

On the other hand, if we force the icosahedral cage to have $4n + 2$ electrons, fulfilling Wade's rules, the Mn center will have an unusual d^8 configuration. Computational study suggests that this cluster has a triplet ground state, consistent with the surprising d^8 configuration for Mn ($5\alpha3\beta$) [82]. However, it should be noted that spin polarization can be significant in such species. The strong Coulomb repulsion between Mn d electrons leads to contracted α d orbitals, while the β unpaired electrons would be pushed away from the metal center. Hence it has been proposed that this cluster is better described as $[Mn^{2+}@(Pb_{12})^{5-}]$. The Mn^{2+} center adopts a rather stable half-filled d^5 configuration, while the outer cage has three electrons more than the one predicted by Wade's rules, leading to an antiferromagnetic coupling between the endohedral center and peripheral cage, as well as the observed (first-order) Jahn-Teller distortion from the perfect I_h symmetry.

It should however be noted that a symmetry-lowering distortion is not always a result of incompletely occupied degenerate orbitals, as exemplified by the $[Co@Ge_{12}]^{3-}$ cluster discussed in the previous subsection [69]. The distorted structure of the latter originates from the size mismatch between the endohedral center and the cage cavity, which leads to a second-order Jahn-Teller distortion. Such possibility suggests that our empirical rules for both "structure" and "bonding" could potentially be violated, complicating the analysis of cluster compounds.

4.3 Competing Isomers of Endohedral Clusters

Deviation from the empirical structural rule can occur way beyond mere symmetry-lowering Jahn-Teller distortion as introduced in the last subsection. The potential energy surface of a cluster compound can be so complicated that, under certain circumstances, the structure could undergo an extensive rearrangement into a completely different shape, challenging our established understanding.

4.3.1 10-Vertex Clusters

A representative case for such a rearrangement could be seen even in very simple endohedral 10-vertex group 14 clusters. Wade's rules predict a 10-vertex *closo* $[E_{10}]^{2-}$ cluster would adopt a bicapped square antiprismatic geometry in a D_{4d} point group. According to our discussion in Sect. 4.1, we might expect that a similar situation would occur in endohedral cluster, and indeed $[Ni@Pb_{10}]^{2-}$ does exhibit a typical pattern of d^{10} center enclosed by a cluster following Wade's rules.

However, the $[Co@Ge_{10}]^{3-}$ cluster (Fig. **24**), which could be seen as an isoelectronic analog of $[Ni@Pb_{10}]^{2-}$, was found to possess a completely different shape [83]. The 10 Ge atoms now arrange in a pentagonal prism, and the cluster seems to conform to octet rule at first glance, each having an external lone pair and three bonds with neighboring atoms. Such bonding scheme would require 50 valence electrons in total (10 lone pairs and 15 Ge-Ge bonds). Electron counting, however, does not support such a bonding scheme, since its total number of valence electrons is 52 ($4 \times 10 + 9 + 3$), different from that required by the octet configuration, not to mention it requires the central metal to be in a very high oxidation state (+7) if 50 electrons are assigned to the outer cage.

Another closely related cluster, $[Fe@Ge_{10}]^{3-}$, also has a pentagonal prismatic structure (Fig. **25**), despite that it has 1 electron less than the Co-centered analog. Computational study suggests that its single electron is predominantly localized on the d_{z2} orbital of the Fe center, assuming the z axis is coincident with the fivefold axis [84].

What further complicates the situation is the characterization of a $[Fe@Sn_{10}]^{3-}$ cluster (Fig. **26**), which is isoelectronic with $[Fe@Ge_{10}]^{3-}$ in composition, but has a geometry that differs from all of the other 10-vertex clusters introduced above. It has

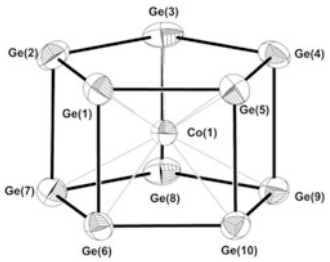

Fig. 24 Crystal structure of $[Co@Ge_{10}]^{3-}$ [83] (Reprinted from [83], Copyright (2009), with permission from John Wiley and Sons)

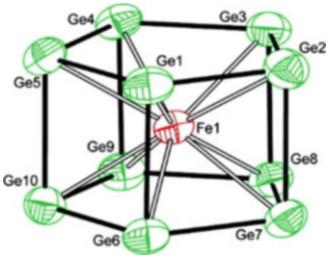

Fig. 25 Crystal structure of $[Fe@Ge_{10}]^{3-}$ [84] (Reprinted with permission from [84]. Copyright (2009) American Chemical Society)

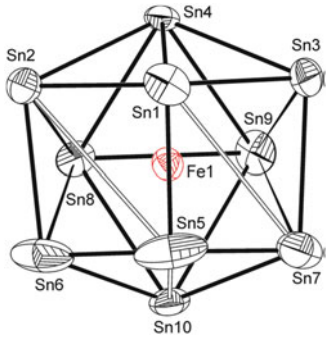

Fig. 26 Structure of $[Fe@Sn_{10}]^{3-}$ [85] (Reproduced from Ref. [85] with permission from The Royal Society of Chemistry)

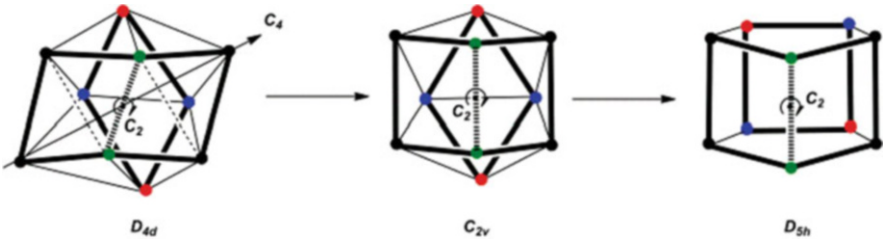

Fig. 27 Isomeric relationship among various geometries of $[M@E_{10}]$ [85] (Reproduced from Ref. [85] with permission from The Royal Society of Chemistry)

an unusual C_{2v} geometry, which has been described as an intermediate structure between the two aforementioned D_{4d} and D_{5h} geometries (Fig. **27**) [85].

A systematic computational study suggests that there is a universal trend in the energy differences among D_{5h}, D_{4d}, and C_{2v} structures of 51-electron or 52-electron $[M@E_{10}]$ species (Fig. **28**) [85]. With respect to the D_{4d} structure as a reference, late transition metals always prefer the D_{5h} structure to a greater extent, while the C_{2v} structure in most cases lies in between. Compared to the $[M@Ge_{10}]$ series, the tin variants also have a higher tendency to deform toward the D_{4d} structure, although the C_{2v} structure can sometimes be even more stable than both, giving rise to the unexpected C_{2v} $[Fe@Sn_{10}]^{3-}$ species.

The competition among multiple low-lying isomers has also been found in related 10-vertex group 13 cluster compounds with 50 electrons such as $[Zn@In_{10}]^{8-}$ [86] and $[Ni@In_{10}]^{10-}$ [87], where the candidate structures are, respectively, bicapped square antiprism (D_{4d}) and tetracapped trigonal prism (C_{3v}, c.f. $[B_{10}H_{10}]$) [85].

4.3.2 12-Vertex Clusters

A somewhat similar scenario occurs in some 12-vertex group 14 clusters. Typical 12-vertex clusters are certainly of icosahedral shape with $4n + 2 = 50$ valence electrons, or 60 if there is an endohedral d^{10} center. Variants with 62 electrons

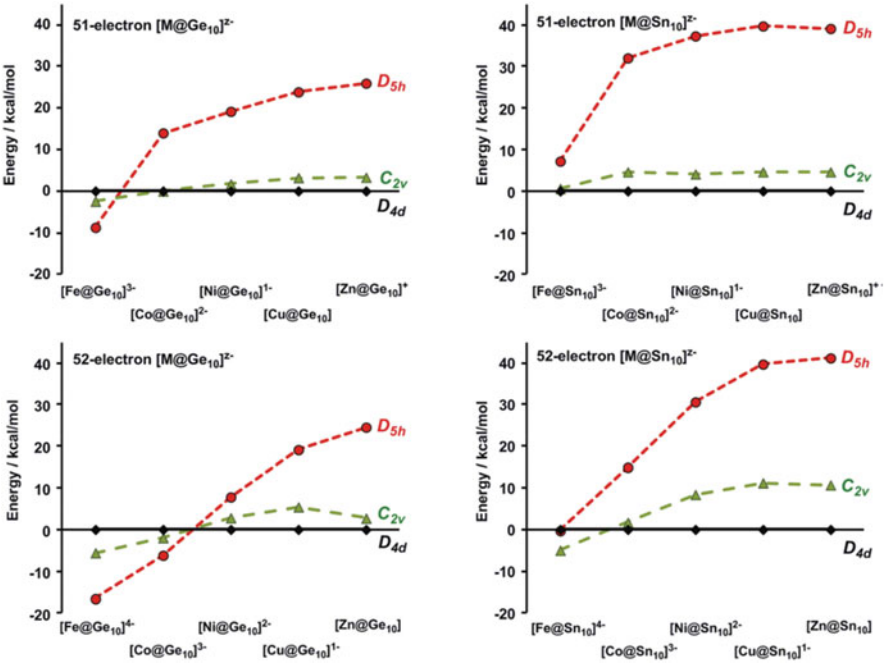

Fig. 28 Geometric preference of $[M@E_{10}]^{q-}$ clusters where each panel showing the energies of various geometric isomers relative to the D_{4d} structure across the periodic table for different tetrel elements and electron counts [85] (Reproduced from Ref. [85] with permission from The Royal Society of Chemistry)

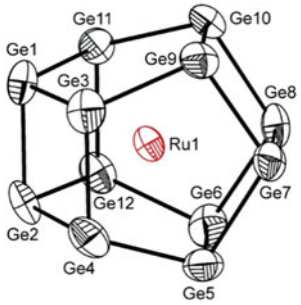

Fig. 29 Structure of $[Ru@Ge_{12}]^{3-}$ [88] (Reprinted with permission from [88]. Copyright (2014) American Chemical Society)

($[Au@Pb_{12}]^{3-}$) or 58 electrons ($[Mn@Pb_{12}]^{3-}$, albeit a high spin species) are also known as discussed in Sect. 4.2, which, though distorted, still roughly retain icosahedral shapes.

Other isomers are possible, however, including hexagonal prismatic (D_{6h}) and bicapped pentagonal prismatic (D_{2d}) structures. One cluster with the latter geometry, $[Ru@Ge_{12}]^{3-}$ (Fig. **29**), has been synthesized and structurally characterized. Similar

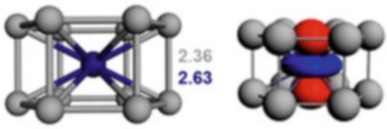

Fig. 30 Optimized structure of the prismatic cluster [$CrSi_{12}$] and its LUMO with metal d_{z2} nature [95] (Reprinted with permission from [95]. Copyright (2014) American Chemical Society)

to the $[Co@Ge_{10}]^{3-}$ case (Fig. **24**), the Ge atoms in the outer cage of $[Ru@Ge_{12}]^{3-}$ seem to retain octet configurations at first glance, each having a lone pair and forming three covalent bonds. But electron counting shows this cluster has 59 ($4 \times 12 + 8 + 3$) valence electrons, one less than the electron count 60 (12 lone pairs and 18 Ge-Ge bonds) required by octet assignment.

A representative of hexagonal prismatic group 14 clusters would be the [$CrSi_{12}$] cluster, which has 54 ($4 \times 12 + 6$) valence electrons. This cluster has only been detected in mass spectroscopy [89, 90], but has attracted special interest because it seems that the cluster can be viewed as an analog of the coordination complex [$Cr(C_6H_6)_2$] [91], if one considers all carbon atoms to be replaced with isoelectronic silicon atoms and all equatorial C-H bonds to be replaced by vertical Si-Si bonds. For this reason, this complex has once been proposed to follow the 18-electron rule for coordination complexes, since it does not follow any known electron-counting rules for clusters [92–94]. But detailed orbital analysis revealed that this cluster does not follow the 18-electron rule in an orbital sense, as demonstrated by the fact that the Cr d_{z2} orbital is found to be the LUMO of the cluster (Fig. **30**) [95].

Computational studies have been performed to understand the geometric preference of various 12-vertex group 14 clusters among icosahedron (Ih), hexagonal prism (HP), hexagonal antiprism (HAP), puckered hexagonal prism (PHP), and bicapped pentagonal prism (BPP) (Fig. **31**) [96]. Although a general understanding is hard to achieve from the computational results, it is yet interesting to notice that, when compared to Si counterparts, Ge-containing clusters in general favor more the icosahedral geometry as predicted by Wade's rules. This is in accordance with the finding in the case of 10-vertex clusters in which heavier elements also prefer traditional Wadean geometries.

While in these competing cases we do not yet have a systematic rule for correlating their electron counts and geometries, we are still fortunate in the sense that these clusters still possess relatively high symmetry and nearly spherical shapes, which offers great help to our orbital analyses. Even though there are clusters with intermediate symmetries (e.g., the 10-vertex C_{2v} structure and the 12-vertex D_{2d} structure) that their superatomic electronic configurations might be difficult to assign, comparison against more symmetric structures still offers insight to the governing rules of structure and bonding.

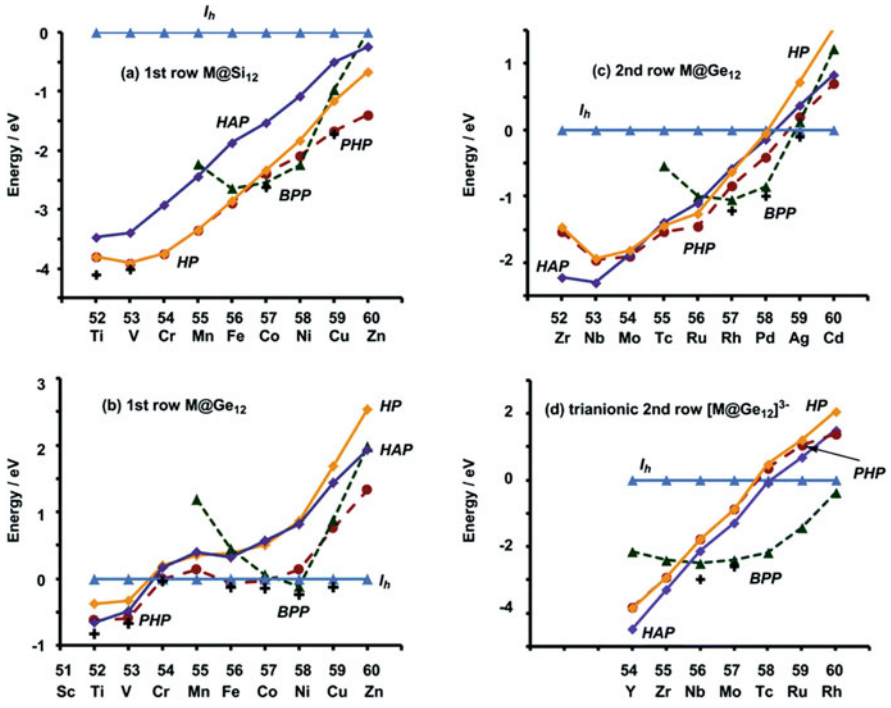

Fig. 31 Geometric preference of $[M@E_{12}]^{q-}$ clusters with each panel showing the energies of various geometric isomers relative to the D_{4d} structure for each tetrel element and each overall charge [96] (Reproduced from Ref. [96] with permission from The Royal Society of Chemistry)

5 Cluster Assemblies

Most clusters discussed up to this point are largely based on one single (quasi-) spherical unit. But these units can be further extended into more complicated clusters, sometimes in an unapparent way. Even so, a modular picture connecting the bonding of fragments to that of large systems is often a very powerful aid in chemical understanding. Hence in this section, we are going to discuss a number of more complicated cluster compounds, and decipher their bonding with the established bonding rules and models discussed in previous sections to show their transferability. This kind of understanding on how clusters can interact with each other or with other chemical moieties would then serve as an important step toward modelling of larger clusters.

5.1 Clusters with Transition Metal Vertex

One simple extension to (quasi-)spherical clusters is to take into account of their interaction with transition metal centers. Apart from endohedral clusters discussed in the previous section, there are also many metal doped group 14 clusters in which the metal center lies on the same surface as the cluster's (quasi-) spherical skeleton, thus itself could also be considered as one vertex on the polyhedron.

In Mingos' PSEPT, it has already been stated how we could view an electron-deficient cluster that combines main group and transition metal vertices. As an illustrative example, let us first take a look at the clusters $[E_9ZnPh]^{3-}$ (E = Si, Ge, Sn or Pb) (Fig. **32**) [97–99]. These clusters adopt a perfect bicapped square antiprismatic geometry, with the transition metal moiety being one of the vertices. The cluster can clearly be understood by Wade's rules, by considering the fact that a $[ZnPh]^-$ moiety has 4 valence electrons (if Zn is considered as a main group, or 14 as a transition metal; either way leads to the same analysis), isoelectronic with a tetrel element, making the whole cluster isoelectronic with a *closo* $[E_{10}]^{2-}$ cluster with 42 valence electrons.

The same analysis would apply to the cluster $[Ge_9R_3EtPd(PPh_3)]$ (Fig. **33**) [100], which has 52 valence electrons (4 × 9 + 1 × 3 + 1 + 10 + 2) and is also isoelectronic

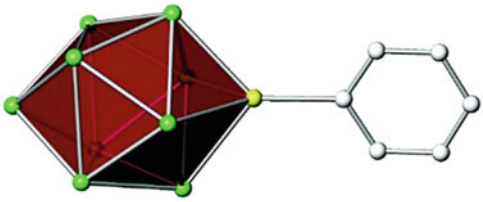

Fig. 32 Structure of $[E_9ZnPh]^{3-}$, where E = Si, Ge, Sn, or Pb [97] (Reprinted with permission from [97]. Copyright (2006) American Chemical Society)

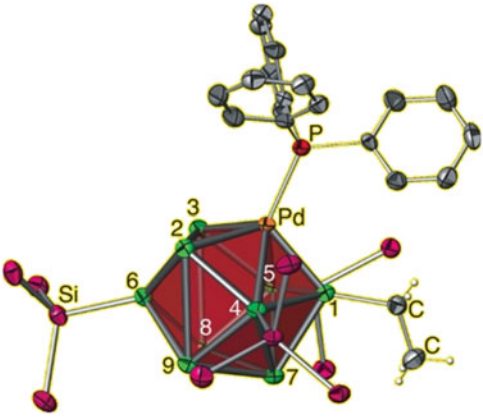

Fig. 33 Structure of $[Ge_9Hyp_3EtPd(PPh_3)]$ [100] (Adapted from [100], Copyright (2016), with permission from John Wiley and Sons)

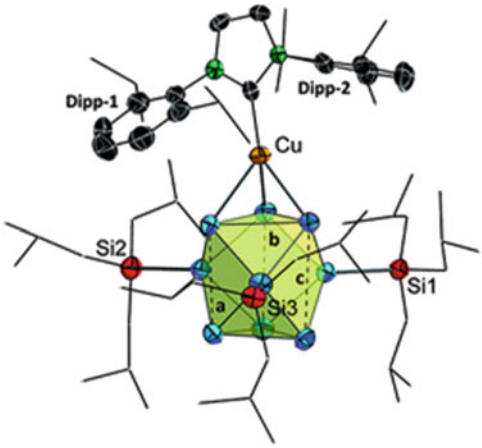

Fig. 34 Structure of $[Ge_9(Si^iBu_3)_3CuNHC^{Dipp}]$ [107] (Adapted from [107], Copyright (2016), with permission from John Wiley and Sons)

with $[E_{10}]^{2-}$ clusters noting that the additional 10 electrons arise from the d^{10} shell of the transition metal Pd center. However, this cluster differs from the $[E_9ZnPh]^{3-}$ cluster in the sense that the transition metal center occupies the antiprismatic vertex, instead of a capping position as in $[E_9ZnPh]^{3-}$.

The reason that the transition metal atoms Zn and Pd occupy different sites in the above two cases is actually not yet well understood. In fact, the preferred occupation site of transition metal can even be altered by the ligand exchange on the metal center in the case of $[Ge_9R_3RhL_2]$ [101]. It has been proposed that different structural isomers of a bicapped square antiprismatic cluster can rapidly interconvert to each other under certain circumstances [102], based on the existence of both isomers of $[E_9M(CO)_3]^{4-}$ (E = Sn, Pb, M = Cr, Mo, W) species [102–105]. Early studies based on perturbative approach suggest that site preference might be related to factors like electronegativities of the heteroatom, interaction strengths, and connectivities of different sites [106].

Apart from variants of the bicapped square antiprismatic structure, there exists another competing structure for $[E_9M]$-based 10-vertex clusters. The cluster $[Ge_9(Si^iBu_3)_3CuNHC^{Dipp}]$ (Fig. **34**) adopts a tetracapped trigonal prismatic structure that may seem to resemble the *hyper-closo* $[B_{10}H_{10}]$. However, its valence electron count sums up to 52 ($4 \times 9 + 3 + 11 + 2$), which is isoelectronic with the *closo* cluster $[B_{10}H_{10}]^{2-}$ but not the *hyper-closo* cluster $[B_{10}H_{10}]$. To understand this anomaly, one should notice that the $[Ge_9(Si^iBu_3)_3]$ moiety itself has a flexible electron count for $[E_9]$ clusters and may exist in tricapped trigonal prismatic structure as discussed in Sect. 3.2. Hence the copper doped cluster could be understood simply as a coordination complex in which the $[Ge_9R_3]^-$ moiety acts as a ligand, donating to the $[CuL]^+$ fragment.

Such a fragment-based view of transition metal doped clusters is convenient in explaining the various geometries adopted by the $[E_9]$ moiety when interacting with a transition metal fragment. Just as what we have elaborated in Sect. 3.2, $[E_9]$ fragment is very flexible in its geometry and electron count, which could explain

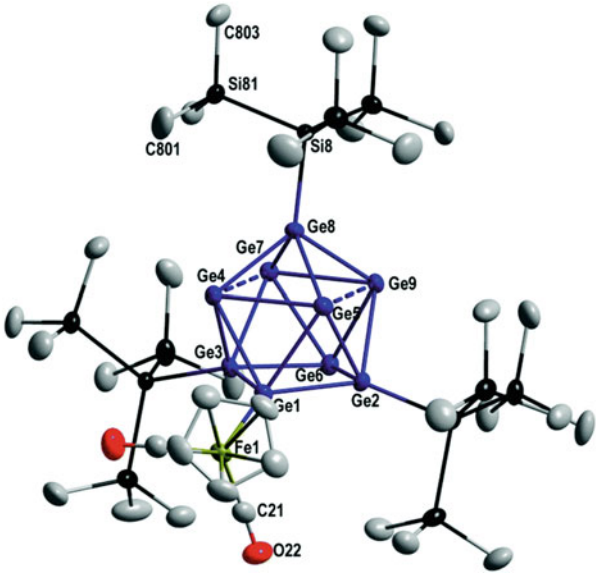

Fig. 35 Structure of $[Ge_9(Hyp)_3FeCp(CO)_2]$ [108] (Reproduced from [108] – Published by The Royal Society of Chemistry, used under CC BY-NC 3.0)

its versatility in interacting with transition metal centers in different clusters. The $[E_9M]$-based 10-vertex clusters could be considered as a *closo* bicapped square antiprismatic cluster in which the transition metal center interacts with $[E_9]$ in η^4 or η^5 modes. Alternatively, it could adopt a structure that can be described as a transition metal center interacting with a tricapped trigonal prismatic $[E_9]$ in an η^3 mode. In addition, as each vertex of the $[E_9]^{4-}$ fragment has an out-pointing lone pair, it is also possible for the fragment to coordinate to the transition metal center in an η^1 manner via one of its lone pairs, for example, in the $[Ge_9(Hyp)_3FeCp(CO)_2]$ cluster (Fig. **35**) [108].

To better understand the role of the $[E_9]^{4-}$ cage as a ligand, let us take a look at the $[(\eta^1\text{-}Ge_9R_3)Cr(CO)_5]^-$ and $[(\eta^5\text{-}Ge_9R_3)Cr(CO)_3]^-$ compounds [109, 110] (Fig. **36**). In the former, the Cr center is coordinated by one lone pair of the $[Ge_9R_3]^-$ cage as well as 5 carbonyl ligands, hence conforming to the 18-electron rule. Similarly, in the latter species the Cr center also conforms to the 18-electron rule because the $[\eta^5\text{-}Ge_9R_3]^-$ ligand donates 6 electrons to the metal center (in analogy with a Cp^- ligand in coordination chemistry). Similar analysis applies to all of the mentioned clusters in this section, where the doping transition metal atoms all conform to the 18-electron rule and follow our traditional understanding in coordination chemistry, despite the presence of cluster moiety as a mono- or multi-dentate "ligand".

As discussed before, deviations from the $(n + 1)$ rule are not uncommon. The cluster $[Ni@Ge_9Ni(CO)]^{2-}$ (Fig. **37**) is another example of this, which can actually be viewed as an endohedral Ni center inside a $[Ge_9Ni(CO)]^{2-}$ cage. If we make our first guess by assigning the endohedral Ni center as Ni(0) with a d^{10} configuration, the outer cage would be left with 50 valence electrons ($4 \times 9 + 10 + 2 + 2$), different from what we have introduced above. On the other hand, one should note that

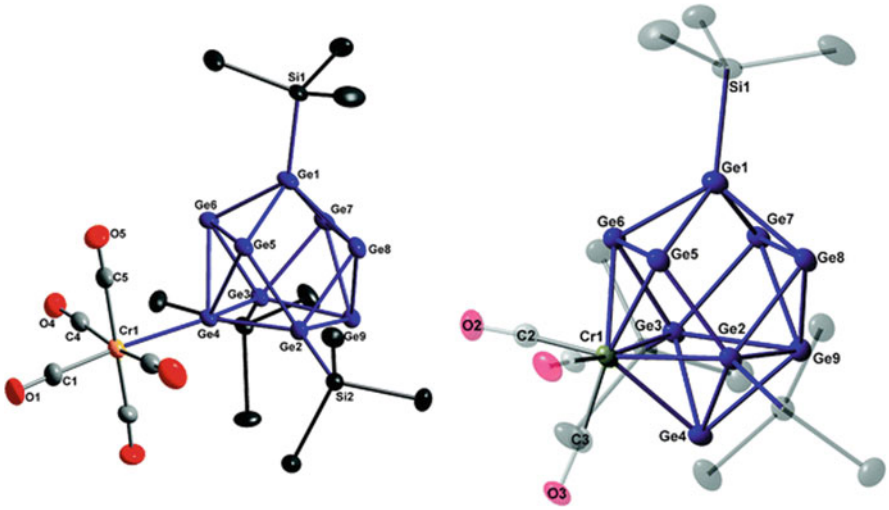

Fig. 36 Structure of $[Ge_9R_3Cr(CO)_5]^-$ and $[Ge_9R_3Cr(CO)_3]^-$, where R = $Si(SiMe_3)_3$ [109] (Reproduced from Ref. [109] with permission from The Royal Society of Chemistry)

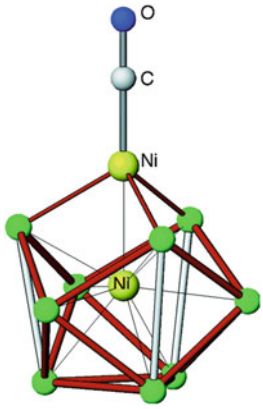

Fig. 37 Crystal structure of $[Ni@Ge_9Ni(CO)]^{2-}$ [79] (Reprinted with permission from [79]. Copyright (2006) American Chemical Society)

although this cluster also adopts a tetracapped trigonal prismatic structure that seems to resemble the $[Ge_9(Si^iBu_3)_3CuNHC^{Dipp}]$ structure shown in Fig. **34**, it is actually isoelectronic with the *hyper-closo* cluster $[B_{10}H_{10}]$ in Fig. **5**, which is different from the previously discussed examples in electron count.

To understand this, we note that there are two different ways to describe a tricapped trigonal prismatic $[E_9]$ cage. If one takes it as a whole and considers it as a nine-vertex *closo* cluster, Wade's rules predict it to be $[E_9]^{2-}$, although we have discussed in Sect. 3.2 that its low-lying LUMO makes it possible to adopt $[E_9]^{4-}$ configuration within D_{3h} point group under certain circumstances. On the other

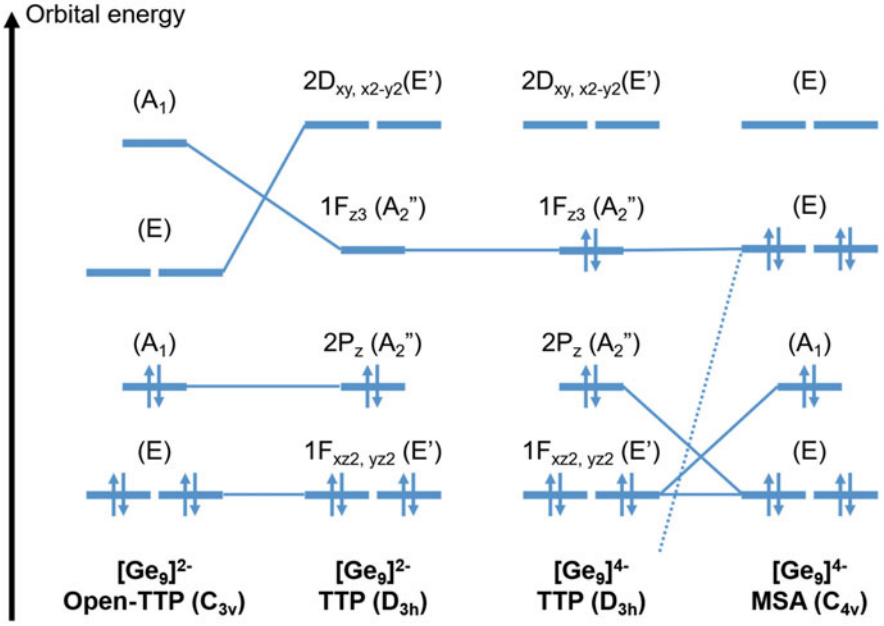

Fig. 38 Frontier molecular orbital diagram of the $[Ge_9]$ cluster with different charges at different geometries

hand, one can view it as a "*hyper-nido*" structure derived from a hypothetical *hyper-closo* $[E_{10}]$ cluster (analogous with the *hyper-closo* $[B_{10}H_{10}]$) by removing its top vertex on its threefold axis. Compared to the ordinary *closo* $[E_9]^{2-}$ cluster, this hypothetical "*hyper-nido*" cluster has one of its trigonal bases slightly open when interacting with the 10^{th} vertex, but its electronic structure is essentially the same as the ordinary one except that its frontier orbitals could be rearranged a bit due to slight geometric distortion.

Similarly, the $[Ni@Ge_9Ni(CO)]^{2-}$ cluster can also be understood in two different ways. Taking the cluster as a whole would result in a 50-electron *hyper-closo* 10-vertex cluster, isoelectronic with the borane cluster $[B_{10}H_{10}]$, while considering it as a coordination complex would lead to a *closo* nine-vertex $[Ni@Ge_9]^{2-}$ cluster conforming to Wade's rules coordinated to the transition metal moiety [Ni(CO)].

Relationship among different geometries and electron counts could be better understood by taking a closer look at their frontier orbitals. The right-hand side of Fig. **38** shows the arrangement of the frontier orbitals of *nido* $[E_9]^{4-}$ in the monocapped square antiprism (MSA) geometry. As discussed in Sect. 3.2, MSA can also rearrange into tricapped trigonal prism (TTP) without significant energy penalty. One can see that at TTP geometry, the HOMO of $[E_9]^{4-}$ is singly degenerate, consistent with our prediction of the *closo* TTP $[E_9]^{2-}$ (with the topmost electron pair removed) based on Wade's rules. When it comes to the "*hyper-nido*" structure which has a triangular base face opened up compared to the ordinary TTP structure, such a distortion will lead to a rearrangement of the LUMOs but the

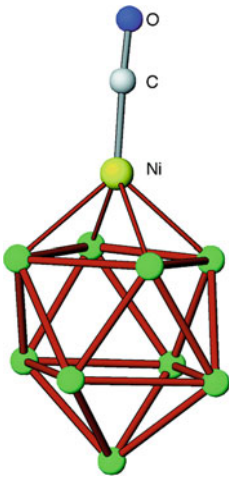

Fig. 39 Crystal structure of open-shell cluster $[Ge_9Ni(CO)]^{3-}$ [79] (Reprinted with permission from [79]. Copyright (2006) American Chemical Society)

occupied orbitals still show clear correspondence in terms of symmetry as shown in the leftmost column of Fig. **38**. It turns out that such "open-TTP" structure would serve as an important fragment for understanding many tetrel clusters, which will be further discussed in later analyses.

While the above two approaches to understand $[Ge_9Ni_2L]^{2-}$ make no essential difference in its bonding, the fragment-based approach, which considers a cluster fragment as a ligand, can be more flexible when extended to clusters that do not follow Wade's rules. Because of the electronic flexibility of the $[E_9]$ cage, not only the Wadean 50-electron η^3-coordinated clusters and the 52-electron η^4-coordinated clusters can be formed, but we are also able to obtain 52-electron η^3-coordinated clusters such as the aforementioned $[(\eta^3\text{-}Ge_9R_3)CuL]$ (shown in Fig. **34**), or even 50-electron η^4-coordinated clusters such as $[Co@Ge_9NiL]^{3-}$ (E = Ge, L = CO; E = Sn, L = C_2H_4) [80]. Open-shell species can also exist, including $[\{\eta^4\text{-}Ge_9\}Ni(CO)]^{3-}$ (Fig. **39**), $[\{\eta^4\text{-}Ge_9\}PdPPh_3]^{3-}$, $[\{\eta^1\text{-}Ge_9(SiSiMe_3)_3)_3\}TiCp_2(NCMe)]$, $[\{\eta^3\text{-}Ge_9(Hyp)_3\}Ni(dppe)]$, $[\{\eta^3\text{-}Ni@Ge_9\}Ni(en)]^{3-}$, and $[\{\eta^4\text{-}Ni@Sn_9\}Ni(CO)]^{3-}$ [79, 111–114]. However, given that both an $[E_9]$ cluster and a transition metal can have the potential to form open-shell species, whether the unpaired electron(s), when present, actually locate on the cage or on the transition metal center has to be determined on a case-by-case basis, and no general rule of thumb is currently available.

Finally, a rather surprising case is associated with the cluster $[Pd@Sn_9SnCy_3]^{3-}$ (Fig. **40**) in which there is an $SnCy_3$ group attached to a $[Pd@Sn_9]$ cluster in an unprecedented η^2 manner [115]. Despite the substituent $SnCy_3$ is not a transition metal here, the cluster can still be understood as a coordination adduct of $[Pd@Sn_9]^{4-}$ and $[SnCy_3]^+$. While it has been shown that the stannyl group, which is isolobal to H, Me, or AuL, can serve as a flexible bridging group bonded to the cluster in multiple ways (Fig. **41**) [33], the preference among different coordination modes under different situations is still not clear.

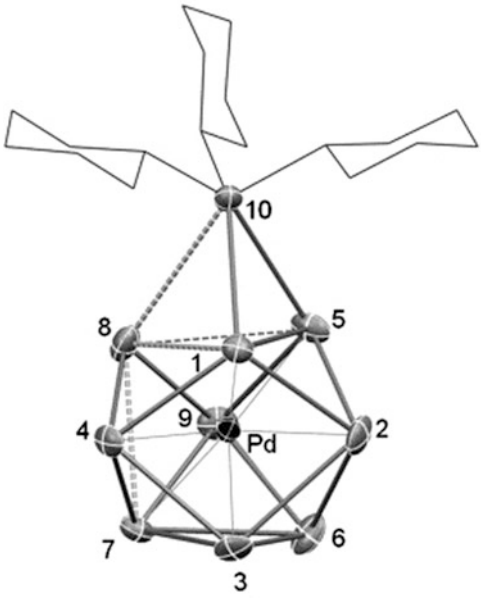

Fig. 40 Structure of $[Pd@Sn_9SnCy_3]^{3-}$ [115] (Adapted from [115], Copyright (2011), with permission from John Wiley and Sons)

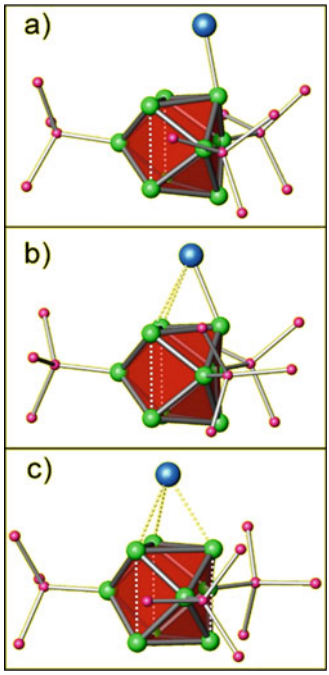

Fig. 41 Three different units simultaneously existing in the crystal structure of $[Ge_9\{Si(SiMe_3)_3\}_3Sn^nBu_3]$ with different coordination modes where substituents on the capping Sn atom (blue) are not shown for clarity [33] (Adapted with permission from [33]. Copyright (2014) American Chemical Society)

Table 1 List of transition metal doped group 14 clusters arranged by electron counts and coordination modes of [E_9] moiety

Electron count	η^3	η^4	η^5
51		$[Ge_9Ni(CO)]^{3-}$ [79] $[Ge_9PdPPh_3]^{3-}$ [111]	
52	$[Ge_9\{Si(SiMe_3)_3\}_3M(NHC^{Dipp})]$ (M = Cu, Ag, Au) [116] $[\{Si(SiMe_3)_3\}_3Ge_9Cu(P^iPr_3)]$ [117] $[Ge_9\{P(N^iPr_2)_2\}_3Cu(NHC^{Dipp})]$ [118] $[Ge_9\{Si(^tBu)_3\}_3CuNHC^{Dipp}]$ [107] $[Ge_9\{Si(SiMe_3)_3\}_2(PR_2)Cu(NHC^{Dipp})]$ [119]	$[E_9ZnPh]^{3-}$ (E = Si, Ge, Sn, Pb) [97] $[E_9ZnR]^{3-}$ (E = Ge, Sn, Pb; R = Mes, ^{i}Pr) [99] $[E_9CdR]^{3-}$ (R = Ph, E = Sn, Pb; R = Sn^{n}Bu$_3$, E = Sn) [98] $[E_9M(CO)_3]^{4-}$ (E = Sn, Pb, M = Cr, Mo, W) [102–105] $[Ge_9R_3Rh(COD)]$ [101] $[E_9Ir(COD)]^{3-}$ (E = Sn, Pb) [65, 120] $[Sn_9\text{-}Ag(NHC^{Dipp})]^{3-}$ [121] $[Ge_9Cu(PR_3)]^{3-}$ (R = ^{i}Pr, Cy) [122] $[Sn_9M(NHC^{Dipp})]^{3-}$ (M = Cu, Ag, Au) [121]	$[Ge_9R_3EtPdPPh_3]$ [100] $[Ge_9R_3Rh(dppe)]$ [101] $[Sn_9W(CO)_3]^{4-}$ [102] $[Pb_9Mo(CO)_3]^{4-}$ [105] $[Ge_9\{Si(SiMe_3)_3\}_3M(CO)_3]^-$ (M = Cr, Mo, W) [109, 110]
60	$[Pt@Sn_9Pt(PPh_3)]^{2-}$ [112] $[Co@Sn_9Pt(PPh_3)]^{3-}$ [80] $[Co@Ge_9AuPh]^{3-}$ [80] $[Ni@Ge_9Ni(CO)]^{2-}$ [79] $[Ni@Ge_9Ni(CCPh)]^{3-}$ [79] $[Ni@Ge_9NiPPh_3]^{2-}$ [123] $[Ni@Ge_9PdPPh_3]^{2-}$ [111]	$[Co@Ge_9Ni(CO)]^{3-}$ [80] $[Co@Sn_9Ni(C_2H_4)]^{3-}$ [80]	
61	$[Ni@Ge_9Ni(en)]^{3-}$ [79]	$[Ni@Sn_9Ni(CO)]^{3-}$ [112]	

To summarize, a list of transition metal doped group 14 clusters is given in Table **1**, in which the [E_9] moiety may adopt η^3, η^4, or η^5 coordination modes. The structural flexibility of the [E_9]-based clusters results in a very rich chemistry of transition metal doped group 14 clusters. One will see in later parts that the fragment-based understanding of cluster compounds introduced in this section can actually serve as the basis for a more general bonding picture to understand the electronic structure of more complicated clusters.

5.2 Metal-Bridged Cluster Assemblies

With the interaction between transition metal and group 14 clusters being well elucidated above, we can proceed to discuss clusters having metal center(s) as bridges which link various (quasi-)spherical clusters together. Specifically, the previously introduced nine-vertex group 14 clusters are important building blocks in large cluster compounds, and multiple [E_9] units can be connected in a variety of ways.

In the class of $[MGe_{18}R_6]^{q-}$ (q = 0, M = Zn, Cd, Hg, Mn; q = 1, M = Cu, Ag, Au; q = 2, M = Pd) clusters, there are two $[Ge_9R_3]^-$ cages bridged by a transition metal center (Fig. **42**) [114, 116, 124–129]. Note that all metal centers adopt d^{10} configurations (except Mn which adopts a half-filled d^5 configuration) and have 6 neighboring Ge atoms arranged in octahedral geometry. The Ge-Ge distances in the coordinating triangular base face (2.87 Å in the case of Pd) are significantly longer than those in the uncoordinated triangular faces (2.63 Å in the case of Pd), suggesting a D_{3h}-to-C_{3v} distortion within each $[E_9R_3]^-$ unit in the overall cluster, implying a combination of the donation from the HOMOs of the $[Ge_9R_3]^-$ unit to the metal center and the back-donation from the metal center to the LUMOs of the cluster unit. The same scenario also holds for other metal-bridged group 14 clusters including but not limited to $[RAu \leftarrow Sn_9R_3 \rightarrow Au \leftarrow Sn_9R_3 \rightarrow AuR]^-$, $[Ge_9R_3 \rightarrow Cu \leftarrow Ge_9R_3 \rightarrow CuPPh_3]$ and $[RZn \leftarrow Ge_9R_3 \rightarrow Pt \leftarrow Ge_9R_3 \rightarrow ZnR]$ (Fig. **42**) [124, 130, 131].

Multiple bare [E_9] units can also be bridged via different coordination modes. In the cluster $[Ge_9 \rightarrow Hg \leftarrow Ge_9 \rightarrow Hg \leftarrow Ge_9 \rightarrow Hg \leftarrow Ge_9]^{10-}$, for example, it features a union of multiple Hg^{2+} and $[Ge_9]^{4-}$ moieties in which η^1 and η^2 coordination modes exist at the same time [132] (Fig. **43**). Such a coordination chain can grow in length and result in a polymer as in the $[K_2HgGe_9]$ compound, though the coordination in the polymeric structure consists of both η^1 and η^3 modes instead [133]. Besides, other coordination modes can also coexist, such as $[(\eta^4\text{-}Ge_9)\text{-}Cu\text{-}(\eta^1\text{-}Ge_9)]^{7-}$, $[(\eta^4\text{-}Sn_9)\text{-}Ag\text{-}(\eta^1\text{-}Sn_9)]^{7-}$, $[(\eta^4\text{-}Ge_9)\text{-}Zn\text{-}(\eta^3\text{-}Ge_9)]^{6-}$, $[(\eta^2\text{-}Sn_9)\text{-}Hg\text{-}(\eta^2\text{-}$

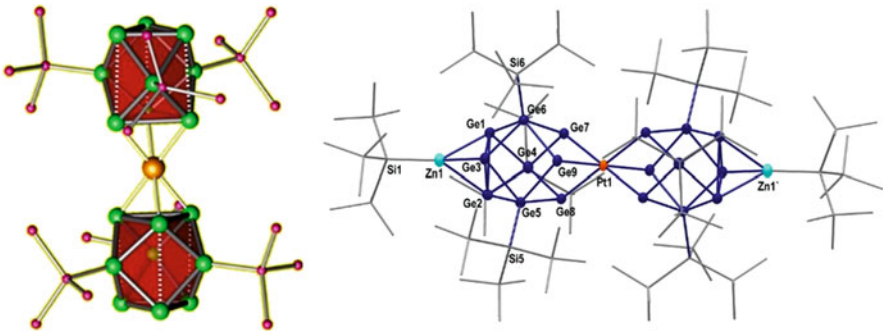

Fig. 42 Structures of $[Ge_9R_3\text{-}Pd\text{-}Ge_9R_3]^{2-}$ and $[RZn\text{-}Ge_9R_3\text{-}Pt\text{-}Ge_9R_3\text{-}ZnR]$ [124, 131] (Adapted with permission from [124, 131]. Copyright (2015) and (2018) American Chemical Society)

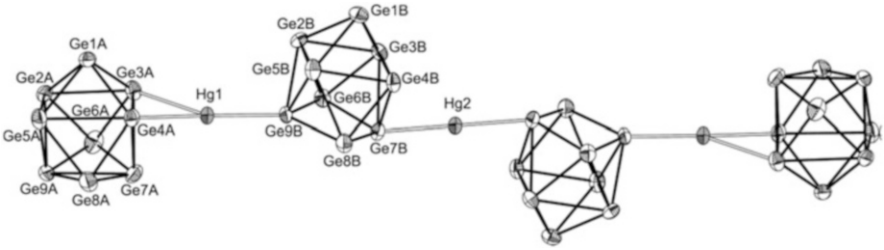

Fig. 43 Crystal structure of $[Ge_9\text{-}Hg\text{-}Ge_9\text{-}Hg\text{-}Ge_9\text{-}Hg\text{-}Ge_9]^{10-}$ [132] (Reproduced from Ref. [132] with permission from The Royal Society of Chemistry)

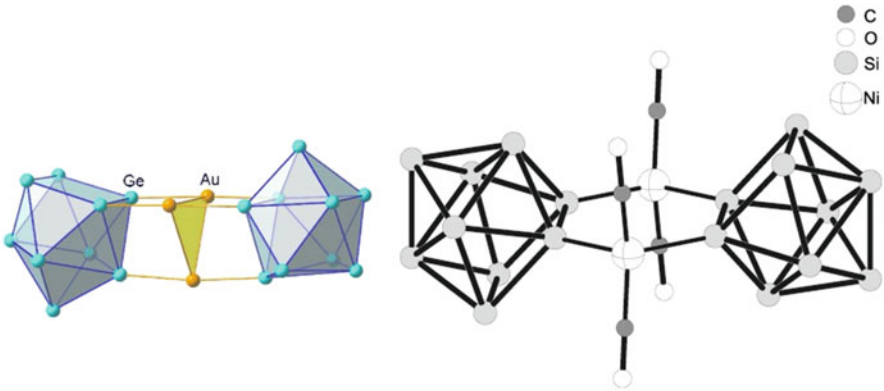

Fig. 44 Structures of $[Ge_9\text{-}Au_3\text{-}Ge_9]^{5-}$ and $[Si_9\text{-}\{Ni(CO)_2\}_2\text{-}Si_9]^{8-}$ [138, 140] (Reprinted from [138, 140], Copyright (2007) and (2009), with permission from John Wiley and Sons)

$Sn_9)]^{6-}$, $[(\eta^4\text{-}Ge_9)\text{-}Zn\text{-}\{\mu_2(\eta^4\text{:}\eta^1\text{-}Ge_9)\}\text{-}Zn\text{-}(\eta^4\text{-}Ge_9)]^{8-}$, and polymeric $_\infty[Zn\{\mu_2(\eta^4\text{:}\eta^1\text{-}Ge_9)\}]^{2-}$ [121, 122, 134–136]. The main group metal-bridged cluster $[(Ni@Sn_9)In(Ni@Sn_9)]^{5-}$ exhibits a similar structural isomerism among $\eta^4\text{:}\eta^4$, $\eta^4\text{:}\eta^3$ and $\eta^3\text{:}\eta^3$ isomers [137].

The cluster $[Au_3Ge_{18}]^{5-}$ (Fig. **44**) provides another possibility of bridging two $[E_9]$ moieties with an $[Au_3]$ triangle [138]. While each Au center has a formal charge of +1 and seems to be repulsive with each other, we would also expect the aurophilic interaction commonly discovered in multinuclear gold(I) compounds can hold multiple Au(I) centers together and in turn bridge the two $[E_9]$ cages [139]. Additional ligands can also be present at the bridging moiety, for example the $[\{Ni(CO)_2\}_2(Si_9)_2]^{8-}$ cluster is an assembly of two $[Si_9]^{4-}$ moieties bridged by two separated $Ni(CO)_2$ fragments (Fig. **44**) [117, 119, 140]. Each Ni center is Ni(0) with four ligands arranged in a tetrahedral geometry, perfectly satisfying its own coordination chemistry.

Another example, the $[Ni_3Ge_{18}]^{4-}$ cluster, may seem to be three endohedral Ni centers in a $[Ge_{18}]$ cage [78] (Fig. **45**). However, the 18 Ge atoms are actually

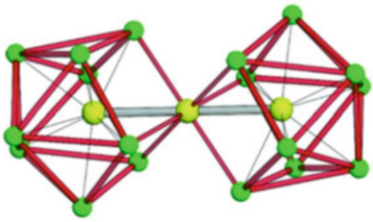

Fig. 45 Structure of $[Ni@Ge_9\text{-}Ni\text{-}Ni@Ge_9]^{4-}$ [78] (Reprinted from [78], Copyright (2005), with permission from John Wiley and Sons)

separated into two groups of atoms, and hence this cluster is better described as two $[Ni@Ge_9]^{2-}$ cages linked by a Ni(0) center [141].

5.3 *Directly Bonded Cluster Assemblies*

In addition, multiple $[E_9]$ units can also be explicitly bonded together via covalent bonds or other direct interactions. Recall that in the $[Ge_9R_2]^{2-}$ cluster discussed in Sect. 3.1, the $[Ge_9]$ moiety is directly bonded with two substituents with localized covalent bonds. In addition to having a substituent in the traditional sense, a Ge vertex could also be bonded to another $[Ge_9]$ moiety. This is the case in the cluster $[R\text{-}Ge_9\text{-}Ge_9\text{-}R]^{4-}$ (R = alkyls, $SbPh_2$ or ER'$_3$ where E = Ge, Sn and R' = Me, Ph) (Fig. **46**), in which each $[Ge_9]$ cage has two covalent bonds, one bonded with substituent and the other bonded with another cage [56, 142, 143]. The skeletal bonding of each cage still resembles that of the $[Ge_9R_2]^{2-}$ cluster, hence it is totally expected that each cage in $[R\text{-}Ge_9\text{-}Ge_9\text{-}R]^{4-}$ adopts a *nido* MSA geometry. The same analysis also applies to the $[Ge_{18}]^{6-}$ (Fig. **46**) with two $[Ge_9]$ cages bonded via a single bond [144, 145]. Other examples include $[Ag(Sn_9\text{-}Sn_9)]^{5-}$ (Fig. **46**) and $[InPh(Ge_9\text{-}Ge_9)]^{4-}$, each with both a Ge-Ge σ-bond and a metal ion that bridges two Ge_9 cages [121, 146, 147]. The cluster polymer $_\infty[Ge_9]^{2-}$ shows extended inter-cage bonding (Fig. **47**), illustrating how these interactions could be utilized in much larger structures [148–150].

The $[E_9]$ building blocks can also be linked in a more delocalized manner. The clusters $[Pd_3Ge_{18}R_6]^{2-}$ (R = Sn^{i}Pr$_3$, Si^{i}Pr$_3$) provide specific examples for such scenario [151, 152]. Each cluster has two $[Ge_9R_3]$ cages bridged by a Pd_3 triangle in between and may be described as a pair of icosahedral cages linked by a common Pd_3 triangular face (Fig. **48**). Given our discussion on $[R_6Ge_{18}Pd]^{2-}$ in Sect. 5.2, one might follow our previous analysis and assign each $[Ge_9R_3]$ cage to be $[Ge_9R_3]^-$ and each Pd to be Pd(0). However, it is interesting to notice that the $[Ge_9R_3]$ cages are different in these two clusters. Compared to $[PdGe_{18}R_6]^{2-}$, the cluster $[Pd_3Ge_{18}R_6]^{2-}$ has two $[Ge_9R_3]$ cages each with one base face widely open, a structure that we have often seen in the previously discussed coordinated clusters. As mentioned in Sect. 5.1, a $[Ge_9R_3]$ cage in an open-TTP conformation has its frontier orbitals reordered, hence $[Ge_9R_3]^-$ is expected to have degenerate HOMO

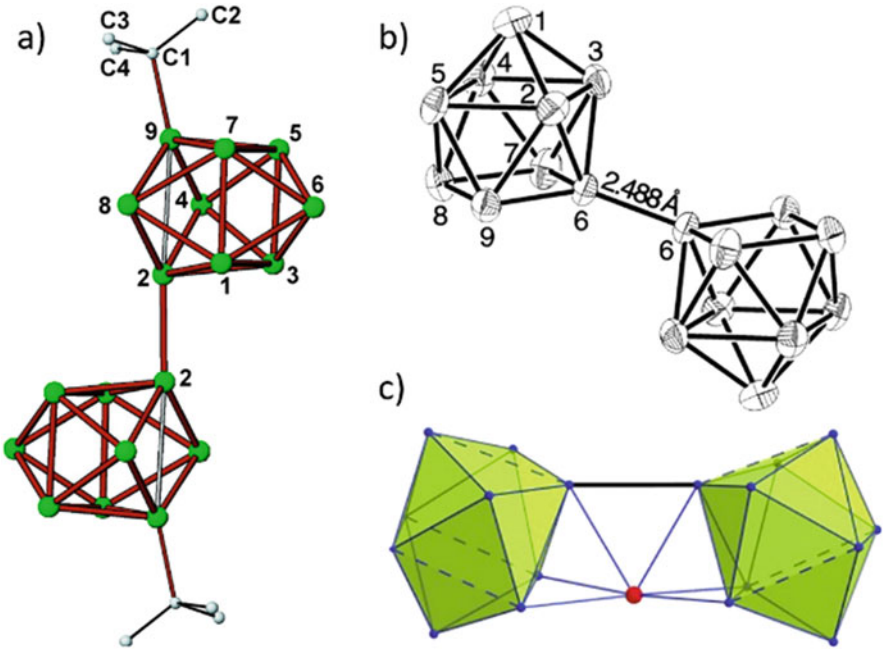

Fig. 46 Structures of $[^t\text{Bu-Ge}_9\text{-Ge}_9\text{-}^t\text{Bu}]^{4-}$, $[\text{Ge}_{18}]^{6-}$ and $[\text{Ag}(\text{Sn}_9\text{-Sn}_9)]^{5-}$ [143, 145, 146] (Reprinted with permission from [143, 145], Copyright (2007) and (1999) American Chemical Society; and from [146], Copyright (2010) John Wiley and Sons)

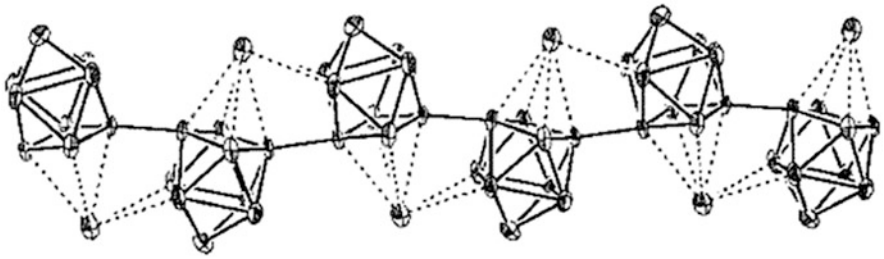

Fig. 47 Crystal structure of polymeric $_\infty[\text{KGe}_9]^-$ [150] (Reprinted with permission from [150]. Copyright (2004) American Chemical Society)

and LUMO in the open-TTP geometry if electrons are forced to be paired up. In this sense, the $[\text{Ge}_9\text{R}_3]^-$ cage is better described as a triplet fragment in this scenario. Formally, these two triplet cages form a pair of delocalized π-bonds (Fig. **48**). Although the two cages lie across the Pd_3 triangle and such a delocalized bonding seems remote and unstable, the cage SOMOs are actually quite localized on the three Ge atoms on its open face [151]. This also explains the eclipsed conformation of the $[\text{Pd}_3\text{Ge}_{18}\text{R}_6]^{2-}$ clusters which bring the two open faces close to each other to stabilize the "remote π-bonds" [151].

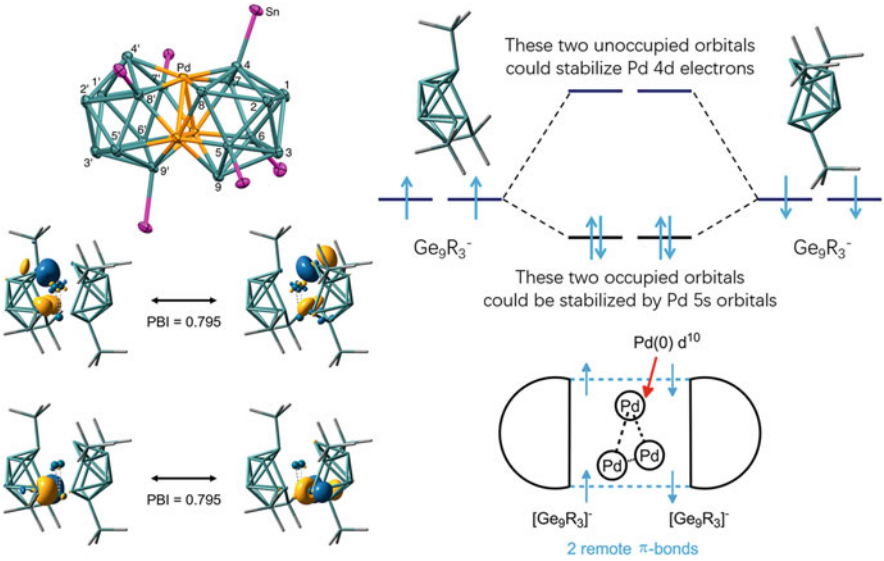

Fig. 48 Crystal structure of $[Ge_{18}Pd_3\{Sn^iPr_3\}_6]^{2-}$ and its principal interacting orbital analysis revealing its bonding scheme [153] (Adapted with permission from [152, 153]. Copyright (2017) and (2019) American Chemical Society)

Such an atypical delocalized bonding is not unique to $[Pd_3Ge_{18}R_6]^{2-}$. The clusters $[Pd_2E_{18}]^{4-}$ (E = Ge, Sn) also have two $[E_9]$ cages close to each other [154, 155] (Fig. **49**). But different from the previous case, the two cages now adopt a staggered conformation. Compared to the Pd_3 triangle in $[Pd_3Ge_{18}R_6]^{2-}$, the Pd-Pd distance in $[Pd_2E_{18}]^{4-}$ is even longer, hence there should not be any Pd-Pd bond. Therefore, each Pd center is again expected to be Pd(0), and the $[E_9]$ cage is assigned to be $[E_9]^{2-}$, which is expected to be at singlet state at an open-TTP structure. The interaction between the two $[E_9]$ cages is thus different from the case in $[Pd_3Ge_{18}R_6]^{2-}$. Specifically, their frontier orbital interactions give rise to three pairs of mutual delocalization, which hold the two cages together although their formal bond order is zero [31, 141] (Fig. **49**).

In fact, when we cross-compare different cases, we can understand the role of an $[E_9]$ unit in a unified framework. If we examine the "principal interacting orbitals" (PIOs) [31, 32] of the formal $[E_9]$ units (together with their substituents or endohedral center) in $[Ge_9Ni_2L]^{2-}$ (Fig. **37**), $[Pd_2E_{18}]^{4-}$ (Fig. **49**), and $[Pd_3Ge_{18}R_6]^{2-}$ (Fig. **48**), we would find very similar PIOs among different cases (as illustrated by the resemblance of π-type PIOs in Figs. **48** and **49**), giving rise to a more generalized picture of the "frontier interactions" of the $[E_9]$ unit [31, 153].

Finally, it should be noted that not all $[E_9]$-based clusters have been well studied. The clusters $[Ge_{27}]^{6-}$ and $[Ge_{36}]^{8-}$ are two of such examples (Fig. **50**). Our knowledge introduced in this chapter can still be used to understand their bonding patterns despite the absence of computational results. These clusters are apparently

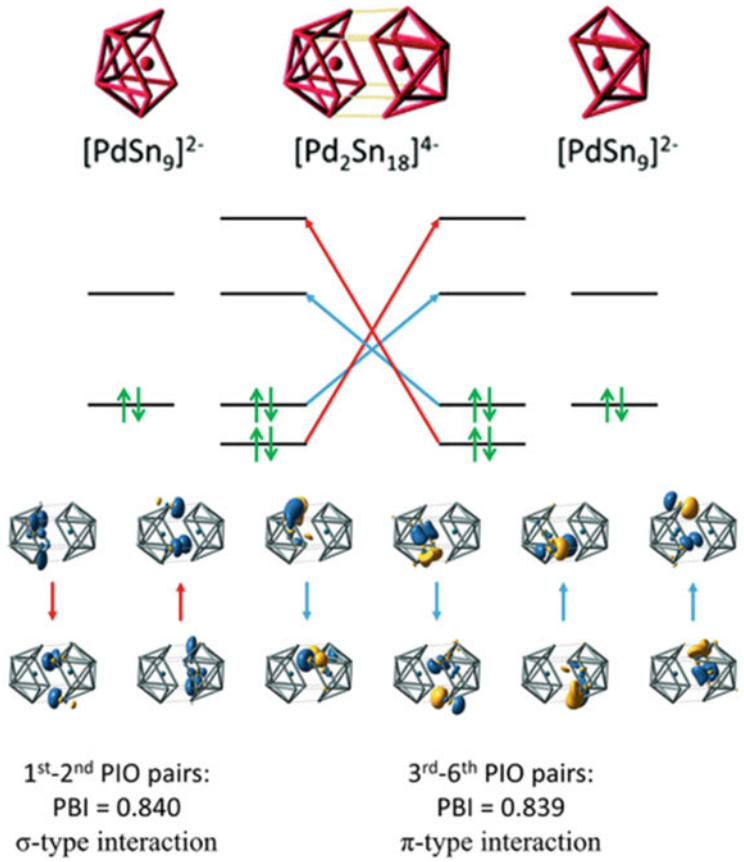

Fig. 49 Crystal structure of $[Pd_2Sn_{18}]^{4-}$ and its principal interacting orbital analysis revealing its bonding Scheme [31, 141, 155] ([31, 141] – Adapted by permission of The Royal Society of Chemistry (2017) and John Wiley and Sons (2018))

made up of three and four $[Ge_9]^{2-}$ units, respectively. However, adjacent $[Ge_9]$ units are doubly connected, with two close Ge-Ge contacts in the range of 2.546 ~ 2.752 Å. The Ge-Ge distances are longer than typical Ge-Ge single bond lengths of approximately 2.48 Å, hence distinguishing these cases from the aforementioned $[Ge_{18}]^{6-}$ cluster (Fig. **46**), which has two *nido*-Ge_9^{3-} moieties linked by a Ge-Ge single bond. Even if we ignore the atypical Ge-Ge bond length and assume that there are two localized bonds between adjacent $[Ge_9]$ units, the middle $[Ge_9]^{2-}$ unit will formally be isoelectronic with $[Ge_9R_4]^{2-}$, an *arachno* cluster according to the total number of valence electrons and Wade's rules. This is different from the familiar skeletal bonding patterns for nine-vertex group 14 clusters. We thus expect these $[Ge_9]$ units are not connected by localized single bonds but are bonded in a rather delocalized manner.

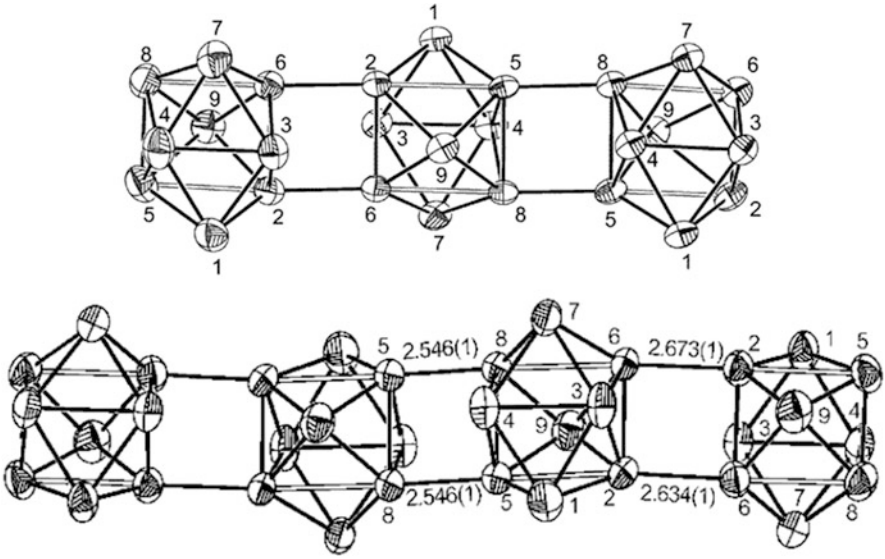

Fig. 50 Crystal structure of $[Ge_{27}]^{6-}$ and $[Ge_{36}]^{8-}$ [156, 157] (Reprinted with permission from [156, 157], Copyright (2002) and (2003) American Chemical Society)

Noting that the structure of each $[Ge_9]$ unit in Fig. **50** is close to the MSA geometry, with the open square face vertices being connected with adjacent units, we may speculate their electronic structures based on the established models introduced in Sect. 3.2 and 5.1, in which the degenerate frontier orbitals are localized on the square face. As a starting point, the (almost) degenerate frontier orbitals are only partially filled for each $[Ge_9]^{2-}$ unit. Then the linear combination of these two frontier orbitals will span two bands, with their partial occupation finally giving rise to weakly bonded $[Ge_9]^{2-}$ units with each individual unit still resembling typical nine-vertex group 14 clusters. Such a delocalized bonding picture is, however, much harder to illustrate through traditional bonding analysis methods, because most of them are based on identifying localized bonds among a couple of adjacent atoms. But with the recent development of computational tools, it is still conceivable that a general bonding picture for these extended clusters could be achieved in the near future.

6 Clusters Beyond Wade's Rules

In the previous sections, we have introduced Wade's rules and their application on a wide variety of group 14 clusters. We have shown that many group 14 clusters can be interpreted using Wade's rules if more specific orbital interactions are introduced. There are still some clusters which require rather different approaches. We will briefly examine some representative examples in this section.

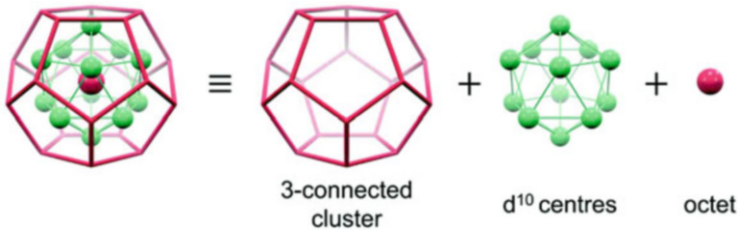

Fig. 51 Crystal structure of $[Sn@Cu_{12}@Sn_{20}]^{12-}$ and its bonding Scheme [159] – Reproduced by permission of The Royal Society of Chemistry

Although in a large part of this chapter we have greatly relied on the "isolobal relationship" among [BH], [E], and $[ER]^+$, we have discussed in Sect. 3 that they do have some differences. In particular, we have briefly mentioned in Sect. 3.1 the role of substituents in stabilizing electron-deficient "carbon cluster." We have also discussed the relationship of tetrel clusters to Jellium model due to the relatively active lone pair in Sect. 3.2. In fact, the availability of skeletal electron pairs and the total electron count can shift the governing bonding models from one to the other.

Recall the two examples we mentioned in Sect. 2: $[B_4Cl_4]$ and $[C_4H_4]$, we considered $[B_4Cl_4]$ to follow a variant of Wade's rules, and described C_4H_4 simply with localized bonding, but what they actually differ is the total electron count.

In fact, similar case also occurs in group 15 clusters where they are often described by a dedicated electron-counting rule for these octet-conforming cases: the 5*n* rule. Because in the case of pnictogen clusters, this often means each vertex would have 3 bonds, and clusters of this kind are therefore often also called "3-connected clusters" [4].

Tetrel elements have 4 valence electrons, hence in most cases electroneutrality principle forces group 14 clusters to fall into the class of Wadean clusters as opposed to 3-connected clusters. However, more electrons could be present in skeletal bonding if the overall cluster is particularly stable. A typical example, albeit complicated, is the Matryoshka cluster $[Sn@Cu_{12}@Sn_{20}]^{12-}$ (Fig. **51**), which has a highly symmetric three-layer geometry [158]. Despite its compositional complexity, its bonding can be simply deciphered via a divide-and-conquer approach like peeling an onion: the innermost tin atom fulfills the octet rule, the sandwiched layer simply consists of 12 Cu centers all with a closed-shell d^{10} configuration, and the outermost layer is a 3-connected cluster in which each tin atom holds an external lone pair and forms three covalent bonds with neighboring vertices, also fulfilling the octet rule. Such assignment indicates that this cluster can be formally written as $[(Sn^{4-})@(Cu^{+})_{12}@(Sn^{-})_{20}]$, where each individual layer is isoelectronic with that in another famous transition metal doped pnictogen Matryoshka cluster $[(As^{3-})@Ni_{12}@As_{20}]$ [159, 160].

Generally, group 14 clusters in most cases cannot sustain such a high negative charge of an electron-precise cluster and require substituents to balance and stabilize

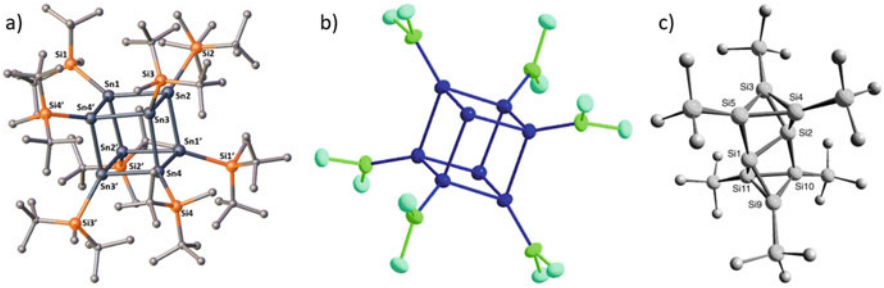

Fig. 52 Crystal structure of a) $[Sn_8(Si^tBu_2Me)_8]$, b) $[Ge_8\{N(SiMe_3)_2\}_6]$ and c) $[Si_8(Si^tBu_3)_6]$ [161, 167, 168] (Reprinted from [161, 167, 168], Copyright (2020), (2003), and (2005), with permission from John Wiley and Sons)

the charge. For example, the substituent-stabilized clusters $[E_nR_m]^{(n-m)-}$ ($n = 4$, E = Si, Ge; $n = 8$, E = Sn) follow the desired valence electron count for 3-connected clusters (not counting substituents in the connectivity) [161–166] (Fig. 52a). Hence these clusters are isoelectronic to corresponding pnictogen clusters $[Pn_n]$ and polyhedranes $[C_nH_n]$.

In many cases, substituent-decorated group 14 clusters fall into the intermediate regime between Wadean and 3-connected clusters, with intermediate valence electron counts between $4n + 2$ for Wadean *closo* clusters and $5n$ for 3-connected clusters. Taking 8-vertex clusters as an example, an $[E_8R_x]$ cluster has $32 + x$ valence electrons. The case with $x = 2$ corresponds to a Wadean *closo* cluster while the case with $x = 8$ corresponds to a 3-connected cluster. The cases with $x = 4$ or $x = 6$ are predicted to adopt *nido* or *arachno* structures, respectively, according to Wade's rules, which are deltahedral clusters with one or two vertices removed.

On the other hand, experimentally synthesized and characterized $[E_8R_4]$ and $[E_8R_6]$ molecules are seen to adopt (distorted) cubic structures, including $[Ge_8\{N(SiMe_3)_2\}_6]$ (Fig. 52b), $[Ge_8\{C_6H_3(O^tBu)_2\}_6]$, $[Sn_8(2,6\text{-}Mes_2C_6H_3)_4]$, and $[Sn_8(Si^tBu_3)_6]$ [164, 167, 169, 170]. In terms of electron count, more edges could be added to the cubic structure to increase electron-sharing and formally make all vertices tetravalent, although the undecorated vertices may not maintain the typical tetrahedral tetravalent geometry in main group chemistry.

At the same time, their isoelectronic silicon analog, $[Si_8(Si^tBu_3)_6]$ (Fig. 52c), has a completely different structure [168]. This cluster has a Si_2 moiety sandwiched by two Si_3R_3 moieties, in which all Si atoms are tetravalent and fulfilling octet rule, showing a rather localized bonding pattern. These compounds clearly show the diversity in structure and bonding of cluster compounds because geometrically similar clusters may have different electron counts while isoelectronic clusters may adopt diverse geometries. It remains a question why these clusters do not follow Wade's rules but instead adopt a 3-connected structure. We anticipate more clusters in this transition regime synthesized in the future could help us understand their preferences.

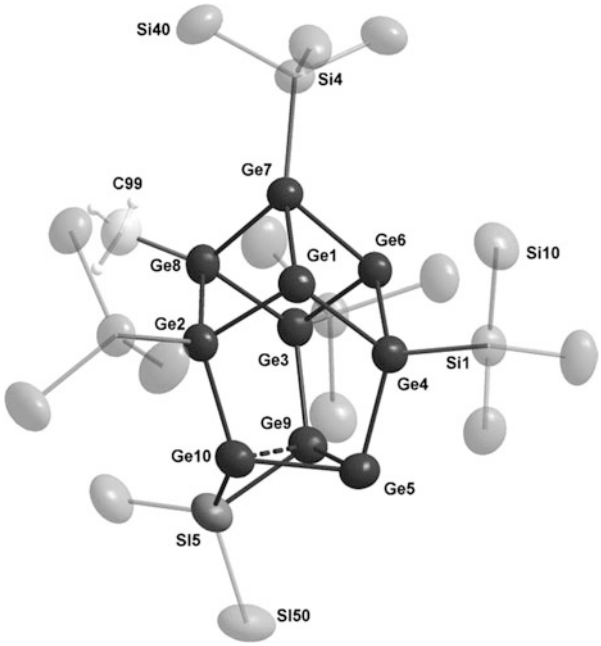

Fig. 53 Crystal structure of $[Ge_{10}\{Si(SiMe_3)_2\}(Hyp)_4Me]^-$ [171] (Reproduced from Ref. [171] with permission from The Royal Society of Chemistry)

When it comes to 10-vertex substituted clusters, the diverse scenario is somewhat similar. The cluster $[Ge_{10}\{Si(SiMe_3)_2\}(Hyp)_4Me]^-$ (Fig. **53**) has a $[Ge_{10}]$ skeleton with 7 attached substituents and hence can be formally described as a $[Ge_{10}R_7]^-$ if we consider that the substituents are singly bonded to the skeletal atoms (note that SiR2 is counted as two separate substituents) [171]. Thus, this cluster has 48 valence electrons ($4 \times 10 + 7 + 1$), two less than that required by a 3-connected bonding scheme, although each vertex has three closest neighboring Ge atoms in around 2.5 Å (except that one of the edges, Ge9-Ge10, has a bond length of 2.74 Å). Based on the electron count, one might assign an additional Ge1-Ge6 bond, despite its relatively long bond length of 2.96 Å. However, this assignment will again lead to non-tetrahedral Ge atoms which are not typical for tetravalent main group elements.

Nevertheless, the locally inverted geometries might not be evident enough to eliminate the possibility of an additional bond between unsubstituted tetrel atoms in above clusters. It is well established that an inverted bond can exist in the [1.1.1] propellane molecule (Fig. **54**) with charge-shift bonding character [172–174]. We would not judge the charge-shift bonding character in the aforementioned cluster compounds here, but would still like to point out that the inverted nature of local center does not completely exclude the possibility of tetravalency.

The cluster $[Sn_{10}R_8]$ (Fig. **55**) is an isoelectronic analog with the previously discussed cluster shown in Fig. **53**, which again adopts a different geometry [175]. There are 4 apparent trivalent Sn atoms, in addition to 6 tetravalent Sn

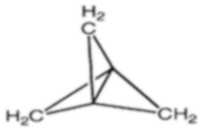

Fig. 54 Structure of [1.1.1]propellane in which there is believed to be an inverted bond between the two opposite carbon atoms [172] (Adapted from [172], Copyright (2009), with permission from John Wiley and Sons)

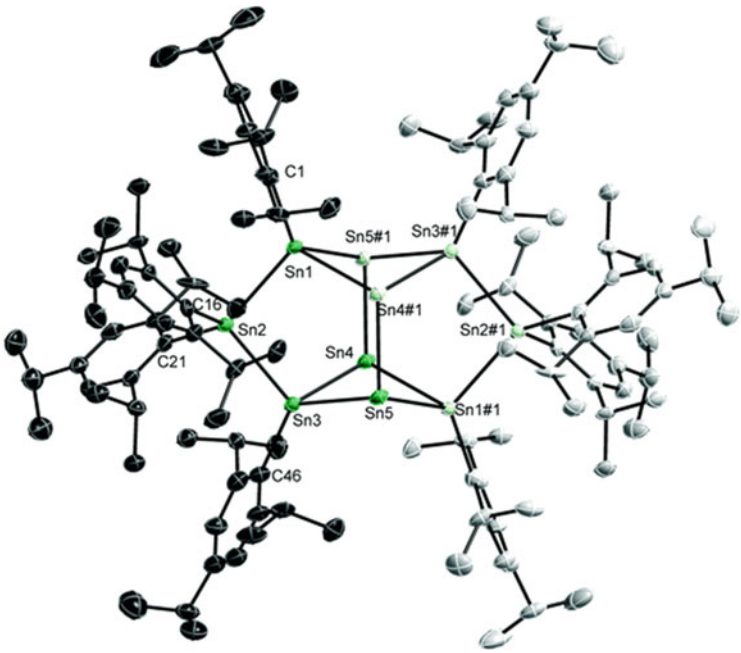

Fig. 55 Crystal structure of $[Sn_{10}R_8]$ [175] – Published by The Royal Society of Chemistry, used under CC BY-NC 3.0

atoms. Since this cluster is only short by two electrons to fulfill the electron count for a 3-connected cluster, the central four Sn atoms must share three lone pairs. In other words, this cluster exhibits a 4-center-6-electron delocalized bonding pattern in the middle, even though the overall structure largely resembles a 3-connected geometry.

We may find other examples of intermediate 10-vertex clusters with even fewer valence electrons. The cluster $[Ge_{10}(Si^tBu_3)_6I]^+$ (Fig. **56**) has 46 valence electrons ($4 \times 10 + 6 + 1–1$), four electrons less than that required by $5n$ rules, despite its apparent 3-connected structure with 15 close Ge-Ge contacts and 7 external bonds [176]. On the other hand, if one deducts the 22 localized bonding electron pairs from overall valence electrons, one would find that there are two remaining electrons while three Ge atoms are not tetravalent yet. This will lead us to assign a 3-center-2-

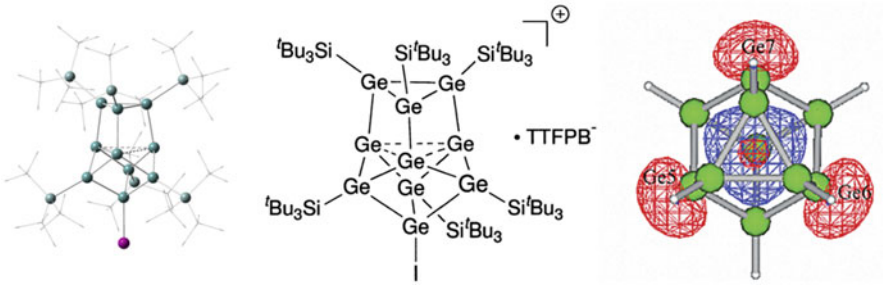

Fig. 56 Crystal structure of $[Ge_{10}(Si^tBu_3)_6I]^+$ and its HOMO showing the 3-center-2-electron bonding character [176] (Adapted with permission from [176]. Copyright (2002) American Chemical Society)

electron bond among the three trivalent Ge atoms, with each Ge atom contributing its external orbital that is normally associated with a lone pair in 3-connected cluster but is now sharing a common electron pair with the other two Ge atoms.

The above 3-center-2-electron bond is not unique in this single cluster. In fact, 2-center-2-electron localized bond, 3-center-2-electron semi-localized bond, and multi-centered bonding (following Wade's rules) can be present in a single cluster at the same time. In the very complicated cluster $[Au_3Ge_{45}]^{9-}$ (Fig. **57**), there are four Ge_9 moieties in typical *closo* or *nido* geometries, while the remaining 9 Ge atoms appear to arrange in a 3-connected manner [177]. Further inspection shows that the central $[Ge_9]$ skeleton has a similar structure with the $[Ge_9]$ skeleton in $[Ge_{10}(Si^tBu_3)_6I]^+$ discussed above, while the $[Ge_9]$ unit IV plays the role of iodine substituted Ge atom, and the $[Ge_9]$ units I, II, and III play the role of the silyl substituents [177]. Eventually, there is a 3-center-2-electron bond among Ge54, Ge55, and Ge56, in addition to the delocalized bonding within the four $[Ge_9]$ units and the localized 2-center-2-electron bonds within the central $[Ge_9]$ skeleton.

In the above seemingly 3-connected clusters, there are vertices that clearly conform to the octet rule and vertices that do not, but this is not always the case. The cluster $[Ge_{14}R_5]^{3-}$ (R = $Ge(SiMe_3)_3$) (Fig. **58**a) has a 3-connected skeletal geometry with 5 out of 14 Ge atoms decorated by substituents [178]. However, this cluster only has 64 ($4 \times 14 + 5 + 3$) valence electrons, much smaller than $5n = 70$ as required by a typical 3-connected cluster predicted by PSEPT. Its electron count does not follow either $4n + 2$ or $5n$ rule and the cluster shows non-deltahedral geometry, both suggesting the inapplicability of Wade's rules on this cluster.

A closely related cluster is the intermetalloid cluster $[Pd_3Sn_8Bi_6]^{4-}$ (Fig. **58**c), in which tetrel and pnictogen atoms are mixed in the 14-vertex peripheral cage [180]. The geometry of this cluster is very similar to that of $[Ge_{14}R_5]^{3-}$, except that there are three endohedral Pd atoms arranged in a triangle. If we follow the usual rule-of-thumb for endohedral centers and assign each Pd to be Pd^0 (d^{10} configuration), then the cage would have 66 valence electrons ($4 \times 8 + 5 \times 6 + 4$), still 4 electrons short when compared to that for a regular 3-connected cluster. However,

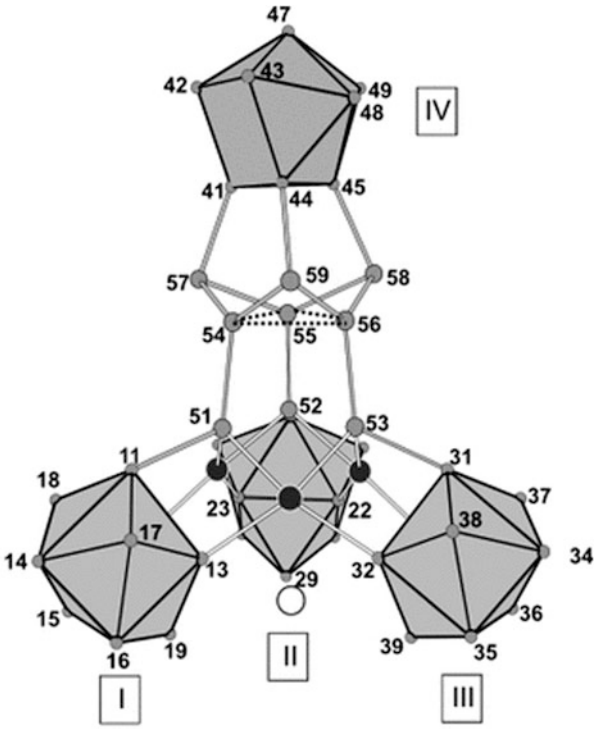

Fig. 57 Crystal structure of $[Au_3Ge_{45}]^{9-}$ [177] (Reprinted from [177], Copyright (2007), with permission from John Wiley and Sons)

3-connected clusters with similar composition do exist, as demonstrated by the clusters $[Nb@Ge_8As_6]^{3-}$ and $[Eu@Sn_6Bi_8]^{4-}$ (Fig. **58**b) [179, 181], both of which have similar geometries with $[Ge_{14}R_5]^{3-}$ and $[Pd_3Sn_8Bi_6]^{4-}$. Nb is an early transition metal with small electronegativity, hence it is hard to imagine Nb to adopt a d^{10} configuration in $[Nb@Ge_8As_6]^{3-}$. Instead, if we consider Nb to be Nb^{5+}, then the outer cage will become $[Ge_8As_6]^{8-}$, isoelectronic with $[As_{14}]$ having 70 valence electrons, thus conforming to the electron count of a 3-connected cluster. The f-block element doped endohedral cluster $[Eu@Sn_6Bi_8]^{4-}$ can be deciphered in a similar way, if we notice that the outer cage should be $[Sn_6Bi_8]^{6-}$ in order to be 3-connected, hence the Eu center is Eu^{2+} with a half-filled f^7 configuration.

These examples again demonstrate the great flexibility in electron count for group 14 clusters. Despite such flexibility, one can also find patterns among them. From a geometric point of view, the clusters $[Nb@Ge_8As_6]^{3-}$ and $[Eu@Sn_6Bi_8]^{4-}$ are fairly spherical, while $[Ge_{14}R_5]^{3-}$ and $[Pd_3Sn_8Bi_6]^{4-}$ are oblate (Fig. **58**d). Clearly there is a relationship between valence electron count and sphericity, implying that the additional 4/6 electrons would have vertical anti-bonding character.

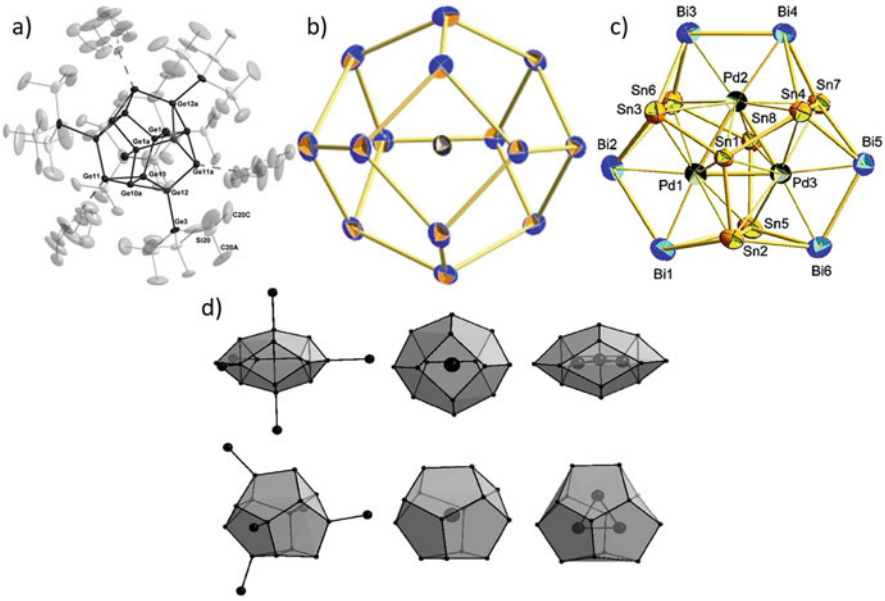

Fig. 58 Crystal structure of $[Ge_{14}\{Ge(SiMe_3)_3\}_5]^{3-}$, $[Eu@Sn_6Bi_8]^{4-}$ and $[Pd_3Sn_8Bi_6]^{4-}$ and comparison among their geometries [178–180] (Reprinted with permission from [178], Copyright (2008) The Royal Society of Chemistry; from [179], Copyright (2010) John Wiley and Sons; and from [180], Copyright (2011) American Chemical Society)

While the previous examples with intermediate electron counts feature 3-connected geometries to some extent, there are also a number of other examples with intermediate electron counts closely resembling Wadean clusters. For example, the clusters $Sn_{10}(Hyp)_6$ (Fig. **59**), $[Sn_{10}(Hyp)_5]^-$, $[Sn_{10}(Hyp)_4]^{2-}$, and $[Pb_{10}(Hyp)_6]$ all have $46 = 4n + 6$ valence electrons, but adopt *arachno* geometries that do follow the prediction of Wade's rules [182–186].

Similarly, the 12-vertex $[Pb_{12}(Hyp)_6]$ cluster (Fig. **59**) has an approximately icosahedral skeleton, with six out of twelve Pb atoms decorated with substituents [183]. This cluster has a valence electron count of 54 ($4 \times 12 + 6$), 4 electrons more than that required by a Wadean cluster (50) but still less than that in $5n$ rule. While skeletal bonding has been partially broken because of the additional electrons, leading to a kernel in (approximate) D_{3d} symmetry, the unexpected hypervalent interaction between silyl groups with another proximate Pb atom shortens the bridge edge, further reducing the molecular symmetry to a pseudo-C_{2h} point group. Although it has been proposed based on electron counting that the overall cluster should be described as an *arachno*-type cluster as predicted by Wade's rules [183], the narrow spread of the bond lengths of the icosahedral edges hints a different electronic structure from its isoelectronic *arachno* borane cluster $[B_{12}H_{18}]$, which has a macropolyhedral geometry [187].

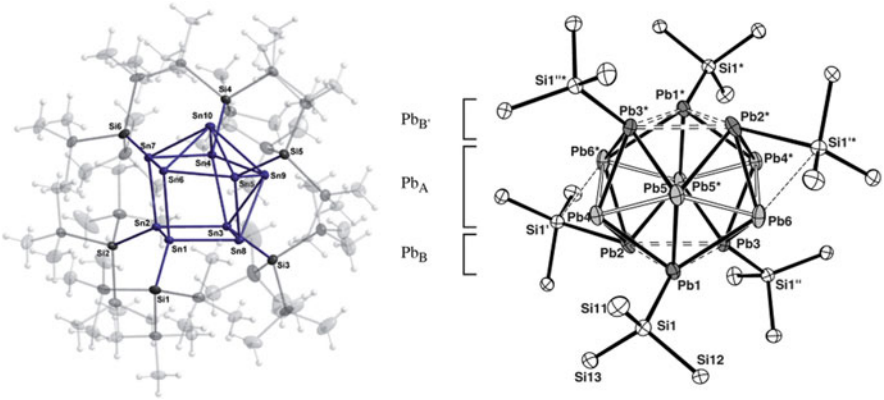

Fig. 59 Crystal structures of $[Sn_{10}(Hyp)_6]$ and $[Pb_{12}(Hyp)_6]$ [182, 183] (Reproduced from Ref. [182] with permission from The Royal Society of Chemistry (2009), and from Ref. [183] with permission from John Wiley and Sons (2004))

From these examples, we can see that group 14 clusters made up of heavier tetrel elements may not necessarily share the same geometry as those made up of lighter tetrel elements with the same number of electrons. On the other hand, without going into detailed comparison among individual cases, we can still see a similar trend as previously discussed in Sect. 4.3, that heavier tetrel elements seem to have a greater tendency to form Wadean clusters while lighter tetrel elements are more likely to adopt 3-connected structures. The failure of Wade's rules on the above examples as well as these subtle features again reveals the difference between tetrel atoms and [BH] units and even between lighter and heavier tetrel atoms, and demonstrates the incompleteness of only applying Wade's rules to understand the electronic structures of group 14 clusters. Nevertheless, Wade's rules still serve as a good reference and a guiding principle when we first face the constantly synthesized novel clusters, since detailed analysis on their electronic structures is often given on top of Wade's bonding description of cluster compounds.

7 Perspective

Cluster chemistry always challenges our perception and interpretation of their structures using the current bonding models, manifesting why this field is particularly fascinating. Although Wade's rules cannot fully explain the electronic structures of all group 14 clusters, it has become a norm to treat them as a starting point when a new cluster is synthesized. The role of Wade's rules in cluster chemistry is similar to the role of the octet rule in classical inorganic chemistry: not all atoms conform to the octet rule in all molecules, but it is always a good starting point when understanding the bonding of a molecule. We often draw a Lewis structure for a

molecule to see whether a satisfactory bonding picture can be achieved. If not, extra attention will be paid to explore the special bonding mode. Although individual atoms in cluster compounds do not necessarily follow the octet rule, we can similarly draw a "Lewis-like structure" in a modular way for many cluster compounds, on the basis of Wade's rules and polyhedral skeletal electron pair theory [188]. In such a modular representation, we can identify the Wadean units in a large cluster and treat them as "superatoms" that can form covalent and dative bonds with other moieties (see Sects. 5.2 and 5.3). Such a modular bonding picture allows us to understand the structure and bonding for each constituent unit in a cluster. In this way, cluster compounds are nothing more than an aggregation of multiple units, each of which falls into the scope of an existing bonding model.

Still, there are a couple of cluster compounds out there that do not follow Wade's rules or their extensions, nor conform to the octet rule as in 3-connected clusters, which encourages us to explore their bonding patterns more carefully and thoroughly, and to develop new bonding models that not only explain the electronic structure of a single cluster, but also have the potential to be transferred to a number of other clusters.

So far, a lot of efforts have been paid to formulate a better understanding for more clusters, and many models arise. For example, aromaticity is a longstanding concept that has been extensively used across various contexts when one intends to describe certain unexpected stability of a compound, and has also been widely applied in group 14 clusters. The Jellium model, which originated from alkali metal clusters and has been widely used for gold clusters, can also be used to understand the electronic structures of some group 14 clusters, as introduced in Sect. 3.2.

While both Wade's rules and Jellium model were developed to understand electronic structure for species with a near-spherical shape, bonding rules proposed for vertex capping and cluster fusion described in the polyhedral skeletal electron pair theory are important steps toward complicated non-spherical clusters. Following this spirit, new bonding models based on the nine-vertex cluster units have been developed, inspired by their frequent presence in cluster assemblies, to understand a number of group 14 cluster assemblies as introduced in Sect. 5.

Nevertheless, cluster compounds covered in this chapter are still far from comprehensive. There are a lot of clusters for which a general bonding model has not emerged. While we are halfway toward a comprehensive understanding of cluster chemistry, the bonding models introduced in this chapter are powerful tools that we are armed with to explore this terra incognita ahead of us.

In particular, the $[E_{10}]$-fused clusters $[Co_2Ge_{16}]^{4-}$ and $[Rh_3Sn_{24}]^{5-}$ [189, 190], though very different in composition and shape, feature the geometries in which identical cluster fragments are fused, which may hint us to adopt a fragment-based approach to understand their relationship, similar to what we have presented in Sect. 5.

The bonding model we discussed for the gold-bridged group 14 cluster $[Au_3Ge_{18}]$, which is a coordination bridged cluster with no explicit Au-Au bonding, could potentially be used to understand the gold-bridged clusters $[Au_8Pb_{33}]^{6-}$ and $[Au_{12}Pb_{44}]^{8-}$ [191] where Au-Au bonding is apparent and a joint model that bridges group 14 clusters and group 11 clusters becomes obligatory, although the existence

of the icosahedral cluster $[Au@Pb_{12}]^{3-}$, which does not conform to Wade's rules, hints us there might be a more complicated chemistry ahead.

Nevertheless, new clusters are constantly synthesized, challenging our established chemistry and urging us to develop new bonding models. After all, this is why Wade's rules were proposed and all the succeeding models were developed. We anticipate novel clusters and innovative models will persistently arise in the future, presenting us with new chemistry.

Acknowledgments We would like to dedicate this chapter to the memory of Roy Johnston who made seminal contribution in the application of molecular orbital theory to the understanding of structure and bonding in molecular cluster compounds. We would also like to acknowledge the financial support from the Hong Kong Research Grants Council (HKUST 16305119).

References

1. Fässler TF, Hoffmann R (1999) Novel synthetic route to soluble polyanions: synthesis and crystal structure of $[K(18\text{-crown-}6)]_4[Pb_9]\cdot en\cdot tol$†. J Chem Soc Dalton Trans:3339–3340
2. Wade K (1971) The structural significance of the number of skeletal bonding electron-pairs in carboranes, the higher boranes and borane anions, and various transition-metal carbonyl cluster compounds. J Chem Soc Chem Commun 0:792–793
3. Mingos DMP (1984) Polyhedral skeletal electron pair approach. Acc Chem Res 17:311–319
4. Mingos DMP, Wales DJ (1990) Introduction to cluster chemistry. Prentice-Hall
5. Stone AJ (1981) New approach to bonding in transition-metal clusters and related compounds. Inorg Chem 20:563–571
6. Welch AJ (2013) The significance and impact of Wade's rules. Chem Commun 49:3615–3616
7. Johnston RL, Mingos DMP (1986) Molecular orbital calculations relevant to the hypercloso vs. iso-closo controversy in metallaboranes. Inorg Chem 25:3321–3323
8. Bould J, Greenwood NN, Kennedy JD, McDonald WS (1982) Quantitative ortho-cycloboronation of P-phenyl groups in metallaborane chemistry and the crystal and molecular structure of the novel iso-closo-ten-vertex metallaborane $[1,1,1\text{-}H(PPh_3)(Ph_2P\text{-ortho-}C_6H_4)\text{-iso-closo-}(1\text{-}IrB_9H_8\text{-}2\text{-})]$. J Chem Soc Chem Commun:465–467
9. King RB (2011) Structure and bonding in zintl ions and related main group element clusters. In: Fässler TF (ed) Zintl ions Princ. Recent dev. Springer, Berlin, pp 1–24
10. Fässler TF (2011) Relationships between soluble zintl anions, ligand-stabilized cage compounds, and intermetalloid clusters of tetrel (Si–Pb) and pentel (P–bi) elements. In: Fässler TF (ed) Zintl ions Princ. Recent dev. Springer, Berlin, pp 91–131
11. Scharfe S, Kraus F, Stegmaier S, Schier A, Fässler TF (2011) Zintl ions, cage compounds, and intermetalloid clusters of group 14 and group 15 elements. Angew Chem Int Ed 50:3630–3670
12. Liu C, Sun Z-M (2019) Recent advances in structural chemistry of group 14 Zintl ions. Coord Chem Rev 382:32–56
13. Hoch C, Wendorff M, Röhr C (2003) Synthesis and crystal structure of the tetrelides $A_{12}M_{17}$ (A=Na, K, Rb, Cs; M=Si, Ge, Sn) and A_4Pb_9 (A=K, Rb). J Alloys Compd 361:206–221
14. Edwards PA, Corbett JD (1977) Stable homopolyatomic anions. Synthesis and crystal structures of salts containing the pentaplumbide(2-) and pentastannide(2-) anions. Inorg Chem 16:903–907
15. Goicoechea JM, Sevov SC (2004) Naked deltahedral silicon clusters in solution: synthesis and characterization of Si_9^{3-} and Si_5^{2-}. J Am Chem Soc 126:6860–6861
16. Campbell J, Schrobilgen GJ (1997) The closo-Ge_5^{2-} anion: synthesis, crystal structure, and raman spectrum of $(2,2,2\text{-crypt-}K^+)_2Ge_5^{2-}\cdot THF$. Inorg Chem 36:4078–4081

17. Corbett JD, Edwards PA (1975) Stable homopolyatomic anions: the crystal structures of salts of the anions pentaplumbide(2–) and enneastannide(4–). J Chem Soc Chem Commun:984–985
18. Suchentrunk C, Korber N (2006) Ge_5^{2-} Zintl anions: synthesis and crystal structures of [K([2.2.2]-crypt)]$_2$Ge$_5$·4NH$_3$ and [Rb([2.2.2]-crypt)]$_2$Ge$_5$·4NH$_3$. New J Chem 30:1737–1739
19. Goicoechea JM, Sevov SC (2005) Ligand-free deltahedral clusters of silicon in solution: synthesis, structure, and electrochemistry of Si_9^{2-}. Inorg Chem 44:2654–2658
20. Belin CHE, Corbett JD, Cisar A (1977) Homopolyatomic anions and configurational questions. Synthesis and structure of the nonagermanide(2-) and nonagermanide(4-) ions, Ge_9^{2-} and Ge_9^{4-}. J Am Chem Soc 99:7163–7169
21. Spiekermann A, Hoffmann SD, Fässler TF (2006) The zintl ion $[Pb_{10}]^{2-}$: a rare example of a homoatomic closo cluster. Angew Chem Int Ed 45:3459–3462
22. Cui L-F, Huang X, Wang L-M, Zubarev DY, Boldyrev AI, Li J, Wang L-S (2006) Sn_{12}^{2-}: stannaspherene. J Am Chem Soc 128:8390–8391
23. Cui L-F, Huang X, Wang L-M, Li J, Wang L-S (2006) Pb_{12}^{2-}: plumbaspherene. J Phys Chem A 110:10169–10172
24. Cui L-F, Wang L-S (2008) Stable icosahedral hollow cage clusters: stannaspherene and plumbaspherene. Int Rev Phys Chem 27:139–166
25. Corbett JD, Edwards PA (1977) The nonastannide(4-) anion Sn_9^{4-}, a novel capped antiprismatic configuration (C4.Upsilon.). J Am Chem Soc 99:3313–3317
26. Yong L, Hoffmann SD, Fässler TF (2006) $_\infty^2$[K$_4$Pb$_9$] – a low-dimensional arrangement of $[Pb_9]^{4-}$ clusters in [K(18-crown-6)]2K$_2$Pb$_9$·(en)$_{1.5}$. Inorg Chim Acta 359:4774–4778
27. Schnering HGV, Baitinger M, Bolle U et al (1997) Binary alkali metal compounds with the zintl anions $[Ge_9]^{4-}$ and $[Sn_9]^{4-}$. Z Für Anorg Allg Chem 623:1037–1039
28. Campbell J, Dixon DA, Mercier HPA, Schrobilgen GJ (1995) The nido-Pb_9^{4-} and the Jahn-Teller distorted closo-Pb_9^{3-} Zintl anions: syntheses, X-ray structures, and theoretical studies. Inorg Chem 34:5798–5809
29. Joseph S, Suchentrunk C, Kraus F, Korber N (2009) Si_9^{4-} anions in solution – structures of the solvates Rb$_4$Si$_9$·4.75NH$_3$ and [Rb(18-crown-6)]Rb$_3$Si$_9$·4NH$_3$, and chemical bonding in Si_9^{4-}. Eur J Inorg Chem 2009:4641–4647
30. Wiesler K, Brandl K, Fleischmann A, Korber N (2009) Tetrahedral $[Tt_4]^{4-}$ zintl anions through solution chemistry: syntheses and crystal structures of the ammoniates Rb$_4$Sn$_4$·2NH$_3$, Cs$_4$Sn$_4$·2NH$_3$, and Rb$_4$Pb$_4$·2NH$_3$. Z Für Anorg Allg Chem 635:508–512
31. Zhang J-X, Sheong FK, Lin Z (2018) Unravelling chemical interactions with principal interacting orbital analysis. Chem Eur J 24:9639–9650
32. Zhang J-X, Sheong FK, Lin Z (2020) Principal interacting orbital: a chemically intuitive method for deciphering bonding interaction. WIREs Comput Mol Sci 10:e1469
33. Li F, Sevov SC (2014) Synthesis, structures, and solution dynamics of tetrasubstituted nine-atom germanium deltahedral clusters. J Am Chem Soc 136:12056–12063
34. Geitner FS, Dums JV, Fässler TF (2017) Derivatization of phosphine ligands with bulky deltahedral zintl clusters – synthesis of charge neutral zwitterionic tetrel cluster compounds [(Ge$_9${Si(TMS)$_3$}$_2$)^{t}Bu$_2$P]M(NHC^{Dipp}) (M: Cu, Ag, Au). J Am Chem Soc 139:11933–11940
35. Sevov SC, Goicoechea JM (2006) Chemistry of deltahedral zintl ions. Organometallics 25:5678–5692
36. Rios D, Gillett-Kunnath MM, Taylor JD, Oliver AG, Sevov SC (2011) Addition of a thallium vertex to empty and centered nine-atom deltahedral zintl ions of germanium and tin. Inorg Chem 50:2373–2377
37. Hull MW, Sevov SC (2007) Organo-zintl clusters soluble in conventional organic solvents: setting the stage for organo-zintl cluster chemistry. Inorg Chem 46:10953–10955
38. Hull MW, Sevov SC (2009) Functionalization of nine-atom deltahedral zintl ions with organic substituents: detailed studies of the reactions. J Am Chem Soc 131:9026–9037
39. Schnepf A (2003) [Ge$_9${Si(SiMe$_3$)$_3$}$_3$]$^-$: a soluble polyhedral Ge$_9$ cluster stabilized by only three silyl ligands. Angew Chem Int Ed 42:2624–2625

40. Li F, Muñoz-Castro A, Sevov SC (2012) $[Ge_9\{Si(SiMe_3)_3\}_3SnPh_3]$: a tetrasubstituted and neutral deltahedral nine-atom cluster. Angew Chem Int Ed 51:8581–8584
41. Hull MW, Sevov SC (2007) Addition of alkenes to deltahedral zintl clusters by reaction with alkynes: synthesis and structure of $[Fc–CH–CH–Ge_9–CH–CH–Fc]^{2-}$, an organo-zintl–organometallic anion. Angew Chem Int Ed 46:6695–6698
42. Ugrinov A, Sevov SC (2002) $[Ph_2Bi–(Ge_9)–BiPh_2]^{2-}$: a deltahedral zintl ion functionalized by exo-bonded ligands. J Am Chem Soc 124:2442–2443
43. Hogeveen H, Kwant PW (1974) Chemistry and spectroscopy in strongly acidic solutions. XL. $(CCH_3)_6^{2+}$, an unusual dication. J Am Chem Soc 96:2208–2214
44. Jašík J, Gerlich D, Roithová J (2014) Probing isomers of the benzene dication in a low-temperature trap. J Am Chem Soc 136:2960–2962
45. Malischewski M, Seppelt K (2017) Crystal structure determination of the pentagonal-pyramidal hexamethylbenzene dication $C_6(CH_3)_6^{2+}$. Angew Chem Int Ed 56:368–370
46. Faessler TF, Hunziker M (1994) Ge_9^{3-} and Pb_9^{3-}: two novel, naked, homopolyatomic zintl ions with paramagnetic properties. Inorg Chem 33:5380–5381
47. Critchlow SC, Corbett JD (1983) Homopolyatomic anions. The synthesis and characterization of the novel paramagnetic nonastannide(3-) anion Sn_9^{3-}, a D_{3h} cluster with 21 skeletal electrons. J Am Chem Soc 105:5715–5716
48. Zubarev DY, Boldyrev AI (2008) Developing paradigms of chemical bonding: adaptive natural density partitioning. Phys Chem Chem Phys 10:5207–5217
49. Tkachenko VN, Boldyrev AI (2019) Multiple local σ-aromaticity of nonagermanide clusters. Chem Sci 10:5761–5765
50. King BR, Silaghi-Dumitrescu I (2008) The role of "external" lone pairs in the chemical bonding of bare post-transition element clusters: the Wade–Mingos rules versus the jellium model. Dalton Trans 0:6083–6088
51. Knight WD, De Heer WA, Saunders WA, Clemenger K, Chou MY, Cohen ML (1987) Alkali metal clusters and the jellium model. Chem Phys Lett 134:1–5
52. Lin Z, Slee T, Mingos DMP (1990) A structural jellium model of cluster electronic structure. Chem Phys 142:321–334
53. Walter M, Akola J, Lopez-Acevedo O, Jadzinsky PD, Calero G, Ackerson CJ, Whetten RL, Grönbeck H, Häkkinen H (2008) A unified view of ligand-protected gold clusters as superatom complexes. Proc Natl Acad Sci 105:9157–9162
54. Li F, Sevov SC (2012) Rational synthesis of $[Ge_9\{Si(SiMe_3)_3\}_3]^-$ from its parent zintl ion Ge_9^{4-}. Inorg Chem 51:2706–2708
55. Downie C, Mao J-G, Guloy AM (2001) Synthesis and structure of $[K^+$-(2,2)diaza-[18]-crown-6$][K_3Ge_9]$·2Ethylenediamine: stabilization of the two-dimensional layer $_\infty^2[K_3Ge_9^{1-}]$. Inorg Chem 40:4721–4725
56. Ugrinov A, Sevov SC (2004) Rationally functionalized deltahedral zintl ions: synthesis and characterization of $[Ge_9–ER_3]^{3-}$, $[R_3E–Ge_9–ER_3]^{2-}$, and $[R_3E–Ge_9–Ge_9–ER_3]^{4-}$ (E=Ge, Sn; R=Me, Ph). Chem Eur J 10:3727–3733
57. Johnston RL, Mingos DMP (1987) A group theoretical paradigm for describing the skeletal molecular orbitals of cluster compounds. Part 2. Bispherical clusters. J Chem Soc Dalton Trans:1445–1456
58. Chen Z, Neukermans S, Wang X, Janssens E, Zhou Z, Silverans RE, King RB, Schleyer P von R, Lievens P (2006) To achieve stable spherical clusters: general principles and experimental confirmations. J Am Chem Soc 128:12829–12834
59. Fässler TF, Hoffmann SD (2004) Endohedral zintl ions: intermetalloid clusters. Angew Chem Int Ed 43:6242–6247
60. Zhao J, Du Q, Zhou S, Kumar V (2020) Endohedrally doped cage clusters. Chem Rev 120:9021–9163
61. Arcisauskaite V, Jin X, Goicoechea JM, McGrady JE (2016) Electronic properties of endohedral clusters of group 14. In: Mingos DMP (ed) Chem bond 100 years old get. Stronger. Springer, Cham, pp 181–197

62. Esenturk EN, Fettinger J, Lam Y-F, Eichhorn B (2004) $[Pt@Pb_{12}]^{2-}$. Angew Chem Int Ed 43:2132–2134
63. Esenturk EN, Fettinger J, Eichhorn B (2006) The Pb_{12}^{2-} and Pb_{10}^{2-} zintl ions and the $M@Pb_{12}^{2-}$ and $M@Pb_{10}^{2-}$ cluster series where M = Ni, Pd, Pt. J Am Chem Soc 128:9178–9186
64. Yi W, Lu-Lu W, Hua-Peng R, Ben-Long L, Rui-Li S, Li X (2015) Synthesis and characterization of the endohedral plumbaspherene$[Rh@Pb_{12}]^{3-}$. Chin J Struc Chem 34:1253–1258
65. Wang J-Q, Stegmaier S, Wahl B, Fässler TF (2010) Step-by-step synthesis of the endohedral stannaspherene $[Ir@Sn_{12}]^{3-}$ via the capped cluster anion $[Sn_9Ir(cod)]^{3-}$. Chem Eur J 16:1793–1798
66. Xing X, Tian Z, Liu H, Tang Z (2003) Magic bimetallic cluster anions of M/Pb (M = Au, Ag and Cu) observed and analyzed by laser ablation and time-of-flight mass spectrometry. Rapid Commun Mass Spectrom 17:1411–1415
67. Neukermans S, Wang X, Veldeman N, Janssens E, Silverans RE, Lievens P (2006) Mass spectrometric stability study of binary MSn clusters (S=Si, Ge, Sn, Pb, and M=Cr, Mn, Cu, Zn). Int J Mass Spectrom 252:145–150
68. Cui L-F, Huang X, Wang L-M, Li J, Wang L-S (2007) Endohedral stannaspherenes $M@Sn_{12}^{-}$: a rich class of stable molecular cage clusters. Angew Chem Int Ed 46:742–745
69. Liu C, Li L-J, Popov IA, Wilson RJ, Xu C-Q, Li J, Boldyrev AI, Sun Z-M (2018) Symmetry reduction upon size mismatch: the non-icosahedral intermetalloid cluster $[Co@Ge_{12}]^{3-}$. Chin J Chem 36:1165–1168
70. Esenturk EN, Fettinger J, Eichhorn B (2005) The closo-Pb_{10}^{2-} Zintl ion in the $[Ni@Pb_{10}]^{2-}$ cluster. Chem Commun:247–249
71. Scharfe S, Fässler TF, Stegmaier S, Hoffmann SD, Ruhland K (2008) $[Cu@Sn_9]^{3-}$ and $[Cu@Pb_9]^{3-}$: intermetalloid clusters with endohedral Cu atoms in spherical environments. Chem Eur J 14:4479–4483
72. Gillett-Kunnath MM, Paik JI, Jensen SM, Taylor JD, Sevov SC (2011) Metal-centered deltahedral zintl ions: synthesis of $[Ni@Sn_9]^{4-}$ by direct extraction from intermetallic precursors and of the vertex-fused dimer $[\{Ni@Sn_8(\mu\text{-}Ge)_{1/2}\}_2]^{4-}$. Inorg Chem 50:11695–11701
73. Hlukhyy V, He H, Jantke L-A, Fässler TF (2012) The neat ternary solid $K_{5-x}Co_{1-x}Sn_9$ with endohedral $[Co@Sn_9]^{5-}$ cluster units: a precursor for soluble intermetalloid $[Co_2@Sn_{17}]^{5-}$ clusters. Chem Eur J 18:12000–12007
74. Yue C-Y, Wang M-F, Yuan Z-D, Zhou F-X, Zhang H-P, Lei X-W (2013) $K_{13}CoSn_{17-x}$ (x = 0.1): a new ternary phase containing -cobalt centered $[Sn_9]$ cluster synthesized via high-temperature reaction. Z Für Anorg Allg Chem 639:911–917
75. Hlukhyy V, Stegmaier S, van Wüllen L, Fässler TF (2014) Endohedrally filled $[Ni@Sn_9]^{4-}$ and $[Co@Sn_9]^{5-}$ clusters in the neat solids $Na_{12}Ni_{1-x}Sn_{17}$ and $K_{13-x}Co_{1-x}Sn_{17}$: crystal structure and ^{119}Sn solid-state NMR spectroscopy. Chem Eur J 20:12157–12164
76. Benda CB, Waibel M, Köchner T, Fässler TF (2014) Reactivity of liquid ammonia solutions of the zintl phase $K_{12}Sn_{17}$ towards Mesitylcopper(I) and Phosphinegold(I) chloride. Chem Eur J 20:16738–16746
77. Witzel BJL, Klein W, Dums JV, Boyko M, Fässler TF (2019) Metallocages for metal anions: highly charged $[Co@Ge_9]^{5-}$ and $[Ru@Sn_9]^{6-}$ clusters featuring spherically encapsulated Co^{1-} and Ru^{2-} anions. Angew Chem Int Ed 58:12908–12913
78. Goicoechea JM, Sevov SC (2005) $[(Ni\text{-}Ni\text{-}Ni)@(Ge_9)_2]^{4-}$: a linear triatomic Nickel filament enclosed in a dimer of nine-atom germanium clusters. Angew Chem Int Ed 44:4026–4028
79. Goicoechea JM, Sevov SC (2006) Deltahedral germanium clusters: insertion of transition-metal atoms and addition of organometallic fragments. J Am Chem Soc 128:4155–4161
80. Liu C, Li L-J, Jin X, McGrady JE, Sun Z-M (2018) Reactivity studies of $[Co@Sn_9]^{4-}$ with transition metal reagents: bottom-up synthesis of ternary functionalized zintl clusters. Inorg Chem 57:3025–3034
81. Li L-J, Pan F-X, Li F-Y, Chen Z-F, Sun Z-M (2017) Synthesis, characterization and electronic properties of an endohedral plumbaspherene $[Au@Pb_{12}]^{3-}$. Inorg Chem Front 4:1393–1396

82. Zhou B, Krämer T, Thompson AL, McGrady JE, Goicoechea JM (2011) A highly distorted open-shell endohedral zintl cluster: $[Mn@Pb_{12}]^{3-}$. Inorg Chem 50:8028–8037
83. Wang J-Q, Stegmaier S, Fässler TF (2009) $[Co@Ge_{10}]^{3-}$: an intermetalloid cluster with archimedean pentagonal prismatic structure. Angew Chem Int Ed 48:1998–2002
84. Zhou B, Denning MS, Kays DL, Goicoechea JM (2009) Synthesis and isolation of $[Fe@Ge_{10}]^{3-}$: a pentagonal prismatic zintl ion cage encapsulating an interstitial iron atom. J Am Chem Soc 131:2802–2803
85. Krämer T, Duckworth JCA, Ingram MD, Zhou B, McGrady JE, Goicoechea JM (2013) Structural trends in ten-vertex endohedral clusters, $M@E_{10}$ and the synthesis of a new member of the family, $[Fe@Sn_{10}]^{3-}$. Dalton Trans 42:12120–12129
86. Sevov SC, Corbett JD (1993) Potassium indium zinc compound $K_8In_{10}Zn$: interstitially-stabilized analogs of early-transition-metal halide clusters. Inorg Chem 32:1059–1061
87. Sevov SC, Corbett JD (1993) $K_{10}In_{10}Z$ (Z = Ni, Pd, Pt): Zintl phases containing isolated decaindium clusters centered by transition elements. J Am Chem Soc 115:9089–9094
88. Espinoza-Quintero G, Duckworth JCA, Myers WK, McGrady JE, Goicoechea JM (2014) Synthesis and characterization of $[Ru@Ge_{12}]^{3-}$: an endohedral 3-connected cluster. J Am Chem Soc 136:1210–1213
89. Beck SM (1987) Studies of silicon cluster–metal atom compound formation in a supersonic molecular beam. J Chem Phys 87:4233–4234
90. Janssens E, Gruene P, Meijer G, Wöste L, Lievens P, Fielicke A (2007) Argon physisorption as structural probe for endohedrally doped silicon clusters. Phys Rev Lett 99:063401
91. Pandey R, Rao BK, Jena P, Blanco MA (2001) Electronic structure and properties of transition metal−benzene complexes. J Am Chem Soc 123:3799–3808
92. Khanna SN, Rao BK, Jena P (2002) Magic numbers in metallo-inorganic clusters: chromium encapsulated in silicon cages. Phys Rev Lett 89:016803
93. Ulises Reveles J, Khanna SN (2006) Electronic counting rules for the stability of metal-silicon clusters. Phys Rev B 74:035435
94. Guo L, Zhao G, Gu Y, Liu X, Zeng Z (2008) Density-functional investigation of metal-silicon cage clusters MSi_n (M=Sc, Ti, V, Cr, Mn, Fe, Co, Ni, Cu, Zn; n=8–16). Phys Rev B 77:195417
95. Abreu MB, Reber AC, Khanna SN (2014) Does the 18-electron rule apply to $CrSi_{12}$? J Phys Chem Lett 5:3492–3496
96. Goicoechea JM, McGrady JE (2015) On the structural landscape in endohedral silicon and germanium clusters, $M@Si_{12}$ and $M@Ge_{12}$. Dalton Trans 44:6755–6766
97. Goicoechea JM, Sevov SC (2006) Organozinc derivatives of deltahedral zintl ions: synthesis and characterization of closo-$[E_9Zn(C_6H_5)]^{3-}$ (E = Si, Ge, Sn, Pb). Organometallics 25:4530–4536
98. Zhou B, Denning MS, Chapman TAD, Goicoechea JM (2009) Coupling reactions of functionalized zintl ions $[E_9Cd(C_6H_5)]^{3-}$ (E = Sn, Pb) with tributyltinhydride: synthesis and isolation of $\{Sn_9CdSn[(CH_2)_3CH_3]_3\}^{3-}$. Inorg Chem 48:2899–2907
99. Zhou B, Denning MS, Jones C, Goicoechea JM (2009) Reductive cleavage of Zn–C bonds by group 14 Zintl anions: synthesis and characterisation of $[E_9ZnR]^{3-}$ (E = Ge, Sn, Pb; R = Mes, ^{i}Pr). Dalton Trans 0:1571–1578
100. Li F, Muñoz-Castro A, Sevov SC (2016) $[(Me_3Si)Si]_3EtGe_9Pd(PPh_3)]$, a pentafunctionalized deltahedral zintl cluster: synthesis, structure, and solution dynamics. Angew Chem Int Ed 55:8630–8633
101. Townrow OPE, Chung C, Macgregor SA, Weller AS, Goicoechea JM (2020) A neutral heteroatomic zintl cluster for the catalytic hydrogenation of cyclic alkenes. J Am Chem Soc 142:18330–18335
102. Kesanli B, Fettinger J, Eichhorn B (2001) The closo-$[Sn_9M(CO)_3]^{4-}$ zintl ion clusters where M=Cr, Mo, W: two structural isomers and their dynamic behavior. Chem Eur J 7:5277–5285
103. Eichhorn BW, Haushalter RC (1990) Closo-$[CrPb_9(CO)_3]^{4-}$: a 100 year history of the nonaplumbide tetra-anion. J Chem Soc Chem Commun:937–938

104. Campbell J, Mercier HPA, Franke H, Santry DP, Dixon DA, Schrobilgen GJ (2002) Syntheses, crystal structures, and density functional theory calculations of the closo-[1-M(CO)$_3$(η^4-E$_9$)]$^{4-}$ (E = Sn, Pb; M = Mo, W) cluster anions and solution NMR spectroscopic characterization of [1-M(CO)$_3$(η^4-Sn$_9$)]$^{4-}$ (M = Cr, Mo, W). Inorg Chem 41:86–107
105. Yong L, Hoffmann SD, Fässler TF (2005) Crystal structures of [K(2.2.2-crypt)]$_4$[Pb$_9$Mo(CO)$_3$] – isolation of the novel isomers [(η^5-Pb$_9$)Mo(CO)$_3$]$^{4-}$ beside [(η^4-Pb$_9$)Mo(CO)$_3$]$^{4-}$. Eur J Inorg Chem 2005:3663–3669
106. Mingos DMP, Zhenyang L (1989) Site preference effects in heterometallic clusters. Comments Inorg Chem 9:95–122
107. Schiegerl LJ, Geitner FS, Fischer C, Klein W, Fässler TF (2016) Functionalization of [Ge$_9$] with small silanes: [Ge$_9$(SiR$_3$)$_3$]$^-$ (R = ^{i}Bu, ^{i}Pr, Et) and the structures of (CuNHC^{Dipp})[Ge$_9$\{Si(^{i}Bu)$_3$\}$_3$], (K-18c6)Au[Ge$_9$\{Si(^{i}Bu)$_3$\}$_3$]$_2$, and (K-18c6)$_2$[Ge$_9$\{Si(^{i}Bu)$_3$\}$_2$]. Z Für Anorg Allg Chem 642:1419–1426
108. Michenfelder NC, Gienger C, Schnepf A, Unterreiner A-N (2019) The influence of the FeCp(CO)$_2^+$ moiety on the dynamics of the metalloid [Ge$_9$(Si(SiMe$_3$)$_3$)$_3$]$^-$ cluster in thf: synthesis and characterization by time-resolved absorption spectroscopy. Dalton Trans 48:15577–15582
109. Schenk C, Schnepf A (2009) \{Ge$_9$R$_3$Cr(CO)$_5$\}$^-$ and \{Ge$_9$R$_3$Cr(CO)$_3$\}$^-$: a metalloid cluster (Ge$_9$R$_3^-$) as a flexible ligand in coordination chemistry [R = Si(SiMe$_3$)$_3$]. Chem Commun:3208–3210
110. Henke F, Schenk C, Schnepf A (2011) [Si(SiMe$_3$)$_3$]$_3$Ge$_9$M(CO)$_3^-$ (M = Cr, Mo, W): coordination chemistry with metalloid clusters. Dalton Trans 40:6704–6710
111. Sun Z-M, Zhao Y-F, Li J, Wang L-S (2009) Diversity of functionalized germanium zintl clusters: syntheses and theoretical studies of [Ge$_9$PdPPh$_3$]$^{3-}$ and [Ni@(Ge$_9$PdPPh$_3$)]$^{2-}$. J Clust Sci 20:601–609
112. Kesanli B, Fettinger J, Gardner DR, Eichhorn B (2002) The [Sn$_9$Pt$_2$(PPh$_3$)]$^{2-}$ and [Sn$_9$Ni$_2$(CO)]$^{3-}$ complexes: two markedly different Sn$_9$M$_2$L transition metal zintl ion clusters and their dynamic behavior. J Am Chem Soc 124:4779–4786
113. Geitner FS, Klein W, Storcheva O, Tilley TD, Fässler TF (2019) Early-transition-metal complexes of functionalized nonagermanide clusters: synthesis and characterization of [Cp$_2$(MeCN)Ti(η^1-Ge$_9$\{Si(TMS)$_3$\}$_3$)] and K$_3$[Cp$_2$Ti(η^1-Ge$_9$\{Si(TMS)$_3$\}$_2$)$_2$]. Inorg Chem 58:13293–13298
114. Kysliak O, Schrenk C, Schnepf A (2016) Reactivity of [Ge$_9$\{Si(SiMe$_3$)$_3$\}$_3$]$^-$ towards transition-metal M^{2+} cations: coordination and redox chemistry. Chem Eur J 22:18787–18793
115. Kocak FS, Zavalij P, Eichhorn B (2011) Reactions of exo-substituted RSn$_9^{3-}$ clusters with Pd: endohedral cluster formation and oxidative insertion. Chem Eur J 17:4858–4863
116. Geitner FS, Fässler TF (2016) Introducing tetrel zintl ions to N-heterocyclic carbenes – synthesis of coinage metal NHC complexes of [Ge$_9$\{Si(SiMe$_3$)$_3$\}$_3$]$^-$. Eur J Inorg Chem 2016:2688–2691
117. Mayer K, Schiegerl LJ, Fässler TF (2016) On the reactivity of silylated Ge$_9$ clusters: synthesis and characterization of [ZnCp*(Ge$_9$\{Si(SiMe$_3$)$_3$\}$_3$)], [CuP^{i}Pr$_3$(Ge$_9$\{Si(SiMe$_3$)$_3$\}$_3$)], and [(CuP^{i}Pr$_3$)$_4$\{Ge$_9$(SiPh$_3$)$_2$\}$_2$]. Chem Eur J 22:18794–18800
118. Geitner FS, Klein W, Fässler TF (2018) Synthesis and reactivity of multiple phosphine-functionalized nonagermanide clusters. Angew Chem Int Ed 57:14509–14513
119. Geitner FS, Wallach C, Fässler TF (2018) On the variable reactivity of phosphine-functionalized [Ge$_9$] clusters: zintl cluster-substituted phosphines or phosphine-substituted zintl clusters. Chem Eur J 24:4103–4110
120. Downing DO, Zavalij P, Eichhorn BW (2010) The closo-[Sn$_9$Ir(cod)]$^{3-}$ and [Pb$_9$Ir(cod)]$^{3-}$ zintl ions: isostructural Ir^I derivatives of the nido-E$_9^{4-}$ anions (E = Sn, Pb). Eur J Inorg Chem 2010:890–894
121. Geitner FS, Klein W, Fässler TF (2017) Formation of the intermetalloid cluster [AgSn$_{18}$]$^{7-}$ – the reactivity of coinage metal NHC compounds towards [Sn$_9$]$^{4-}$. Dalton Trans 46:5796–5800

122. Scharfe S, Fässler TF (2010) Varying bonding modes of the zintl ion $[Ge_9]^{4-}$ in Cu^I complexes: syntheses and structures of $[Cu(\eta^4\text{-}Ge_9)(PR_3)]^{3-}$ (R = ^{i}Pr, Cy) and $[Cu(\eta^4\text{-}Ge_9)(\eta^1\text{-}Ge_9)]^{7-}$. Eur J Inorg Chem 2010:1207–1213
123. Esenturk EN, Fettinger J, Eichhorn B (2006) Synthesis and characterization of the $[Ni_6Ge_{13}(CO)_5]^{4-}$ and $[Ge_9Ni_2(PPh_3)]^{2-}$ Zintl ion clusters. Polyhedron 25:521–529
124. Li F, Sevov SC (2015) Coordination of tri-substituted Nona–Germanium clusters to Cu(I) and Pd(0). Inorg Chem 54:8121–8125
125. Schenk C, Schnepf A (2007) $[AuGe_{18}\{Si(SiMe_3)_3\}_6]^-$: a soluble Au–Ge cluster on the way to a molecular cable? Angew Chem Int Ed 46:5314–5316
126. Henke F, Schenk C, Schnepf A (2009) $[Si(SiMe_3)_3]_6Ge_{18}M$ (M = Zn, Cd, Hg): neutral metalloid cluster compounds of germanium as highly soluble building blocks for supramolecular chemistry. Dalton Trans:9141–9145
127. Schenk C, Henke F, Santiso-Quiñones G, Krossing I, Schnepf A (2008) $[Si(SiMe_3)_3]_6Ge_{18}M$ (M = Cu, Ag, Au): metalloid cluster compounds as unusual building blocks for a supramolecular chemistry. Dalton Trans:4436–4441
128. Kysliak O, Schrenk C, Schnepf A (2015) $\{Ge_9[Si(SiMe_3)_2(SiPh_3)]_3\}^-$: ligand modification in metalloid germanium cluster chemistry. Inorg Chem 54:7083–7088
129. Kysliak O, Kunz T, Schnepf A (2017) Metalloid $Ge_9R_3^-$ clusters with various silyl substituents: from shielded to open cluster cores. Eur J Inorg Chem 2017:805–810
130. Binder M, Schrenk C, Block T, Pöttgen R, Schnepf A (2017) [Hyp-Au-Sn_9(Hyp)$_3$-Au-Sn_9(Hyp)$_3$-Au-Hyp]$^-$: the longest intermetalloid chain compound of tin. Chem Commun 53:11314–11317
131. Kysliak O, Nguyen DD, Clayborne AZ, Schnepf A (2018) $[PtZn_2Ge_{18}(Hyp)_8]$ (Hyp = Si(SiMe$_3$)$_3$): a neutral polynuclear chain compound with $Ge_9(Hyp)_3$ units. Inorg Chem 57:12603–12609
132. Denning MS, Goicoechea JM (2008) $[Hg_3(Ge_9)_4]^{10-}$: a nanometric molecular rod precursor to polymeric mercury-linked cluster chains. Dalton Trans:5882–5885
133. Nienhaus A, Hauptmann R, Fässler TF (2002) $_\infty{}^1[HgGe_9]^{2-}$ – a polymer with zintl ions as building blocks covalently linked by heteroatoms. Angew Chem Int Ed 41:3213–3215
134. Bentlohner MM, Jantke L-A, Henneberger T, Fischer C, Mayer K, Klein W, Fässler TF (2016) On the nature of bridging metal atoms in intermetalloid clusters: synthesis and structure of the metal-atom-bridged zintl clusters $[Sn(Ge_9)_2]^{4-}$ and $[Zn(Ge_9)_2)]^{6-}$. Chem Eur J 22:13946–13952
135. Yong L, Boeddinghaus MB, Fässler TF (2010) $[Sn_9HgSn_9]^{6-}$: an intermetalloid zintl ion with two Sn_9 connected by heteroatom. Z Für Anorg Allg Chem 636:1293–1296
136. Mayer K, Jantke L-A, Schulz S, Fässler TF (2017) Retention of the Zn−Zn bond in $[Ge_9Zn{-}ZnGe_9]^{6-}$ and formation of $[(Ge_9Zn){-}(Ge_9){-}(ZnGe_9)]^{8-}$ and polymeric $[-(Ge_9Zn)^{2-}-]$. Angew Chem Int Ed 56:2350–2355
137. Zhang C, Morgan HWT, Wang Z-C, Liu C, Sun Z-M, McGrady JE (2019) Structural isomerism in the $[(Ni@Sn_9)In(Ni@Sn_9)]^{5-}$ Zintl ion. Dalton Trans 48:15888–15895
138. Spiekermann A, Hoffmann SD, Kraus F, Fässler TF (2007) $[Au_3Ge_{18}]^{5-}$ – a gold–germanium cluster with remarkable Au–Au interactions. Angew Chem Int Ed 46:1638–1640
139. Schmidbaur H (2000) The aurophilicity phenomenon: a decade of experimental findings, theoretical concepts and emerging applications. Gold Bull 33:3–10
140. Joseph S, Hamberger M, Mutzbauer F, Härtl O, Meier M, Korber N (2009) Chemistry with bare silicon clusters in solution: a transition-metal complex of a polysilicide anion. Angew Chem Int Ed 48:8770–8772
141. Sheong FK, Chen W-J, Zhang J-X, Li Y, Lin Z (2017) Structure and bonding of $[Pd_2Sn_{18}]^{4-}$: an interesting example of the mutual delocalisation phenomenon. Dalton Trans 46:2214–2219
142. Ugrinov A, Sevov SC (2003) Derivatization of deltahedral zintl ions by nucleophilic addition: $[Ph{-}Ge_9{-}SbPh_2]^{2-}$ and $[Ph_2Sb{-}Ge_9{-}Ge_9{-}SbPh_2]^{4-}$. J Am Chem Soc 125:14059–14064

143. Hull MW, Ugrinov A, Petrov I, Sevov SC (2007) Alkylation of deltahedral zintl clusters: synthesis of $[R-Ge_9-Ge_9-R]^{4-}$ (R = ^{t}Bu, ^{s}Bu, ^{n}Bu, ^{t}Am) and structure of $[^t Bu-Ge_9-Ge_9-^t Bu]^{4-}$. Inorg Chem 46:2704–2708
144. First Synthesis of Group-14 Polyanions by Extraction of a Binary Alloy with dmf and a Novel Conformation of the $(Ge_9-Ge_9)^{6-}$ Dimer: Crystal Structures of $[K_6(Ge_9-Ge_9)](dmf)_{12}$, $[Rb_6(Ge_9-Ge_9)](dmf)_{12}$ and $[K_{2.5}Cs_{3.5}(Ge_9-Ge_9)](dmf)_{12}$ (2006) Z Für Anorg Allg Chem 632:1752–1758
145. Xu L, Sevov SC (1999) Oxidative coupling of deltahedral $[Ge_9]^{4-}$ zintl ions. J Am Chem Soc 121:9245–9246
146. Wang J-Q, Wahl B, Fässler TF (2010) $[Ag(Sn_9–Sn_9)]^{5-}$: a homoleptic silver complex of a dimeric Sn_9 zintl anion. Angew Chem Int Ed 49:6592–6595
147. Hansen DF, Zhou B, Goicoechea JM (2012) Further studies into the reactivity and coordination chemistry of $[Ge_9]^{4-}$ zintl ions. The indium-containing anions $[In(Ge_9)_2]^{5-}$, $[(Ge_9)_2In(C_6H_5)]^{4-}$ and $[Ge_9\{In(C_6H_5)_3\}_2]^{4-}$. J Organomet Chem 721–722:53–61
148. Ugrinov A, Sevov SC (2005) Synthesis of a chain of nine-atom germanium clusters accompanied with dimerization of the sequestering agent. Comptes Rendus Chim 8:1878–1882
149. Downie C, Tang Z, Guloy AM (2000) An unprecedented $_\infty{}^1[Ge_9]^{2-}$ polymer: a link between molecular zintl clusters and solid-state phases. Angew Chem 112:346–348
150. Downie C, Mao J-G, Parmar H, Guloy AM (2004) The role of sequestering agents in the formation and structure of germanium anion cluster polymers. Inorg Chem 43:1992–1997
151. Perla LG, Sevov SC (2016) A stannyl-decorated zintl ion $[Ge_{18}Pd_3(Sn^iPr_3)_6]^{2-}$: twinned icosahedron with a common Pd_3-face or 18-vertex hypho-deltahedron with a Pd_3-triangle inside. J Am Chem Soc 138:9795–9798
152. Perla LG, Muñoz-Castro A, Sevov SC (2017) Eclipsed- and staggered-$[Ge_{18}Pd_3\{E^iPr_3\}_6]^{2-}$ (E = Si, Sn): positional isomerism in deltahedral zintl clusters. J Am Chem Soc 139:15176–15181
153. Zhang J-X, Sheong FK, Lin Z (2019) Remote bonding in clusters $[Pd_3Ge_{18}R_6]^{2-}$: modular bonding model for large clusters via principal interacting orbital analysis. Inorg Chem 58:3473–3478
154. Goicoechea JM, Sevov SC (2005) $[(Pd-Pd)@Ge_{18}]^{4-}$: a palladium dimer inside the largest single-cage deltahedron. J Am Chem Soc 127:7676–7677
155. Sun Z-M, Xiao H, Li J, Wang L-S (2007) $Pd_2@Sn_{18}{}^{4-}$: fusion of two endohedral stannaspherenes. J Am Chem Soc 129:9560–9561
156. Ugrinov A, Sevov SC (2002) $[Ge_9Ge_9Ge_9]^{6-}$: a linear trimer of 27 germanium atoms. J Am Chem Soc 124:10990–10991
157. Ugrinov A, Sevov SC (2003) $[Ge_9Ge_9Ge_9Ge_9]^{8-}$: a linear tetramer of nine-atom germanium clusters, a nanorod. Inorg Chem 42:5789–5791
158. Stegmaier S, Fässler TF (2011) A bronze matryoshka: the discrete intermetalloid cluster $[Sn@Cu_{12}@Sn_{20}]^{12-}$ in the ternary phases $A_{12}Cu_{12}Sn_{21}$ (A = Na, K). J Am Chem Soc 133:19758–19768
159. Sheong FK, Chen W-J, Kim H, Lin Z (2015) Peeling the onion: a revised model of the electron count for matryoshka clusters. Dalton Trans 44:7251–7257
160. Moses MJ, Fettinger JC, Eichhorn BW (2003) Interpenetrating As_{20} fullerene and Ni_{12} icosahedra in the onion-skin $[As@Ni_{12}@As_{20}]^{3-}$ ion. Science 300:778–780
161. Bashkurov R, Kratish Y, Fridman N, Bravo-Zhivotovskii D, Apeloig Y (2021) A high yield synthesis of an octastannacubane and a Bis(silyl) stannylene via reductive elimination of a silane. Angew Chem Int Ed 60:2898–2902
162. Wiberg N, Finger CMM, Polborn K (1993) Tetrakis(tri-tert-butylsilyl)-tetrahedro-tetrasilane $(^tBu_3Si)_4Si_4$: the first molecular silicon compound with a Si4 tetrahedron. Angew Chem Int Ed Engl 32:1054–1056
163. Wiberg N, Hochmuth W, Nöth H, Appel A, Schmidt-Amelunxen M (1996) Tetrakis(tri-tert-butylsilyl)-tetrahedro-tetragermane $(^tBu_3Si)_4Ge_4$ – the first molecular germanium compound with a Ge_4 tetrahedron. Angew Chem Int Ed Engl 35:1333–1334

164. Wiberg N, Lemer H-W, Wagner S, Nöth H, Seifert T (1999) Über das Octastannandiid $R^*_6Sn_8[Na(THF)_2]_2$ und zur möglichen Existenz des Octastannans $R^*_6Sn_8$ [1] / on an Octastannanediide $R^*_6Sn_8[Na(THF)_2]_2$ and the possible existence of an octastannane $R^*_6Sn_8$ [1]. Z Für Naturforschung B 54:877–880
165. Ichinohe M, Toyoshima M, Kinjo R, Sekiguchi A (2003) Tetrasilatetrahedranide: a silicon cage anion. J Am Chem Soc 125:13328–13329
166. Klapötke TM, Vasisht SK, Fischer G, Mayer P (2010) A reactive Si_4 cage: $K(Si^tBu_3)_3Si_4$. J Organomet Chem 695:667–672
167. Schnepf A, Köppe R (2003) $[Ge_8\{N(SiMe_3)_2\}6]$: a ligand-stabilized Ge cluster compound with formally zero-valent Ge atoms. Angew Chem Int Ed 42:911–913
168. Fischer G, Huch V, Mayer P, Vasisht SK, Veith M, Wiberg N (2005) $Si_8(Si^tBu_3)_6$: a hitherto unknown cluster structure in silicon chemistry. Angew Chem Int Ed 44:7884–7887
169. Eichler BE, Power PP (2001) Synthesis and characterization of $[Sn_8(2,6\text{-}Mes_2C_6H_3)_4]$ (Mes=2,4,6-$Me_3C_6H_2$): a main group metal cluster with a unique structure. Angew Chem 113:818–819
170. Schnepf A, Drost C (2005) Ge8R6: the ligands define the bonding situation within the cluster core. Dalton Trans:3277–3280
171. Schnepf A (2006) $\{Ge_{10}Si[Si(SiMe_3)_3]_4(SiMe_3)_2Me\}^-$: a $Ge_{10}Si$ framework reveals a structural transition onto elemental germanium. Chem Commun:192–194
172. Wu W, Gu J, Song J, Shaik S, Hiberty PC (2009) The inverted bond in [1.1.1]propellane is a charge-shift bond. Angew Chem Int Ed 48:1407–1410
173. Shaik S, Danovich D, Wu W, Hiberty PC (2009) Charge-shift bonding and its manifestations in chemistry. Nat Chem 1:443–449
174. Shaik S, Danovich D, Galbraith JM, Braïda B, Wu W, Hiberty PC (2019) Charge-shift bonding: a new and unique form of bonding. Angew Chem Int Ed 59:984–1001
175. Wiederkehr J, Wölper C, Schulz S (2016) Synthesis and solid state structure of a metalloid tin cluster $[Sn_{10}(trip_8)]$. Chem Commun 52:12282–12285
176. Sekiguchi A, Ishida Y, Kabe Y, Ichinohe M (2002) The cation cluster of heavier group 14 elements: a free germyl cation with trishomoaromaticity. J Am Chem Soc 124:8776–8777
177. Spiekermann A, Hoffmann SD, Fässler TF, Krossing I, Preiss U (2007) $[Au_3Ge_{45}]^{9-}$ – a binary anion containing a Ge_{45} cluster. Angew Chem Int Ed 46:5310–5313
178. Schenk C, Schnepf A (2008) $Ge_{14}[Ge(SiMe_3)_3]_5Li_3(THF)_6$: the largest metalloid cluster compound of germanium: on the way to fullerene -like compounds? Chem Commun:4643–4645
179. Lips F, Clérac R, Dehnen S (2011) $[Eu@Sn_6Bi_8]^{4-}$: a mini-fullerane-type zintl anion containing a lanthanide ion. Angew Chem Int Ed 50:960–964
180. Lips F, Clérac R, Dehnen S (2011) $[Pd_3Sn_8Bi_6]^{4-}$: a 14-vertex Sn/bi cluster embedding a Pd_3 triangle. J Am Chem Soc 133:14168–14171
181. Mitzinger S, Broeckaert L, Massa W, Weigend F, Dehnen S (2015) $[V@Ge_8As_4]^{3-}$ and $[Nb@Ge_8As_6]^{3-}$: encapsulation of electron-poor transition metal atoms. Chem Commun 51:3866–3869
182. Schrenk C, Schellenberg I, Pöttgen R, Schnepf A (2010) The formation of a metalloid $Sn_{10}[Si(SiMe_3)_3]_6$ cluster compound and its relation to the α↔β tin phase transition. Dalton Trans 39:1872–1876
183. Klinkhammer KW, Xiong Y, Yao S (2004) Molecular lead clusters – from unexpected discovery to rational synthesis. Angew Chem Int Ed 43:6202–6204
184. Schrenk C, Helmlinger J, Schnepf A (2012) $Sn_{10}[Si(SiMe_3)_3]_5^-$: an anionic metalloid tin cluster from an isolable Sn^I halide solution. Z Für Anorg Allg Chem 638:589–593
185. Schrenk C, Gerke B, Pöttgen R, Clayborne A, Schnepf A (2015) Reactions with a metalloid tin cluster $Sn_{10}[Si(SiMe_3)_3]_4^{2-}$: ligand elimination versus coordination chemistry. Chem Eur J 21:8222–8228
186. Schrenk C, Winter F, Pöttgen R, Schnepf A (2015) $Sn_{10}[Si(SiMe_3)_3]_4^{2-}$: a highly reactive metalloid tin cluster with an open ligand shell. Chem Eur J 21:2992–2997

187. Kiani FA, Hofmann M (2006) Cluster increments for macropolyhedral boranes. Dalton Trans:5515–5520
188. Sheong FK, Zhang J-X, Lin Z (2017) Localized bonding model for coordination and cluster compounds. Coord Chem Rev 345:42–53
189. Liu C, Popov IA, Li L-J, Li N, Boldyrev AI, Sun Z-M (2018) $[Co_2@Ge_{16}]^{4-}$: localized versus delocalized bonding in two isomeric intermetalloid clusters. Chem Eur J 24:699–705
190. Liu C, Jin X, Li L-J, Xu J, McGrady JE, Sun Z-M (2019) Synthesis and structure of a family of rhodium polystannide clusters $[Rh@Sn_{10}]^{3-}$, $[Rh@Sn_{12}]^{3-}$, $[Rh_2@Sn_{17}]^{6-}$ and the first triply-fused stannide, $[Rh_3@Sn_{24}]^{5-}$. Chem Sci 10:4394–4401
191. Shu C-C, Morgan HWT, Qiao L, McGrady JE, Sun Z-M (2020) A family of lead clusters with precious metal cores. Nat Commun 11:3477